AR TARGET SHEET

The following document was too large to scan as one unit, therefore, it has been broken down into sections.

EDMC#:	0056409
SECTION:	2 of 4
DOCUMENT #:	RPP-7884, REV 000
TITLE:	Field Investigation Report for WMA S-SX

Figure B.16. Trace Metals Calculated from Sediment Water Extracts and Actual Porewaters for 299-W23-19 Sediment

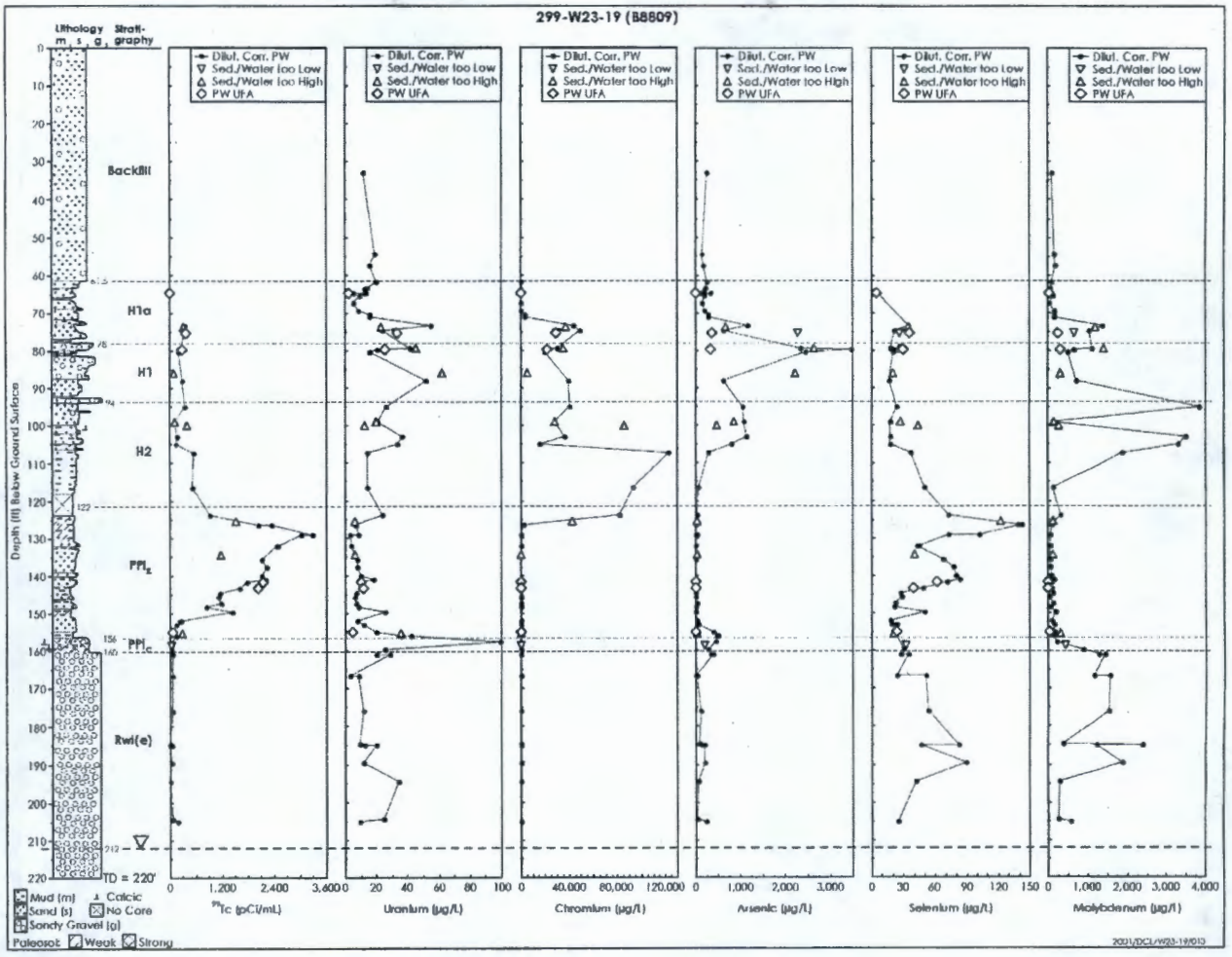

B.3.5 CHEMICAL INTERACTIONS

No specific experiments were completed on soils from this borehole to quantify geochemical reactions influencing contaminant migration. Dominant chemical reactions affecting radionuclides and tank fluid chemicals are inferred from the relative location of these constituents in the soil column, comparison of acid-leachable versus water-leachable concentrations for specific contaminants, and general knowledge of the tank fluid chemistry. Greater contaminant mobility is inferred from the occurrence of high concentration zones deeper in the vadose zone and smaller differences in concentrations leached by water versus acid.

Generally speaking, the data suggest that tank SX-115 fluid chemistry, other than providing increased amounts of certain constituents to the soil column, had little effect on the chemical behavior of contaminants in the sense that chemical reactions between tank fluid constituents and the soil column environment were largely controlled by soil-soil water reactions. Constituent anions (e.g., nitrate and technetium-99) have migrated the most rapidly and mark the leading edge of vertical tank fluid migration at this location. Chromium was slightly retarded relative to technetium-99 and nitrate, presumably because of oxidation reduction, allowing fixation on soil. Constituent cations have migrated varying distances depending on the strength of retardation mechanisms. Cesium-137 sorbed very strongly as soon as tank fluid entered the soil column. Sodium concentrations, being relatively high, successfully completed for sorption sites in vadose zone soils, were somewhat retarded. Calcium, magnesium, and indigenous strontium were displaced by sodium and pushed ahead of sodium during migration.

B.3.6 GROUNDWATER MEASUREMENTS

Groundwater contaminants in this borehole are characterized by the largest technetium-99 concentrations currently seen in the monitoring network. Recent analyses are listed in Appendix C, Table C.17. Also, nitrate and chromium concentrations are high.
The technetium-99/nitrate ratios (0.11 pCi/μg) are similar to those postulated for tank fluids. This observation, coupled with the location of borehole 299-W23-19 strongly indicates the tank SX-115 leak as the source of this groundwater contamination.

B.4.0 TANK SX-108 SLANT BOREHOLE

This section summarizes data reported in *Geologic and Geochemical Data Collected from Vadose Zone Sediments from Slant Borehole [SX-108] in the S/SX Waste Management Area and Preliminary Interpretations* (Serne et al. 2001d) except for the groundwater sample data, which are reported in the WMA S-SX RCRA groundwater monitoring report (Johnson and Chou 2000). The SX-108 slant borehole was completed to further characterize the nature and extent of vadose zone contaminants supplied by a tank SX-108 leak. This borehole was drilled specifically to sample soils as close the tank leak site as possible and to investigate tank fluid migration underneath the tank, an area which has received no evaluation other than gross gamma measurements along laterals in the 1970s. Soils analyses from the slant borehole combined with analyses from borehole 41-09-39 provides a means of comparing tank fluid migration in two different locations with somewhat different conditions occurring. In addition to being closer to the tank leak, the slant borehole goes through the 'umbrella' region under the tank where little if any natural infiltration is anticipated, compared to the region between the tanks. Also, the addition of second borehole data provides a better idea of the three-dimensional aspect of the migrating leak distribution.

The most significant data provided by this characterization effort were soil measurements of radionuclides and chemicals attributed to this leak. Elevated concentrations of several constituents were measured in soils throughout the length of the slant borehole from 17 and 41 m (55 and 135 ft) bgs. This depth interval includes subunits H1 and H2 of the Hanford formation and part of subunit PPlz) of the Plio-Pleistocene unit. The primary radionuclides present in this zone are cesium-137 and technetium-99. Maximum cesium-137 concentrations are present between 17 and 27 m (55 and 88 ft) bgs in subunit H1 and the top part of subunit H2. Maximum technetium-99 concentrations are present in the bottom part subunit H2 and the top part of subunit PPlz between 26 and 42 m (85 and 138 ft) bgs. The primary chemical characteristics attributed to tank fluid-soil interaction within this zone are elevated: pH, sodium, chromium, and nitrate. The depth of maximum technetium-99 concentration coincides with high nitrate concentrations and marks the leading edge of vertical tank fluid migration at this location. Also, this is the only borehole in which iodine-129 has been detected. Iodine-129 occurs between 24 and 40 m (80 and 130 ft) bgs at about 18,000 to 43,000 pCi/L.

It is of note that most constituents show more than one peak concentration with depth within their respective highest concentration ranges. Several mechanisms may have played a role in creating these patterns of contaminant concentration, including stratigraphic heterogeneities that encourage layering, thermal cycling effects that temporarily created circulating fluids in the soil column, and/or multiple leaks. None of these various options are clearly preferred.

Moisture content measurements are somewhat dry and in situ temperatures are elevated relative to undisturbed Hanford formation soils. Both conditions plus the presence of the tank suggest that relatively little drainage is occurring in this area. The lack of tank fluid contaminants below the Plio-Pleistocene unit and the low concentrations of technetium-99 and nitrate in groundwater samples from nearby borehole 41-09-39 indicate that contaminants from this area have not reached the unconfined aquifer at this location.

B.4.1 GEOLOGY

The SX-108 slant borehole intersected three primary stratigraphic units: (1) backfill, which was not sampled, (2) the Hanford formation, and (3) the top of the Plio-Pleistocene unit. The backfill appears to extend to about 16.2 m (53 ft) bgs where it contacts the Hanford formation. The next 2.6 m (8 ft) bgs is interpreted to correlate with the upper fine sand and mud sequence of the Hanford formation subunit H1a. Below this lies the 4.2 m (14 ft) thick middle coarse sand and gravel sequence of subunit H1. The contact between the Hanford formation and the Plio-Pleistocene unit is interpreted to occur at 38.5 m (126 ft) bgs. The frequency and manner in which the samples were taken limits the completeness of the geologic description that can be made.

B.4.1.1 Backfill

The backfill was not sampled. The contact depth of the backfill with the Hanford formation at 16.2 m (53.1 ft) bgs is supported by tank farm engineering drawings (H-2-37985 sheet 2 of 2), an increase in blow counts required to advance the casing, and an increase in apparent moisture content as indicated in the neutron moisture log.

B.4.1.2 Hanford formation

All three Hanford formation subunits (H1a, H1, and H2) were present at the SX-108 slant borehole and sampled.

- **Subunit H1a** – This subunit, the upper fine sand and mud sequence, is believed to be approximately 2.6 m (8.4 ft) thick extending from the base of the backfill to a vertical depth of approximately 18.7 m (61.5 ft) bgs. The location of this contact is supported by a slight increase in the blow counts and a sharp decrease in the neutron-neutron moisture log response. Layering was evident in the single sample retrieved from subunit H1a. From 16.6 to 16.9 m (54.5 to 55.3 ft) bgs the sample exhibited a layer of dry gray muddy (silty) sand containing some possible rock flour, overlying a moist muddy, medium sand.

- **Subunit H1** – This subunit, the middle coarse sand and gravel sequence, is estimated to be approximately 4.2 m (13.8 ft) thick extending to a vertical depth of approximately 22.9 m (75.3 ft) bgs. The depth to this contact is supported by a sharp decrease in blow counts and an increase in the neutron-neutron moisture log response. The moisture log response is further substantiated by an increase in gravimetric moisture content below the contact. Two samples were recovered from subunit H1. One sample was lost. The recovered samples show some coarse layering. Sample S0070-03 was described as a dry grayish-brown medium to fine sand with some mud and gravel fragments (up to medium pebble). Sample S0070-04 contained some fine gray powder (rock flour) and the remainder of the sample was a salt and pepper textured medium to fine sand; no gravel was noted.

- **Subunit H2** – This subunit, the lower fine sand and mud sequence, is estimated to be about 15.6 m (51.1 ft) thick, extending to a vertical depth of approximately 38.5 m (126.4 ft) bgs. This depth is supported by a slight increase in the blow counts and a sharp increase in the neutron-neutron moisture log response. There is a parallel increase in

gravimetric moisture content of the samples below the contact. Ten split-spoon samples were collected through this horizon between 22.9 and 38.5 m (75.3 to 126.4 ft) bgs. Subunit H2 is composed of stratified sand, muddy sand and mud. The laminar nature of this unit is one of its outstanding characteristics. Thin laminations of mud and sand commonly separate the sand strata.

B.4.1.3 Plio-Pleistocene Unit

The Plio-Pleistocene unit was penetrated but its lower contact was not encountered in the slant borehole. Three split-spoon samples were collected from this horizon. The unit is composed of interstratified mud and muddy, very fine sand with occasional very fine sand strata (i.e., PPlz subunit). The sandier strata were described as friable and frequently exhibiting finely laminated muds.

B.4.2 GEOPHYSICAL AND PHYSICAL PROPERTY MEASUREMENTS

Several geophysical logging techniques were used during and after installation of the SX-108 slant borehole. These techniques included the following:

- Gyroscopic borehole surveys
- Casing wall temperature logging using an infrared sensor
- Neutron-neutron moisture logging
- High-purity germanium spectral gamma logging
- High-rate gamma logging.

A composite of the temperature, moisture, spectral gamma, and high-rate gamma logs (Gardner and Reynolds 2000) is shown in Figure B.17.

The neutron-neutron moisture log recorded the average volumetric moisture content within a 20 to 30 cm (8 to 12 in.) radius. A slightly increased moisture content was noted between vertical depths of 15 and 18 m (50 and 60 ft) bgs, and second significant moisture content change noted at 33 m (107 ft) bgs. These moisture content changes correlate well with changes in the geologic materials.

Several spectral-gamma and high-rate gamma logging events were conducted using different logging systems, shielding configurations, and counting times. Cesium-137 was the only gamma-emitting contaminant detected. Above 16 m (52 ft) bgs, cesium-137 concentrations were generally less that 20 pCi/g, and were attributed (most likely) to internal casing contamination (Gardner and Reynolds 2000). This internal casing contamination resulted from the loss of sample S0070-02 down the borehole. Between depths of 16 and 27 m (53 and 90 ft) bgs very high concentrations of cesium-137 (on the order of 10^8 pCi/g) were measured. Internal contamination and/or dragdown most likely dominate contamination detected below 27 m (90 ft) bgs (Gardner and Reynolds 2000).

Figure B.17. Geophysics Logging Graph for SX-108 Slant Borehole

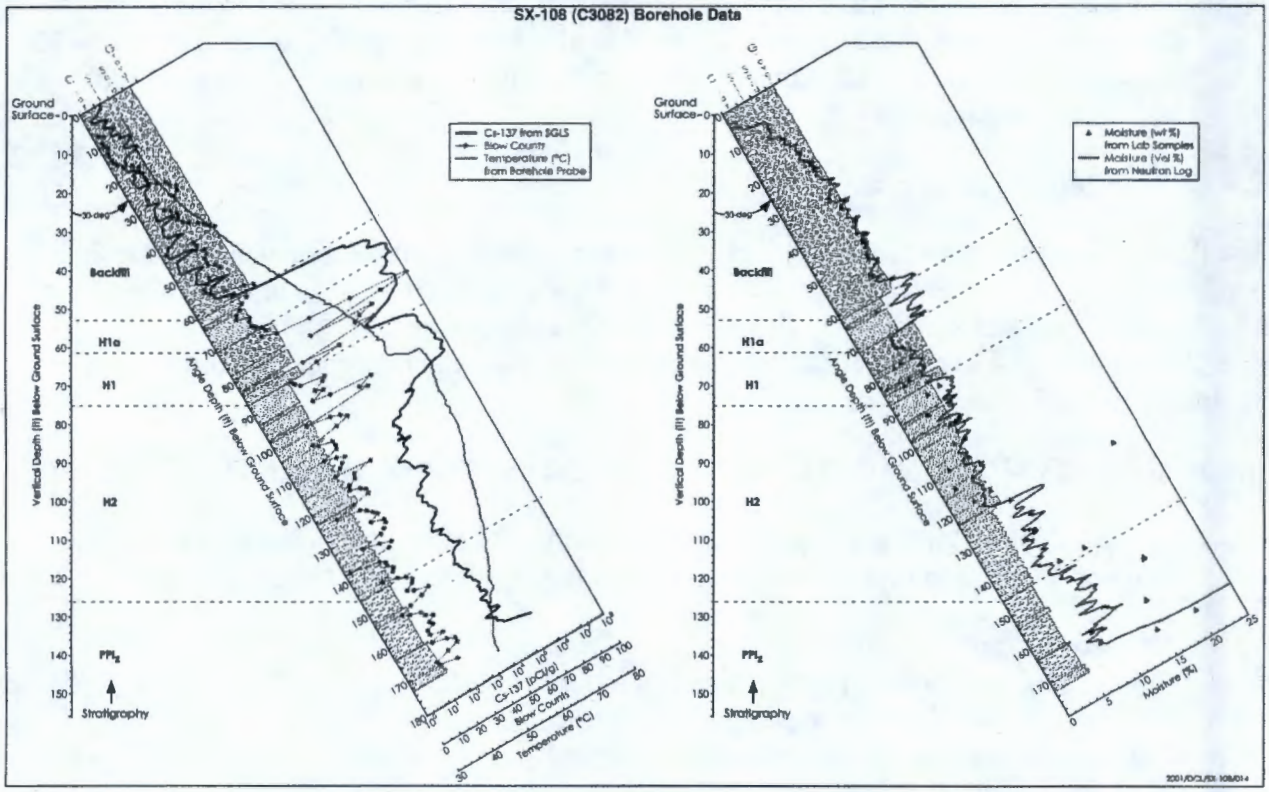

Laboratory measurements of soil moisture content (Table B.12 and Figure B.18) show similar trends in relative concentrations as the neutron-neutron moisture measurements. The moisture profile shows one high peak in subunit H2 at a laminated sand facies with a silt tringer at 32 m (105 ft) bgs. With the exception of one sample, the Plio-Pleistocene unit soils show generally the highest moisture content in the soil column.

B.4.3 SOIL WATER CHEMISTRY MEASUREMENTS

In addition to soil physical property measurements (Section B.4.2), an extensive water chemistry analysis has been completed for samples collected at the SX-108 slant borehole between 17 and 44 m (55 and 145 ft) bgs. The primary means of measuring porewater composition was to add deionized water to soil samples to generate enough water for performing analyses. By back-calculating for the dilution introduced by the added water, 'true' concentrations were derived. For a few samples porewater was directly separated from the same soil sample or one nearby and analyzed directly. By comparing the dilution-corrected water extract data with the porewater data in these few samples, an indication of the closeness of the water extract chemistry to original water chemistry was determined. In general, comparisons were not exact but concentration values were generally within a factor of two or better, agreement improved with increasing constituent concentration, and both sets of data showed similar concentrations versus soil depth correlations. Thus, the water extract method is an effective tool for evaluating tank fluid interactions with vadose zone soil.

Water extract pH and electrical conductivity measurements with depth are listed in Table B.13 and graphed in Figure B.19. Elevated pH values (greater than 9.) are measured between 17 and 25 m (55 and 85 ft) bgs primarily in subunits H1a and H1 and the top part of subunit H2. Because pH values are expected to decrease as increasing interaction with soil and soil water occurs, the location of maximum pH values suggests the approximate initial depth of tank fluid interaction with the vadose zone at this location. As with most chemical indicators at this borehole in the zones of elevated value, an apparent bimodal distribution of pH values is created by the low pH value (8) measured in the middle of the elevated zone at 25 m (80.6 ft) bgs. Increases in electrical conductivity values compared to undisturbed soil water values are also an indicator of tank fluid occurrence in soil. Maximum values of approximately 100,000 to 133,000 μS/cm are measured between 26 and 30 m (85 and 97 ft) bgs. A secondary range of elevated electrical conductivity values occurs between 35 and 40 m (114 and 130 ft) bgs, primarily at the bottom of subunit H2 and the top of the Plio-Pleistocene subunit PPlz. Maximum electrical conductivity values are an indicator of location for mobile tank fluid constituents and maximum vertical penetration of tank fluids.

Table B.12. Moisture Content (wt%)
SX-108 Slant Borehole Sediments

Lithologic Unit	Sample ID	Vertical Depth (ft bgs)	Moisture (%)
H1A	01B	54.5-54.9	ND
H1A	01A	54.9-55.3	4.33
H1	02B	63.0-63.5	NS
H1	02A	63.5-63.7	NS
H1	03B	67.3-67.7	3.76
H1	03A	67.7-68.1	2.76
H1	04B	71.5-71.9	3.55
H1	04A	71.9-72.4	2.77
H2	05B	75.7-76.2	6.48
H2	05A	76.2-76.6	4.69
H2	06B	79.9-80.4	3.50
H2	06A	80.4-80.8	3.68
H2	07B	84.1-84.6	6.60
H2	07A	84.6-85.0	6.18
H2	08B	88.3-88.8	4.52
H2	08A	88.8-89.2	6.02
H2	09B	92.5-92.9	5.32
H2	09A	92.9-93.3	2.35
H2	10B	96.6-97.1	4.62
H2	10A	97.1-97.5	1.91
H2	11B	101.0-101.5	5.50
H2	11A	101.5-101.9	3.15
H2	12B	104.9-105.4	7.02
H2	12A	105.4-105.8	21.35
H2	13B	113.1-113.6	7.95
H2	13A	113.6-114.0	7.64
PPlz	14B	121.3-121.7	8.51
PPlz	14A	121.7-122.2	11.95
PPlz	15B	129.4-129.9	17.50
PPlz	15A	129.9-130.3	17.42
PPlz	16B	137.5-138-0	15.13
PPlz	16A	138.0-138.4	7.50
PPlz	17B	144.0-144.4	14.49
PPlz	17A	144.4-144.9	19.70

ND = not determined.
NS = no sample.

Figure B.18. Moisture Content (wt%) in Vadose Zone Sediment Profile at SX-108 Slant Borehole

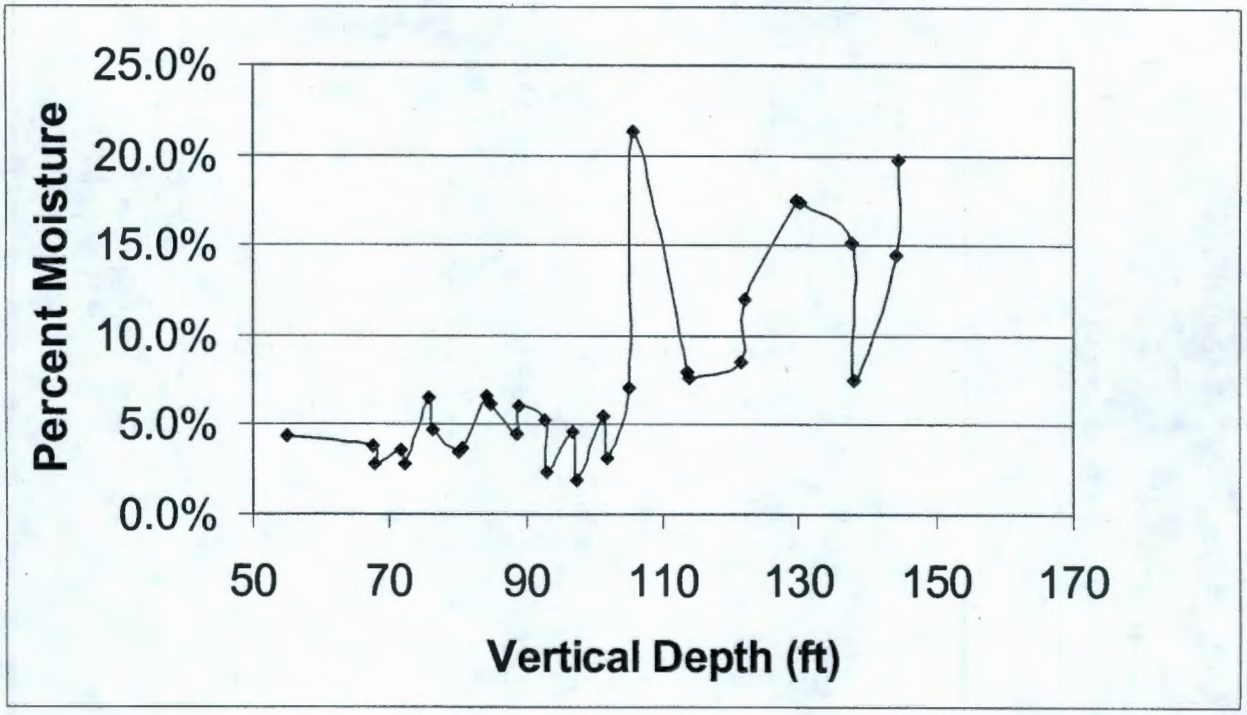

Table B.13. Water Extract pH and Electrical Conductivity Values at SX-108 Slant Borehole

Sample ID	Vertical Depth (ft bgs)	Dilution Factor	1:1 pH	1:1 EC (mS/cm)	Pore EC (mS/cm)
01A	55.1	23.13	9.16	0.404	9.34
02A	63.02	NS	NS	NS	NS
03AB	67.9	36.88	9.58	0.701	25.85
04A	72.2	36.15	9.54	0.576	9.57
05A	76.4	21.36	9.78	0.877	14.21
06A	80.6	27.18	8.00	16.71	454.2
07A	84.8	16.20	9.55	54.62	1166.5
08A	89.0	16.61	7.83	49.01	1771.6
09A	93.1	42.56	7.88	31.76	1009.3
10A	97.3	52.34	8.23	25.56	1337.7
11A	101.7	31.78	8.38	13.93	592.8
12A	105.6	4.69	8.02	2.36	11.04
13A	113.8	13.38	7.99	29.78	398.4
14A	122.0	8.69	7.82	30.24	262.8
15A	130.1	5.74	7.45	40.01	229.7
16A	138.2	13.31	7.24	5.80	77.16
17A	144.6	5.08	7.22	3.47	17.63

EC = electrical conductivity.
NS = no sample was available.

Figure B.19. SX-108 Slant Borehole pH and Electrical Conductivity Profiles with Depth

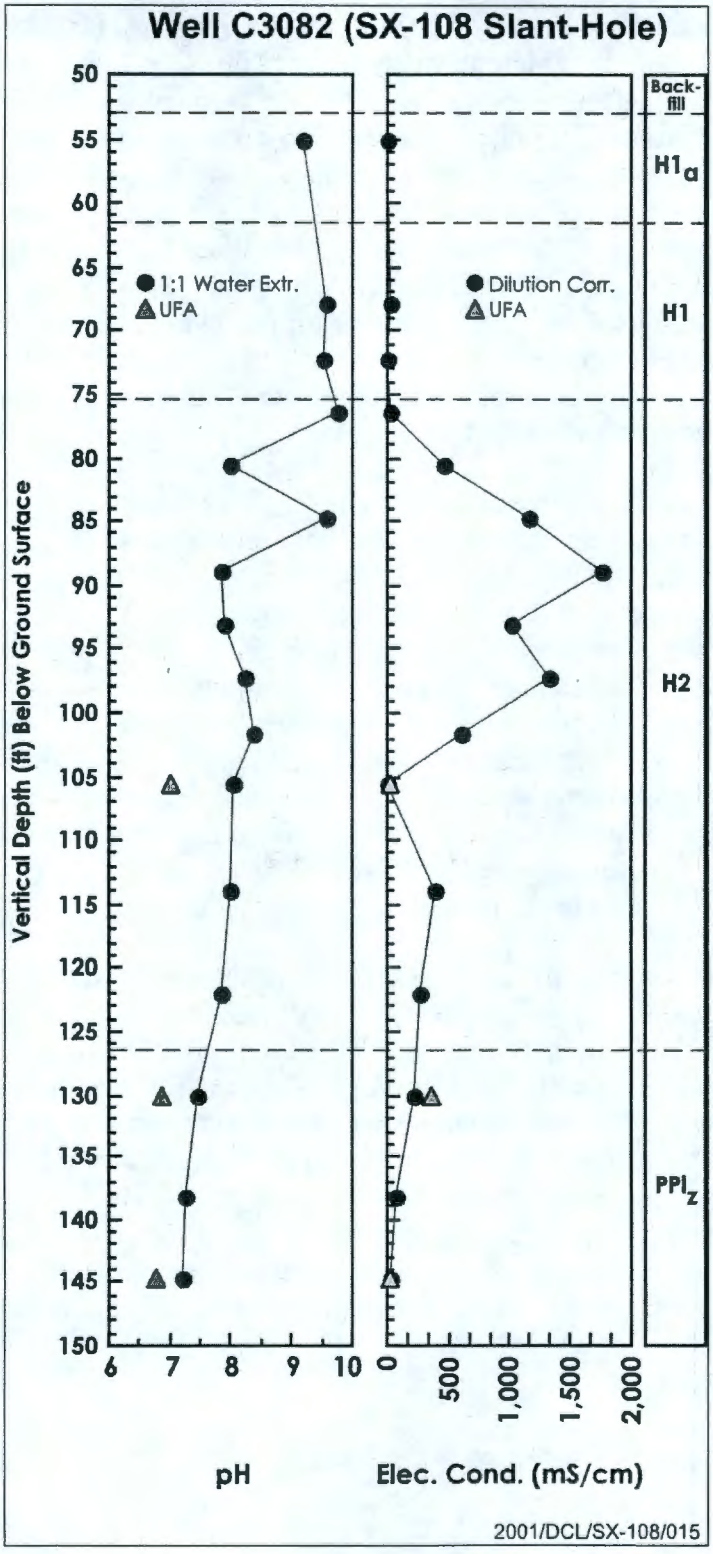

Water extract anion concentrations as a function of depth are listed in Table B.14. Nitrate, chloride, and sulfate concentrations with depth are shown in Figure B.20. The primary indicator of tank fluid occurrence is elevated nitrate concentrations, which are measured through the borehole with maximum values between 180,000 and 995,000 mg/L between 25 and 39 m (81 and 130 ft) bgs. An apparent bimodal distribution of nitrate values is created by the low nitrate value (7,191 mg/L) measured in the middle of the elevated zone at 32 m (105.6 ft) bgs. It is probable that the bottom of the nitrate range was not reached in this sampling effort. Elevated levels of chloride (between 26 and 44 m [85 and 145 ft]) and sulfate (between 20 and 39 m [65 and 127 ft]) are also observed. Chloride maximum concentrations (between 27 and 30 m [89 and 130 ft] bgs) and sulfate maximum concentrations between 25 and 40 m (81 and 130 ft) bgs track closely with nitrate in subunit H2 and subunit PPlz. The minimum chlorine and sulfate concentrations (109 and 147 mg/L, respectively) at 32 m (105.6 ft) bgs establishes an apparent bimodal distribution for both anions. Overall, the anion concentrations appear to be diminishing rapidly in the deepest sample and indicate the leading edge of the tank fluid migration near the bottom of the borehole (44 m [145 ft]).

Water extract cation concentrations as a function of depth are listed in Table B.15 and graphed in Figure B.21. Among the cations, elevated sodium concentrations are the primary tank fluid indicator and occur throughout the SX-108 slant borehole. Maximum values begin abruptly at 25 m (81 ft) bgs, remain elevated above 65,000 mg/L through 40 m (130 ft) bgs except at 32 m (105.6 ft) bgs where sodium concentration drops to 691 mg/L. The potassium concentration distribution with depth mimics sodium. Calcium, magnesium, barium, and natural strontium show depleted concentrations above the high sodium depth range at 17 to about 27 m (55 to 90 ft) bgs and elevated concentrations between 27 and 44 m (90 and 145 ft) bgs, a depth range slightly ahead of the high sodium range. The relative positioning of sodium and perhaps potassium concentration ranges versus that of the other cations supports the hypothesis that sodium and potassium preferentially replace these cations in sorption sites as they migrate vertically and push them ahead to the leading edge of the plume.

The last group of constituents analyzed included radionuclides and trace metals. Of these, cesium-137, technetium-99, and chromium are clearly present in concentrations above background and are attributed to have originated in the tank fluid. Gamma log concentrations of cesium-137 are listed in Table B.16 and distribution is shown in Figure B.22.
Above background cesium-137 concentrations are measured throughout the borehole.
The primary contamination zone is in subunit H1 and the upper half of subunit H2 between 21 and 27 m (68 and 90 ft) bgs. In this zone two peaks occur at 21 and 24 to 26 m (68 and 80 to 85 ft) bgs at concentration levels of 2×10^7 and 9×10^7 pCi/g. Overall, the vast majority of cesium-137 mass resides in the upper half of subunit H2 between 24 and 26 m (80 and 85 ft) bgs. Just below these peaks, cesium-137 concentrations drop by orders of magnitude (less than 1000 pCi/g at 28 m [93 ft] bgs and below).

Table B.14. Anion Content of Water Extracts of SX-108 Slant Borehole Sediment

Sample ID	Depth (ft bgs)	Dilution Factor	Water:Soil Ratio	1:1 Extracts (mg/L)							Dilution Corrected Porewater (mg/L)						
				Nitrate	Fluoride	Nitrite	Chloride	Sulfate	Phosphate	Alk*	Nitrate	Nitrite	Chloride	Sulfate	Phosphate	Fluoride	Alk*
1A	55.1	23.13	1.00	6.95	1.94	<0.1	1.76	20.0	<0.5	211	161	<2.31	40.7	462	<11.6	44.7	4884
1A-Dup	55.1	23.13	1.00	6.07	1.71	<0.1	1.27	17.5	<0.5	519	140	<2.31	29.4	405	<11.6	39.6	12007
3AB	67.9	36.88	1.02	29.1	3.69	0.36	3.38	21.7	0.87	382	1072	13.1	125	801	0.88	136	14105
4A	72.2	36.15	1.00	23.5	2.27	0.31	1.51	11.5	0.68	387	851	11.2	54.7	415	0.68	81.9	13977
5A	76.4	21.36	1.00	92.9	3.24	0.34	3.92	27.3	1.06	407	1984	7.30	83.8	584	1.06	69.3	8701
6A	80.6	27.18	1.00	11743	ND	ND	<10	70.9	<5	587	319225	ND	<272	1926	<136	ND	15945
7A	84.8	16.20	1.00	46645	<10	ND	26.0	607	<50	1702	755649	ND	421	9833	<810	<162	27577
8A	89.0	16.61	1.00	39713	<10	87.5	83.3	566	<50	886	659796	1453	1383	9412	<831	<166	14725
9A	93.1	42.56	1.00	22852	<10	57.1	123	566	<50	504	972499	2429	5213	24092	<2128	<426	21439
10A	97.3	52.34	1.00	18994	<10	59.0	128	276	<50	484	994113	3088	6713	14465	<2617	<523	25335
11A	101.7	31.78	1.00	9524	<1	<10	130	46.8	<50	130	302677	318	4121	1486	<1589	<31.8	4130
12A	105.6	4.69	1.00	1535	<1	<1	23.3	31.4	<5	100	7191	<46.9	109	147	<23.4	<4.69	467
13A	113.8	13.38	1.02	22223	<10	72.5	213	293	<50	704	297334	970	2846	3923	<669	<134	9418
14A	122.0	8.69	1.04	21496	<10	46.3	187	339	<50	389	186815	402	1624	2945	<435	<86.9	3381
14A-Dup	122.0	8.38	1.00	24084	<10	31.9	212	387	<50	436	201786	267	1773	3246	<419	<83.8	3650
15A	130.1	5.74	1.00	34574	<10	34.4	331	507	<50	541	198485	198	1903	2908	<287	<57.4	3104
16A	138.2	13.31	1.00	4193	<1	<10	56.2	11.4	<5	219	55822	<133	749	151	<66.6	<13.3	2914
17A	144.6	5.08	1.00	2395	<1	<1	34.7	11.6	<5	123	12155	<5.08	176	59.1	<25.4	<5.08	622

*Alk = alkalinity as mg/L of $CaCO_3$.
ND = not determined.

Figure B.20. Anions Calculated and Actual Porewaters for SX-108 Slant Borehole Sediments

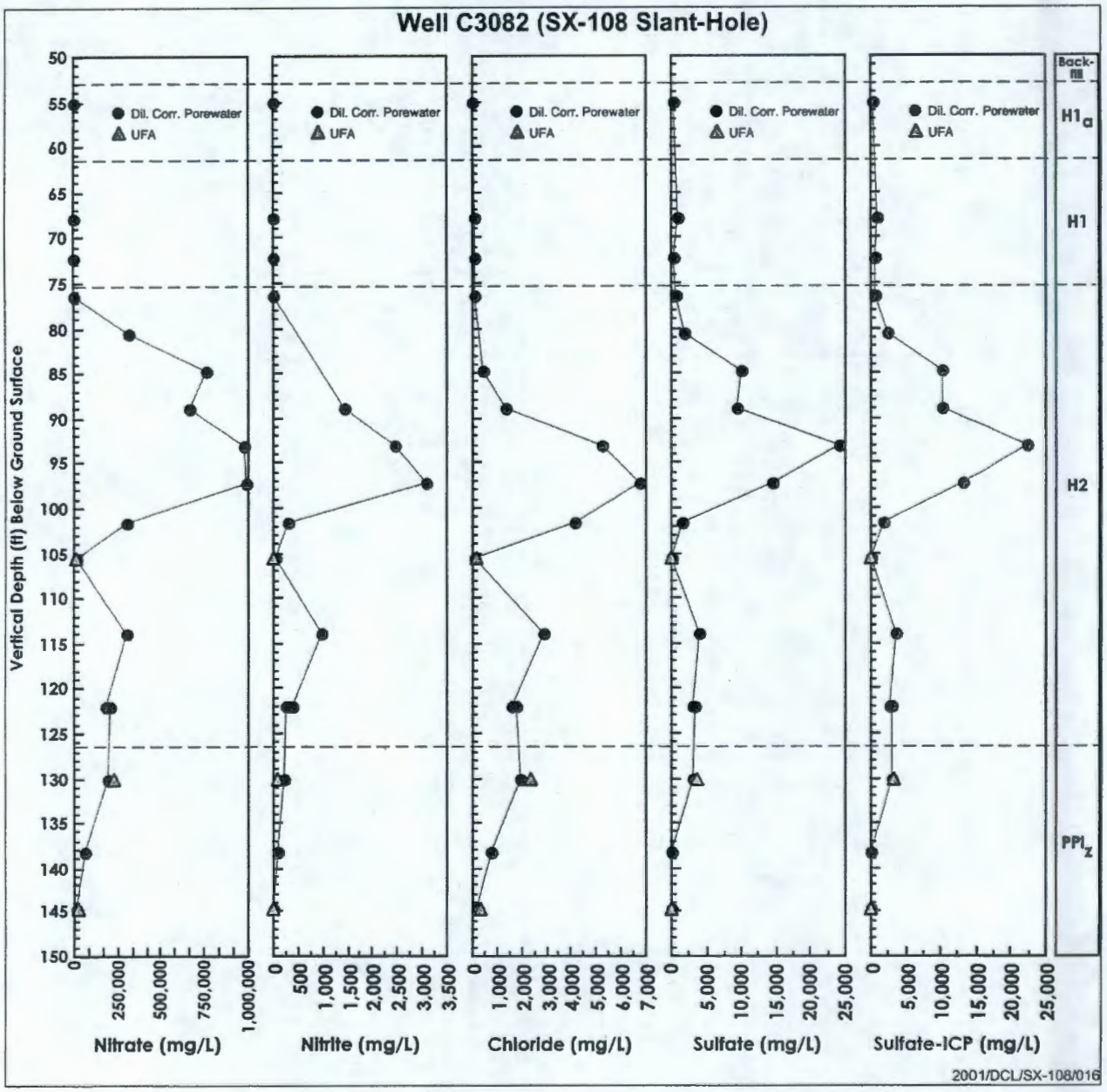

Table B.15. Calculated Porewater Cation Composition from Water Extracts of Vadose Zone Sediments from SX-108 Slant Borehole

Sample ID	Depth (ft bgs)	Dilution Factor	Water:Soil Ratio	Aluminum (µg/L)	Barium (µg/L)	Calcium (mg/L)	Iron (µg/L)	Potassium (mg/L)	Magnesium (mg/L)	Sodium (mg/L)	Silicon (mg/L)	Strontium (µg/L)	Sulfate (mg/L)	Manganese (µg/L)
1A	55.1	23.13	1.00	16351	(375)	28.23	16197	(77)	(5.7)	2378	420	(259)	451	(585)
1A-Dup	55.1	23.13	1.00	15702	(409)	25.51	14623	(82)	(5.3)	2344	398	<23130	427	(526)
3A	67.9	36.88	1.02	66585	1073	(34.97)	67342	(131)	27.18	6829	734	(265)	855	(1349)
4A	72.2	36.15	1.00	50399	(819)	(32.95)	56108	(86)	(16.9)	7195	865	<36150	526	(882)
5A	76.4	21.36	1.00	26641	(468)	(17.97)	29374	(43)	(4.8)	5716	367	<21360	657	(375)
6A	80.6	27.18	1.00	10769	(223)	1647.9	9997	703	101	153069	(193)	(8131)	2329	<1359
7A	84.8	16.20	1.00	8598	2809	39.59	8481	1339	(3.3)	345472	170.3	(2794)	10402	<810
8A	89.0	16.61	1.00	(3405)	(207)	1966	(3397)	2961	118	305019	(99)	31612	10320	<831
9A	93.1	42.56	1.00	(4924)	(527)	4303	(5271)	4388	151	370034	(225)	45684	22196	<2128
10A	97.3	52.34	1.00	(11869)	1695	1821.3	(12356)	3604	128	391103	(295)	(36890)	13276	<2617
11A	101.7	31.78	1.00	<7945	29778	37905	<7945	1358	3143	65257	(285)	421747	1902	1813
12A	105.6	4.69	1.00	(929)	1739	1309	(929)	87	213	691	66	7485	113	(91)
13A	113.8	13.38	1.02	(2006)	548	1583	(2124)	1001	137	110749	(102)	23332	3600	<669
14A	122.0	8.69	1.04	(1297)	653	1678	(1297)	566	163	68587	(74)	27027	2836	<435
14A-Dup	122.0	8.38	1.00	(1146)	587	1855	(1125)	611	175	73859	(71)	29976	3042	<419
15A	130.1	5.74	1.00	(370)	507	2555	(357)	555	270	70723	82	37277	2891	<287
16A	138.2	13.31	1.00	(577)	18286	10030	(577)	348	2259	4404	164	64992	147	2287
17A	144.6	5.08	1.00	(412)	3519	2169	(412)	113	593	649	60	11816	59	541

Notes: In Sample ID column, Dup represents a duplicate water extract on a separate aliquot of sediment. Note that some analytes are reported as µg/L and others as mg/L. Depth represents the vertical depth in feet.; the S values have been converted to sulfate to allow comparison to the anion data in Table 4.4.

Figure B.21. Cations Calculated and Actual Porewaters for SX-108 Slant Borehole Sediments

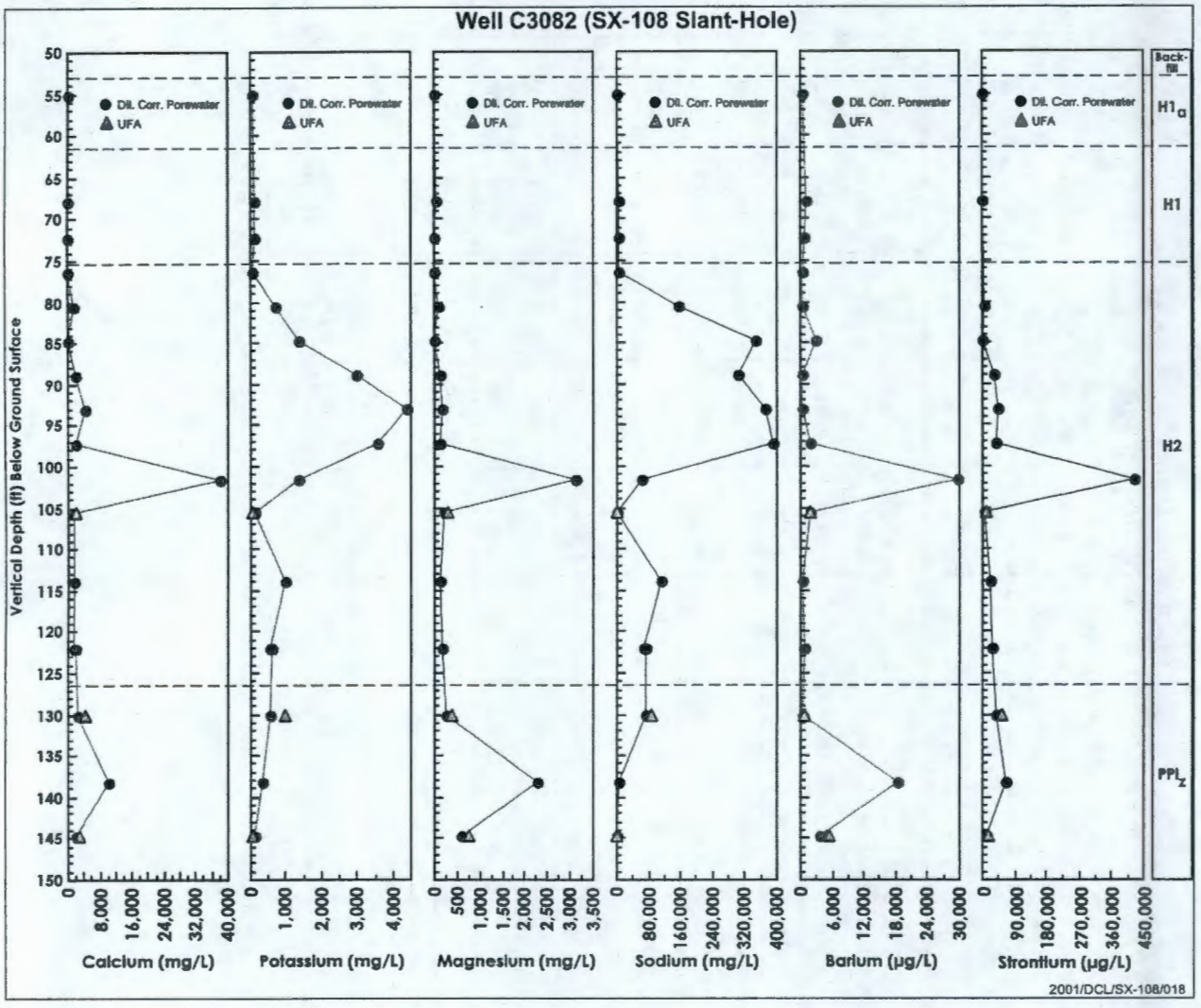

Table B.16. Gamma Energy Analysis of Vadose Zone Sediments at SX-108 Slant Borehole

Sample ID	Depth (ft bgs)	Cesium-137	± uncertainty	Potassium-40	± uncertainty
		pCi/g		pCi/g	
Hanford Subunit H1a (Sand)					
1A	55.1	3.06E+06	8.55E+04	<3.88E+03	--
Hanford Subunit H1 (Coarse Sand/Gravel)					
3BA	67.9	1.94E+07	5.37E+05	<1.45E+04	--
4B	71.5	8.16E+06	2.27E+05	<7.66E+03	--
4A	72.2	1.38E+06	3.94E+04	<7.21E+03	--
Hanford Subunit H2 (Fine Laminated Sand)					
5B	75.7	3.78E+06	1.05E+05	<6.40E+03	--
5A	76.4	6.52E+06	1.81E+05	<2.59E+04	--
6B	79.9	3.63E+07	1.64E+06	<4.17E+04	--
6A	80.6	5.31E+07	2.41E+06	<6.29E+04	--
7B	84.1	8.06E+06	2.26E+05	<4.16E+04	--
7A	84.8	2.14E+07	5.97E+05	<5.20E+04	--
7A1	84.6	9.57E+07	4.34E+06	--	--
8B	88.3	5.03E+06	1.41E+05	<9.86E+03	--
8A	89.0	5.55E+05	1.69E+04	<1.22E+03	--
9B	92.5	1.29E+04	1.91E+02	1.23E+01	3.19E+00
9A	93.1	1.71E+02	3.28E+00	2.49E+01	4.40E+00
10B	96.6	6.31E+02	1.00E+01	1.55E+01	1.45E+00
10A	97.3	4.51E+02	7.23E+00	1.82E+01	1.52E+00
11B	101	1.19E+04	1.86E+02	<2.46E+01	--
11A	101.7	9.12E+02	1.46E+01	2.73E+01	3.55E+00
12B	104.9	7.81E+02	1.23E+01	2.20E+01	2.82E+00
12A	105.6	3.37E+02	5.50E+00	2.66E+01	3.58E+00
13B	113.1	5.82E+03	8.95E+01	2.01E+01	3.08E+00
13A	113.8	5.21E+02	8.12E+00	1.64E+01	1.83E+00
14B	121.3	1.16E+03	1.78E+01	1.98E+01	3.37E+00
14A	122.0	8.37E+02	2.40E+01	3.01E+01	2.70E+00
Plio-Pleistocene Subunit (Fine-Grained Mud) [PPlz]					
15B	129.4	5.31E+02	8.65E+00	2.53E+01	5.50E+00
15A	130.1	5.92E+02	9.78E+00	2.47E+01	1.66E+00
16B	137.5	4.62E+03	7.13E+01	2.57E+01	4.11E+00
16A	138.2	9.79E+01	2.09E+00	2.52E+01	1.94E+00
17B	144	7.43E+02	1.17E+01	2.05E+01	5.16E+00
17A	144.6	1.75E+02	3.08E+00	2.58E+01	3.25E+00

Figure B.22. Cesium-137 in Vadose Sediments at the SX-108 Slant Borehole

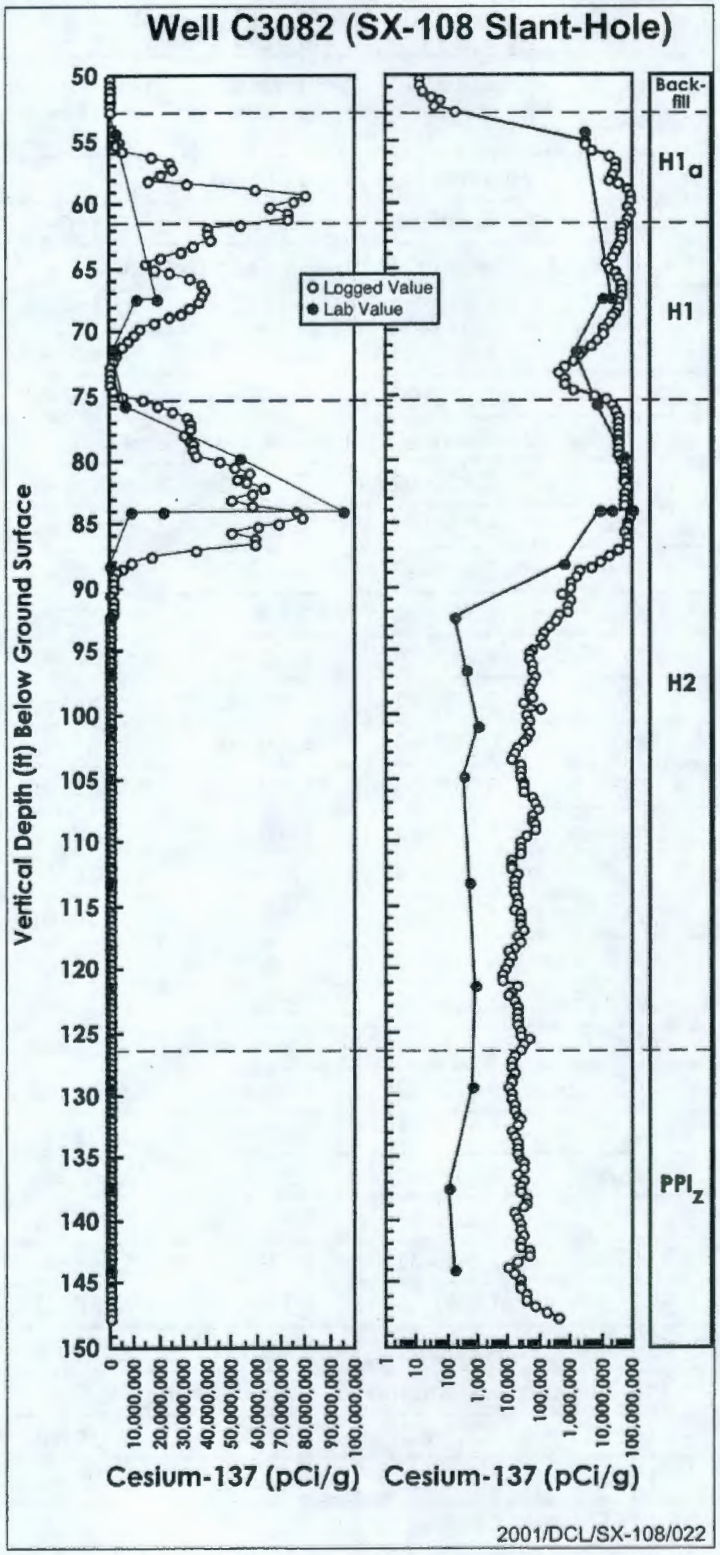

Technetium-99 is found at elevated concentrations throughout the SX-108 slant borehole. The technetium-99 elevated concentration pattern (listed as pCi/mL in Table B.17) shows an apparent bimodal distribution in the primary high contamination zone between 26 and 40 m [85 and 130 ft] bgs in the bottom half of subunit H2 and in subunit PPlz (Figure B.23). As with other constituents, the low technetium-99 concentration at 32 m (105.6 ft) bgs creates this distribution. The largest concentration peak occurs at 30 m (97 ft) bgs at a maximum concentration of about 237,000 pCi/mL. This pattern closely mimics the nitrate concentration distribution. It is probable that the bottom of the technetium-99 range was not reached in this sampling effort. Chromium concentration values (listed as mg/L in Table B.17) increase above background beginning at 20 m (68 ft) bgs and show maximum values between 25 and 40 m (81 and 130 ft) bgs. The peak concentrations of greater than 22,000 mg/L occur at 30 m (97 ft) bgs. The deepest entire chromium range may have been captured by these soil samples as indicated by very small concentrations in the two deepest samples. The occurrence of the maximum chromium range slightly higher in the soil column relative to technetium-99 indicates some retarding chemical mechanism has slowed chromium migration relative to technetium-99. Work completed by the S&T activity (Appendix D, Section D.4.1) indicates that iron(II)-rich minerals in the vadose zone soil reduce the oxidation state of a fraction of the chromium in solution from +6 to +3. In the +3 state, chromium is removed from solution by sorption or coprecipitation in iron(II)-rich minerals.

Other constituents that may have been placed into the soil column by the tank SX-108 leak include iodine-129, selenium, and molybdenum. The iodine-129 measurements are difficult to obtain and often suspect, but in this case there does appear to be measurable concentrations between 24 and 40 m (80 and 130 ft) bgs in 4 samples. The maximum concentration of about 43,000 pCi/L occurs at 24 m (80 ft) bgs and values decrease to about 19,000 pCi/L at the bottom of the SX-108 slant borehole, suggesting that the bottom of the iodine-129 contamination zone occurs below the borehole. These concentrations are three orders of magnitude less than technetium-99 concentrations in the same depth interval. Elevated selenium concentrations show a pattern that is nearly identical to technetium-99. Elevated molybdenum concentrations are more restricted and lie between 24 and 28 m (80 and 93 ft) bgs.

B.4.4 CONTAMINANT CONCENTRATIONS

Contaminant concentrations at the SX-108 slant borehole were not analyzed.

B.4.5 CHEMICAL INTERACTIONS

No specific experiments were completed on soils from the SX-108 slant borehole to quantify geochemical reactions influencing contaminant migration. Dominant chemical reactions affecting radionuclides and tank fluid chemicals are inferred from the relative location of these constituents in the soil column, comparison of acid-leachable versus water-leachable concentrations for specific contaminants, and general knowledge of the tank fluid chemistry. Greater contaminant mobility is inferred from the occurrence of high concentration zones deeper in the vadose zone and smaller differences in dissolved concentrations leached by water versus acid. Empirical in situ distribution coefficient estimates are summarized in Table B.18.

Table B.17. Calculated Porewater Trace Metal Composition for Water Extracts of Sediments from SX-108 Slant Borehole

Sample ID	Vertical Depth (ft bgs)	Dilution Factor	Water:Soil Ratio	Tc-99 (pCi/mL)	U (μg/L)	Cr* (mg/L)	As (μg/L)	Se (μg/L)	Mo (μg/L)	Ag (μg/L)	Cd (μg/L)	Pb (μg/L)
1A	55.1	23.13	1.00	<392	(35.9)	(0.21)	(875)	<1157	305	(2.31)	(30.1)	253389
1A-Dup	55.1	23.13	1.00	<392	(28.9)	(0.22)	(798)	<1157	347	<57.8	<57.8	4196
3A	67.9	36.88	1.02	(125)	140.14	(29.1)	(1239)	<1844	11446	<92.2	(3.69)	(679)
4A	72.2	36.15	1.00	(61)	209.67	(27.8)	(3687)	<1808	2176	<90.4	<90.4	(95.8)
5A	76.4	21.36	1.00	(217)	(98.3)	75.1	(1772)	(145)	3036	(32.0)	<53.4	(334)
6A	80.6	27.18	1.00	1106	(32.6)	13150	(266)	(1298)	127610	(216)	279	(78.8)
7A	84.8	16.20	1.00	16485	1433.7	5018	(2019)	984.2	90874	(183)	211	(953)
8A	89.0	16.61	1.00	47439	(43.2)	13782	(507)	2477	40238	(276)	105	(74.7)
9A	93.1	42.56	1.00	168400	(46.8)	21817	(1290)	5612	7510	(12.8)	(4.26)	(1221)
10A	97.3	52.34	1.00	237279	(55.0)	20838	(1675)	8615	871	(15.7)	<131	(325)
11A	101.7	31.78	1.00	144287	(6.36)	28.1	(753)	3849	184	<79.5	<79.5	(89.0)
12A	105.6	4.69	1.00	2792	(2.35)	0.98	(23.5)	(37.5)	56.7	<11.7	<11.7	(9.8)
13A	113.8	13.38	1.02	96874	(13.4)	5766	(561)	3182	3180	(8.03)	(14.7)	(33.5)
14A	122.0	8.69	1.04	58820	(5.65)	2588	(422)	1954	258	(5.21)	(0.87)	(45.2)
14A-Dup	122.0	8.38	1.00	64773	(7.12)	2913	(440)	2249	231	(5.03)	<21.0	(21.8)
15A	130.1	5.74	1.00	66072	6.89	1931	(443)	2360	78.6	(3.44)	(0.00)	(12.6)
16A	138.2	13.31	1.00	19255	(18.6)	(0.26)	(82.5)	(419)	181	<33.3	(2.66)	(58.6)
17A	144.6	5.08	1.00	2800	5.08	(0.02)	(20.8)	(69.1)	100	(0.51)	<12.7	(26.9)

Note: Values in parentheses are those that are below limit of quantification.

*Higher chromium values are from ICP-OES, not ICP-MS. Note chromium values are in mg/L.

ICP = inductively coupled plasma.
MS = mass spectrometer.
OES = optical emission spectroscopy.

Figure B.23. Trace Metals Calculated and Actual Porewaters for SX-108 Slant Borehole Sediments

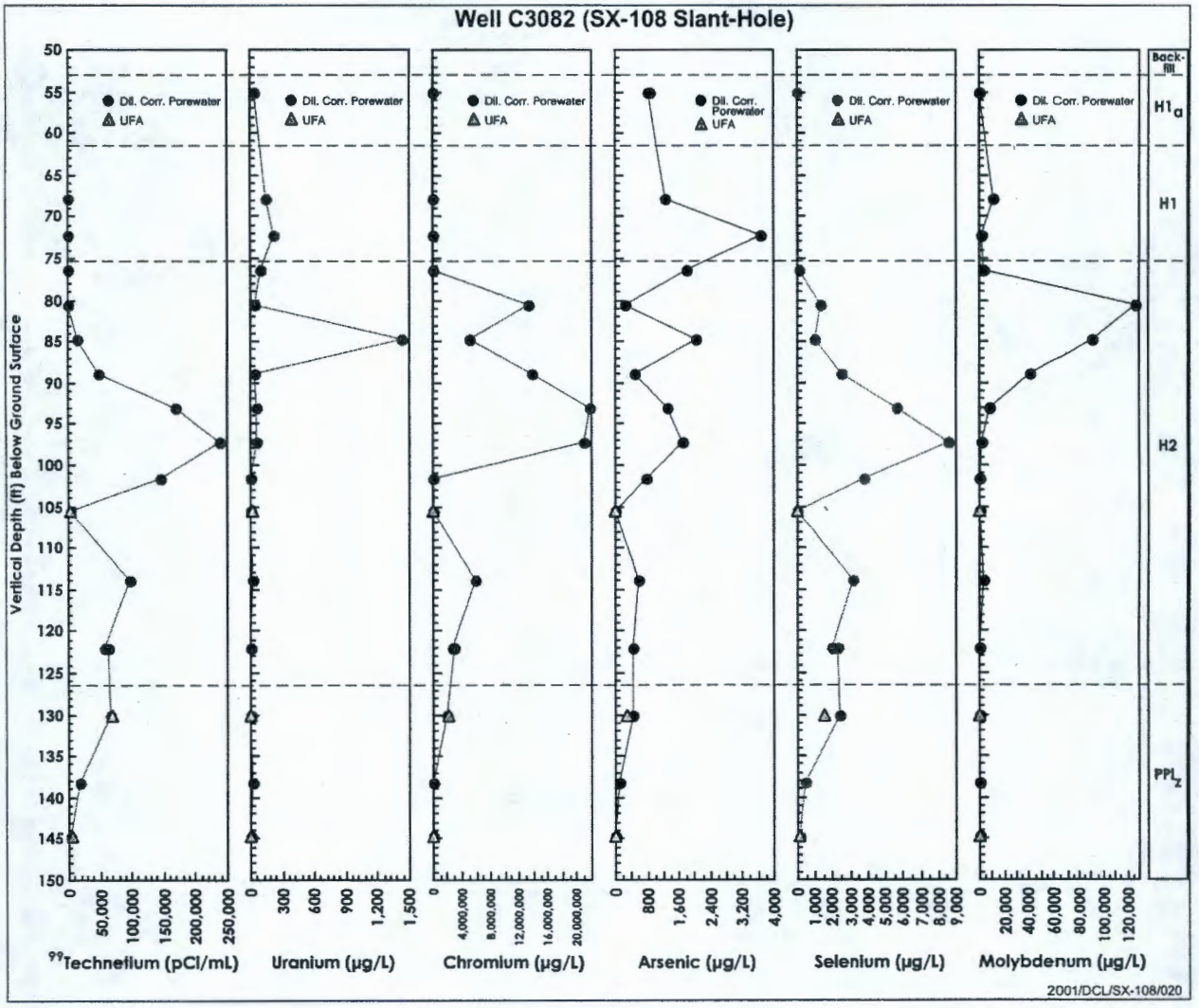

Table B.18. In Situ Distribution Coefficient Values for Contaminants Desorbing from SX-108 Slant Borehole Vadose Zone Sediments

Sample ID	Depth (ft bgs)	Lith. Unit	Distribution Coefficient Values (mL/g)						
			Cesium-137	Technetium-99	Uranium	Chromium	Arsenic	Selenium	Molybdenum
01A	55.1	H1a	230.3	indeterm.	13	423	3.02	indeterm.	1.53
01A-dup	55.1	H1a	--	indeterm.	14	749	8.34	0.11	18.26
03A	67.9	H1	25.7	0.04	5	4.26	1.44	indeterm.	0.16
04A	72.2	H2	72.9	indeterm.	3	4.32	0.64	indeterm.	0.42
05A	76.4	H2	99.3	-0.01	8	2.92	2.68	1.26	0.44
06A	80.6	H2	2.3	0.01	24	0.01	16	0.11	0.06
07A	84.8	H2	4.2	-0.01	0	0.18	2.37	0.21	0.00
08A	89	H2	24.8	-0.02	18	0.05	10	0.06	0.19
09A	93.1	H2	6.5	0.00	14	0.01	3.38	0.02	0.04
10A	97.3	H2	10.2	0.00	12	0.01	2.49	0.02	0.46
11A	101.7	H2	>49.7	0.00	114	1.04	5.74	0.04	3.01
12A	105.6	H2	>120.7	-0.02	588	24.1	461	7.52	4.72
13A	113.8	H2	>46.5	0.00	459	0.04	10	0.06	0.79
14A	122	H2	307.4	0.01	168	0.06	14	0.10	3.21
14A-dup	122	H2	--	-0.01	132	0.03	13	0.12	3.36
15A	130.1	PPlz	>136.7	-0.02	139	0.04	8.32	0.10	7.84
16A	138.2	PPlz	>13.9	0.02	63	84.9	39	0.55	3.02
17A	144.6	PPlz	35.6	0.11	223	1864	303	4.58	15.7

Generally speaking, the data suggest that tank SX-108 fluid chemistry had a substantial, but limited, effect on contamination behavior at the SX-108 slant borehole. Given the depth below the tank SX-108 bottom at which very high concentrations of cesium-137 occur (essentially, the entire thickness of subunit H2), cesium-137 was initially highly mobile in the leaked tank fluid. Various types of sorption experiments completed by the S&T group (Appendix D, Section D.3.0) shows that the very high concentrations of cesium-137, sodium, and to a lesser extent potassium in the tank SX-108 fluid created local conditions where sodium preferentially occupied soil sorption sites in soils and preventing cesium-137 sorption. These conditions were short-lived and confined to subunits H1 and H2 as shown by the current limited distribution of cesium-137. Over time natural infiltration and recharge subsequently separated sodium from cesium-137, permitting cesium-137 to sorb in situ. The current degree of cesium-137 mobility was determined by comparing the amount of cesium-137 removed by water versus total activity measured by gamma. The in situ distribution coefficient for cesium-137 varies from about 2 to 300 mL/g in the sediments in the borehole where distribution coefficient values tend to correspond inversely to the salinity level.

Tank fluids also increased amounts of other constituents in the soil column, but had little effect on the chemical behavior of contaminants other than cesium-137 in the sense that chemical reactions between tank fluid constituents and the soil column environment were largely controlled by soil-soil water reactions. Constituent anions (e.g., nitrate and technetium-99) have migrated the most rapidly and mark the leading edge of vertical tank fluid migration. The technetium-99 in situ distribution coefficient was determined by comparing acid versus water leached concentrations and does not exceed 0.11 mL/g over the whole zone of contamination. Chromium was slightly retarded relative to technetium-99 and nitrate, presumably because of oxidation reduction, allowing fixation on soil. Generally, the in situ distribution coefficient values were very small except for the soil samples between 17 and 23 m (55 and 76 ft) bgs where the distribution coefficient value between about 3 and 430 mL/g was estimated. These numbers suggest that maximum oxidation reduction occurred near the tank bottom.

Other constituent cations have migrated varying distances depending on the strength of retardation mechanisms. Sodium concentrations, being relatively high, successfully completed for sorption sites in vadose zone soils, were somewhat retarded. Calcium, magnesium, and indigenous strontium were displaced by sodium and pushed ahead of sodium during migration.

B.4.6 GROUNDWATER MEASUREMENTS

Groundwater measurements were not taken at the SX-108 slant borehole.

B.5.0 BOREHOLE SEDIMENT ANALYSIS

This section summarizes data reported in *Characterization of Uncontaminated Sediments from the Hanford Reservation – RCRA Borehole Core and Composite Samples* (Serne et al. 2001a) taken from two boreholes (299-W22-48 and 299-W22-50) drilled east of the S and SX tank farms (Figure B.1) as RCRA groundwater monitoring wells. Relative to vadose zone characterization, soil samples taken in the vadose zone represent undisturbed soils that have the soil characteristics found under the S and SX tank farms prior to contamination from tank leaks. The most important data collected from these boreholes include the physical soil properties and the porewater chemistry derived from water extractions, acid extractions, and porewater squeezings.

B.5.1 GEOLOGY

Geology at boreholes 299-W22-48 and 299-W22-50 are described in the following sections.

B.5.1.1 Borehole 299-W22-48

Borehole 299-W22-48 was drilled for the RCRA Groundwater Monitoring Project. Samples were collected via continuous split spoon to a depth of 59 m (193.5 ft) bgs; the sampling effort was sponsored by the S&T activity. Grab samples were taken at 1.5 m (5 ft) intervals. Samples were obtained to support S&T activity research addressing characteristics of noncontaminated sediments.

B.5.1.1.1 Hanford formation. Sediments of the Hanford formation were penetrated from the surface to 41.3 m (135 ft) bgs. Subunits H1 an H2 were present.

- **Subunit H1** – Two distinct coarse-grained intervals (gravelly sand to gravel) were identified within relatively uniform medium-grained sand; an upper zone at 12.5 to 15.3 m (41 to 50 ft) bgs and a lower zone at 17.7 to 18.6 m (58 to 61 ft) bgs. These gravelly intervals have been identified in surrounding vadose zone boreholes and wells based on geophysical log correlations (Sobczyk 2000) but have not been readily identified in the geologic grab samples. The base of subunit H1 is estimated to lie at 18.6 m (61 ft) bgs.

- **Subunit H2** – Subunit H2 extends to 41.3 m (135 ft) bgs, and has been described as a fine to medium-grained sand which becomes finer with depth. Numerous silt laminae are noted in the split-spoon samples collected from this subunit at this location.

B.5.1.1.2 Plio-Pleistocene Unit. The two Plio-Pleistocene subunits include the upper subunit PPlz, characterized by a relatively high silt content, and the lower subunit PPlc, characterized by secondary, pedogenic, calcium-carbonate cement.

- **Subunit PPlz** – Subunit PPlz is recognized on the gamma logs and is present from 41.3 to 44.6 m (135 to 146 ft) bgs. This gamma signature reflects the downward decreasing grain size from silty sand to silt typical of the unit in this area.

- **Subunit PPlc** – Subunit PPlc is present from 44.6 to 45.5 m (146 to 149 ft) bgs at this location. The carbonate-rich unit is at a moderately higher elevation at this location than at sites further south.

B.5.1.1.3 Ringold Formation. Two subunits of the Ringold Formation have been tentatively identified at borehole 299-W22-48, the member of Taylor Flat and the member of Wooded Island. The interpretation of the Ringold Formation in this borehole differs significantly from other nearby wells.

- **Member of Taylor Flat** – At borehole 299-W22-48, a fairly uniform, silty, sandy, gravel unit extending from 45.5 to 58.6 m (149 to 192 ft) bgs has been tentatively identified as the member of Taylor Flat. This unit has not been identified elsewhere in the near vicinity and may actually be representative of the more commonly identified member of Wooded Island unit E.

- **Member of Wooded Island** – Member of Wooded Island unit E silty-sandy gravels have been identified by an increase in moisture at 58.6 m (192 ft) bgs that extends to the water table at 69 m (226 ft) bgs.

B.5.1.2 Borehole 299-W22-50

The vadose zone portion of borehole 299-W22-50 penetrated strata belonging to the Hanford formation, the Plio-Pleistocene unit, and the Ringold Formation. The upper 6.1 m (20 ft) of this borehole were not sampled, drilling in this portion of the borehole was done with a cable-tool deployed core barrel, and no intact samples were available for geologic logging.
Field descriptions of that portion of the borehole indicate it penetrated fine sand, coarse sand, and gravel/sand facies.

B.5.1.2.1 Hanford formation. Sediments of the Hanford formation were penetrated from the ground surface to an estimated depth of 39.3 m (129 ft) bgs. Subunits H1 and H2 were present.

- **Subunit H1** – From a depth of 6.1 m (20 ft) bgs to approximately 16.1 m (53 ft) bgs the sediments logged consist of fine sand facies with lesser coarse sand facies. Stratification commonly observed in this interval include planar laminae, normally graded bedding and silty interbeds. Some evidence of planar and trough cross-bedding in the form of low-angle bedding intersections were observed. A few structures suggestive of clay skins on clastic dikes were noted. Minor pebble gravel, occurring as isolated clasts, is found in the lowermost 0.9 m (3 ft) of the interval.

  Approximately 2.9 m (9.5 ft) of the gravel/sand facies underlies the sandy strata. The contact between these intervals is relatively sharp. Evidence of poorly developed planar and low angle bedding, suggested by coarse-fine grain size alterations is present. No clast-supported pebble gravel was observed in this interval.

- **Subunit H2** – A sandy interval from 19 to 39.3 m (62.5 to 129 ft) bgs is interpreted to be subunit H2. The upper 1.7 m (5.5 ft) consist predominately of well-stratified, friable, coarse sand. This sand appears to be unweathered and displays a mixed mafic/felsic mineralogy similar to the matrix sand in the overlying gravelly interval. The remainder

of this sand interval consists predominantly of planar laminated to ripple cross-laminated fine sand facies. Other observed stratification includes normally graded bedding, planar cross bedding and trough cross bedding. Two paleosols are present in the sandy interval at 22.9 m (75 ft) bgs and 31.4 m (103 ft) bgs. Poorly developed blocky peds, possible burrow traces, organic debris, and increased calcium carbonate content is evident in the uppermost of the two paleosols. The deeper paleosol is less well developed, displaying poorly developed traces of burrowing and mottling.

B.5.1.2.2 Plio-Pleistocene Unit. The two Plio-Pleistocene subunits include the upper subunit PPlz, characterized by a relatively high silt content, and the lower subunit PPlc, characterized by secondary, pedogenic, calcium-carbonate cement.

- **Subunit PPlz** – A fine sand/silt facies becomes dominant at 39.3 m (129 ft) bgs. This facies is consistent with the unit described as subunit PPlz in other boreholes in the vicinity of borehole 299-W22-50. This facies displays an increase in the occurrence of silt and the appearance of intercalated silt facies horizons greater than 0.15 m (0.5 ft) thick. Ripple cross-lamination and planar laminae are well developed in the sandy portions of the interval, which extends to 41.9 m (137.5 ft) bgs.

- **Subunit PPlc** – A well-developed paleosol at 41.9 m (137.5 ft) bgs marks the top of subunit PPlc. This paleosol is 0.15 m (0.5 ft) thick and displays moderately well developed beds, bedding is disrupted to massive, and stage I/II calcium carbonate is present. The remainder of the carbonate-rich interval consists of approximately 1.4 m (4.5 ft) of silt, sand, and gravel divided into: (1) approximately 0.46 m (1.5 ft) of conglomerate with a carbonate overprint; (2) somewhat greater than 0.3 m (1 ft) of silty paleosol; and (3) a basal conglomerate with carbonate overprint. The presence of stage II/III carbonate in the form of clast coatings, discontinuous stringers, and concretions indicates this is the Plio-Pleistocene carbonate rich subunit PPlc.

B.5.1.2.3 Ringold Formation. The top of the Ringold Formation is encountered at 43.4 m (142.5 ft) bgs where calcium carbonate content decreases markedly. The uppermost Ringold Formation strata encountered in this well consist of variably indurated conglomerate about 3.7 m (12 ft) thick that has a mixed basaltic/felsic sand matrix. The more felsic portions of the interval display yellow to yellow-brown color typical of many Ringold Formation deposits. However, the mafic content of these sediments is high enough to give the sand matrix a non-typical salt and pepper appearance.

In the interval 47.1 to 49.7 m (154.5 to 163 ft) bgs, coarse, variably indurated, crudely stratified sand with minor pebbles is present. The mineralogy of this sand is similar to the matrix sand in the overlying conglomerate. From 49.7 to 50.5 m (163 to 165.5 ft) bgs another conglomerate unit is penetrated. From 50.5 to 53.8 m (165.5 to 175 ft) bgs a sandy unit is present. This sandy unit is locally silty and displays abundant evidence of disrupted bedding and a white-gray color in the silty parts. The sand is calcium carbonate poor and the mafic content is greater than 25%.

At 53.5 m (175 ft) bgs conglomerate was again encountered, and at 53.8 ft (176.5 ft) bgs split-spoon sampling was suspended. Based on the abundance of gravel and absence of paleosol

facies in the Ringold Formation in this borehole the entire interval is assigned to the member of Wooded Island unit E.

B.5.2 GEOPHYSICAL AND PHYSICAL PROPERTY MEASUREMENTS

Downhole geophysical and physical measurements (Figures B.24 and B.25) for the RCRA borehole sediments analysis included high-purity germanium spectral gamma logs; laboratory measurements of soil moisture content, neutron-neutron logs from the surface to the unconfined aquifer of both boreholes (249 ft [76 m] and 247 ft [75m] for 299-W22-48 and 299-W22-50, respectively); and soil suction measurements (Figure B.12). Outstanding geophysical data that distinguish stratigraphic units in the vadose zone include high moisture content and low natural gamma levels in subunit PPlc. Subunit PPlz shows relatively high natural gamma levels and low moisture content. Small silt-rich zones are indicated in subunit H2 by high moisture content. Soil suction measurements generally show drainage in the Hanford formation but not in the Plio-Pleistocene unit and below.

B.5.3 SOIL WATER CHEMISTRY MEASUREMENTS

In addition to soil physical property measurements (Section B.5.2), an extensive water chemistry analysis has been completed for samples collected between the surface and 59 m (192 ft) bgs in borehole 299-W22-48 and between the surface and 53 m (174 ft) bgs for borehole 299-W22-50. The primary means of measuring porewater composition was to add deionized water to soil samples to generate enough water for performing analyses. By back-calculating for the dilution introduced by the added water, 'true' concentrations were derived. For a few samples porewater was directly separated from the same soil sample or one nearby and analyzed directly. By comparing the dilution-corrected water extract data with the porewater data in these few samples, an indication of the closeness of the water extract chemistry to original water chemistry was determined. In general, comparisons were not exact but concentration values were generally within a factor of two or better, agreement improved with increasing constituent concentration, and both sets of data showed similar concentrations versus soil depth correlations. Thus, the water extract method is an effective tool for evaluating tank fluid interactions with vadose zone soil.

Water extract pH and electrical conductivity measurements with depth are listed and graphed in Table B.19 and Figure B.26 for borehole 299-W22-48 and listed in Table B.20 for borehole 299-W22-50. The pH values in both boreholes fall into a normal range (7 to 8.5) except at 18 to 21 m (60 to 68 ft) bgs in borehole 299-W22-50 where elevated pH values (about 10 and 9) are measured. The reason for this increase is not known. Elevations in electrical conductivity values are not observed. A range of 50 to 500 μS/cm are present in these samples.

Water extract anion concentrations as a function of depth are listed in Table B.19 for borehole 299-W22-48. Nitrate, chloride, and sulfate concentrations with depth are shown in Figure B.27. Other than enrichment of subunit PPlc in nitrate and sulfate, the profiles are undistinguished. In borehole 299-W22-50, anion data have no distinguishing features other than slight elevations of nitrate and sulfate in subunits PPlz and PPlc.

Figure B.24. Vadose Zone Stratigraphy for Borehole 299-W22-48

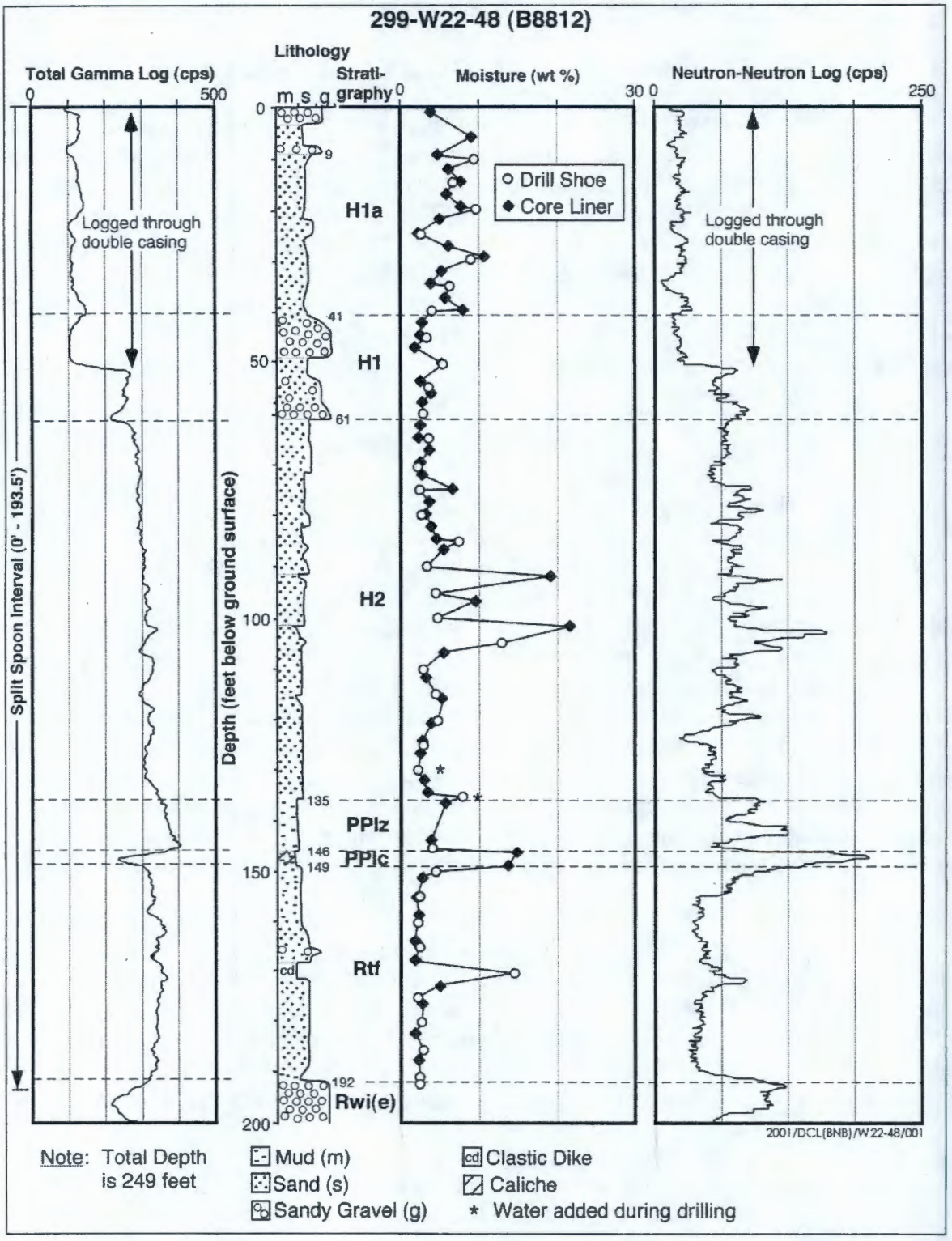

Figure B.25. Vadose Zone Stratigraphy for Borehole 299-W22-50

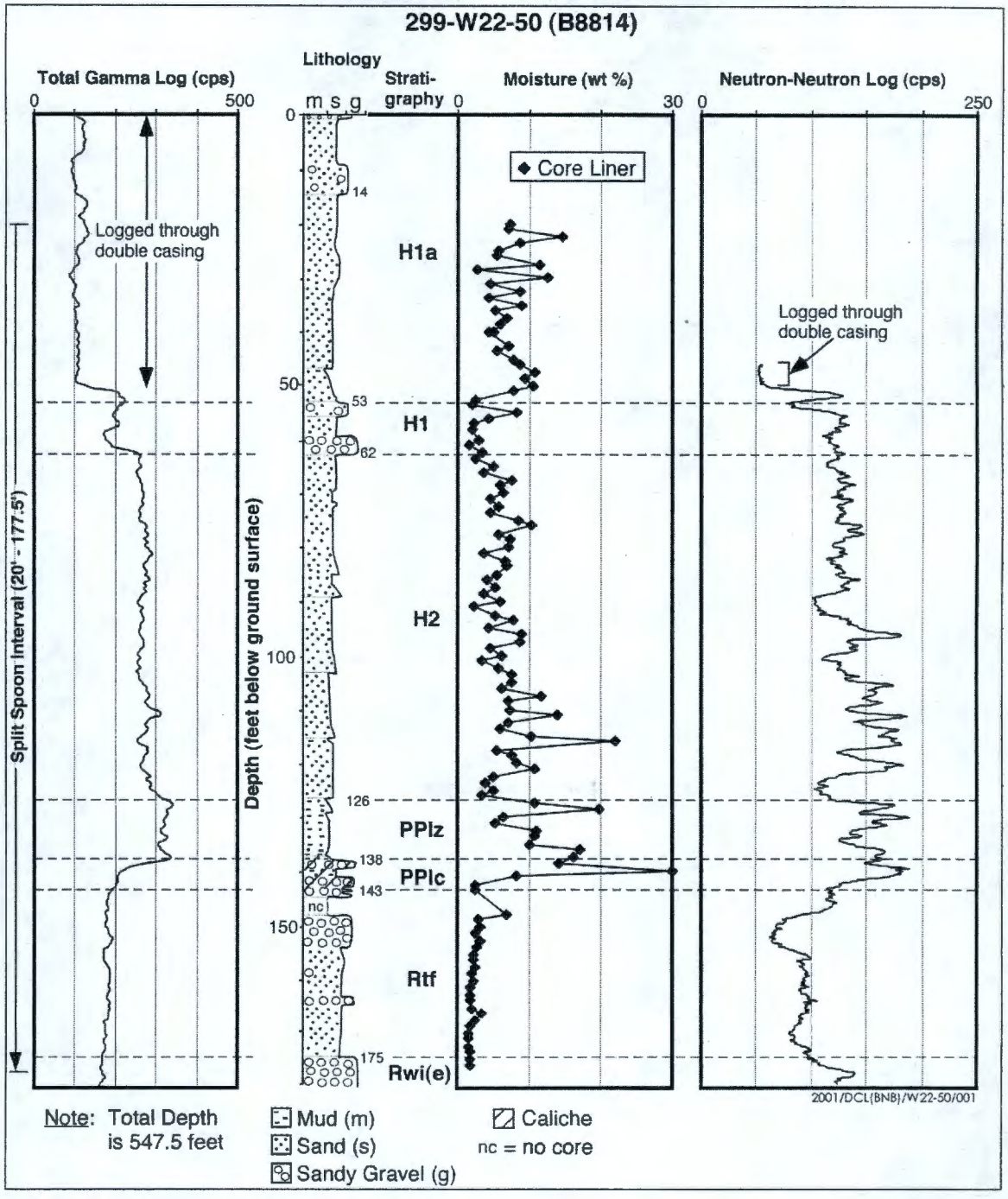

Table B.19. Borehole 299-W22-48 pH, Electrical Conductivity, Alkalinity, and Anions in 1:1 Water Extracts (2 Sheets)

Constituent Sample		pH	EC (µS/cm)	Alk (mg/L $CaCO_3$)	F (mg/L)	Cl (mg/L)	NO_2 (mg/L)	NO_3 (mg/L)	PO_4 (mg/L)	SO_4 (mg/L)
Depth (ft bgs)	Strat. Unit									
1	H1a				1.56	1.27	<0.1	7.06	0.21	2.42
6	H1a				1.90	0.42	<0.1	7.94	<0.1	5.48
9.5	H1a				1.43	0.39	<0.1	5.89	0.27	8.79
12.5	H1a				3.04	0.32	<0.1	4.37	0.24	5.64
14.5	H1a				2.65	0.30	<0.1	4.46	0.29	14.62
17	H1a				2.66	0.35	<0.1	7.10	0.37	15.20
19.5	H1a				1.74	0.72	<0.1	9.79	<0.1	15.70
22	H1a				1.03	0.49	<0.1	14.50	0.35	16.90
24.5	H1a				0.95	0.37	<0.1	5.27	0.34	18.20
27	H1a				1.39	0.49	<0.1	11.00	0.28	18.30
29.5	H1a	7.38	224	47.94	*0.95**	*0.32**	<0.1	*7.89**	*0.27**	*20.68**
32	H1a	7.97	171	41.60	*0.62*	*0.26*	<0.1	*6.97*	*0.30*	*9.14*
34.3	H1a				0.79	0.39	<0.1	5.20	0.63	9.88
37	H1a				0.72	1.43	<0.1	11.90	0.28	14.80
39.5	H1a	7.39	180	33.14	*0.55*	*0.65*	<0.1	*13.75*	*<0.24*	*14.75*
42	H1				*0.74*	*0.43*	<0.1	*3.99*	*0.13*	*11.85*
44.5	H1				0.63	0.42	<0.1	3.69	0.18	18.40
47	H1	7.30	126	28.91	**0.58****	**0.24****	**<0.1**	**2.76****	**0.13**	**9.26****
50	H1				0.65	0.84	<0.1	10.90	0.25	12.10
53.5	H1				0.49	0.53	<0.1	2.46	<0.1	10.10
56	H1	7.20	142	NA	*0.45*	*1.05*	<0.1	*1.00*	*0.13*	*11.47*
57.5	H1				0.57	1.72	<0.1	7.07	0.12	13.40
74.5	H2	*7.395*	*216*	*36.00*	*0.50*	*5.06*	<0.1	*7.28*	*0.33*	*24.06*
91.5	H2				0.60	4.83	<0.1	8.44	0.39	13.60
101.5	H2				*0.63*	*5.48*	<0.1	*9.82*	*0.34*	*17.15*
106.5	H2	7.70	177	33.84	0.33	6.45	<0.1	5.19	<0.1	10.40
115.5	H2	7.39	182	38.07	0.36	2.28	<0.1	7.55	0.38	12.30
136	PPlz	7.20	214	40.19	0.45	1.32	<0.1	22.70	0.50	11.90
143.5	PPlz	7.12	186	34.55	0.27	0.71	<0.1	16.20	0.35	11.10
146	PPlc	*7.39*	*441*	*47.47*	*0.91*	*3.57*	<0.1	*75.20*	*0.17*	*44.40*
148.5	PPlc	7.48	291	41.6	1.27	1.84	<0.1	42.80	<0.1	16.90

Table B.19. Borehole 299-W22-48 pH, Electrical Conductivity, Alkalinity, and Anions in 1:1 Water Extracts (2 Sheets)

Constituent Sample		pH	EC (μS/cm)	Alk (mg/L $CaCO_3$)	F (mg/L)	Cl (mg/L)	NO_2 (mg/L)	NO_3 (mg/L)	PO_4 (mg/L)	SO_4 (mg/L)
Depth (ft bgs)	Strat. Unit									
151	Rtf	7.56	208	49.35	1.21	1.68	<0.1	4.16	<0.1	5.45
163.5	Rtf	7.46	117	29.96	0.49	0.45	<0.1	6.95	0.11	1.69
170	Rtf	7.40	116	31.02	0.46	0.49	<0.1	7.34	0.21	1.84
172.5	Rtf	7.33	190	31.73	0.50	0.40	<0.1	1.96	<0.1	1.50
187	Rtf	7.58	53	15.51	0.48	0.59	<0.1	9.91	<0.1	1.86
192	Rwi(e)	7.78	120	18.33	1.37	1.55	<0.1	9.10	0.29	10.00

Note: *Data in *italics* type are average of duplicate extracts. **Data in **bold** type are the average of triplicate extracts.

EC = electrical conductivity.
NA = not analyzed.

Figure B.26. Moisture Content (wt%) of Sediment, pH and Dilution-Corrected Electrical Conductivity of Water Extract and Actual Porewater versus Depth and Stratigraphy for Borehole 299-W22-48

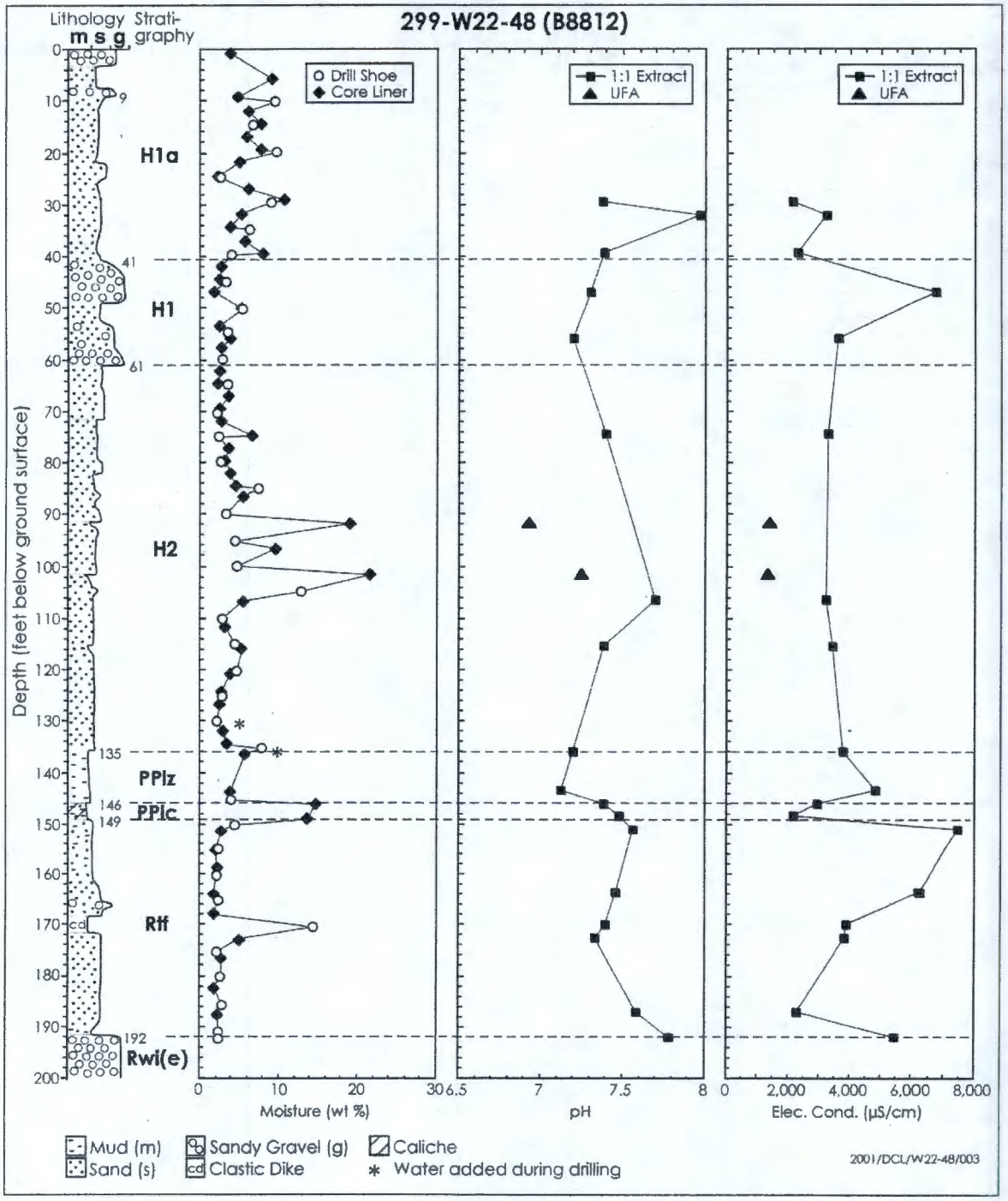

Table B.20. Borehole 299-W22-50 pH, Electrical Conductivity, Alkalinity, and Anions in 1:1 Water Extracts

Constituent Sample		pH	EC (µS/cm)	Alk mg/L $CaCO_3$	F (mg/L)	Cl (mg/L)	NO_2 (mg/L)	NO_3 (mg/L)	PO_4 (mg/L)	SO_4 (mg/L)
Depth (ft bgs)	Strat. Unit									
20	H1a	7.78	188	52.88	0.72	0.45	<0.1	5.89	0.1	8.56
22.5	H1a	7.72	221	26.79	0.74	1.08	<0.1	4.51	<0.1	13.52
25	H1a	7.68	214	31.73	0.72	0.76	<0.1	3.42	0.2	9.78
27.5	H1a	7.60	214	48.65	0.7	1.88	<0.1	0.63	0.1	19.56
30	H1a	7.65	217	39.48	0.63	4.85	<0.1	2.64	0.15	20.5
32.5	H1a	7.67	186	43.01	0.56	1.62	<0.1	2.51	0.33	11.64
35	H1a	7.49	222	50.06	0.68	0.82	<0.1	0.68	0.29	13.85
37.5	H1a	7.84	203	45.12	0.61	0.67	<0.1	0.57	<0.1	12.51
40	H1a	7.03	184	47.24	0.5	0.57	<0.1	0.36	<0.1	11.49
42.5	H1a	7.11	223	54.29	0.58	0.99	<0.1	1.15	0.16	17.54
45*	H1a	7.46±0.1	224±3	35±19	0.60±0.05	0.82±0.01	<0.1	1.46±0.52	<0.1	17.6±1.1
47.5	H1a	7.40	224	34.55	0.57	0.83	<0.1	0.46	<0.1	16.37
51	H1a	7.90	181	56.40	0.59	0.45	<0.1	3.09	0.1	8.62
52.5	H1a	7.44	181	32.43	0.39	0.85	<0.1	0.72	<0.1	16.15
55	H1	7.32	216	54.99	0.47	1.34	<0.1	0.25	<0.1	19.18
56	H1	7.35	129	25.38	0.28	0.54	<0.1	1.25	0.12	8.37
60	H1	10.33	553	60.63	0.41	9.33	<0.1	1.82	<0.1	35.71
67.5	H2	9.00	276		0.38	4.84	<0.1	5.49	0.21	21.9
76	H2	8.55	223	21.86	0.36	4.4	<0.1	8.85	0.18	29.7
96*	H2	7.44±0.02	298±15	35±5	0.39±0.06	23.7±13	<0.1	10.0±1.0	0.20±0.06	28.7±1.0
111	H2	7.45	296	58.52	0.49	11.47	<0.1	25.51	0.15	23.01
115	H2	7.51	309	55.70	0.51	14.41	<0.1	29.8	0.17	16.6
130	PPlz	7.66	231	89.54	0.41	2.01	<0.1	6.32	0.16	9.63
135	PPlz	8.50	226.5	62.04	0.46	2.31	<0.1	20.99	0.2	18.02
141	PPlc	8.12	246	67±36	0.80±0.08	3.3±0.5	<0.1	11±1.3	<0.1	22±2.8
150.5	Rtf	7.77	191	6.35	1.1	1.49	<0.1	<0.1	<0.1	8.62
160.5	Rtf	7.74	135	31.02	0.62	0.76	<0.1	<0.1	<0.1	3.13
174	Rtf	7.75	88	18.33	0.99	4.77	<0.1	10.9	0.13	2.57

*Data are average of duplicate extracts.

EC = electrical conductivity.

Figure B.27. Dilution-Corrected Anion Content of Water Extracts and Anion Concentration in Actual Porewater versus Depth and Stratigraphy for Borehole 299-W22-48

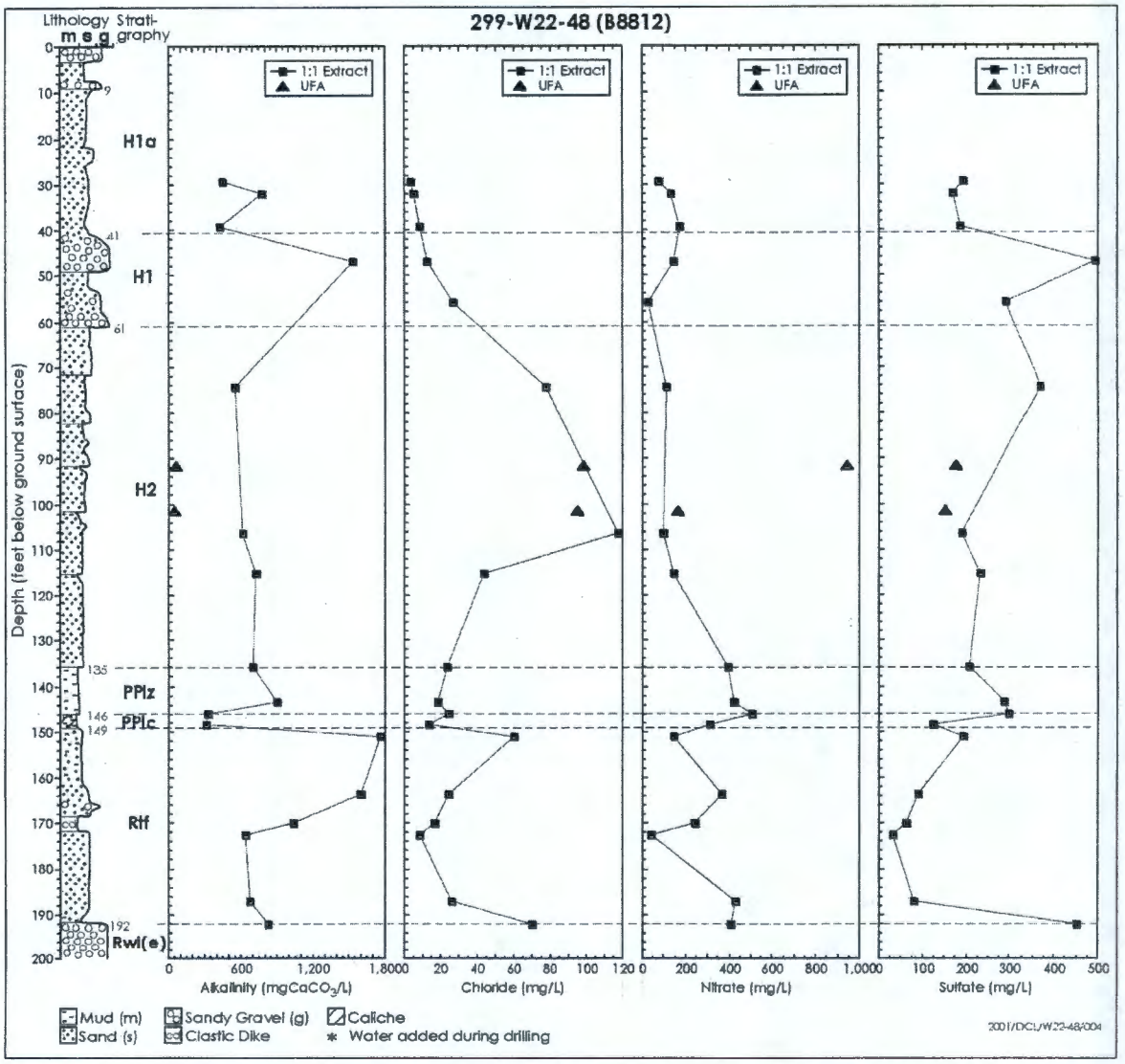

Water extract cation concentrations as a function of depth are listed in Table B.21 and graphed in Figure B.28 for borehole 299-W22-48. Table B.22 provides cation concentrations for borehole 299-W22-50. In both boreholes slight elevations of calcium and natural strontium occur in subunit PPlc because of the relatively high quantities of calcium carbonate. A calcium enrichment anomaly occurs at 60 ft (18 m) bgs in borehole 299-W22-50, which is unexplained.

Trace metal concentrations are shown in Tables B.23 and B.24 for boreholes 299-W22-48 and 299-W22-50, respectively. Slight molybdenum enrichment is seen in subunit PPlc at both boreholes. Also, in borehole 299-W22-48 slight enrichment of selenium occurs in subunit PPlc.

B.5.4 CONTAMINANT CONCENTRATIONS

Contaminant concentrations were not analyzed in the RCRA borehole sediments analysis.

B.5.5 CHEMICAL INTERACTIONS

Chemical interactions were not analyzed in the RCRA borehole sediments analysis.

B.5.6 GROUNDWATER MEASUREMENTS

Groundwater contaminants are present in boreholes 299-W22-48 and 299-W-22-50. The contaminants are apparently derived both from large regional contaminant plumes (whose sources are a variety of crib, ditch, and trench discharges) and from tank waste. Available contaminant data are listed in Appendix C, Table C.16. Small concentrations of technetium-99, chromium, nitrate, and carbon tetrachloride are present in borehole 299-W22-48. The carbon tetrachloride is ubiquitous in this region. Technetium-99 appears to be increasing and may be derived from S tank farm contamination. The carbon tetrachloride and the nitrate that occur 75 to 80 m (246 to 263 ft) bgs in well 299-W22-50 are assumed to be derived from regional sources. The technetium-99 and nitrate occurring near the top of the aquifer may be derived from the tank SX-115 leak as indicated by the elevated technetium-99/nitrate ratio of 0.1 pCi/μg the same ratio found at well 299-W23-19 (Figure C.25). A more extensive discussion of these and other data postulated as relevant to tank SX-115 leak is provided in Section 3.4.2 of the main text.

Table B.21. Major Cations in 1:1 Water Extracts of Borehole 299-W22-48 Sediment Samples

Stat Unit (ft bgs)	Na (mg/L)	Mg (mg/L)	Al (µg/L)	Si (mg/L)	P (µg/L)	S (mg/L)	K (mg/L)	Ca (mg/L)	Mn (µg/L)	Fe (µg/L)	Sr (µg/L)	Ba (µg/L)
29.5-H1a	28.97	1.42	(35)	17.71	(91)	7.18	4.67	6.78	(1)	49.2	29.7	27.6
32.0-H1a	21.10	1.16	(49)	16.46	(113)	2.95	4.12	6.00	(1)	68.8	21.1	12.2
39.5-H1a	20.09	1.24	(29)	10.57	<500	4.54	3.83	6.66	(1)	(17)	24.3	15.5
47.0-H1	12.70	1.07	(48)	10.46	(2)	3.26	2.93	5.28	(1)	42.5	25.4	21.2
56.0-H1	15.36	2.29	50.7	9.06	(135)	4.00	4.70	8.89	(3)	43.1	37.4	(5)
74.5-H2	**16.45**	**3.56**	**76.1**	**9.55**	**(83)**	**8.98**	**4.36**	**10.75**	**(1)**	**45.0**	**62.0**	**17.3**
91.5-H2	19.14	2.86	286	12.80	(197)	5.30	3.47	9.55	(2)	93.2	49.9	17.0
101.5-H2	20.19	2.75	272	13.64	(169)	6.36	3.45	11.95	(3)	90.9	59.3	29.9
106.5-H2	14.21	2.15	85.0	8.94	(36)	4.14	3.60	9.65	(1)	63.2	48.5	16.9
115.5-H2	14.81	2.27	54.8	11.33	(21)	4.94	3.36	10.47	(1)	58.7	57.1	27.9
136.0-PPlz	16.50	3.21	68.5	11.76	(110)	4.78	3.84	12.92	(1)	39.2	65.9	32.3
143.5-PPlz	11.32	3.66	(10)	8.83	(88)	4.21	3.27	11.23	(1)	(8)	61.0	29.5
146.0-PPlc	**22.44**	**12.21**	**(5)**	**26.28**	**(207)**	**15.83**	**5.00**	**29.60**	**(0)**	**(5)**	**186**	**29.6**
148.5-PPlc	15.29	7.52	(8)	28.10	<500	6.40	3.99	18.47	(0)	95.5	121	24.9
151.0-Rtf	17.55	4.70	(29)	18.91	(81)	2.39	6.11	10.39	(4)	(19)	60.9	16.5
163.5-Rtf	7.24	2.68	(25)	11.73	<500	0.83	2.47	6.65	(0)	(16)	38.2	11.9
170.0-Rtf	7.13	2.93	(31)	12.78	<500	0.89	2.82	7.30	(2)	33.2	41.3	44.6
172.5-Rtf	8.22	2.80	(29)	13.06	(18)	0.70	3.62	7.01	(1)	(21)	39.3	19.0
187.0-Rtf	4.74	0.51	(28)	12.70	(145)	0.77	1.58	1.31	(2)	46.3	(7)	(8)
192.0-Rwi(e)	13.95	0.74	65.2	11.65	(125)	3.84	4.22	1.75	(2)	40.7	(10)	16.5

Note: Values in parenthesis are just below level of quantification but spectra looked good; thus, a tentative value was attributed to data. Data in **bold** are average of duplicate extracts.

Figure B.28. Dilution-Corrected Cation Content of Water Extracts and Cation Concentrations in Actual Porewater versus Depth for Borehole 299-W22-48

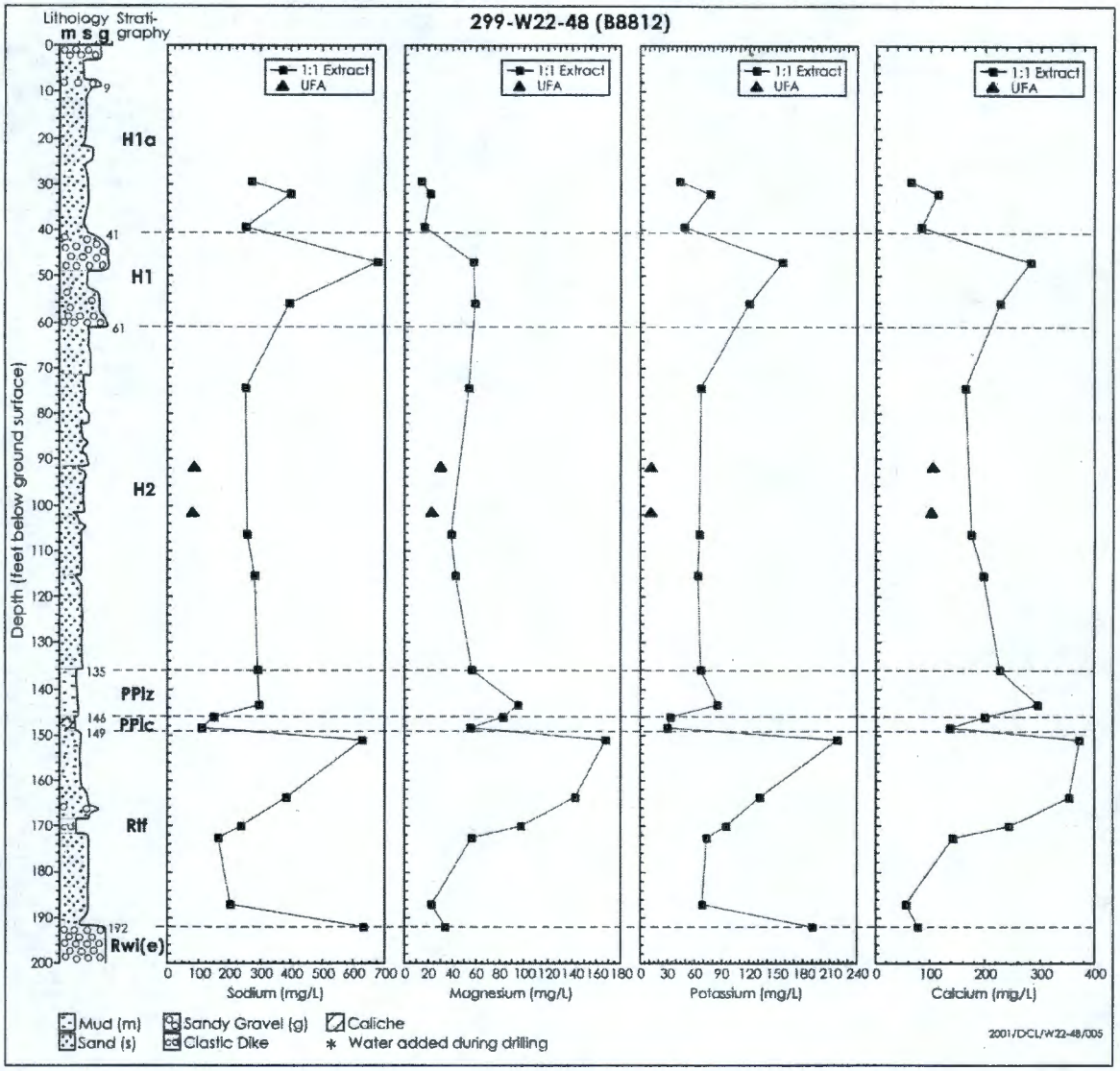

Table B.22. Major Cations in 1:1 Water Extracts for Borehole 299-W22-50

Depth (ft bgs)	Strat. Unit	Na mg/L	Mg mg/L	Al µg/L	Si mg/L	P µg/L	S mg/L	K mg/L	Ca mg/L	Mn µg/L	Fe µg/L	Sr µg/L	Ba µg/L
20	H1a	19.63	1.65	(29)	16.34	(33)	3.11	5.40	7.14	(0)	33.9	31.6	16.9
22.5	H1a	24.74	2.08	(45)	16.61	<500	4.76	6.48	9.49	(1)	96.2	40.2	20.0
25	H1a	20.05	1.40	(30)	14.22	(91)	3.51	5.41	6.32	(0)	30.6	27.5	18.5
27.5	H1a	22.40	2.35	(38)	15.60	(42)	7.10	6.69	10.72	(2)	76.7	48.1	28.8
30	H1a	20.15	2.42	(20)	17.47	(59)	7.18	5.98	11.24	(0)	45.6	52.1	19.9
32.5	H1a	19.79	1.67	(23)	15.40	(91)	4.48	4.86	7.95	(0)	26.3	34.6	18.2
35	H1a	25.40	2.15	(30)	16.63	(54)	5.56	6.82	10.91	(1)	31.7	49.0	26.3
37.5	H1a	22.52	1.97	(21)	16.02	(80)	5.08	6.37	9.98	(0)	33.2	44.7	19.8
40	H1a	18.18	2.07	(28)	15.41	(37)	4.72	6.18	9.98	(0)	27.5	46.3	23.5
42.5	H1a	22.12	2.62	(25)	17.63	<500	6.85	7.09	12.86	(0)	(22)	55.9	17.5
45	H1a	**21.62**	**2.52**	**(30)**	**18.01**	**(50)**	**7.06**	**7.19**	**12.28**	**(0)**	**(22)**	**55.5**	**21.3**
47.5	H1a	22.33	2.63	(25)	17.90	(41)	6.47	7.31	13.13	(0)	(23)	59.9	21.1
51	H1a	17.25	1.84	(22)	17.61	(126)	3.39	5.20	9.15	(0)	35.2	39.9	13.7
52.5	H1a	15.17	2.17	(34)	13.94	(52)	6.26	5.57	10.12	(0)	(19)	46.3	20.3
55	H1	19.45	2.79	(36)	15.40	(56)	7.31	6.56	12.72	(1)	33.7	58.3	27.5
56	H1	11.06	1.77	(47)	9.01	(76)	3.20	4.09	5.74	(1)	(21)	26.8	14.6
60	H1	28.12	0.03	379	28.04	(145)	13.61	10.05	51.55	<10	(7)	176	44.9
67.5	H2	16.36	3.03	103	10.67	(154)	8.21	4.69	12.62	(1)	109	56.8	15.3
76	H2	16.34	2.79	75.1	10.51	(81)	10.64	4.01	14.10	(0)	59.7	58.7	16.4
96	H2	**23.18**	**4.29**	**(27)**	**9.95**	**(139)**	**11.20**	**5.93**	**19.17**	**(0)**	**(18)**	**85.6**	**26.7**
111	H2	22.41	3.93	(14)	11.51	(67)	9.01	5.66	17.85	(0)	(11)	79.7	30.1
115	H2	24.33	4.15	(26)	10.23	(51)	6.75	5.49	18.50	(3)	33.1	85.4	35.5
116	H2	17.48	2.14	308	14.43	(257)	4.05	2.66	10.45	(2)	98.6	46.1	25.8
130	PPlz	18.37	4.03	(29)	9.96	(78)	4.13	3.78	16.15	(2)	(19)	71.8	28.6
135	PPlz	20.96	4.61	(13)	10.58	(179)	7.07	4.72	15.73	(0)	(12)	70.3	28.7
140	PPlc	17.01	3.51	277	14.99	(131)	6.16	3.04	11.41	(3)	117	57.4	34.0
141	PPlc	**20.13**	**5.28**	**(20)**	**21.56**	**(33)**	**8.93**	**4.71**	**17.09**	**(0)**	**(13)**	**82.9**	**22.7**
150.5	Rtf	17.33	3.31	370	13.81	(129)	3.87	4.63	10.44	15.2	352	59.6	15.3
160.5	Rtf	10.02	2.33	(38)	13.98	(88)	1.52	3.60	8.41	(2)	(24)	40.5	16.8
174	Rtf	6.69	0.90	106	13.81	(123)	1.13	2.20	2.98	(2)	44.7	(14)	(5)

Note: Values in parenthesis are just below level of quantification but spectra looked good; thus, a tentative value was attributed to data. Data in **bold** are the average of duplicate extractions.

Table B.23. Trace Metals in 1:1 Water Extracts of Borehole 299-W22-48 Sediments

Units (ft bgs)	B (µg/L)	Cr* (µg/L)	Co (µg/L)	Ni (µg/L)	Cu (µg/L)	Zn (µg/L)	As* (µg/L)	Se* (µg/L)	Mo* (µg/L)	Tc* (µg/L)	Pb* (µg/L)	U* (µg/L)
29.5-H1a	(8)	(0.32)	<10	<100	<25	30.9	37.5	(0.69)	3.97	(0.00)	(0.16)	2.84
32.0-H1a	(3)	(0.37)	1.4	<100	<25	15.0	32.1	(0.15)	2.35	(0.00)	(0.03)	1.47
39.5-H1a	(0)	(0.39)	<10	<100	<25	22.7	21.6	(1.06)	4.81	(0.00)	(0.29)	1.76
47.0-H1	<100	(0.19)	1.1	<100	<25	22.3	9.45	(0.29)	1.20	(0.00)	(0.25)	0.530
56.0-H1	(4)	(0.07)	1.0	<100	<25	16.3	9.52	(0.23)	11.35	(0.00)	(0.16)	1.47
74.5-H2	**(6)**	**0.470**	**<10**	**<100**	**<25**	**23.1**	**21.6**	**(0.65)**	**7.08**	**(0.00)**	**(0.18)**	**0.430**
91.5-H2	2003	0.551	1.3	<100	<25	15.7	22.5	(3.84)	17.64	(0.00)		0.455
101.5-H2	1996	0.985	<10	<100	<25	20.0	19.2	5.77	24.2	<0.025		0.430
106.5-H2	(6)	0.530	<10	<100	<25	24.5	17.1	(2.25)	12.1	(0.00)	(0.22)	0.375
115.5-H2	(10)	0.940	1.8	<100	(0)	26.9	21.2	(3.15)	10.6	(0.00)	(0.31)	0.530
136.0-PPlz	(8)	0.665	1.5	<100	<25	44.1	26.4	12.9	9.5	(0.00)	(0.14)	0.510
143.5-PPlz	(7)	(0.21)	1.1	<100	<25	25.6	9.20	6.55	17.3	<0.025	(0.14)	0.970
146.0-PPlc	**(11)**	**1.86**	**1.4**	**<100**	**<25**	**29.3**	**8.44**	**36.50**	**57.2**	**(0.00)**	**(0.08)**	**7.90**
148.5-PPlc	(3)	0.690	<10	<100	<25	23.3	10.8	14.8	9.9	(0.00)	(0.75)	5.68
151.0-Rtf	(4)	(0.07)	0.9	<100	(2)	22.1	8.56	(3.22)	7.58	(0.00)	(0.04)	2.48
163.5-Rtf	<100	(0.05)	2.0	<100	<25	27.8	15.0	(2.67)	5.17	(0.00)	(0.01)	0.245
170.0-Rtf	(0)	(0.24)	0.0	<100	<25	86.8	12.4	(3.39)	5.99	<0.025	(0.22)	0.565
172.5-Rtf	(1)	(0.17)	2.2	<100	<25	23.8	10.6	(1.80)	6.94	(0.00)	(0.06)	0.920
187.0-Rtf	<100	(0.19)	1.4	<100	<25	26.3	6.31	4.25	3.54	(0.00)	(0.09)	0.000
192.0-Rwi(e)	(9)	(0.26)	0.8	<100	<25	96.7	6.80	5.78	7.14	<0.025	(0.13)	0.032

Note: Values in parenthesis are just below level of quantification but spectra looked good; thus, a tentative value was attributed to data. Data in **bold** are average of duplicate extractions.

*ICP-MS instrument was used.

Table B.24. Trace Metals in 1:1 Water Extracts of Samples for Borehole 299-W22-50

Depth (ft bgs)	Strat. Unit	B (µg/L)	Cr* (µg/L)	Co (µg/L)	Ni (µg/L)	Cu (µg/L)	Zn (µg/L)	As* (µg/L)	Se* (µg/L)	Mo* (µg/L)	Tc* (µg/L)	Pb* (µg/L)	U* (µg/L)
20	H1a	(8)	0.910	<10	(6)	(1)	30.3	39.3	<5	1.89	(0.00)	(0.35)	1.11
22.5	H1a	(6)	(0.31)	0.5	(6)	(2)	41.4	34.4	<5	4.81	(0.00)	(0.28)	1.73
25	H1a	(4)	(0.28)	<10	(4)	(1)	48.8	41.3	(0.02)	3.52	(0.00)	(0.84)	1.55
27.5	H1a	(3)	(0.47)	0.1	(2)	(1)	33.6	34.0	(0.14)	6.57	(0.00)	(0.13)	1.44
30	H1a	(5)	(0.32)	<10	(3)	(2)	31.5	13.5	(0.27)	1.62	(0.00)	(0.09)	0.805
32.5	H1a	(3)	(0.41)	0.4	(3)	(1)	30.8	27.0	(0.24)	2.12	(0.00)	(0.01)	1.61
35	H1a	(2)	0.510	0.0	(2)	(1)	31.3	24.3	(0.28)	9.68	(0.00)	(0.03)	2.08
37.5	H1a	(3)	0.625	<10	(2)	(3)	28.6	22.8	(0.21)	12.8	(0.00)	(0.25)	1.72
40	H1a	(4)	0.535	<10	(3)	(1)	42.4	10.1	(0.07)	4.32	(0.00)	(0.02)	1.07
42.5	H1a	(6)	0.590	<10	(4)	(1)	46.7	11.5	(0.17)	6.74	(0.00)	(0.00)	1.15
45	H1a	**(5)**	**(0.49)**	**<10**	**(2)**	**(3)**	**35.2**	**13.2**	**(0.58)**	**6.05**	**(0.00)**	**(0.22)**	**1.15**
47.5	H1a	(5)	(0.49)	<10	(3)	(1)	29.8	11.2	(0.13)	12.54	<0.02	(0.08)	1.21
51	H1a	(0)	(0.39)	<10	(3)	(0)	26.7	12.4	(0.18)	1.03	(0.00)	(0.00)	0.710
52.5	H1a	(2)	(0.32)	<10	(3)	<25	34.8	9.60	(0.50)	3.35	(0.00)	(0.25)	0.565
55	H1	(4)	(0.48)	<10	(4)	(2)	26.9	7.09	(0.31)	14.9	(0.00)	(0.02)	0.820
56	H1	<100	(0.15)	<10	(2)	<25	33.3	9.16	(0.42)	2.81	(0.00)	(0.02)	0.565
60	H1	(11)	48.8	<10	(2)	(3)	33.5	2.95	(0.66)	10.21	(0.00)	(0.02)	0.000
67.5	H2	(3)	0.715	<10	(4)	(2)	34.3	16.6	(0.66)	9.96	(0.00)	(0.21)	0.885
76	H2	(4)	0.760	<10	(4)	(0)	31.4	14.7	(1.14)	4.77	(0.00)	(0.14)	0.565
96	H2	**(11)**	**0.775**	**<10**	**(2)**	**<25**	**30.2**	**12.7**	**(1.22)**	**14.5**	**(0.00)**	**(0.10)**	**0.567**
111	H2	(12)	1.85	<10	(8)	(5)	27.7	13.8	(1.64)	20.2	(0.00)	(0.00)	0.615
115	H2	(14)	0.500	0.0	(6)	(4)	28.7	11.7	(3.40)	17.6	(0.00)	(0.05)	0.810
116	H2	2161	0.705	0.1	(3)	(4)	19.9	29.7	(1.43)	11.1	(0.00)		0.348
130	PPlz	(9)	(0.39)	<10	(3)	(4)	25.5	9.81	(3.12)	15.1	(0.00)	(0.02)	0.935
135	PPlz	(12)	1.65	<10	(5)	(3)	33.3	6.76	5.38	28.1	(0.00)	(0.07)	0.870
140	PPlc	2089	0.925	1.2	<100	(1)	21.1	9.51	(2.00)	25.7	(0.00)		0.975
141	PPlc	**(8)**	**0.725**	**<10**	**(4)**	**(3)**	**34.9**	**18.1**	**(3.14)**	**63.6**	**(0.00)**	**(0.17)**	**10.24**
150.5	Rtf	(5)	0.565	<10	(5)	(3)	31.4	3.61	(0.10)	8.23	(0.00)	(0.10)	0.775
160.5	Rtf	(5)	(0.29)	0.0	(6)	(4)	30.8	3.82	(0.95)	5.96	(0.00)	(0.04)	0.438
174	Rtf	(1)	0.610	<10	(5)	(5)	32.0	3.44	(3.41)	1.61	(0.00)	(0.24)	0.005

Note: Values in parenthesis are just below level of quantification but spectra looked good; thus, a tentative value was attributed to data. Data in **bold** are average of duplicate extractions.

*ICP-MS instrument was used.

B.6.0 S TANK FARM SHALLOW SOILS INVESTIGATION

A shallow soils investigation (Bratton et al. 2001a) was conducted in the S tank farm to address the source and extent of contamination associated with tank S-104, as well as other nearby locations that could have contributed to the identified vadose zone contamination. Cesium-137 had been reported in the vicinity of this tank (GJPO 1998) through the baseline spectral gamma logging program. Cesium-137 was noted at concentrations greater than the resolution capability of the 35% high-purity germanium tool used. Research into the history of 241-S-104 operations revealed that the tank was subjected to an overfill in 1965. After thorough review of the tanks' construction, a hypothesis was developed that proposed that when the tank was overfilled, the resulting moderate overpressurization caused tank wastes to exit the tank through one or more spare inlet ports. The location of the well shown by the spectral gamma logging to be contaminated is in close proximity to a bank of spare inlet ports at the four o'clock position on the tank. This hypothesis could be tested by collecting gamma distribution data near the tank wall at this position.

A gamma tool deployed via a cone penetrometer was selected as the preferred method of collecting data. The cone penetrometer can be rapidly pushed to the depth of the tank farm excavation, gross gamma data collected as the cone is advanced and spectral gamma analysis could be run to determine those contaminants contributing to the gross gamma signature. Gamma spectra were obtained during this deployment, but are not reported due to the limited window of concentration that can be defined (Bratton et al. 2001b). Finally, it would be feasible to attempt collecting samples should threshold sampling criteria be met.

Eight locations (Figure B.29) were selected to be characterized. These locations were screened for underground utilities using ground-penetrating radar. These ground-penetrating radar screens revealed that the primary site was in close proximity to a shallow electrical service. This site was hand excavated to reveal the true location of the electrical service and then an elongate area demarked through which the cone penetrometer was deployed.

B.6.1 GEOLOGY

The investigation only went through the backfill material. See Appendix C, Section C.4.0 for a description of the backfill.

B.6.2 GEOPHYSICAL AND PHYSICAL PROPERTY MEASUREMENTS

Three locations (CP-04-03, CP-04-04, and CP-04-05) showed gross gamma signatures (Bratton et al. 2001a). Two of these locations (CP-04-04 and CP-04-05) show a bimodal distribution of gross gamma counts (Figures B.30 and B.31). The lowermost zone of high counts, present at all three locations, resides at the base of the tank farm excavation from 12.2 to 13.7 m (40 to 45 ft) bgs. Count rates in this zone ranged from 60,000 to 125,000 counts per second resulting in an instrument dead time exceeding 90%. The upper zone resides between 8.8 and 9.8 m (28.75 and 32 ft) bgs, well above and separated from the base of the excavation. The highest count rates in these two zones were 15,000 and 80,000 counts per second.

Figure B.29. Cone Penetrometer Test Locations in the S Tank Farm

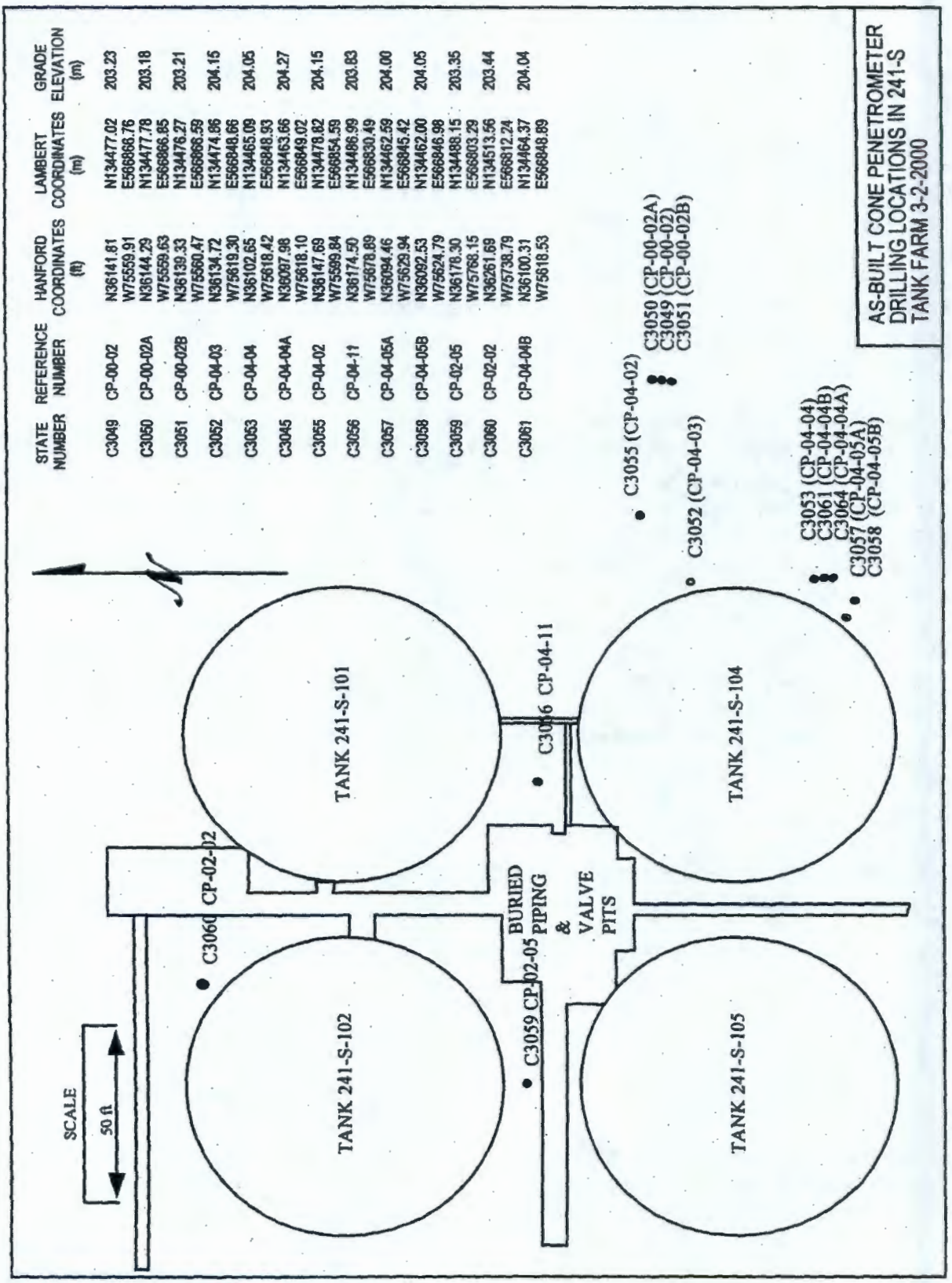

Figure B.30. Distribution of Gross Gamma Concentrations at Location CP-04-04 Down to 50 ft (16 m) Below Ground Surface

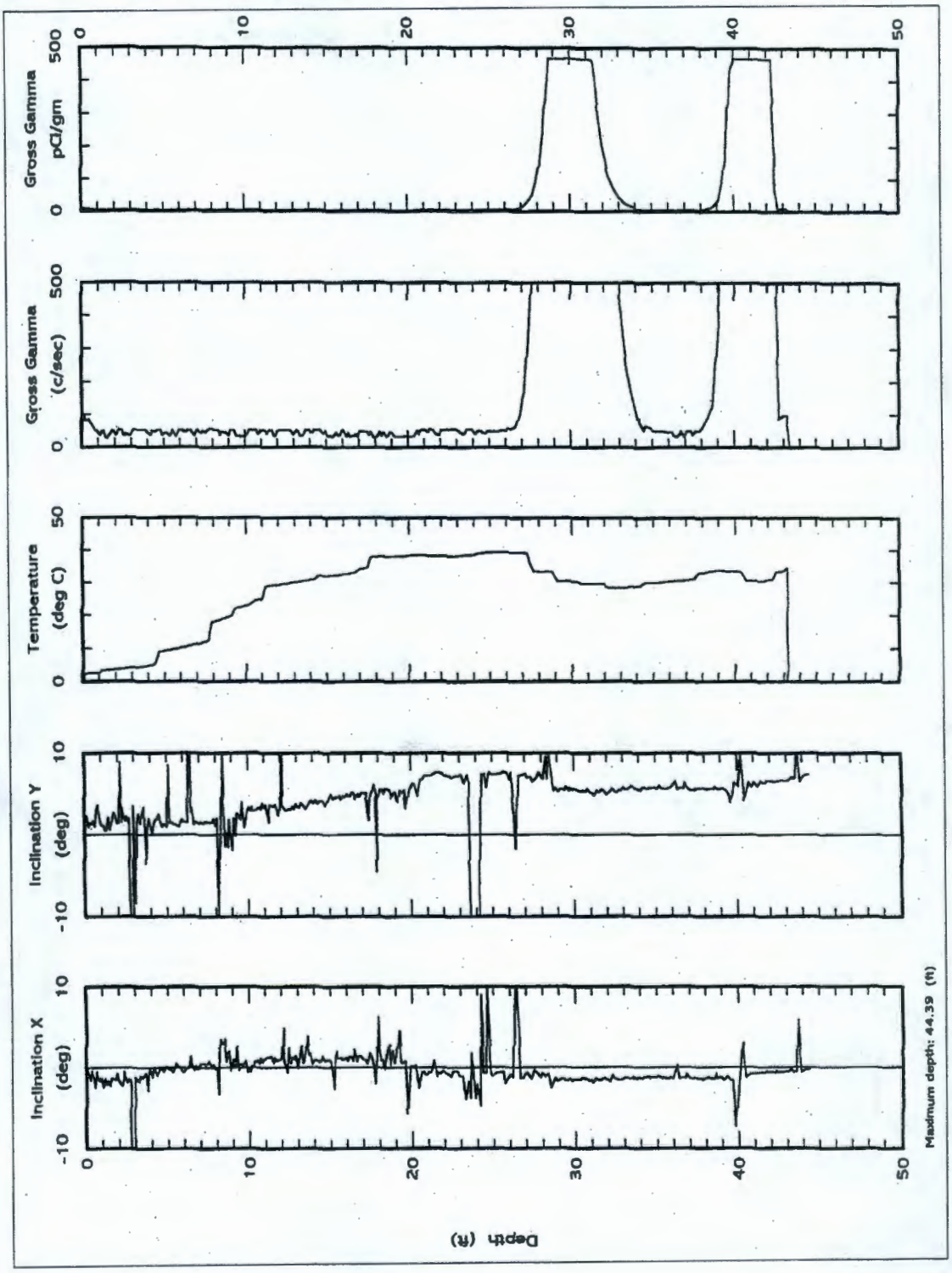

Figure B.31. Distribution of Gross Gamma Concentrations at Location CP-04-05 Down to 50 ft (16 m) Below Ground Surface

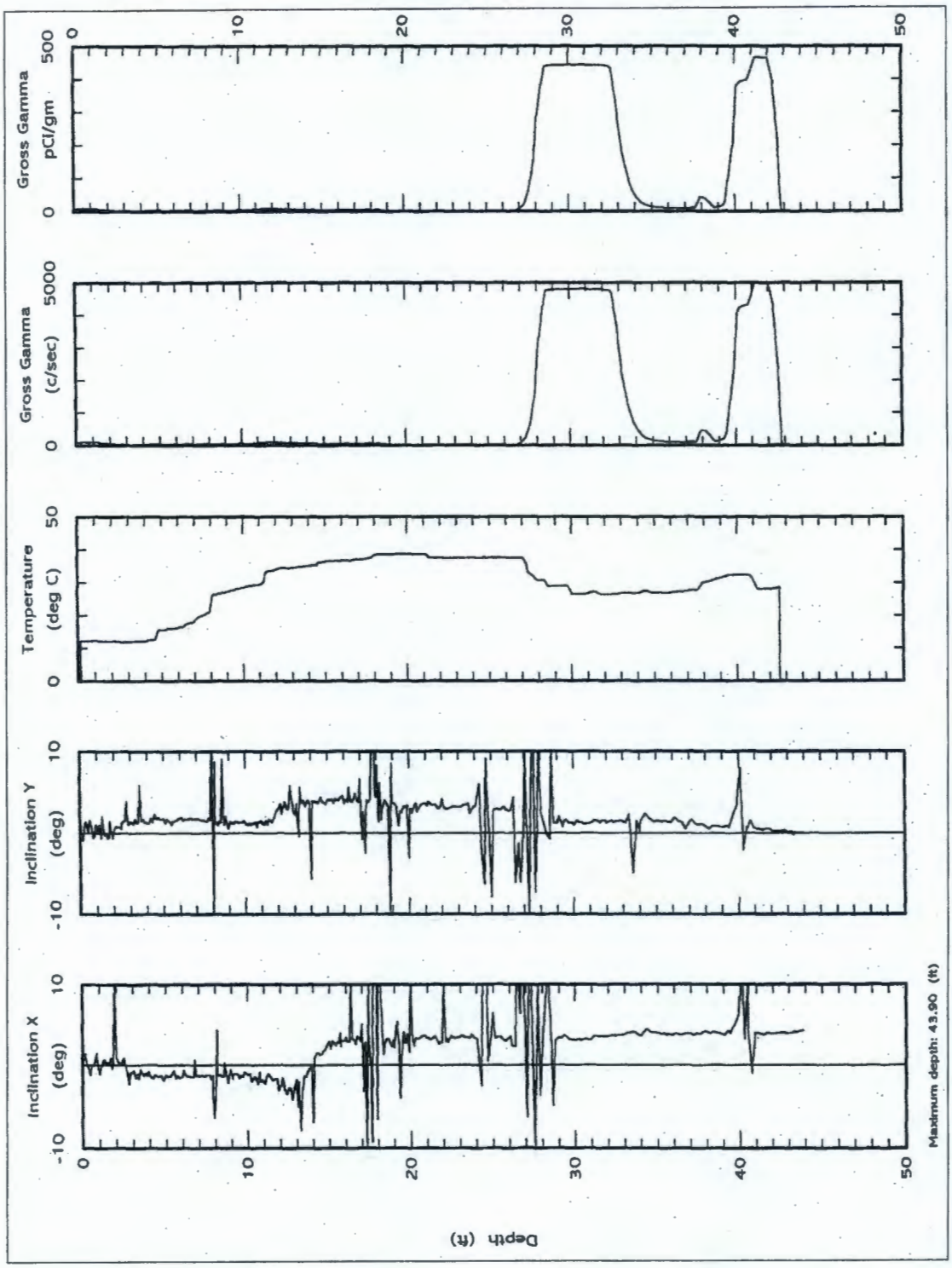

Samples were collected from immediately below the upper zones of contamination and submitted for laboratory analysis. Because the spectral gamma mode analysis of these portions of the holes did not show a characteristic peak for cesium, the possibility of strontium-90 based Brehmsstrahlung-induced peaks were hypothesized. Laboratory analysis of recovered samples showed no contamination. No samples were collected from the highly contaminated lower zones to preclude contamination of people and equipment during recovery.

B.6.2.1 Interpretation of Results Measurements

Each of the cone penetrations was extended to refusal. The majority of the pushes were within the S tank farm excavation. Pushes CP-00-02, -02A and -02B were outside the farm excavation as evidenced by the limited depth to refusal (Table B.25). The base of the farm in all areas investigated is a compacted surface, likely due to extended vehicular compaction during the construction process. (Construction specifications HW-3937, indicate that the zone under the tanks was likely not mechanically compacted prior to placement of the tank bases.)

The compacted portions of the tank farm excavation provide a surface upon which tank derived fluids would spread. Evidence supporting this interpretation is the high count rate materials found in CP-03, -04 and -05 locations in the range of 12.2 to 13.7 m (40 to 45 ft) bgs. The full volume of impacted sediments could not be determined due to the limited depth that could be interrogated. It is probable that contamination resulting from an overfill would also extend beneath the tank.

Two push locations, CP-04 and CP-05, where a high gamma signature was found above the base of the excavation at 9.2 and 9.1 m (30.25 and 29.75 ft) bgs, respectively, support the hypothesis that this S tank farm contamination is due to an overfill of tank S-104. Limitations on how close to a tank wall a mechanized excavation can be performed severely impact full resolution of this leak hypothesis. Figure B.32 is a conceptualization of the extent of contamination associated with tank S-104.

B.6.2.2 Estimate of Inventory Based on Measurements

It was necessary to make a number of assumptions to estimate the possible inventory held in the vadose zone beneath tank S-104. The following outline those assumptions.

- **Extent of contamination** – The contaminants are symmetrically dispersed about the hypothesized source in a circle that is an approximately 12 m (39 ft) radius.
- **Depth of contamination** – Total thickness is 0.3 m (1 ft) based on the depth of greater than 10^6 pCi/g cesium concentration that is cited in GJPO (2000).
- **Concentration** – The maximum concentration reported for borehole 40-04-05 (GJPO 2000), which is 2.0×10^6 pCi/g
- **Soil Density** – Throughout subject area is assumed to be 1.8 g/cc.

Table B.25. Summary of Data from Gamma Cone Penetrometers in the S Tank Farm

Location/ Well #	Final Depth (ft)	Cone Datafile	Spectrum Datafile	Spectrum Depth (ft)	Counts/ sec	Sample Depth
CP-00-02 C3049	33.01	527J0001C.DAT				
CP-00-02A C3050	8.10	528J0002C.DAT	28JANB.CHN 28JANC.CHN 28JAND.CHN 28JANE.CHN 28JANF.CHN	1.05 2.05 3.85 5.35 6.85	60 60 45 45 45	
CP-00-02B C3051	15.00	528J0003C.DAT	28JANI.CHN 28JANJ.CHN 28JANK.CHN 28JANL.CHN 28JANM.CHN	1.13 2.55 4.05 5.55 6.75	45 45 45 45 45	
CP-04-03 C3052	46.35	531J0001C.DAT	31JANB.CHN 31JANC.CHN 31JAND.CHN 31JAN3.CHN	43.25 43.65 44.05 45.15	500 2,000 12,000 180,000	
CP-04-04 C3053	44.40	501F0001C.DAT	01FEBB.CHN 01FEBC.CHN 01FEBD.CHN 01FEBE.CHN 01FEBF.CHN 01FEBG.CHN	27.25 28.75 30.25 31.75 38.75 40.25	300 8,700 15,000 2,200 320 60,000	31.75-33.75 28.75-30.70
CP-04-02 C3055	47.02	502F0003C.DAT				
CP-04-11 C3056	50.74	503F0001C.DAT				
CP-04-05 C3057	43.95	503F0004C.DAT	03FEBD.CHN 03FEBE.CHN 03FEBF.CHN 03FEBG.CHN 03FEBH.CHN 03FEBI.CHN 03FEBJ.CHN 03FEBK.CHN	27.05 28.25 29.75 31.25 32.75 34.25 39.25 40.75	450 9,000 80,000 35,000 3,500 300 350 125,000	31.25-33.75
CP-02-05 C3059	39.5	507F0003C.DAT				
CP-02-02 C3060	42.9	508F0001C.DAT				

Figure B.32. Estimated Extent of Shallow Contamination Zone Down to 50 ft (16 m) Below Ground Surface Near Tank S-104

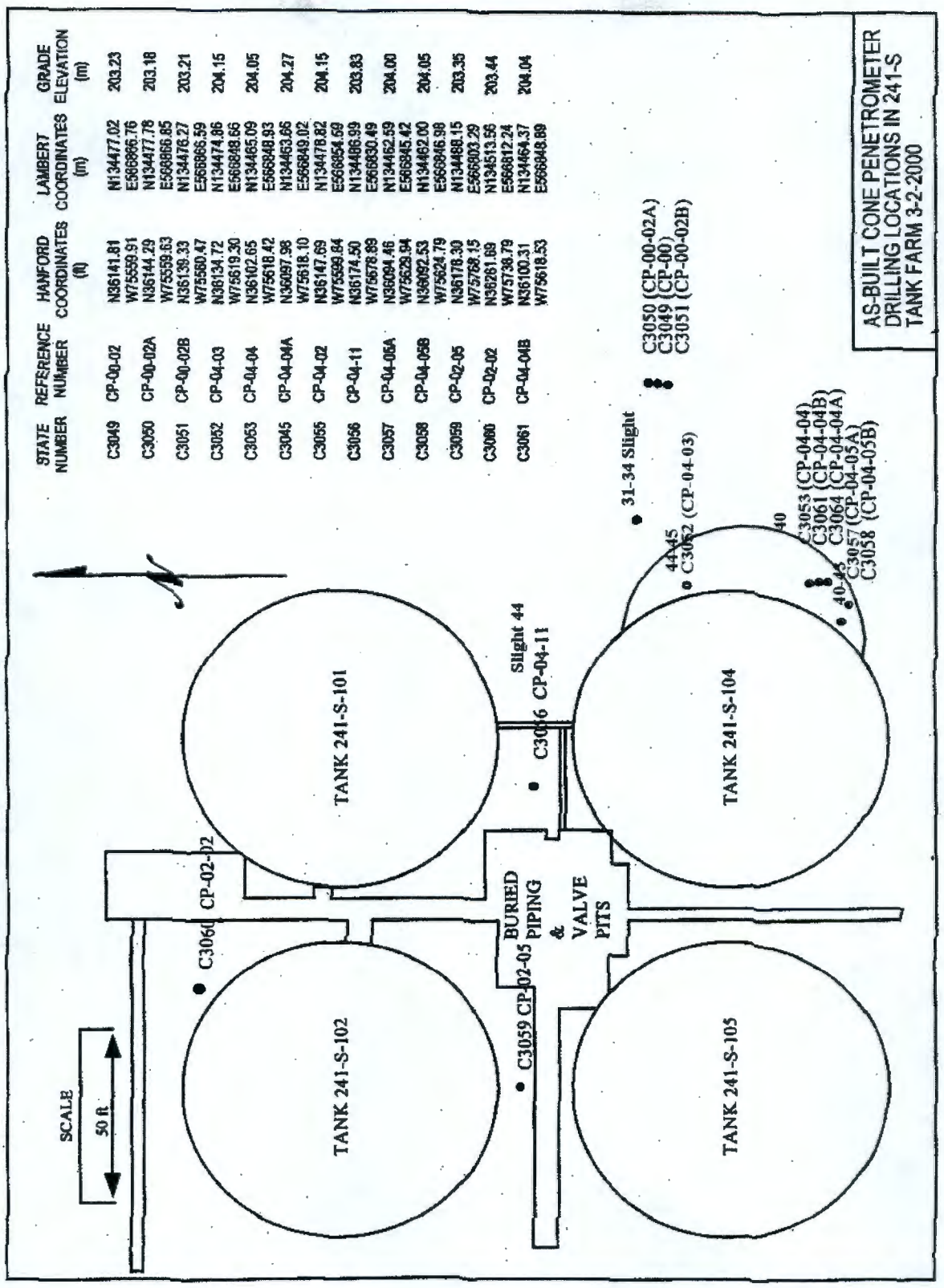

Based on this gross calculation, approximately 500 curies of cesium-137 would be included in the plume. The total inventory of cesium-137 calculated by MACTEC-ERS (GJPO 2000) is about 10 curies. Neither of these inventory estimates supports the reported 91,000 L (24,000 gal) leak (Hanlon 2001). Based on Jones et al. (2000) the cesium-137 inventory that would result from the reported 91,000 L (24,000 gal) loss would be approximately 1.14×10^4 Ci.

B.6.3 SOIL WATER CHEMISTRY MEASUREMENTS

Soil water chemistry measurements were not taken during the S tank farm shallow soils investigation.

B.6.4 CHEMICAL INTERACTIONS

Chemical interactions were not analyzed during the S tank farm shallow soils investigation.

B.6.5 GROUNDWATER MEASUREMENTS

Groundwater measurements were not applicable to the S tank farm shallow soils investigation.

B.7.0 REFERENCES

Bratton, W. L., W. C. Dickerson, and T. J. Hazon, 2001a, *Cone Penetrometer Tests with Gross and Spectral Gamma at the S-Tank Farm, 200 West Area, Hanford Site, Richland, Washington*, RPP-6108, Applied Research Associates Inc., Richland, Washington.

Bratton, W. L. and W. E. Dickerson, 2001b, *Calibration of the Cone Penetrometer Gamma Probe*, RPP-7547, Applied Research Associates, Richland, Washington.

Gardner, M. G., and K. D. Reynolds, 2000, *SX-108 Slant Borehole Completion Report*, RPP-6917, Rev. 0, CH2M HILL Hanford Group, Inc., Richland, Washington.

General Electric Company, 1949, *Specifications HW-3937 Waste Disposal Facility 241-S and 207-S, 200 West Area*, HW-3937, General Electric Company, Richland, Washington.

GJPO, 1998, *Hanford Tank Farms Vadose Zone S Tank Farm Report*, GJO-97-31-TAR, U.S. Department of Energy, Albuquerque Operations Office and Grand Junction Project Office, Grand Junction, Colorado.

GJPO, 2000, *Hanford Tank Focus Vadose Zone Addendum to the S Tank Focus Report*, GJPO-97-31-TARA, GJPO-HAN-17, U.S. Department of Energy, Grand Junction Projects Office, Grand Junction, Colorado.

H-2-37985, 1974, *Civil North Section Contoured Excavation 241-SX Tank Farm*, Rev. 0, sheet 2 of 2, Kaiser Engineers Hanford, Richland, Washington.

Hanlon, B. M., 2001, *Waste Tank Summary Report for Month Ending March 31, 2001*, HNF-EP-0182, Rev. 156, CH2M HILL Hanford Group, Inc., Richland, Washington.

Johnson, V. G. and C. J. Chou, 2001, *RCRA Groundwater Quality Assessment Report for Waste Management Area S-SX (November 1997 through April 2000)*, PNNL-13441, Pacific Northwest National Laboratory, Richland, Washington.

Jones, T. E., R. A. Watrous, G. T. Maclean, 2000, *Inventory Estimates for Single-Shell Tank Leaks in S and SX Tank Farms*, RPP-6285, Rev. 0, CH2M HILL Hanford Group, Inc., Richland, Washington.

Lindsey, K. A., S. E. Kos, and K. D. Reynolds, 2000, *Vadose Zone Geology of Boreholes 299-W22-50 and 299-W23-19 S-SX Waste Management Area Hanford Site, South-Central Washington*, RPP-6149, Rev. 0, Daniel B. Stephens & Associates, Richland, Washington.

MACTEC-ERS, 1997, *Assessment of Log Data for Borehole 41-09-39 and Correlation with Borehole 41-09-04 in the SX Tank Farm*, GJO-97-4-TAR, March 1997, MACTEC-ERS, Grand Junction Office, Grand Junction, Colorado.

Myers, D. A., D. L. Parker, G. Gee, V. G. Johnson, G. V. Last, R. J. Serne, and D. J. Moak, 1998, *Findings of the Extension of Borehole 41-09-39, 241-SX Tank Farm*, HNF-2855, Lockheed Martin Hanford Company, Richland, Washington.

Resource Conservation and Recovery Act of 1976, Public Law 94-580, 90 Stat. 2795, 42 USC 901 et seq.

Serne, R. J., H. T. Schaef, B. N. Bjornstad, B. A. Williams, D. C. Lanigan, D. G. Horton, R. E. Clayton, V. L. LeGore, M. J. O'Hara, C. F. Brown, K. E. Parker, I. V. Kutnyakov, J. N. Serne, A. V. Mitroshkov, G. V. Last, S. C. Smith, C. W. Lindenmeier, J. M. Zachara, and D. B. Burke, 2001a, *Characterization of Uncontaminated Sediments from the Hanford Reservation-RCRA Borehole Core and Composite Samples,* PNNL-2001-1, Pacific Northwest National Laboratory, Richland, Washington.

Serne, R. J., G. V. Last, G. W. Gee, H. T. Schaef, D. C. Lanigan, C. W. Lindenmeier, R. E. Clayton, V. L. LeGore, R. D. Orr, M. J. O'Hara, C. F. Brown, D. B. Burke, A. T. Owen, I. V. Kutnyakov, T. C. Wilson, and D. A. Myers, 2001b, *Geologic and Geochemical Data Collected from Vadose Zone Sediments from Borehole SX 41-09-39 in the S/SX Waste Management Area and Preliminary Interpretations*, PNNL-2001-2, Pacific Northwest National Laboratory, Richland, Washington.

Serne, R. J., H. T. Schaef, B. N. Bjornstad, D. C. Lanigan, G. W. Gee, C. W. Lindenmeier, R. E. Clayton, V. L. LeGore, R. D. Orr, M. J. O'Hara, C. F. Brown, G. V. Last, I. V. Kutnyakov, D. B. Burke, T. C. Wilson, and B. A. Williams, 2001c, *Geologic and Geochemical Data Collected from Vadose Zone Sediments from Borehole 299-W23-19 [SX-115] in the S/SX Waste Management Area and Preliminary Interpretations*, PNNL-2001-3, Pacific Northwest National Laboratory, Richland, Washington.

Serne, R. J., H. T. Schaef, G. V. Last, D. C. Lanigan, C. W. Lindenmeier, C. C. Ainsworth, R. E. Clayton, V. L. LeGore, M. J. O'Hara, C. F. Brown, R. D. Orr, I. V. Kutnyakov, T. C. Wilson, K. B. Wagnon, B. A. Williams, and D. B. Burke, 2001d, *Geologic and Geochemical Data Collected from Vadose Zone Sediments from Slant Borehole [SX-108] in the S/SX Waste Management Area and Preliminary Interpretations*, PNNL-2001-4, Pacific Northwest National Laboratory, Richland, Washington.

Sobczyk, S. M., 2000, *Subsurface Interpretation of the SX Tank Farm Hanford Site, Washington Based on Gamma Ray Logging*, Nez Pierce ERWM Program, Lapwai, Idaho.

APPENDIX C

NON-WORK PLAN SPECIFIC WORK AND ASSOCIATED RESULTS

This page intentionally left blank.

CONTENTS

FIGURES

TABLES

LIST OF TERMS

bgs	below ground surface
ESP	Environmental Simulation Program
HDW	Hanford defined waste (model)
HGL	HydroGeologic, Inc.
HLW	high-level waste
MSU	Montana State University
RCRA	*Resource Conservation and Recovery Act of 1976*
REDOX	reduction-oxidation
SST	single-shell tank
WMA	waste management area

C.1.0 INTRODUCTION

The work plan addenda associated with waste management area (WMA) S-SX were developed for the primary purpose of directing field work (Myers 1997; Henderson 1999; Rogers and Knepp 2000). During the course of conducting the identified field work, other activities were identified that would either complement or supplement that field work. Some 'projects-of-opportunity' that fit within the general scope of the Tank Farm Vadose Zone Project were undertaken. Included in this category were sampling and geological mapping associated with *Resource Conservation and Recovery Act of 1976* (RCRA) groundwater monitoring wells that were drilled to enhance or maintain the WMA S-SX groundwater monitoring program. Included are the data derived from the monitoring of well 299-W23-19 that was drilled to characterize the vadose zone but converted to a groundwater monitoring well due to the technetium-99 activity of the single sample identified in the work plan (Henderson 1999). Efforts to fully document the history of S and SX tank farm activities continued even though the majority of the information had been garnered for the subsurface conditions description report (Johnson et al. 1999).

As noted in Jones et al. (1998), determination of the contaminant inventory that was lost to the vadose zone is the most pressing need. This inventory was estimated using historical data and then revised based on the data gathered during the drilling of the characterization boreholes called out in the work plan addenda.

An effort to characterize the distribution of moisture in the southern portion of the SX tank farm was undertaken in an attempt to determine if pressurized water lines in that portion of the farm were a possible source of recharge. Those measurements added to the drive to cut-off unnecessary pressurized water lines leading to the tank farm. These measurements also added to the database used by the Science and Technology Program modeling effort reported in Appendix D.

Geochemical characterization of sediments collected from cores during construction of the RCRA groundwater monitoring wells provide a basis against which to judge the impact of tank waste lost to the environment.

Finally, data and analysis of the groundwater provide additional insight into the overall conceptual model of contaminant flow and transport through the vadose zone and into the unconfined aquifer.

C.2.0 TANK FARM HISTORY

Operating history of the S and SX tank farms was compiled and documented in Johnson et al. (1999). As work proceeded in conjunction with the various work plan addenda, that history was correlated with the new field data and the interpretations of that data. No additional incidents in the history of actual tank farm operations were identified.

Adjacent facilities and operations have been scrutinized in an attempt to further define the potential impact; some potentially important historic records could not be located. The most important of those records concern the inventory of technetium-99 disposed to the 216-S-25 trench during the U-1, U-2 pump-and-treat era. This pump-and-treat system used ion exchange columns to remove uranium from groundwater. The resins were used until uranium breakthrough occurred; this mode of operation ensured that technetium-99 was returned to the environment through the trench. The Hanford Environmental Information System was interrogated to ascertain the levels of technetium-99 in wells surrounding the 200-UP-1 and 200-UP-2 pump and treat operation. The values contained in Hanford Environmental Information System show technetium-99 to have been in the range of 3,000 to 4,000 pCi/L maximum.

C.3.0 LEAK INVENTORY ESTIMATES

The development of credible inventory estimates of chemicals and radionuclides lost to the WMA S-SX vadose zone represents a major component of the characterization activities. This inventory estimate provides both quantitative data for transport modeling and constrains the range of components that need be considered in the risk evaluation. The development of these estimates was based on an extensive review of historical records, previously developed methods for estimating tank waste compositions, extensive field investigation data, and statistical modeling of certain data sets. Highlights of these activities are discussed in Section 3.0 of the main text of this report. More extensive data tables are included in this section.

C.3.1 WASTE COMPOSITION ESTIMATES

There has long been an interest in using flowsheet data from various Hanford Site chemical processes coupled with waste transfer records to develop tank waste inventory estimates (Jungfleish 1984). Researchers at Los Alamos National Laboratory, supported by many individuals associated with the Hanford tank waste characterization program (Agnew 1997) brought the approach developed by Jungfleish to fruition. The Los Alamos National Laboratory task involved two major activities.

- The extensive waste transfer records were centralized into a single document, *Waste Status and Transfer Record Summary (WSTRS Rev. 4)* (Agnew et al. 1997).

- Flowsheet information was coupled with an understanding of the chemistry of each waste stream to develop estimates of solid and liquid compositions for each waste stream.

The composition of each major waste stream was coupled with the waste volumes for each of the transfers into and out of each Hanford Site waste tank. Using simple waste mixing rules for the sum of waste transfers through individual tanks, current waste compositions and total inventories were calculated for each Hanford Site waste tank. This approach is termed the Hanford defined waste (HDW) model (Agnew 1997). The HDW model develops two waste composition estimates:

- Sludge composition, estimated by the tank layering model
- Supernatant composition, estimated by the supernatant mixing model.

The waste composition estimates from the supernatant mixing model module are a combination of liquid and salt cake (Agnew 1997).

Although the driver for the HDW model was to develop 'current' tank inventory estimates, the HDW model provides the capability for developing inventory estimates at any point in time in each tank. As noted above, the HDW model results for selected SX tank farm high-heat tanks are used in Agnew and Corbin (1998) to develop the 'Hanford leak model,' which projects preliminary leak volume estimates for tanks SX-108, SX-109, SX-111, and SX-112. The Agnew and Corbin (1998) approach for developing tank composition estimates at specific points in time was used in estimating tank leak events in WMA S-SX (Jones et al. 2000a). Tables C.1 and C.2 list the waste composition estimates at the times tanks were suspected to have leaked for 10 tanks in the S and SX tank farms (for more details in the development of these tables see discussion in Jones et al. 2000a).

Table C.1. Summary of Chemical Tank Supernate/Salt Concentrations at Time of Leak (2 Sheets)

Tank	S-104	SX-107	SX-108	SX-109	SX-110	SX-111	SX-112	SX-113	SX-114	SX-115
Assumed Leak Date / Chemicals	1965 (mol/L)	Ave. 64-67 (mol/L)	Ave. 65-66 (mol/L)	Ave. 64-67 (mol/L)	1974 (mol/L)	1973 (mol/L)	1969 (mol/L)	1962 (mol/L)	1972 (mol/L)	1964 (mol/L)
Na	8.671E+00	1.873E+01	1.960E+01	1.519E+01	6.068E+00	5.310E+00	1.319E+01	7.982E+00	8.852E+00	3.593E+00
Al	1.556E+00	3.273E+00	3.361E+00	2.560E+00	7.336E-01	5.270E-01	2.167E+00	1.267E+00	9.692E-01	8.258E-01
Total Fe	3.543E-03	6.878E-03	7.209E-03	5.598E-03	4.216E-03	5.323E-03	3.542E-03	2.967E-03	7.436E-03	2.111E-03
Cr	1.647E-01	3.919E-01	4.128E-01	3.211E-01	6.793E-02	5.862E-02	2.065E-01	1.712E-01	1.015E-01	5.088E-02
Bi	8.951E-09	0.000E+00	0.000E+00	0.000E+00	1.139E-04	1.179E-04	6.395E-06	0.000E+00	1.475E-04	6.627E-08
La	2.205E-14	0.000E+00	0.000E+00	0.000E+00	8.532E-10	1.326E-09	1.575E-11	0.000E+00	1.720E-09	1.632E-13
Hg	3.541E-06	1.154E-07	1.966E-09	0.000E+00	1.518E-06	1.586E-06	1.006E-06	0.000E+00	1.864E-06	6.293E-06
Zr (as ZrO(OH)2)	8.935E-10	0.000E+00	0.000E+00	0.000E+00	1.953E-05	1.614E-05	6.383E-07	0.000E+00	1.959E-05	6.615E-09
Pb	5.666E-04	1.846E-05	3.146E-07	0.000E+00	2.093E-04	2.206E-04	1.596E-04	0.000E+00	2.569E-04	1.007E-03
Ni	3.101E-03	6.187E-03	6.488E-03	5.038E-03	2.012E-03	1.942E-03	3.187E-03	2.671E-03	3.005E-03	1.732E-03
Sr	0.000E+00	0.000E+00	0.000E+00	0.000E+00	0.000E+00	0.000E+00	0.000E+00	0.000E+00	0.000E+00	0.000E+00
Mn	6.515E-08	0.000E+00	0.000E+00	0.000E+00	2.254E-03	3.538E-03	4.655E-05	0.000E+00	4.565E-03	4.824E-07
Ca	1.595E-02	3.096E-02	3.245E-02	2.520E-02	1.012E-02	9.760E-03	1.594E-02	1.336E-02	1.505E-02	9.502E-03
K	3.069E-02	6.989E-02	7.386E-02	5.763E-02	2.632E-02	2.451E-02	5.094E-02	3.106E-02	3.951E-02	1.105E-02
Density (g/cc)	1.397E+00	1.840E+00	1.874E+00	1.674E+00	1.255E+00	1.218E+00	1.583E+00	1.349E+00	1.366E+00	1.181E+00
Void Frac.	0.000E+00	0.000E+00	0.000E+00	0.000E+00	0.000E+00	0.000E+00	0.000E+00	0.000E+00	0.000E+00	0.000E+00
wt.% H2O	5.153E+01	2.325E+01	2.089E+01	3.139E+01	6.465E+01	6.807E+01	3.815E+01	5.480E+01	5.276E+01	7.507E+01
TOC wt% C	8.391E-06	0.000E+00	0.000E+00	0.000E+00	2.959E-01	3.911E-01	5.289E-03	0.000E+00	4.950E-01	7.345E-05
free OH	0.000E+00	0.000E+00	0.000E+00	0.000E+00	0.000E+00	0.000E+00	0.000E+00	0.000E+00	0.000E+00	0.000E+00
OH	9.009E+00	1.980E+01	2.049E+01	1.571E+01	4.745E+00	3.510E+00	1.331E+01	7.968E+00	6.429E+00	4.171E+00
NO3	3.006E+00	4.891E+00	5.464E+00	4.485E+00	1.714E+00	1.534E+00	3.486E+00	2.818E+00	2.476E+00	1.197E+00
NO2	1.638E+00	4.485E+00	4.418E+00	3.225E+00	1.256E+00	1.131E+00	3.132E+00	1.336E+00	1.864E+00	7.840E-01
CO3	1.596E-02	3.096E-02	3.245E-02	2.520E-02	1.802E-01	2.263E-01	2.055E-02	1.336E-02	3.169E-01	9.550E-03

Table C.1. Summary of Chemical Tank Supernate/Salt Concentrations at Time of Leak (2 Sheets)

Tank	S-104	SX-107	SX-108	SX-109	SX-110	SX-111	SX-112	SX-113	SX-114	SX-115
Assumed Leak Date / Chemicals	1965 (mol/L)	Ave. 64-67 (mol/L)	Ave. 65-66 (mol/L)	Ave. 64-67 (mol/L)	1974 (mol/L)	1973 (mol/L)	1969 (mol/L)	1962 (mol/L)	1972 (mol/L)	1964 (mol/L)
PO4	5.792E-07	0.000E+00	0.000E+00	0.000E+00	1.140E-02	1.317E-02	4.138E-04	0.000E+00	1.791E-02	4.288E-06
SO4	3.206E-02	9.299E-02	9.229E-02	6.775E-02	9.641E-02	1.226E-01	6.646E-02	2.879E-02	1.714E-01	1.920E-02
Si (as SiO32-)	2.806E-02	9.803E-02	9.334E-02	6.561E-02	3.481E-02	3.425E-02	5.563E-02	2.229E-02	5.508E-02	1.279E-02
F	4.617E-07	0.000E+00	0.000E+00	0.000E+00	5.400E-03	5.272E-03	3.299E-04	0.000E+00	6.534E-03	3.418E-06
Cl	1.412E-01	3.215E-01	3.397E-01	2.651E-01	1.017E-01	8.848E-02	2.215E-01	1.429E-01	1.488E-01	5.071E-02
C6H5O7	4.771E-07	0.000E+00	0.000E+00	0.000E+00	1.810E-02	2.602E-02	3.408E-04	0.000E+00	3.548E-02	3.532E-06
EDTA	1.858E-08	0.000E+00	0.000E+00	0.000E+00	3.213E-04	4.655E-04	1.328E-05	0.000E+00	5.988E-04	1.376E-07
HEDTA	1.543E-08	0.000E+00	0.000E+00	0.000E+00	5.799E-04	9.256E-04	1.102E-05	0.000E+00	1.202E-03	1.142E-07
glycolate	6.734E-07	0.000E+00	0.000E+00	0.000E+00	3.077E-02	1.215E-02	4.811E-04	0.000E+00	3.811E-02	4.985E-06
acetate	6.989E-08	0.000E+00	0.000E+00	0.000E+00	2.233E-04	5.419E-05	4.993E-05	0.000E+00	3.255E-05	5.175E-07
oxalate	2.888E-14	0.000E+00	0.000E+00	0.000E+00	1.118E-09	1.738E-09	2.063E-11	0.000E+00	2.253E-09	2.138E-13
DBP	4.231E-07	0.000E+00	0.000E+00	0.000E+00	1.082E-02	1.686E-02	3.023E-04	0.000E+00	2.136E-02	3.133E-06
butanol	4.231E-07	0.000E+00	0.000E+00	0.000E+00	1.082E-02	1.686E-02	3.023E-04	0.000E+00	2.136E-02	3.133E-06
NH3	2.051E-02	1.122E-01	1.051E-01	7.226E-02	3.248E-02	3.205E-02	6.916E-02	2.123E-02	5.011E-02	1.305E-02
Fe(CN)6	0.000E+00	0.000E+00	0.000E+00	0.000E+00	0.000E+00	0.000E+00	0.000E+00	0.000E+00	0.000E+00	0.000E+00

Source: Jones et al. (2000a).

Note: This chart selects a single waste composition (from a single selected year or average of a range of years) for each tank that leaked. The objective is to provide the Tank Farm Vadose Zone Project with an unambiguous set of leak composition values. Data source is HDW model-SMM concentrations for selected tanks and for each year.

HDW = Hanford defined waste (model).
SMM = supernatant mixing model.
TOC = total organic compound.

Table C.2. Summary of Radionuclide Tank Supernate/Salt Concentrations at Time of Leak (3 Sheets)

Tank	S-104	SX-107	SX-108	SX-109	SX-110	SX-111	SX-112	SX-113	SX-114	SX-115
Assumed Leak Date / Radionuclides	1965 (Ci/L)	Ave. 64-67 (Ci/L)	Ave. 65-66 (Ci/L)	Ave. 64-67 (Ci/L)	1974 (Ci/L)	1973 (Ci/L)	1969 (Ci/L)	1962 (Ci/L)	1972 (Ci/L)	1964 (Ci/L)
H-3	7.812E-05	6.640E-04	6.013E-04	3.960E-04	1.661E-04	1.531E-04	4.208E-04	8.092E-05	2.548E-04	7.551E-05
C-14	6.059E-06	3.044E-05	2.876E-05	1.996E-05	2.218E-05	2.942E-05	2.028E-05	6.264E-06	4.091E-05	3.657E-06
Ni-59	7.660E-07	3.543E-06	3.373E-06	2.361E-06	1.201E-06	1.418E-06	1.712E-06	7.828E-07	2.078E-06	4.413E-07
Ni-63	7.157E-05	3.475E-04	3.291E-04	2.290E-04	1.186E-04	1.403E-04	1.675E-04	7.309E-05	2.053E-04	4.315E-05
Co-60	2.420E-06	3.097E-05	2.744E-05	1.755E-05	2.491E-05	3.360E-05	1.961E-05	2.473E-06	4.646E-05	3.550E-06
Se-79	1.287E-06	5.756E-06	5.507E-06	3.878E-06	1.904E-06	1.984E-06	3.275E-06	1.330E-06	3.107E-06	7.007E-07
Sr-90	4.961E-02	1.166E-01	1.225E-01	9.516E-02	5.514E-02	6.636E-02	6.020E-02	5.044E-02	9.720E-02	1.777E-02
Y-90	4.962E-02	1.166E-01	1.226E-01	9.519E-02	5.515E-02	6.638E-02	6.022E-02	5.046E-02	9.722E-02	1.777E-02
Zr-93	6.075E-06	2.853E-05	2.715E-05	1.900E-05	9.435E-06	9.899E-06	1.631E-05	6.278E-06	1.544E-05	3.455E-06
Nb-93m	4.963E-06	2.047E-05	1.977E-05	1.407E-05	6.690E-06	6.949E-06	1.154E-05	5.133E-06	1.090E-05	2.510E-06
Tc-99	4.247E-05	2.435E-04	2.272E-04	1.553E-04	1.593E-04	2.080E-04	1.602E-04	4.385E-05	2.912E-04	2.904E-05
Ru-106	1.820E-11	7.971E-09	6.766E-09	4.071E-09	4.222E-09	4.573E-09	4.831E-09	6.907E-12	7.089E-09	8.857E-10
Cd-113m	1.878E-05	1.334E-04	1.223E-04	8.175E-05	5.331E-05	5.863E-05	8.581E-05	1.935E-05	8.880E-05	1.570E-05
Sb-125	3.669E-06	1.158E-04	9.998E-05	6.166E-05	1.065E-04	1.452E-04	7.206E-05	3.631E-06	2.000E-04	1.307E-05
Sn-126	1.976E-06	8.667E-06	8.312E-06	5.868E-06	2.869E-06	2.979E-06	4.920E-06	2.044E-06	4.675E-06	1.054E-06
I-129	8.158E-08	4.604E-07	4.302E-07	2.945E-07	3.066E-07	4.016E-07	3.033E-07	8.423E-08	5.616E-07	5.496E-08
Cs-134	6.935E-08	7.004E-06	5.972E-06	3.617E-06	9.609E-07	4.299E-07	4.180E-06	6.248E-08	1.077E-06	7.764E-07
Cs-137	1.249E-01	8.378E-01	7.712E-01	5.185E-01	1.272E-01	5.765E-02	5.329E-01	1.288E-01	1.415E-01	9.885E-02
Ba-137m	1.182E-01	7.925E-01	7.296E-01	4.905E-01	1.204E-01	5.454E-02	5.042E-01	1.218E-01	1.339E-01	9.351E-02
Sm-151	4.591E-03	2.021E-02	1.937E-02	1.367E-02	6.685E-03	6.948E-03	1.148E-02	4.746E-03	1.090E-02	2.465E-03
Eu-152	4.539E-07	5.471E-06	4.860E-06	3.121E-06	2.014E-06	2.388E-06	2.600E-06	4.657E-07	3.527E-06	6.185E-07
Eu-154	5.843E-05	7.543E-04	6.680E-04	4.271E-04	3.916E-04	4.777E-04	4.733E-04	5.974E-05	6.919E-04	8.618E-05
Eu-155	2.150E-05	2.785E-04	2.466E-04	1.576E-04	1.160E-04	1.412E-04	1.323E-04	2.198E-05	2.057E-04	3.158E-05

Table C.2. Summary of Radionuclide Tank Supernate/Salt Concentrations at Time of Leak (3 Sheets)

Tank	S-104	SX-107	SX-108	SX-109	SX-110	SX-111	SX-112	SX-113	SX-114	SX-115
Assumed Leak Date / Radionuclides	1965 (Ci/L)	Ave. 64-67 (Ci/L)	Ave. 65-66 (Ci/L)	Ave. 64-67 (Ci/L)	1974 (Ci/L)	1973 (Ci/L)	1969 (Ci/L)	1962 (Ci/L)	1972 (Ci/L)	1964 (Ci/L)
Ra-226	8.936E-11	2.125E-10	2.235E-10	1.735E-10	6.432E-11	6.273E-11	1.098E-10	9.199E-11	1.017E-10	2.893E-11
Ra-228	2.064E-12	9.465E-15	8.319E-15	5.265E-15	1.060E-08	4.447E-09	1.474E-09	6.165E-16	3.049E-09	1.528E-11
Ac-227	5.177E-10	1.234E-09	1.298E-09	1.008E-09	3.845E-10	3.764E-10	6.374E-10	5.341E-10	5.958E-10	1.657E-10
Pa-231	1.917E-09	6.197E-09	6.190E-09	4.567E-09	1.971E-09	2.053E-09	3.381E-09	1.986E-09	3.134E-09	7.760E-10
Th-229	1.631E-13	6.367E-13	5.954E-13	4.081E-13	2.714E-10	1.442E-10	3.554E-11	1.176E-13	1.075E-10	4.400E-13
Th-232	2.767E-13	2.681E-14	2.351E-14	1.483E-14	9.589E-10	7.156E-10	1.965E-10	1.635E-15	6.976E-10	2.039E-12
U-232	4.198E-11	6.790E-11	6.427E-11	4.481E-11	1.125E-07	1.272E-07	1.496E-08	1.449E-11	1.092E-07	1.808E-10
U-233	8.080E-11	1.721E-12	1.715E-12	1.266E-12	4.326E-07	4.899E-07	5.718E-08	5.523E-13	4.218E-07	5.933E-10
U-234	4.484E-07	8.120E-07	8.406E-07	6.458E-07	3.239E-07	3.572E-07	5.165E-07	3.297E-07	5.050E-07	3.818E-07
U-235	1.894E-08	3.188E-08	3.357E-08	2.623E-08	1.314E-08	1.460E-08	2.051E-08	1.419E-08	2.065E-08	1.473E-08
U-236	1.063E-08	4.325E-08	3.908E-08	2.572E-08	1.186E-08	1.202E-08	2.506E-08	5.216E-09	1.755E-08	2.257E-08
U-238	4.340E-07	6.400E-07	6.979E-07	5.629E-07	3.227E-07	3.424E-07	4.263E-07	3.365E-07	4.740E-07	2.823E-07
U-Total (M)	5.463E-03	8.064E-03	8.792E-03	7.089E-03	3.662E-03	4.149E-03	5.314E-03	4.234E-03	5.818E-03	3.558E-03
Np-237	2.765E-07	9.534E-07	9.424E-07	6.878E-07	5.653E-07	7.119E-07	6.576E-07	2.846E-07	1.011E-06	1.256E-07
Pu-238	2.491E-07	1.221E-06	1.121E-06	7.521E-07	7.478E-07	9.538E-07	5.906E-07	1.840E-07	1.358E-06	3.270E-07
Pu-239	1.567E-05	3.012E-05	3.163E-05	2.461E-05	2.267E-05	3.027E-05	1.560E-05	1.313E-05	4.187E-05	9.276E-06
Pu-240	2.265E-06	5.382E-06	5.436E-06	4.069E-06	4.002E-06	5.309E-06	2.731E-06	1.879E-06	7.383E-06	1.552E-06
Pu-241	1.399E-05	6.011E-05	5.611E-05	3.844E-05	5.033E-05	6.614E-05	2.938E-05	1.105E-05	9.275E-05	1.469E-05
Pu-242	6.017E-11	3.360E-10	3.086E-10	2.071E-10	2.825E-10	3.669E-10	1.620E-10	5.068E-11	5.195E-10	5.893E-11
Pu-Total (g/L)	2.622E-04	5.089E-04	5.335E-04	4.142E-04	2.509E-04	3.001E-04	2.621E-04	2.196E-04	4.331E-04	1.562E-04
Am-241	2.168E-05	8.798E-05	8.515E-05	6.073E-05	3.039E-05	3.018E-05	4.951E-05	2.239E-05	4.863E-05	1.093E-05
Am-243	2.033E-10	3.430E-09	3.008E-09	1.898E-09	1.159E-09	9.826E-10	1.814E-09	2.094E-10	1.753E-09	3.769E-10
Cm-242	1.034E-08	2.514E-07	2.183E-07	1.358E-07	7.703E-08	9.701E-08	8.209E-08	1.071E-08	1.414E-07	2.676E-08

Table C.2. Summary of Radionuclide Tank Supernate/Salt Concentrations at Time of Leak (3 Sheets)

Tank	S-104	SX-107	SX-108	SX-109	SX-110	SX-111	SX-112	SX-113	SX-114	SX-115
Assumed Leak Date / Radionuclides	1965 (Ci/L)	Ave. 64-67 (Ci/L)	Ave. 65-66 (Ci/L)	Ave. 64-67 (Ci/L)	1974 (Ci/L)	1973 (Ci/L)	1969 (Ci/L)	1962 (Ci/L)	1972 (Ci/L)	1964 (Ci/L)
Cm-243	2.370E-10	2.490E-08	2.124E-08	1.288E-08	7.487E-09	9.285E-09	8.166E-09	2.455E-10	1.365E-08	2.598E-09
Cm-244	7.224E-09	2.482E-07	2.141E-07	1.319E-07	8.013E-08	9.639E-08	8.123E-08	7.484E-09	1.455E-07	2.621E-08

Note: This chart selects a single waste composition (from a single selected year or average of a range of years) for each tank that leaked.
Objective is to provide the Tank Farm Vadose Zone Project with an unambiguous set of leak composition values.
Data source (HDW model-SMM Concentrations for selected tanks and for each year).

HDW = Hanford defined waste (model).
SMM = supernatant mixing model.

Once developed, waste compositions can be coupled with leak volumes to develop specific leak inventory estimates. However, published leak volume estimates (Hanlon 2001) are highly uncertain for a number of the SX tank farm leaks (Jones et al. 2000a). Thus, it was necessary to use other data sources to develop leak volume estimates. This process is discussed in the following sections.

C.3.2 GAMMA LOGGING DATA

Since the early 1960s gamma logging data have been used as a secondary tank leak monitoring system (Isaacson and Gasper 1981). In practice, strategically placed shallow boreholes (24.4 to 45.7 m [80 to 150 ft] below ground surface [bgs]), called 'drywells,' were routinely monitored for changes in total gamma activity. Hence, the activity is known as gross gamma logging. Drywells were located approximately 3.1 m (10 ft) from the tanks and generally 4 to 8 drywells surrounded each 'active' tank (that is, leak monitoring concentrated on tanks currently being used to store liquid wastes). Tanks known to have leaked (e.g., tank SX-113) where all pumpable liquids had been removed, were not given high priority to be monitored for additional leakage. For additional leak monitoring capability, 10 of the 15 tanks in the SX tank farm had laterals (i.e., horizontal pipes radiating from a central caisson) installed approximately 3.0 m (10 ft) below the base of the tank. Except for tank SX-113, each tank had three laterals radiating from a nearby caisson. As the prototype for the laterals tank leak monitoring system, tank SX-113 had five laterals installed under it.

During the routine gamma logging program, changes in gamma activity in a borehole would suggest potential leakage from a nearby waste storage tank. Although the gross gamma logging data were stored electronically from 1974 to the end of the logging program in 1994, data comparisons within any specific drywell were restricted to short time intervals. Gross gamma logging data were treated as being of value only for 'real-time' leak monitoring of active single-shell tanks (SSTs).

As part of the WMA S-SX vadose zone characterization, historic gross gamma logging data are assessed in Myers (1999a), and Myers (1999b). Although the gamma logging instrumentation underwent major modifications (particularly the probes) over the 20 years of data collection, the data exhibited surprising reproducibility. The data analysis also provided useful information about the potential movement of gamma emitting radionuclides over the 20-year period.

The validity of gross gamma logging methodology as a tank leak detection system was critically evaluated in *A Scientific Basis for Establishing Dry-Well Monitoring Frequencies* (Isaacson and Gasper 1981). One of the conclusions from the evaluation was that the gross gamma data provided far more insight into the migration of radionuclides in the soil than it did about potential leaks in active tanks. With the passage of time and thus decay of the short-lived mobile gamma emitting radionuclides such as ruthenium-106, the 1981 conclusions are more valid than ever.

In 1994, a baseline spectral gamma-logging program was initiated to assess the nature and extent of gamma emitting radionuclides in the tank farms vadose zone (DOE-GJPO 1995a, 1995b, 1995c; DOE-RL 1996a) by using the unique radiation emitted to identify and quantify the radionuclides. Essentially all existing drywells within each tank farm were logged with a system

designed to provide specific isotopic composition of gamma emitting radionuclides. Baseline spectral gamma logging results were published for each tank farm. The gamma-logging probe selected for the initial logging runs became saturated at approximately 1,000 pCi/g of cesium-137. Thus, in the most highly contaminated zones, quantitative values were not determined. At a later date the highly contaminated zones were re-logged using a less sensitive probe and updated results were published in supplemental tank farm reports. Ninety-eight drywells were logged in the SX tank farm and results were published in *Vadose Zone Characterization Project at the Hanford Tank Farms, SX Tank Farm Report* (DOE-GJPO 1996) and its supplement, *Addendum to the SX Tank Farm Report* (DOE-GJPO 2000). Seventy-two drywells were logged in the S tank farm and results were published in DOE-GJPO (1998) and its supplement, *Addendum to the S Tank Farm Report* (DOE-GJO 2000).

The baseline spectral gamma-logging program has made major contributions to the current tank farm vadose zone characterization efforts. The main radionuclide found was cesium-137. Only very small amounts (i.e., a few pCi/g) of cobalt-60 and/or europium-154 were found in the S and SX tank farm drywells.

C.3.3 KRIGING ANALYSIS

The SX tank farm gamma logging and soil analysis data for cesium-137 represent 'point measurements' along a vertical, horizontal, or slant direction. The goal of kriging analysis of the cesium-137 data was to establish mathematically defensible inventory estimates associated with the gamma contamination around each tank in the SX farm. Two separate data analyses were conducted. The first, conducted by Professor Dan Goodman, Montana State University (MSU) beginning in 1998, combined gross gamma and spectral gamma logging data with soil analysis data from borehole 41-09-39 and historical soils data (Raymond and Shdo 1966) (Goodman 2000). The MSU results are referred to as 'MSU kriging results' in this document. The second statistical analysis of the SX tank farm cesium-137 data, conducted by HydroGeologic, Inc. (HGL) (Sullivan et al. 2001), began with the same data set as used by MSU but also included newly acquired soils analysis data from the SX-108 slant borehole (Serne 2001d) and the updated spectral gamma logging results (DOE-GJPO 2000b).

The MSU statistical analysis focused on two objectives.

- The gross gamma logging data were evaluated to establish calibration curves so as to use the gross gamma data to develop 'data patches' for the regions of the spectral gamma data set lost because of detector saturation in the initial spectral gamma logging.
- The resulting enhanced gamma logging-based cesium-137 data set was coupled with soils analysis data to develop cesium-137 inventory estimates for the regions around each tank in the SX farm.

The projected cesium-137 inventory estimate for each of tank in the SX tank farm is listed in Table C.3. Inventory estimates are reported at both the 50 and 95 percentiles.

Table C.3. SX Tank Farm Cesium-137 Inventory Estimates from Kriging Analyses

Tank	MSU 50% (pCi)	MSU 95% (pCi)	HGL 50% (pCi)
SX-101	9.1E+09	2.1E+10	2.3E+10
SX-102	0.0E+00	0.0E+00	1.5E+10
SX-103	0.0E+00	0.0E+00	2.1E+10
SX-104	2.7E+08	1.6E+09	7.7E+09
SX-105	5.5E+09	1.3E+10	1.3E+10
SX-106	0.0E+00	0.0E+00	5.9E+09
SX-107	8.0E+15	1.5E+16	4.2E+16
SX-108	1.4E+16	3.6E+16	3.9E+16
SX-109	7.2E+14	2.3E+15	1.6E+15
SX-110	2.0E+12	1.3E+13	7.5E+12
SX-111	2.3E+11	1.1E+12	2.3E+11
SX-112	1.8E+13	9.5E+13	2.9E+13
SX-113	0.0E+00	0.0E+00	6.4E+07
SX-114	0.0E+00	0.0E+00	1.9E+08
SX-115	N/R	N/R	1.1E+14

HGL = HydroGeologic, Inc.
MSU = Montana State University.
N/R = not reported.

The second kriging analysis was focused on understanding the impact of the addition of the cesium-137 soils analysis data from the SX-108 slant borehole investigation on the overall cesium-137 inventory estimate. Also included in the second kriging analysis were the updated spectral gamma logging data for cesium-137 from highly contaminated zones (DOE-GJPO 2000b). Thus, the data patches from historical gross gamma data developed by MSU for that kriging analysis were not required for the HGL kriging analysis.

The first step in any kriging process is the development of a variogram model. Vertical and horizontal correlation lengths are determined during the variogram analysis. Significantly different correlation lengths were reported between the two kriging analyses.

- MSU variogram analysis led to a horizontal correlation length of 8.2 m (26.9 ft) and a vertical correlation length of 3 m (10 ft)
- HGL variogram analysis led to horizontal and vertical correlation lengths of 15 m (49 ft) and 20 m (66 ft), respectively.

The practical result of longer correlation lengths is the projection of somewhat larger plume volumes with the existing data set.

There are a number of reasons for the large correlation lengths reported in the HGL kriging analysis (Sullivan et al. 2001). The most obvious reason is the addition of the cesium-137 concentrations along the SX-108 slant borehole, giving much better definition of the vertical contamination directly below tank SX-108. However, there were also differences in approach. The MSU variogram analysis treated all of the available data within the SX tank farm while the HGL variogram analysis focused on the area around tank SX-108. The decision to estimate correlation lengths using data only from around tank SX-108 focused the analysis in the area where the maximum amount of data was available. The correlation lengths derived from the analysis of data around tank SX-108 were then used in the kriging analysis for all of the SX tank farm data. The intent was to apply the knowledge gained from detailed field investigations around tank SX-108 to the contamination found around and under other SX farm tanks.

This was justified because very similar waste types leaked from all failed SX farm tanks and the geology was assumed reasonably similar across the SX tank farm. The HGL kriging analysis also reports results of sensitivity studies associated with data processing decisions.

The cesium-137 inventory estimates developed in the HGL kriging analysis are also listed by tank in Table C.3. An example of the graphical representation of cesium-137 activity generated in the HGL kriging analysis is shown in Figures C.1 through C.7. This series of figures provide a graphical representation of the projected cesium-137 contamination as a function of activity levels.

The comparison between projected cesium-137 inventory estimates for each tank in the SX tank farm is shown in Figure C.8.

There are subjective decisions that are made in any statistical analysis involving large and diverse data sets such as those reported here where data compression is required. The HGL kriging analysis explored potential impacts of these decisions on reported results. The HGL analysis results are discussed briefly in the following paragraphs.

Both kriging analyses were forced to reduce the size of the data set prior to computations because the data set was too large to be processed with available computer systems. Both groups separated the tank farm area into a 1 m by 1 m grid size. MSU used a 1 m depth to form 1 m^3 sections. The geometric mean of all cesium-137 concentration values with the 1 m^3 was assigned to the center of the cube. The variogram analysis and kriging were completed with this reduced data set. The HGL data process approach was quite similar except the grid size was 1 m (3 ft) by 1 m (3 ft) by 0.5 m (1.5 ft) depth.

The geometric mean is commonly used as an approach for compressing large environmental data sets, where values span multiple orders of magnitudes (e.g., HGL data in the SX tank farm). However, other approaches could be taken. For example, a more conservative approach would be to assign the data value of the volume space as the maximum value reported within that grid volume. Or, one might chose to use the arithmetic mean. Results of the three data compression alternatives are shown in Figure C.9 for tank SX-107. A more detailed comparison between 'geometric mean' and 'maximum' values for all SX farm tanks are shown in Tables C.4 and C.5 (Sullivan et al. 2001).

Figure C.1. Three-Dimensional Perspective of Cesium-137 Contaminated Soil Above 5×10^1 pCi/g

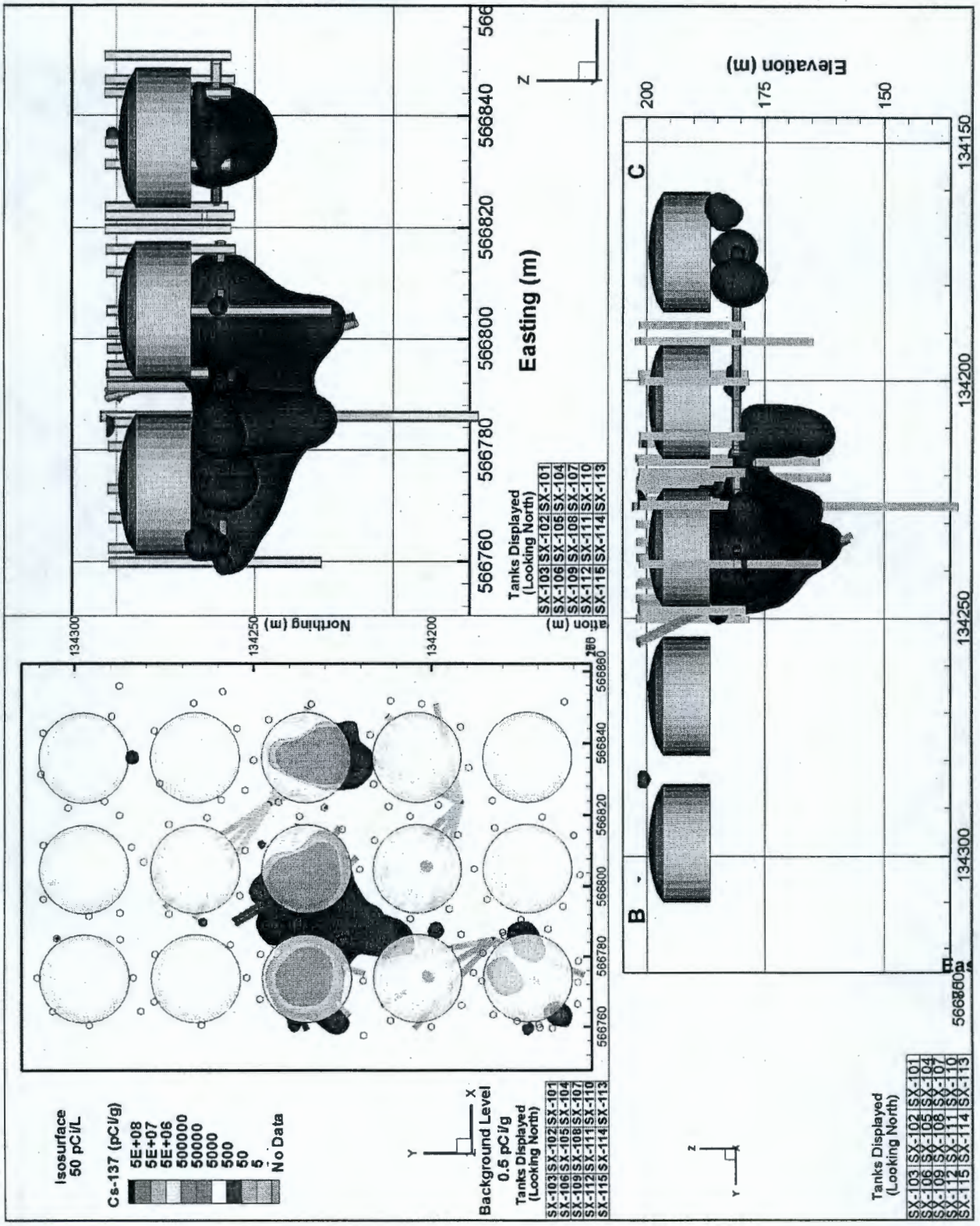

Figure C.2. Three-Dimensional Perspective of Cesium-137 Contaminated Soil Above 5×10^2 pCi/g

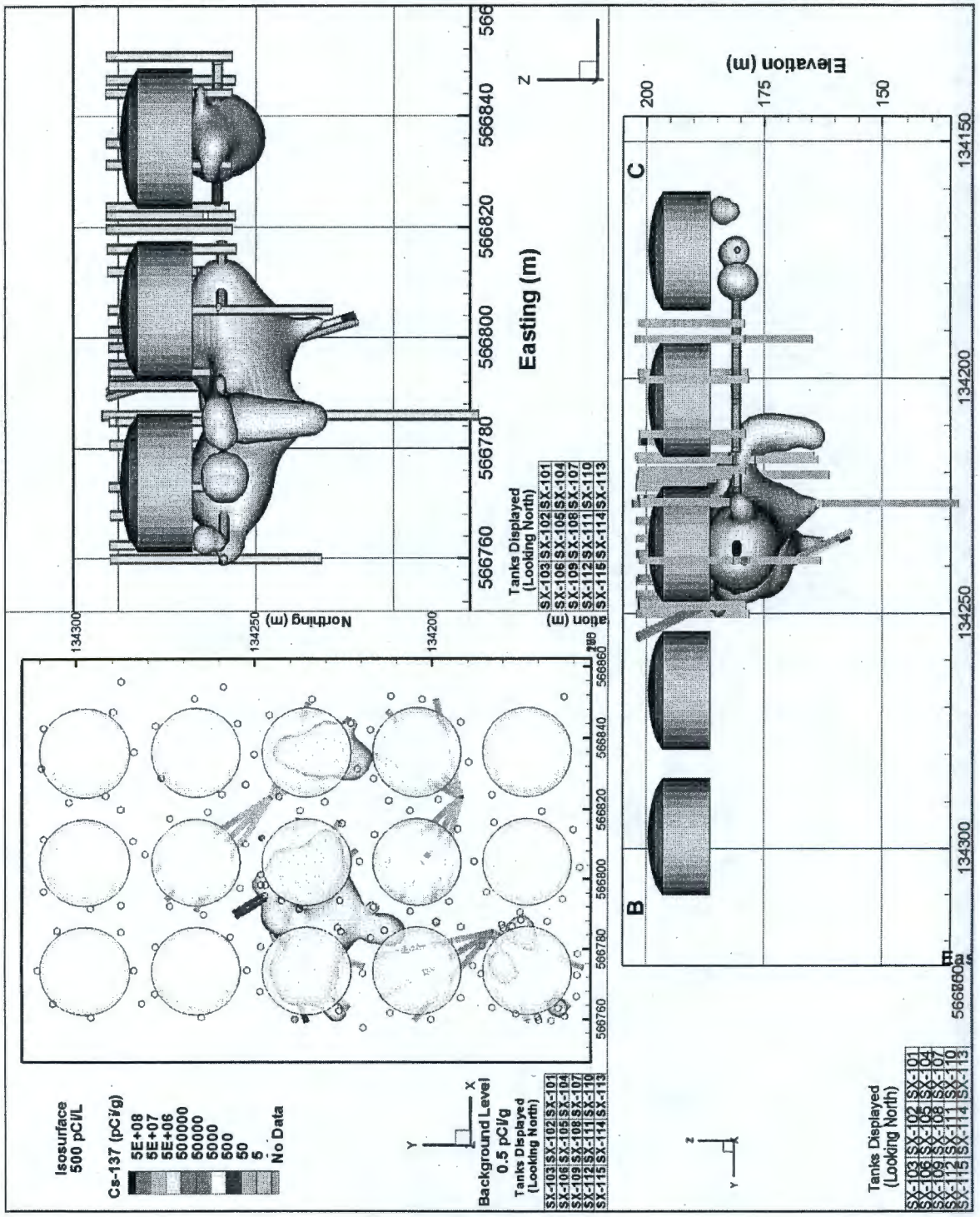

Figure C.3. Three-Dimensional Perspective of Cesium-137 Contaminated Soil Above 5×10^3 pCi/g

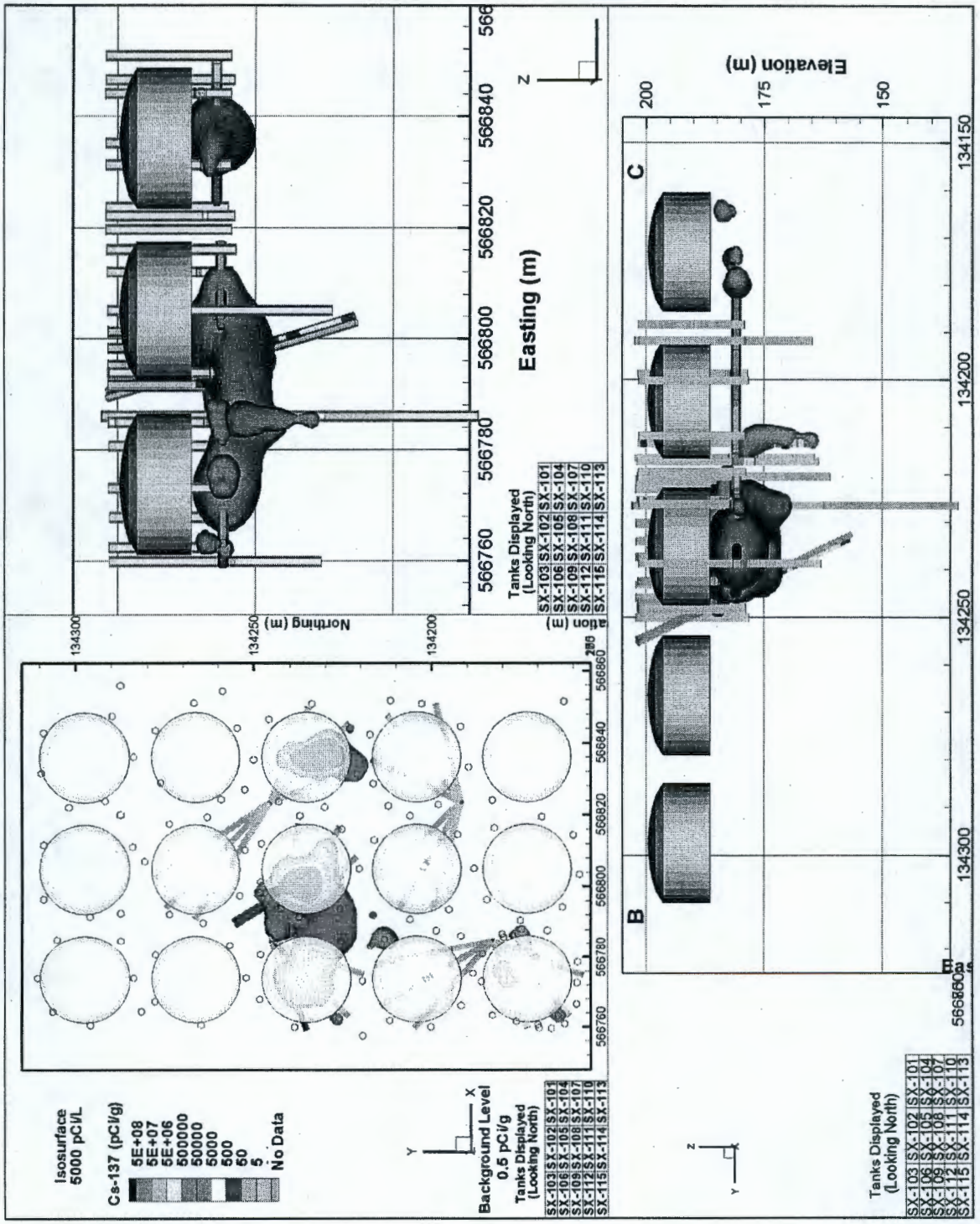

Figure C.4. Three-Dimensional Perspective of Cesium-137 Contaminated Soil Above 5×10^4 pCi/g

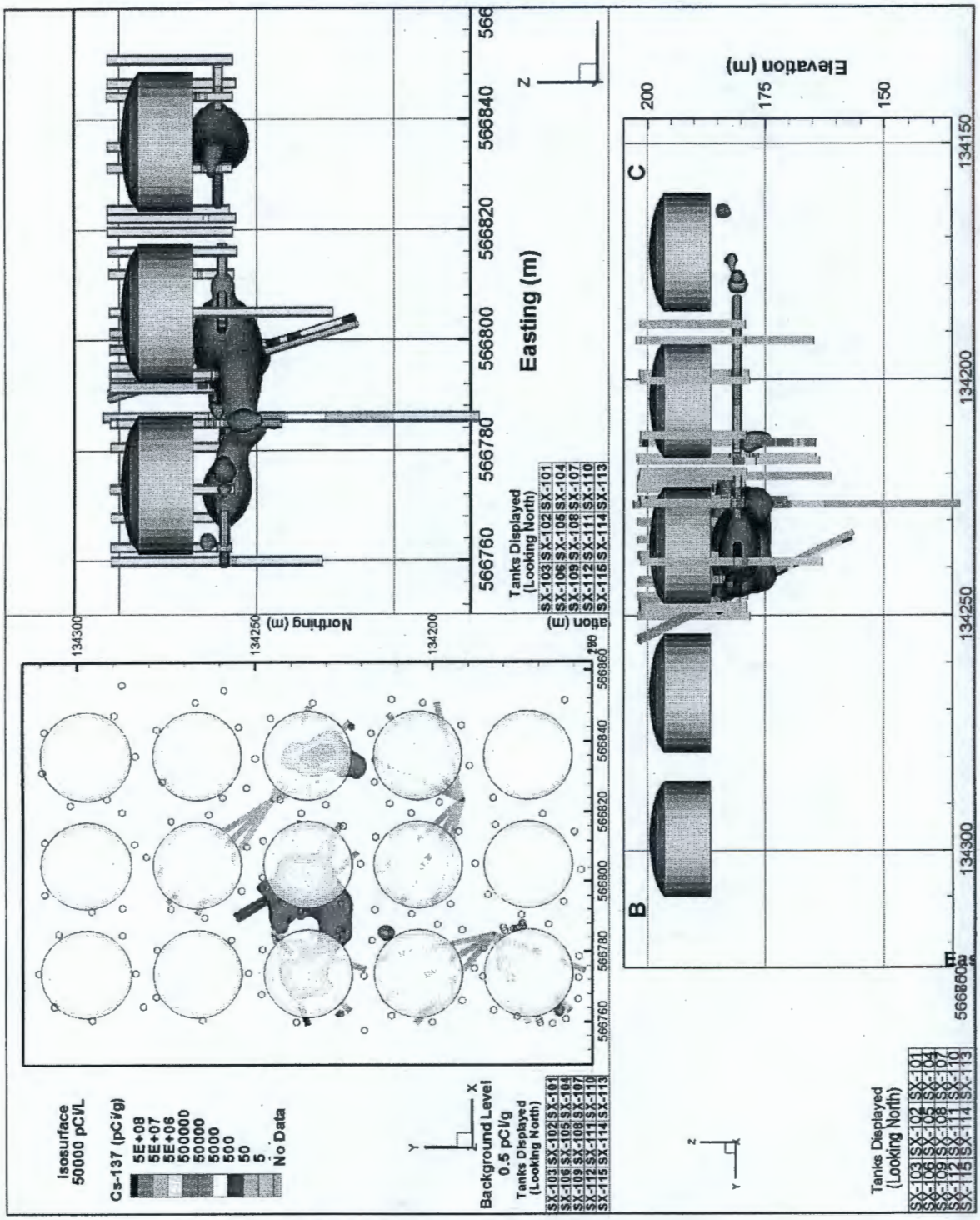

Figure C.5. Three-Dimensional Perspective of Cesium-137 Contaminated Soil Above 5×10^5 pCi/g

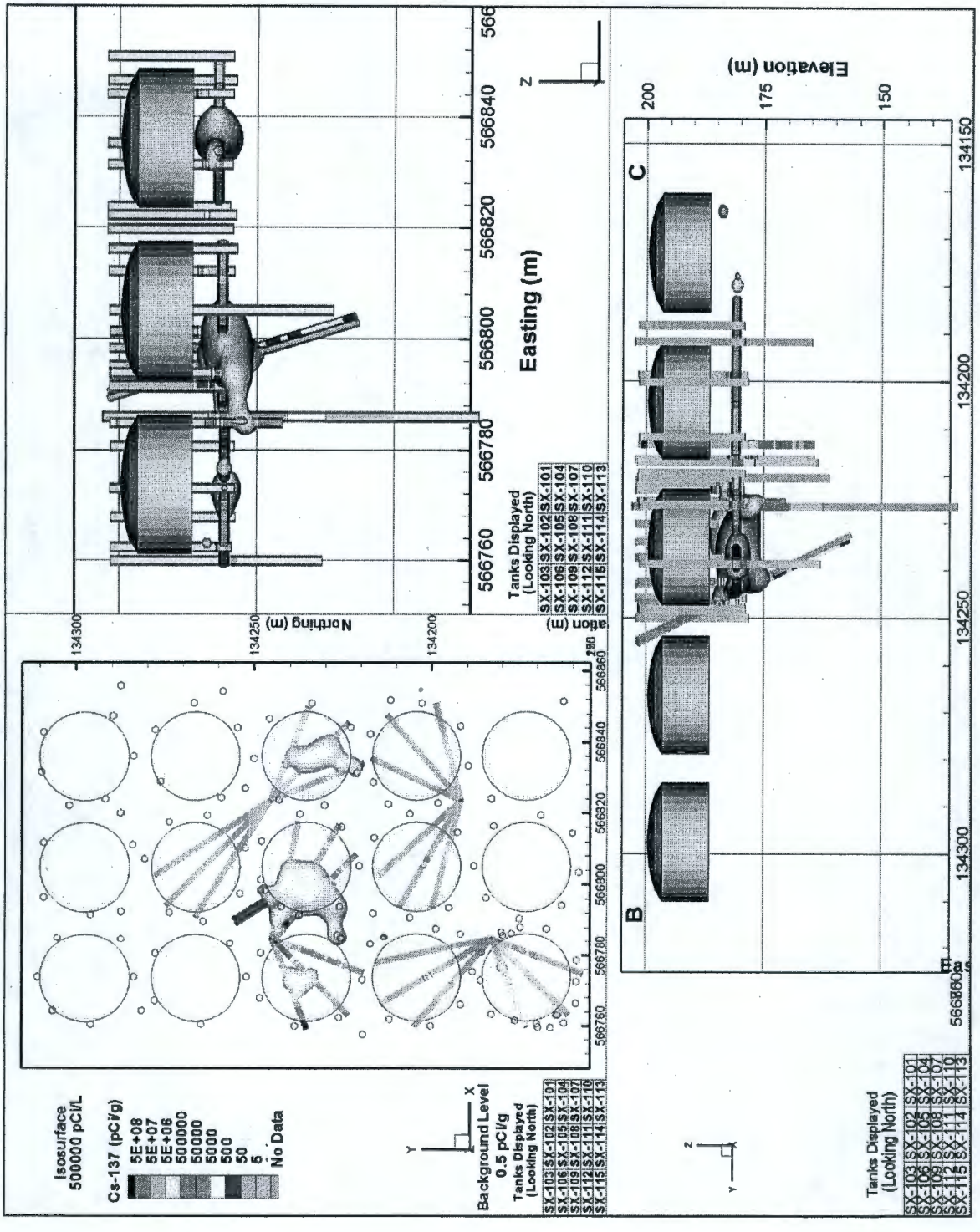

Figure C.6. Three-Dimensional Perspective of Cesium-137 Contaminated Soil Above 5×10^6 pCi/g

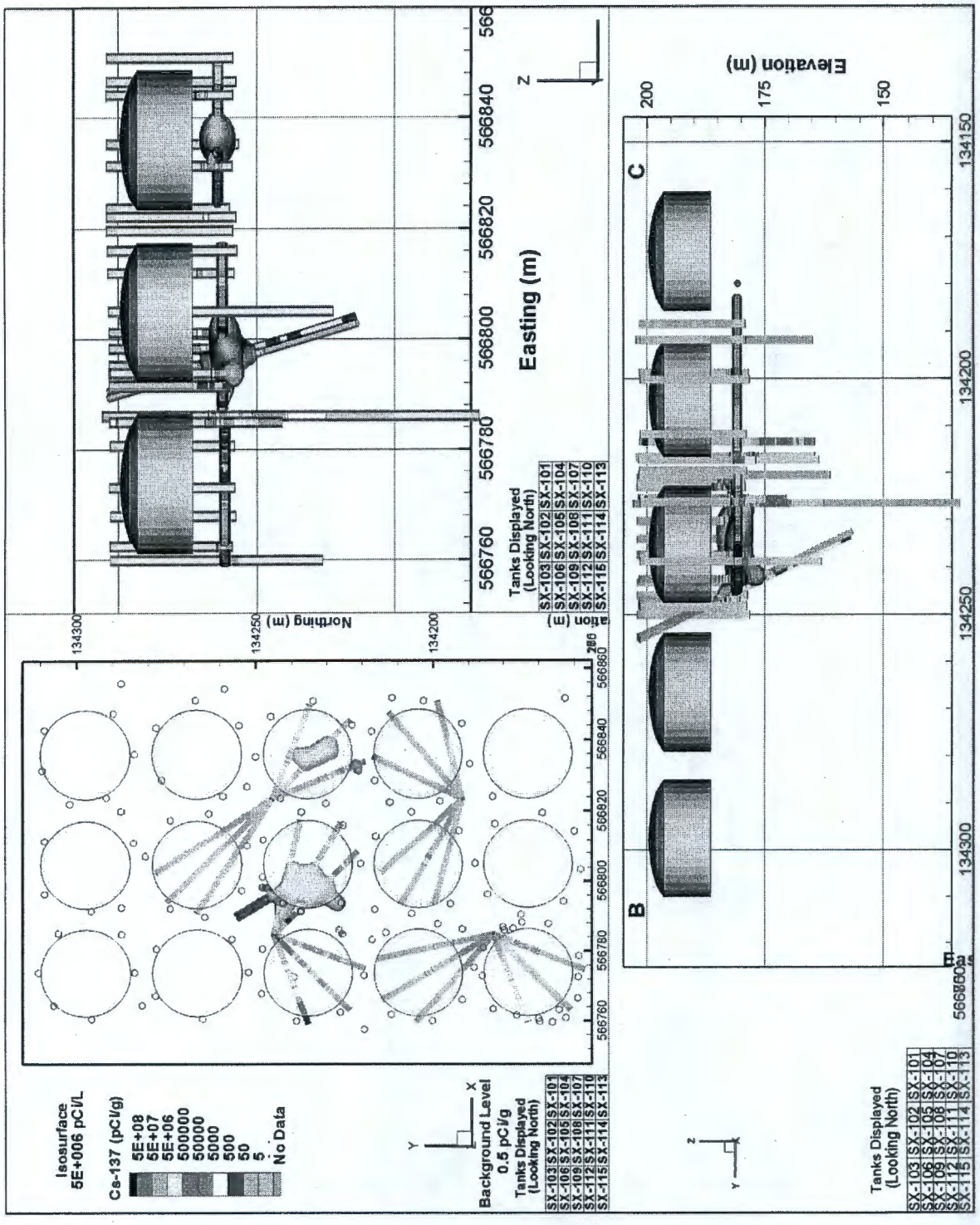

Figure C.7. Three-Dimensional Perspective of Cesium-137 Contaminated Soil Above 5×10^7 pCi/g

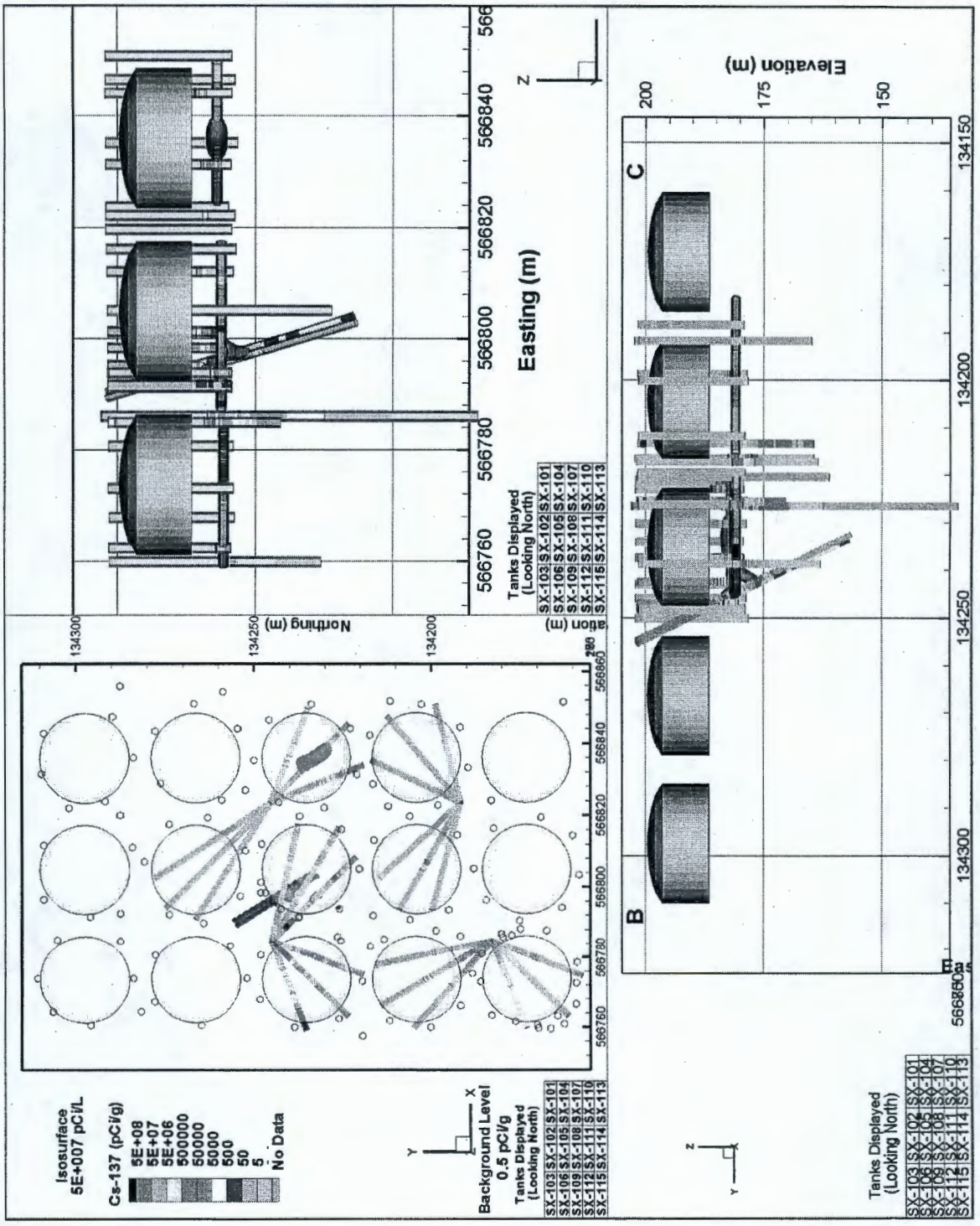

Figure C.8. Total Pico-Curies of Cesium-137 Inventory by Tank

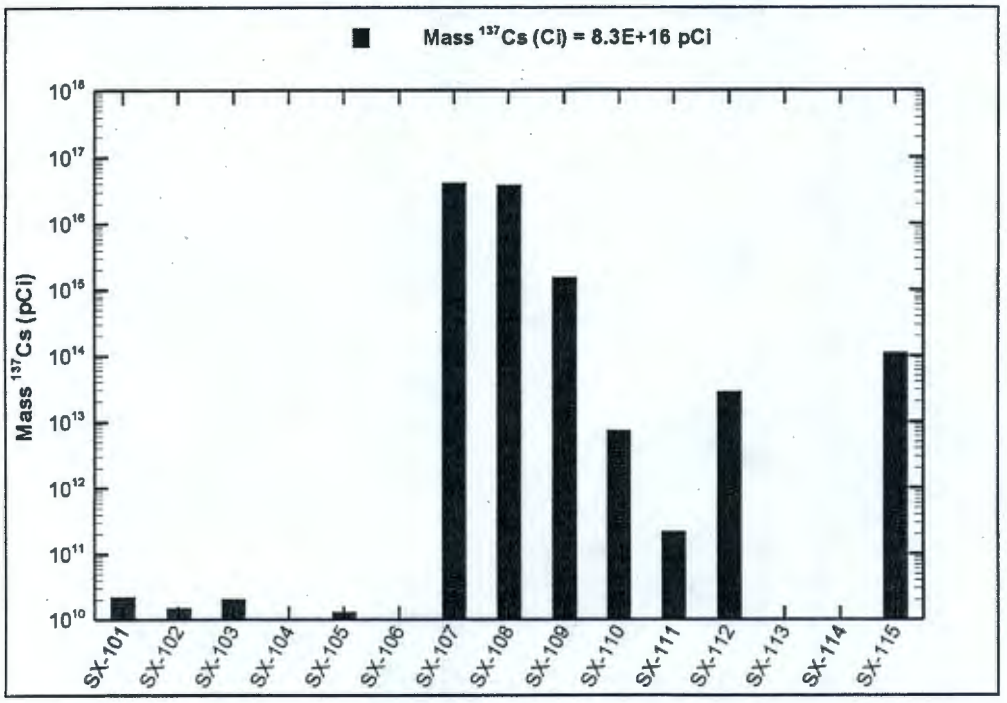

Figure C.9. Estimated Activity Levels and Estimated Contaminated Soil Volume Using Max, Mean, and Geometric Mean Sample Data Filtering for Tank SX-107

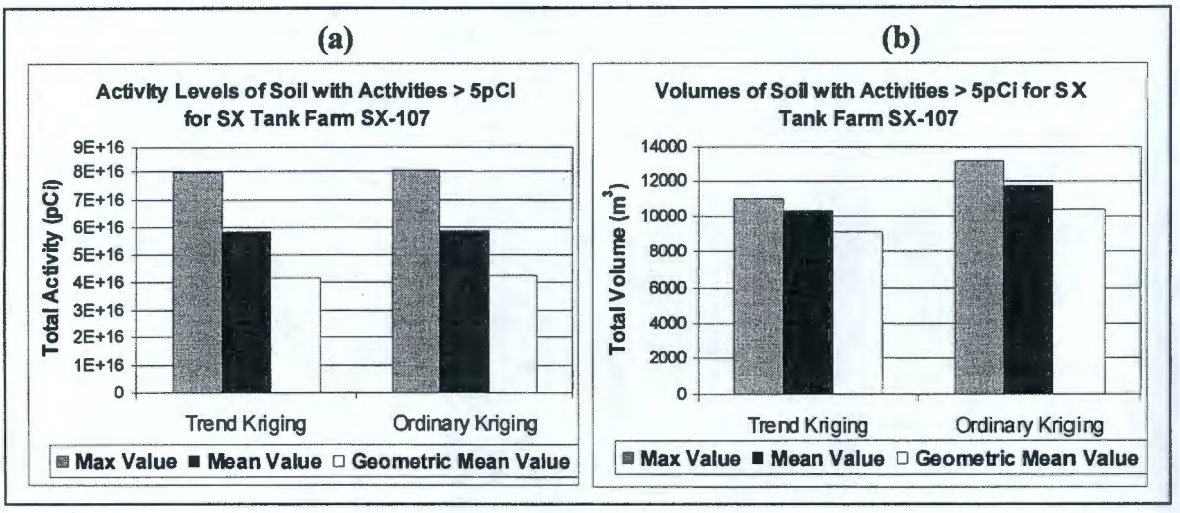

Table C.4. Summary of Activity and Volume Estimates by Tank and Activity Threshold with Geometric Mean Filtering

Tank	Activity/ Volume	Activity Threshold							
		5 (pCi/g)	50 (pCi/g)	500 (pCi/g)	5,000 (pCi/g)	50,000 (pCi/g)	500,000 (pCi/g)	5E+06 (pCi/g)	5E+07 (pCi/g)
SX-101	Activity (pCi)	2.30E+10	4.11E+09	0.00E+00	0.00E+00	0.00E+00	0.00E+00	0.00E+00	0.00E+00
	Volume (m^3)	1.10E+03	2.05E+01	0.00E+00	0.00E+00	0.00E+00	0.00E+00	0.00E+00	0.00E+00
SX-102	Activity (pCi)	1.53E+10	0.00E+00	0.00E+00	0.00E+00	0.00E+00	0.00E+00	0.00E+00	0.00E+00
	Volume (m^3)	1.14E+03	0.00E+00	0.00E+00	0.00E+00	0.00E+00	0.00E+00	0.00E+00	0.00E+00
SX-103	Activity (pCi)	2.12E+10	2.24E+08	0.00E+00	0.00E+00	0.00E+00	0.00E+00	0.00E+00	0.00E+00
	Volume (m^3)	1.31E+03	2.00E+00	0.00E+00	0.00E+00	0.00E+00	0.00E+00	0.00E+00	0.00E+00
SX-104	Activity (pCi)	7.75E+09	0.00E+00	0.00E+00	0.00E+00	0.00E+00	0.00E+00	0.00E+00	0.00E+00
	Volume (m^3)	5.23E+02	0.00E+00	0.00E+00	0.00E+00	0.00E+00	0.00E+00	0.00E+00	0.00E+00
SX-105	Activity (pCi)	1.33E+10	7.62E+08	0.00E+00	0.00E+00	0.00E+00	0.00E+00	0.00E+00	0.00E+00
	Volume (m^3)	1.03E+03	3.00E+00	0.00E+00	0.00E+00	0.00E+00	0.00E+00	0.00E+00	0.00E+00
SX-106	Activity (pCi)	5.90E+09	3.35E+08	0.00E+00	0.00E+00	0.00E+00	0.00E+00	0.00E+00	0.00E+00
	Volume (m^3)	4.93E+02	2.00E+00	0.00E+00	0.00E+00	0.00E+00	0.00E+00	0.00E+00	0.00E+00
SX-107	Activity (pCi)	4.22E+16	4.22E+16	4.22E+16	4.22E+16	4.22E+16	4.20E+16	4.06E+16	3.32E+16
	Volume (m^3)	7.82E+03	4.33E+03	2.90E+03	2.00E+03	1.36E+03	8.05E+02	3.57E+02	1.18E+02
SX-108	Activity (pCi)	3.91E+16	3.91E+16	3.91E+16	3.91E+16	3.90E+16	3.86E+16	3.55E+16	6.20E+15
	Volume (m^3)	1.83E+04	1.07E+04	7.02E+03	4.69E+03	3.06E+03	1.82E+03	9.02E+02	5.35E+01
SX-109	Activity (pCi)	1.56E+15	1.56E+15	1.56E+15	1.55E+15	1.48E+15	1.13E+15	2.20E+14	0.00E+00
	Volume (m^3)	1.74E+04	1.04E+04	6.58E+03	3.69E+03	1.58E+03	3.81E+02	1.55E+01	0.00E+00
SX-110	Activity (pCi)	7.51E+12	7.50E+12	7.47E+12	7.30E+12	6.63E+12	3.88E+12	0.00E+00	0.00E+00
	Volume (m^3)	5.15E+02	2.05E+02	9.10E+01	3.50E+01	1.20E+01	3.00E+00	0.00E+00	0.00E+00
SX-111	Activity (pCi)	2.26E+11	1.91E+11	1.07E+11	2.97E+10	0.00E+00	0.00E+00	0.00E+00	0.00E+00
	Volume (m^3)	1.72E+03	3.42E+02	4.90E+01	1.50E+00	0.00E+00	0.00E+00	0.00E+00	0.00E+00
SX-112	Activity (pCi)	2.92E+13	2.91E+13	2.87E+13	2.67E+13	2.05E+13	7.45E+12	0.00E+00	0.00E+00
	Volume (m^3)	7.14E+03	2.27E+03	9.53E+02	2.82E+02	5.35E+01	6.00E+00	0.00E+00	0.00E+00
SX-113	Activity (pCi)	6.41E+07	0.00E+00	0.00E+00	0.00E+00	0.00E+00	0.00E+00	0.00E+00	0.00E+00
	Volume (m^3)	6.00E+00	0.00E+00	0.00E+00	0.00E+00	0.00E+00	0.00E+00	0.00E+00	0.00E+00
SX-114	Activity (pCi)	1.90E+08	0.00E+00	0.00E+00	0.00E+00	0.00E+00	0.00E+00	0.00E+00	0.00E+00
	Volume (m^3)	1.25E+01	0.00E+00	0.00E+00	0.00E+00	0.00E+00	0.00E+00	0.00E+00	0.00E+00
SX-115	Activity (pCi)	1.14E+14	1.14E+14	1.14E+14	1.13E+14	1.07E+14	9.27E+13	5.50E+13	0.00E+00
	Volume (m^3)	4.24E+03	1.46E+03	6.12E+02	2.46E+02	6.70E+01	1.70E+01	3.00E+00	0.00E+00
SX Tank Farm Totals	Activity (pCi)	8.3011E+16	8.3011E+16	8.3011E+16	8.2997E+16	8.2814E+16	8.1834E+16	7.6375E+16	3.940E+16
	Volume (m^3)	62,750	29,375	18,205	10,945	6,133	3,032	1,278	172

Table C.5. Summary of Activity and Volume Estimates by Tank and Activity Threshold with Maximum Value Filtering

Tank	Activity/ Volume	Activity Threshold Level							
		5 (pCi/g)	50 (pCi/g)	500 (pCi/g)	5,000 (pCi/g)	50,000 (pCi/g)	500,000 (pCi/g)	5E+06 (pCi/g)	5E+07 (pCi/g)
SX-101	Activity (pCi)	6.29E+10	1.54E+10	1.96E+09	0.00E+00	0.00E+00	0.00E+00	0.00E+00	0.00E+00
	Volume (m^3)	2.56E+03	7.55E+01	1.50E+00	0.00E+00	0.00E+00	0.00E+00	0.00E+00	0.00E+00
SX-102	Activity (pCi)	5.62E+10	0.00E+00	0.00E+00	0.00E+00	0.00E+00	0.00E+00	0.00E+00	0.00E+00
	Volume (m^3)	3.19E+03	0.00E+00	0.00E+00	0.00E+00	0.00E+00	0.00E+00	0.00E+00	0.00E+00
SX-103	Activity (pCi)	7.60E+10	9.26E+09	0.00E+00	0.00E+00	0.00E+00	0.00E+00	0.00E+00	0.00E+00
	Volume (m^3)	3.50E+03	6.80E+01	0.00E+00	0.00E+00	0.00E+00	0.00E+00	0.00E+00	0.00E+00
SX-104	Activity (pCi)	3.61E+10	1.53E+09	0.00E+00	0.00E+00	0.00E+00	0.00E+00	0.00E+00	0.00E+00
	Volume (m^3)	1.74E+03	1.30E+01	0.00E+00	0.00E+00	0.00E+00	0.00E+00	0.00E+00	0.00E+00
SX-105	Activity (pCi)	7.03E+10	1.19E+10	9.85E+09	4.77E+09	0.00E+00	0.00E+00	0.00E+00	0.00E+00
	Volume (m^3)	3.66E+03	1.25E+01	2.50E+00	5.00E-01	0.00E+00	0.00E+00	0.00E+00	0.00E+00
SX-106	Activity (pCi)	5.71E+10	5.78E+09	4.03E+09	0.00E+00	0.00E+00	0.00E+00	0.00E+00	0.00E+00
	Volume (m^3)	3.09E+03	1.05E+01	2.00E+00	0.00E+00	0.00E+00	0.00E+00	0.00E+00	0.00E+00
SX-107	Activity (pCi)	8.08E+16	8.08E+16	8.08E+16	8.08E+16	8.08E+16	8.05E+16	7.86E+16	6.44E+16
	Volume (m^3)	9.94E+03	5.22E+03	3.54E+03	2.52E+03	1.79E+03	1.19E+03	6.38E+02	2.12E+02
SX-108	Activity (pCi)	5.02E+16	5.02E+16	5.02E+16	5.02E+16	5.01E+16	4.96E+16	4.60E+16	9.84E+15
	Volume (m^3)	2.27E+04	1.16E+04	7.60E+03	5.24E+03	3.51E+03	2.14E+03	1.08E+03	8.15E+01
SX-109	Activity (pCi)	3.77E+15	3.77E+15	3.77E+15	3.76E+15	3.67E+15	3.06E+15	9.61E+14	0.00E+00
	Volume (m^3)	2.19E+04	1.26E+04	8.33E+03	5.20E+03	2.68E+03	8.49E+02	6.60E+01	0.00E+00
SX-110	Activity (pCi)	1.11E+14	1.11E+14	1.11E+14	1.10E+14	1.09E+14	1.04E+14	8.35E+13	0.00E+00
	Volume (m^3)	1.50E+03	2.83E+02	1.37E+02	6.50E+01	3.00E+01	1.15E+01	4.00E+00	0.00E+00
SX-111	Activity (pCi)	1.16E+12	1.08E+12	9.70E+11	4.52E+11	1.11E+11	0.00E+00	0.00E+00	0.00E+00
	Volume (m^3)	4.16E+03	5.92E+02	1.79E+02	1.65E+01	5.00E-01	0.00E+00	0.00E+00	0.00E+00
SX-112	Activity (pCi)	6.16E+13	6.14E+13	6.07E+13	5.82E+13	4.82E+13	2.76E+13	0.00E+00	0.00E+00
	Volume (m^3)	1.21E+04	3.50E+03	1.26E+03	4.57E+02	8.90E+01	1.30E+01	0.00E+00	0.00E+00
SX-113	Activity (pCi)	8.42E+08	0.00E+00	0.00E+00	0.00E+00	0.00E+00	0.00E+00	0.00E+00	0.00E+00
	Volume (m^3)	7.00E+01	0.00E+00	0.00E+00	0.00E+00	0.00E+00	0.00E+00	0.00E+00	0.00E+00
SX-114	Activity (pCi)	6.16E+09	0.00E+00	0.00E+00	0.00E+00	0.00E+00	0.00E+00	0.00E+00	0.00E+00
	Volume (m^3)	4.64E+02	0.00E+00	0.00E+00	0.00E+00	0.00E+00	0.00E+00	0.00E+00	0.00E+00
SX-115	Activity (pCi)	2.69E+14	2.69E+14	2.69E+14	2.68E+14	2.60E+14	2.27E+14	1.46E+14	0.00E+00
	Volume (m^3)	5.30E+03	1.82E+03	8.27E+02	3.97E+02	1.54E+02	3.80E+01	6.00E+00	0.00E+00
SX Tank Farm Totals	Activity (pCi)	1.35E+17	1.35E+17	1.35E+17	1.35E+17	1.35E+17	1.34E+17	1.26E+17	7.43E+16
	Volume (m^3)	95,867	35,735	21,873	13,894	8,260	4,232	1,795	294

C.3.4 INVENTORY ESTIMATES FOR WASTE MANAGEMENT AREA S-SX TANK LEAKS

Leak volume estimates and projected inventory estimates for WMA S-SX tank leaks are listed in Tables C.6 and C.7 (Jones et al. 2000a). Leak inventory estimates for tanks SX-107, SX-108, and SX-109 were based on cesium-137 inventories developed by the MSU kriging analysis (Goodman 2000). Leak volumes for these three tanks were estimated from cesium-137 inventory estimates (Goodman 2000) coupled with waste composition estimates (see Section C.3.1). Inventory estimates for tanks S-104, SX-113, and SX-115 were based on documented leak volumes (Hanlon 2001; Jones et al. 2000a). For these three cases, leak volumes were combined with tank waste inventory estimates (see Section C.3.1) to develop inventory estimates for each tank leak.

The following discussion focuses on potential modifications to the published WMA S-SX inventory estimates based on the updated HGL kriging results.

Inventory and leak volume estimates developed in Jones et al. (2000a) are listed in Tables C.6 and C.7. The estimates were made using the waste tank compositions (discussed in Section C.3.1) and the leak volumes as estimated from the cesium-137 inventory in the soil (discussed in Section C.3.3). The inventory estimates shown in Tables C.6 and C.7 for tanks SX-107, SX-108, and SX-109 were developed using 95 percentile cesium-137 data from MSU (Goodman 2000). That is, these inventory estimates were biased high by using the 95 percentile data rather than the mean or 50 percentile values. The decision to use the higher values was driven by an assumption that the cesium-137 plume estimates failed to reflect realistic estimates of the cesium-137 inventories directly below the tanks. (This was one of the conclusions discussed in the MSU report [Goodman 2000] and was used as one of the technical justifications for drilling the SX-108 slant borehole.)

Those estimates remain as reasonable estimates for use in leak impact assessment studies. The HGL kriging analysis was more robust than the MSU efforts because only experimentally determined measurements were used by HGL, and HGL correlation lengths were based on a single tank (i.e., tank SX-108) where the most data were available then applied to all SX farm tanks.

The inventory estimates for tanks SX-107, SX-108, and SX-109 were developed using the 95 percentile MSU kriging data. If the HGL kriging results had been used in developing the inventory estimates, the values for tanks SX-108 and SX-109 listed in Tables C.6 and C.7 would have changed very little. However, the tank SX-107 inventory estimates would have been slightly higher than those reported for tank SX-108 in Tables C.6 and C.7. Leak inventory estimates for tanks S-104, SX-113, and SX-115 were based on historical leak volumes. Leak volumes from tanks SX-113 and SX-115 are well documented (Hanson et al. 1962; Raymond and Shdo 1966) whereas the leak volume from tank S-104 is significantly more uncertain. The 24,000 gal (91,000 L) leak volume currently reported in *Waste Tank Summary Report for Month Ending March 31, 2001* (Hanlon 2001) for tank S-104 is based on long-term liquid level decreases (Agnew et al. 1997). However, the waste footprint projected from field investigations using cone penotrometer techniques and spectral gamma logging data fail to document the inventory estimates shown in Tables C.6 and C.7 for tank S-104. Thus, the tank S-104 inventory estimates listed in Tables C.6 and C.7 are conservative.

Table C.6. Estimated Inventory Lost to Vadose Zone in the S and SX Tank Farms (2 Sheets)

Chemical	Estimated S-104 Inventory Loss (kg)	Estimated SX-107 Inventory Loss (kg)	Estimated SX-108 Inventory Loss (kg)	Estimated SX-109 Inventory Loss (kg)	Estimated SX-113 Inventory Loss (kg)	Estimated SX-115 Inventory Loss (kg)
Leak Vol.	**24,000 gal[a]**	**63,500 gal[b]**	**15,200 gal[b]**	**989 gal[b]**	**15,000 gal[a]**	**50,000 gal[a]**
Na	1.82E+04	9.90E+03	2.37E+04	1.54E+03	1.05E+04	1.57E+04
Al3	3.83E+03	2.00E+03	4.78E+03	3.11E+02	1.95E+03	4.24E+03
Fe (Total)	1.81E+01	8.87E+00	2.12E+01	1.38E+00	9.47E+00	2.25E+01
Cr	7.81E+02	4.71E+02	1.13E+03	7.33E+01	5.08E+02	5.03E+02
Bi	1.71E-04	0.00E+00	0.00E+00	0.00E+00	0.00E+00	2.63E-03
La	2.79E-10	0.00E+00	0.00E+00	0.00E+00	0.00E+00	4.31E-09
Hg	6.49E-02	1.90E-04	4.54E-04	2.95E-05	0.00E+00	2.40E-01
ZrO(OH)2	1.15E-05	0.00E+00	0.00E+00	0.00E+00	0.00E+00	1.77E-04
Pb	1.07E+01	3.13E-02	7.48E-02	4.87E-03	0.00E+00	3.96E+01
Ni	1.66E+01	8.36E+00	2.00E+01	1.30E+00	8.94E+00	1.93E+01
Sr	0.00E+00	0.00E+00	0.00E+00	0.00E+00	0.00E+00	0.00E+00
Mn	3.27E-04	0.00E+00	0.00E+00	0.00E+00	0.00E+00	5.04E-03
Ca	5.82E+01	2.85E+01	6.82E+01	4.44E+00	3.05E+01	7.22E+01
K	1.09E+02	6.33E+01	1.52E+02	9.86E+00	6.92E+01	8.21E+01
U-Total	1.19E+02	4.58E+01	1.10E+02	7.14E+00	5.74E+01	1.61E+02
Pu-Total	2.39E-02	1.17E-02	2.80E-02	1.82E-03	1.25E-02	2.97E-02
TOC wt% C	1.28E+02	0.00E+00	0.00E+00	0.00E+00	0.00E+00	0.00E+00
free OH	0.00E+00	0.00E+00	0.00E+00	0.00E+00	0.00E+00	0.00E+00
OH	1.40E+04	7.66E+03	1.83E+04	1.19E+03	7.72E+03	1.35E+04
NO3	1.70E+04	7.40E+03	1.77E+04	1.15E+03	9.96E+03	3.87E+03
NO2	6.87E+03	4.49E+03	1.07E+04	6.99E+02	3.50E+03	9.23E+03
CO3	8.73E+01	4.28E+01	1.02E+02	6.66E+00	4.57E+01	8.35E+01
PO4	5.02E-03	0.00E+00	0.00E+00	0.00E+00	0.00E+00	4.89E-02
SO4	2.81E+02	1.95E+02	4.68E+02	3.04E+01	1.58E+02	3.46E+02
Si (as SiO32-)	1.94E+02	1.57E+02	3.76E+02	2.45E+01	9.66E+01	2.33E+02
F	8.00E-04	0.00E+00	0.00E+00	0.00E+00	0.00E+00	4.94E-02
Cl	4.57E+02	2.65E+02	6.33E+02	4.12E+01	2.89E+02	1.83E+02
C6H5O7	8.22E-03	0.00E+00	0.00E+00	0.00E+00	0.00E+00	1.27E-01
EDTA	1.69E-06	0.00E+00	0.00E+00	0.00E+00	0.00E+00	7.32E-03
HEDTA	1.41E-06	0.00E+00	0.00E+00	0.00E+00	0.00E+00	5.75E-03
glycolate	6.14E-05	0.00E+00	0.00E+00	0.00E+00	0.00E+00	7.10E-02
acetateE-	6.37E-06	0.00E+00	0.00E+00	0.00E+00	0.00E+00	5.80E-03
oxalate	2.63E-12	0.00E+00	0.00E+00	0.00E+00	0.00E+00	3.58E-09

Table C.6. Estimated Inventory Lost to Vadose Zone in the S and SX Tank Farms (2 Sheets)

Chemical	Estimated S-104 Inventory Loss (kg)	Estimated SX-107 Inventory Loss (kg)	Estimated SX-108 Inventory Loss (kg)	Estimated SX-109 Inventory Loss (kg)	Estimated SX-113 Inventory Loss (kg)	Estimated SX-115 Inventory Loss (kg)
Leak Vol.	**24,000 gal[a]**	**63,500 gal[b]**	**15,200 gal[b]**	**989 gal[b]**	**15,000 gal[a]**	**50,000 gal[a]**
DBP	3.86E-05	0.00E+00	0.00E+00	0.00E+00	0.00E+00	9.58E-02
butanol	3.86E-05	0.00E+00	0.00E+00	0.00E+00	0.00E+00	4.40E-02
NH3	1.87E+00	3.96E+01	9.48E+01	6.17E+00	2.06E+01	4.21E+01
Fe(CN)6	0.00E+00	0.00E+00	0.00E+00	0.00E+00	0.00E+00	0.00E+00

[a]Leak volumes from Hanlon (2001).

[b]Leak volumes estimated from Montana State University kriging analysis of gamma logging data (Goodman 2000).

Table C.7. Estimated Inventory Lost to Vadose Zone in the S and SX Tank Farms (Radionuclides) (2 Sheets)

Radionuclide	Estimated S-104 Inventory Loss Ci	Estimated SX-107 Inventory Loss Ci	Estimated SX-108 Inventory Loss Ci	Estimated SX-109 Inventory Loss Ci	Estimated SX-113 Inventory Loss Ci	Estimated SX-115 Inventory Loss Ci
H-3	7.12E+00	1.34E+01	3.20E+01	2.08E+00	4.61E+00	1.43E+01
C-14	5.53E-01	6.37E-01	1.52E+00	9.92E-02	3.57E-01	6.95E-01
Ni-59	6.99E-02	7.46E-02	1.79E-01	1.16E-02	4.46E-02	8.38E-02
Ni-63	6.53E+00	7.28E+00	1.74E+01	1.13E+00	4.17E+00	8.20E+00
Co-60	2.21E-01	6.11E-01	1.46E+00	9.52E-02	1.41E-01	6.74E-01
Se-79	1.17E-01	1.22E-01	2.92E-01	1.90E-02	7.58E-02	1.33E-01
Sr-90	4.52E+03	2.69E+03	6.44E+03	4.19E+02	2.88E+03	3.38E+03
Y-90	4.53E+03	2.69E+03	6.44E+03	4.19E+02	2.88E+03	3.38E+03
Zr-93	5.54E-01	6.01E-01	1.44E+00	9.36E-02	3.58E-01	6.56E-01
Nb-93m	4.53E-01	4.37E-01	1.05E+00	6.80E-02	2.93E-01	4.77E-01
Tc-99	3.87E+00	5.03E+00	1.21E+01	7.84E-01	2.50E+00	5.52E+00
Ru-106	1.66E-06	1.51E-04	3.62E-04	2.36E-05	3.94E-07	1.68E-04
Cd-113m	1.71E+00	2.71E+00	6.50E+00	4.23E-01	1.10E+00	2.98E+00
Sb-125	3.35E-01	2.23E+00	5.34E+00	3.48E-01	2.07E-01	2.48E+00
Sn-126	1.80E-01	1.84E-01	4.40E-01	2.86E-02	1.16E-01	2.00E-01
I-129	7.44E-03	9.53E-03	2.28E-02	1.48E-03	4.80E-03	1.04E-02
Cs-134	6.32E-03	1.33E-01	3.19E-01	2.08E-02	3.56E-03	1.48E-01
Cs-137	1.14E+04	1.71E+04	4.10E+04	2.67E+03	7.34E+03	1.88E+04
Ba-137m	1.08E+04	1.62E+04	3.87E+04	2.52E+03	6.94E+03	1.78E+04
Sm-151	4.19E+02	4.28E+02	1.03E+03	6.67E+01	2.71E+02	4.68E+02
Eu-152	4.14E-02	1.08E-01	2.59E-01	1.69E-02	2.65E-02	1.18E-01
Eu-154	5.33E+00	1.49E+01	3.56E+01	2.32E+00	3.41E+00	1.64E+01
Eu-155	1.96E+00	5.49E+00	1.31E+01	8.55E-01	1.25E+00	6.00E+00
Ra-226	8.15E-06	4.90E-06	1.17E-05	7.64E-07	5.24E-06	5.50E-06
Ra-228	1.88E-07	1.85E-10	4.44E-10	2.89E-11	3.51E-11	2.90E-06
Ac-227	4.72E-05	2.85E-05	6.81E-05	4.43E-06	3.04E-05	3.15E-05
Pa-231	1.75E-04	1.36E-04	3.26E-04	2.12E-05	1.13E-04	1.47E-04
Th-229	1.49E-08	1.32E-08	3.16E-08	2.05E-09	6.70E-09	8.36E-08
Th-232	2.52E-08	5.24E-10	1.25E-09	8.16E-11	9.32E-11	3.87E-07
U-232	3.83E-06	1.42E-06	3.41E-06	2.22E-07	8.26E-07	3.44E-05
U-233	7.37E-06	3.78E-08	9.05E-08	5.89E-09	3.15E-08	1.13E-04
U-234	4.09E-02	1.85E-02	4.43E-02	2.88E-03	1.88E-02	7.25E-02
U-235	1.73E-03	7.37E-04	1.77E-03	1.15E-04	8.09E-04	2.80E-03
U-236	9.69E-04	8.69E-04	2.08E-03	1.35E-04	2.97E-04	4.29E-03

Table C.7. Estimated Inventory Lost to Vadose Zone in the S and SX Tank Farms (Radionuclides) (2 Sheets)

Radionuclide	Estimated S-104 Inventory Loss Ci	Estimated SX-107 Inventory Loss Ci	Estimated SX-108 Inventory Loss Ci	Estimated SX-109 Inventory Loss Ci	Estimated SX-113 Inventory Loss Ci	Estimated SX-115 Inventory Loss Ci
U-238	3.96E-02	1.53E-02	3.66E-02	2.38E-03	1.92E-02	5.36E-02
Np-237	2.52E-02	2.08E-02	4.97E-02	3.24E-03	1.62E-02	2.39E-02
Pu-238	2.27E-02	2.49E-02	5.96E-02	3.87E-03	1.05E-02	6.21E-02
Pu-239	1.43E+00	6.95E-01	1.66E+00	1.08E-01	7.48E-01	1.76E+00
Pu-240	2.07E-01	1.20E-01	2.87E-01	1.86E-02	1.07E-01	2.95E-01
Pu-241	1.28E+00	1.24E+00	2.98E+00	1.94E-01	6.30E-01	2.79E+00
Pu-242	5.49E-06	6.85E-06	1.64E-05	1.07E-06	2.89E-06	1.12E-05
Am-241	1.98E+00	1.88E+00	4.50E+00	2.93E-01	1.28E+00	2.08E+00
Am-243	1.85E-05	6.70E-05	1.60E-04	1.04E-05	1.19E-05	7.16E-05
Cm-242	9.43E-04	4.87E-03	1.17E-02	7.59E-04	6.11E-04	5.09E-03
Cm-243	2.16E-05	4.75E-04	1.14E-03	7.39E-05	1.40E-05	4.94E-04
Cm-244	6.59E-04	4.78E-03	1.14E-02	7.44E-04	4.27E-04	4.98E-03

C.3.5 SPECIATION ANALYSIS

Significant quantities of high-level waste (HLW) were lost to the soil column from large underground tanks in WMA S-SX during long-term storage of the wastes produced in the Reduction-Oxidation (REDOX) Plant. An understanding of the mechanisms of soil/waste reactions controlling the movement of tank waste through the vadose zone requires knowledge of waste components on a molecular level. However, this level of tank waste chemistry is generally not available since this level of understanding was not required for the original plant operations or for long-term storage and waste management. *REDOX Technical Manual* (GE 1951) and the updated flowsheets from *Standard Inventories of Chemicals and Radionuclides in Hanford Site Tank Wastes* (Kupfer et al. 1998) provide clear guidance as to the conditions required for successful operations of separations process but only limited understanding of the underlying fundamental chemistry. Thus, the most practical approach for developing an understanding of the chemical species present in leaked tank waste comes from a chemical equilibria-based computer model that develops speciation of bulk waste components.

Chemical thermodynamic-based models of aqueous systems can be applied to predict reaction products if the controlling thermodynamic parameters are sufficiently well understood. However, the tank waste mixtures are extremely complex and many of the required thermodynamic parameters are only poorly understood. Any thermodynamic-based modeling exercise involving a tank waste matrix requires many approximations and assumptions. Thus, speciation modeling results must be treated with considerable caution.

The initiative was to conduct preliminary scoping studies using the Environmental Simulation Program (ESP), a thermodynamic-based chemical process simulator that has been widely applied at the Hanford Site (MacLean and Eager 1998). ESP is currently used to simulate transfers, mixing, and treatment of tank wastes for both the waste feed delivery project and vitrification pretreatment. It has been used to simulate processing of plutonium solutions, the clean salt waste treatment process, sluicing of tank wastes, and other nuclear-waste related processing.

The ESP is designed to model the processing of complex, concentrated aqueous solutions, organic liquids, solids, and vapors. It uses sophisticated thermodynamic models to predict the activity coefficients and equilibrium constants of most species and equilibrium relationships that can exist in tank wastes, or during processing of plant wastes. It can be used to calculate the equilibrium or time dependent composition of mixtures of solids, liquids, and gases.

The ESP calculates the thermodynamic equilibrium of all phases by minimizing the chemical potential of a system in an iterative process (Sterner et al. 1997). The equilibrium constants for aqueous and solid species are calculated using the Helgeson-Kirkham-Flowers Equation of State (Sterner et al. 1997), thermodynamic properties, or temperature and pressure dependent correlations of experimental data. Activity coefficients, partial molar densities, and other properties of aqueous species are calculated using the Bromely-Zemaitis or Pitzer excess property models (Sterner et al. 1997).

ESP comes with several databanks covering most of the elements and compounds found or expected in Hanford Site tank wastes (Sterner et al. 1996). These are supplemented with custom databanks that have been prepared specifically for simulating the processing of tank wastes.

Special databanks combined with associated chemistry models are used for almost all waste-related simulations.

As discussed in Section C.3.1, the compositions of the wastes in SSTs at the time of suspected leaks were developed using the HDW model (Agnew 1997). The HDW model provides supernatant compositions that were combined with leak volumes to project leak inventory estimates (Jones et al. 2000a). The tank waste supernatant compositions were then used as input to the ESP model with the goal of developing a better understanding of chemical speciation of the wastes at the time of suspected leaks. One of the weak points of the HDW model is its inability to reliably predict acid/base parameters such as pH or free hydroxide ion concentrations. However, the historical records (GE 1951; Harmon 1949; Barney 1976) clearly show that it was well known that the solution chemistry of REDOX HLW was dominated by the aluminum ion solubility and the aluminum solubility was controlled by the free hydroxide ion concentration. The selection of the free hydroxide concentration will dictate the thermodynamic modeling results for the REDOX HLW systems. Thus, much of the speciation modeling work discussed here focused on developing a better understanding of aluminum ion chemistry in the REDOX waste matrix. Such an understanding is potentially important in geochemical processes impacting tank waste movement in the subsurface.

The speciation calculation results reported in Jones et al. (2000a) use the tank waste compositions predicted by the HDW model at the times of the leaks for tanks S-104, SX-108, and SX-115. The previously reported results are supplemented here with additional modeling runs addressing the free hydroxide issue. These results are compared with results from Litchner et al. (2001). Corrections to errors in technetium-99 speciation estimates in Jones et al. (2000a) are also discussed briefly.

C.3.5.1 Aluminum Solubility in Reduction-Oxidation Wastes

One of the major characteristics of the REDOX HLW was the very high aluminum ion concentrations found in this waste stream (GE 1951). Aluminum ion solubility is closely coupled with the 'free' hydroxide ion concentration. An understanding of the aluminum ion chemistry in the REDOX HLW matrix is required in order to develop reasonable leak inventory estimates and address questions about waste-soil chemical reactions.

Aluminum nitrate was used as a 'salting out' agent in the REDOX liquid-liquid exchange columns to facilitate transfer of uranium and plutonium from the aqueous to organic phase. The high aluminum ion levels in the waste streams led to the development of carefully controlled processes for concentrating and neutralizing the HLW stream prior to being discharged to the SSTs (GE 1951). Considerable care was taken to avoid the precipitation of aluminum oxides during the concentration and neutralization processes because the formation of aluminum oxide solids in the waste stream led to problems in pumping the wastes. Since the long-term HLW management goals (Tomlinson 1963) required many waste transfers between tanks and processing facilities prior to final solidification, it is reasonable to assume that the free hydroxide concentration in the REDOX HLW streams would have been maintained at high enough levels to maintain essentially all of the aluminum ions in the solution phase (Barney 1975). However, there are inconsistencies in the historical records.

GE (1951) states that it was necessary to neutralize the HLW stream to a pH 13 to obtain a 'nearly clear liquid.' However, the manual also states that 25% to 30% excess caustic was required to reach that pH. Because the aluminum neutralization involved the reaction of 1 mole of aluminum with 4 moles of hydroxide to form sodium aluminate ($NaAl(OH)_4$), a 25% to 30% excess caustic leads to 1 to 1.2 moles excess hydroxide being added per mole aluminum, during the neutralization process. Because the total aluminum concentration in the neutralized waste stream was approximately 1.2 moles, one would expect the free hydroxide concentration to be as high as 1.2 to 1.4 moles. However, some of the excess hydroxide would be neutralized by the excess nitric acid (1.2%), dichromate, iron, and uranium. Nevertheless, the excess hydroxide concentration in the waste stream going to the SSTs, would likely have been around 1 mole. The free hydroxide concentration would, of course, increase as the wastes were concentrated by self-evaporation in the tanks. REDOX boiling wastes were concentrated by a factor of approximately two until the beginning of 1963. After that point it appears the REDOX wastes were concentrated by a factor of closer to three in tanks SX-107, SX-108, and SX-109.

The arbitrary selection of 0.1 mole hydroxide for the preliminary speciation calculations reported in Jones et al. (2000a) was based on statements in GE (1951). However, the statement in GE (1951) that the waste was neutralized to pH 13 probably has little relationship to the hydrogen ion (or hydroxide ion) concentration in the waste. It is likely the pH 13 simply reflected an operations parameter that, in reality, only reflects the potential developed between a glass electrode and the reference electrode (likely to have been a calomel electrode). In a well-controlled laboratory environment, pH measurements can be converted to hydrogen ion activity (and concentration) in relatively simple systems. However, such a conversion is likely impossible in the REDOX waste matrix. Glass pH electrodes are, by design, highly selective for hydrogen ions but many also respond to sodium ion activity. Above pH 10, this 'sodium ion error' can become quite significant. There are also issues associated with the liquid junction potentials in the reference electrode. Finally, pH measurements are meaningful only if matrix-matched standards are available to calibrate the pH measurement system. Little is known about the pH monitoring systems or their operations in the REDOX Plant. Analysis of the REDOX process flowsheets leads to the conclusion that the hydroxide was at least an order of magnitude higher that the value used in Jones et al. (2000a).

The initial ESP speciation modeling of REDOX HLW, reported in Jones et al. (2000a), assumed a 0.1 mole free hydroxide concentration resulting in essentially all of the aluminum residing in the solid phase as aluminum hydroxide. Because of the uncertainty about the correct hydroxide concentration in the REDOX HLW, a sensitivity study was completed using the ESP model to assess the aluminum ion solubility in the waste matrix over a range of free hydroxide concentrations. The projected aluminum solubility data at 50 and 100 °C (122 and 212 °F) are shown in Figures C.10 and C.11. The aluminum solubility increases with increasing hydroxide reaching a maximum at 1 mole at 100 °C (212 °F) and 2 moles at 50° C (122 °F), with essentially all of the aluminum in solution, as aluminum hydroxide. GE (1951) states that acidic REDOX HLW was cooled to slightly less than 50 °C (122 °F) prior to neutralization with 50% caustic. It is also stated that the wastes were neutralized to a 'near-clear' solution. Statements from GE (1951) coupled with aluminum solubility modeling results would suggest that the wastes contained in excess of 1 mol/L free hydroxide. Thus, it is almost certain that the HLW leaving the REDOX Plant would have contained in excess of 1 mol/L free hydroxide. The modeling results show the solubility to increase at higher temperatures therefore is likely that essentially all

aluminum ions remained in the solution phase during the boiling phase of the REDOX waste processing in the SX tank farm. This suggests that leaked tank wastes would have contained high levels of both aluminum ions and free hydroxide. This conclusion is supported by speciation calculations reported in Litchner (2001). The Litchner (2001) results are briefly described in Section C.3.5.2.

Figure C.10. Solubility of Aluminum in Tank SX-108 Waste at 100 °C (212 °F)

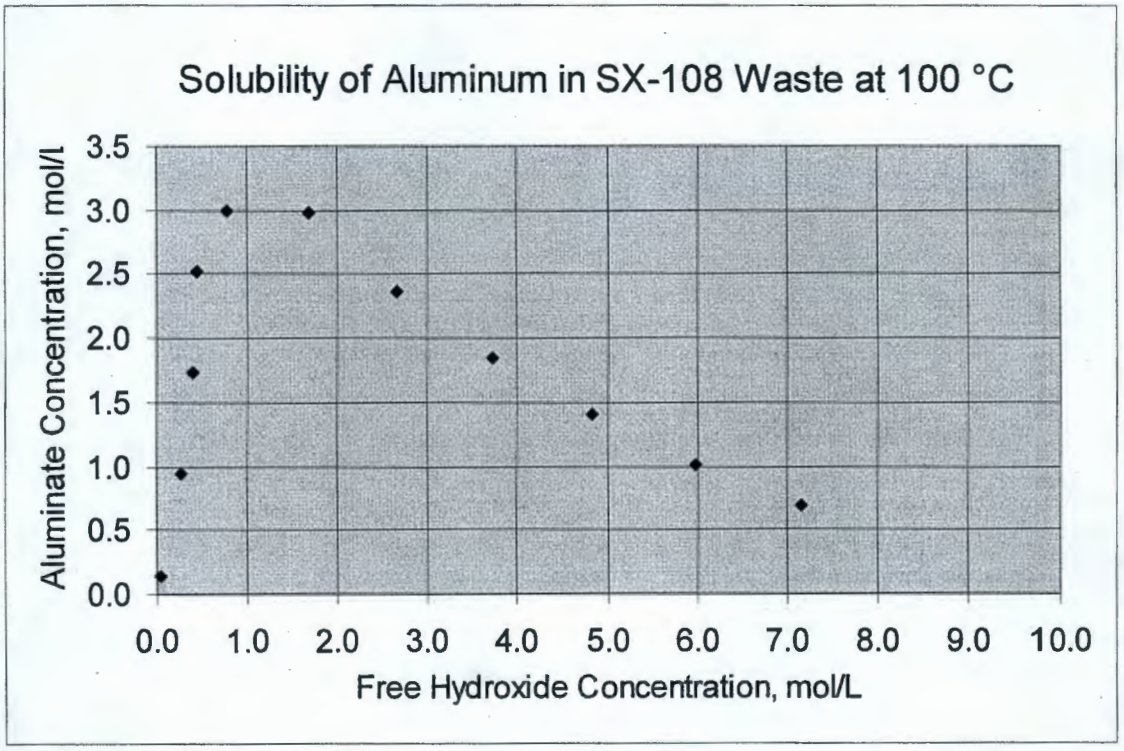

Figure C.11. Solubility of Aluminum in Tank SX-108 Waste at 50 °C (122 °F)

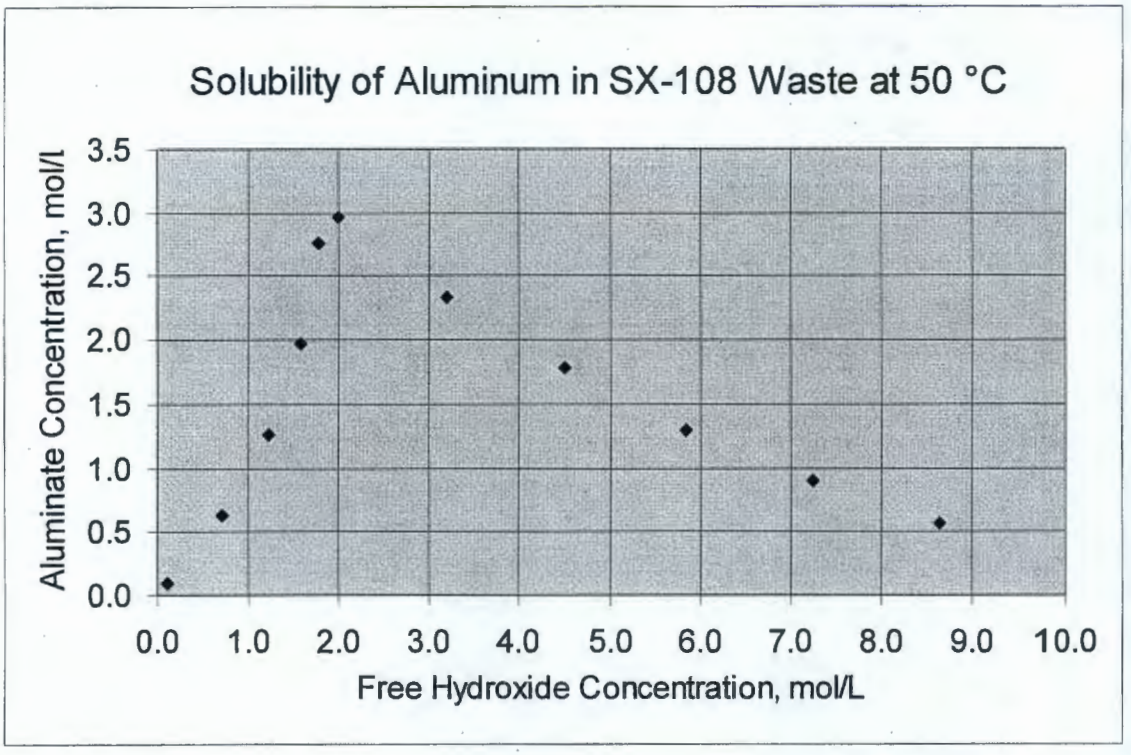

The second speciation modeling run evaluated the changes in solution composition as water was removed from the system. A REDOX HLW waste composition containing only major components was taken from GE (1951). Maximum aluminum ion solubility required 2.60 mol/L free hydroxide. The results shown in Tables C.8 and C.9 indicate the sodium nitrate is the first solid that precipitates from solution as water is removed. The aluminum ion solubility is not exceeded until approximately 45 % of the water is removed. These results are consistent with evaporator operations while removing water from high aluminum wastes (Barney 1975). Results are shown graphically in Figure C.12.

Table C.8. REDOX High-Level Waste Components During Volume Reduction (with Constant OH^-)

REDOX High-Level Waste (50 °C) – moles								Liq. Vol.
OH-	Al(OH)4-	NaAlO2	NO3-	NaNO3aq	Total NO3aq	NaNO3	Liq. Dens.	
2.60	1.40	0.00	2.02	2.21	4.23	0.00	1.36	1.00
2.60	1.40	0.00	1.79	2.44	4.23	0.00	1.40	0.91
2.60	1.40	0.00	1.42	2.48	3.90	0.33	1.43	0.82
2.60	1.40	0.00	0.87	1.99	2.86	1.37	1.43	0.73
2.60	1.40	0.00	0.41	1.50	1.91	2.32	1.45	0.64
2.60	1.05	0.36	0.14	1.05	1.19	3.04	1.46	0.56
2.60	0.37	1.03	0.03	0.63	0.66	3.57	1.47	0.47
2.60	0.05	1.36	0.00	0.23	0.23	4.00	1.53	0.38

Table C.9. REDOX High-Level Waste Components Assuming Water Removal Only

moles/liter					Liq. Vol.	Solid Vol.	Solid Vol. Frac.
OH-	Al(OH)4-	NaAlO2	NO3-	NaNO3aq			
2.60	1.40	2.02	2.22	4.23	1.00	0.000	0.000
2.86	1.54	1.96	2.68	4.65	0.91	0.000	0.000
3.22	1.73	1.75	3.07	4.82	0.81	0.013	0.016
3.82	2.06	1.29	2.92	4.21	0.68	0.052	0.071
4.68	2.52	0.73	2.70	3.43	0.56	0.088	0.137
6.18	2.48	0.34	2.48	2.82	0.42	0.134	0.241
9.43	1.34	0.12	2.28	2.40	0.28	0.191	0.409
16.60	0.29	0.00	1.48	1.48	0.16	0.226	0.591

Figure C.12. REDOX Waste Chemistry During Water Removal

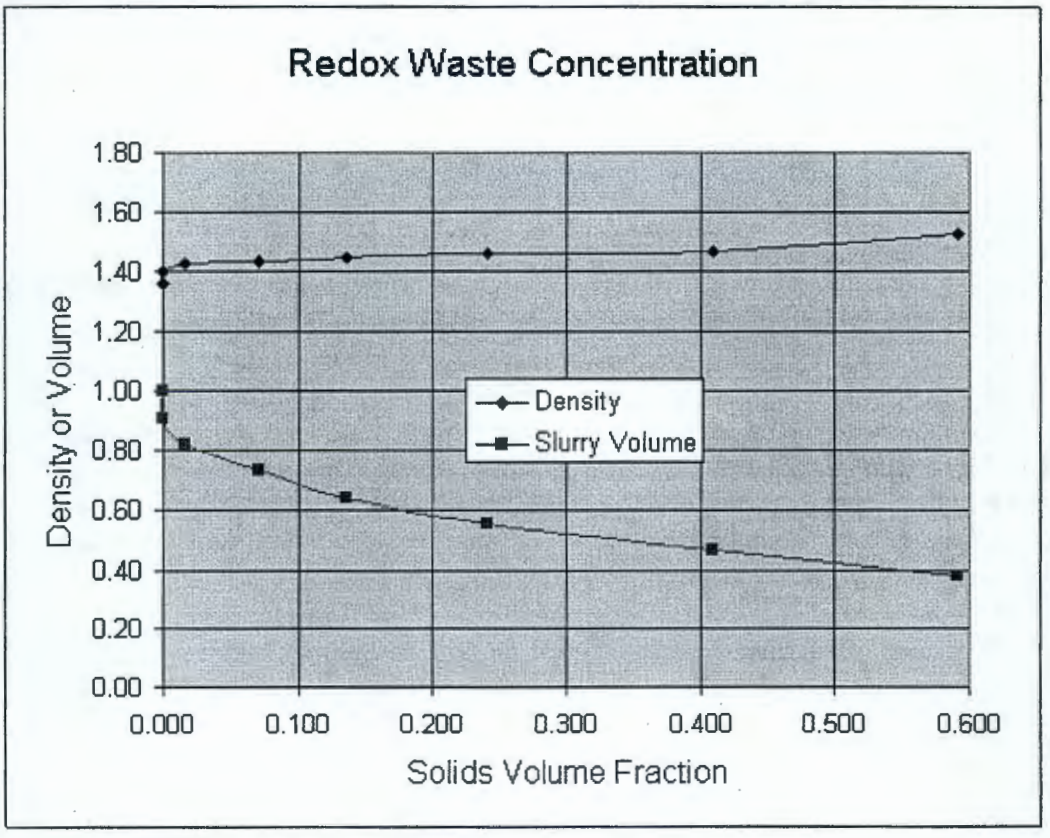

C.3.5.2 Los Alamos National Laboratory Speciation Results for Tank SX-108

The results reported in Litchner (2001) represent a far more detailed solution thermodynamic investigation than the results reported in Jones et al. (2000a). Litchner (2001) uses the Pitzer-based formulation for calculation activity coefficients. This approach is more consistent with contemporary goechemical modeling studies.

Any assessment of the soil-waste reactivity requires reasonable estimates of the chemical species present in the tank waste at the time of the leak. Litchner (2001) begins with estimated tank waste compositions reported in Jones et al. (2000a). The initial step in any speciation modeling exercise is the development a charge balance for the system. Jones et al. (2000a) fixes the hydroxide at 0.1 mole and allows the sodium ion to vary until the overall charge balance is reached, leading to sodium ion concentration near 12 moles. Litchner (2001) chooses to maintain the sodium ion concentration developed by the HDW model and allows hydroxide to be varied until a charge balance is reached. At equilibrium in tank SX-108 at 100 °C (212 °F), Litchner (2001) predicts the hydroxide to be 5.1 moles and a pH of 14.1 with essentially all of the aluminum to be in solution as aluminum hydroxide. The Litchner (2001) speciation results are consistent with the conditions one would predict from process flowsheet data. Thus, these results are the preferred data set for geochemical modeling studies.

C.3.5.3 Technetium-99 Speciation

Technetium-99 has been identified as the major radioisotope of concern in recent risk evaluations at the Hanford Site. Based on theoretical calculations and Hanford Site reactor production records, it is believed that approximately 33,000 Ci of technetium-99 were produced at Hanford and processed through the various plutonium recovery processes (Kupfer et al. 1998). Currently, the fate of this technetium-99 is unclear. Although it is assumed in Kupfer et al. (1998) that for tank inventory estimates all of the technetium-99 produced in the plutonium-production reactors is currently stored in the 177 HLW tanks at the Hanford Site, it is widely understood that some fraction of the technetium-99 was shipped offsite as an impurity in the recovered uranium (Roberts et al. 1962), lost during intentional discharges of tank wastes to the soil column in the 1950s (Waite 1991; Corbin et al. 2001), and lost during various tank waste leak events. In addition to the uncertainty about the quantities and location of technetium-99 within the Hanford HLW tanks, there is considerable uncertainty about the chemical species of technetium-99 in individual tanks (Kovach et al. 1999). Thus, the preliminary speciation modeling results suggesting that major fractions of the technetium-99 could reside in the solid phase as potassium pertechnetate ($KTcO_4$) in highly concentrated REDOX HLW (Jones et al. 2000a) were of considerable interest.

Initial modeling runs indicated that the majority of technetium-99 in wastes in tank SX-108 was incorporated into the solid phase as potassium pertechnetate but in the more dilute tank SX-115 wastes the technetium-99 remained in the solution phase (Jones et al. 2000a). The implication was that technetium-99 was being 'salted out' of solution because of extremely high salt concentrations of these supernates. If the technetium-99 were predominately in the solid phase then the quantity of technetium-99 lost during a leak event would be reduced, as would the long-term risk. The possibility of technetium-99 being salted out of solution because of high ionic strengths could have had significant impacts on other tank waste related activities such as

waste retrieval and vitrification operations. Thus, the technetium-99 modeling results were critically reviewed.

A detailed review of the supporting information reported along with the speciation modeling results indicated that the potassium pertechnetate solubility was being driven by an unrealistically large activity coefficient term. Resolution of this issue was referred back to OLI Systems[1], the software vendor, for resolution. The vendor reported that a programming error was found in the code. Basically, the silicate ion activity was being summed with pertechnetate activity leading to errors in solubility estimates. After correcting this programming error, the model predicted that all technetium-99 remained in the solution phase in each SX farm tank waste composition. Although, to date, no technetium-99 analysis data have been found for REDOX HLW, the suggestion that technetium-99 tends to remain in the solution phase is consistent with experimental data for plutonium-uranium extraction HLW (Godfrey 1971).

[1] OLI Systems, Inc., Morris Plains, New Jersey.

C.4.0 GEOLOGY

This section presents a general discussion on the vadose zone geology in the vicinity of the SX tank farm.

C.4.1 REGIONAL GEOLOGIC SETTING

The Hanford Site is located within the Columbia Plateau of southeastern Washington State. This broad plain, situated between the Cascade Mountains to the west and the Rocky Mountains to the east, is underlain by a thick sequence of Miocene age tholeiitic basalt flows (the Columbia River Basalt Group). These basalt flows have been folded and faulted, creating broad structural and topographic basins, separated by asymmetric anticlinal ridges. Sediments of late Miocene, Pliocene, and Pleistocene age have accumulated up to 518 m (1,700 ft) thick in some of these basins. The Hanford Site lies within one of the larger of these basins, the Pasco Basin. This basin is partially bisected by the Umtanum-Gable Mountain anticline creating two subordinate synclinal basins. The largest of these is the Cold Creek syncline, which is further subdivided into two basins, the Wye Barricade depression and the Cold Creek depression. The Cold Creek depression underlies the principal WMAs of the Hanford Site, the 200 East and 200 West Areas.

The generalized stratigraphy beneath the Hanford Site consists of, in ascending order, the Columbia River Basalt Group, the Ringold Formation, the Plio-Pleistocene unit, and the Hanford formation (Figure C.13). Thin veneers of Holocene alluvium, colluvium, and/or eolian sediments discontinuously overlie these principal geologic units. More thorough descriptions of the regional geology, including the saturated zone of this area, are found in *Geology of the Separations Areas, Hanford Site, South-Central Washington* (Tallman et al. 1979), *Consultation Draft Site Characterization Plan* (DOE 1988); *200 West Groundwater Aggregate Area Management Study Report* (DOE-RL 1993); and "Geohydrologic Setting of the Hanford Site, South-Central Washington" (Lindsey et al. 1994).

C.4.2 GEOLOGY OF THE S AND SX TANK FARMS

The S and SX tank farms were constructed into the upper Hanford formation sediments underlying 200 West Area, along the north limb of the Cold Creek syncline. Stratigraphic units underlying or adjacent to the tank farms (in descending order) include backfill materials, lower Hanford formation sediments, the Plio-Pleistocene unit, and the Miocene- to Pliocene-age Ringold Formation.

Figure C.13. Generalized, Composite Stratigraphy for the Late Cenozoic Sediments Overlying the Columbia River Basalt Group on the Hanford Site

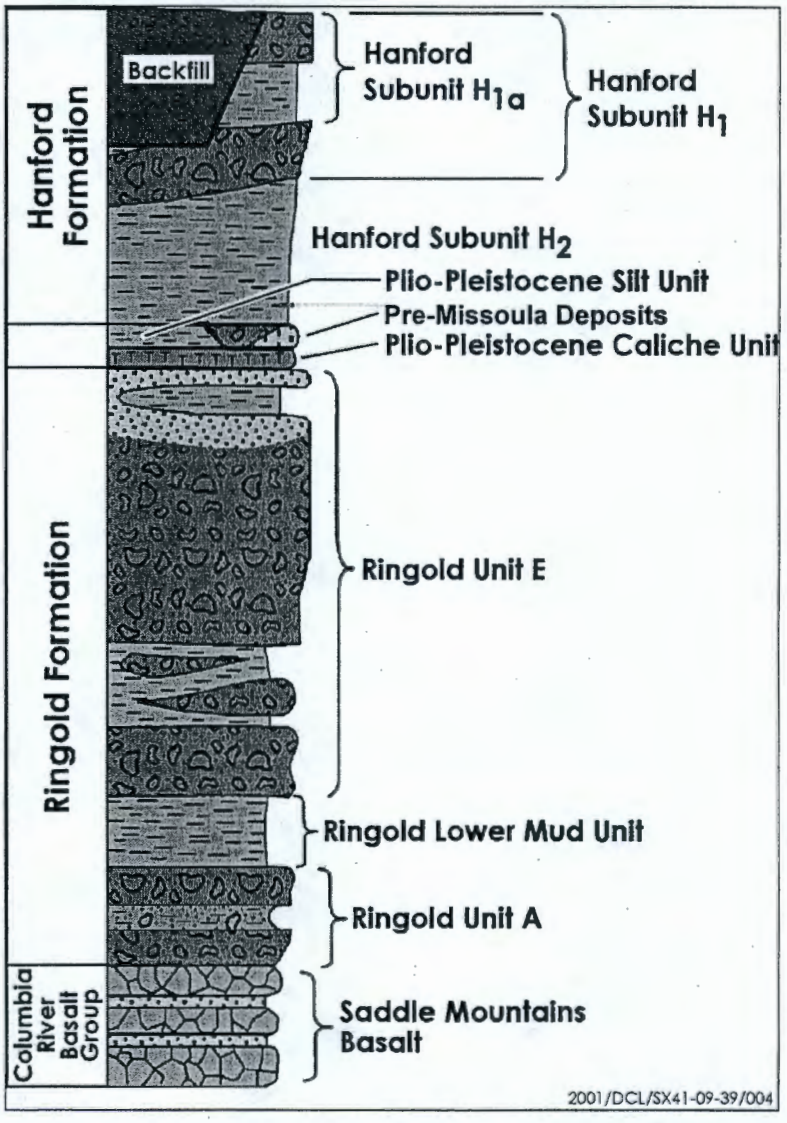

Sources: Johnson and Chou (1998); Johnson and Chou (1999).

The geology beneath the S and SX tank farms has been the subject of numerous reports. *Geology of the 241-SX Tank Farm* (Price and Fecht 1976a) presents an initial detailed interpretation of the geology. *Vadose Zone Characterization Project at the Hanford Tank Farms* (DOE 1996) presents an interpretation of the geology that is based primarily on groundwater monitoring wells constructed around the perimeter of the tank farm in the early 1990s. *Results of Phase I Groundwater Quality Assessment for Single-Shell Tank Waste Management Areas S-SX at the Hanford Site* (Johnson and Chou 1998) updates and refines the geologic interpretation. *Findings of the Extension of Borehole 41-09-39, 241-SX Tank Farm* (Myers et al. 1998) and *Geologic and Geochemical Data Collected from Vadose Zone Sediments from Borehole SX 41-09-39 in the S/SX Waste Management Area and Preliminary Interpretations* (Serne et al. 2001b) present detailed discussions on the geologic materials penetrated by the extension of borehole 41-09-39 (299-W23-234). *Subsurface Conditions Description for the S-SX Waste Management Area* (Johnson et al. 1999) further describes the geology and other subsurface contaminants. *Vadose Zone Geology of Boreholes 299-W22-50 and 299-W23-19 S-SX Waste Management Area Hanford Site, South-Central Washington* (Lindsey et al. 2000) provides additional interpretations on the geology, facilitated by the collection of near continuous split-spoon samples from boreholes 299-W22-50 and 299-W23-19. Geochemical analyses on vadose zone samples collected from borehole 299-W23-19, drilled through a contaminated zone immediately adjacent to SST SX-115, is the focus of this report (Figure C.14).

Borehole Data Package for Wells 299-W22-48, 299-W22-49, and 299-W22-50 at Single Shell Tank Waste Management Areas S-SX at the Hanford Site (Horton and Johnson 2000) contains a compilation of data packages on three groundwater monitoring wells (299-W22-48, 299-W22-49, and 299-W22-50) completed near the SX tank farm in 1999 and 2000. Most recently, *Subsurface Interpretation of the SX Tank Farm, Hanford Site, Washington Based on Gamma-Ray Logging* (Sobczyk 2000) presents a reinterpretation on the geology based on gross gamma-ray logs of 98 boreholes within the SX tank farm and the most recently published geology reports of the area (Johnson et al. 1999; Lindsey et al. 2000). Lastly, *Modeling Data Package for S-SX Field Investigation Report* (Khaleel et al. 2000) contains a detailed data package to support numerical simulation of the S and SX tank farms.

A hydrogeologic cross-section, constructed from a series of densely spaced boreholes beneath the SX tank farm is presented in Figure C.15. Some slight discrepancies may occur between the depths of the geologic contacts presented in this appendix and those presented in other documents, due to the various source of uncertainty in the geologic data sets and an individual geologist's interpretation. Johnson et al. (1999) describes the various sources of uncertainty for locating the stratigraphic contacts within a borehole as well as those uncertainties for drawing correlations between boreholes. That document identifies the principal sources of uncertainty as related to the drilling and sampling techniques, logging of the boreholes, and uncertainties in the geometric shape of the sedimentary units. Two different geostatistical techniques are used in Johnson et al. (1999) to evaluate the stratigraphy/depth uncertainty and finds that both techniques indicate that the stratigraphy beneath the S and SX tank farms is relatively consistent across the area. The optimal depths for stratigraphic correlations between different data sets were also found to be typically accurate to within 0.6 to 3 m (2 ft to 10 ft).

Figure C.14. SX Tank Farm and Vicinity Showing Location of Borehole 299-W23-19

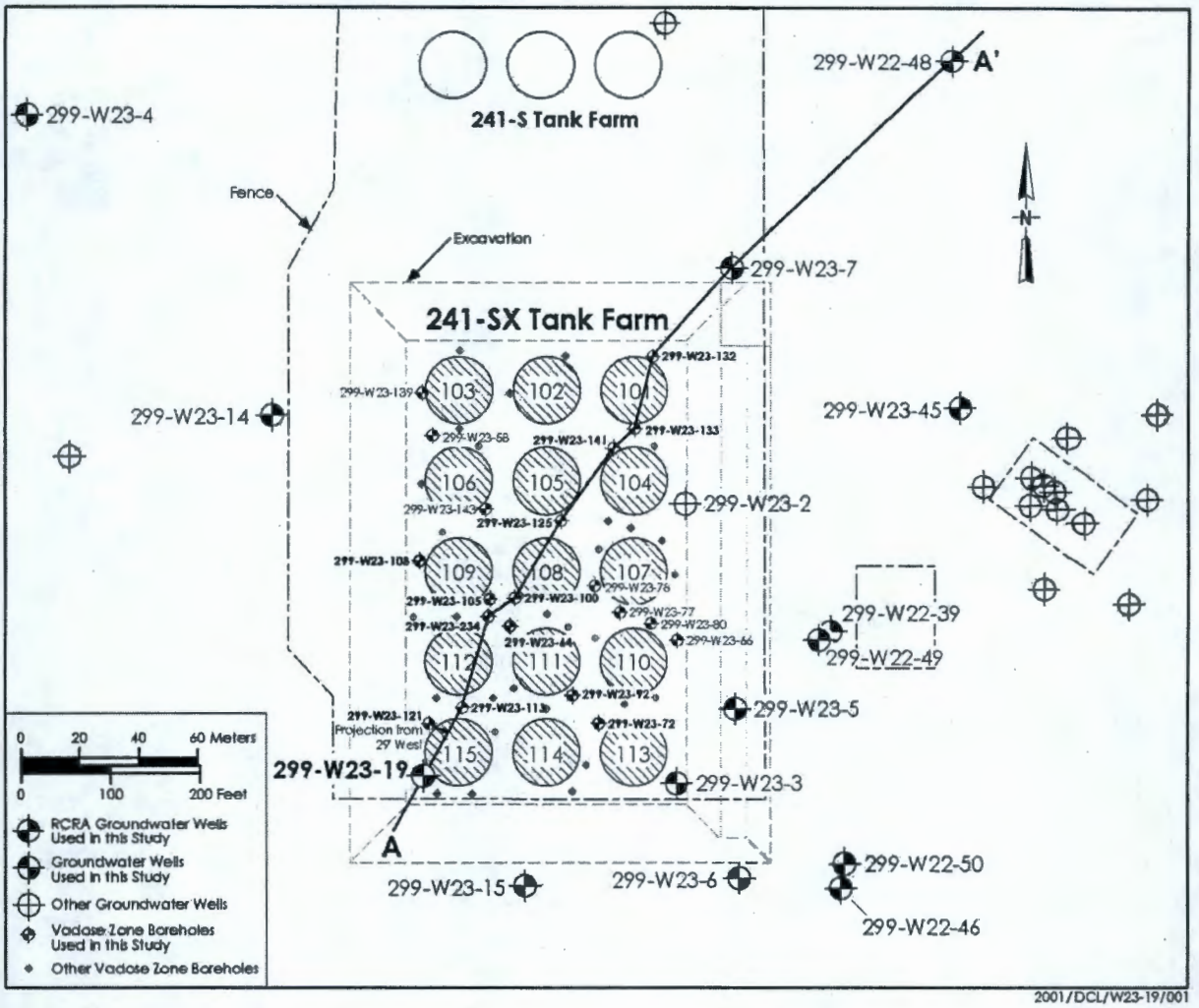

Note: Location of cross-section A-A', represented in Figure C.15.

Figure C.15. Hydrogeologic Cross-Section of the Vadose Zone Beneath the SX Tank Farm

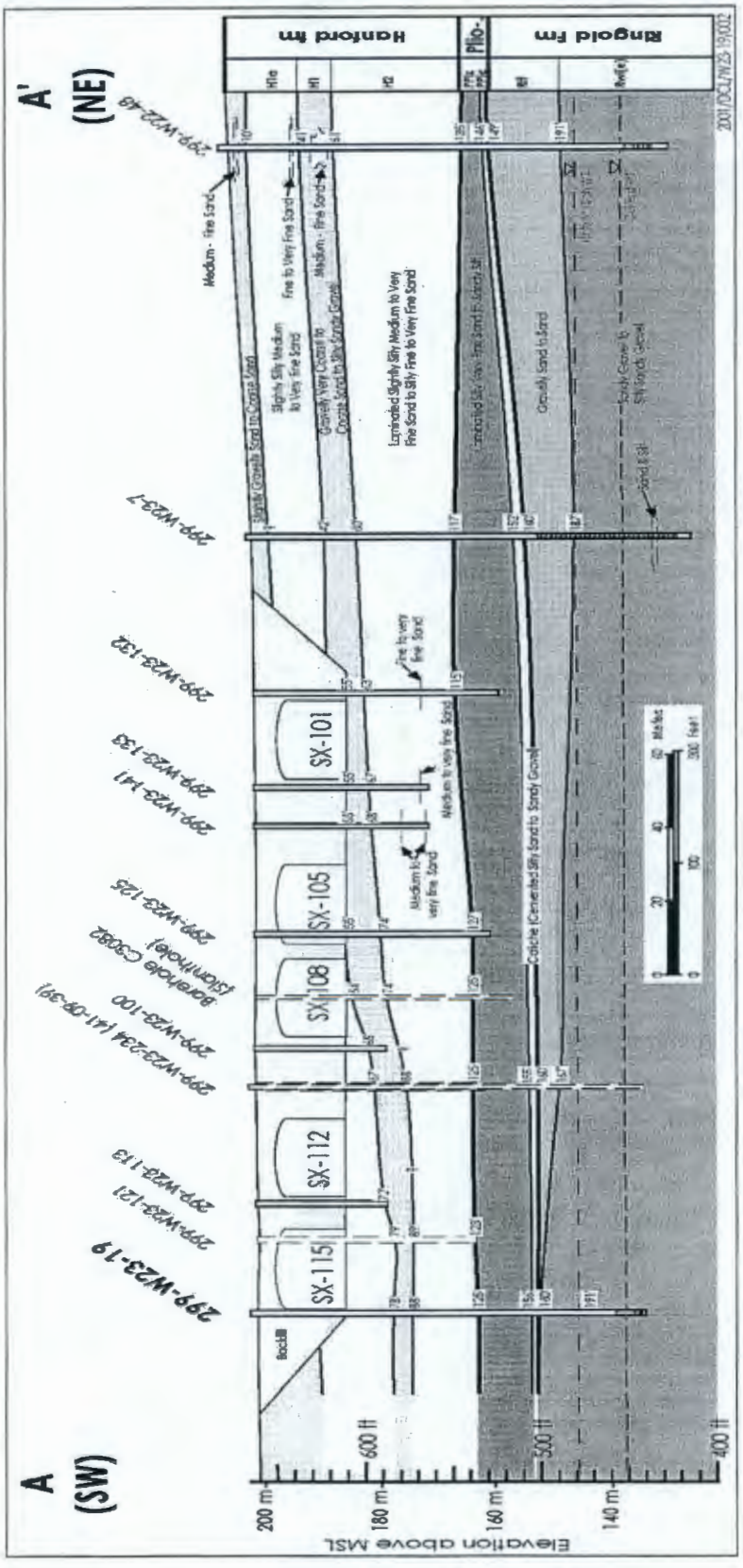

The stratigraphic terminology used in this report is summarized in Table C.10. The general stratigraphic interpretation presented here differs somewhat from that presented in Lindsey et al. (2000). The coarse (gravelly) materials found near the middle of the Hanford formation (correlative with Hanford H1 unit in Lindsey et al. [2000]) are interpreted to correlate across the tank farm and to represent a laterally continuous coarse unit distinct from the overlying and underlying finer sand units. Lindsey et al. (2000) suggests that these coarser materials are not continuous but rather represent thin, lenticular, discontinuous gravelly beds within stratified sand sheets of the Hanford formation. These differences are in interpretation only.

C.4.2.1 Columbia River Basalt Group

The Columbia River Basalt Group (composed of approximately 50 basalt flows) is more than 3,000 m (10,000 ft) thick and forms the bedrock beneath the Hanford Site. Sedimentary interbeds are sandwiched between the basalt flows, particularly in the uppermost Saddle Mountains Basalt. These interbeds, along with the porous basalt flow tops and flow bottoms, form confined aquifers that extend across the Pasco Basin (Reidel 1997).

The surface of the Columbia River Basalt Group lies at an elevation of approximately 26 m (85 ft) above mean sea level beneath the S and SX tank farms (a depth of approximately 175 m [575 ft] and dips gently to the southwest towards the axis of the Cold Creek syncline (Price and Fecht 1976a; DOE-RL 1993).

C.4.2.2 Ringold Formation

The Ringold Formation lies directly on top of the Columbia River Basalt Group and is approximately 125 m (410 ft) thick beneath the S and SX tank farms. The group locally consists of three principal stratigraphic units: (1) the fluvial gravels of unit A, (2) a fine-grained, paleosol-lacustrine sequence referred to as the lower mud unit, and (3) fluvial gravels of unit E (Figure C.13). The Ringold unit E gravels, depicted as Rwi(e) on Table C.10, are interpreted as equivalent to the Ringold Member of Wooded Island exposed along the White Bluffs, located along the eastern margin of the Hanford Site (Lindsey 1996). Ringold unit E grades upwards into fluvial sands of the upper Ringold unit (DOE-RL 1993), interpreted as an equivalent to the Ringold member of Taylor Flat (Rtf on Table C.10). Ringold unit E forms the main unconfined aquifer beneath the 200 West Area.

DOE-RL (1993) shows that the thickness of fluvial Ringold unit A is approximately 30 m (100 ft). Tallman et al. (1979) describes this unit as a silty-sandy gravel that is composed predominantly of gravel supported by a coarse-to-fine sand matrix with intercalated, lenticular beds of sand and silt.

The thickness of the lower mud unit is approximately 12 to 30 m (40 to 100 ft) (Tallman et al. 1979; DOE-RL 1993). This unit consists of predominantly mud (i.e., silt and clay); the lower portion contains well-developed argillic to calcic paleosol sequence (DOE 1988). The high clay content (up to 43% by weight) and the low hydraulic conductivity (perhaps as low as 10^{-12} ft/day) of this sequence acts to locally confine groundwater within unit A and form a base for the uppermost unconfined aquifer (Last et al. 1989).

Table C.10. Stratigraphic Terminology Used in this Report for the Vadose Zone Beneath the SX Tank Farm

Stratigraphic Symbol*	Formation	Facies/Subunit	Description	Genesis
Holocene/Fill	NA	Backfill	**Poorly sorted gravel to medium sands and silt** derived from the Hanford formation (Price and Fecht 1976a).	Anthropogenic
H1a	Hanford formation	Unit H1b - gravelly sand	**Top coarse sand and gravel sequence** equivalent to the Johnson et al. (1999) 'Gravel Unit B.'	Cataclysmic flood deposits
		Unit H1a - slightly silty sand	**Upper fine sand and silt sequence**	
H1		Unit H1	**Middle Coarse Sand and Gravel Sequence** equivalent to 'Gravel Unit A' described by Johnson et al. (1999) and 'Hanford Unit A' described by Sobcyzk (2000).	
H2		Unit H2	**Lower Fine Sand and Silt Sequence**	
PPlz and/or H/PPl	Plio-Pleistocene unit	Upper	**Very Fine Sand to Clayey Silt Sequence** is interstratified silt to silty very fine sand and clay deposits at least partially correlative with the 'early Palouse soils' described by Tallman et al. (1979) and DOE (1988) and the 'unnamed Hanford formation [?] or Plio-Pleistocene Deposits [?]' described by Lindsey et al. (2000), and the H/PP deposits in Wood et al. (2001).	Fluvial and/or eolian deposits (with some weakly developed paleosols)
PPlc		Lower	**Carbonate-Rich Sequence.** Weathered and naturally altered sandy silt to sandy gravel, moderately to strongly cemented with secondary pedogenic calcium carbonate.	Well-developed calcic paleosol or sequence of calcic soils.
Rtf	Ringold Formation	Member of Taylor Flat	**Interstratified sand and silt deposits,** equivalent to the Upper Ringold unit described by Tallman et al. (1979) and DOE (1988).	Fluvial and overbank-paleosol deposits
Rwi(e)		Member of Wooded Island, subunit E	**Moderate to strongly cemented, well-rounded gravel and sand deposits,** and interstratified finer-grained deposits.	Fluvial

*After Lindsey et al. (2000).

The thickness of unit E is estimated to be approximately 75 to 85 m (250 to 280 ft) (Tallman et al. 1979; DOE-RL 1993). This unit consists of well-rounded, clast-supported pebbles and small cobbles in a matrix of sand and mud. The amount of cementation is variable, with the lower portion of this unit described as moderately to well-indurated conglomerate (Tallman et al. 1979). However, zones of poorly indurated gravel and sand also occur within this zone. The upper part of the unit is generally poorly indurated. Borehole data in the immediate vicinity of the SX tank farm indicate that this upper portion is dominated by sandy gravel and muddy sandy gravel, with sand to muddy sand beds becoming more prevalent toward the top of the unit.

A relict erosional and weathered surface occurs at the top of the Ringold Formation beneath the SX tank farm (DOE 1988; Slate 1996; Slate 2000). The uppermost portion of this paleosurface is highly weathered and often cemented with secondary pedogenic calcium carbonate, referred to in this appendix as the carbonate-rich facies (subunit PPlc) of the Plio-Pleistocene unit (Table C.10). The northwest-southeast trending trough-shaped surface appears to conform to an ancestral Cold Creek channel and drainage system that developed following late Pliocene incision of the Ringold Formation, and prior to early Pleistocene cataclysmic flooding, during the period between approximately 2 to 3 million years ago (DOE 1988). The SX tank farm lies north of the ancestral Cold Creek paleochannel and the eroded Ringold paleosurface dips to the southwest beneath the SX tank farm. The attitude on this surface may have increased since late Pliocene-early Pleistocene time as a result of tectonic deformation associated with the Cold Creek syncline (Slate 1996; Slate 2000).

C.4.2.3 Plio-Pleistocene Unit

The Plio-Pleistocene unit lies unconformably on the tilted and truncated Ringold Formation that formed following incision and downcutting of the Ringold Formation by the ancestral Columbia River system, which began about 3.4 million years ago (DOE 1988). These deposits are inferred to have a late Pliocene to early Pleistocene age on the basis of stratigraphic position. The Plio-Pleistocene unit includes all material overlying the Ringold Formation, including the weathered horizon at the top of the Ringold Formation, and beneath cataclysmic flood deposits of the Hanford formation (Lindsey et al. 1994). The Plio-Pleistocene unit includes the 'early Palouse soils' described in *An Eolian Deposit Beneath 200-West Area* (Brown 1960), Tallman et al. (1979), and DOE (1988); the 'Pre-Missoula Gravels' (or equivalent); the 'unnamed Hanford Formation [?] or Plio-Pleistocene Deposits [?]' described in Lindsey et al. (2000); and H/PP(?) deposits described in *Subsurface Conditions Description of the T-TX-TY Waste Management Area* (Wood et al. 2001).

Two distinct facies of the Plio-Pleistocene unit are recognized beneath the SX tank farm; these consist of an upper (PPlz) and lower (PPlc) subunit (Table C.10). The upper subunit PPlz is characterized by an abundance of silt, signified by the letter 'z,' and the lower subunit PPlc is characterized by an abundance of pedogenic calcium carbonate cement, signified by the letter 'c.' The combined total thickness of the Plio-Pleistocene unit is up to 13.1 m (43 ft) in the vicinity of the SX tank farm (Figure C.15). Subunit PPlz is relatively thick (up to 10.7 m [35 ft]), compared to the subunit PPlc, which measures only 1 to 4 m (4 to 13 ft) in thickness.

Subunit PPlc. The lower subunit PPlc represents a highly weathered paleosurface that developed atop the Ringold Formation (Brown 1959; Brown 1960), which represents a long period of surficial weathering in a semi-arid climate, similar to climatic conditions that exist today. Root traces and animal borrows, as well as other relict soil structures, point to a pedogenic origin for the calcium carbonate, although "Buried Carbonate Paleosols Developed in Pliocene-Pleistocene Deposits of the Pasco Basin, South-Central Washington" (Slate 1996) and *Nature and Variability of the Plio-Pleistocene Unit in the 200 West Area of the Hanford Site* (Slate 2000) also suggest the calcium carbonate could be associated with precipitation from paleo-groundwater levels. Calcium carbonate contents as high as 70 wt% have been reported within subunit PPlc elsewhere within the 200 West Area; however, the calcium carbonate content generally does not exceed 25 wt% in the vicinity of the SX tank farm. The calcium carbonate content from 3 randomly chosen boreholes within the SX tank farm did not exceed 10 wt%. Other names used for subunit PPlc, including 'caliche' and 'calcrete' are somewhat misleading because they imply a single, homogeneously cemented layer, which is not the case. Considerable internal variation exists, within subunit PPlc, often with multiple carbonate-cemented zones present (Bjornstad 1990; Slate 1996; Slate 2000; Wood et al. 2001).

The calcium carbonate overprint may occur on a variety of lithologies including silt, sand, felsic sand, and gravel as well as basaltic sand and gravel (Lindsey et al. 2000). In places, pedogenic alteration occurs directly on top of Ringold gravels (Rwi[e]) or sands (Rtf). In other places, the carbonate horizons occur within younger, pedogenically altered, fine-grained, eolian or sidestream-alluvial deposits overlying the Ringold Formation. The top of subunit PPlc is well defined by a coincident significant increase in calcium carbonate and decrease in mud content and sorting accompanied by a sudden and sustained decrease in total gamma activity (i.e., potassium-40) on borehole geophysical logs (DOE 1988; Last et al. 1989; Bjornstad 1990; Wood et al. 2001). In general, the top of subunit PPlc is easily identified by a sudden drop in total gamma activity that is usually, but not always, accompanied by a significant increase in calcium carbonate.

While the top subunit PPlc is relatively easy to recognize, considerable variation may exist internally within the subunit due to natural heterogeneity inherent of soils and soil processes that vary under different physical, chemical, and biological conditions (e.g., moisture, grain size, aspect, mineralogy, bioturbation, microbial activity). Added to this is the complicating factor that the land surface during Plio-Pleistocene time was undergoing many changes under the influence of local fluvial and eolian activity resulting in variable rates of aggradation, degradation, and soil development. Normally, only a single paleosol horizon is present within the lower Plio-Pleistocene unit within the SX tank farm, suggesting slow or negligible aggradation and/or subsequent erosion during paleosol development. This is in contrast to other areas to the west and south, which show up to five separate calcic horizons (Figure C.16) separated by relatively noncalcareous, uncemented sand; silt; and even indigenous, basaltic sand and/or gravel (Slate 1996; Slate 2000; Wood et al. 2001). Multiple carbonate horizons within the subunit PPlc are indicative of several periods of calcic-soil development interrupted temporarily by periodic aggradational events (e.g., localized overbank flood, eolian accumulation, channel fill). The evolution of calcic paleosols and their morphogenetic development are discussed further in Slate (1996; 2000) and Wood et al. (2001).

Figure C.16. Lithofacies Distribution for the Lower Plio-Pleistocene Subunit PPlc

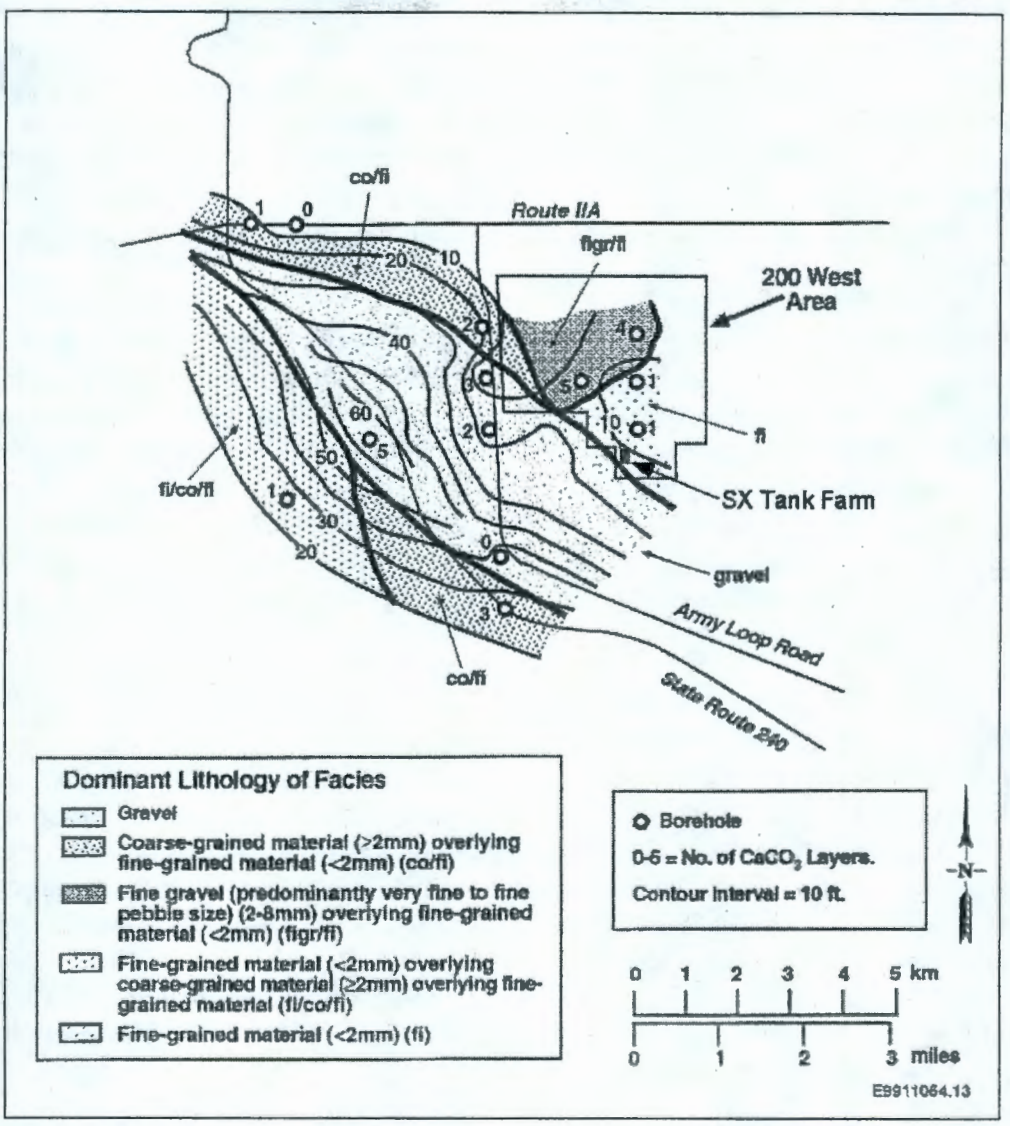

Modified from Slate (2000).

In WMA T-TX-TY, which is 1,800 m (5,900 ft) north of the SX tank farm, the top of subunit PPlc dips to the southwest at about 1° (Wood et al. 2001). At least some of the dip reflects the paleo-topography that existed during subaerial weathering of the eroded Ringold Formation surface. This is inferred based on the relief on top of subunit PPlc, which is almost double that of the underlying Ringold Formation lower mud unit. Therefore, it appears that during development of subunit PPlc there was a gentle dip to the land surface to the southwest toward the Cold Creek valley axis. Since Plio-Pleistocene time this surface has been steepened further by continued long-term downwarping along the north limb of the Cold Creek syncline (DOE 1988).

Another recognized facies of the Plio-Pleistocene unit is a coarse-grained side-stream-alluvial facies (Bjornstad 1984; DOE 1988; Slate 1996; Slate 2000), which is laterally equivalent to subunit PPlc to the south and west of SX tank farm. The side-stream alluvial facies (gravel facies in Figure C.16) fills and is restricted to the northwest-southeast trending, ancestral Cold Creek channel, located south and west of the 200 West Area. The eastern edge of this gravel facies occurs along the southwest boundary of 200 West Area near the SX tank farm (Figure C.16). North and east of the 200 West Area, the Plio-Pleistocene unit is generally not present, having been scoured away during either post-Ringold erosion and/or Pleistocene cataclysmic flooding.

C.4.2.3.1 Subunit PPlz. Unconformably overlying subunit PPlc is the upper subunit PPlz which consists of interstratified, uncemented fine sand, silt, and/or clay that only displays occasional, very weak soil development in the vicinity of the SX tank farm. Based on its fine-grained texture and relatively high natural-gamma activity on geophysical logs, this unit can be correlated across most of the 200 West Area (Wood et al. 2001). Subunit PPlz sediments appear to be predominantly fluvial-overbank type deposits intercalated with some eolian deposits (Lindsey et al. 2000; Slate 2000; Wood et al. 2001). Subunit PPlz is at least partially correlative with the 'early Palouse soils' described by previous reports (Brown 1960; Tallman et al. 1979; Bjornstad 1984; Last et al. 1989; Bjornstad 1990; and DOE 1988); the 'unnamed Hanford Formation [?] or Plio-Pleistocene Deposits [?]' described in Lindsey et al. (2000); and the H/PP(?) unit described in Wood et al (2001).

The upper Plio-Pleistocene unit contains moderate amounts (up to a few weight percent) of calcium carbonate (Table C.11), generally more than the overlying Hanford formation. As discussed previously, however, subunit PPlz may also locally have more calcium carbonate than the underlying subunit PPlc if samples from subunit PPlc come from noncalcic zones between paleosols within subunit PPlc.

Table C.11. Example of Granulometric and Calcium Carbonate Data from Drive-Barrel Samples of Subunit PPlz Encountered Beneath the SX Tank Farm

Borehole /Depth	$CaCO_3$ %	Gravel >2 mm	Sand					Mud <0.063 mm	Class
			Very Coarse 1-2 mm	Coarse 0.5-1.0 mm	Medium 0.25-0.5 mm	Fine 0.125-0.25 mm	Very Fine 0.063-0.125 mm		
299-W23-5 120 ft	2.6	0.0	1.8	1.9	4.8	12.3	31.1	48	mS
299-W23-5 125 ft	2.3	0.0	1.6	7.0	9.2	7.3	8.1	66.8	sM

The source of the calcium carbonate within the two subunits appears distinctly different. Within subunit PPlc, most of the calcium carbonate appears as stringers or in massive horizons, which formed in situ as a result of pedogenesis (Wood et al. 2001). Within subunit PPlz, on the other hand, the calcium carbonate is evenly disseminated and does not occur in discrete zones; therefore, it is interpreted to be detrital in origin (Wood et al. 2001). In fact, the bulk of the detrital, calcium carbonate mineral grains in subunit PPlz are probably derived from the disintegration and mechanical re-working and re-deposition of the underlying subunit PPlc.

The contact between subunits PPlz and PPlc is distinctive and easily identified. Subunit PPlz consists of relatively loose, stratified, non-pedogenically altered, well-sorted silt to very fine sand in contrast to poorly-sorted, weathered, and carbonate-cemented deposits of subunit PPlc. Also distinctive is a sudden increase in total gamma activity upward across the contact (DOE 1988; Last et al. 1989; Bjornstad 1990; Johnson et al. 1999). The upper contact of subunit PPlz with the overlying Hanford formation, on the other hand, often appears gradational, both texturally and structurally, and thus is often difficult to identify based on lithologic observations alone, especially in the vicinity of the SX tank farm. Because of this uncertainty, in the past subunit PPlz has been combined and queried with the lower Hanford formation in some recent reports (Lindsey et al. 2000; Wood et al. 2001). For the purposes of this study it was determined that the total gamma activity on borehole geophysical logs can effectively be used to identify the upper contact for the Plio-Pleistocene unit. Accordingly, a subtle decrease in total gamma activity appears to be associated with the top of subunit PPlz, probably as a result of a lower silt/clay content within the Hanford formation. Therefore, we recommend that this change in total-gamma activity and grain size be used to define the upper contact for subunit PPlz.

C.4.2.4 Hanford Formation

Pleistocene-age deposits of the Hanford formation overlie the Plio-Pleistocene unit and represent the dominant vadose zone materials directly beneath the SX tank farm. The Hanford formation is the informal name given to all deposits from Ice Age cataclysmic floods including any intercalated non-flood deposits.

The Hanford formation can generally be divided into three facies: (1) gravel-dominated, (2) sand-dominated, and (3) silt-dominated, also referred to as coarse-grained deposits, plane-laminated sand facies, and rhythmite facies, respectively (Baker et al. 1991). The coarse-grained facies have also been referred to as the 'Pasco gravels,' and the rhythmite

facies as 'Touchet Beds.' The Hanford formation is thickest (up to 65 m [215 ft]) in the vicinity of the 200 Areas beneath Cold Creek bar (Figure C.17).

The gravel-dominated facies generally consists of poorly-sorted coarse-grained basaltic sand and granule to boulder gravel. These deposits occasionally display an open framework texture, massive bedding, plane to low-angle bedding, and large-scale fore-set bedding in outcrop. The gravel clasts (dominated by basalt) are usually subangular to subrounded. The gravel-dominated facies was deposited by high-energy floodwaters in or immediately adjacent to the main cataclysmic flood channel ways (Figure C.17).

The sand-dominated facies consists of fine- to coarse-grained sand and granule gravel displaying plane lamination and bedding and, less commonly, plane bedding and channel-fill sequences in outcrop. These sands may contain small pebbles and rip-up clasts in addition to pebble-gravel interbeds and silty interbeds less than 1 m (3 ft) thick. The silt content of these sands is variable, but where it is low a well-sorted and open framework texture is common. These sands typically are basaltic, commonly being referred to as black, gray, or 'salt-and-pepper' sands. The laminated sand facies was deposited at higher elevations where the floodwaters were starved of gravel, and/or adjacent to main flood channel ways during the waning stages of flooding (Figure C.17). This is a transitional facies between the gravel-dominated facies and the silt-dominated facies. The sand-dominated facies is the predominant facies of the Hanford formation beneath the SX tank farm.

The silt-dominated facies consists of rhythmically bedded, ripple-cross-laminated sand and silt, and fine- to coarse-grained sand grading upward to plane laminated silt. Individual rhythmites range from a few centimeters to several tens of centimeters thick (Myers and Price 1979; DOE 1988; Baker et al. 1991). These sediments were deposited under slack-water conditions and in back-flooded areas (DOE 1988), mostly around the margins of the basins (Figure C.17). The silt-dominated facies is the predominant facies of the Hanford formation south and west of the SX tank farm.

The Hanford formation beneath the SX tank farm is mostly represented by sand-dominated facies consisting of fine-grained sands intercalated with coarse sand and gravel and thinner lenses of silt. The basal portion of the Hanford formation is predominantly silty fine sand, described by DOE (1996) and Lindsey et al. (2000) as Hanford subunit H2 (Table C.10). A sandy gravel to coarse sand facies dominates the middle portion of the Hanford formation, which is then overlain by a slightly silty medium sand and finally by a slightly gravelly coarse sand. The middle coarse sand to gravel facies makes up the Hanford subunit H1 described in DOE (1996), Johnson et al. (1999), and Lindsey et al. (2000). The slightly silty medium sand and overlying slightly gravelly coarse sand is equivalent to the Hanford subunit H1a (Johnson et al. 1999; Lindsey et al. 2000).

Figure C.17. Digital Elevation Model Map of a Portion of the Pasco Basin Showing Routes and Facies Distributions for the Last Pleistocene Cataclysmic Floods

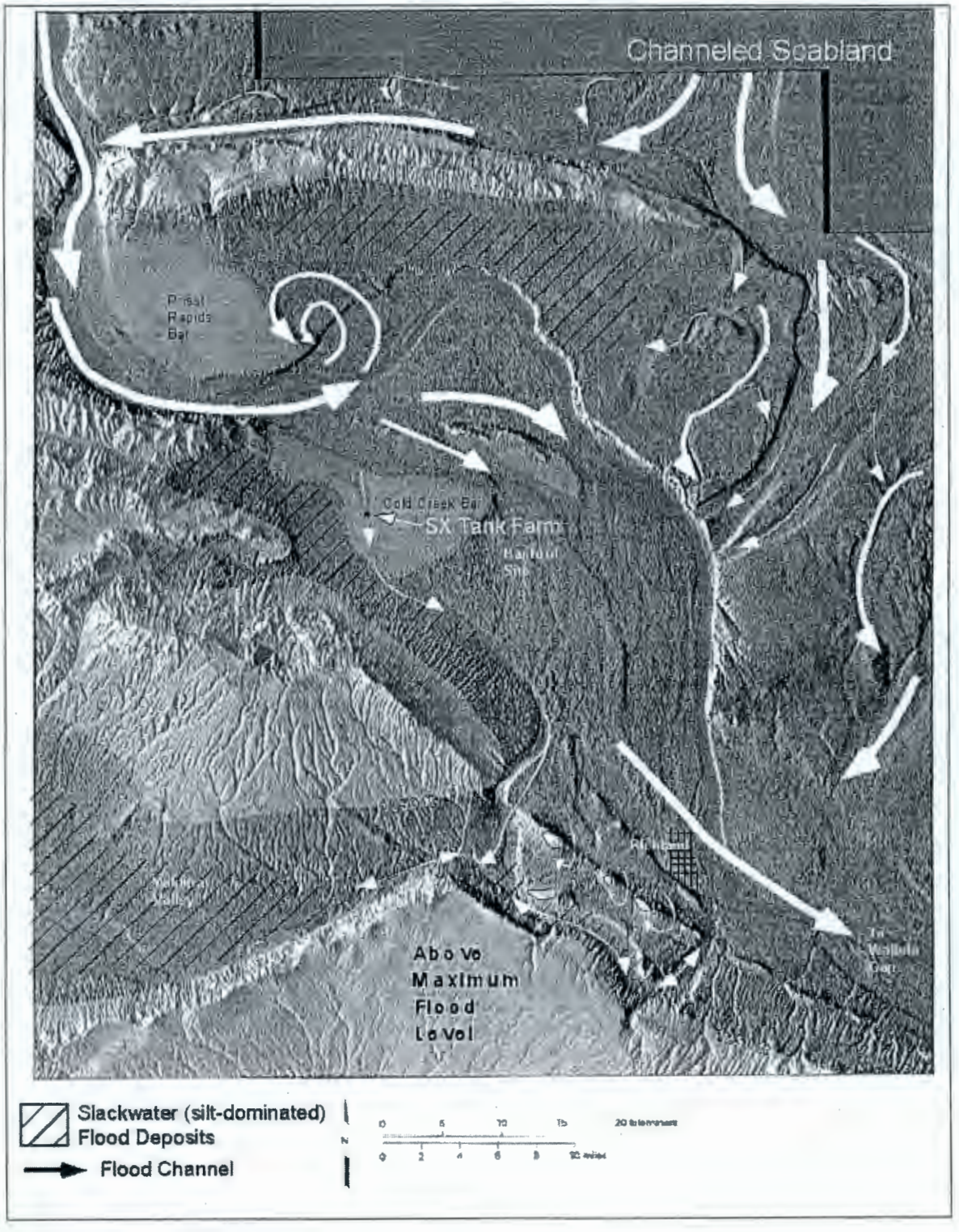

C.4.2.4.1 Subunit H2. The lower fine sand and silt sequence of the Hanford formation, H2 subunit, consists primarily of interstratified silty sands. This sequence generally thins from about 24.3 m (80 ft) east of the SX tank farm to approximately 10.7 m (35 ft) west of the tank farm (Figure C.15). Johnson and Chou (1998) suggests that this thinning may signify some scouring on top of the subunit, perhaps associated with a secondary flood channel similar to the north-south trending flood channel that bisects Cold Creek bar in Figure C.17. The grain-size within the Hanford H2 subunit appears to coarsen upward slightly (see Table C.12). Sobcyzk (2000) and Johnson et al. (1999) report that the top of this unit generally dips about 6° to the southwest with some local relative highs and lows present throughout. Below subunit H2 are slightly finer-grained deposits of interstratified very fine sand, silt, and clay associated with the upper Plio-Pleistocene subunit PPlz. As mentioned previously, the base of the Hanford formation is indicated by a diagnostic increase in total-gamma activity on borehole geophysical logs.

C.4.2.4.2 Subunit H1. Subunit H2 is bounded above by subunit H1, and is a coarse unit dominated by gravel to gravelly sand and intercalated coarse sand (Table C.12) that appears to correlate beneath the SX tank farm (Figure C.15). This middle sequence—referred to as 'Gravel Unit A' in Johnson et al. (1999) and as 'Hanford Unit A' in Sobcyzk (2000)—is equivalent to the H1 unit described in DOE (1996) and Lindsey et al. (2000). Subunit H1 ranges in thickness from 1 m (3 ft) to nearly 10 m (30 ft) beneath the SX tank farm. Sobcyzk (2000) reports subunit H1 to be thickest beneath tank SX-102 (Figure C.14) where coarse-grained flood deposits backfilled an apparent channel eroded into the top of the underlying subunit H2.

Recent particle size results using dry sieving for 100 selected samples from 7 wells drilled in and around the tank farm reveal that this unit averages approximately 30% gravel, 66% sand, and only 4 % mud (see Appendix A). This is compared to the materials directly above and below it, that both average less than 1% gravel, nearly 90% sand, and 9% mud. Based on the modified Folk/Wentworth classification scheme, the classification of the average particle size for subunit H1 falls near the boundary between the sandy gravel and gravelly sand classes.

C.4.2.4.3 Subunit H1a. Above the middle coarse facies of the subunit H1 lies an upper fine sand to silty-sand sequence equivalent to subunit H1a described in Lindsey et al. (1994; 2000), and the 'silty sand' described in Sobcyzk (2000). This sequence consists predominantly of interstratified slightly-silty medium to very fine sands (Table C.12) and ranges in thickness from 0 m (0 ft) where it was removed during excavation of the tank farm to about 9 to 12 m (30 to 40 ft) to the southwest (Figure C.15). Sobcyzk (2000) reports that the top of this unit dips slightly (approximately 2°) to the southwest. Sobcyzk (2000) also suggests that this unit may become coarser textured to the west.

C.4.2.4.4 Top Coarse Sand and Gravel Sequence (Hanford Subunit H1 - Coarse Unit B). A coarse-grained sand to gravelly sand unit (Table C.12) overlies the fine sand sequence of subunit H1a, and may be intercalated with some sandy gravel to the west. This unit is equivalent to Gravel Unit B (Johnson et al. 1999) and Hanford Unit B (Sobcyzk 2000). It is the uppermost stratigraphic unit in the tank farm area, but is completely missing beneath the tank farm, where it was removed during construction. In surrounding boreholes, however, this unit ranges from a few meters in thickness to east to up 12 m (40 ft) to the west.

Table C.12. Data from Drive Barrel and Split-Spoon Samples of the Hanford Formation Beneath SX Tank Farm located in Figure C.14

Hanford Subunit	Borehole /Depth	$CaCO_3$ %	Gravel >2 mm	Sand (mm)					Mud <0.06 3 mm	Class	Average Bulk Density from 299-W22-50[a]
				Very Coarse 1-2 mm	Coarse 0.5-1.0 mm	Medium 0.25-0.5 mm	Fine 0.125-0.25	Very Fine 0.063-0.125 mm			
H1a	299-W23-72 55 ft	1.4	0.4	0.5	1	19.1	43.1	22.1	13.9	(m)S	1.95
	299-W23-92 80 ft	NA	2.1	3	12.1	20.4	31.2	19.8	11.4	(m)S	
H1	299-W23-72 70 ft	1.7	10.7	23.7	28.7	16.7	8.3	6.0	6.0	gS	2.27
	299-W23-92 90 ft	NA	16.3	16.9	27.9	18.5	8.1	5.7	6.6	gS	
	299-W23-108 85 ft	NA	41.8	24.5	14.5	7.1	3.9	3.3	5.0	sG	
H2	299-W23-72 100 ft	1.7	0.0	0.2	2.1	37.6	29.7	15.2	15.3	(m)S	2.05
	299-W23-92 110 ft	NA	0.8	1.0	9.4	40.0	22.2	14.6	12.0	(m)S	
	299-W23-92 120 ft	NA	2.8	2.2	1.7	9.6	33.5	34.9	15.4	(m)S	
	299-W23-108 110 ft	NA	1.8	0.1	1.8	13.2	26.6	30.9	15.7	mS	

Source: Horton and Johnson (2000).
NA = not analyzed.

C.4.2.5 Backfill

Geology of the 241-SX Tank Farm (Price and Fecht 1976a) describes the backfill surrounding the HLW tanks of the SX tank farm as consisting predominantly of poorly sorted cobbles, pebbles, and coarse to medium sands to silt derived from the Hanford formation. Lindsey et al. (2000) describes the backfill as relatively non-cohesive, friable, massive sand with variable amounts of silt and pebbles. A hardened zone at the base of the backfill, extending to a depth of approximately 18.6 m (61 ft) that was significantly harder and drier than the overlying materials was also observed.

Engineering drawings (H-237985, Sheets 1 and 2) show that the tank farm was excavated to create three terraces for construction of cascading tanks. This excavation extended to an elevation of 185.3 m (608 ft) on the west side and 185.9 m (610 ft) on the east side.

C.4.2.6 Clastic Dikes

Clastic dikes are vertical to near-vertically oriented sedimentary structures that cut across horizontal bedding planes. These dikes have been observed in all types and ages of geologic materials found beneath the Hanford Site including basalt; interbed sediments; the Ringold Formation; and the sands, mud, and gravels of the Hanford formation (Fecht et al. 1999). They are especially notable within the sand- and silt-dominated facies of the Hanford formation where they have been observed to be a few centimeters to more than a meter thick and extend to depths of 36 m (120 ft) or more. Clastic dikes may significantly impact contaminant transport through the vadose zone based on their differing orientation versus the traditional horizontal strata common in the Hanford formation.

Price and Fecht (1976a) states that clastic dikes were detected in the SX tank farm but that they could not be mapped. Clastic dikes (and/or polygonally patterned ground often associated with them) have also been observed at a number of locations surrounding the SX tank farm, including the SY tank farm to the north, the Environmental Restoration and Disposal Facility to the east, and throughout Cold Creek Valley to the south and west (including the former 216-S-16 pond). Tallman et al. (1979) indicates that identification of clastic dikes in this area was also based on examination of cable-tool drilling samples. Horton and Johnson (2000) reports that possible clastic dikes had been encountered by two or three recently installed RCRA groundwater monitoring wells (299-W22-48 and 299-W22-50). Lindsey et al. (2000) also notes a few structures suggestive of clay skins on clastic dikes in split-spoon samples from well 299-W22-50.

Figure C.18 illustrates one of the clastic dikes observed in walls of the excavation for the SY tank farm located approximately 300 m (1,000 ft) to the north of the SX tank farm (Price and Fecht 1976b).

Figure C.18. Clastic Dike in the SY Tank Farm Excavation

Johnson et al. (1999) projects a plausible network of clastic dikes for the SX tank farm (Figure C.19) based on polygonally patterned ground mapped between Army Loop Road and State Highway 240 and scaled based on the best cell size estimate from *An Atlas of Clastic Injection Dikes of the Pasco Basin and Vicinity* (Fecht et al. 1999).

Figure C.19. Projection of a Hypothetical Network of Clastic Dikes onto Waste Management Area S-SX

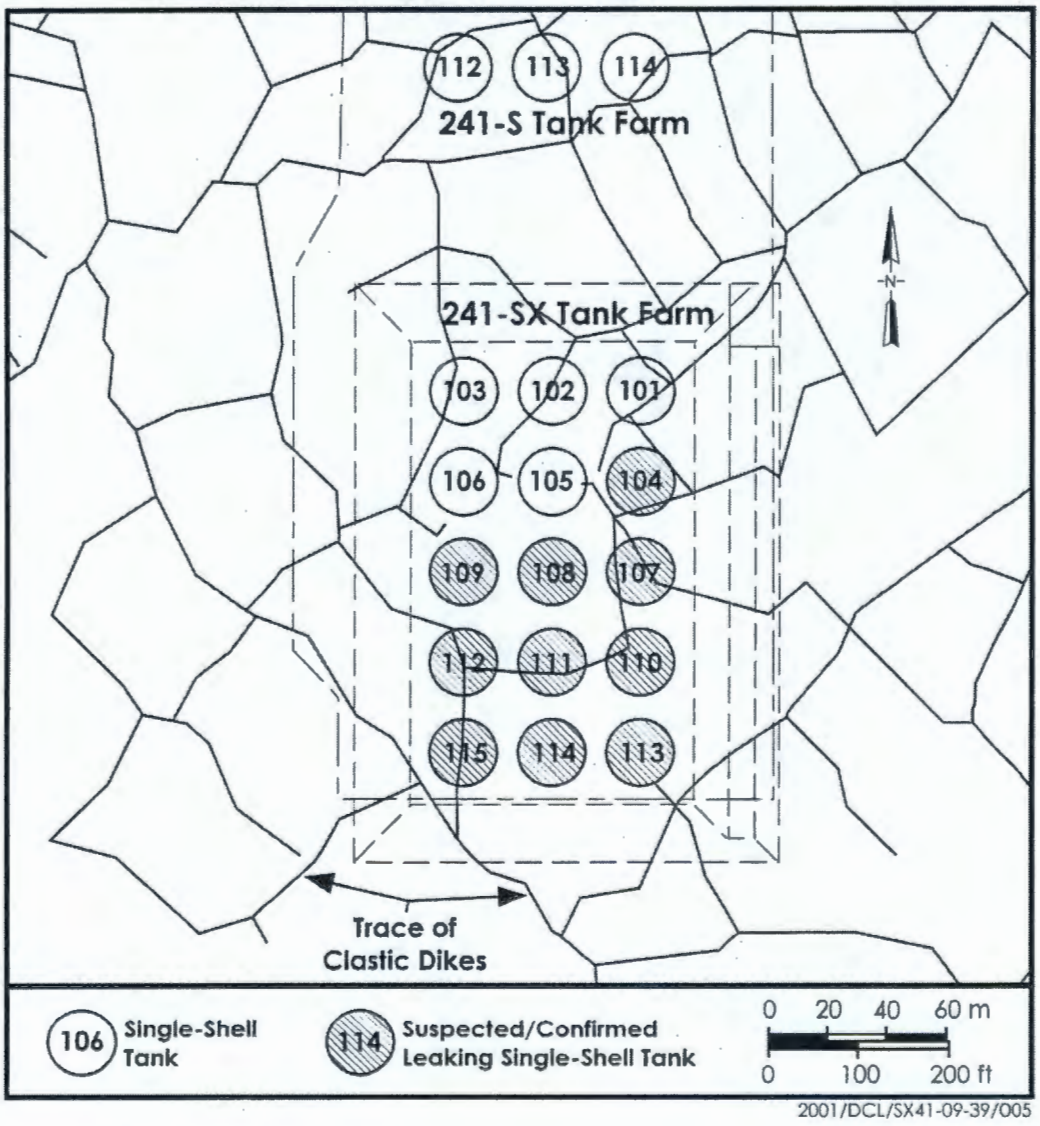

Source: Johnson et al. (1999).

C.5.0 MOISTURE CONTENT AND MATRIC POTENTIAL MEASUREMENTS

Moisture content and matric potential measurements are available for a number of boreholes in WMA S-SX (Myers 2000; Serne et al. 2001a, 2001b, 2001c). Many of the conclusions based on the measured matric potentials (Serne et al. 2001a, 2001b, 2001c) are presented in Section 3.2.1, in the context of recharge estimates for the tank farms. The primary purpose of this section is to present the measured data on moisture content and matric potential.

Moisture content measurements were made for sediments in the drywells surrounding the SX tank farm (Myers 2000). Matric potentials were measured for samples from two clean RCRA boreholes, 299-W22-48 and 299-W22-50 (Serne et al. 2001a), and also for the two contaminated boreholes: borehole 41-09-39 near tank SX-108 (Serne et al 2001b) and borehole 299-W23-19 south of the SX tank farm (Serne et al. 2001c).

C.5.1 MOISTURE CONTENT FOR DRYWELL SEDIMENTS

The drywells at SX tank farm are generally within 1.5 to 3 m (5 to 10 ft) from the outside walls of the tanks. The drywells extend to various depths, typically between 22.8 and 30 m (75 and 100 ft). There are presently 98 drywells within the SX tank farm.

Within the backfill surrounding the SX tank farm, the measurements suggest that there is relatively consistent moisture content of 8 to 10 % (volumetric), with a moderate increase in moisture at the base of the excavation (Figure C.20). The increased moisture content is possibly due to the increased compaction that took place during farm construction. In the undisturbed soils beneath the excavation, the presence of gravelly zones results in much lower moisture content, typically in the range of 4 to 6 vol%, with some drier zones. Thin zones of higher moisture content are evident below the tank farm excavation (Figure C.21). These thin zones are consistent with the presence of lenses or beds of silty fine sands noted in the Hanford formation. Deeper drywells exhibit a consistent increase in moisture content at a depth of about 38 m (125 ft) (Figure C.21). This depth corresponds to the approximate depth of the more massive fine, silty sands and sandy silts of the lower Hanford formation or Plio-Pleistocene unit.

Regions of greater than 12 % moisture content (volumetric) were detected (Figure C.20). One of these zones was located east of tank SX-115. This location is defined by the high moisture content in a narrow zone in a single drywell at a depth about 21.3 m (70 ft). A second zone of high moisture content was identified north of tank SX-109 and appears as a halo starting at about 1.5 m (5 ft) bgs (Figure C.21). Research into the location of utilities serving the tank farm reveals that these readings are from a depth close to the terminus of an active water line. The presence of areas of noticeably wetter zones in vicinity of water distribution pipes points to the probability that these pipes may be significant sources of recharge.

In summary, the geologic environment of the SX tank farm plays a significant role in controlling the distribution of moisture with increasing depth. The distribution of moisture content, on the basis of drywell measurements, helps to identify areas where potential sources of recharge from water-line leaks may exist.

Figure C.20. Measured Moisture Contents for the Drywell Sediments Beneath SX Tank Farm

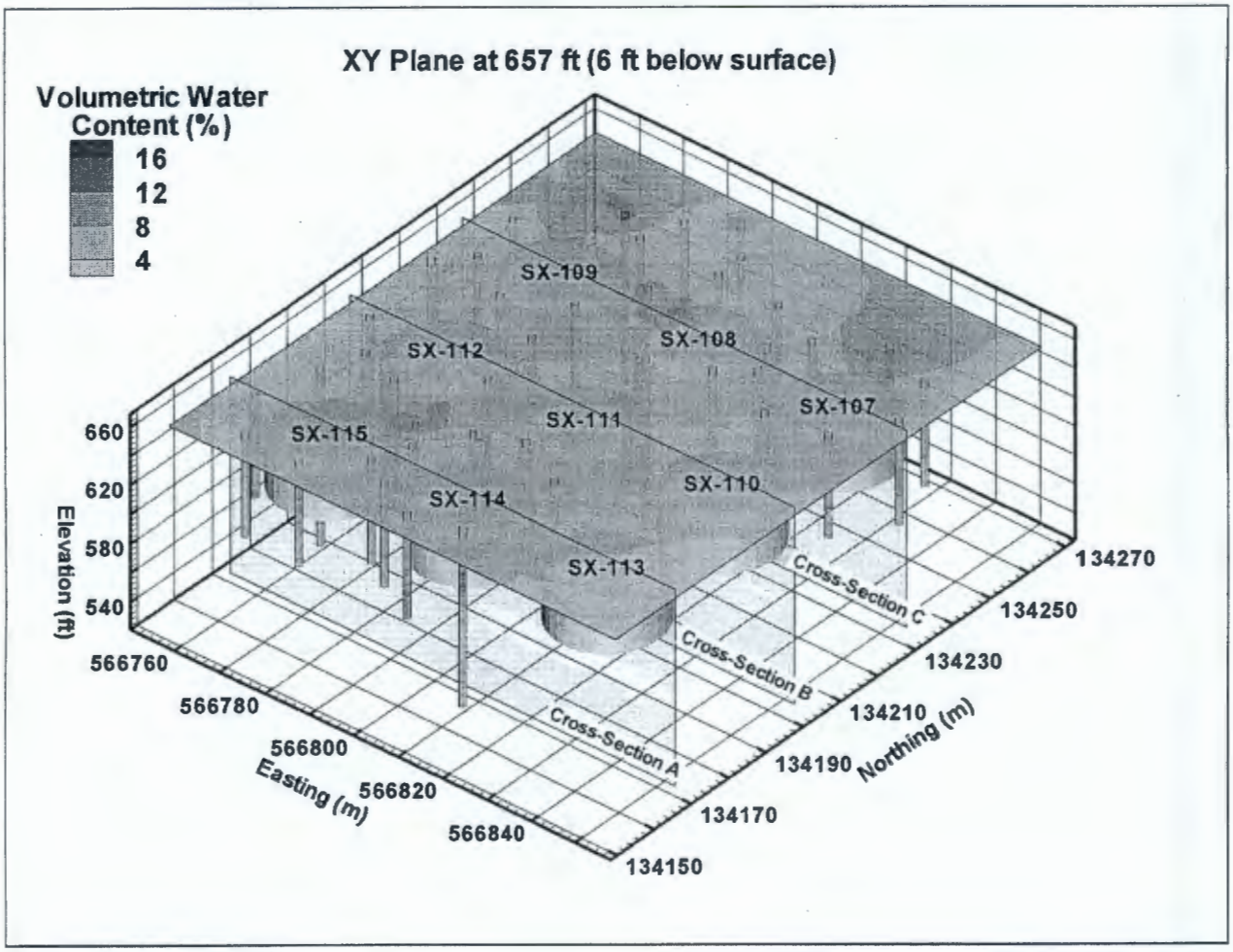

Source: Myers (2000).

Figure C.21. Moisture Content Distribution for the Drywell Sediments for Three Cross-Sections

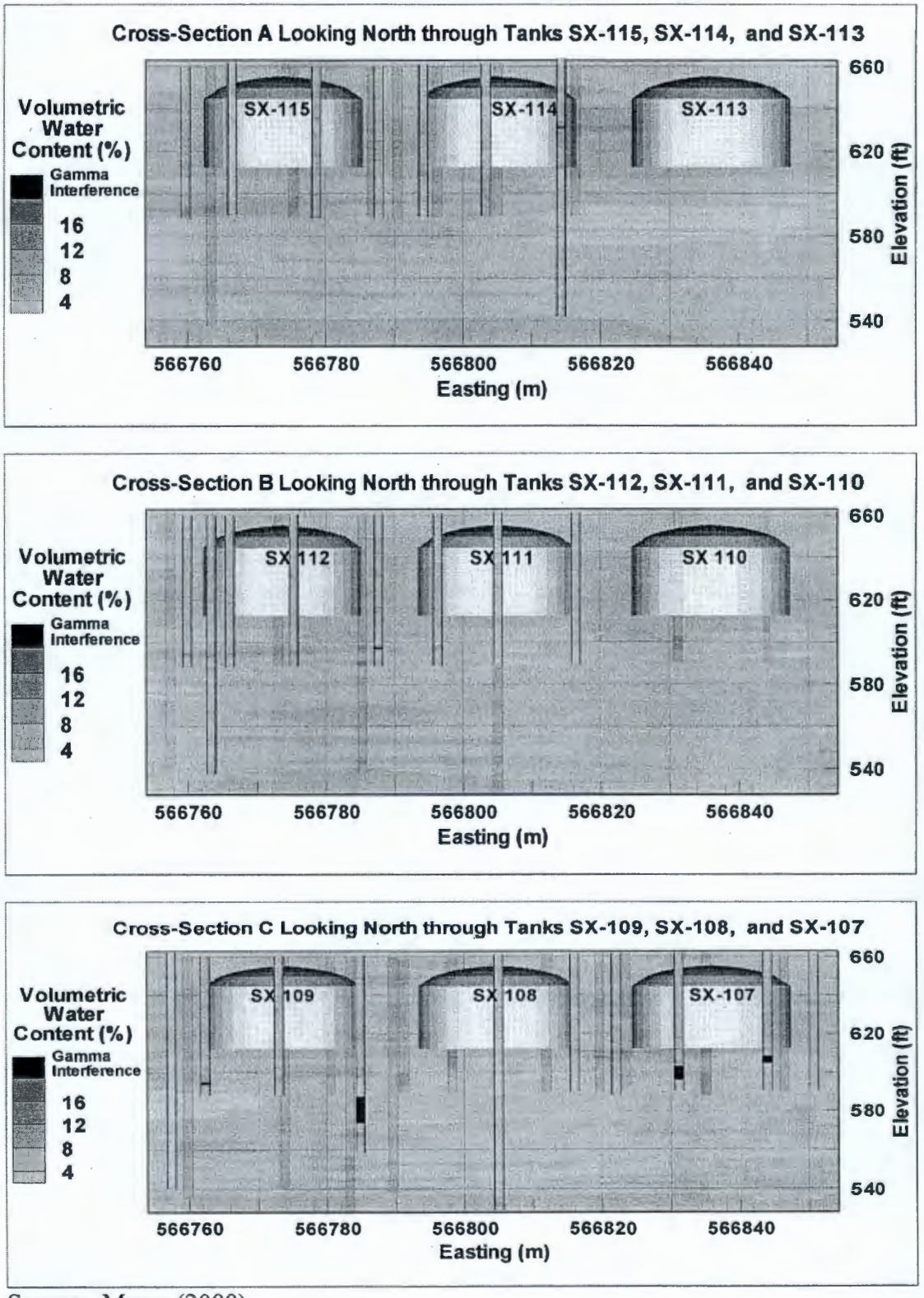

Source: Myers (2000).

C.5.2 MEASUREMENTS FOR BOREHOLES 299-W23-19, 299-W22-48, AND 299-W22-50

The gravimetric moisture content for sediments from borehole 299-W23-19 are shown in Figure C.22. The moisture content profile shows several high peaks within the Hanford formation coarse facies and the Hanford formation fine laminated sands. At 26.5 and 28.7 m (87 and 94 ft) bgs within the coarse unit, the higher moisture contents correspond to thin lenses of finer grained material. Within the fine unit there are wetter zones at 31 and 36 m (102 and 118 ft) bgs that do not seem to correlate with subtle changes in particle size. Within the Plio-Pleistocene unit fine gained facies there are 3 wet zones at 38.7, 43, and 45.7 m (127, 141, and 150 ft) bgs that correspond to thin zones of finer grained material. Wetter zones within the Ringold Formation may correspond to zones where water was added during hard tooling. Hard tooling was initiated at 49 m (161 ft) bgs and continued periodically down to 63.4 m (208 ft) bgs.

Figure C.22. Gravimetric Moisture Content Distribution for the Sediment Profile at Borehole 299-W23-19

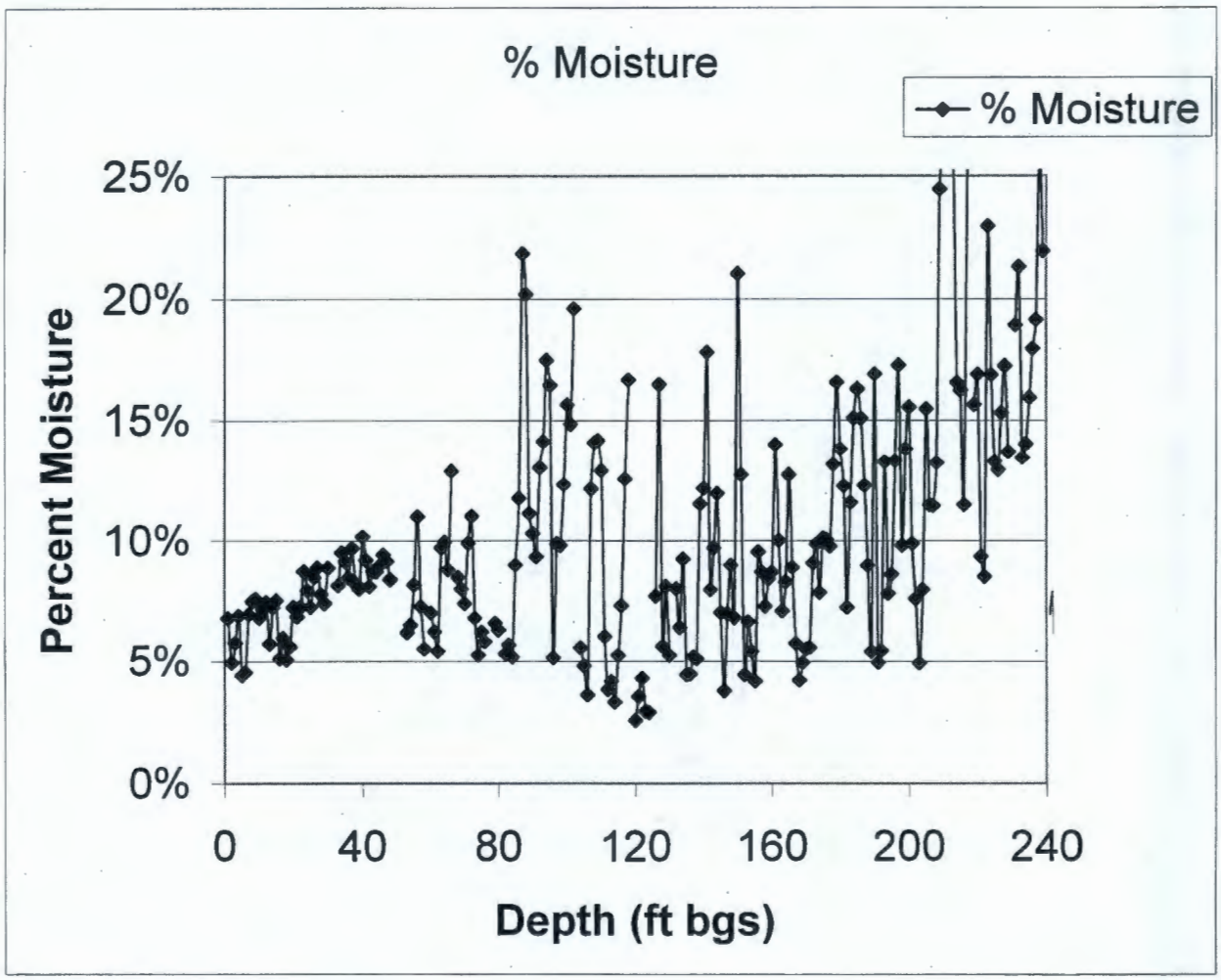

Source: Serne et al. (2001c).

The moisture content profile in Figure C.22 is consistent with the measured data in Figure C.20 for near-surface sediments. The profile data in Figure C.22 are also consistent with those in Figure C.21 at about 21 m (70 ft) bgs and at about 37 m (120 ft) bgs. However, the observed high moisture contents at about 27 m (90 ft) bgs in Figure C.22 are not present in Figure C.21 near tank SX-115.

Matric potential measurements for samples from borehole 299-W23-19 and clean RCRA boreholes (299-W22-48 and 299-W22-50) are shown in Figure C.23. The soil suction (negative of matric potential) data are reported as head values in feet, consistent with reported depths bgs.

The higher the suction values, the less recharge is expected. On Figure C.23, an equilibrium line is also shown. Measured soil suction values to the left of the equilibrium line indicate that drainage (recharge) is occurring while values to the right of the line indicate that evaporation (drying or upward flow) conditions persist. As discussed in *Geologic and Geochemical Data Collected from Vadose Zone Sediments from Borehole 299-W23-19 [SX-115] in the S/SX Waste Management Area and Preliminary Interpretations* (Serne et al. 2001c), for RCRA boreholes 299-W22-48 and 299-W22-50 it appears that water from winter rains and snowmelt (or perhaps other sources) have penetrated the soil profile to depths of about 30 m (100 ft) bgs. However, below that depth the sediments from these two uncontaminated boreholes are significantly drier (i.e., to the right of the equilibrium line) compared to the sediments found in contaminated borehole 299-W23-19.

For borehole 299-W23-19 3 m ([10 ft] to the south-south-west of the side of tank SX-115), the suctions are low (sediments are relatively wet) throughout the profile and drainage is predicted to be the highest of any of the three boreholes. Note that borehole 299-W23-19 was drilled using air rotary and therefore no water was added during drilling. This is unlike the RCRA groundwater wells 299-W23-48 and 299-W22-50 boreholes, where water was added during hard tooling process of cable tool drilling. As discussed in Serne et al. (2001c), unit gradient conditions persist throughout the profile for borehole 299-W23-19 sediments but not for two clean boreholes outside the tank farm operations area. The accelerated drainage from water-line leaks south of tank SX-115 is believed to be the primary reason for the relatively low suction values (and higher recharge) for sediments from borehole 299-W23-19. Nonetheless, as discussed in Serne et al. (2001c), for this location an estimated recharge rate of between 50 to 100 mm/yr (2 to 4 in./yr) would be in line with the observed drainage rates from bare gravel surface soils at the Hanford Site (Gee et al. 1992).

C.5.3 MEASUREMENTS FOR BOREHOLE 41-09-39

Thirty sleeve sediment samples from the extension borehole for 41-09-39 near tank SX-108 were analyzed for and moisture content and matric suction. The data, tabulated in Table C.13 and shown in Figure C.24, indicate that of the 30 samples 18 are at matric suctions lower (wetter) than the elevation of the sample above the water table (Serne at al. 2001b). As shown in Figure C.24, when the suction for a sample is less than the sample's elevation-above the water table, the sample is draining. As discussed in Serne at al. (2001b), in contrast to the other contaminated borehole 299-W23-19 matric suction values for samples from borehole 41-09-39 suggest a much drier moisture regime. Note that, because of extreme variability and uncertainty in some of the measurements, not all the data (Table C.13) are plotted in Figure C.24.

Figure C.23. Soil Suction Profiles for 299-W22-48, 299-W22-50 and 299-W23-19 Borehole Samples

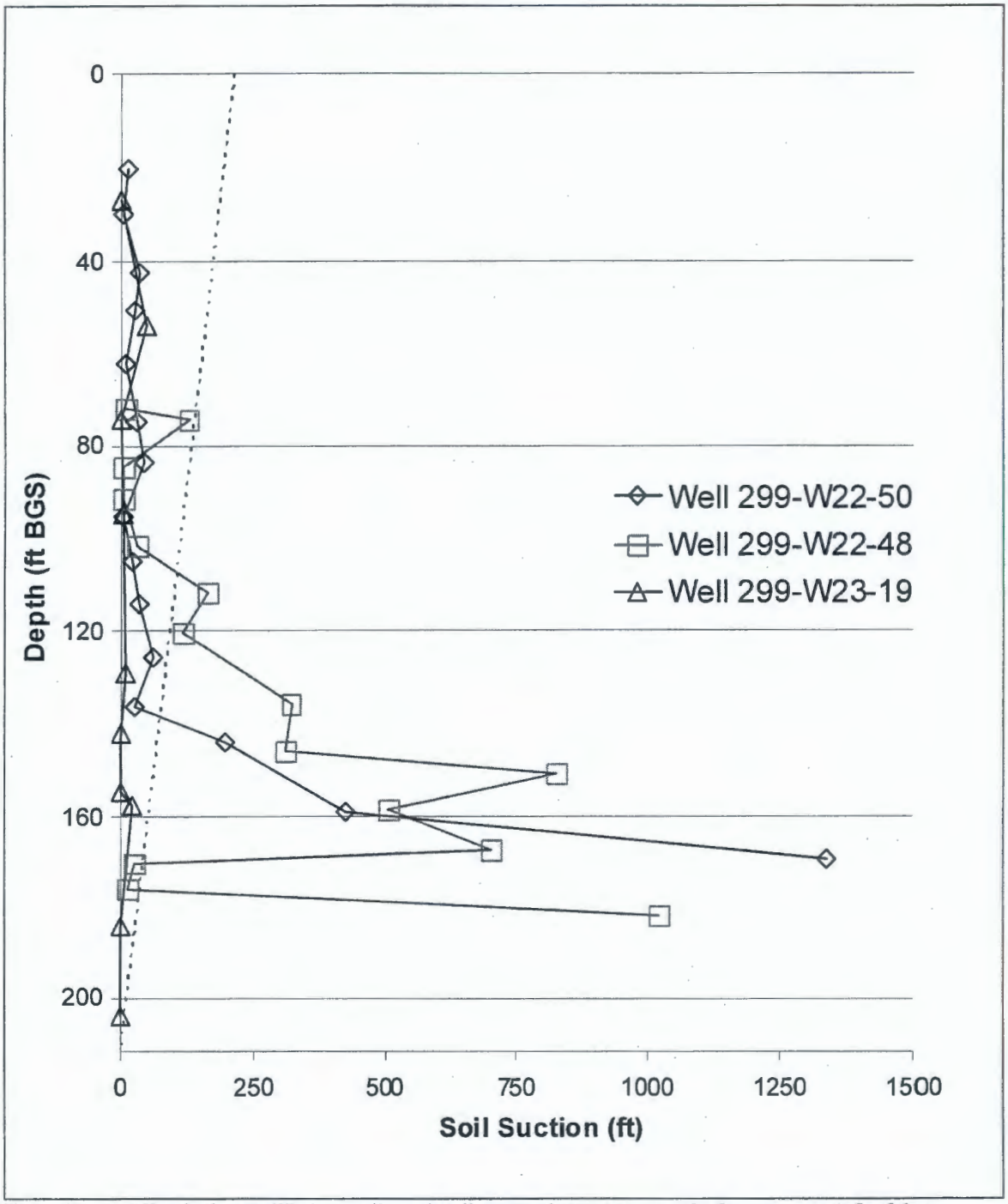

Note: Dashed line is the equilibrium soil suction line. Drainage occurs only for values to left of the equilibrium line.

Source: Serne et al. (2001c).

Table C.13. Water Content and Matric Suction Values for Samples from Borehole 41-09-39

Sample	Depth (ft bgs)	Water content (g/g)	Suction (m)	Sample	Depth (ft bgs)	Water Content (g/g)	Suction (m)
6F	141.9	0.11	3.93	37C	186.2	0.026	21.08
6E	142.4	0.096	5.38	38C	187.8	0.029	8.42
6D	143.3	0.218	12.74	38B	188.3	0.019	4.65
6C	144.1	0.26	3.3	39A	189.5	0.018	50.16
6B	144.7	0.229	5.03	40A	190.7	0.051	12.83
7C	146.4	0.112	26.81	47C	196.4	0.066	3.53
8C	148.3	0.074	14.99	50A	199.4	0.039	96.42
8B	149.9	0.097	9.6	56C	204.3	0.077	5.34
9A	152.8	0.139	6.04	56B	205.0	0.066	27.75
10C	153.4	0.136	24.86	56A	205.6	0.054	30.77
10B	153.9	0.147	2	58C	208.1	0.102	2.97
10A	154.5	0.196	4.8	58B	208.6	0.106	4.34
16D	162.3	0.133	0.25	59C	209.8	0.125	0.33
16C	162.8	0.135	2.21	59A	210.9	0.25	0.02
22B	172.0	0.052	5.54	64A	213.3	0.132	0.03

Source: Serne et al. (2001b).

Figure C.24. Matric Suction Profile for Samples from Borehole 41-09-39

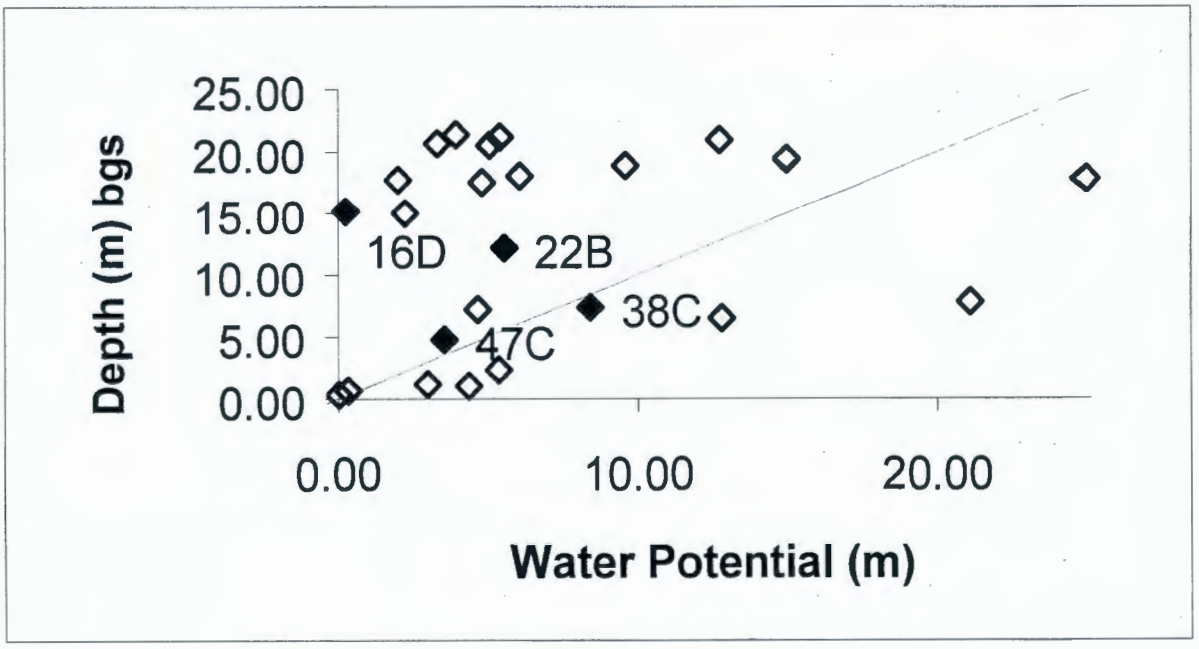

Source: Serne et al. (2001b).

Serne et al. (2001b) presents three possibilities for the borehole 41-09-39 core samples having higher matric suction. The first is that much less drainage (recharge) is occurring at this borehole location than was observed at the other location at borehole 299-W23-19. The second is that the samples were disturbed enough during coring that the water content and possibly the density were altered enough to increase the matric suction values. The third is the possible drying effect due to heat load from the high-heat tank SX-108.

C.6.0 GEOCHEMISTRY

Numerous studies have been completed during the characterization of the WMA S-SX vadose zone that provide geochemistry information related to vadose zone contamination. Data provided by these studies are discussed in other sections and appendices of this WMA S-SX Field Investigation Report. Those investigations are briefly described here with appropriate references to other sections of this document for more detailed discussion.

The first and most extensive effort is the characterization of soil samples from the boreholes that have been drilled in support of this RCRA facility investigation. These include three characterization boreholes within WMA S-SX and two RCRA groundwater monitoring boreholes east of WMA S-SX. Soil samples were extensively analyzed for mineralogy and particle size distribution. Water and acid extracts were taken to measure water chemistry and radionuclide content. In a few samples, porewater was extracted without dilution from the soils and analyzed. These data are discussed in greater detail in Appendix B.

Several laboratory studies were completed to determine the chemical reactions controlling the mobility of cesium-137 and chromium. The results show that cesium-137 sorption is strongly influenced by the concentration of competing cations (primarily sodium and to a lesser extent potassium) for sorption sites and cesium-137 mobility has ranged from very high to very low. Chromium studies indicate that some retardation of chromium migration can occur by oxidation-reduction reactions. Cesium-137 and chromium studies are discussed in greater detail in Appendix D, Sections D.3.0 and D.4.0, respectively. Isotopic fission products were measured in borehole soils to gain insight on multiplicity of tank sources and their distribution in the soil column (Appendix D, Sections D.6.1, D.6.2, and D.6.3).

Finally, several modeling studies were completed to evaluate or incorporate geochemical parameters and their influence on contaminant migration. These included thermodynamic simulations to predict tank fluid chemistry (Appendix D, Section D.7.3) and flow and transport estimates of aqueous species migration (Appendix D, Section D.7.1 and D.7.4)

C.7.0 GROUNDWATER CONTAMINATION

Several groundwater monitoring wells around WMA S-SX have been contaminated during the last decade by constituents (primarily technetium-99, nitrate, and chromium) whose sources are postulated to be derived from one or more tank leaks (Johnson and Chou 1998; Johnson and Chou 1999b). Relatively high technetium-99 concentrations downgradient of WMA S-SX and occurrences of relatively high technetium-99/nitrate ratios similar to presumed tank liquid ratios have been the primary observations suggesting a link between observed groundwater contamination and tank leak contamination in the vadose zone. These data are also summarized in Johnson et al (1999). Since that report was issued, additional groundwater contamination data have been collected. This section summarizes some of the additional data provided in Johnson and Chou (2001). Where relevant to the discussion, data collected more recently than Johnson and Chou (2001) are also discussed in the main text.

The most recent groundwater contamination data from groundwater samples in several groundwater monitoring wells continue to support the hypothesis that the tank farm is the source of the contaminants. Sampling with depth was conducted at 4 new wells including well 299-W23-19 near tank SX-115, well 299-W22-48 east of S tank farm, well 299-W22-49 east of SX tank farm, and well 299-W22-50 at the southeast corner of the SX tank farm. Chemical species and radionuclide concentrations measured in these wells are listed in Tables C.14, C.15, and C.16. Technetium-99/nitrate and tritium/technetium-99 ratios are shown in Figures C.25 and C.26, respectively. Some outstanding features include the following.

- **Well 299-W23-19** – Shallow samples (0 to 6 cm and 1 m [0 to 5.5 in. and 3 ft]) were first taken in October 1999. Later samples in 2000 were taken at greater depth. There is relatively little variability with depth. Of note are the very high technetium-99 concentrations which continue to be high. Also, maximum technetium-99/nitrate ratios of 0.11 are observed, indicating a tank waste source.

- **Well 299-W22-48** – Moderate contaminant concentrations are observed. However, intermediate technetium-99/nitrate ratios of 0.039 occur, which may indicate a tank waste source.

- **Well 299-W22-49** – Moderate amounts of contaminants occur. The relatively high tritium/technetium-99 ratio indicates a non-tank farm source.

- **Well 299-W22-50** – Moderate contaminant concentrations occur. Maximum technetium-99/nitrate ratios of 0.11 are observed, indicating a tank waste source. The presence of increased nitrate and carbon tetrachloride at about 68 m (223 ft) indicates that an additional source, presumably the regional contamination plumes created by crib discharges, has contributed to contamination at this location.

In particular, technetium-99 groundwater concentrations measured in March 2001 have reached 81,500 pCi/L in well 299-W23-19.

Table C.14. Observed Contaminant Concentrations in Shallow and Extended Well 299-W23-19 Completions Near Tank SX-115

Constituent (unit)	Shallow Temporary Screen (1.5 m)		Permanent Screen (9.1 m)	
	October 1999[a]		March 2000	June 2000
	Passive (Kabis, 0–6 cm)	Pumped[b] (1 m)	Pumped[c] (2 m)	Pumped[c] (2 m)
Technetium-99 (pCi/L)[d]	48,050	39,000	52,300	63,700
Chromium (μg/L)[e]	84	63	90	87
Nitrate, as NO_3^- (mg/L)	560	434	491	562
Tritium (pCi/L)	92,000	91,000	95,800	92,000
Specific Conductance (μS/cm)	1,199	1,003	968	1,237
Sulfate (mg/L)	18	16	18	17
Calcium (mg/L)	118	96	127	120
Magnesium (mg/L)	39	32	41	40
Sodium (mg/L)	34	34	42	43
Chloride (mg/L)	15	12	16	16

[a]Values reported represent duplicate averages.
[b]1.5 m (5 ft) screened interval with pump intake set at 1 m (3 ft) below the static water level.
[c]9.1 m (30 ft) screened interval with pump intake set at 2 m (6 ft) below the static water level.
[d]Concentration values of 81,500 pCi/L were measured in the March 2001 sample.
[e]Concentration values of 138 μg/L were measured in the March 2001 sample.

Table C.15. Depth Distribution of Key Contaminants at SX Tank Farm Wells

Well	Sample Date	Depth (m)	Mode	Contaminants					
				^{99}Tc (pCi/L)	NO_3 (μg/L)	Cr (μg/L)	^{3}H (pCi/L)	U (μg/L)	CCl_4 (μg/L)
299-W22-48	10/26/99	0.6	DT/B	39.5	17,132	3.2U	122U	0.2	0.4
	03/30/00	2.3	S	720	18,593	7.1	249U	3.23	4
299-W22-49	11/04/99	0.5	DT	32.5	13,546	3.2U	22,000	0.82	0.6
	03/30/00	2.3	S	58.3	9,296	4.6U	22,000	3.27	6
	11/08/99	6.7	DT	2.96U	7,880	3.2U	18,900	0.92	1
299-W22-50	11/23/99	0.2	DT/B	4,240	57,991	3.0U	31,400	0.78	13
	04/03/00	2.3	S	3,230	30,102	10.4	24,200	4.29	11
	11/29/99	6.7	DT	812	12,838	3.0U	19,900	3.34	5.6
	12/14/99	11.9	DT	7.03U	2,125	3.0U	969	1.09	0.94
	12/15/99	28.7	DT	0U	1,151	3.0U	304	0.58	1.5
	12/17/99	53.0	DT	0U	3,187	3.0U	185U	0.79	5.6
	12/22/99	67.7	DT	0.577U	12,838	3.0U	0U	0.43	0.89
	01/12/00	99.4	DT	0U	4,869	3.0U	0U	30.90	0.23

*Depth is below water table.
DT = sampled during drilling using temporary pump/screen and packer assembly.
DT/B = bailed during drilling.
S = sample collected by pumping from 4.5 m (15 ft) screened interval.
U = analytical result is not detected.

Table C.16. Hydrochemical Parameters at SX Tank Farm Wells

Well	Hydrochemical Parameters								
	pH	Conductivity (µS/cm)	Alkalinity (µg/L)	SO_4 (µg/L)	Cl (µg/L)	Na (µg/L)	Ca (µg/L)	Mg (µg/L)	Na/Ca
299-W22-48	7.97	263	74,000	21,300	6,910	26,300	19,400	5,070	1.36
	8.59	295	---	19,200	5,900	27,000	22,200	6,910	1.22
299-W22-49	8.94	245	90,000	13,900	5,330	25,600	16,200	5,070	1.58
	9.09	240	---	11,900	2,800	23,300	17,600	5,960	1.32
	8.1	244	86,000	15,400	3,660	26,000	16,400	5,320	1.59
299-W22-50	---	---	100,000	14,200	4,800	28,200	23,200	7,300	1.22
	8.14	278	---	13,400	3,100	23,900	22,600	7,100	1.06
	8.1	235	101,000	12,500	2,500	20,400	17,800	6,020	1.15
	8.2*	228	106,000	14,400	3,100	11,600	26,300	9,250	0.44
	7.9*	242	114,000	14,400	4,400	12,700	28,700	10,200	0.44
	7.9*	307	126,000	16,100	15,200	14,300	33,400	12,400	0.43
	7.7*	323	115,000	19,300	10,000	15,500	33,000	12,500	0.47
	8.5*	234	96,000	18,900	5,800	16,600	20,200	8,010	0.82

*Laboratory result.

Figure C.25. Technetium-99/Nitrate Ratios for Waste Management Area S-SX Network Wells

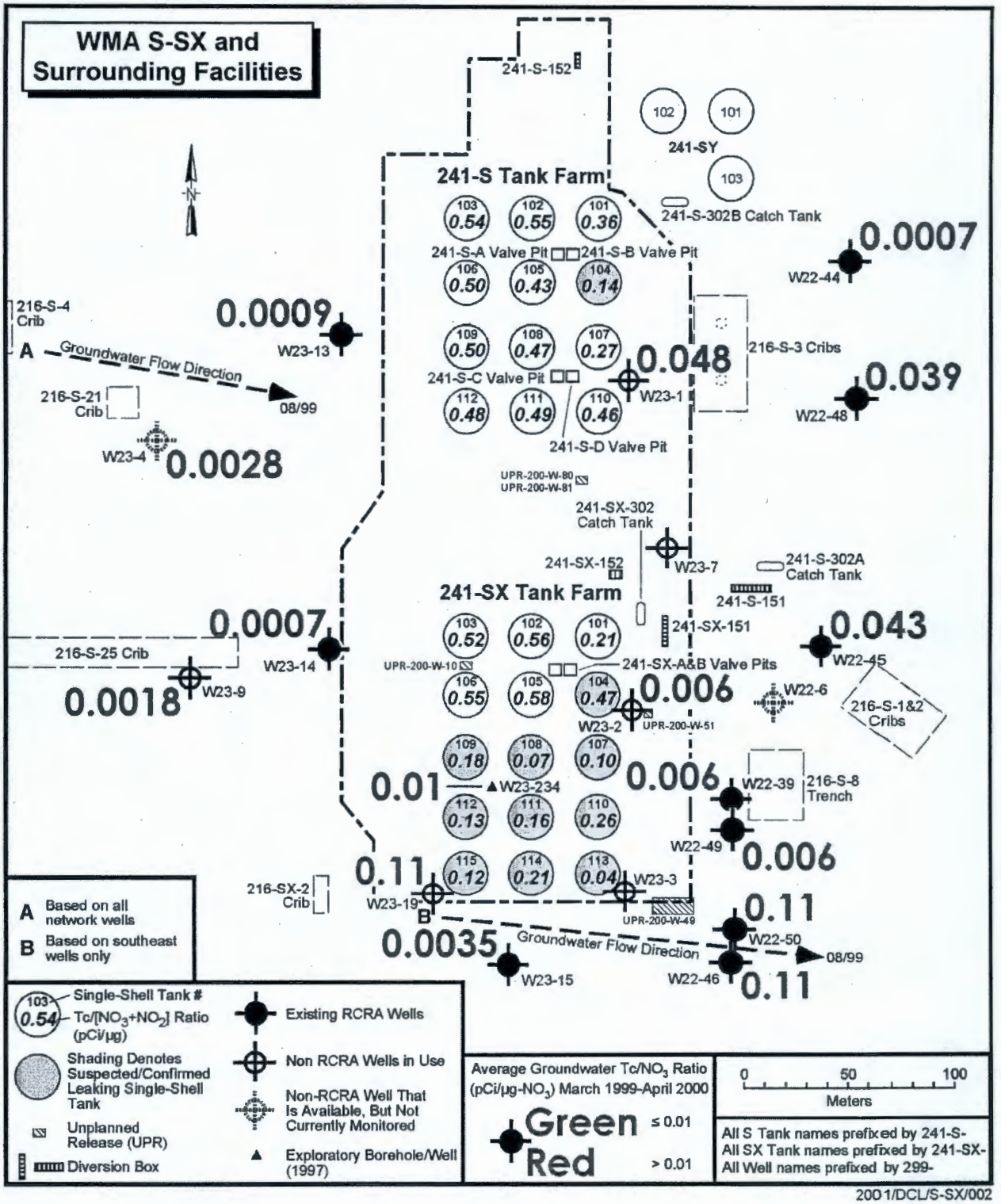

Figure C.26. Tritium/Technetium-99 Ratios for Waste Management Area S-SX Network Wells

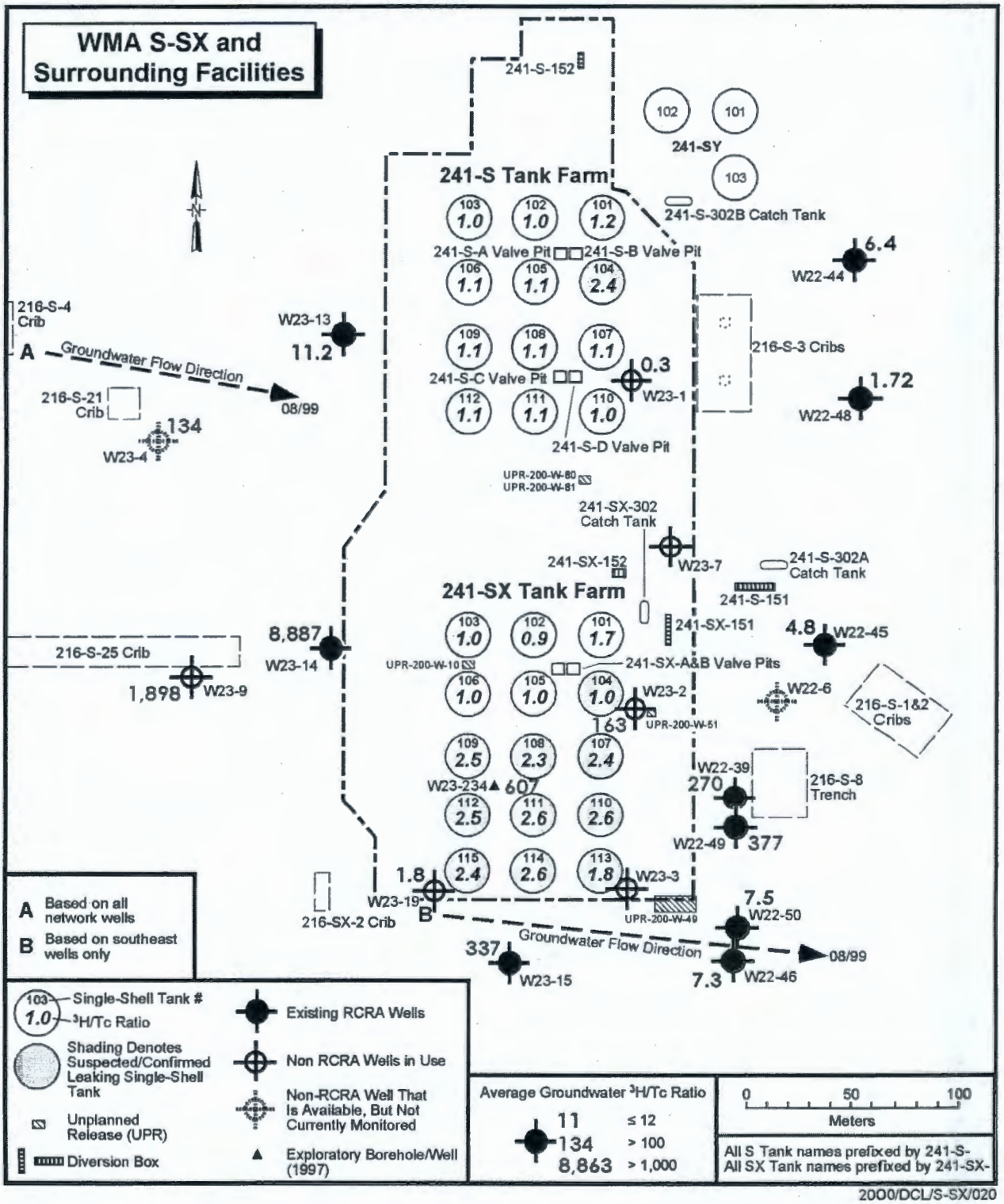

Given the well distribution showing relatively high technetium-99 concentrations, it appears that more than one tank waste source may be contributing to groundwater contamination. The largest technetium-99 concentrations (Table C.17) that have been recorded since 1997 occur at the southern end of the SX tank farm. This contamination is attributed to the tank SX-115 leak. A plausible plume distribution is shown in Figure C.27. The characteristics of this distribution are a 10-year plume narrowly constrained to the east-southeast whose source is in the vadose zone at or southwest of tank SX-115. The wells most clearly associated with this postulated plume are 299-W23-19, 299-W22-50, and 299-W22-46. All show identical technetium-99/nitrate ratios (Figure C.25) and show good fit with relative concentrations. There is some indication that this plume has rotated slightly over time to a more easterly direction because technetium-99/nitrate ratios and technetium-99 concentrations were high in well 299-W23-15. The technetium-99 plume has since moved away from this location (Figure C.27).

Other wells suggesting the occurrence of tank waste contaminants include 299-W23-1, 299-W22-48, and 299-W22-45 towards the north of WMA S-SX. The technetium-99/nitrate values in these wells are elevated relative to crib associated values west of WMA S-SX, but not as high as those at the south end of the SX tank farm. This suggests some vadose zone source under the S tank farm upgradient of these wells. Historical knowledge identifies only the tank S-104 leak as a source of relatively high technetium-99 content. Because the technetium-99 concentrations may still be rising in wells 299-W22-48, 299-W22-44, and 299-W22-45 (Figure C.28), future changes in contamination levels are uncertain here.

Figure C.27. Theoretical Groundwater Plume Dispersion Pattern from a Tank Leak Source in the SX Tank Farm Monitoring Efficiency Model

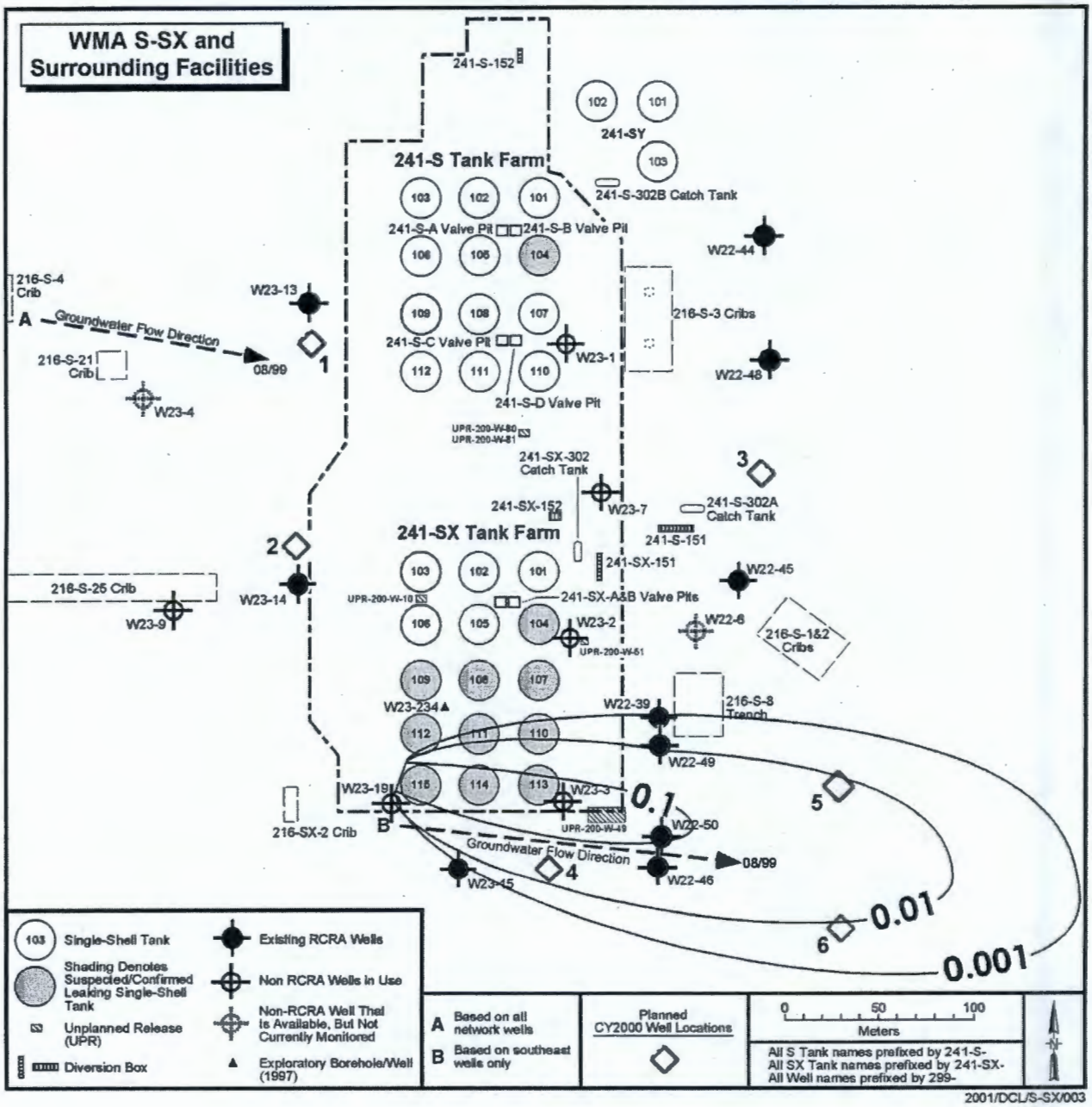

Figure C.28. Technetium-99 for Waste Management Area S-SX Network Wells

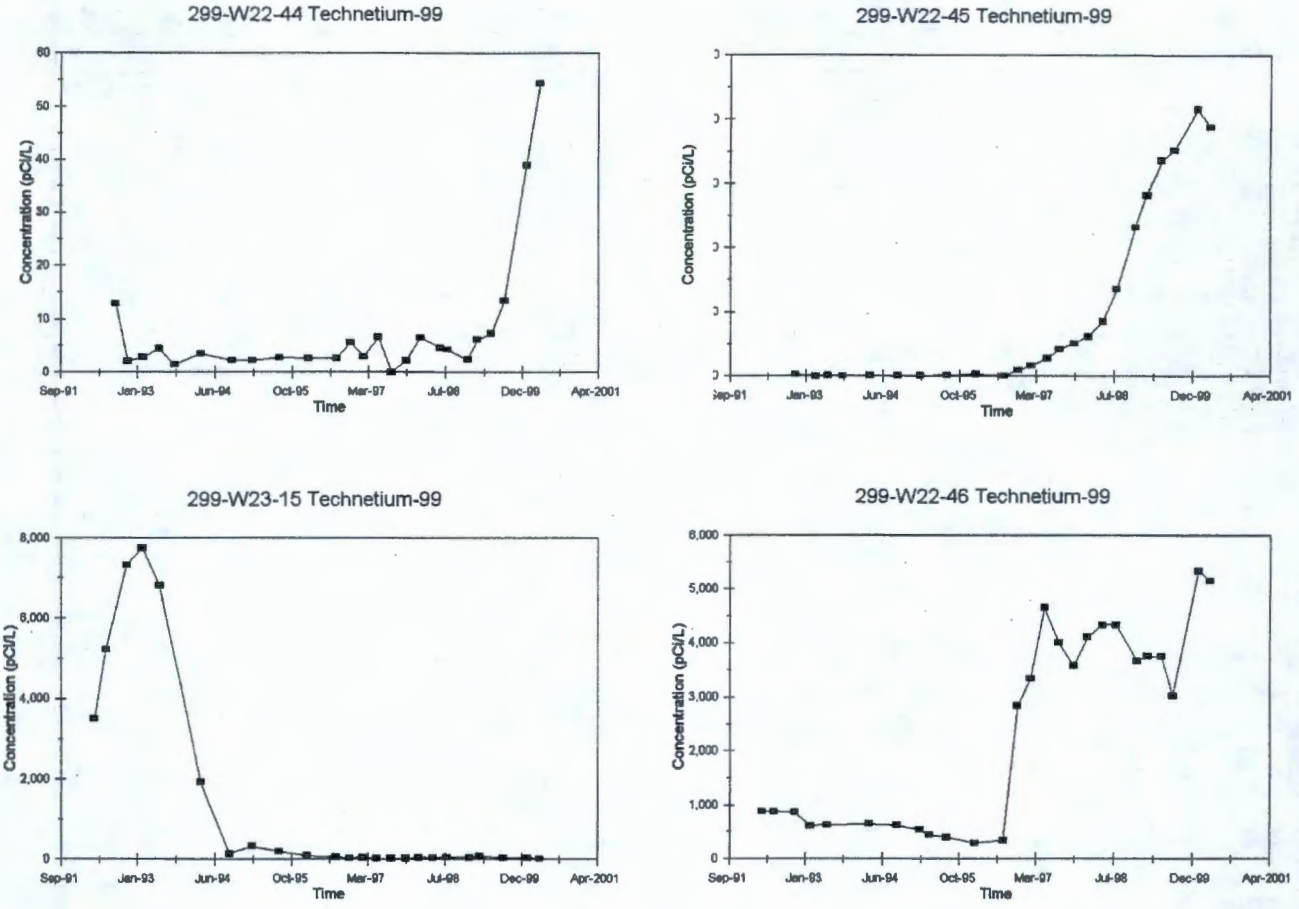

Table C.17. Maximum Contaminant Concentrations for Groundwater Samples Collected from Waste Management Area S-SX Network Wells (November 1997 to April 2000)

Analyte	MCL	W22-39	W22-44	W22-45	W22-46	W22-48	W22-49	W22-50	W23-1	W23-2
Chromium[a] (µg/L)	100	16.3	5[b]	27.4[b]	26	7.1	4.6U	10.4	29	6.1
^{99}Tc (pCi/L)	900	120	56	2,080	5,330	720	58.3	4,240	2,890	75.6
Nitrate (as NO_3) (µg/L)	45,000	16,822	37,628	47,367	49,580	18,593	13,546	57,991	50,023	11,952
Uranium (µg/L)	20	4.81	6.48	7.97	5.91	3.23	3.27	**30.9**	8.06	6.57
Gross alpha (pCi/L)	15	3.56	4.81	6.36	4.36	1.21	2.24	20.9	5.68	4.65
Gross beta (pCi/L)	50	37.5	20.7	768	1,836	223	22	1,420	1,090	29.3
Tritium (pCi/L)	20,000	27,100	238U	18,800	58,700	249U	22,000	31,400	1,010	12,700
^{90}Sr (pCi/L)	8	0.261U	0.295U	1.4U	4.92U	0U	0U	1.03U	**7.54**	0.205U
^{137}Cs (pCi/L)	200	1.82U	2.42U	2.78U	4.59U	0U	1.7U	0U	1.82U	0U
Iron[a] (µg/L)	300	118	146[b]	65.9	122	54.9	85.8[b]	95.5[b]	59	39.5
Manganese[a] (µg/L)	50	7.7	8.1[b]	3.8	4.3	**306**	244	167	7	11.8
Carbon tetrachloride (µg/L)	5	3.8	6.2	12	30	4	6	19	--	--
Fluoride (µg/L)	4,000	473	400	480	440	490	550	**730**	458	424
Aluminum[a] (µg/L)	50	51	58.3U	41.8U	45.7	41.8U	64.6	**93.2**	31.3U	20.6U
pH	[6.5, 8.5]	[7.93, 8.48]	[7.92, 8.25]	[8.07, 8.35]	[7.89, 8.33]	[7.97, 8.59]	[8.1, 9.09]	[8.1, 8.14]	[7.33, 8.19]	[8.11, 8.26]

Analyte	W23-4[c]	W23-9[c]	W23-13[c]	W23-14[c]	W23-15	W23-19[e]	W23-234	Max[d]	Max/MCL
Chromium[a] (µg/L)	4.6U	8.5	33.9	12.5	8.1[b]	**89.8**	7.5	89.8	0.9
^{99}Tc (pCi/L)	21.1	408	10.6U	218	72.1	**52,300**	80.4	52,300	58.1
Nitrate (as NO_3) (µg/L)	4,869	165,562	7,698	134,575	14,697	**562,204**	19,080	562,204	12.5
Uranium (µg/L)	24.4	25.8	16.5	18	14.6	17.6	3.4	30.9	1.5
Gross alpha (pCi/L)	14.5	17.3	11.7	9.82	10.8	**21.9**	--	21.9	NA
Gross beta (pCi/L)	15	56.6	11.4	19.7	27.8	**23,000**	--	23,000	NA
Tritium (pCi/L)	1,540	**502,000**	215U	382,000	22,200	95,800	138,000	502,000	25.1
^{90}Sr (pCi/L)	0.222U	0.481U	0.189U	0.425U	0.36U	9.63U	0.2U	7.54	0.94
^{137}Cs (pCi/L)	3.96U	0U	1.33U	1.71U	2.31U	1.63U	1.3U	Not detected	NA
Iron[a] (µg/L)	81.5	83.3	154	110	**938**	46	48.2	938	3.1
Manganese[a] (µg/L)	2.4	30.3	10.2	12.7	20.1	203	5.7	306	6.1
Carbon tetrachloride (µg/L)	100	2	11	0.51	**140**	22	--	140	28
Fluoride (µg/L)	340	319	390	350	490	340	497	730	0.2
Aluminum[a] (µg/L)	41.8U	41.8U	41.8U	33.5U	83.2	41.8U	33.5U	93.2	1.9
pH	[8.0, 8.09]	[7.72, 8.1]	[7.72, 8.58]	[7.78, 8.52]	[7.74, 8.12]	8.05	8.54	[7.33, 9.09]	NA

Note: All well numbers prefixed by 299-. U denotes analytical result is not detected. **Bold** indicates well with maximum.

[a]Filtered sample results.
[b]Outliers removed.
[c]Upgradient wells.
[d]Maximum across all network wells.
[e]Subsequent groundwater sample analyses show increases in chromium and technetium-99 concentrations (138 µg/L and 81,500 pCi/L, respectively) as of March 2001.

C.8.0 REFERENCES

Agnew S. F., 1997, *Hanford Tank Chemical and Radionuclide Inventories: HDW Model Rev. 4*, LA-UR-96-3860, Los Alamos National Laboratory, Los Alamos, New Mexico.

Agnew, S. F., and R. A. Corbin, 1998, *Analysis of SX Farm Leak Histories—Historical Leak Model (HLM)*, LA-UR-96-3537, Los Alamos National Laboratory, Los Alamos, New Mexico.

Baker, V. R., B. N. Bjornstad, A. J. Busacca, K. R. Fecht, E. P. Kiver, U. L. Moody, J. G. Rigby, D. F. Stradling, and A. M. Tallman, 1991, "Quaternary Geology of the Columbia Plateau," in R. B. Morrison, ed., *Quaternary Nonglacial Geology, Conterminous U.S.*, Boulder, Colorado, Geological Society of America, The Geology of North America, v. K-2.

Barney, G. S., 1976, *Vapor Liquid Phase Equilibria of Radioactive Sodium Salt Wastes at Hanford*, ARH-ST-133, Atlantic Richfield Company, Richland, Washington.

Bjornstad, B. N., 1984, *Suprabasalt Stratigraphy With and Adjacent to the Reference Repository Location*, SD-BWI-DP-039, Rockwell Hanford Operations, Richland, Washington.

Bjornstad, B. N, 1990, *Geohydrology of the 218-W-5 Burial Ground, 200 West Area, Hanford Site*, PNL-7336, Pacific Northwest Laboratory, Richland, Washington.

Brown, D. J, 1959, *Subsurface Geology of the Hanford Separations Areas*, HW-61780, General Electric Company, Richland, Washington.

Brown, D. J, 1960, *An Eolian Deposit Beneath 200-West Area*, HW-67549, General Electric Company, Richland, Washington.

Corbin, R. A., B. C. Simpson, and S. F. Agnew, 2001, *Hanford Soil Inventory Model*, BHI-01496, Rev. 0, Bechtel Hanford, Inc., Richland, Washington.

DOE, 1996, *Vadose Zone Characterization Project at the Hanford Tank Farms, SX Tank Farm Report*, GJPO-HAN-4, Final Draft, U.S. Department of Energy, Richland Operations Office, Richland, Washington.

DOE, 1988, *Consultation Draft Site Characterization Plan*, DOE/RW-0164, 9 volumes, U.S. Department of Energy, Richland Operations Office, Richland, Washington.

DOE-GJO, 2000, *Addendum to S Tank Farm Report*, GJO-97-31-TARA, U.S. Department of Energy, Albuquerque Operations Office and Grand Junction Projects Office, Grand Junction Colorado.

DOE-GJPO, 2000, *Addendum to the SX Tank Farm Report SX Supplement*, GJPO-HAN-4, U.S. Department of Energy, Albuquerque Operations Office, Grand Junction Projects Office, Grand Junction, Colorado.

DOE-RL, 1993, *200 West Groundwater Aggregate Area Management Study Report*, DOE/RL-92-16, Rev. 0, U.S. Department of Energy, Richland Operations Office, Richland, Washington.

Fecht, K. R., K. A. Lindsey, D. G. Horton, G. V. Last, and S. P. Reidel, 1999, *An Atlas of Clastic Injection Dikes of the Pasco Basin and Vicinity*, BHI-01103, Rev. 0, Bechtel Hanford, Inc., Richland, Washington.

GE, 1951, *REDOX Technical Manual*, HW-18700, General Electric Company, Richland, Washington.

Gee, G. W., M. J. Fayer, M. L. Rockhold, and M. D. Campbell, 1992, "Variations in Recharge at the Hanford Site," *Northwest Science*, 66:237-250.

Godfrey, W. L., 1971, *Inventory of Rhodium, Palladium, and Technetium Stored in Hanford Tanks*, ARH-1979, Atlantic Richfield Hanford Company, Richland, Washington.

Goodman, D., 2000, *Estimation of SX-Farm Vadose Zone Cs-137 Inventories From Geostatistical Analysis of Drywell and Soil Core Data*, HNF-5782, Rev. 0, Montana State University, Bozeman, Montana.

H-2-37985, 1974, *Civil North Section Contoured Elevation 241-SX Tank Farm*, Rev. 0, Atlantic Richfield Hanford Corporation, Richland, Washington.

Hanlon, B. M., 2001, *Waste Tank Summary Report for Month Ending March 31, 2001*, HNF-EP-0182, Rev. 156, CH2M HILL Hanford Group, Inc., Richland, Washington.

Harmon, M. K., 1949, *Neutralization of REDOX Aqueous Waste Streams*, HW-12566, General Electric Company, Richland, Washington.

Henderson, J. C., 1999, *Preliminary Site-Specific Work Plan Addendum for WMA S-SX*, HNF-4380, Rev. 1, Lockheed Martin Hanford Corporation, Richland, Washington.

Horton, D. G., and V. G. Johnson, 2000, *Borehole Data Package for Wells 299-W22-48, 299-W22-49, and 299-W22-50 at Single-Shell Tank Waste Management Area S-SX*, PNNL-13200, Pacific Northwest National Laboratory, Richland, Washington.

Johnson, V., and C. J. Chou, 1998, *Results of Phase I Groundwater Quality Assessment for Single-Shell Tank Waste Management Areas S-SX at the Hanford Site*, PNNL-11810, Pacific Northwest National Laboratory, Richland, Washington.

Johnson, V., and C. J. Chou, 1999, *Addendum to the RCRA Assessment Report for Single-Shell Tank Waste Management Areas S-SX at the Hanford Site*, PNNL-11810 ADD. 1., Pacific Northwest National Laboratory, Richland, Washington.

Johnson, V. L., and C. J. Chou, 2001, *RCRA Groundwater Quality Assessment Report for Waste Management Area S-SX (November 1997 through April 2000)*, PNNL-13441, Pacific Northwest National Laboratory, Richland, Washington.

Johnson, V. G., T. E. Jones, S. P. Reidel, and M. I Wood, 1999, *Subsurface Conditions Description For the S-SX Waste Management Area*, HNF-4936, Rev. 0, Lockheed Martin Hanford Corporation, Richland, Washington.

Jones, T. E., R. Khaleel, D. A. Myers, J. W. Shade, and M. I. Wood, 1998, *A Summary and Evaluation of Hanford Site Tank Farm Subsurface Contamination*, HNF-2603, Rev. 0, Lockheed Martin Hanford Corporation, Richland, Washington.

Jones, T. E., R. A. Watrous, and G. T. Maclean, 2000a, *Inventory Estimates for Single-Shell Tank Leaks in S and SX Tank Farms*, RPP-6285, Rev. 0, CH2M HILL Hanford Group, Inc., Richland, Washington.

Khaleel, R., T. E. Jones, A. J. Knepp, F. M. Mann, D. A. Myers, P. M. Rogers, R. J. Serne, and M. I. Wood, 2000, *Modeling Data Package for S-SX Field Investigation Report (FIR)*, RPP-6296, Rev. 0, CH2M HILL Hanford Group, Inc., Richland, Washington.

Kovach, J. L., 1998, *TWRS Technetium Workshop*, Letter Report prepared by an Independent Review Plan for the U.S. Department of Energy, Richland Operations Office, Richland, Washington.

Kupfer, M. J., A. L. Boldt, K. M. Hodgson, L. W. Shelton, B. C. Simpson, R. A. Watrous, M. D. LeClair, G. L. Borsheim, R. T. Winward, B. A. Higley, R. M. Orme, N. G. Colton, S. L. Lambert, D. E. Place, and W. W. Schulz, 1998, *Standard Inventories of Chemicals and Radionuclides in Hanford Site Tank Wastes*, HNF-SD-WM-TI-740, Rev. 8, prepared by Lockheed Martin Hanford Corporation for Fluor Daniel Hanford, Inc., Richland, Washington.

Last, G. V., B. N. Bjornstad, M. P. Bergeron, D. W. Wallace, D. R. Newcomer, J. A. Schramke, M. A. Chamness, C. S. Cline, S. P. Airhart, and J. S. Wilbur, 1989, *Hydrogeology of the 200 Areas Low-Level Burial Grounds - An Interim Report*, PNL-6820, 2 volumes, Pacific Northwest Laboratory, Richland, Washington.

Lindsey, K. A., 1996, *The Miocene to Pliocene Ringold Formation and Associated Deposits of the Ancestral Columbia River System, South-Central Washington and North-Central Oregon*, Open-File Report 96-8, Washington Division of Geology and Earth Resources, Olympia, Washington.

Lindsey, K. A., S. P. Reidel, K. R. Fecht, J. L. Slate, A. G. Law, and A. M. Tallman, 1994, "Geohydrologic Setting of the Hanford Site, South-Central Washington", in D.A. Swanson and R. A. Hagerud, eds., *Geologic Field Trips in the Pacific Northwest: 1994 Geological Society of America Meeting*, Chapter 1C, Geological Society of America, Boulder, Colorado, p. 1C-1 to 1C-16.

Lindsey, K. A., S. E. Kos, and K. D. Reynolds, 2000, *Vadose Zone Geology of Boreholes 299-W22-50 and 299-W23-19 S-SX Waste Management Area Hanford Site, South-Central Washington*, RPP-6149, Rev. 0, Daniel B. Stephens & Associates, Richland, Washington.

MacLean, G. T., and K. M. Eager, 1998, *Evaluation of the Environmental Simulation Program (ESP) as a Computer Simulator of Nuclear Waste Processing*, HNF-3257, Rev. 0, Numatec Hanford Company, Richland, Washington.

Myers, C. W. and S. M. Price, 1979, *Geologic Studies of the Columbia Plateau -- A Status Report*, RHO-BWI-ST-4, Rockwell Hanford Operations, Richland, Washington.

Myers, D. A., 1997, *Activity Plan: Extension of Borehole 41-09-39, SX Tank Farm*, HNF-SD-WM-AP-044, Rev. 0, Lockheed Martin Hanford Corporation, Richland, Washington.

Myers, D. A., D. L. Parker, G. Gee, V. G. Johnson, G. V. Last, R. J. Serne, and D. J. Moak, 1998, *Findings of the Extension of Borehole 41-09-39, 241-SX Tank Farm*, HNF-2855, Lockheed Martin Hanford Corporation, Richland, Washington.

Myers, D. A, 2000, *Moisture Content in the S-SX Tank Farm*, RPP-7613, CH2M HILL Hanford Group, Inc., Richland, Washington.

Price, W. H., and K. R. Fecht, 1976a, *Geology of the 241-SX Tank Farm*, ARH-LD-134, Atlantic Richfield Hanford Company, Richland, Washington.

Price, W. H., and K. R. Fecht, 1976b, *Generalized Geology of the 241-SY Tank Farm*, ARH-LD-139, Atlantic Richfield Hanford Company, Richland, Washington.

Raymond, J. R., and E. G. Shdo, 1966, *Characterization of Subsurface Contamination in the SX Tank Farm*, BNWL-CC-701, Pacific National Laboratory, Richland, Washington.

Resource Conservation and Recovery Act of 1976, Public Law 94-580, 90 Stat. 2795, 42 USC 901 et seq.

Reidel, S. P., 1997, "Geologic Setting" in *Hanford Site Groundwater Monitoring for Fiscal Year 1996*, Pacific Northwest National Laboratory, Richland, Washington.

Rogers, P. M., and A. J. Knepp, 2000, *Site-Specific SST Phase 1 RFI/CMS Work Plan Addendum for WMA S-SX*, HNF-5085, Rev. 1, CH2M HILL Hanford Group, Inc., Richland, Washington.

Serne, R. J., H. T. Schaef, B. N. Bjornstad, B. A. Williams, D. C. Lanigan, D. G. Horton, R. E. Clayton, V. L. LeGore, M. J. O'Hara, C. F. Brown, K. E. Parker, I. V. Kutnyakov, J. N. Serne, A. V. Mitroshkov, G. V. Last, S. C. Smith, C. W. Lindenmeier, J. M. Zachara, and D. B. Burke, 2001a, *Characterization of Uncontaminated Sediments from the Hanford Reservation-RCRA Borehole Core and Composite Samples*, PNNL-2001-1, Pacific Northwest National Laboratory, Richland, Washington.

Serne, R. J., G. V. Last, G. W. Gee, H. T. Schaef, D. C. Lanigan, C. W. Lindenmeier, R. E. Clayton, V. L. LeGore, R. D. Orr, M. J. O'Hara, C. F. Brown, D. B. Burke, A. T. Owen, I. V. Kutnyakov, T. C. Wilson, and D. A. Myers, 2001b, *Geologic and Geochemical Data Collected from Vadose Zone Sediments from Borehole SX 41-09-39 in the S/SX Waste Management Area and Preliminary Interpretations*, PNNL-2001-2, Pacific Northwest National Laboratory, Richland, Washington.

Serne, R. J., H. T. Schaef, B. N. Bjornstad, D. C. Lanigan, G. W. Gee, C. W. Lindenmeier, R.E. Clayton, V. L. LeGrove, R. D. Orr, M. J. O'Hara, C. F. Last, I. V. Kutnyakov, D.B. Burke, T. C. Wilson, and B. A. Williams, 2001c, *Geologic and Geochemical Data Collected from Vadose Zone Sediments from Borehole 299-W23-19 [SX-115] in the S/SX Waste Management Area and Preliminary Interpretations*, PNNL-2001-3, Pacific Northwest National Laboratory, Richland, Washington.

Siddall III, T. H., 1959, *Behavior of Technetium in the PUREX Process*, DP-634, E. I. du Pont & Co., Aiken, South Carolina.

Slate, J. L, 1996, "Buried Carbonate Paleosols Developed in Pliocene-Pleistocene Deposits of the Pasco Basin, South-Central Washington, USA," *Quaternary International*, Vol. 34-36, pp. 191-196.

Slate, J. L, 2000, *Nature and Variability of the Plio-Pleistocene Unit in the 200 West Area of the Hanford Site*, BHI-01203, Rev. 0, Bechtel Hanford, Inc., Richland, Washington.

Sobczyk, S. M., 2000, *Subsurface Interpretation of the SX Tank Farm Hanford Site, Washington Based on Gamma-Ray Logging*, Nez Perce Tribe Environmental Restoration Waste Management Program, Ladwai, Idaho.

Sterner, S. M.; J. R. Rustad; and A. R. Felmy, 1996, *The Hanford Thermochemical Databank: v 1.00 with Parameters for the ESP and Pitzer Models*, Pacific National Laboratory, Richland, Washington.

Sterner, S. M.; A. R. Felmy; J. R. Rustad; and K. S. Pitzer, 1997, *Thermodynamic Analysis of Aqueous Solutions Using INSIGHT*, PNWD-SA-4436, Pacific National Laboratory, Richland, Washington.

Sterner, S. M., J. R. Rustad, and A. R. Felmy, 1996, *The Hanford Thermochemical Databank: v 1.00 with Parameters for the ESP and Pitzer Models*, Pacific Northwest National Laboratory, Richland, Washington.

Sullivan, P., M. P. Connelly, and T. E. Jones, 2001, *Geostatistical Analysis of Gamma-Emitting Radionuclides in the SX Tank Farm Vadose Zone*, RPP-8209, Rev. 0, CH2M Hill Hanford Group, Inc., Richland, Washington.

Tallman, A. M., K. R. Fecht, M.C. Marratt, and G. V. Last, 1979, *Geology of the Separations Areas, Hanford Site, South-Central Washington*, RHO-ST-23, Rockwell Hanford Operations, Richland, Washington.

Tomlinson, R. E., 1963, *Waste Management Program Chemical Processing Department*, HW 76352, General Electric Company, Richland, Washington.

Waite, J. L., 1991, *Tank Wastes Discharged Directly to the Soil at the Hanford Site*, WHC-MR-0227, Westinghouse Hanford Company, Richland, Washington.

WHC, 1992a, *Tank 241-SX-108 Leak Assessment*, WHC-MR-0300, Westinghouse Hanford Company, Richland, Washington.

WHC, 1992b, *Tank 241-SX-109 Leak Assessment*, WHC-MR-0301, Westinghouse Hanford Company, Richland, Washington.

WHC, 1992c, *Tank 241-SX-115 Leak Assessment*, WHC-MR-0302, Westinghouse Hanford Company, Richland, Washington.

Wood, M. I., T. E. Jones, R. Schalla, B. N. Bjornstad, and F. N. Hodges, 2001, *Subsurface Conditions Description of the T-TX-TY Waste Management Area*, RPP-7123, Rev. 0, CH2M HILL Hanford Group, Inc., Richland, Washington.

APPENDIX D

DIGEST OF S&T PROGRAM EVALUATIONS

This page intentionally left blank.

CONTENTS

FIGURES

TABLES

This page intentionally left blank.

D.1.0 OVERVIEW AND SUMMARY

The Hanford Science and Technology Program (S&T Program) was initiated in 1998 with the overall goal of coordinating and performing mission-oriented scientific research in support of environmental management decision making for the 200 Areas at Hanford. The scope of the S&T Program, as well as the major site milestones that it supports, has been described in the Science and Technology Roadmap for the Hanford vadose zone (DOE 2000). The S&T Program consists of focused, site-specific investigations funded by DOE-Richland Operations through the Groundwater/Vadose Zone Integration Project, and Environmental Management Science Program (EMSP) projects funded in the FY 1999 vadose zone call.

The Integration Project has used the process of roadmapping, where problem holders (such as the U.S. Department of Energy (DOE), Tribal Nations, regulators, stakeholders, and remediation contractors) come together with problem solvers (such as scientists and engineers from universities and the DOE national laboratories) to define the problems and establish a path to solution. The scope and outcomes of S&T Program activities, linkages of the outcomes to the Integration Project or other Hanford Site projects, and the schedule, budget, and priorities for these activities are documented in the S&T Program roadmap, which was issued and revised once (DOE 1999; DOE 2000).

This particular appendix contains research performed by three elements of the Hanford S&T Program: Representative Sites Research, Reactive Transport Modeling, and Vadose Zone Field Experiments. This scientific input by the S&T Program to the Waste Management Area (WMA) S-SX Field Investigation Report represents a specific milestone in the S&T Program roadmap. The research addressed a number of key scientific issues associated with tank waste source terms; the chemical speciation of Reduction-Oxidation (REDOX) tank wastes, water and contaminant fluxes through the vadose zone at WMA S-SX; and the geochemical behavior of ^{137}Cs, Cr, and ^{99}Tc. These issues were studied through experiments with uncontaminated (borehole B8812) and contaminated subsurface sediments (299-W23-19, 41-09-39, tank SX-108) from the S and SX tank farms (Representative Sites); modeling studies of heat, water, and contaminant flux through the S-SX vadose zone (Reactive Transport Modeling); and field injection experiments at the Vadose Zone Transport Studies Site.

This appendix summarizes key results of the S&T Program research that have important implications to (1) conceptual models of water and waste migration in the vadose zone, and (2) future migration and in-ground chemical behavior as it may influence future discharges to groundwater, need for corrective actions, and leak-loss limits for tank waste sluicing. In the interest of brevity, many details and the supporting experimental, theoretical, and computational information have not been included in the scientific summaries that follow. Readers desiring full disclosure of methods and results are best directed to the peer-reviewed publications that are resulting from this work.

D.1.1 KEY FINDINGS

The most important findings of the S&T Program investigations and their implications are summarized below. Details of these findings and other equally important conclusions may be found in the individual technical sections.

(1) Laboratory studies Environmental Management Science Program of the interaction of highly basic REDOX waste simulants with S-SX sediments have shown that significant mineral alteration and precipitation (e.g., of zeolites) occurs as a result of waste-sediment reaction. As a result, it was speculated that a large/deep mineral alteration aereole would surround the leaked tanks, which would impact contaminant behavior. Field observations, in contrast, showed that this alteration zone was much reduced in depth (e.g., only 67.27 ft, sample 3A in SX-108 core), although clearly apparent through microscopic analysis of the sediment grains. Most contaminants were observed at depths deeper than the mineral transformation zone, suggesting that such reactions were of minimal consequence to contaminant retardation and need not be considered in terms of future mobility issues in the S and SX tank farms. Mineral and surface analyses of sample 5A from the SX-108 core, which contained low contaminant levels, showed that surfaces were pristine, indicating that reactive tank wastes did not migrate through this sediment. A heterogeneous vertical migration pattern is inferred.

(2) The ^{137}Cs distribution coefficient is not constant over the range of sodium, potassium, calcium, and cesium concentrations found in the tank farm inventory and in the vadose zone porewater. Vadose zone processes, such as dilution from infiltrating rainwater (or water leaking from pipes), or concentration from boiling waste, will dramatically alter the ^{137}Cs-K_d over time and space. The multi site cation exchange model developed by EMSP researchers captures many of the chemical effects responsible for the dependence of ^{137}Cs-K_d on competing cation and Cs concentrations, and is a significant improvement over a constant K_d to model ^{137}Cs transport from tank leaks and to predict its future in-ground behavior.

(3) The deep penetration of ^{137}Cs may be explained as resulting from the competitive ion exchange effects of high Na and K present in REDOX wastes and possibly by the bypassing of exchange sites in immobile regions during unsaturated flow. New, charge-balanced calculations performed to estimate the total composition and speciation of leaked wastes from tanks SX-108 and SX-109 suggest that the Na^+ concentration was higher than previously thought, possibly approaching 19.6 and 15.2 mol/L for tanks SX-108 and SX-109, respectively. The chemical effects of these high electrolyte concentrations, alone, yielded predicted values of ^{137}Cs retardation (2 to 3) that were remarkably close to observed values below tank SX-108 (2.5 to 3), although these conclusions were based on one-dimensional flow and transport simulations that may not be applicable to the complex flow system developed around the boiling tank SX-108. The current in-ground Cs is in approximate ion exchange equilibrium with its surroundings.

(4) Approximately 50% of the large in-ground adsorbed $^{133,135,137}Cs$ pool in WMA S-SX sediments is labile and exchangeable with the aqueous phase. The fission-derived Cs is

sorbed to micas and smectites, with no other phase associations observed. Significant desorption and transport, as could feasibly occur if fluids were released by waste sluicing, however, is not expected unless aqueous concentrations of Na and K exceed those present in the original, leaked REDOX wastes. Such conditions are considered highly unlikely.

(5) X-ray absorption (XAS) measurements by EMSP investigators showed that Cr existed in two valence states (III, VI) in contaminated sediments from both 41-09-39 and tank SX-108. Cr(III), which is relatively immobile, is believed to result from the heterogeneous reduction of CrO_4^{2-} in the REDOX tank wastes by Fe(II) contained in sediment minerals (biotite, ilmenite) to insoluble hydroxide precipitates. Laboratory studies indicated that this reaction was base (e.g., OH^-) facilitated and may no longer be operative. The water extractable Cr was consistent with that present as Cr(VI) (CrO_4^{2-}). Approximately 30 to 60% of the Cr present in tank waste was immobilized in sediment as Cr(III) precipitate, with the remainder present as water-soluble CrO_4^{2-}. Fission-derived Mo (presumably as MoO_4^{2-}) appeared to follow similar reductive processes to Cr, while $^{79/82}Se$ (SeO_4^{2-}) and $^{99}TcO_4^-$ were freely mobile. These mass balance issues must be considered when using Cr(VI) concentrations in groundwater as indications of tank waste contribution.

(6) The isotopic ratios of trace anionic fission products ($^{127}I/^{129}I$; $^{95}Mo/^{98}Mo$) in water extracts varied significantly between regions of the SX-108 core showing peak concentrations in mobile constituents (e.g., NO_3, Cr, ^{99}Tc). These isotopic ratios provide a means for tracing waste sources and leak events if the "fill history" of the tank and its time variant isotopic signature is sufficiently documented. The trace isotope analyses of waters extracted from tank SX-108 indicate that wastes of different isotopic composition were discharged to the vadose zone from tank SX-108. The results may imply the time-separated intrusion of leaked waste of different composition into the subsurface, most likely associated with the two known fillings of the tank in 1959 and 1963. Further evaluations of the tank fill history and the isotopics of the REDOX and other comingled wastes (Al-cladding waste and condensate) are needed to formulate a consensus conclusion on the implications of the measurements.

(7) An assessment of the $^{87}Sr/^{86}Sr$ isotopic ratios in the B8812 core indicated an average water infiltration flux of 30 ±20 mm/yr to the vadose zone over the past 100 to 1000 years. In contrast, infiltration estimates for the S and SX tank farms based on a method that uses winter precipitation and surface soil texture data, calibrated by 20 years of Hanford lysimeter data, place the average value at 56 mm/yr with a range of 20 to more than 150 mm/yr, depending on climatic conditions. Regardless of precise value, these results suggest that natural infiltration and drainage is significant for moving mobile species (e.g., NO_3, Cr, ^{99}Tc, $^{127/129}I$, $^{79/82}Se$) toward groundwater over time periods of decades to hundreds of years. The estimated vadose transit time for meteoric waters in the S and SX tank farms range from 60 to 500 years depending on assumptions and model.

(8) A microbiological enumeration was performed on contaminated SX-108 sediments to determine if microorganisms were present that could influence the long-term fate of the

in-ground contaminants. Culturable microorganism populations of chemoheterotrophic bacteria were found in samples 1a, 4a, 7a, 9a 12a, 16a, and 17a. Some of the organisms found can use nitrate as an electron acceptor in the absence of O_2 and reduce contaminant metals/radionuclides [Cr(VI), Tc(VII)] to insoluble species in presence of a sufficient energy source. Radiation-resistant-bacteria, closely related to *Deinococcus radiodurans*, was isolated from two core samples containing high levels of ^{137}Cs. This is the first time that *D. radiodurans* has been isolated from a radionuclide-contaminated environment.

(9) Significant horizontal movement of water along the top of the Plio-Pleistocene caliche was implied by moisture content, isotopic measurements, and solute displacement from B8812 core materials. While the source of these waters and the entrained contaminants has not been identified, the observations affirm that water perching and lateral transport may occur on the Plio-Pleistocene contact beneath the S and SX tank farms.

(10) Field injection experiments at the Vadose Zone Test Facility performed by a team of EMSP and S&T Program investigators near PUREX in 200 East indicated that subtle changes in sediment texture can induce the lateral spreading of draining vadose zone waters and their entrained contaminants. In particular, the layering anisotropy of fine over coarse sediments can produce significant lateral spreading of a plume that generally retards and reduces the downward migration of solutes. These findings provide a physical model for various observations in the S and SX tank farms, including (1) elevated water contents found at depth in 41-09-39, tank SX-108, and 299 W23-19 associated with layer sequences of finer-textured sediments, and (2) heterogeneous localization of ^{137}Cs in specific lithologies and apparent horizontal migration as inferred by downhole gamma spectral logging.

(11) Nonisothermal model simulations indicate that the thermal load from the boiling waste tanks altered water seepage patterns and caused large-scale redistributions in moisture. During periods of high heat load in the 1950s and 1960s, fluid and heat flow near the tank was dominated by vapor-liquid counterflow. Such counterflow concentrated dissolved solids near the heat source as precipitates. The heat load caused formation dry-out beneath the tank that was also accompanied by near-tank solute precipitation. Salt precipitates may have been remobilized at later times when tank temperatures declined and previously dried out regions began rewetting. Such effects may complicate the interpretation of solute distribution patterns in the SX-108 core. It is expected that solute distribution profiles in the infiltration shadow beneath the center of the tank will be different than in the region of enhanced seepage fluxes around the tank perimeter because of dilution and solubilization effects of dry-out induced salt precipitates.

(12) When compared with simulations done under isothermal conditions, nonisothermal model calculations indicate slightly faster transport through the vadose zone to the water table even when transport begins at present. Lower saturations induced by the tank heat result in shorter travel times and more lateral migration toward the compliance boundary. This effect may increase when the thermal impact of tank leaks (e.g., ^{137}Cs decay) is also considered. The model simulations (isothermal,

nonisothermal), however, assumed a constant recharge of 100 mm/yr at the soil surface and did not allow for evaporation. Residual heat from the tanks may enhance surface evaporation and reduce recharge, an effect that would slow solute migration toward groundwater. Additional nonisothermal modeling will address such issues.

(13) The vertical distribution of anionic and cationic solutes in borehole 299-W23-19 were well matched with a three-dimensional transport model that included multicomponent cation exchange as the primary chemical retardation mechanism. The model was parameterized with laboratory measurements of cation exchange capacity and ion selectivity and assumed that all cation exchange sites in the sediment were accessible to the tank solutes. While the 3D simulations used laboratory CECs and selectivity coefficients without calibration, the tank fluids leaking into the vadose zone had to be diluted from the charge-balanced estimates. In addition, some questions remain whether the 3D flow model, despite having used the accepted hydrostratigraphy of the Hanford formation, captured the full effects of the heterogeneities present. However, the good agreement between model and data suggested that sediment exchange sites were not being bypassed in the transport event. Accordingly, there is presently no evidence that the solute distributions were influenced by phenomena associated with expedited migration such as fast flow pathways or transport-limited sorption in immobile water zones. By analogy, it appears that the enhanced migration of ^{137}Cs noted beneath tank SX-108 was a result of its different chemical environment (e.g., high Na), although the higher temperatures associated with tank SX-108 may have produced a substantially different flow regime.

D.1.2 OBJECTIVE OF THE INTEGRATION PROJECT AND THE S&T PROGRAM

The Integration Project was established by DOE to ensure protection of the Columbia River environment, including river-dependent life and users of river resources. The Integration Project is accountable for the integrated management of vadose zone, groundwater, and Columbia River activities at the Hanford Site. This role involves five elements designed to:

- integrate characterization and assessment work affecting long-term risk assessments (Integration)
- assess the potential long-term effects of Hanford contaminants (System Assessment Capability [SAC])
- enhance the role of science and technology in cleanup decisions (S&T Program)
- ensure productive involvement by parties interested in influencing Hanford's cleanup (Public Involvement)
- ensure independent technical reviews and management oversight of the Integration Project (Technical Review).

These are described in Volume I of the *Project Summary Description* document.

The objective of the S&T Program is to provide new knowledge, data, tools, and the understanding needed to enable the Integration Project's mission. The S&T Program is focused on resolving key technical issues that help inform and influence decisions on remediation and closure of tank farms and contaminated soil sites, in partnership with both the SAC and core projects (those projects that are influenced by the Integration Project).

D.1.3 APPROACH

For each of the technical elements contributing to the S&T evaluation of WMA S-SX, a approach was developed.

D.1.3.1 Tank SX-108 Implementation Plan

The ORP Tank Farm Vadose Zone Project developed a plan for characterizing samples from the slant borehole at tank SX-108. This characterization was performed to determine the general state of conditions (chemical/radiological and physical) beneath tank SX-108. The results of the tank SX-108 analyses were integrated with those from the uncontaminated boreholes (e.g., B8812 and B8814), the decommissioning of 41-09-39, and the SX-115 borehole. Together with the contributions from the S&T Program effort, a greatly improved conceptual model of subsurface tank waste migration at WMA S-SX was developed.

The scientific studies of the uncontaminated and contaminated samples complemented the ORP Tank Farm Vadose Zone Project characterization with definition of the physical, chemical, and mineralogic association of contaminants; their chemical status and environment; their degree of immobilization or reversibility; their potential for future mobilization; and other such issues. The planning of the wraparound science was, in part, accomplished through EMSP vadose zone workshops held at Pacific Northwest National Laboratory in November 1999 and November 2000. These workshops brought together the principal investigators of EMSP projects and Hanford Site personnel, including staff of the ORP.

To prepare for the characterization activity at tank SX-108, the ORP developed inventory estimates for tank waste in tank SX-108 at the time of the leak, and a leak history scenario. The inventory estimate allowed identification of primary contaminants of concern (COCs; ^{137}Cs, ^{99}Tc, CrO_4^{2-}) and their potential concentration ranges, and other constituents (e.g., Na, NO_3^{2-}, OH^-, $Al(OH)_4^-$) that will impact contaminant mobility. In addition, the best estimate of tank SX-108 composition at the time of the leak(s) was substantially greater (by at least a factor of five) than that estimated for tank SX-115. The concentration range is significant in that the advanced scientific equipment that may be used to investigate the chemical environment and reactivity of contaminants (e.g., optical and X-ray absorption spectroscopy and microscopy) requires certain minimal concentrations for effective application.

The plan for the SX-108 slant borehole was to retrieve samples immediately beneath the leaked tank, and from the distal region of the vadose zone plume using a 2-inch diameter, 1-foot long shielded split spoon. Precautions were taken to seal the retrieved core to prevent drainage and oxygenation after collection as soon as radiation protection and environment, safety, and health procedures allowed. Approximately 500 g of each sample were made available for S&T Program research. Poor core recovery may further limit sample availability. The high potential radioactivity of the core materials resulting from sorbed ^{137}Cs mandates that extreme care be taken in distributing and handling the core materials and that all appropriate environment, safety, and health and radiation protection procedures be followed at Pacific Northwest National Laboratory and receiving institutions. A separate environment, safety, and health plan for the distribution of these samples was developed and implemented. All samples were distributed to investigators, retrieved, and dispositioned without incident.

D.1.3.2 Transport Modeling

The Transport Modeling element performed analyses to identify appropriate detail in process models for Hanford Site assessments and provide technical defensibility for their use in predicting long-term contaminant behavior. The S&T Program modeling is based on historical data for the Hanford Site as well as the results of recent characterization efforts and scientific investigations. The data used by the modeling team have been or are being developed by other entities (e.g., other national laboratories through the S&T Program or EMSP, Site contractors, etc.) for a variety of purposes. Most of these data were previously not examined in a comprehensive modeling framework for consistency. An important role for the S&T Program modeling, therefore was to identify inconsistencies between observations and process-level understanding and identify areas that merit additional investigation.

The S&T Program modeling addressing the nonisothermal multiphase fluid flow modeling was performed in two-dimensional cross sections, with the TOUGH2 (Pruess et al. 1999) and STOMP (White and Oostrom 2000a, b) codes. In each effort, two-dimensional cross sections were used to represent the vadose zone beneath WMA S-SX. The STOMP simulations used the data package (Khaleel et al. 2000) developed for the Tank Farm Vadose Zone Project projections of solute transport under isothermal conditions. The S&T Program modeling was performed to test the isothermal assumption by performing nonisothermal multiphase simulations.

Reactive transport modeling was performed on the tank SX-115 leak by coupling the reactive transport code CRUNCH (Steefel 2001) with the multiphase flow and heat transport code NUFT (Nitao 1998). In addition to the flow and transport parameters documented in Khaleel et al. (2000), the reactive transport simulations used ion exchange parameters extracted from batch and transport experiments performed as part of the WMA S-SX S&T Program investigations.

D.1.3.3 Vadose Zone Transport Field Studies

The detailed test plan (Ward and Gee 2000) outlines the overall scope of the field experiments. The first 2 years of field experiments were performed at a test location in the 200 East area previously known as the Sisson and Lu site (299-E24-111) where a previous injection experiment was performed and extensive characterization data already were compiled. Data were collected in several phases: (1) characterization of background conditions at the site, and (2) process characterization that occurred during and after the field injection experiment. Background moisture conditions at the site were determined, and a series of fluid injections, designed to simulate a leak from a high-level waste tank, was performed over a 3-month period. The field test involved water and tracers to simulate dilute tank wastes. A second injection experiment is being conducted during FY 2001 involving dense saline fluids with tracers to simulate high-salt wastes. Nine monitoring technologies were used, including neutron logging, electrical resistance tomography, cross-borehole radar and seismic, high-resolution resistively, electromagnetic imaging, advanced tensiometry, and isotopic tracers. Water contents, obtained by neutron probe logging and coring, provided baseline measurements for comparison of other geophysical measurements.

D.1.4 REFERENCES

DOE, 1999, *Groundwater/Vadose Zone Integration Project Science and Technology Summary Description*, DOE/RL-98-48, Vol. III, Rev. 0, U.S. Department of Energy, Richland, Washington.

DOE, 2000, *Groundwater/Vadose Zone Integration Project Science and Technology Summary Description*, DOE/RL-98-48, Vol. III, Rev. 1, U.S. Department of Energy, Richland, Washington.

DOE-RL, 2000, *Groundwater/Vadose Zone Integration Project Science and Technology Summary Description*, DOE/RL-98-48, Vol. III, Rev. 1, U.S. Department of Energy, Richland Operations Office, Richland, Washington.

Khaleel, R., T. E. Jones, A. J. Knepp, F. M. Mann, D. A. Myers, P. M. Rogers, R. J. Serne, and M. I. Wood, 2000, *Modeling Data Package for S-SX Field Investigation Report (FIR)*. RPP-6296, Rev. 0, CH2M Hill Hanford Group, Inc., Richland, Washington.

Nitao, J., 1998, *Reference Manual for the NUFT Flow and Transport Code, Version 2.0*, UCRL-MA-130651, Lawrence Livermore National Laboratory, Livermore, California.

Pruess, K., C. Oldenburg, and G. Moridis, 1999, *TOUGH2 User's Guide, Version 2.0*, LBNL-43134, Lawrence Berkeley National Laboratory, Berkeley, California.

Steefel, C. I., 2001, "CRUNCH: Software for Modeling Multicomponent-Multidimensional Reactive Transport. 1 ed. User's Manual," Lawrence Livermore National Laboratory (In press)

Ward, A. L. and G. W. Gee, 2000, *Vadose Zone Transport Field Study: Detailed Test Plan for Simulated Leak Tests*, PNNL-13263, Pacific Northwest National Laboratory, Richland, Washington.

White, M. D. and M. Oostrom, 2000a, *STOMP, Subsurface Transport Over Multiple Phases, Version 2.0, Theory Guide*, PNNL-12030, Pacific Northwest National Laboratory, Richland, Washington.

White, M. D. and M. Oostrom, 2000b, *STOMP, Subsurface Transport Over Multiple Phases, Version 2.0, User's Guide*, PNNL-12034, Pacific Northwest National Laboratory, Richland, Washington.

D.2.0 S-SX SITE MINERALOGY

James P. McKinley[1], John M. Zachara[1], Paul L. Gassman[1], Calvin C. Ainsworth[1], Bruce Arey[1], Susan McKinley[1], Todd Schaef[1], Steven C. Smith[1], Jean Kimberling[1], David L. Bish[2], Steve J. Chipera[2], and Peg Snow[2]

[1]Pacific Northwest National Laboratory, Richland, Washington 99352

[2]Los Alamos National Laboratory, Los Alamos, New Mexico 87545

D.2.1 INTRODUCTION

The sediment mineralogy beneath the SX tank farm directly impacted the mobility and fate of caustic wastes that leaked from compromised tanks. The impacted sediments were fine sand with potentially reactive mineral components (Bjornstad et al. 1987), including the micaceous minerals muscovite and biotite, laumontite, smectite and kaolinite clays, and a lithic component that was dominated by basalt clasts. The latter included abundant volcanic glass, which might preferentially react with alkaline wastes. The alkaline waste reacted with sediment surfaces, and the reacted waste had lower alkalinity and precipitated secondary minerals. These minerals may have incorporated radionuclides as impurities, and they may have provided reactive surface sites to bind contaminant ions. The binding of contaminant ions at the solid-solution interface of sediment minerals was an important factor in determining contaminant mobility in the vadose zone. The selective surface reaction of dissolved components with indigenous mineral phases, particularly micas, contributed to radionuclide immobilization and retardation.

The study of sediment mineralogy, as it was before and after reaction with tank waste, can provide valuable insights into the mechanisms of radionuclide retardation and the potential for long-term in-ground immobilization. These aspects of waste-sediment interaction were investigated by determining the mineralogy of unaltered sediment and contrasting it with the mineralogy of synthetically altered sediments and with sediments extracted from beneath the SX tank farm. All of the sediments were examined using X-ray diffraction (XRD) and scanning electron microscopy (SEM) to provide a systematic set of observations for determining the effects of tank waste on SX sediments.

The geology of the SX tank farm is extensively summarized elsewhere (Serne et al. 2001a, b) and the stratigraphic locations are given here for reference to those summaries. The samples from the SX-108 slant borehole comprised a set of sediments that transected a tank-waste plume. The numbered samples included in this study were targeted to capture the range of chemical affects of alkaline waste on sediments from several stratigraphic horizons. The uppermost sample, 1A, originated near the interface between tank farm backfill and the Hanford Upper Sand. The next lower sample, 3A, showed the most pronounced visible effects of tank waste alteration and was stratigraphically located within the Hanford Coarse Sand sequence. Samples 4 through 14 were within the Lower Hanford Laminated Sand, and the lowermost samples were within the Hanford Plio-Pleistocene interval. The texture and mineralogy of these samples are described below.

D.2.2 EXPERIMENTAL PROCEDURES

The mineralogic composition of contaminated and uncontaminated sediments from the S and SX tank farms and nearby environment was analyzed by various methods. Some results are presented in summary here and described in greater detail in the documents cited, including uncontaminated composite samples from different locations at Hanford (Serne et al. 2001b), uncontaminated samples from boreholes 299-W22-48 (Serne et al. 2001b) and 299-W22-50 (Serne et al. 2001b), and contaminated samples from borehole 41-09-39 (Serne et al. 2001a). Samples from boreholes SX-108 slant (contaminated) and B8812 (uncontaminated) were examined explicitly for this study.

Additionally, this study investigated the mineralogic products resulting from the contact of base (NaOH) with an S and SX tank farms composite sediment. These experiments were intended to elucidate the types of mineralogic changes that could result from the reaction (base hydrolysis) of REDOX wastes (which contained high levels of free hydroxide [OH^-]) with sub-tank sediments. The composite sediment representative of the upper Hanford formation was termed the "Above B" composite. This study material was created by compositing core samples from the depth range of 9-21 m bgs from RCRA boreholes 299-W23-14, 299-W23-15, 299-W22-46, 299-W22-39, and 299-W23-45. This same uncontaminated composite material was used in batch and column studies of Cs^+ retardation in Section D.3.0.

D.2.2.1 Textural Analysis

Sediment samples were epoxy imbedded, wafered, polished, and mounted to glass slides. Mosaic images of the polished sections were made using backscattered electron detection in SEM. The digitized images were analyzed using Prismview image analysis software. A composite Hanford Fine Sand sample (B8814) was sieved to determine size fractions by weight percent.

D.2.2.2 X-Ray Diffraction

XRD analyses were done at PNNL and at LANL. At LANL, the instrument was a Siemens D500 diffractometer, using Cu K_α radiation with a solid-state detector. Data were collected from 2 to 70° 2θ in 0.02° increments with a 4-second step. At PNNL, the instrument was a Scintag diffractometer, using Cu K_α radiation with a solid-state detector, with operating conditions identical to those at LANL. At both laboratories, bulk samples were prepared by crushing to a powder with analysis as random mounts, and clay fractions separated by sedimentation in water were analyzed as oriented mounts, air-dried and glycol solvated. An alumina standard was used at LANL in conjunction with full-pattern fitting methods to provide quantitative mineralogical analyses. For semiquantitative analysis, various mineral standards were used at PNNL (Serne et al. 2001b). At PNNL, all phases with a nonexpansible 100 nm peak were termed "illite," at LANL such phases were termed "mica."

D.2.2.3 Scanning Electron Microscopy

Samples from SX-108 slant borehole were surveyed to assess the effects of caustic waste on sediment minerals. Samples reacted with simulated waste (NaOH) in the laboratory were

examined to determine the hypothetical effects of waste fluids on sub-tank sediments. Samples for SEM were prepared by sprinkling sediment directly onto sticky tape on a 1-inch SEM stub. For contaminated sediments from SX-108 slant borehole, a glass cylinder was rolled over the dispersed sediment to firmly fix it to the tape. This step caused some disaggregation of agglomerated clasts and mica flakes. The sediment was sputter coated with carbon for conductivity; individual clasts nevertheless exhibited poor conductivity ('charging') in some cases. Samples were imaged at PNNL using a JEOL 840 SEM. Images were captured using a Gatan CCD device and elemental analysis was via an Oxford energy dispersive spectrometer (EDS).

D.2.2.4 Sediment-Base Reaction Studies

Laboratory studies were performed to investigate the mineralogic products of base-sediment reaction using the "Above B" composite sediment from the S and SX tank farms. The sediment was pretreated by sieving to remove the less than 56 μm fraction, treated with sodium acetate, and dialyzed to equilibration with sodium bicarbonate. For each treatment, 0.8 g of soil was added to a polypropylene Oakridge centrifuge tube. Also, 25 mL of 1M $NaNO_3$ was added to each tube and the tubes were gently shaken for 30 minutes. This yielded a suspension density of 25 g/L. After shaking, the tubes were centrifuged at 2500 x G for 10 minutes and the supernatant removed and discarded. This washing process was repeated three times. After washing the sediment, the tubes were refilled with $NaNO_3$ solution and concentrated (10 M) NaOH to yield final concentrations of 1 M $NaNO_3$, and 0.113 M, 1 M, 3 M, or 5 M NaOH and retain a suspension density of 25 g/L. The tubes were incubated at 50 °C for 14, 28, 56, or 112 days. All tubes were stored inside of sealed buckets that had a constant flow of nitrogen to preclude introduction of carbon dioxide from air. At the end of the incubation periods, sample tubes were centrifuged at 2500 × G for 10 minutes and the supernatant removed. Soils were filter washed with pH adjusted 0.01 M $NaNO_3$ (pH 7.5) to remove excess salt and then air-dried. Dried soils were analyzed by XRD and SEM.

D.2.3 RESULTS

D.2.3.1 Sediment Texture

The sediments had a broad distribution in grain size (Table D.2.3.1), but all were dominated by the fine fraction on the basis of grain-counting methodology (SEM image processing). At the scale of the sediment mosaics, the resolution of the analysis software was limited by the ratio of the pixel density to the smallest grain sizes: the resultant resolution limit was approximately 14 μm. The mean particle diameter was approximately uniform at ca. 37 μm, with the sediments predominated by fines having a particle diameter in the silt category (diameter less than 62 μm) or less. The samples had a large variation in grain size distributions. The standard deviations varied widely, and the grain diameter maximum ranged from 1031 μm to 334 μm. Samples 1, 3, and 5 included particularly large lithic clasts; Sample 7 was relatively uniformly fine-grained; the lower samples were coarser, and sample 17 included several large soil fragments. The dominant abundance of fines suggests that all sediment horizons should have significant reactivity with respect to alkaline tank wastes. While grain counting suggests that fines predominate, sieving and analysis according to mass shows (for a composite uncontaminated sample, Table D.2.3.1) that on a weight percent basis, the sediments are by far predominated by clasts larger than 100 μm.

Table D.2.3.1. Statistical Summary of the Grain Size Distribution for SX-108 Samples. A) Based on Digital Image Analysis of the Backscattered-Electron Mosaics. All Values in μm; Minimum Diameters are at or Near the Minimum Measurable at the Scale of the Photomosaics. (13 mm width). B) Based on sieving, to nearest weight percent.

A. SX-108 Samples				
Sample No.	Mean Diam.	Std. Dev.	Min. Diam.	Max. Diam.
SX-108 01	37.7	54.0	14.1	702
SX-108 03	41.1	71.8	14.1	1031
SX-108 05	39.4	54.2	15.5	997
SX-108 07	36.8	34.2	15.0	347
SX-108 08	37.0	47.7	13.7	768
SX-108 11	39.7	51.8	13.2	640
SX-108 13	37.4	39.1	15.0	637
SX-108 17	32.0	33.4	14.1	334

B. B8814 Hanford Fine Sand Composite					
Size Fract. μm	Wt. %	Size Fract. μm	Wt. %	Size Fract. μm	Wt. %
>850	2	180-40	43	5-1.5	2
850-425	11	40-18	1	<1.5	1
425-180	30	18-5	3		

D.2.4 X-RAY DIFFRACTION

D.2.4.1 Pristine Sediments

Table D.2.4.2 includes typical mineralogic results, with approximate weight percent abundances from the studies of Serne et al. (2001a, b) (Note that the tabulated values are to illustrate typical relative abundances for comparison only. More detailed tabulations can be found in the references). The bulk sediment mineralogy was dominated by abundant quartz, potassium feldspar, plagioclase feldspar, and less abundant calcite. Mica was not reported. The clay mineral fraction included quartz, smectite, illite (mica), chlorite, kaolinite, and subordinate calcite and potassium feldspar.

Table D.2.4.2. Typical SX Mineralogy, Weight Percent Values, From (Serne et al. 2001a, b). Totals were not Constrained to 100 Percent.

Bulk Mineralogy							
Well or Location	**Quartz**	**K-Spar**	**Plagioclase**	**Calcite**			
Site Composite	50	10	20				
299-W22-48	60	20	10	10			
299-W22-50	60	10	25				
41-09-39	50	5	50				
Clay Mineralogy							
Well or Location	**Quartz**	**K-Spar**	**Calcite**	**Smectite**	**Illite**	**Chlorite**	**Kaolinite**
Site Composite	5			30	40	20	5
299-W22-48	10			20	30	20	10
299-W22-50	5		10	30	15	10	10
41-09-39	10	10		5	30	20	10

The samples from borehole B8812 were examined with attention to detection of minor phases. The sediments were also size-fractionated. The Hanford Fine Sand contained laumontite ($CaAl_2Si_4O_{12}\cdot 4H_2O$), a zeolite, in fractions finer than 150 μm (Figure D.2.4.1). Analysis with attention to the overall mineralogy of phases detected at low X-ray incidence angles (e.g., zeolites and clay minerals) showed the presence of smectite, mica, laumontite, amphibole, and chlorite with variable abundance in different fractions. Other minerals occurring significantly were quartz, potassium feldspar, plagioclase feldspar, hematite, magnetite, and calcite. The abundances of these phases in bulk sediments and as a function of grain size in the sample collected at 64 ft deep are presented in Tables D.2.4.3 and D.2.4.4 respectively. Mica (biotite) increased in abundance as the mean grain size decreased; this increase may be significant for the retention of ^{137}Cs in these fractions. The XRD results from PNNL and LANL

differed with respect to the minor phases detected; bulk major minerals in all the sediments included smectite, chlorite, quartz, potassium feldspar, plagioclase feldspar, mica (whether termed illite or mica or biotite) and calcite. Kaolinite was observed in the samples examined at PNNL but not in those examined at LANL. The effort to observe minor minerals at LANL yielded identification of hematite, magnetite, amphibole, and laumontite, all at abundances of about 1 wt% or less.

Figure D.2.4.1. Comparison of Diffraction Patterns of Size Fractions of the 63.5 to 64 ft. Sample. Green Markers Show the Positions of Laumontite Reflections.

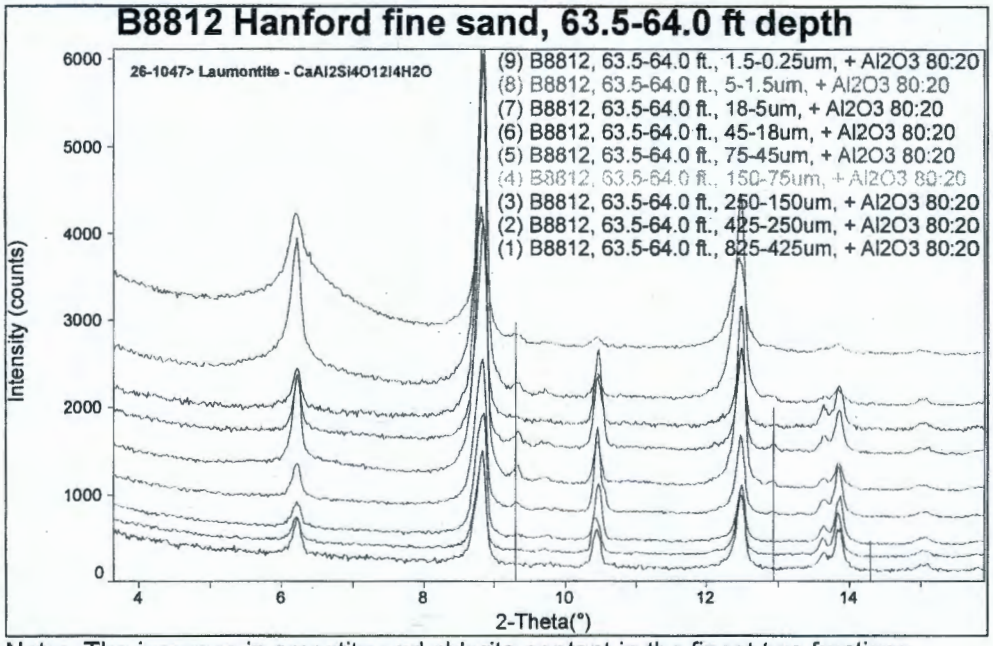

Note: The increase in smectite and chlorite content in the finest two fractions.

Table D.2.4.3. Quantitative X-ray Powder Diffraction Analyses for Bulk Samples (wt%).

Sample	Smectite	Laumontite	Chlorite	Quartz	K-Spar	Plagioclase	Hematite	Biotite	Magnetite	Amphibole	Calcite	Total
B8812 63.5-64.0'Bulk	8.5	0.2	1.2	28.4	10.2	33.8	0.2	13.2	0.4	1.2	1.1	98.3
B8812 64.0-64.5' Bulk	6.9	0.3	1.3	38.4	9.6	31.7	0.1	7.9	0.3	2.9	1.1	100.4
B8812 76.0-76.5' Bulk	8.8	0.3	1.2	38.7	8.2	32.3	0.2	6.3	0.2	3.3	0.8	100.3
B8812 76.5-77.0' Bulk	8.6	0.4	1.0	26.7	9.4	36.2	0.3	11.1	0.2	2.5	0.8	97.1
B8814 Bulk Hanford Sand	10.6	0.4	1.0	42.9	7.4	30.6	0.2	4.5	0.1	2.0	0.7	100.4

Table D.2.4.4. Quantitative X-ray Powder Diffraction Analyses for Size Fractions of the B8812 63.5-64.0' Sample (wt%).

Sample	Smectite	Laumontite	Chlorite	Quartz	K-Spar	Plagioclase	Hematite	Biotite	Magnetite	Amphibole	Calcite	Total
B8812 63.5-64.0' Bulk	8.5	0.2	1.2	28.4	10.2	33.8	0.2	13.2	0.4	1.2	1.1	98.3
825-425μm	5.2	---	1.2	46.2	9.4	31.5	0.1	5.2	0.2	1.4	0.7	101.2
425-250μm	4.3	---	1.0	45.2	8.4	32.6	0.1	6.2	0.5	1.4	0.7	100.5
250-150μm	5.8	0.3	0.9	40.2	8.9	32.4	0.2	5.8	0.9	1.8	1.1	98.3
150-75μm	7.5	0.5	1.3	37.4	8.0	37.0	0.2	5.9	0.7	2.1	0.9	101.6
75-45μm	7.5	0.6	1.1	34.5	9.4	34.4	0.1	8.2	0.1	2.4	1.1	99.4
45-18μm	9.4	1.1	1.7	33.4	9.2	34.3	0.1	5.4	0.5	2.8	2.5	100.4
18-5μm	14.7	0.8	3.2	25.2	9.2	30.3	0.1	11.3	0.3	1.4	2.9	99.4
5-1.5μm	24.9	0.9	5.2	18.5	9.9	26.1	0.2	10.4	0.1	0.9	3.0	101.1
1.5-0.25μm	52.7	0.6	3.2	7.1	7.9	17.5	0.1	10.1	0.0	0.5	2.6	102.1

D.2.4.2 Base-Reacted Sediments

Diffraction patterns for 5 M base-reacted sediments indicated that there was no zeolite in these samples. The diffraction patterns suggested the presence of a zeolite phase (Figure D.2.4.2), either tetranatrolite ($NaAl_2Si_3O_{10}\cdot 2H_2O$) or an unnamed phase ($Na_{14}Al_{12}Si_{13}O_{51}\cdot 6H_2O$). Close examination of the figure revealed an imperfect match between the zeolite library diffraction files and the reacted sediment, a possible result of chemical/structural differences between the precipitated phase and the library phases. Alternatively, the observed diffraction peaks may have come from feldspars in the bulk sediment. XRD results for the bulk reacted sediment were similar to those for the bulk pristine sediment, with coarse-grain mineralogy consisting of quartz, potassium feldspar, and plagioclase feldspar (the sediments had been sieved to remove fines less than 75 μm in diameter.)

Figure D.2.4.2. Diffraction Patterns for Bulk Post-Reaction Samples from Sediment-Base Reaction Experiments. Result Suggest that a Na-Zeolite is Present.

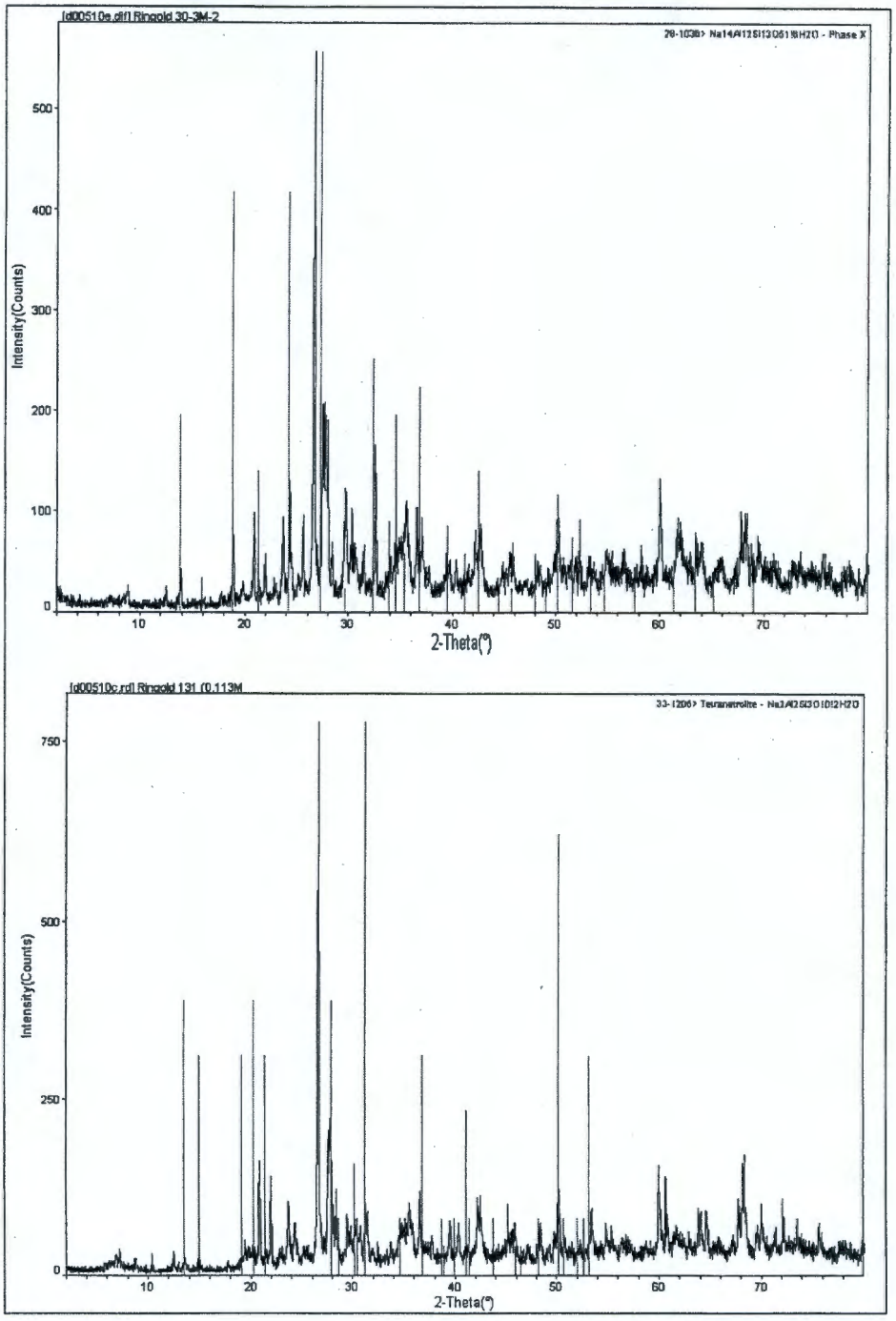

D.2.4.3 Tank SX-108 Samples

Three samples from tank SX-108 were intensively studied to identify possible effects of waste interaction on sediment mineralogy. Figure D.2.4.3 compares a pristine sample from borehole BB8812 with SX-108 samples 3A, 6A, and 7A. The same major minerals were present in the pristine and contaminated sediments, as was laumontite. Chabazite, a calcium-bearing zeolite, may have been present in sample 7A only. Also present in 7A, and perhaps in 6A was the secondary mineral nitratine, $NaNO_3$, a likely precipitate from tank wastes. Mica, chlorite, amphibole, and smectite were definitively identified in the clay fraction (Figure D.2.4.4), and kaolinite may have been present. All of these phases were also observed in the pristine samples. A comparison of SX-108 sediments with a pristine sample (Figure D.2.4.5), with overlain peak markers for tetranatrolite and the unnamed hydrated sodium aluminum silicate, indicated that these zeolitic phases were not present. Potential library-sample matches for them could be explained by other common phases such as feldspars.

Figure D.2.4.3. XRD of Three Contaminated Samples and One Pristine Sample (offset for clarity).

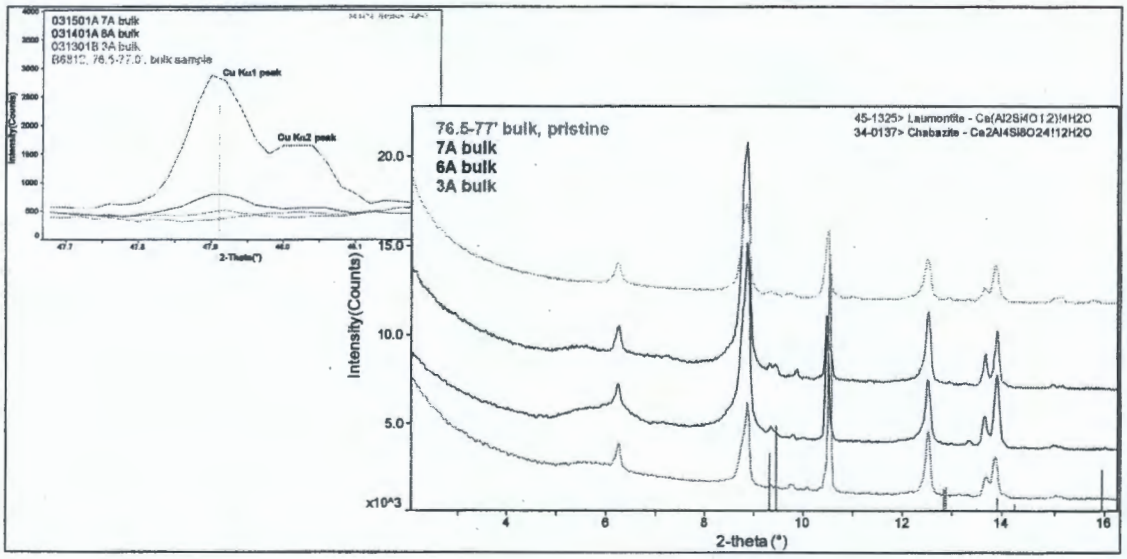

Note: The presence of a small amount of laumontite in all samples, plus the possible presence of chabazite in Sample 7A. Chabazite has not been identified in any pristine sample. Inset shows the presence in 7A of nitratine, $NaNO_3$.

Figure D.2.4.4. Diffraction Patterns of the Clay Fraction of Samples 3A, 6A, and 7A, after Solvation with Ethylene Glycol.

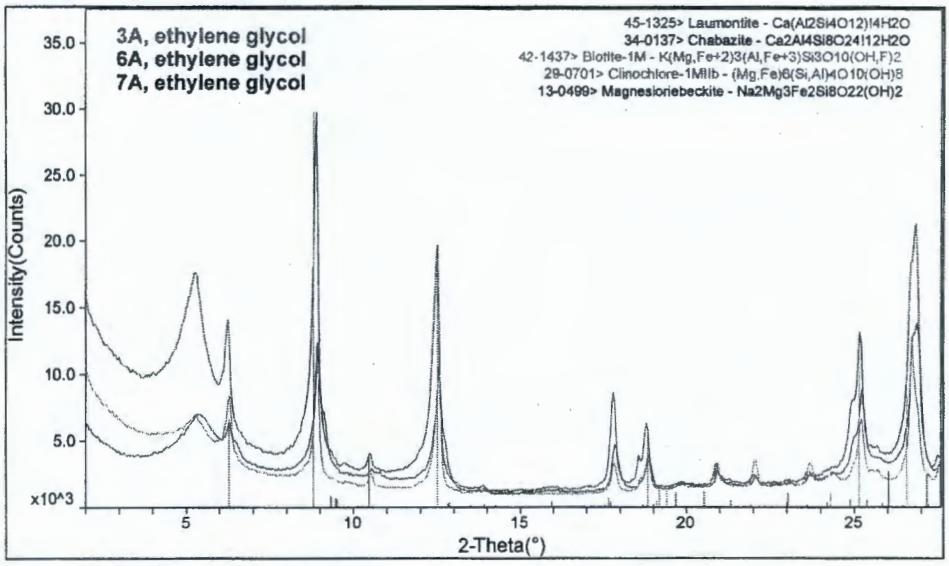

Note: The presence of mica (denoted by biotite), chlorite, an amphibole (denoted by magnesioriebeckite), and smectite, shown by the broad peaks centered around 5.5° 2θ. The peak just above 25° 2θ has a low-angle shoulder, suggesting the presence of kaolinite in these samples. Although present in the bulk samples of 3A, 6A, and 7A, laumontite (and chabazite in 7A) is not apparent in the clay fraction of these samples.

Figure D.2.4.5. A Portion of the XRD Patterns for Altered Samples 3A, 6A, and 7A, with that for the Pristine Sample from 76.5 to 77' Depth. The Latter Pattern has been Displaced Vertically for Clarity. Peak Markers for Tetranatrolite (red) and for Hydrated Na-Al Silicate (green) are Superimposed at the Bottom.

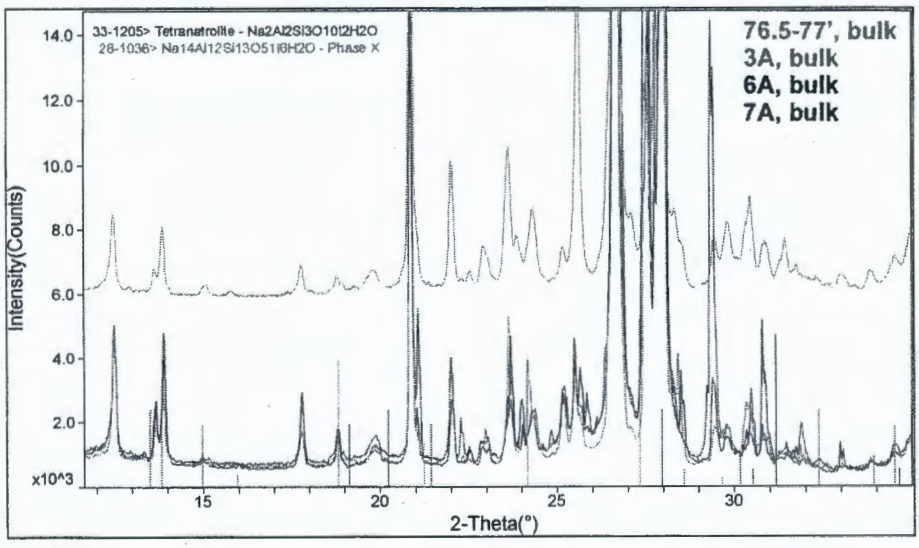

Note: That where potential matches to these phases exist, they exist in both pristine and altered samples and are due to other common phases such as feldspars.

D.2.5 SCANNING ELECTRON MICROSCOPY

D.2.5.1 Pristine Sediments

SEM inspection of uncontaminated sediments from borehole B8812 allowed the identification of minerals whose abundance was too low for detection by bulk XRD. These minerals were observed in very small quantities. In addition to minerals identified by XRD, barite, Fe-oxides, rutile, pyroxene, apatite, zircon, and rare-earth-element minerals were identified. Fe-oxides were observed on the surfaces of some micas.

D.2.5.2 Laboratory Base Reacted Sediments

Sediments reacted with base in the laboratory ("Above B" composite) were considered to be representative of subsurface sediments and the possible types of mineral surface reactions and secondary mineralization products that might be observed in waste-impacted sediments. Three sets of images are presented as illustrations of the mineral transformations observed in the laboratory.

Micas were drastically altered by NaOH (Figure D.2.5.6). The surfaces and edges of the mica were encrusted with secondary minerals, and the edges were dulled by dissolution and weathering. Distinctive clusters of zeolitic minerals were precipitated (Figure D.2.5.7). These took the form of starred clusters and balls, but also included cemented aggregates of plates and blades. Zeolites also formed distinctive colonies and clusters on mineral surfaces (Figure D.2.5.8). The secondary phases formed radiating clusters, cluster aggregates, and singular balls on mica surfaces. These phases were apparently not detected by XRD (see discussion above), indicating that they did not compose a significant mass fraction of the sediment.

Figure D.2.5.6. Micas Altered During Base Interaction Experiments.

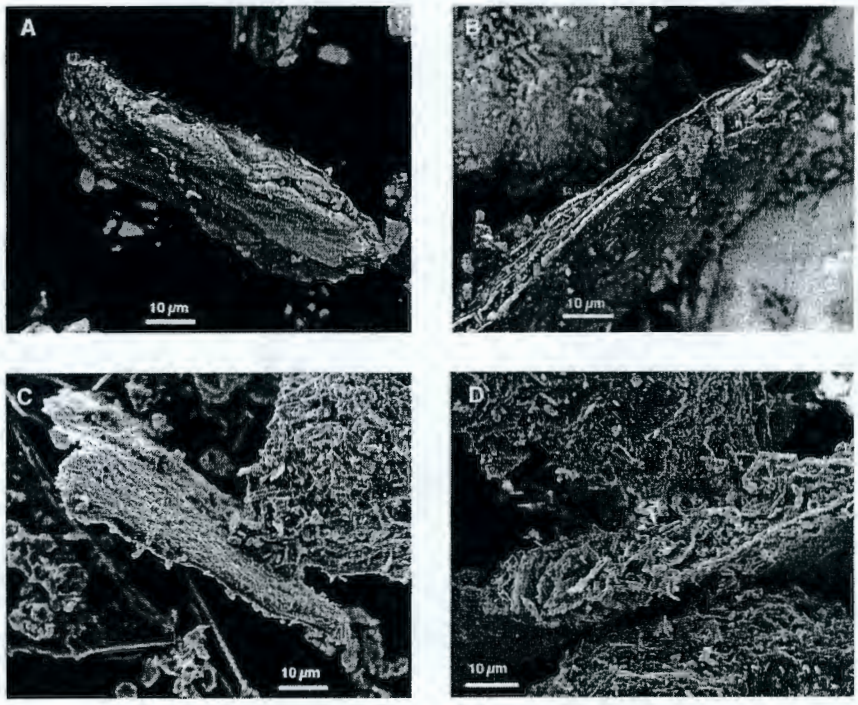

Figure D.2.5.7. Zeolite Crystals Formed During Base Interaction Experiments.

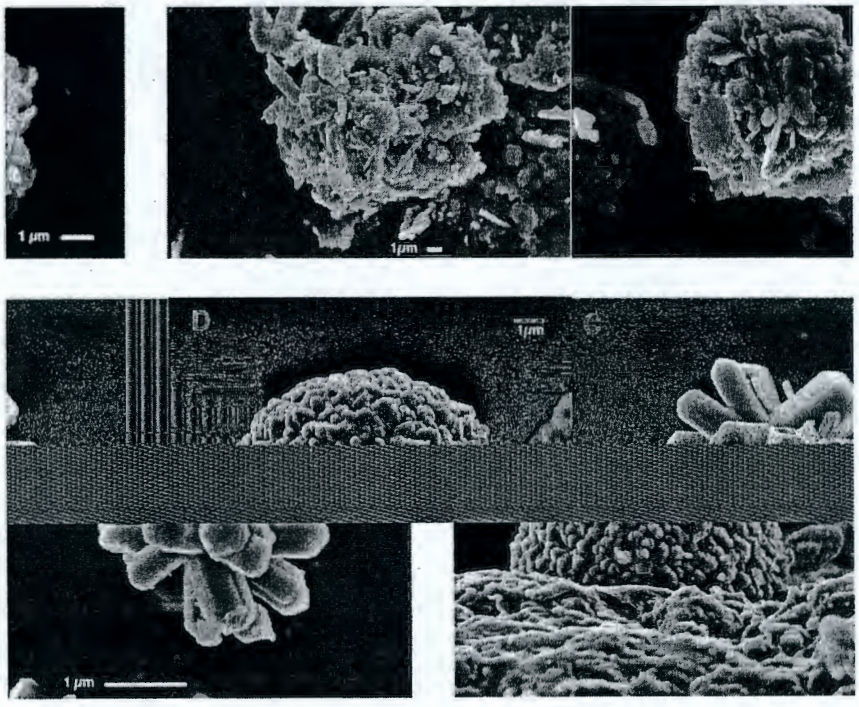

Figure D.2.5.8. Zeolites Precipitated on Mineral Surfaces During Base Interaction Experiments.

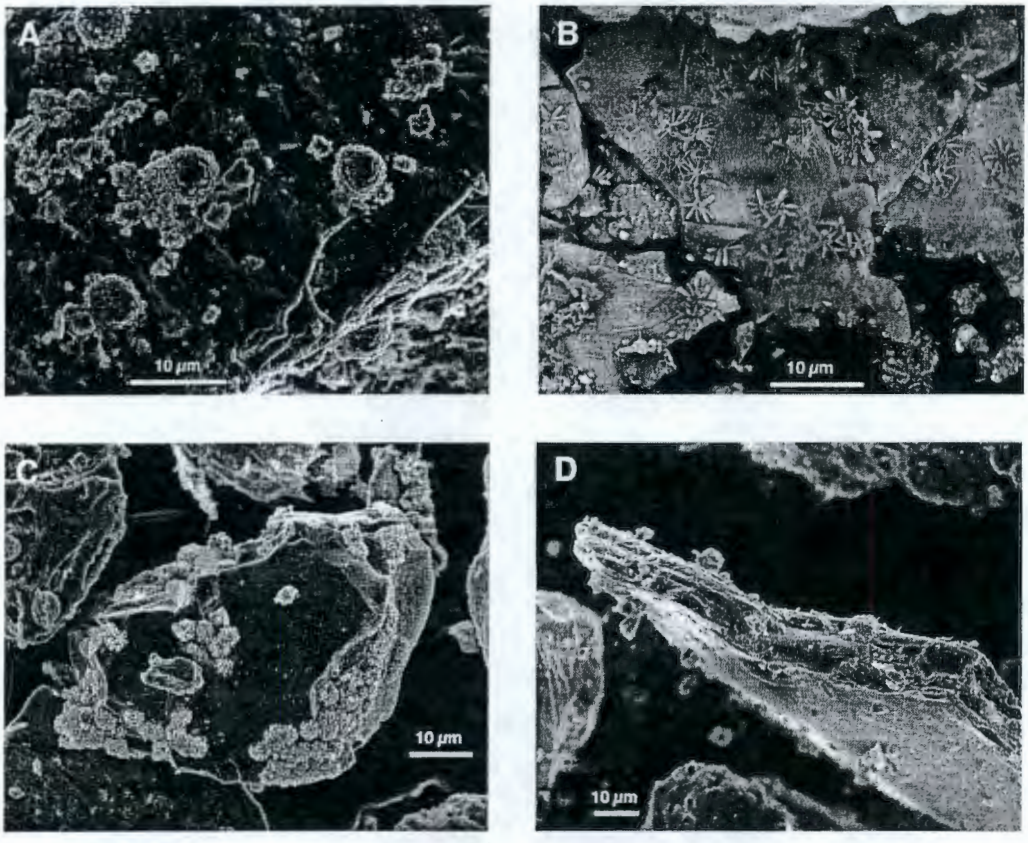

D.2.5.3 SX-108 Samples

Samples 1A, 3A, 5A, 7A, 8A, 11A, 13A, and 17A from the SX-108 slant borehole were examined (all with S0070 prefixes). The first four of these samples included high activities of ^{137}Cs. The highest activity was observed in sample 7A (2.14×10^7 pCi g^{-1}). Sample 3A also contained high levels of ^{137}Cs (1.95×10^7 pCi g^{-1}) and was chalky in appearance, suggesting mineral alteration.

Three attributes that were clearly evident by electron microscopy were used to assess the chemical impact of tank leakage on sediments: the development of secondary mineralization on sediment clasts, the occurrence of clay-cemented agglomerates of clasts, and the alteration of mica. The latter was a sensitive indicator of chemical alteration. In pristine samples (e.g., 13A) the micas were clear of surface-precipitated secondary minerals, and the edges of individual lamina were sharp and clean. In altered micas, flake surfaces were covered with fine aluminosilicate precipitates, and edges were blunt and obscured by secondary mineralization. The formation of cemented agglomerates was also indicative of alteration but was not diagnostic. In the notably altered sample 3A, agglomerations of silicate clasts were abundant. Agglomerates were also present but were sparse in deeper, apparently unaltered sediments; their abundance was the important discriminator in sample 3A. The abundance of secondary mineralization was also apparently higher in waste-impacted sediments. In these sediments, silicate clasts such as quartz and feldspar were abundantly coated with secondary aluminosilicates. The compositions of

these secondary minerals were consistent with those of quartz and smectite. Smectite (an aluminosilicate clay mineral with minor Fe, Mg, Ca, and Na) was the apparent cement for agglomerates, which always contained a significant mica component. Other secondary phases had compositions that included silicon oxide, iron oxide, calcium phosphate, and aluminum silicate; these were presumably quartz, iron oxide, apatite, and kaolinite, all observed in XRD studies. Secondary minerals occurred in close heterogeneous association of very fine individual grains.

The occurrence of smectite as a product of interaction with alkaline wastes was not apparent in XRD studies. The poor crystallinity of this mineral and the preexisting smectite in unreacted sediments could have prevented its detection by the relatively insensitive XRD method. The synthesis of smectite by exposure to alkaline wastes is consistent with the experimental synthesis of smectites from mineral and oxide components in alkaline conditions (Deer et al. 1976b). Zeolite is common in altered volcanic rocks and volcanic sediments, and these minerals were expected in waste-impacted sediments, but only very rare occurrences of minerals that could be zeolites were observed in these samples.

Figures D.2.5.9 through D.2.5.19 illustrate mineral alteration, top-to-bottom through the borehole. The photomicrographs present examples of the alteration indicators described above. The uppermost four samples, 1A, 3A, 5A, and 7A show unmistakable indications of interaction between tank waste and sediments.

Figure D.2.5.9. Sample 1A. 4A. Feldspar with Secondary Minerals on Surface. A. Smectite, B. Silica. 4B. Agglomerated Clasts Cemented by Secondary Clay. Bladed Mica is Abundant, with Subordinate Silicates.

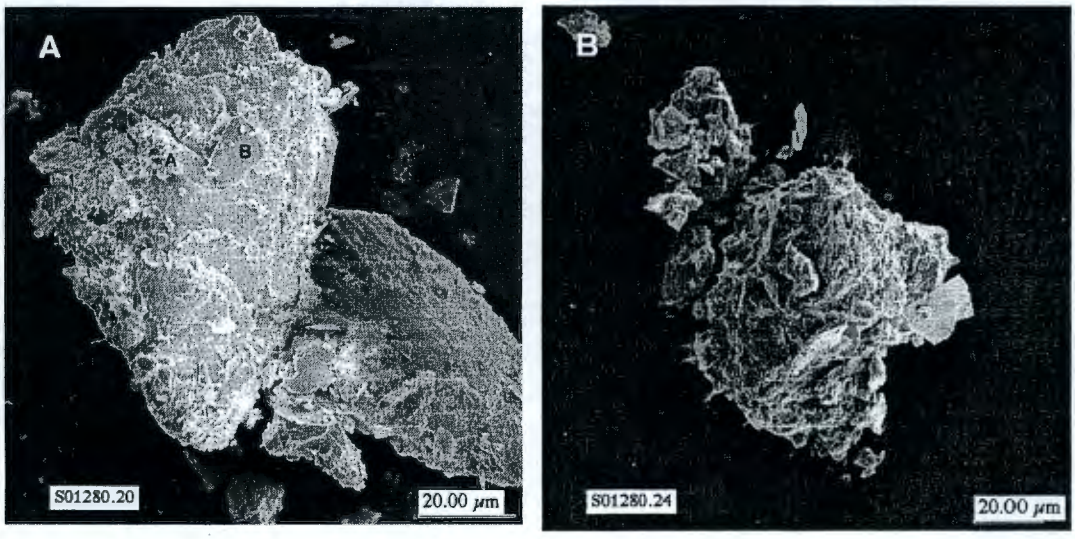

Figure D.2.5.10. Sample 1A. Mica Edge, and Detail (right) Showing Absence of Alteration.

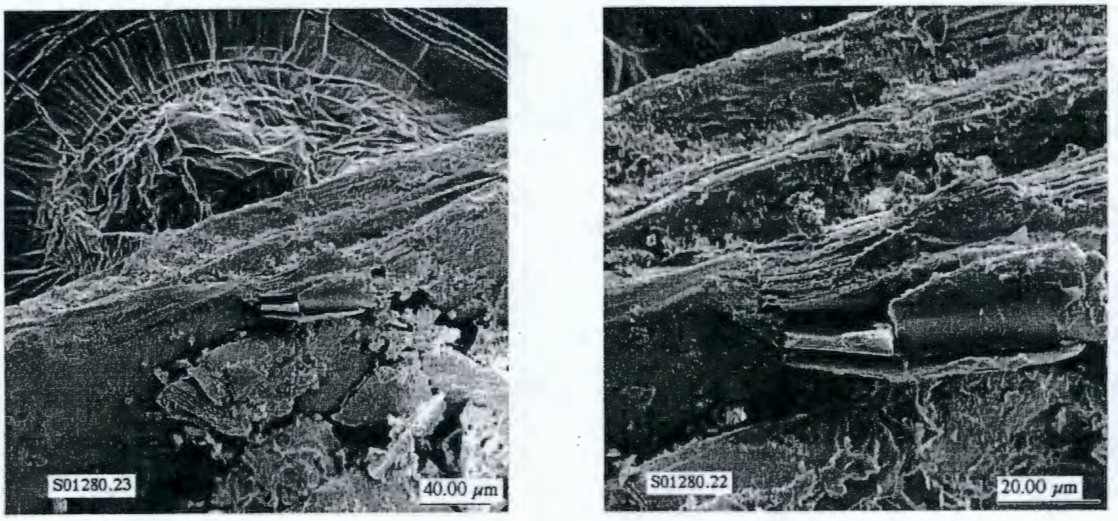

Figure D.2.5.11. Sample 3A. 6A. Agglomerated Clasts Disaggregated During Mounting. A: Plagioclase Feldspar; B: Smectite; C: Mica; D: Potassium Feldspar. 6B. Clay-Cemented and Coated Clasts. Larger Clast (A) is Coated with Smectite; Agglomerated Clast Includes Quartz (B) and Mica (C).

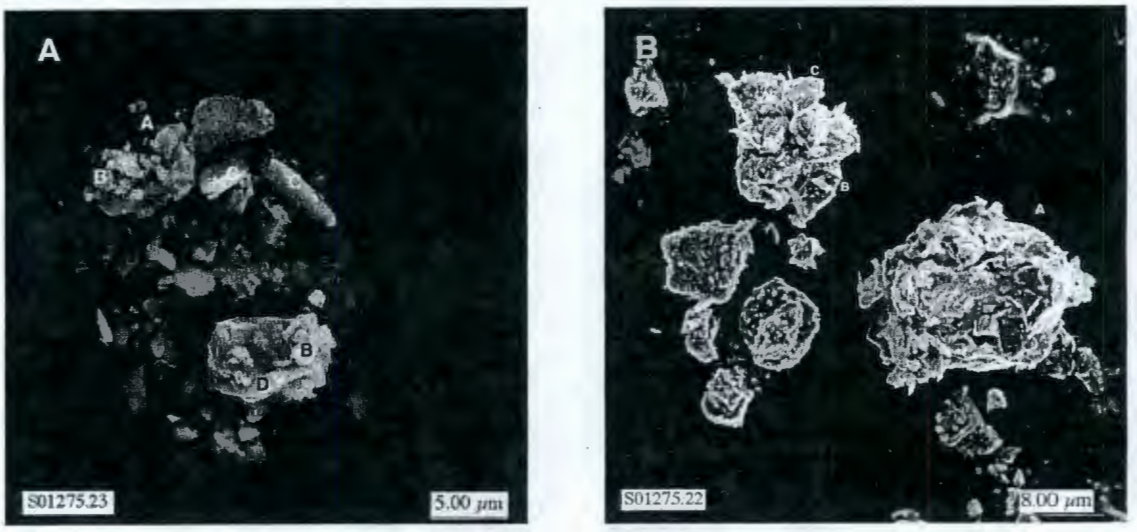

Figure D.2.5.12. Sample 3A. 7A. Very Altered Mica. Lamella are Curled and Altered (A), Surface is Weathered and Coated with Secondary Smectite. 7B. Altered Mica Edge. Delaminated Flake Revealed the Contrast Between the Unaltered and the Extensively Altered Edges and Surface. The Surface is Coated with a Masking Layer of Secondary Smectite (A). The Edges of Mica Flakes are Splayed and Blunted by Chemical Alteration and Deposition of Secondary Phases.

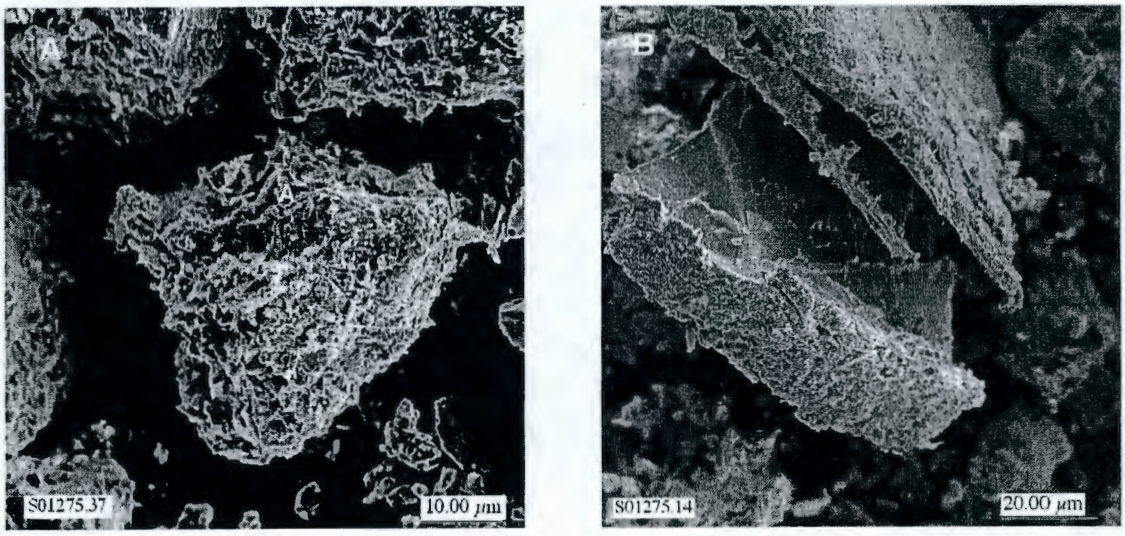

Figure D.2.5.13. Sample 5A. Detail of Unaltered Mica Edge.

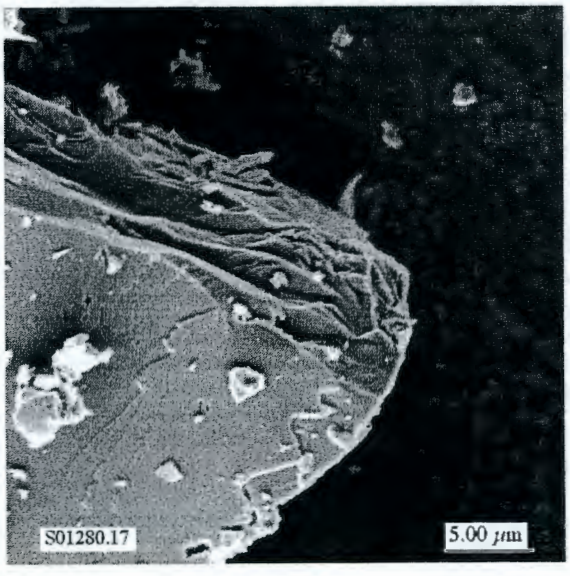

Figure D.2.5.14. Sample 7A. Cemented Agglomerate of Smectite and Mica, with an Associated Grain of and Sodium-Aluminum-Silicate (EDS spectrum) that may be Zeolite.

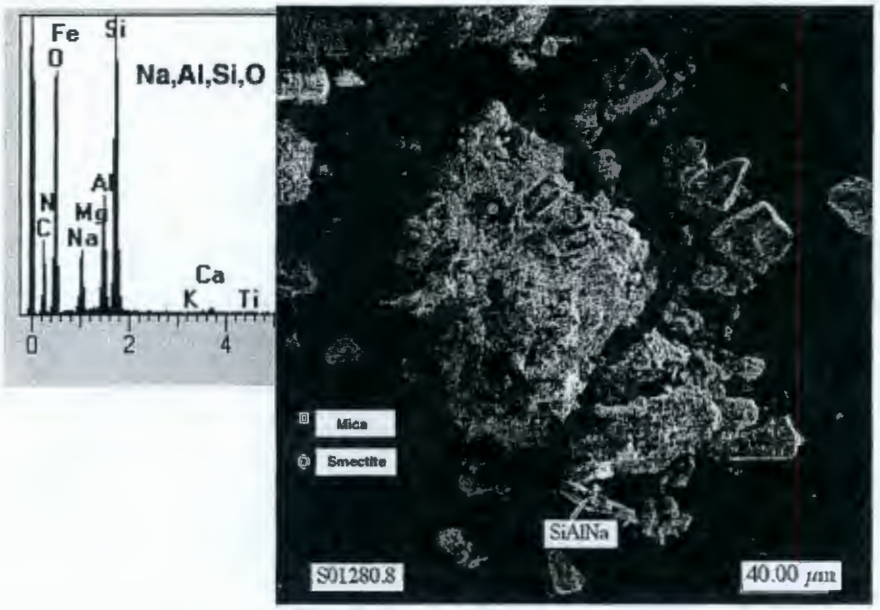

Figure D.2.5.15. Sample 7A. 10A. Altered Mica. Secondary Mineralization on the Surface is not Extensive, but Edge Alteration is Evident. 10B. Unaltered Mica with Few Associated Surface Smectite Grains. Edges are Sharp and Unaltered. This Morphology Predominates.

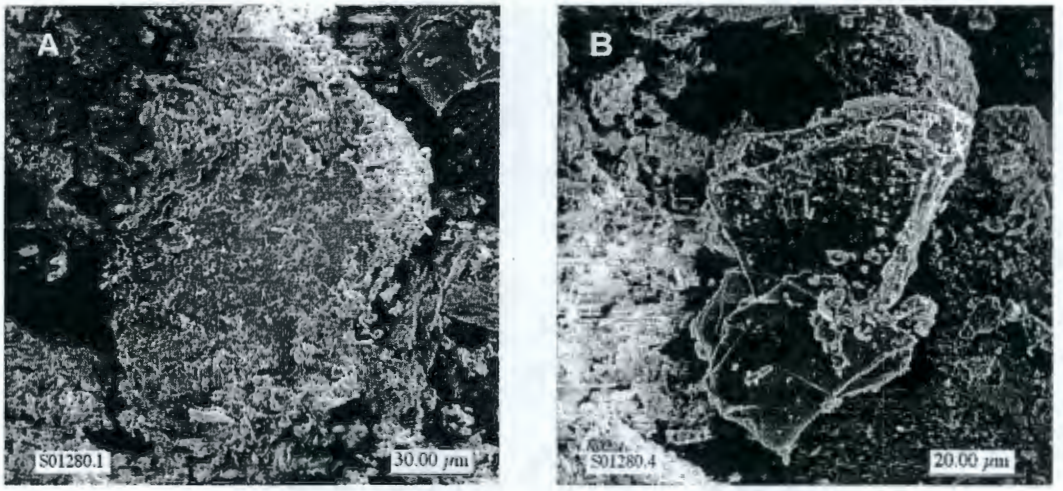

Figure D.2.5.16. Sample 8A. 11A. Detail of Unaltered Mica, Showing Deformed, Sharp, Unaltered Edges. Some Smectite Adheres to the Surface. 11B. Unaltered Mica, some Smectite Adheres to Surface, Edges are Unaltered.

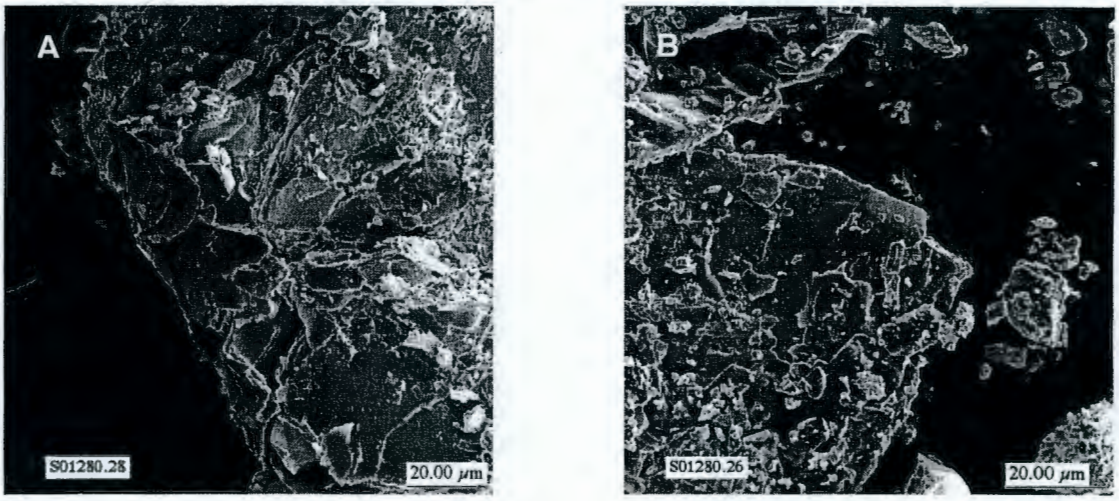

Figure D.2.5.17. 12A, Sample 11A. Unaltered Mica. 12B, Sample 13A. Unaltered Mica.

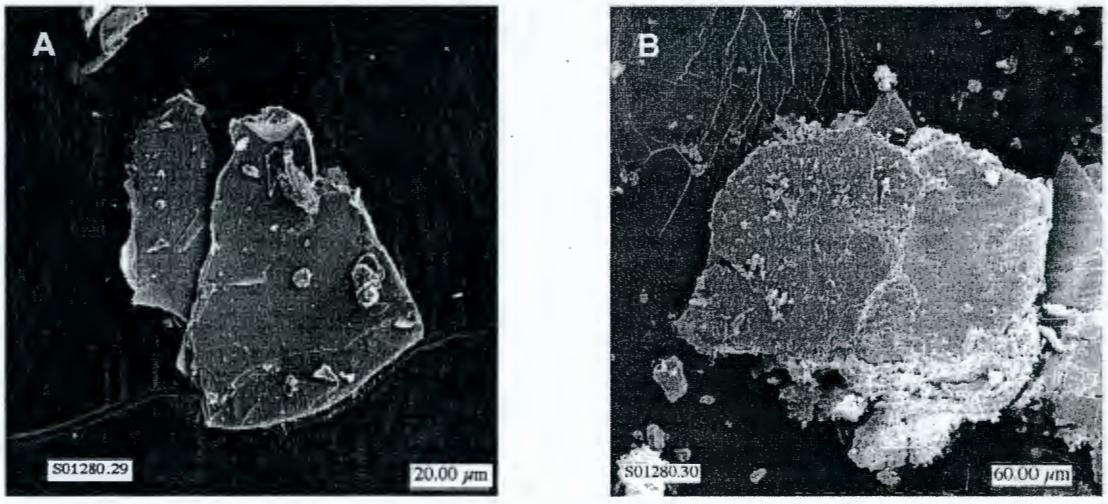

Figure D.2.5.18. Sample 17A. 13A. Several Clasts, A: Potassium Feldspar, B: Unaltered Mica, C: Smectite Cemented Agglomerate Including Mica. 13B. Unaltered Mica. Edges are Bent but Sharp and Unaltered, and there is no Surface Precipitated Secondary Mineralization. Compare to the Mica in Figure D.2.5.12.

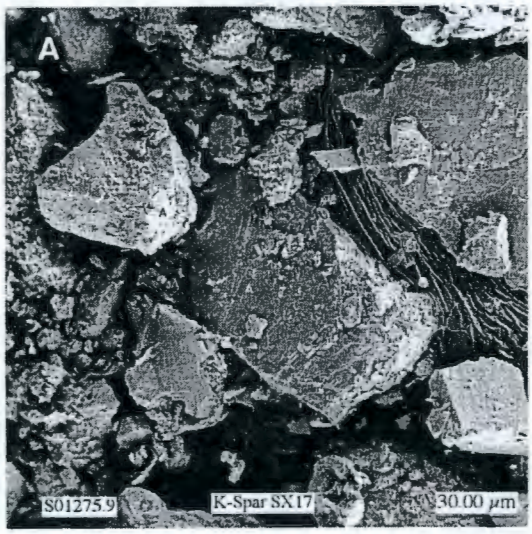

Figure D.2.5.19. Comparison Between SX-108 Sample 03, Quartz Grain with Surface Zeolite Grains, and Zeolite Clusters on a Quartz Grain after a Sediment-Base Interaction Experiment. Natural Samples have much Sparser Occurrence of Zeolite.

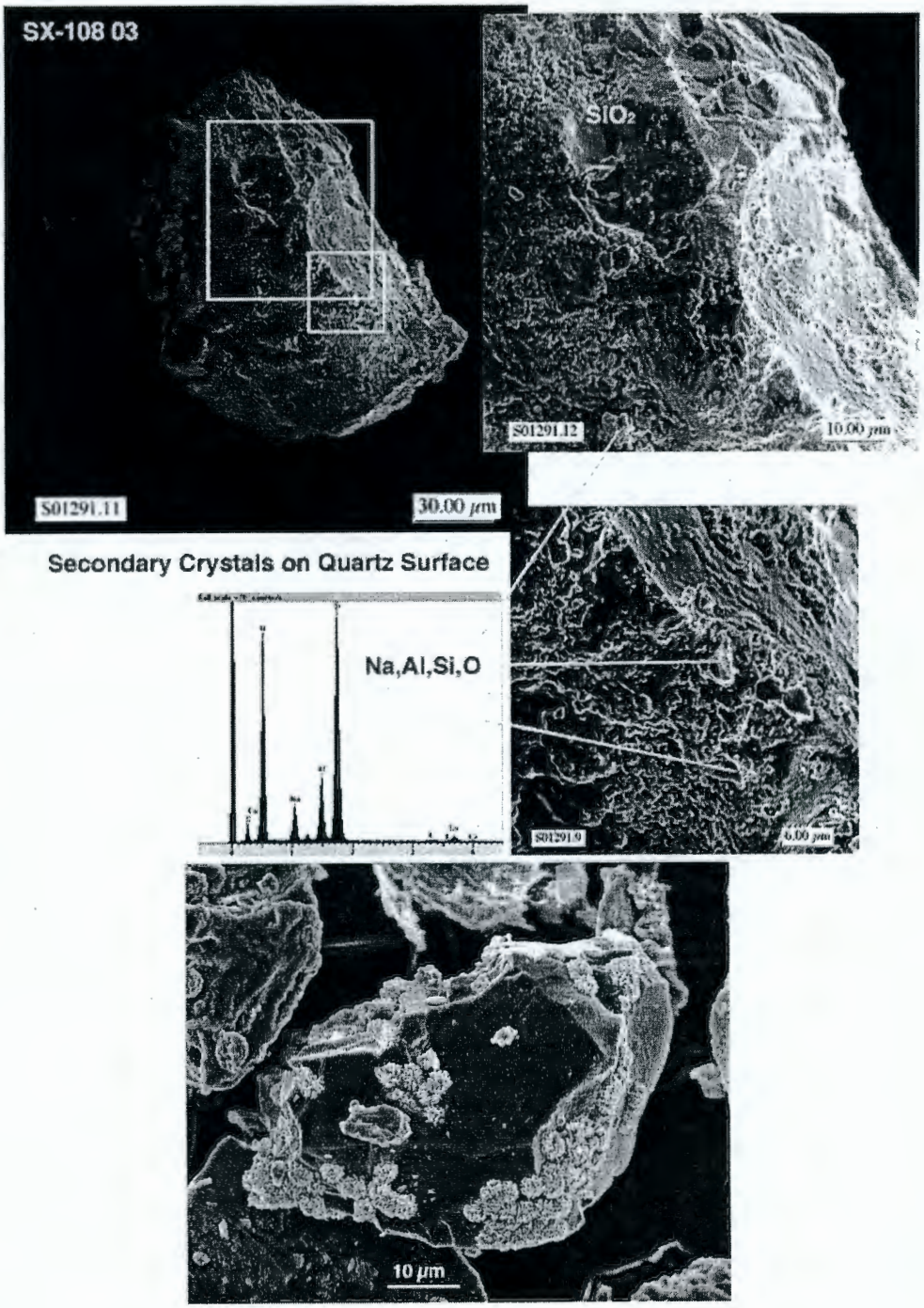

Sample 1A (Figures D.2.5.9 and D.2.5.10) showed moderate effects of interaction, with some secondary minerals on silicate surfaces and some agglomeration. Micas, however, were unaltered.

Sample 3A (Figures D.2.5.11 and D.2.5.12) showed the most pronounced effects of tank waste reaction; the texture of this sample resembled crumbled concrete. Primary silicates were abundantly coated with silica and what appeared to be smectite, producing elemental lines on energy-dispersive X-ray spectra of varying intensities for Si, Al, Na, and Ca, with or without minor inclusion of Fe and Mg. These heterogeneous accumulations of minerals on clast surfaces may include detrital and secondary smectites or poorly crystalline aluminosilicates, with the secondary minerals incorporating differing proportions of their component oxides. These minerals were carefully examined for crystal morphology and chemistry comparable to the zeolites observed in the laboratory experiments with waste simulants (e.g., Figures D.2.5.7 and D.2.5.8 and Figure D.2.5.6, especially cruciate morphology of Na-Al-Si-O composition.) Unambiguous zeolite crystals were not observed. The similarity of components between smectite and Na-zeolite may have hindered the identification of a Na-zeolite if its morphology were not well developed. The morphology of some of the agglomerated crystallites in Figure D.2.5.8A were similar to those observed in the sediments reacted in the laboratory with waste simulants. However, the sediments reacted in the laboratory were sieved to remove the less than 56 μm size fraction. The formation of zeolite may have been masked in the SX-108 samples by the inclusion within or overprecipitation by more abundant aluminosilicate. If a Na-zeolite were present, its abundance was very low, much less than 1 wt%, because Na-rich secondary mineral fragments were very rare and of micron-scale. Agglomerates were common, and varied in the fractional inclusion of smectite cement; some agglomerates were readily disaggregated into discrete constituent clasts, some were more indurated. The presence of abundant secondary aluminosilicate and the abundant smectite-cemented agglomerates may be responsible for the chalky texture of this sediment.

Micas in sample 3A were pervasively altered. The platelets were curled and crenellated (Figure D.2.5.12A), and flake surfaces were generously plated with secondary minerals (Figure D.2.5.12B). Some mica flakes were so altered that they could be mineralogically identified only with the aid of compositional data. Comparison of the altered micas from 3A with the experimentally altered micas (presented above) shows a close similarity. As with smectite, the alteration of micas did not produce a change in XRD results to reflect lower mica abundance (see above). Although mica surfaces were altered, the flake interiors were not (Figure D.2.5.12), so that XRD intensities were not noticeably changed.

Sample 5A was relatively unaltered. Clast surfaces had little secondary mineral deposition. Agglomerates were rare. Micas were unaltered (Figure D.2.5.13). This sample with ^{137}Cs of 6.52×10^{6} pCi g^{-1}, was between 3A, extensively altered and ^{137}Cs activity of 1.95×10^{7} pCi g^{-1}, and 7A, with moderate alteration and the highest ^{137}Cs activity (2.14×10^{7} pCi g^{-1}). This relatively unaltered interval with lesser activity was probably a result of borehole and waste-migration geometry. The borehole was essentially a one-dimensional transect of a three-dimensional waste plume. The plume was not necessarily compact and monolithic in shape, and the borehole seems to have intersected a portion of the subsurface that was less impacted by leaking waste.

Sample 7A (Figures D.2.5.14 and D.2.5.15) was moderately affected by interaction with tank wastes. There was limited secondary mineralization on clast surfaces, agglomerates were few, and micas were unaltered. This interval within the SX-108 slant borehole had the highest ^{137}Cs activity, but was much less altered than sample 3A.

Samples 3A and 7A, on close examination in conjunction with autoradiography results (see Section D.3.5 "Mineralogic Residence of ^{137}Cs in Contaminated Sediments"), showed evidence for the precipitation of zeolites on mineral surfaces. In comparison, however (Figure D.2.5.19), the secondary zeolite-like phases on natural samples are far fewer and less developed than zeolites on experimentally reacted solids.

Samples 8A, 11A, 13A, and 17A (Figures D.2.5.16 through D.2.5.18) were unaltered, and had activity one or more orders of magnitude lower than 1A, 3A, 5A, and 7A. Agglomerates occurred sparsely. Micas in these intervals had little surface-adhering minerals, and the mica edges were sharp and unaltered. The contrast with 3A is evident in comparing Figure D.2.5.18 with Figure D.2.5.12. The 3A mica had bent lamina with blunted edges and a dense surface coating of secondary phases; the 17A mica also had bent lamina, but the edges were sharp and no secondary phases were present.

The micaceous minerals in sample 3A were pervasively altered but sample 3A still retained significant ^{137}Cs, presumably in the relatively unaltered portions of micas. While this sample suffered the most alteration of any examined, a lower sample, 7A, retained the highest mass-normalized level of ^{137}Cs activity. Sample 7A, however was only moderately impacted by caustic waste. These results indicated strong and rapid retardation of OH^- by mineral reaction. If base neutralization by mineral reaction was responsible for the differences in the extent of mineral alteration and secondary mineralization, the reaction was not reflected in the pH of 1:1 suspensions with water. The four upper samples (1A, 3A, 5A, and 7A) retaining significant ^{137}Cs all had suspension pH above 9 (9.16, 9.58, 9.78, and 9.55, respectively; data from Serne, elsewhere in this document). Samples below 7A had slurry pH of approximately 8 by comparison.

D.2.6 CONCLUSIONS AND IMPLICATIONS

Minor mineralogic differences were observed between sediments of differing stratigraphic origin or history of exposure to authentic or simulated tank waste. The differences were primarily in the variability of the relative masses of minerals rather than changes in mineralogic identity. Minor differences were also noted between mineralogic analyses performed at PNNL and LANL. The X-ray diffraction analysis provided a common set of mineral phases in the pristine sediments, base-reacted sediments, and SX-108 core samples. Other than nitratine, $NaNO_3$, apparently precipitated from tank wastes in sample 7A, there was no definitive determination using X-ray diffraction of the addition of a secondary mineral phase to the SX-108 sediments after reaction with tank wastes.

The mineralogy determined by XRD was consistent, regardless of the exposure to alkaline solutions. Within the precision of measurement, the following minerals were present (abundances in weight percent): quartz, 35; potassium feldspar, 10; plagioclase feldspar, 35; mica (biotite or muscovite), 10; smectite, 10. The separation and analysis of clay or silt-sized particles added the detection of minor (generally less than 1 wt% in the bulk) laumontite, kaolinite, amphibole, magnetite, hematite, chlorite, and calcite. Because they are highly crystalline and occur with low surface-to-volume ratios, quartz and the feldspars would not be expected to react extensively with transient alkaline waste. The low reactivity of these phases was supported by SEM results. Smectite is poorly crystalline and theoretically unstable, eventually reacting to form kaolinite (depending on solution composition). However, in the presence of reacting minerals supplying abundant dissolved ions, alkaline conditions favored the formation of smectite and zeolites. The appearance of mica surfaces suggested that micas reacted preferentially, and that a secondary aluminosilicate (perhaps smectite) formed mica surfaces.

The experimental reaction of representative sediments with high concentration of NaOH apparently resulted in the formation of a secondary Na zeolite as suggested by SEM analyses. Zeolite formation is favored in alkaline environments because high pH favors the increased solubility of silica in solution (Newman 1987). Zeolites are also common weathering products of basic (e.g., basaltic) rocks (Deer et al. 1976a), which form a significant fraction of the waste-impacted sediments. The unambiguous identification of the secondary zeolite in experimentally reacted sediments was obscured in XRD results by abundant primary feldspar in the samples, but the morphology and chemistry of secondary phases observed in SEM was consistent with a Na-zeolite. Extensive XRD examination of SX-108 sediments did not show the production of detectable secondary zeolites, and XRD patterns from pristine and impacted sediments were indistinguishable. Again, very minor amounts of a Na aluminosilicate phase were observed that may have been a secondary zeolite.

The experimentally reacted sediments had been size fractionated (fines were removed) prior to reaction, and the secondary zeolites stood out on the surfaces of primary silicates. In the impacted SX-108 sediments, the presence of zeolites may have been obscured by the presence of abundant preexisting smectite, and waste-induced secondary phases that might be zeolite were of low abundance and indistinct morphology. By examining the surfaces of individual clasts with very low ^{137}Cs activity, some secondary phases with the appropriate composition were found. These phases were far too sparse to have affected the results of bulk or clay-size XRD.

The secondary 'zeolites' were present, however, and apparently retained a small, detectable quantity of radiation (see Section D.3.5). The difference in results from the two exposures to high concentrations of NaOH – i.e., the purposeful laboratory experiment and the accidental leakage exposure – may also be largely due to the stark contrast in the conditions of reaction. In the zeolite-producing laboratory experiments, the solids-solution ratio was very low, so that the pH was relatively constant throughout the course of the experiment (e.g., the OH^- reactant was in excess). Beneath the SX tank farm, the solids-solution ratio was very high so that the pH would be rapidly moderated by base-induced hydrolysis of the mineral fraction. The conditions under the tank may thus have had only a transient potential for zeolite precipitation.

Tank wastes altered the sediment composition and mineralogy, generating non-crystalline or poorly crystalline reaction products. These secondary phases were not apparently abundant enough to be detected by XRD, but may have been significant in affecting the behavior of ^{137}Cs. Sample 3A was altered to an extent that affected its appearance and texture, and samples 1A and 7A were also significantly altered. Sample 5A was apparently little impacted and showed few affects of having contacted tank waste; it was apparently in a location that had been impacted little by leaking wastes. The chemical reaction of tank wastes with sediments did not correlate directly with the retention of ^{137}Cs.

D.2.7 REFERENCES

Bjornstad B. N., K. R. Fecht, and A. M. Tallman, 1987, Quaternary Geology of the Pasco Basin, Washington, Rockwell Hanford Operations.

Deer W. A., R. A. Howie, and J. Zussman, 1976a, Rock-Forming Minerals, Vol. 4 Framework Silicates, John Wiley and Sons, Inc.

Deer W. A., R. A. Howie, and J. Zussman, 1976b, Rock-Forming Minerals, Volume 3. Sheet Silicates, Longmans, London.

Newman, A.C.D., 1987, Chemistry of Clays and Clay Minerals, Mineralogic Society Monograph No. 6, John Wiley & Sons.

Serne R. J., G. V. Last, G. W. Gee, H. T. Schaef, D. C. Lanigan, C. W. Lindenmeir, R. E. Clayton, V. L. LeGore, R. D. Orr, C. F. Brown, D. B. Burke, I. V. Kutnyakov, T. C. Wilson, and D. A Myers, 2001a, Geologic and Geochemical Data Collected from Vadose Zone Sediments from Borehole SX 41-09-39 in the S/SX Waste Management Area and Preliminary Interpretations, p. 162, Pacific Northwest National Laboratory, Richland, Washington.

Serne R. J., H. T. Schaef, B. N. Bjornstad, B. A. Williams, D. C. Lanigan, D. G. Horton, R. E. Clayton, V. L. LeGore, M. J. O'Hara, C. F. Brown, D. E. Parker, I. V. Mitroshkov, G. V. Last, S. C. Smith, C. W. Lindenmeir, J. M. Zachara, and D. B. Burke, 2001b, Characterization of Uncontaminated Sediments From the Hanford Reservation—RCRA Borehole Core Samples and Composite Samples, p. 142, Pacific Northwest National Laboratory, Richland, Washington.

D.3.0 GEOCHEMISTRY AND REACTIVE TRANSPORT BEHAVIOR OF ^{137}CS

^{137}Cs ($t^{1/2}$ = 30.07 y) is a high-yield fission product existing in tank wastes at Hanford in significant concentrations (e.g., 10^{-1} - 10^{0} Ci/L). The supernatant concentration of ^{137}Cs in the leaked S-SX single-shell tanks (SSTs) has been estimated to range between 3.05×10^{-5} mol/L – 3.91×10^{-6} mol/L in tanks SX-108, SX-109, and SX-115 (Jones et al. 2000). Single-shell tank leakage in the S and SX tank farms has released approximately 86.9 kCi of ^{137}Cs to the vadose zone in highly alkaline, highly saline ($NaNO_3$- $NaNO_2$) waste solutions, although in-ground inventory estimates vary considerably between authors using different estimation methods and/or assumptions (Jones et al. 2000). All estimates, however, reinforce the fact that ^{137}Cs is the major in-ground radioactive inventory element in the S and SX tank farms, with additional large in-ground inventories site-wide.

Many previous engineering-based measurements of Cs adsorption to Hanford sediments have shown that the migration of Cs in the Hanford subsurface is strongly retarded by ion exchange reactions. It is also known that electrolyte cations (e.g., Na, Ca, Mg, and K) influence Cs migration in Hanford sediments through competitive ion effects, and empirical relationships describing these effects over certain electrolyte concentration ranges have been established. However, the observed subsurface migration of ^{137}Cs beneath the S and SX tank farms is deeper than expected given this knowledge base and current conceptual models of fluid migration in the Hanford vadose zone (Ward et al. 1997). Great concern exists over the future behavior of the enormous in-ground ^{137}Cs inventory. Should corrective measures be applied in the S and SX tank farms, and other tank farms where Cs subsurface contamination is extensive (e.g., B-BX-BY) to prevent its future migration? Of particular concern is whether the extensively sorbed in-ground Cs pool is exchangeable with the aqueous phase and susceptible to remobilization by infiltrating meteoric waters or dilute waste fluids released during tank sluicing.

A series of research activities was performed to provide a more comprehensive understanding of Cs geochemistry and reactive transport in sediments from the S and SX tank farms, because existing information was inadequate to interpret the in-ground concentration profiles of ^{137}Cs in sediments obtained by the spectral gamma logging of dry wells (DOE-GJPO 1996) and direct analyses of core materials beneath leaked tanks (e.g., 41-09-39, SX-108 slant). The new research has involved both Hanford S&T Program and EMSP investigators and includes use of uncontaminated and contaminated subsurface sediments from the S and SX tank farms. The overall objectives of this research have been to provide scientific insights on (1) waste characteristics and reactive transport phenomena that have produced the current in-ground distribution of ^{137}Cs and (2) the susceptibility of sorbed Cs to future migration. The results and implications of this research are described in the following sections: adsorption reactions of Cs in WMA S-SX sediments in presence of high-salt and base, spectroscopic studies of Cs-containing micas to define chemical and structural controls on Cs adsorption, reactive transport experiments and modeling under saturated and unsaturated conditions, mineralogic residence of ^{137}Cs in contaminated sediments, and lability and desorption of the in-ground ^{137}Cs pool.

Reference

DOE-GJPO, 1996, *Vadose Zone Characterization Project at the Hanford Tank Farms – SX Tank Farm Report*, DOE/ID/12584-268, GJPO-HAN-4, U.S. Department of Energy, Albuquerque Operations Office, Grand Junction Projects Office, Grand Junction, Colorado.

Ward, A. L., G. W. Gee, and M. D. White, 1997, *A Comprehensive Analysis of Contaminant Transport in the Vadose Zone Beneath Tank SX-109*, PNNL-11463, Pacific Northwest National Laboratory, Richland, Washington.

D.3.1 ADSORPTION REACTIONS OF CS IN WMA S-SX SEDIMENTS IN PRESENCE OF HIGH SALT AND HIGH BASE

John M. Zachara[1], Chongxuan Liu[1], Steven C. Smith[1], and Calvin C. Ainsworth[1]

[1]Pacific Northwest National Laboratory, Richland, Washington 99352

D.3.1.1 Introduction

The sorption of Cs to geologic materials has been well studied by the scientific community (e.g., Cornell 1993). Cs engages in ion exchange reactions with hydrated cations on the planar sites of smectites and vermiculites and is strongly and selectively sorbed to frayed edge sites (FES) that develop along the weathered periphery of micas (e.g., biotite and muscovite). Multisite adsorption models have been developed that include this phenomenology (Brouwer et al. 1983; Poinssot et al. 1999). The sorption behavior of Cs^+ in a geologic material is a sensitive consequence of the relative concentrations of smectite/vermiculite and mica/illite as the former are the primary contributors of planar sites, and the latter of the strongly sorbing FES.

Hanford sediments contain small but significant concentrations of Cs-sorbing phyllosilicates (smectites and micas) that are ubiquitous components of the Hanford formation flood deposits and underlying Ringold formation. It has long been recognized that Hanford sediments have a strong sorption potential for Cs. Performance assessment models have been used to forecast Cs migration at Hanford using distribution coefficients (K_ds) estimated from empirical regression equations involving sediment cation exchange capacity (CEC), electrolyte composition/ concentration, and Cs retention at tracer concentration (e.g., 10^{-9}-10^{-8} mol/L). Mobility predictions from these models have been adequate for dilute waste streams where Cs is highly retarded (e.g., many disposal cribs), but appear to be inadequate for application to the S and SX tank farms where Cs^+, Na^+, K^+, and OH^- concentrations were high in the leaked waste fluids and Cs migration was more substantial. The waste concentrations of the above ions were in significant excess to those where previous measurements have been made on the sorption of Cs^+ to Hanford sediments.

Here we report on new studies of Cs^+ adsorption to WMA S-SX sediments that were performed over concentration ranges of Cs and other ions selected to bracket those present in leaked REDOX wastes from the S and SX tanks. An experimental design was followed that allowed parameterization and testing of a multisite, multicomponent ion exchange model to compute Cs adsorption (e.g., K_d) from REDOX-like waste solutions. Following model development, other experiments were performed to quantify (1) the impacts of high OH^- on Cs adsorption that might result from near-field waste-sediment reaction (base-induced dissolution and reprecipitation of clay-sized materials) and (2) ^{137}Cs ion exchange behavior in contaminated WMA S-SX sediments. Last, the multisite ion exchange model was applied to Cs distribution data from the SX-108 slant borehole to provide insights on in situ retardation mechanisms. Comprehensive results of these studies may be found in Zachara et al. (2001), Ainsworth et al. (2001a, b), and several other papers in preparation.

D.3.1.2 Experimental Procedures

D.3.1.2.1 Sediment Collection and Analysis. The "Above B" Hanford formation medium/fine sand composite (D.2.2) was used as an experimental medium. The particle size distribution and mineralogy of this sediment is described by Zachara et al. (2001). The composite was divided into two subsamples, with one subsample receiving multiple extractions with pH 4.5 Na-acetate (NaOAc-treated) to remove sodium and calcium carbonates. The other sample was used without specific treatment other than ion saturation with Na^{+}, K^{+}, or Ca^{2+} electrolyte.

The mineralogy of the bulk sediment, separated clay and silt fractions with appropriate ion saturation, and hand-picked micas were determined by X-ray diffraction using "research quality procedures." The cation exchange capacity of NaOAc-treated sediment was determined using Na^{+}, Ca^{2+}, or K^{+} saturated material. Isotopic exchange with either ^{22}Na or ^{45}Ca in 0.002 mol/L $NaNO_3$ or 0.001 mol/L $Ca(NO_3)_2$ electrolytes, respectively, was used to determine the surface excess of these cations. The aqueous phase activity of ^{22}Na and ^{45}Ca after 16 hours equilibration was determined by liquid scintillation counting. The K^{+} exchange capacity of the sediment was measured by extracting with 0.1-mol/L ammonium acetate. The K^{+} concentration in the extract was measured by inductively coupled argon plasma emission spectroscopy.

D.3.1.2.2 Cs Adsorption Experiments. Cesium sorption isotherms on NaOAc-treated "Above B" sediment were measured in $NaNO_3$, KNO_3, and $Ca(NO_3)_2$ electrolytes of various concentrations. Solids were presaturated with the appropriate electrolyte before addition of $CsNO_3$. The solids concentrations in Na electrolyte were 100 g/L, 50 g/L, 10 g/L, and 2 g/L in 7.0/5.0, 1.0, 0.1, and 0.01 mol/L $NaNO_3$, respectively. The solids concentrations were varied between 100 g/L and 2 g/L depending on electrolyte concentration and identity to achieve statistically sound sorption measurements. Cesium nitrate concentrations ranged from 10^{-9} to 10^{-1} mol/L, and were labeled with 7×10^{3} to 2.00×10^{4} dpm/mL ^{137}Cs. The suspensions were shaken in 50 mL high-density polyethylene bottles at 80 rpm and 30 °C for 16 hours. Solid-liquid phase separation was accomplished by centrifugation (5000 rcF for 30 minutes). The ^{137}Cs in the aqueous phase was determined by gamma counting. The suspension pH was measured using a calibrated glass combination electrode.

D.3.1.2.3 Effect of High Base on Cs Adsorption. The leaked REDOX wastes in WMA S-SX are believed to have contained in excess of 1 mol/L free OH^{-} (Lichtner 2001). Hydroxide is highly reactive with aluminosilicate minerals. Two types of experiments were performed to evaluate whether OH^{-} in REDOX wastes may have altered the Cs adsorbability of the Hanford sediment.

In the first experiment, "Above B" composite sediment was contacted with 0.1 mol/L NaOH (in 1 mol/L $NaNO_3$ at 40:1 liquid:solid ratio) in Teflon containers at 10 ° and 50 °C under $N_{2(g)}$ atmosphere. The OH^{-} concentration yielded a $pH_c = 13.2$ and a computed pH of 12.6. The sediment was removed after 56, 112, and 168 days of contact and washed repeatedly with pH 8 electrolyte of decreasing concentration. The reacted sediment was air-dried after soluble salts were removed, and Cs adsorption isotherms were measured in 1 mol/L $NaNO_3$, as described above, at 25 °C. The results allowed evaluation of whether CEC and adsorption site distribution and affinity for Cs were changed by base reaction.

The second experiment investigated the sorption of Cs during OH^-/sediment reaction. Three series of replicate Teflon tubes containing "Above B" sediment were spiked with 3 mol/L carbonate-free NaOH (the approximate free OH^- in tank SX-108) in 1 mol/L $NaNO_3$. Each tube series was then spiked with one of three concentrations of Cs (10^{-9}, 10^{-7}, 10^{-5}) and equilibrated with shaking at 50 °C under $N_{2(g)}$ atmosphere. Replicate tubes were sacrificed at different times out to 120 days, and the aqueous phase analyzed for Cs, Al, Fe, Si, K, Ca, and several other ions. Only results for Cs will be reported here. Other base-weathering/Cs-reaction studies were performed at different temperatures and OH^- concentrations, and results are reported in Ainsworth et al. (2001).

D.3.1.3 Results

D.3.1.3.1 Mineralogy and Cation Exchange Capacity. The cation exchange capacities (CEC) of the "Above B" composite varied with saturating ion (Table D.3.1.1) and were relatively low because the small amount of clay (less than 2%). The higher CEC in K^+ was consistent with the presence of a micaceous mineral fraction, but its large excess over that in Ca^{2+} and Na^+ electrolyte was not easily explained. The CEC measurements were repeated six times to ensure reproducibility. The Na CEC of the composite was very similar to the measured CECs of (1) uncontaminated Hanford fine sands from borehole W22-48 (Serne et al. 2001a), and (2) contaminated Hanford fine sands from boreholes 41-09-39 and SX-108 slant (Table D.3.1.2).

Table D.3.1.1. Cation Exchange Capacities and Cs^+ Sorption Maxima in Different Electrolytes.

Index ion	CEC (eq/g × 10^{-5}) n = 6	Max Cs adsorption (eq/g × 10^{-5}) [a] n = 4
Na^+	4.26 +/- .12	5.79
K^+	8.25 +/- .35	3.61
Ca^+	4.69 +/- .14	6.22

[a]Observed in the lowest ionic strength of each electrolyte.

Table D.3.1.2. Cation Exchange Capacities and Cs^+ Sorption Maxima in Different Electrolytes.

	Na-CEC (eq/g)	Comment
Above-B composite	$4.26 \times 10^{-5} \pm .12$ [a]	Composite of Hanford fine sands from RCRA boreholes on east and west sides of WMA S-SX
Contaminated WMA S-SX sediments		
SX-108 7A	4.44×10^{-5} [a]	Hanford fine sands from contaminated boreholes
41-09-39 7A/B/C	5.10×10^{-5} [a]	
41-09-39 9A/B/C	3.88×10^{-5} [a]	
41-09-39 11C	5.06×10^{-5} [a]	
	CEC = $4.62 \times 10^{-5} \pm 0.57$	
Borehole W22-48		
4-61	$4.2 \pm 0.3 \times 10^{-5}$ [b]	Hanford fine sands from W22-48, immediate east of WMA S-SX
91.5	$4.8 \pm 0.4 \times 10^{-5}$ [b]	
101.5	$6.0 \pm 0.4 \times 10^{-5}$ [b]	

[a]Measured by ^{22}Na isotopic dilution.
[b]Measured by NH_4Cl displacement.

The weight percentages of the mineral constituents varied with particle size. The mineralogic analysis of the bulk sediment showed that quartz was the dominant mineral phase with lesser amounts of plagioclase and potassium feldspars, micas, chlorite, and smectite. Micas, including muscovite, biotite and vermiculitized biotite, were present in all size fractions of the sediment. The feldspar content decreased with decreasing particle size. Most of the feldspar was plagioclase with anorthite being the dominant phase. The clay fraction consisted of smectite, vermiculite, chlorite, and mica. The Mg saturated, glycol-solvated clay displayed an intense but very broad diffraction maxima for smectite. X-ray diffractograms of the clay-sized fraction of the "Above B" sediment were almost identical to the clay-sized fraction of contaminated samples from boreholes 41-09-39 (Serne et al. 2001b) and SX-108 slant (data not shown).

D.3.1.3.2 Cs^+ Adsorption Chemistry from Na^+, K^+, and Ca^{2+} Electrolytes. The adsorption isotherms of Cs^+ in Na^+ and K^+ electrolytes were dependent on electrolyte concentration (Figure D.3.1.1). Electrolyte concentration was less important with Ca^{2+}. The isotherms were of the Freundlich type with slopes below unity (Freundlich 1/n less than 1), implying sorption site heterogeneity. Cs^+ adsorption from K^+ electrolyte was the most linear of those studied (e.g., isotherm slope = 0.85 to 0.95). Increasing salt uniformly displaced the isotherms in both Na^+ and K^+ electrolyte, indicating adsorption by ion exchange.

Figure D.3.1.1. Cs^+ Adsorption Behavior on the "Above B" Sediment Composite From WMA S-SX Presented as Adsorption Isotherms [$(Cs)_{ads}$ versus $(Cs)_{aq}$], Exchange Isotherms [E(CsX) versus $\hat{E}$(Cs-aq)], and K_d Functions [K_d versus $(Cs)_{aq}$].

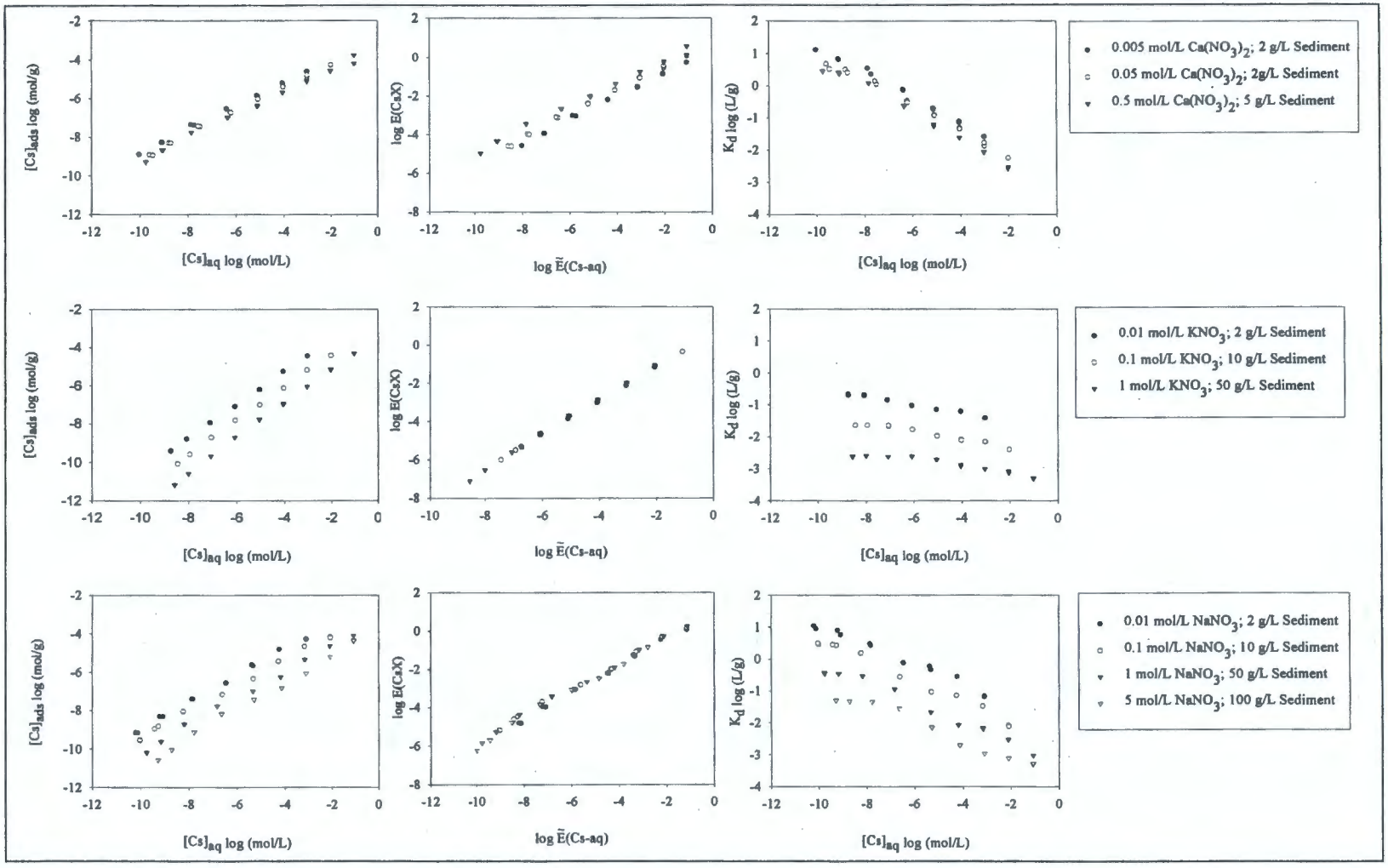

The adsorption data were reformatted in terms of surface (E) and aqueous ($\tilde{E}$) equivalent fractions where

$$E_{Cs} = q_{Cs}/Q \text{ and } \tilde{E}_{Cs} = [Cs^+]/\tilde{Q} \qquad (D.3.1.1)$$

where q_{Cs} was the adsorption density in mole/g, Q was the electrolyte specific CEC (e.g., Table D.3.1.1), $[Cs^+]$ was the aqueous concentration in mole/L and $\tilde{Q}$ was the total solution normality. The Cs^+ adsorption data for the monovalent exchange systems (Na^+, K^+) reduced to single exchange isotherms over wide ranges in surface and aqueous equivalent fractions [log E_{CsX} versus log $\tilde{E}_{Cs(aq)}$], while three parallel but distinct ion exchange isotherms resulted for Ca^{2+} electrolyte (Figure D.3.1.1).

The distribution ratio, K_d [(L/g) = (mol Cs^+/g)/(mol Cs^+/L)], is a parameter used to describe sorption strength in radionuclide performance assessment models. Here, K_d decreased with increasing salt concentration and the total Cs concentration (Figure D.3.1.1). The effect of increasing Na^+ and K^+ were generally comparable. The decrease in K_d with total Cs concentration was smallest in K^+ electrolyte, but was as much as 2 to 3 orders of magnitude in Na^+ and Ca^{2+} electrolyte. At high salt (Na^+ and K^+) and Cs^+ concentrations (e.g., greater than 10^{-4} mol/L), adsorption was negligible [e.g., K_d (mL/g) = 0]. The competitive effect of the electrolyte ions on Cs^+ sorption followed the trend $K^+ >> Na^+ \geq Ca^{2+}$.

D.3.1.3.3 Ion Exchange Modeling. Conditional equilibrium constants (K_c) for Cs^+ exchange were computed from the data in Figure D.3.1.1 according to the following relationships.

$$uCs^+_{(aq)} + AX_u = uCsX + A^{u+}_{(aq)} \qquad (D.3.1.2)$$

$$K_c = [A^{u+}][E_{CsX}]^u/[Cs^+]^u[E_{AXu}] \qquad (D.3.1.3)$$

where $A^{u+} = Na^+$, K^+, or Ca^{2+} and [] is concentration. E_{CsX} (the equivalent fraction of Cs^+ on the exchange fraction) was defined as in equation (D.3.1.1) and E_{AXu} as $1-E_{CsX}$. The resulting K_cs were equivalent to the Vanselow model for homoionic, monovalent exchange (e.g., Na^+-Cs^+, K^+-Cs^+), and to the Gaines and Thomas model for heterovalent exchange (e.g., Ca^{2+}-Cs^+ see Sposito 1981).

The K_cs increased as the fractional occupancy of the CEC by Cs^+ decreased (Figure D.3.1.2). In monovalent electrolyte, K_c increased abruptly below $E_{CsX} = 0.01$, while K_c in Ca^{2+}electrolyte showed a monotonic increase with decreasing equivalent fraction of Cs^+. All experiments showed a leveling or approximately constant K_c below a log $E_{CsX} = -4.5$. The magnitude of these K_c values in the three electrolytes and their trend with respect to adsorption density were similar to those reported for illites (Brouwer et al. 1983; Comans et al. 1991).

Figure D.3.1.2. Computed Condition Equilibrium Constants (K_c) From Figure D.3.1.1 and Results of Multisite Modeling (Lines) with Best-Fit Parameters (Site Concentrations Expressed as a Fraction of the CEC, and Binary Ion Exchange Constants) as Noted.

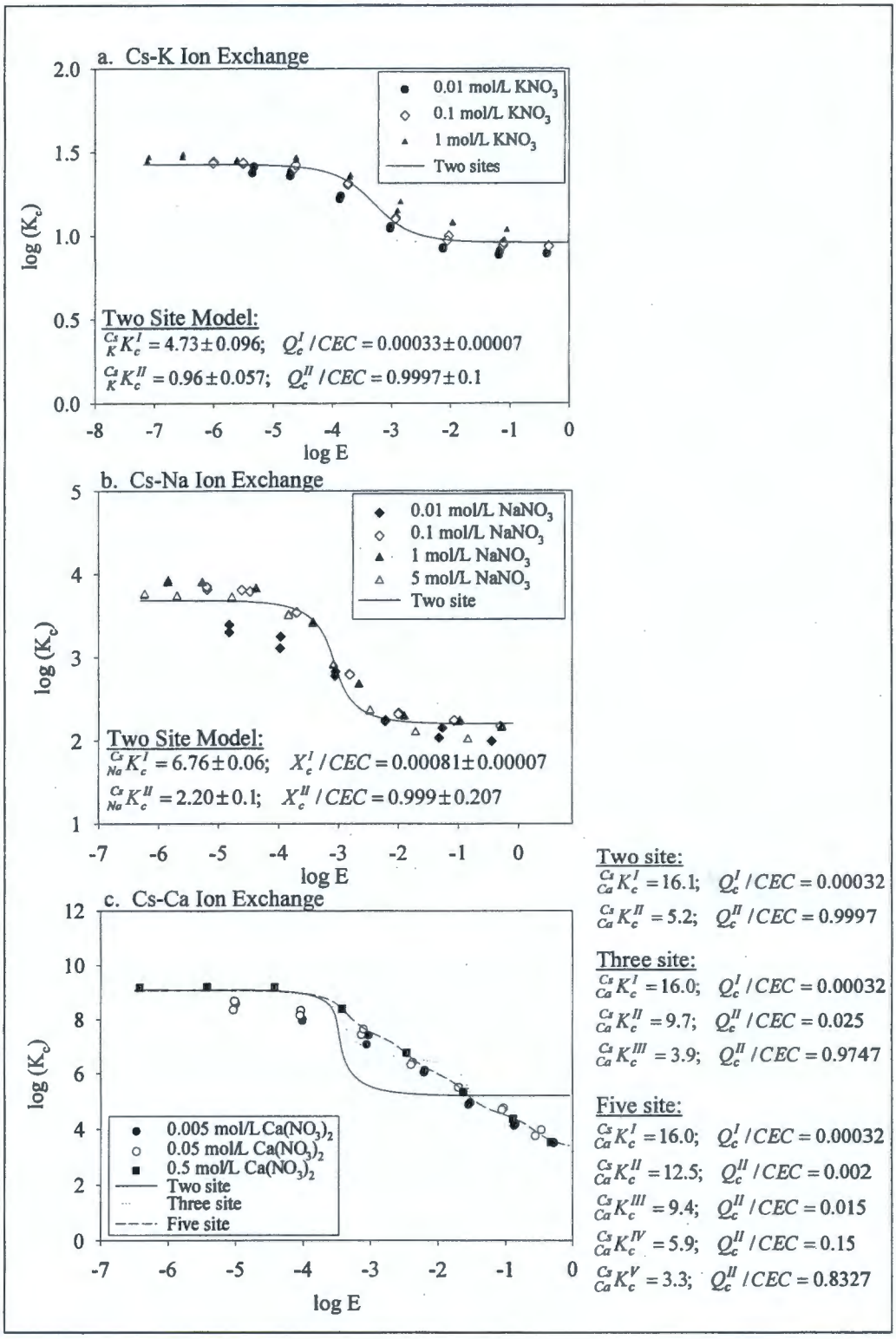

A multisite ion exchange model was applied to the adsorption data (Figure D.3.1.2, solid lines). The model is fully described in Zachara et al. (2001). In the multisite model, the adsorbed concentration is hypothesized to result from the contributions of sorption sites that differ in both affinity (e.g., high and low) and concentration. The measured electrolyte specific CECs (e.g., Table D.3.1.1) were used as the total site concentrations. Previous multisite modeling of Cs^+ adsorption to illite rationalized these different sites as existing on the phyllosilicate basal plane and the frayed edge. The concentration (of Cs) and ionic strength dependence of the homovalent exchange (Cs^+-K^+ and Cs^+-Na^+) was well approximated by a two-site model (Figure D.3.1.2). A one-site model could not reproduce the sorption data from any electrolyte. The primary electrolyte ions in REDOX wastes (K^+ and Na^+) were competitive with Cs^+ for both high- and low-affinity sorption sites.

Modeling the heterovalent exchange (Cs^+-Ca^{2+}) was more challenging and required five distinct sites to adequately fit the data (Figure D.3.1.2). This difficulty in describing Cs^+-Ca^{2+} ion exchange was not considered to be especially significant to the S and SX tank farms, because Cs^+ migration trails the Ca^{2+} plume that was displaced by Na^+ from the ion exchange complex.

D.3.1.3.4 Effects of High Base. Equilibration of the "Above B" sediment with 0.1 mol/L NaOH/1 mol/L $NaNO_3$ leads to a progressive increase in CEC with contact time (Table D.3.1.3), presumably through base-induced hydrolysis and exfoliation of micas. The measured isotherm data on the base-treated sediments was recast as K_cs calculated according to Equations D.3.1.1 through D.3.1.3, using the new CEC data (Figure D.3.1.3a). The "0-day" data in Figure D.3.1.3a was the same as that plotted for 1 mol/L $NaNO_3$ in Figure D.3.1.2. Base treatment had a surprisingly small impact on Cs sorption selectivity to the sediment after the observed increase in CEC was accounted for. There was a slight reduction in K_c below an equivalent fraction of 10^{-3} (0.2 to 0.25 log units) that increased with base contact time, indicating a lessening in the exchange selectivity of the FES for Cs. This experiment and others in this series indicated that base reaction changed the mineralogy of the clay fraction, but had minimal influence on the overall sorptivity of Cs.

Table D.3.1.3. Measured CEC Value of "Above-B" Composite After Reaction with 0.1 mol/L NaOH at 50 °C.

Contact time (d)	CEC [a] (eq/g)
56	$4.71 \pm 0.12 \times 10^{-5}$
112	$6.73 \pm 0.11 \times 10^{-5}$
168	$7.42 \pm 0.89 \times 10^{-5}$

[a]CEC measured by ^{22}Na isotopic dilution, n = 3.

Figure D.3.1.3. Selected Results of Base Reaction Studies with "Above B" Composite.

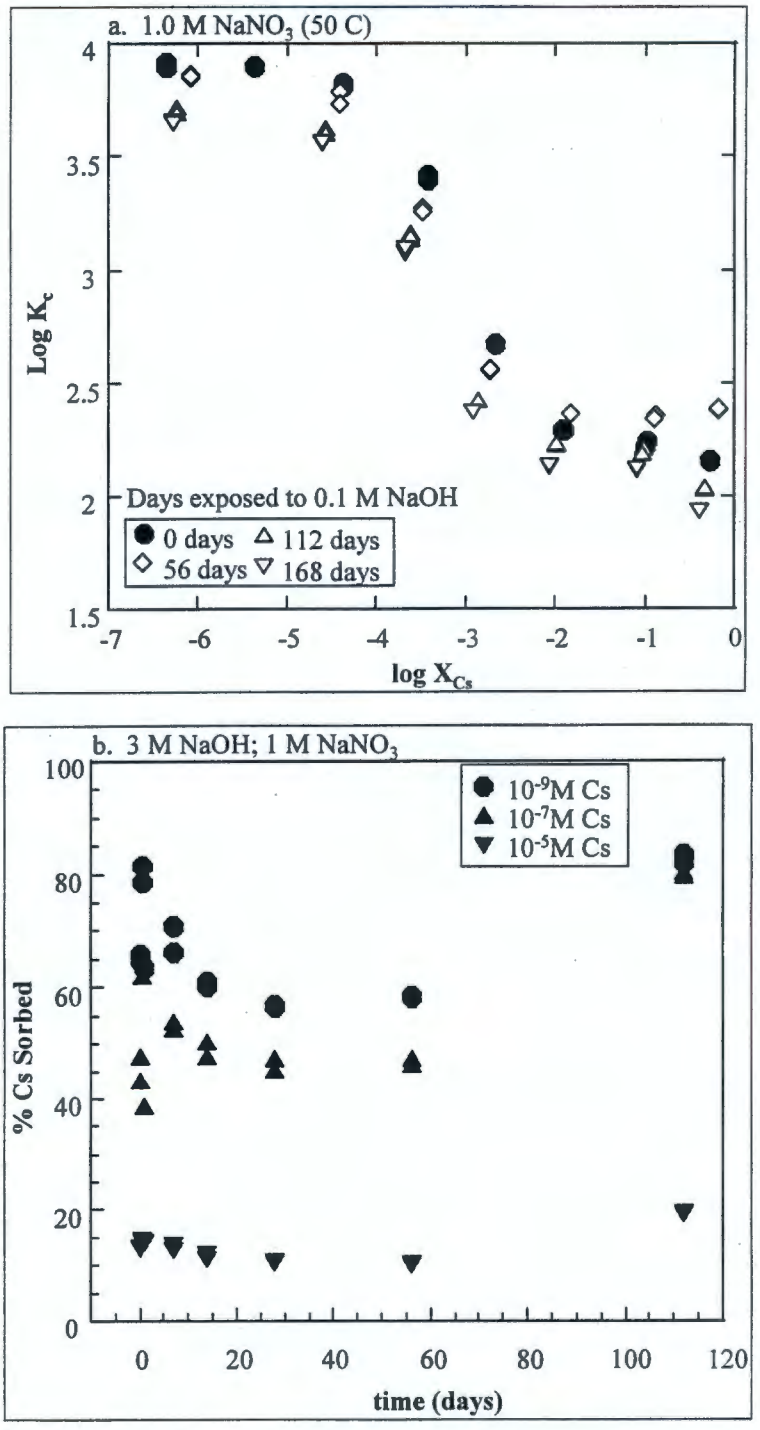

Note: a) Kc values for Cs^+ adsorbed to sediment contacted with 0.1 mol/L NaOH at 50 °C for various time periods. The sediment was washed free of reaction products before adsorption was measured at 25 °C in 1.0 mol/L $NaNO_3$. b) Temporal behavior of Cs sorption when added with 3 mol/L NaOH. The suspension was equilibrated at 50 °C.

All kinetic studies of Cs sorption to Hanford sediment have shown that the ion-exchange reaction occurs rapidly, within the time frame of hours. Some small increases or decreases in Cs sorption relative to the initial ion exchange reaction have been observed with prolonged contact time (e.g., 10 to over 100 days). These long-term changes have been attributed to intraparticle diffusion (increases) and K^+ release through mineral dissolution (decreases). The temporal behavior of Cs sorption in presence of high base (3 mol/L, 50 °C) was markedly different from these past observations (Figure D.3.1.3b). A rapid initial reaction was observed (less than 1 day), followed by a decrease (1 to 24 days), then another increase in Cs adsorption (55 to 110 days). The concentrations of Si, Al, and K^+ in particular, were quite dynamic over this time period indicating an effect of mineral dissolution and precipitation reactions. It is not yet known whether the sorbed state after 110 days in terms of mineral residence and desorbability is similar to that after the initial reaction (1 day). The sediment at experiment termination showed signs of significant mineral alteration and was similar in many respects to sample 3A from the SX-108 slant borehole. This experiment differed from that in Figure D.3.1.3a in that a higher base concentration was used (3 mol/L as compared to 0.1 mol/L) and Cs^+ was present in solution as mineral phases dissolved and precipitated.

D.3.1.3.5 Ion Exchange of ^{137}Cs in Contaminated WMA S-SX Sediments. Four samples of ^{137}Cs-contaminated sediment from 41-09-39 and SX-108 slant were placed in Na^+, K^+, and Rb^+ electrolytes of three different concentrations and equilibrated for 6 days to determine if the sorbed ^{137}Cs was exchangeable. Literature reports indicate that cation selectivity on phyllosilicates generally follows the trend: $Cs^+ \cong Rb^+ > K^+ >> Na^+$ (e.g., Brouwer et al. 1983; Zachara et al. 2001). It was therefore expected that Rb^+ and K^+ would be effective in displacing ^{137}Cs.

The ^{137}Cs aqueous concentrations that resulted were dependent on electrolyte identity and concentration (Figure D.3.1.4); a significant fraction of the sorbed Cs pool was exchangeable with the aqueous phase. Increasing the electrolyte concentration led to an increase in desorbed ^{137}Cs through ion exchange. Consistent with the higher affinity of K^+ and Rb^+ for the FES, these ions were more effective than Na^+ in displacing adsorbed ^{137}Cs. Between 19 and 26.9% of the adsorbed ^{137}Cs was displaced by the highest concentrations of K^+ and Rb^+ (Table D.3.1.4).

Figure D.3.1.4. Observed and Predicted Ion Exchange of ^{137}Cs in Contaminated WMA S-SX Sediments After 6 Days Equilibration in Different Electrolyte Solutions.

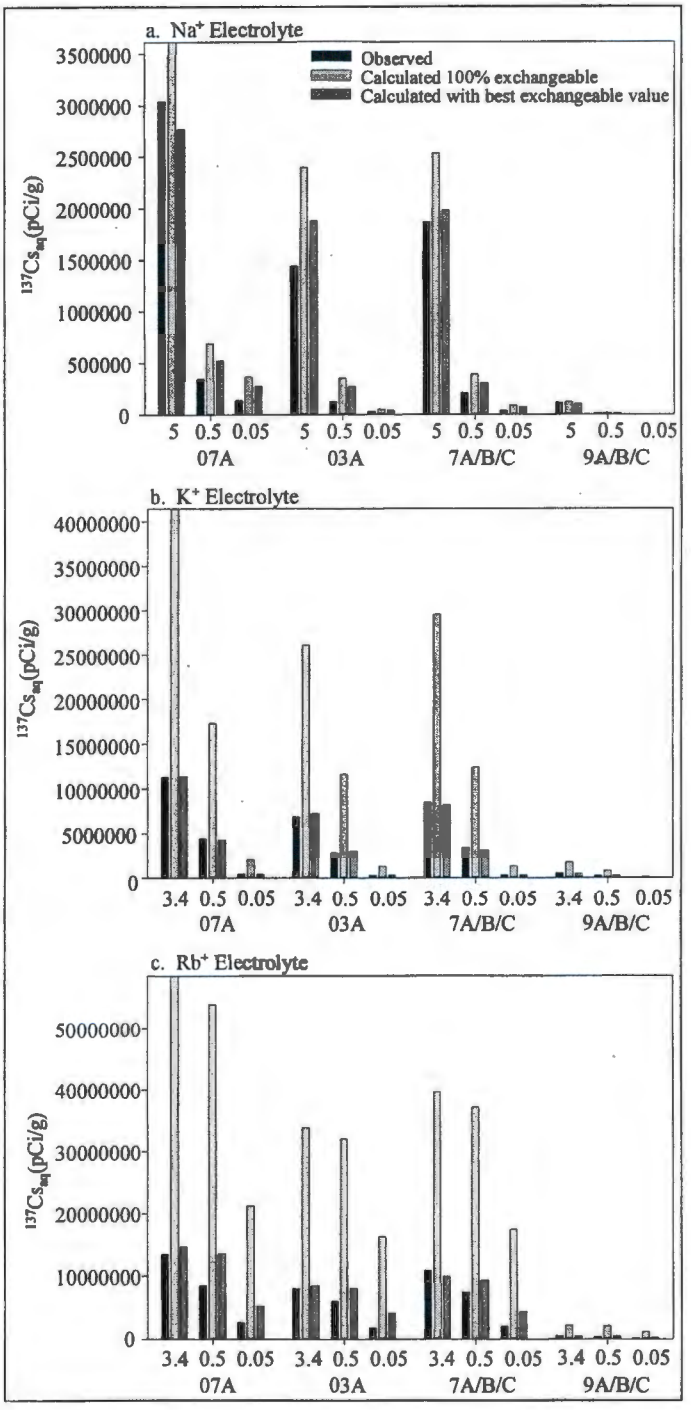

Note: Electrolyte concentrations noted immediately below bars. The predicted values include the assumption of, 1) 100% exchangeability or, 2) partial exchangeability to provide best data fit. a) Na^+ Electrolyte, b) K^+ Electrolyte, and c) Rb^+ Electrolyte.

Table D.3.1.4. Exchange of ^{137}Cs From Contaminated S-SX Sediments Using Different Electrolytes.

Sample	Total ^{137}Cs pCi/g (std dev)	Measured ^{137}Cs Exchange pCi/g (% of total)			Predicted ^{137}Cs Exchange		
					Na	K	Rb
					100% [a]	100% [a]	100% [a]
		5.0 mol/L Na^+	3.4 mol/L K^+	3.4 mol/L Rb^+	(.84) [b]	(.28) [b]	(0.25) [b]
7A	5.94×10^7	3.04×10^6	1.13×10^7	1.34×10^7			
	(1.34×10^7)	(5.12)	(19.0)	(22.4)	6.08	69.7	98.6
					(4.66)	(19.1)	(24.6)
3A	3.42×10^7	1.44×10^6	6.87×10^6	8.03×10^6			
	(1.30×10^6)	(4.21)	(20.1)	(23.5)	7.01	76.3	99.1
					(5.50)	(21.1)	(24.8)
7A/B/C	4.01×10^7	1.87×10^6	8.43×10^6	1.08×10^7			
	(1.04×10^6)	(4.66)	(21.0)	(26.9)	6.31	73.6	99.0
					(4.94)	(20.3)	(24.8)
9A/B/C	2.37×10^6	1.13×10^5	5.03×10^5	5.98×10^5			
	(1.10×10^5)	(4.76)	(22.4)	(25.2)	5.10	67.8	91.9
					(4.27)	(19.7)	(23.0)

[a]Predicted described amount of ^{137}Cs by multi-site model assuming entire adsorbed Cs pool is exchangeable in 6 hours.
[b]Predicted described amount of ^{137}Cs by multi-site model assuming the noted fraction of the adsorbed Cs pool is exchangeable in 6 hours.

The analytically determined isotopic ratio of ^{137}Cs in the aqueous phase of these equilibrations [$^{137}Cs/(^{137}Cs + ^{135}Cs + ^{133}Cs) = 0.2083$], the computed total Cs concentration in the sediment given this abundance value, and the ^{137}Cs activity determined by high-performance germanium counting (HPGe), the CEC measured by ^{22}Na dilution (Table D.3.1.2), and the indigenous ion content of the aqueous and exchanger phases determined by 1:1 water extraction and NH_4^+ displacement, respectively, were used as input to the equilibrium multisite exchange model to predict the expected $^{137}Cs_{(aq)}$ concentrations in the different electrolyte solutions (Figure D.3.1.4). The model used the exchange constants (K_{K-Cs}, K_{Na-Cs}, and K_{K-Na}) and site fractions calculated for the "Above B" composite (Figure D.3.1.3), and a K_{Rb-Cs} estimated from Brouwer et al. (1983). The calculations were first performed with the assumption that all the sorbed Cs was exchangeable over the 6 hours experimental period. This assumption led to calculated $^{137}Cs_{(aq)}$ concentrations that were remarkably close, albeit slightly above the observed values in the Na electrolyte (Figure D.3.1.4a; Table D.3.1.3) given the uncertainty in the ^{137}Cs activity determined by HPGe (error bars). The predicted concentrations for the K^+ and Rb^+ electrolytes significantly exceeded the observed values (Figures D.3.1.4b, c; Table D.3.1.3) but their computed decrease with decreasing electrolyte concentration paralleled the observed trend.

The fraction of exchangeable Cs was adjusted to determine if the model calculations could be improved by assuming a constant value of labile Cs for the sample suite as a whole. Cs may diffuse into the dehydrated, interlamellar regions of phyllosilicates with long contact times (Comans et al. 1991). The fraction of Cs undergoing such diffusion is slowly exchangeable with the aqueous phase. The data was best described by assuming that 84% of the adsorbed Cs was exchangeable in Na electrolyte and 25 to 28% was exchangeable in K and Rb electrolytes. Given these assumptions of exchangeability, the $^{137}Cs_{(aq)}$ concentrations were well described with the multi-site model using parameters developed on the "Above B" composite (Figure D.3.1.4; Table D.3.1.3). The calculations for the Rb electrolyte showed deviations at the intermediate electrolyte concentration that were attributable to the use of a K_{Rb-Cs} that was not specific to the Hanford sediment. Undoubtedly, the Rb calculations could be improved by the measurement of a Hanford specific value. Other measurements of Cs exchangeability and a discussion of causes and implications are provided in other subsections of this Appendix (Ainsworth et al. 2001).

D.3.1.3.6 ^{137}Cs Retardation in WMA S-SX. The multisite model parameters for Cs^+, K^+, and Na^+ summarized in Figure D.3.1.2 were used along with (1) the average CEC for contaminated Hanford fine sands from WMA S-SX (4.62×10^{-5} eq/g; Table D.3.1.2) and (2) the computed free concentrations of Na^+ and K^+ in SX-108, SX-109, and SX-115 tank wastes (Lichtner 2001) to compute K_d functions for Cs in the sub-tank sediments (Figure D.3.1.5a). The calculation shows that Cs retardation is a strong function of its adsorption density, which, in turn, is dependent on the total Cs^+ concentration. For SX-108 and SX-109 wastes, the K_d is virtually 0 above an adsorbed concentration of 10^{-7} mol/g. Adsorbed Na^+ and K^+ block Cs adsorption to all but the high affinity FES sites because of their high aqueous concentration. Because ^{137}Cs represents only 20.83% of the total Cs concentration, the figure suggests that the maximum ^{137}Cs sorption capacity of the Hanford fine sand in presence of SX-108 and SX-109 supernate is reached at approximately 1.5×10^8 - 3.0×10^8 pCi/g ^{137}Cs. These computed values are remarkably close to the highest adsorbed ^{137}Cs concentrations observed in sediments from the SX-108 slant borehole that were collected closest to the tank (1A - 3.7×10^8 pCi/g; 3A - 1.39×10^8 pCi/g). If it

assumed that the underlying Hanford fine sand has a bulk density of 1.4 g/cm^3 and a porosity of 0.3, and it becomes saturated with tank SX-108 waste (3.05×10^{-5} mol/L Cs) and adsorbs 90% of the Cs, then the adsorbed Cs concentration would be approximately 1.22×10^{-9} mol/g of ^{137}Cs or 1.46×10^{7} pCi/g ^{137}Cs. This adsorption density is an order of magnitude below the estimated sorption capacity and is close to the high-end values of sorbed ^{137}Cs noted in deeper core samples from both 41-09-39 and SX-108 slant.

The lower salt concentrations in tank SX-115 allow significantly greater Cs retardation in Hanford fine sands surrounding this tank (e.g., increases in K_d by 3x; Figure D.3.1.5a). For example, a finite K_d (2.5-3.5 ml/g) is observed over an adsorption density range of 10^{-7} to 10^{-5} mol/g as a result of partial Cs^+ accessibility to planar sites on smectites and vermiculites. This lower affinity ion exchange allows for a larger adsorption maximum of ^{137}Cs (approximately 2.0×10^{11} pCi/g). Given this higher retardation potential, it is not surprising that ^{137}Cs was not observed in the borehole proximate to SX-115 (299 W23-19; Serne et al. 2001c).

The multisite model was also used along with the average CEC of the contaminated Hanford fine sands (4.62×10^{-5} eq/g; Table D.3.1.2), the porewater concentrations of Na^+ and K^+ computed from the 1:1 water extraction data of SX-108 (Serne et al. 2001d), and the total Cs determined by direct gamma counting to compute in situ K_d values for comparison with those observed (Serne et al. 2001d). The computed ^{137}Cs-K_d values matched the observed ones quite well in trend over the whole borehole (Figure D.3.1.5b), and were close in value between 80 to 100 feet where the highest Na and K concentrations were found in porewater. Significant deviations were observed in upper region (55 to 71 feet) of the ^{137}Cs accumulation zone (55 to 88 feet), where aqueous Na concentrations were low (0.103-0.313 mol/L) and where mineral alterations as a result of heat and base reaction were observed (Section D.2.1). Variations in CEC beyond the average value (4.62×10^{-5} eq/g), changes in ion exchange affinity as a result of mineral alteration (e.g., K_{Cs-Na}/K_{Cs-K}), and partial Cs fixation within phyllosilicates armored by secondary precipitates are potential causes of discrepancy. Overall, however, the surprisingly good agreement between the computed and observed K_d values suggests that the current in-ground distribution of ^{137}Cs is in approximate ion-exchange equilibrium with the pore water and phyllosilicate sorbents in the sediment phase.

D.3.1.4 Conclusions and Implications

(1) Although Hanford sediments have a high potential to adsorb Cs^+ by selective ion exchange, Na^+ and K^+ are competitive ions that exist in the REDOX wastes that act to strongly suppress Cs^+ sorption even at trace levels. Subsurface mobility is enhanced beyond previously expected values.

(2) The competitive effects of Na^+ and K^+ and the strong concentration dependency of Cs^+ sorption could be well described by an equilibrium, multisite ion exchange model. The model was parameterized using the "Above B" composite sample representative of the sediments in the 12 m below the S and SX tank farms.

Figure D.3.1.5. Multisite Model Simulations Using Site Fractions and Exchange Constants From "Above B" Sediment, Model Calculations of REDOX Tank Waste Composition, and Cs Distribution Data Below SX-108.

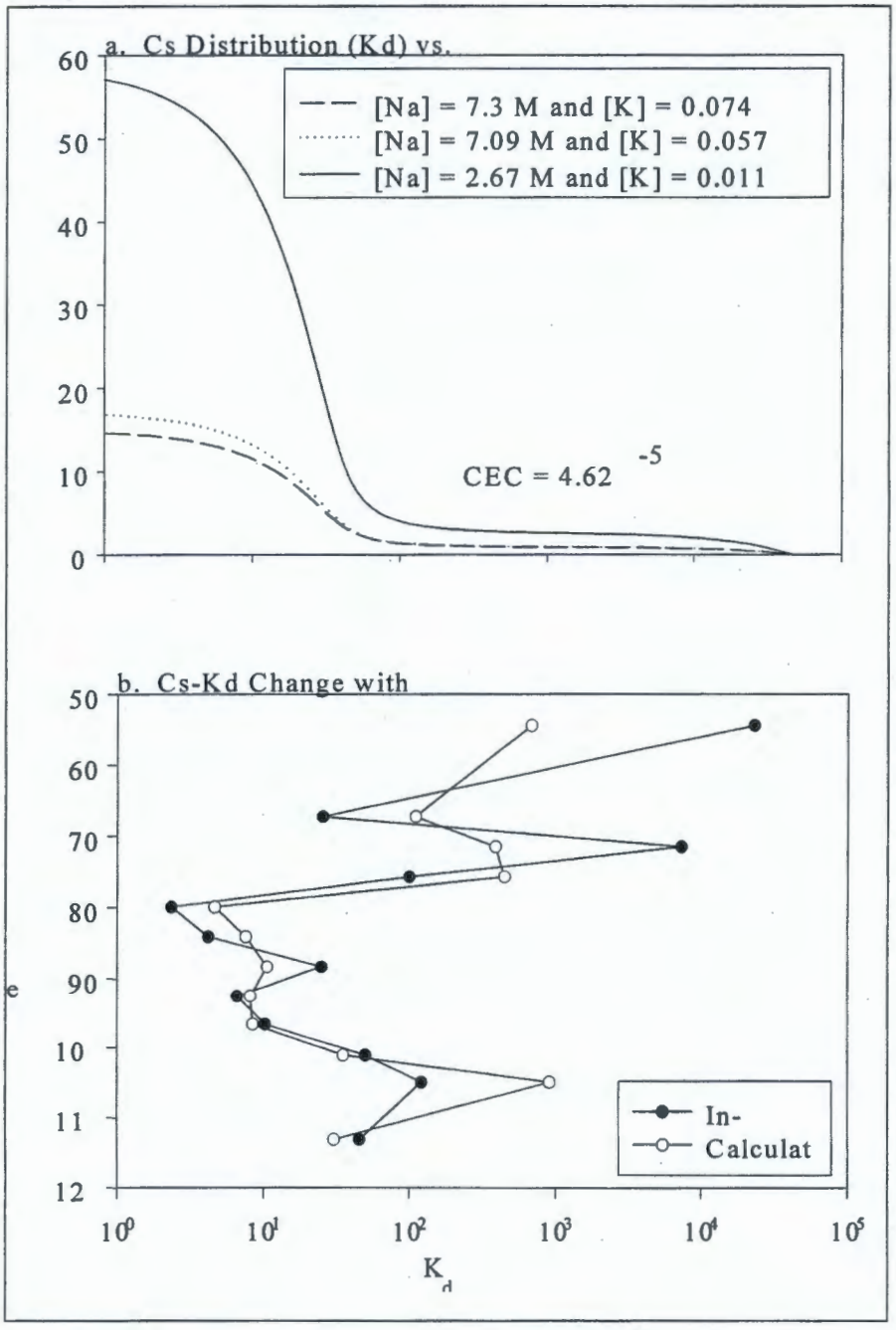

*Calculation was based on previous 2-site equilibrium sorption model and measured aqueous Na, K, and Cs concentrations in SX-108 slant borehole sediments. The CEC was fixed at 4.62×10^{-5} (eq/g).

Note: a) Computed K_d functions for SX-108, 109, and 115 tank waste solutions and b) predicted versus observed in situ K_d values for ^{137}Cs below SX-108.

(3) Reactions of [OH^-], a highly reactive waste component, with the S and SX sediments did not markedly change their sorption behavior for Cs. High base reaction increased the CEC of the sediment by approximately 30%. After accounting for the effect of CEC increase, the ion exchange selectivity was found to decrease only slightly after base reaction at 50 °C.

(4) A significant fraction (greater than 20%) of the adsorbed Cs pool in tank-waste contaminated sediments was exchangeable with the aqueous phase and desorbable by Na^+, K^+, and Rb^+. The multisite model that had been parameterized using the "Above B" composite provided good semiquantitative predictions of Cs release from, and equilibrium concentrations in contact with, contaminated S and SX sediments. Model calculations indicated that an unresolved fraction of adsorbed Cs was less exchangeable with the aqueous phase.

(5) The trend and magnitude of the in situ K_ds for ^{137}Cs beneath tank SX-108 conform generally to multicomponent ion exchange predictions. It appears that the existing in-ground distribution of ^{137}Cs is in approximate ion exchange equilibrium with its solid and aqueous phase surroundings.

Ion exchange experiments with Cs on WMA S-SX sediments showed that the high concentrations of Na^+ and K^+ present in REDOX wastes may have expedited subsurface Cs transport by reducing attenuation and the effective K_d to low values. Uncertainty in the total and free concentrations of both Na^+ and K^+ in the actual leaked solutions prevents more precise statements. However, more recent modeling of the S and SX tank waste solutions indicates Na concentrations were even higher than initially thought and may have reached 19.6 mol/L for tank SX-108 (Section D.7.3). These high concentrations of Na are consistent with the deep penetration of ^{137}Cs. Our findings indicated that sorbed ^{137}Cs in contaminated S and SX sediments is partially labile and its measured aqueous and solid phase distribution appears to conform to a equilibrium state with respect to ion exchange. This current chemical condition is one that undoubtedly evolved over time. It is not necessarily proposed that the in-ground distribution of ^{137}Cs is reflective of an equilibrium transport event at the time of waste implacement. Growing evidence suggests that the waste emplacement event may have been quite rapid. Unsaturated transport experiments show that Cs breakthrough is more rapid than expectation under low moisture content and high flux rates (Section D.3.4). Collectively these studies indicate that the chemical effect of high salt is probably just one of several factors that allowed deep penetration of strongly sorbing Cs.

A sizable fraction of the adsorbed ^{137}Cs pool in contaminated WMA S-SX sediments was replaceable by Na^+, K^+, and Rb^+ (see also Section D.3.6). While these results indicated that much of the sorbed Cs pool is available for transport, they do not necessarily imply that future migration is expected or probable. We employed very high concentrations of the electrolyte ions that were near saturation with their respective NO_3-salts to induce mass-action displacement of ^{137}Cs. It is inconceivable that such high concentrations of K^+ or Rb^+ would ever occur in the Hanford vadose zone. Sodium was less effective in displacing adsorbed ^{137}Cs, but is a ubiquitous ion in the vadose zone originating from tank waste discharge and mineral water reaction. Currently, the Na^+ pulse resulting from tank waste leakage has migrated beyond/deeper

than that of Cs, with more dilute waters following. These dilute waters stabilize ^{137}Cs in the exchange complex and limit desorption.

Our results suggest that future migration of ^{137}Cs is unlikely unless Na concentrations in porewater approach those in the original REDOX waste discharge (e.g., 10 mol/L). Realistic scenarios to achieve such concentrations are few, but do include "leak-losses" from tank sluicing designed to dissolve salt-cake. Leak-losses should not induce ^{137}Cs mobilization if kept sufficiently dilute, and the waste sluicing process should be managed with this issue in mind. The adsorption data and models developed in this section can be used to identify concentration ranges of sluicing solutions that can be safely leaked to the vadose zone without fear of Cs mobilization.

D.3.1.5 Acknowledgement

This research was supported by the DOE Environmental Management Sciences Program (EMSP) through a FY 97 funded project: "Mineral Surface Processes Responsible for the Decreased Retardation (or Enhanced Mobilization) of ^{137}Cs From HLW Tank Discharges" (Zachara, Serne, Bertsch, Ellis).

D.3.1.6 References

Ainsworth, C. C., J. M. Zachara, K. Wagnon, and J. P. McKinley, 2001a, "Effect of Hypersaline and High pH Solutions on the Ion Exchange of Cs in Hanford Formation Sediments," *Soil Science Society of America Journal,* (Submitted).

Ainsworth, C. C., J. M. Zachara, J. P. McKinley, and K. Wagnon, 2001b, "Effect of Hyperalkalinity on Hanford Formation Sediments: Base-Induced Mineral Transformations," *Geochimica et Cosmochimica Acta,* (Submitted).

Brouwer, E., B. Baeyens, A. Maes, and A. Cremers, 1983, "Cesium and Rubidium Ion Equilibria in Illite Clay," *Journal of Physical Chemistry*, Vol. 87:1213-1219.

Comans, R. N. J., M. Haller, and P. De Preter, 1991, "Sorption of Cesium on Illite: Non-Equilibrium Behavior and Reversibility," *Geochimica et Cosmochimica Acta*, Vol. 55:433-440.

Cornell, R. M., 1993, "Adsorption of Cesium on Minerals: A Review," *Journal of Radioanalytical Nuclear Chemistry Articles*, Vol. 171:483-500.

Jones, T. E., R. A. Watrous, and G. T. Maclean, 2000, *Inventory Estimates for Single-Shell Tank Leaks in S and SX Tank Farms*, RPP-6285, Rev. 0, CH2M HILL Hanford Group, Inc., Richland, Washington.

Lichtner, P. C., 2001, *Estimating Tank Supernatant Liquid Compositions*, LA-UR-01-1403, Los Alamos National Laboratory, Los Alamos, New Mexico.

Poinssot, C., B. Baeyens, and M. H. Bradbury, 1999, "Experimental and Modeling Studies of Cesium Sorption on Illite," *Geochimica et Cosmochimica Acta*, Vol. 63:3217-3227.

Serne, R. J., H. T. Schaef, B. N. Bjornstad, B. A. Williams, D. C. Lanigan, D. G. Horton, R. E. Clayton, V. L. LeGore, M. J. O'Hara, C. F. Brown, K. E. Parker, I. V. Kutnyakov, J. N. Serne, A. V. Mitroshkov, G. V. Last, S. C. Smith, C. W. Lindenmeier, J. M. Zachara, and D. B. Burke, 2001a, *Characterization of Uncontaminated Sediments from the Hanford Reservation-RCRA Borehole Core and Composite Samples*, PNNL-2001-1, Pacific Northwest National Laboratory, Richland, Washington.

Serne, R. J., G. V. Last, G. W. Gee, H. T. Schaef, D. C. Lanigan, C. W. Lindenmeier, R. E. Clayton, V. L. LeGore, R. D. Orr, M. J. O'Hara, C. F. Brown, D. B. Burke, A. T. Owen, I. V. Kutnyakov, and T. C. Wilson, 2001b, *Geologic and Geochemical Data Collected from Vadose Zone Sediments from Borehole SX 41-09-39 in the S/SX Waste Management Area and Preliminary Interpretations*, PNNL-2001-2, Pacific Northwest National Laboratory, Richland, Washington.

Serne, R. J., H. T. Schaef, B. N. Bjornstad, D. C. Lanigan, G. W. Gee, C. W. Lindenmeier, R. E. Clayton, V. L. LeGore, M. J. O'Hara, C. F. Brown, R. D. Orr, G. V. Last, I. V. Kutnyakov, D. B. Burke, T. C. Wilson, and B. A. Williams, 2001c, *Geologic and Geochemical Data Collected from Vadose Zone Sediments from Borehole 299 W23-19 [SX-115] in the S/SX Waste Management Area and Preliminary Interpretations*, PNNL-2001-3, Pacific Northwest National Laboratory, Richland, Washington.

Serne, R. J., H. T. Schaef, G. V. Last, D. C. Lanigan, C. W. Lindenmeier, R. E. Clayton, V. L. LeGore, M. J. O'Hara, C. F. Brown, R. D. Orr, I. V. Kutnyakov, T. C. Wilson, D. B. Burke, B. A. Williams and B. N. Bjornstad, 2001d, *Geologic and Geochemical Data Collected from Vadose Zone Sediments from the Slant Borehole under SX-108 in the S/SX Waste Management Area and Preliminary Interpretations*, PNNL-2001-4, Pacific Northwest National Laboratory, Richland, Washington.

Sposito, G., 1981, "Cation Exchange In Soils: An Historical and Theoretical Perspective," In Chemistry in the Soil Environment, pp. 13-30, *American Society of Agronomy*, Madison, Wisconsin.

Zachara, J. M., S. C. Smith, J. P. McKinley, R. J. Serne, and P. L. Gassman, 2001, "Sorption of Cs^+ to Micaceous Subsurface Sediments from the Hanford Site," *Geochimica et Cosmochimica Acta*, (Accepted).

D.3.2 SPECTROSCOPIC STUDIES OF CS-CONTAINING MICAS

James P. McKinley[1], John M. Zachara[1], Steven C. Smith[1], Paul L. Gassman[1], Steven M. Heald[1,2], and Steven Sutton[2]

[1]Pacific Northwest National Laboratory, Richland, Washington 99352

[2]Argonne National Laboratory, Argonne, Illinois 60439

D.3.2.1 Introduction

The micas, including biotite and muscovite in Hanford sediments, have a crystallographic structure that strongly binds poorly-hydrated monovalent cations such as Cs^+. This structure consists of metal ions, principally Al and Si but including isomorphic substitutions of Fe and other metals, in sheets where they are octahedrally and tetrahedrally coordinated with O. These sheets are bound together by K to form a book structure; platy flakes of mica are common components of sedimentary rocks, and are plentiful in the unconsolidated sediments at Hanford. The retention of Cs^+ by micas has been intensively studied using contaminated sediments and laboratory specimens (Comans et al. 1991; Comans and Hockley 1992; Evans et al. 1983; Francis and Brinkley 1976; Sawhney 1970). The resultant conceptual model of the controls on Cs^+ mobility in the environment includes rapid initial and slower continued adsorption, with complimentary dual rates of desorption. Typically, a fraction of adsorbed Cs^+ is intransigent to desorption after an extended residence on the mica surface. The model relies on deductions about different binding sites on the mica surface that have not been documented by direct measurement. These include basal-plane exchange sites, chemically frayed sites at flake edges, and interlayer sites where Cs^+ could displace and substitute for K^+. The significance of the latter binding reaction (diffusion of Cs^+ into interlayer space by displacement of K^+) has been questioned, since solid phase diffusion constants yield infinitesimally slow rates of less than 1 nm per year (Comans et al. 1991).

We carefully examined the spatial residence of Cs^+ on the surfaces and the interiors of Hanford mica flakes to establish the relevance of the conceptual model to the different types of mica found in the Hanford and Ringold formations. Our methods were directed at several questions about the conceptual model and the classes of binding sites on the different mica surfaces. First, was Cs^+ preferentially sorbed to edge sites? If binding to frayed edge sites was stronger than binding to sites on the basal plane, then Cs^+ should be concentrated there. Second, are sites internal to mica flakes accessible to aqueous Cs^+? If these sites were accessible, then the reactive surface area on a mica flake would be much larger than would be estimated by consideration of the area on the edges and basal surfaces of a mica flake alone. We also hoped to observe the diffusive penetration of Cs^+ into interlayer space if it occurred more rapidly than calculated from theoretical considerations.

Our experiments could have significance for determining the fate of contaminant ^{137}Cs at Hanford. For instance, if we observed a heterogeneous localization of Cs at particle edges, the hypothesis of strong binding at edges would be confirmed. Strong binding to particle edges and rapid intraparticle migration (our experiments were short-term) would suggest that desorption and mobilization to future infiltrating waters or waste solutions would proceed slowly.

D.3.2.2 Experimental Procedures

Micas were hand picked from uncontaminated Hanford formation fine sands (35 to 55 ft below ground surface) collected during placement of RCRA monitoring wells around the S and SX tank farms boundary. Three phases were differentiated on the basis of color and morphology: clear muscovite, rust vermiculite, and black biotite. Small numbers of flakes were exposed to varying concentrations of $CsNo_3$ (0.001, 0.01, and 0.08 M) for 28 days, then washed in deionized water and air-dried. Some of the flakes were then mounted to glass slides (exposing the basal plane), while others were imbedded in epoxy and fixed to glass slides as polished, ca. 50 μm-thick thin sections, cut normal to the basal plane. All samples were sputter-coated with carbon to assure electrical conductivity.

The detection of Cs on solid surfaces relied on two types of spectroscopy. Electron microprobe (EMP) analysis used wavelength dispersive spectroscopy (WDS). X-ray microprobe (XMP) analysis used WDS and energy dispersive spectroscopy (EDS), alone and in combination. Both spectrophotometric methods detected induced, characteristic X-radiation. The WDS method relied on Bragg diffraction to eliminate interference from other elements by using a crystal of known d-spacing. Its advantage is a high resolution and low background, but it detects a single element at a time. The EDS discriminated between X-radiation from different elements on the basis of photon energy. Its advantage is the ability to detect and monitor a wide range of elements at once, but it has relatively poor bandwidth and a higher background than WDS.

The EMP analysis on a JEOL 8600 instrument used WDS spectrometers with 30 eV resolution that were tuned to wavelengths for Cs, K, and Fe Kα radiation and left fixed during image acquisition. The samples were examined using an accelerating potential of 20 KeV and a beam current of 20 nA, with the electron beam focused to ca. 50-nm on the sample surface. The beam position was digitally controlled and a digital compositional image of the sample was acquired by rastering the beam over the sample surface at, typically, 100-nm steps with a beam dwell time of 500-ms per step; images were collected overnight.

The x-ray microprobe measurements were performed at the PNC-CAT insertion device beamline (Heald et al. 1999) and at the GSE-CARS beamline, both at the ANL Advanced Photon Source (APS). Focusing was achieved using Kirkpatick-Baez mirrors. The entrance slits were set at 0.7 × 0.7 mm and the beam focused to 5 μm horizontally × 6 μm vertically. Typical flux was about 5×10^{11} ph/sec. The sample was rotated 30-degrees from normal incidence giving an effective horizontal spot of about 6-μm. The beam energy was selected with a Si (111) double crystal monochromator with an energy resolution of $\Delta E/E = 1.4 \times 10^{-4}$. The fluorescence from the sample was detected at PNC-CAT using either a 13-element solid-state detector with typical energy resolution of about 300 eV alone, or in combination with a bent Laue crystal detector (WDS) with 30 eV resolution. At GSE-CARS a tunable WDS detector identical to that used in EMP measurements was used. The Laue crystal detector was tuned to the Cs L_α fluorescence line, and was able to detect about 5×10^9 Cs atoms in the beam spot. Energy windows on the 13-element detector were set to record the fluorescence signals from K, Ca, Ti, Cr, Mn, and Fe as the sample was scanned. For imaging, the incident energy was set to 7110 eV. This only partially excites the Fe signal, avoiding detector saturation from high concentrations of Fe. The detection limit at GSE-CARS was approximately 1-ppm on a mass basis. Weight percent

concentrations were not measured. The detection of Cs was judged against background, and comparative results were obtained by examining and equalizing brightness levels between sample background areas.

D.3.2.3 Results

The laboratory-prepared mica samples with adsorbed Cs^+ were first examined by EMP. Micas that were exposed to different concentrations of $CsNO_3$ did not show discernible differences in surface concentrations; the images shown here all originated from the 0.08 M $CsNO_3$ suspensions. Figure D.3.2.1 is a plan view of biotite, vermiculite, and muscovite flakes, imaged according to the surface concentration of Cs and K. The three mineral species did not retain Cs equally. Biotite retained the highest quantity and had the highest spot concentrations, with Cs distributed very heterogeneously. The vermiculite surface had at best gentle gradations in Cs retention, which was very low. (During laboratory manipulation of "vermiculite" flakes, the surfaces readily delaminated, revealing a "biotite" core. The surface layers of vermiculite were not judged to be a barrier to solution contact with the biotite surface, and vermiculites were not studied further.) Of the micas examined, muscovite retained the least amount of Cs^+.

Figure D.3.2.1. Electron Microprobe Elemental Images of Cs-Exposed Micas.

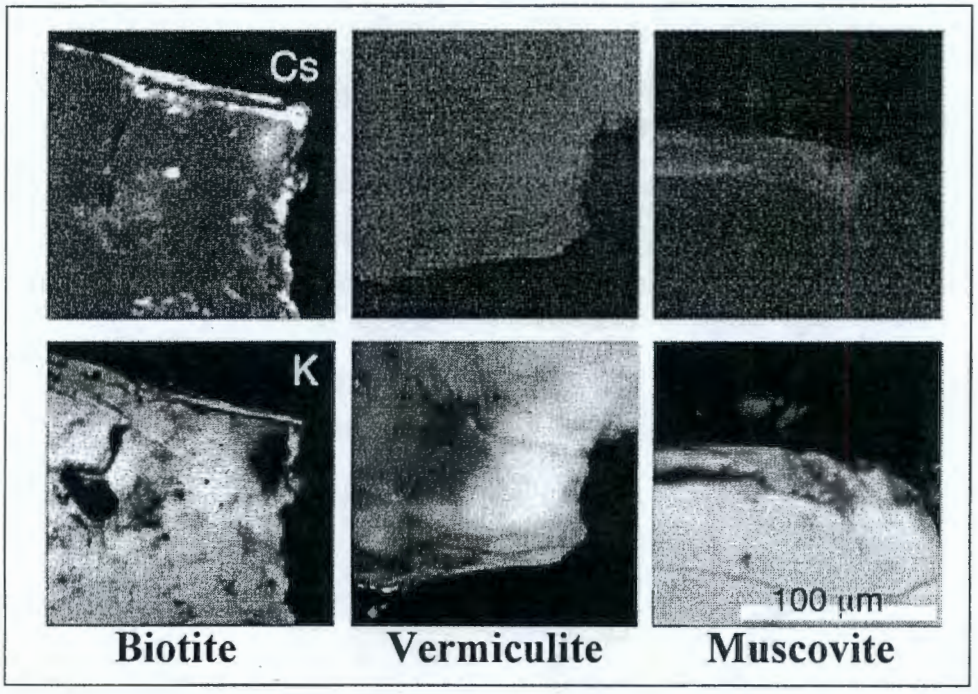

Note: Lower images of K abundance serve well as overall images of morphology. Cs is most abundant at flake edges, and is most abundant where K is depleted. Lower images of K abundance serve well as overall images of morphology. Cs is most abundant at flake edges, and is most abundant where K is depleted.

The Cs images in Figure D.3.2.1 were adjusted digitally for comparison purposes: the background intensity of each image was adjusted to a uniform level so that the relative brightness (Cs concentration) could be observed. The pattern of retention on the mica surfaces

indicated that edge sites strongly sorbed Cs^+. The altered edges in biotite and muscovite showed the highest concentrations. The basal plane sites also retained some Cs^+, as shown by the brightness above background across each flake. The images showing flake morphologies are the complimentary intensities of K radiation for each image. These images were adjusted digitally to best show the contrast of K concentrations within each flake, (e.g., to give a range of black-to-white in each image). On biotite and muscovite, Cs intensities were highest where K was depleted (dark areas in the K images). This was consistent with the hypothetical chemical "fraying" of edges through K^+ depletion, to provide sites with high adsorption affinity for Cs^+. The abundance of iron may also be a positive covariant with Cs.

Figure D.3.2.2 presents comparative images of the (unadjusted) intensities of K, Cs, and Fe for biotite and muscovite. As observed in Figure D.3.2.1, K the biotite surface was depleted in zones where Cs was concentrated. Fe also appeared to be in higher concentration where Cs was present, although the relationship was general; e.g., Fe was broadly more abundant on the right of the biotite flake where Cs was present in patchy concentrations. Because Fe was relatively abundant in biotite, subtle variations in its concentration–as correlated with Cs–were not readily apparent in these X-ray images. The relationship between Fe and Cs on the muscovite flake was easily seen, even though the intensities were lower. The muscovite was very thin, showing apparent transparency in the K image, and Fe was present at low concentrations typical of muscovite. The muscovite image was collected at twice the spatial resolution of the biotite. The relationship between K depletion and Cs abundance was obscured by the mottling caused by the abrupt and significant differences in thickness across the flake, but there was a clear correlation between the abundance of Fe and Cs. This relationship could be the result of weathering that solublized K and perhaps Si, leaving areas abundant in frayed edge sites and insoluble Fe(III).

Samples that were sectioned normal to the C axis after exposure to Cs^+ were used to investigate whether Cs^+ could access the interiors of mica flakes (Figure D.3.2.3, for muscovite). The K image clearly showed structural splaying of the mica edge by weathering. Cs was concentrated at the ends of weathered plates, but was also present above background on the flake interior in the relatively unweathered core (the possible presence of natural Cs in micas was investigated at the PNC-CAT–data not shown–and no detectable Cs was present in natural biotites or muscovites). Again, a correlation of Cs adsorption density with elevated Fe concentrations was observed. Fe has low abundance in muscovite, and the brightness levels in the image were manipulated to enhance contrast.

Figure D.3.2.2. Comparison of K, Cs, and Fe on the Surfaces of Biotite and Muscovite.

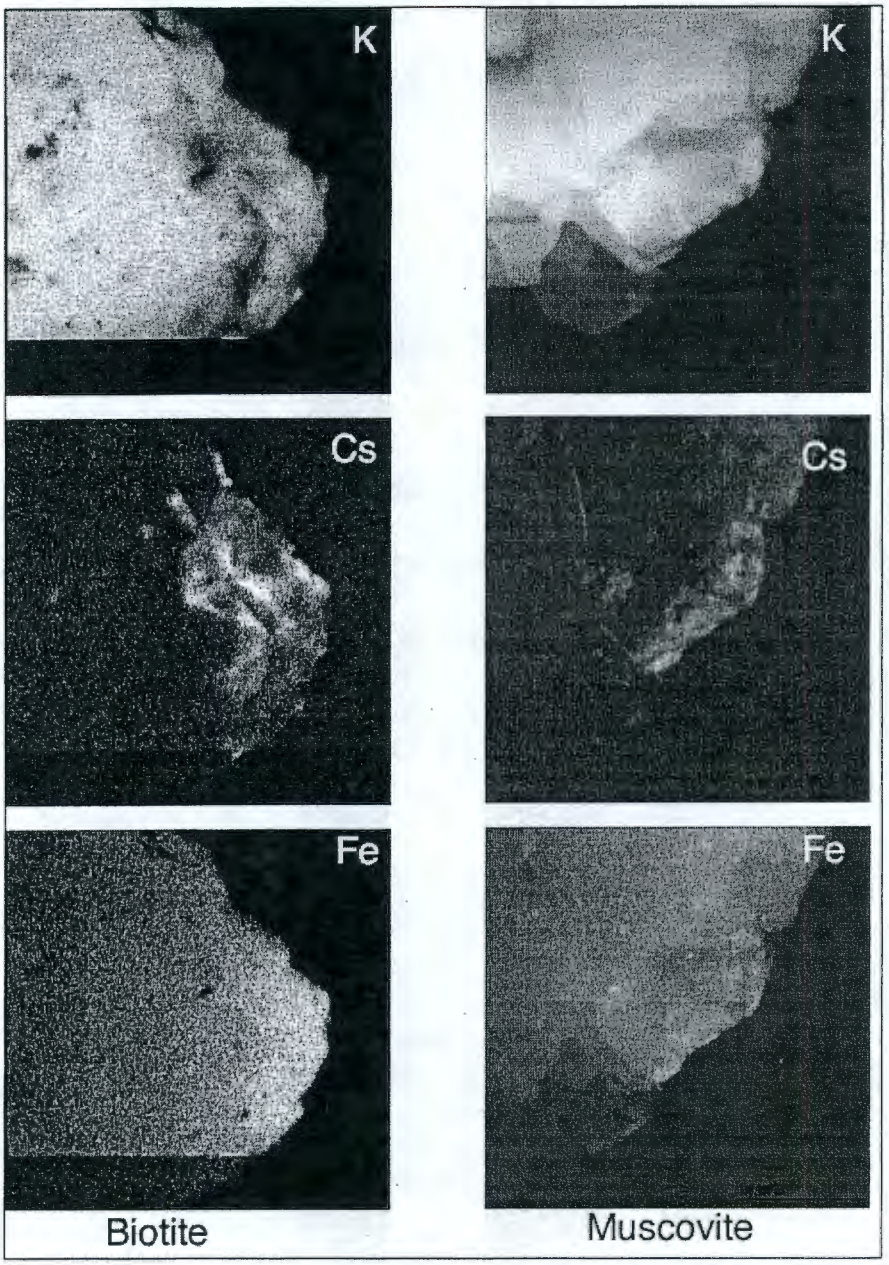

Note: Cs is concentrated where K is depleted and where Fe is enriched. The bottom of the biotite image was partially clipped during data collection. The muscovite image was collected at double the spatial resolution as the biotite image, and the muscovite flake is so thin near the bottom that it appears translucent.

Figure D.3.2.3. Muscovite Section Imaged as K, Cs, and Fe Abundance.

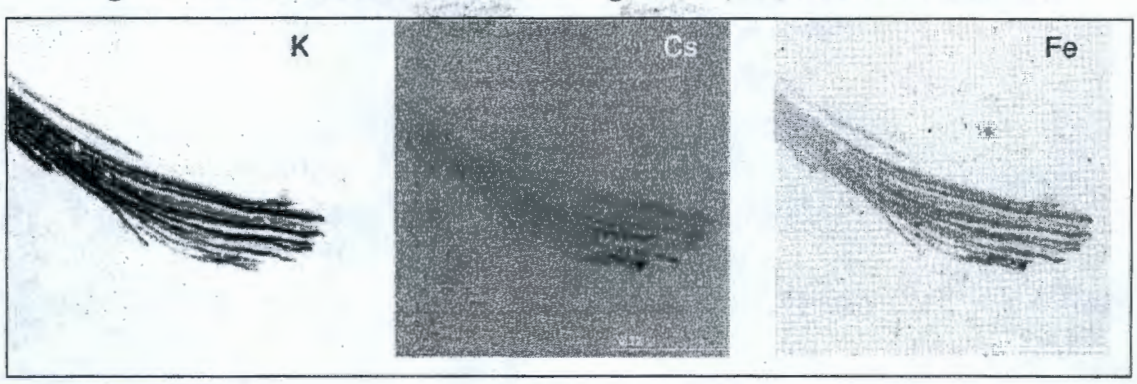

Note: The Mica Flake is weathered and its component plates are splayed where it has been most severely altered. Cs is distributed at the edges of Mica Plates. Fe and Cs are correspondingly enriched near the platelet ends.

There is an inherent difficulty in the use of EMP to define structural locations for metal adsorption (Figure D.3.2.3). Although the optical resolution of the images was high, the detection limit, defined by the ability to perceive Cs above background, was near the level at which Cs^+ was adsorbed. The Cs image in Figure D.3.2.3 was manipulated to show variations in abundance, but the contrast between background and signal was low. Investigations of the internal distribution of Cs in micas required a much lower detection limit, as supplied by the synchrotron-based technique, XMP. XMP provides great elemental sensitivity, but generally poor optical resolution; in some cases the inability to simultaneously monitor multiple signals is problematic. Figure D.3.2.4 allows a comparison of Cs distribution in sectioned biotite as mapped by EMP and XMP. The relatively low-magnification EMP image provided good detail of the distribution of Cs at edges and interlamellar channels, while the higher-magnification XMP image showed a continuum of Cs abundance with a local maximum within interlamellar space.

Figure D.3.2.4. (a) Electron Microprobe (EMP), and (b) X-ray Microprobe (XMP) Images of Cs^+ Distribution in Cross-Sectioned Biotite (brighter false colors denote higher abundance).

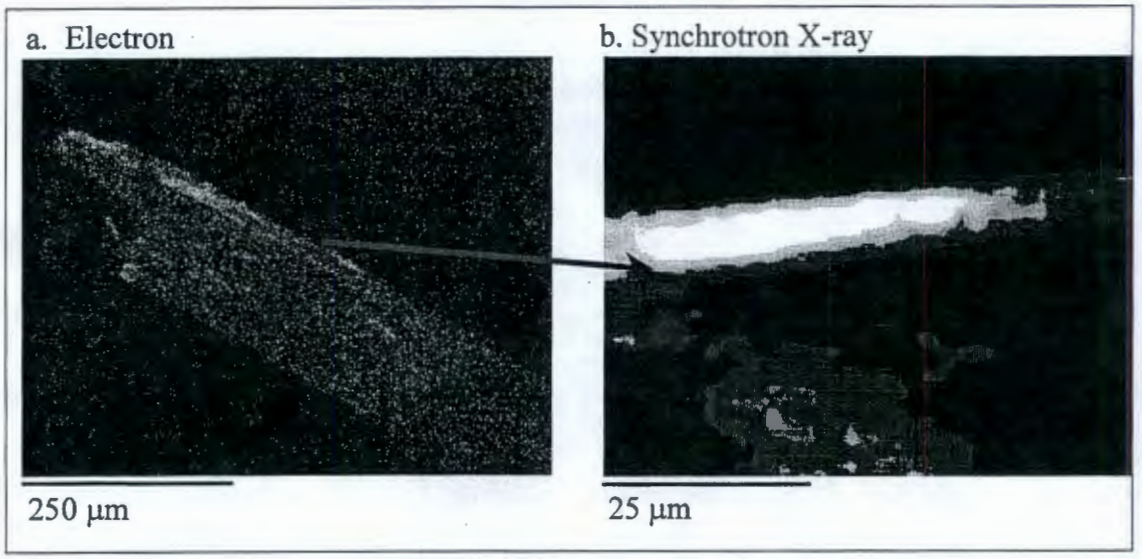

Note: Cs^+ localizes in select surface and edge regions, and in Interlamellar Channels. XMP provides far greater sensitivity.

The lower detection limits and the consequent increased range of abundance measurements afforded by XMP provided confirmation of the distribution of Cs with respect to morphologic features on flake surfaces. On muscovite (Figure D.3.2.5), Cs was concentrated at flake edges and along fractures or cracks on the muscovite surface. In cross section (Figure D.3.2.6), Cs was detected at an estimated operational detection limit of 1-ppm. This image showed several important details of Cs distribution, highlighted by detail insets. At the flake's edge, there are many zones of Cs localization; this is a confirmation of the observed concentration of Cs near the flake edge in Figure D.3.2.3. The sensitivity of XMP showed that these zones were discrete and spatially compressed. Also identified were laterally continuous zones of high Cs^+ adsorption density in the flake interior. These indicated that dissolved Cs^+ was able to access high-energy sorption sites in portions of the flake interior. This result was not expected, since solid-state diffusion limitations would prevent Cs^+ from accessing the interior in the absence of cracks or micro-fissures that would allow fluid transport. As seen dimly in the optical image, the flake has some internal open areas and Cs^+ may have been channeled to the flake interior along cracks and delamination features.

Figure D.3.2.5. Optical Image of Muscovite Flake with Cs Abundance Overlay.

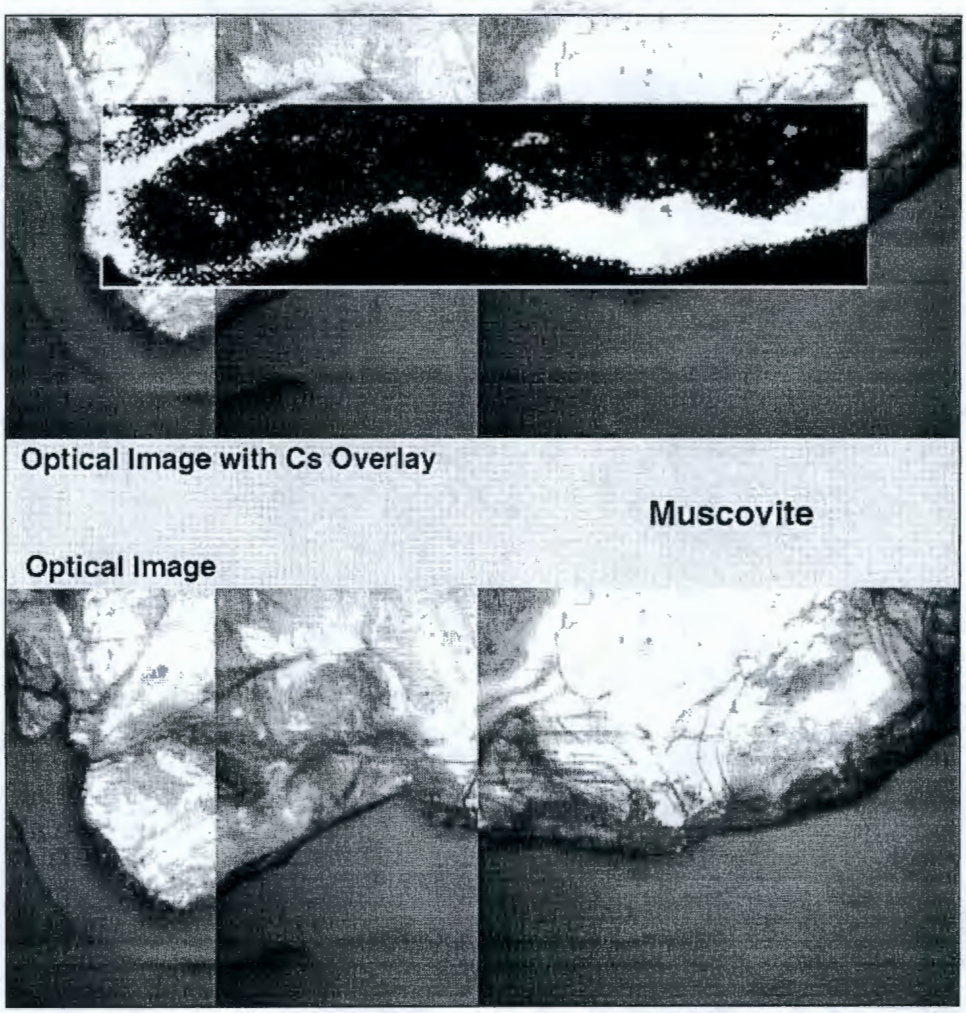

Note: Cs is most abundant at edges and along cracks on the flake surface. Blue is an indication of Cs below detection, white is maximum abundance. The XMP image is 1.3-mm across.

Figure D.3.2.6. The Abundance of Cesium Within a Muscovite Flake.

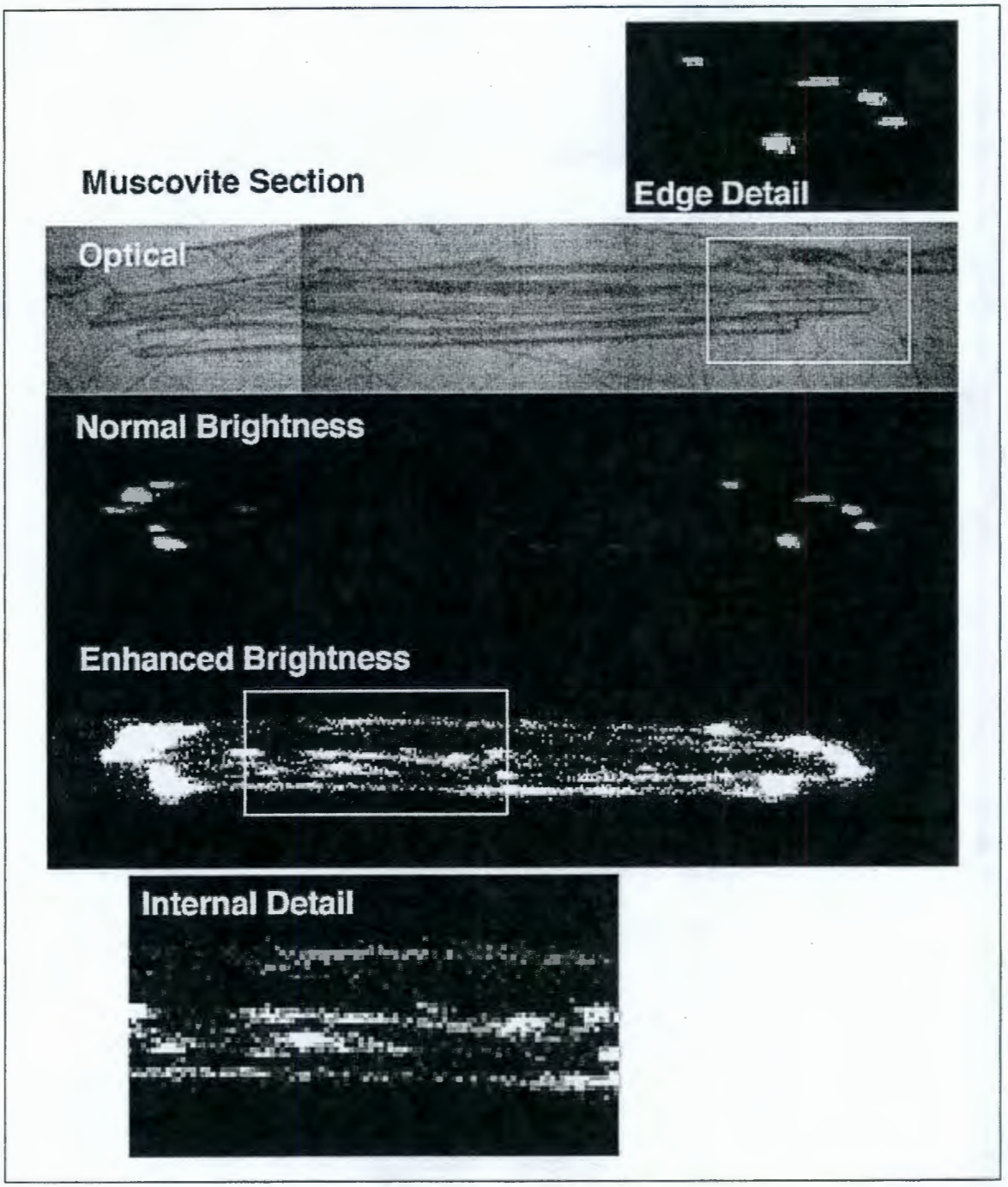

Note: The sectioned flake is ca. 1.2-mm long. Cs is concentrated at platelet edges on the ends of the flake, and within restricted zones in the flake interior.

The distribution of Cs within biotite flakes (Figure D.3.2.7) was similar to muscovite, but the relationship of Cs adsorption density to biotite's more complex chemistry was not clear. As with muscovite, Cs was concentrated at edges, flake ends, and along internal fissures. Cs was more abundant where K was depleted, as previously observed. However, Cs was also more abundant where either Ti or Fe were abundant. Both Fe and Ti are primary components of biotite, and the observed association could be related to the extent of alteration. Ferrous iron may have been dissolved and removed, or dissolved, oxidized, and precipitated to form zones of increased abundance; the weathering process could have formed zones of Fe enrichment or depletion. For Ti, however, dissolution and removal are unlikely, so the apparent enrichment of Ti may be an artifact of more extensive weathering, or the minor inclusion of a Ti specific phase such as ilmenite. If enriched Fe and Ti are taken as indicators of a molecular-level weathering environment, the relationship of Cs with Fe and Ti was consistent with the hypothesized binding of Cs at frayed edge sites.

Measurements of Cs distribution in contaminated samples from tank SX-108 were attempted. Detector sensitivity measurements using a liquid sample indicated a yield of 200 cts/sec when the X-ray beam illuminated 9×10^{10} atoms; the detection limit was taken as ca. 5×10^{9} Cs atoms within the beam. The tank SX-108 sample 07 had approximately 10^{14} Cs atoms, which, if homogeneously distributed, would present ca. 5×10^{7} atoms to the beam. A concentration factor of about 100 was thus required to reach the detection limit, and Cs was not detected. The calculations of Cs abundance may have been marginally incorrect and the necessary concentration factor was apparently not achieved.

D.3.2.4 Conclusions and Implications

Our experiments demonstrated that Cs^{+} was rapidly sorbed by micas extracted from the SX tank farm sediments. Biotite and muscovite each sorbed Cs^{+}, but biotite was more effective than muscovite. The adsorption behavior of Cs^{+} in Hanford sediments has been modeled with a two-site model containing sites of high affinity (mica edges) and low affinity (phyllosilicate basal planes), as described in Section D.3.1. After short contact in our experiments, Cs^{+} was concentrated at edge sites on mica particles and penetrated the mica flakes along planes of delamination and fractures to bind to sites in the flake interiors. The Cs was concentrated at high-energy sites that represented a small fraction of the total surface area. This work confirms the existence on micas of high-energy sites capable of sorbing and immobilizing contaminant Cs^{+} from tank waste leakage. The examination of contaminated sediments from SX-108 slant borehole, using microscopy and autoradiography, confirmed the importance of micas in immobilizing ^{137}Cs (Section D.3.5). The ability of Cs^{+} to access high energy sites internal to mica flakes markedly enhances the sorption capacity of micas, provides a transport limitation to desorption, and increases the overall immobilization of Cs^{+} in these sediments.

D.3.2.5 Acknowledgement

This research was supported in full by the DOE EMSP through a FY 97 funded project: "Mineral Surface Processes Responsible for the Decreased Retardation (or Enhanced Mobilization) of ^{137}Cs from HLW Tank Discharges" (Zachara, Serne, Bertsch, Ellis).

Figure D.3.2.7. XMP False Color Images of Sectioned Biotite: 780 × 165 Microns.

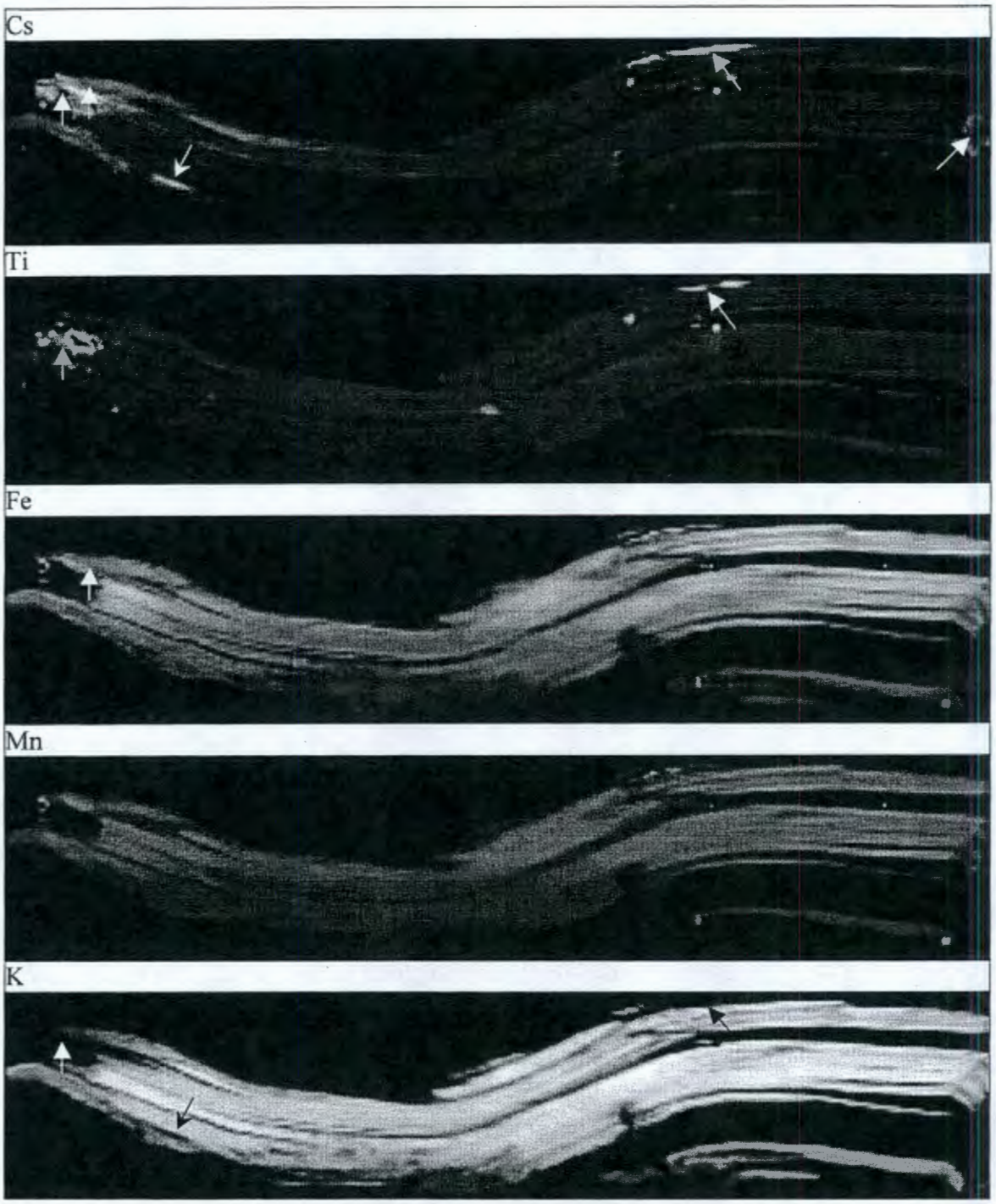

Note: Chemical abundances normalized to the color spectrum are, top to bottom, Cs, Ti, Fe, Mn, and K. Cs is concentrated where K is depleted and dither Ti or Fe are enriched.

D.3.2.6 References

Comans, R. N. J., M. Haller, and P. de Ptreter, 1991, "Sorption of Cesium on Illite: Non-Equilibrium Behavior and Irreversibility," *Geochimica et Cosmochimica Acta*, Vol. 55:433440.

Comans, R. N. J., and D. E. Hockley, 1992, "Kinetics of Cesium Sorption to Illite," *Geochimica et Cosmochimica Acta*, Vol. 56:1157-1164.

Evans, D. W., J. J. Alberts, and A. I. C. Roy, 1983, "Reversible Ion-Exchange Fixation of Cesium-137 Leading to Mobilization From Reservoir Sediments," *Geochimica et Cosmochimica Acta*, Vol. 47:1041-1049.

Francis, C. W., and F. S. Brinkley, 1976, "Preferential Sorption of ^{137}Cs to Micaceous Minerals in Contaminated Freshwater Sediment," *Nature*, Vol. 260:511-513.

Heald, S. M., D. L. Brewe, E. A. Stern, K. H. Kim, F. C. Brown, D. T. Jiang, E. D. Crozier, and R. A. Gordon, 1999, "XAFS and Micro-XAFS at the PNC-CAT Beamlines," *Journal of Syn. Rad.*, Vol. 6:347-349.

Sawhney, B. L., 1970, "Potassium and Cesium Ion Selectivity in Relation to Clay Mineral Structure," *Clays and Clay Minerals*, Vol. 18:47-52.

D.3.3 REACTIVE TRANSPORT EXPERIMENTS INVESTIGATING THE MIGRATION OF ^{137}CS IN SEDIMENTS BENEATH THE HANFORD SX TANK FARM

Susan Carroll[1], Carl Steefel[1], Pihong Zhao[1], and Sarah Roberts[1]

[1]Lawrence Livermore National Laboratory, Livermore, California 94550

D.3.3.1 Introduction

Recent observations in the S and SX tank farms show that cesium (^{137}Cs) has migrated to greater depths than expected (Serne et al. 2001a, b). Various explanations for enhanced Cs migration include: (1) physical processes such as fast flow pathways or bypassing of exchange sites in immobile zones, and (2) chemical processes associated with the very high salt contents and high pH of the tank fluids. Ion exchange processes are clearly indicated in the depth profiles of ^{137}Cs, and potassium (K), sodium (Na), calcium (Ca), and nitrate (NO_3, acting as a tracer) from the boreholes beneath tank SX-108 and tank SX-115. Below both tanks, Cs concentration peaks are retarded with respect to K and Na. The importance of cation concentration on ion exchange is clearly illustrated by the Na and tracer profiles beneath the tanks. Pore water with high Na concentrations at tank SX-108 showed little or no retardation of Na, as indicated by superimposed Na and NO_3 peaks. In contrast, at SX-115, Na was significantly retarded relative to tracers (NO_3 and Tc), presumably due to the lower Na concentration in the SX-115 waste supernatant compared to SX-108 waste supernate. Ca and Mg form very distinct peaks at the leading edge of the Na front under both tanks SX-108 and SX-115. Observations such as these, led Zachara (2001), Section D.3.1, to conduct a series of systematic adsorption experiments over a wide range of Cs and salt concentrations to develop an ion exchange model that could be used to predict Cs migration beneath the Hanford tank farms.

We report reactive transport experiments of Cs sorption to Hanford sediments, with the specific objective of testing the applicability of cation exchange models derived from batch experiments to calculate Cs mobility beneath the Hanford tank farms. These experiments couple Cs exchange thermodynamics determined for Hanford sediments based on the batch experiments (Zachara et al. 2001) and flow and transport using a reactive transport model (Steefel 2001). Our experiments included: (1) binary Na–Cs exchange experiments at two different high salt and Cs concentrations, (2) ternary K–Na–Cs exchange experiment, and (3) high base experiment in which mineral dissolution and precipitation affect Cs exchange. In addition to allowing the testing of the batch-derived exchange model, these experiments provide a more direct measure of Cs retardation in Hanford sediments, which can be used in field-scale analyses of transport (Sections D.3.7 and D.7.4). Our experiments investigated the reversibility of Cs exchange dominated by sorption to high affinity, frayed-edge sites on micas (FES sites), and to basal layers of expandable clay minerals such as smectite and vermiculite (clay sites). Results of the high salt reactive transport experiments form the basis for extending the cesium exchange model to reactive, hot tank wastes containing high base [OH^-].

D.3.3.2 Experimental and Modeling Procedures

D.3.3.2.1 Column Experiments. A total of 6 one-dimensional column experiments using uncontaminated Hanford sediments were carried out at 25 °C to investigate the reactive transport of Cs (Table D.3.3.1). The "Above B" Hanford formation composite (D.2.2, D.3.1.2.1) was used as the experimental medium. The sediment was lightly crushed to pass through a 2-mm sieve, air-dried, and mixed thoroughly. No further fractionation of the sediments was conducted. The sediments were loaded into a reactor column (1.06 cm × 15.27 cm) filled with distilled and deionized water. Sediment density was determined to be 2.67 g/cm^3 by volume displacement. The reactive transport experiments consisted of three phases. In the pretreatment phase, the background electrolyte was passed through the column to replace K, Ca, and Mg with Na on the sediment exchange sites. Complete exchange was achieved in 7 to 10 pore volumes. The pretreatment phase of the experiment also provided an independent measure of the sediment cation exchange capacity (CEC). The pretreatment phase was followed by the Cs sorption experiment in which a CsI and $NaNO_3$ (or mixed KNO_3-$NaNO_3$, or NaOH) solution was passed through the sediment column to measure Cs retardation from the breakthrough curve. The final phase was a Cs desorption experiment in which the background electrolyte solution was passed through the sediment column to displace Cs from the exchange sites to assess the reversibility of the cation exchange reaction. Iodide behaved as a non-reactive tracer and was used to obtain a dispersivity of 1 cm. Aqueous samples exiting the column were analyzed for pH, Al, Ca, Cs, Fe, K, Mn, Mg, Na, and Si. The post-mortem sediments were examined by SEM/EDS and by X-ray diffraction for evidence of mineral reaction.

Table D.3.3.1. One–Dimensional Cesium-Reactive Transport Experiments.

Exp. No.	Inlet salt solution	Inlet Cs M	Flow rate (ml min^{-1})	Darcy flux (cm min^{-1})	Sediment: solution (g/L)	% Porosity
1	1 M $NaNO_3$	10^{-4}	0.1	0.025	3529.0	38.2
2	1 M $NaNO_3$	10^{-4}	0.02	0.113	3682.9	40.4
3	5 M $NaNO_3$	10^{-4}	0.1	0.121	3921.8	40.5
4	1 M NaOH	10^{-4}	0.02	0.023	4195.1	38.9
5	1 M $NaNO_3$	5×10^{-7}	0.1	0.113	3818.1	41.1
6	0.1 M KNO_3 0.9 M $NaNO_3$	10^{-4}	0.1	0.113	3483.5	43.4

The sediment cation exchange capacity of the unreacted sediments were measured from triplicate ^{22}Na isotopic equilibrium experiments. Sodium saturated sediments were rinsed repeatedly with 2 mM $NaNO_3$ until a constant conductivity was reached to remove excess Na from the sediment pore water. The dry, treated sediments were then reacted in 2 mM $NaNO_3$ spiked with ^{22}Na (10^5 dpm/ml ^{22}Na-$NaNO_3$) for 24 hours. After equilibration, the suspensions were centrifuged, and the supernatant was filtered and analyzed for ^{22}Na by liquid scintillation and total Na by ICP-AES. The sediment cation exchange capacity was also measured from the equivalent sum of Ca, K, Mg, and Na eluted with $NaNO_3$ and KNO_3 flushes of the sediments.

D.3.3.2.2 Modeling. Modeling of Cs transport in the column experiments was performed with the reactive transport code CRUNCH (Steefel 2001). The code includes the capability for simulating multi-component ion exchange coupled to aqueous complexation and mineral precipitation and dissolution. Two sets of input were used to carry out the reactive transport simulations. One set of selectivity coefficients and exchange site concentrations were determined from a global fit of all of the batch Cs-Na, Cs-K, and Cs-Ca exchange experiments (Zachara et al. 2001) at background electrolyte concentrations of 5 M or less (Figure D.3.3.1) (these are referred to as the "batch parameters"). The other set of selectivity coefficients and site concentrations was determined from batch and column experiments, with strong weighting of the column experiments in the optimization procedure (these are referred to as the "column parameters"). The fitting was carried out with the general fitting code PEST used in conjunction with speciation calculations carried out by CRUNCH. In this way, the resulting parameter set is fully compatible with the reactive transport simulations of Cs migration in both the column experiments and the field. The difference between the fits to the batch data presented here and those presented by (Zachara et al. 2001) is the inclusion of activity coefficient corrections and aqueous complexation in the fitting procedure presented here.

Figure D.3.3.1. Comparison of Cesium Exchange to Hanford Sediments Measure in Binary Batch Experiments (symbols) with Multi-Cation Exchange Model (solid lines) with Selectivity Coefficients and Exchange Sites Derived from a Global Fit to all of the Binary Data Shown in this Figure. Batch Data are from Zachara et al. (2001).

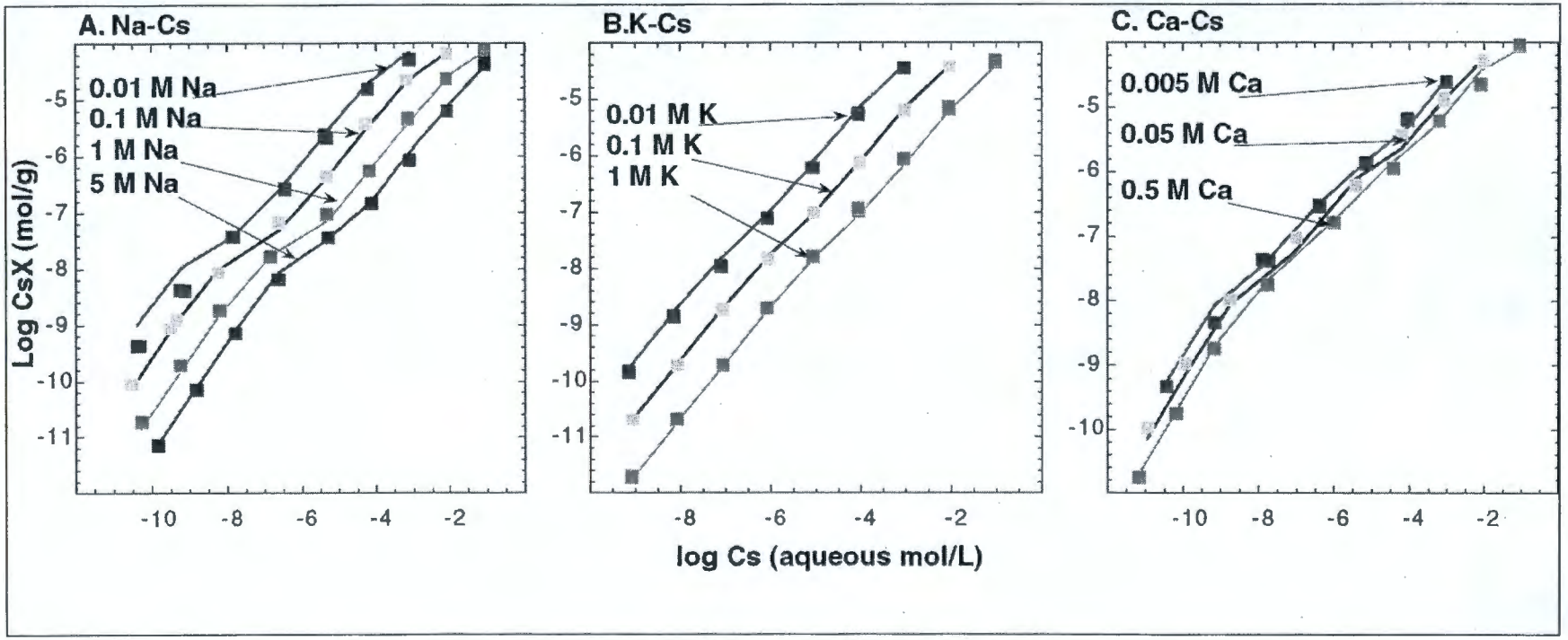

The selectivity coefficients in Table D.3.3.2 were fit assuming the Gapon activity convention:

$$Cs^+ + M_{1/m}X \leftrightarrow CsX + {}^1\!/_m M \qquad (D.3.3.2.1)$$

where M is the exchanging cation (Na^+, K^+, Ca^{2+}) and m is its charge (Appelo and Postma 1996). The exchange reactions can then be used to write a standard mass action equation for binary Cs-M exchange:

$$K_{M/Cs} = \frac{[M_{1/m}X][Cs^+]}{[CsX][M]^{1/m}} \qquad (D.3.3.2.2)$$

Table D.3.3.2. Cesium Exchange Selectivity Coefficients, Ion Pair Formation Constants, and CEC Derived From a Global Fit to Zachara et al. [8] Batch Binary Exchange Experiments (Batch Parameters) and Derived From Fits Heavily Weighted with Column Exchange Experiments (Column Parameters).

Exchange reaction	Batch parameters Log K	Column parameters Log K
$NaX1 + Cs^+ = Na^+ + CsX1$	6.96	6.85
$NaX2 + Cs^+ = Na^+ + CsX2$	3.57	3.00
$NaX3 + Cs^+ = Na^+ + CsX3$	1.64	2.10
$KX1 + Cs^+ = K^+ + CsX1$	4.76	4.50
$KX2 + Cs^+ = K^+ + CsX2$	1.44	3.77
$KX3 + Cs^+ = K^+ + CsX3$	0.95	0.70
$Ca_{0.5}X1 + Cs^+ = 0.5Ca^{2+} + CsX1$	7.53	7.13
$Ca_{0.5}X2 + Cs^+ = 0.5Ca^{2+} + CsX2$	4.55	6.46
$Ca_{0.5}X3 + Cs^+ = 0.5Ca^{2+} + CsX3$	1.44	1.58
$NaNO_3(aq) \rightarrow Na^+ + NO_3$-	0.33	0.26
$CsNO_3(aq) \rightarrow Cs^+ + NO_3$-	0.47	0.50
Bdot parameter (Cs-X)	1.66E-04	-8.90E-02
Exchange site	**CEC (μeq g^{-1})**	**CEC (μeq g^{-1})**
Site 1	0.027	0.037
Site 2	1.43	0.14
Site 3	86.6	102

Multiple exchange sites were needed to capture the large range in Cs- K_d as a function of Cs concentration. The need for multiple sites with differing affinities can also be seen by plotting conditional equilibrium constants as was done by (Zachara et al. 2001; Section D.3.1) who used a 2-site model to fit the data. Zachara et al. (2001) have presented the physical evidence for the

existence of at least two sites with very different affinities for Cs, one associated with the frayed edges of micas and the other with the surfaces of expansible layer silicates. We have fitted Cs exchange with a three-site model because it provides a substantially better fit of the Cs-Ca and, to a lesser extent, the Cs-Na exchange data. The three-site model was used because of the improvement it gave in matching the batch data–there is no clear physical evidence for more than two distinct sites actually present in the Hanford sediments. Detection of ^{137}Cs on mica minerals, but not on smectite minerals, from contaminated sediments beneath tank SX-108 (McKinley et al. 2001) may indicate that the very high Na concentrations estimated by Lichtner (Section D.7.3) in this tank leak suppressed Cs sorption to the basal sites on smectites, thereby leaving the frayed-edge sites on the micas as dominant Cs exchange mechanism. The observation from SX-108 sediments that Cs is associated almost exclusively with micas may not hold for other tank leaks where competing cation concentrations are lower than they are at tank SX-108.

We chose to fit the cation exchange capacity (CEC) rather than using an independently determined value, because there is significant uncertainty in the CEC determined for these Hanford sediments. The highest CEC value was determined by cation elution during preliminary washes of the sediment (CEC = 99 ± 13 μeq/g) [this study]. The next highest CEC value was determined by extraction of K by NH_4 acetate (CEC = 83 μeq/g) [8]. The lowest CEC values were determined by ^{22}Na and ^{45}Ca isotopic equilibria measurements (CEC = 46 ± 3 μeq/g) (Zachara et al. 2001, this study). Additional experiments are planned to help resolve the CEC so that it can be imposed as an independent constraint in the fitting of the exchange selectivity coefficients. The CEC of high affinity sites (as opposed to the total CEC) still needs to be fitted, however, since this cannot be determined with conventional CEC determinations. With the current model, the fits are non-unique as is shown by strong inverse correlation between selectivity coefficients for a particular site and the CEC of that site.

We used a standard Debye-Huckel formulation for activity coefficients augmented with fitting parameters for ion pair formation to describe solution activities accurately in the highly concentrated and variable Hanford system. Free cation activities were calculated by adjusting the log Ks for the ion pairs $CsNO_3(aq)$, $Ca(NO_3)_2(aq)$, and $NaNO_3(aq)$ to match ion activities determined with the Pitzer approach as implemented in the code GMIN (Felmy 1995). In this respect, activity coefficients for the Debye-Huckel and Pitzer formulations do not match, but their ion activities do match. It was also necessary to include an empirical activity coefficient correction for the various Cs exchange species in order to capture the ionic strength dependence of the exchange. This took the form of a "Bdot" correction affecting only the activity of the exchange species:

$$\ln \gamma_{Cs-X} = BI \qquad \text{(D.3.3.2.3)}$$

D.3.3.3 Key Results

D.3.3.3.1 Dependence of K_d on Cesium and Competing Cation Concentration. The refitting of the batch data (Zachara et al. 2001) confirmed the strong variability of the Cs-K_d for Hanford sediments. The dependence of the Cs- K_d on the other cations (Na^+, K^+, and Ca^{2+}) is predicted by the ion exchange theory. We can rewrite Equation D.3.3.2.2 to obtain an expression for the dimensionless form of the distribution coefficient, K'_d:

$$K'_d = \frac{[CsX]}{[Cs^+]} = \frac{1}{K_{M/Cs}} \frac{[M_{1/m}X]}{[M]^{1/m}} \qquad \text{(D.3.3.3.1)}$$

It follows that Cs retardation depends on the concentration of the competing ion because Cs retardation is described by:

$$R = 1 + K'_d = 1 + \frac{\rho_B K_d}{\phi} \qquad \text{(D.3.3.3.2)}$$

where ρ_B is the bulk dry density of the sediment, and ϕ is the porosity. This is shown graphically by plotting the Cs-K_d versus Na concentration in solution (Figure D.3.3.2b). The Cs- K_d is also dependent on the Cs concentration in solution, because the different sites have different affinities for Cs exchange. If aqueous Cs concentrations are close to the concentration of the high affinity frayed-edge sites, then the retardation (or K_d) for Cs will be correspondingly high. However, if Cs concentrations significantly exceed the concentration of the frayed-edge sites, the K_d will be lower because Cs adsorption occurs on low affinity sites on the basal plane of expansible layer silicates. Figure D.3.3.2b shows the effect of Cs concentration on the Cs-K_d.

D.3.3.3.2 Multi-Cation Cesium Exchange Model—Batch-Derived Fits. Our results suggest that the Cs-Ca-Na-K exchange model derived from batch experiments predicts Cs retardation in Hanford sediments when Na or K concentrations are high enough to compete strongly for exchange sites. However, at lower Na and K concentrations, the model based on batch-fitted parameters underpredicts Cs retardation by 25 to 55 percent. In Figure D.3.3.3, we plot the model predictions and the experimental breakthrough curves of Cs. Retardation factors derived from the breakthrough data are summarized in Table D.3.3.3. In high salt solutions, 5 M $NaNO_3$, with relatively high Cs concentrations, 10^{-4} M, retardation is about 8 for both the model prediction and experiment. There is also a good match between model prediction and experiment in solutions containing K (0.1 M KNO_3, 0.9 M $NaNO_3$, and 10^{-4} M Cs), yielding a Cs retardation of about 12. However, in 1 M $NaNO_3$ solutions with no K, the model under predicts Cs retardation at both high and low Cs concentrations. In the 1 M $NaNO_3$ experiments, Cs retardation is 41 at 10^{-4} M Cs and 282 at 5×10^{-7} M Cs, compared to predicted retardation equal to 26 and 226, respectively.

Table D.3.3.3. Comparison of Cesium Retardation Model.

Exp. No.	Inlet salt solution	Inlet Cs M	Observed retardation	Model retardation batch fit	Model retardation column fit
1	1 M $NaNO_3$	10^{-4}	42.9	26.9	36.7
2	1 M $NaNO_3$	10^{-4}	40.3	26.4	36.6
3	5 M $NaNO_3$	10^{-4}	7.6	8.0	7.1
4	1 M NaOH	10^{-4}	38.7	32.4	42.5
5	1 M $NaNO_3$	5×10^{-7}	282.2	225.6	276
6	0.1 M KNO_3 0.9 M $NaNO_3$	10^{-4}	12.6	11.2	11.6

Figure D.3.3.2. The Dependence of Cs K_d on Dissolved Cs (A) and Sodium (B) Concentrations Calculated with the Multi-Cation Exchange Model.

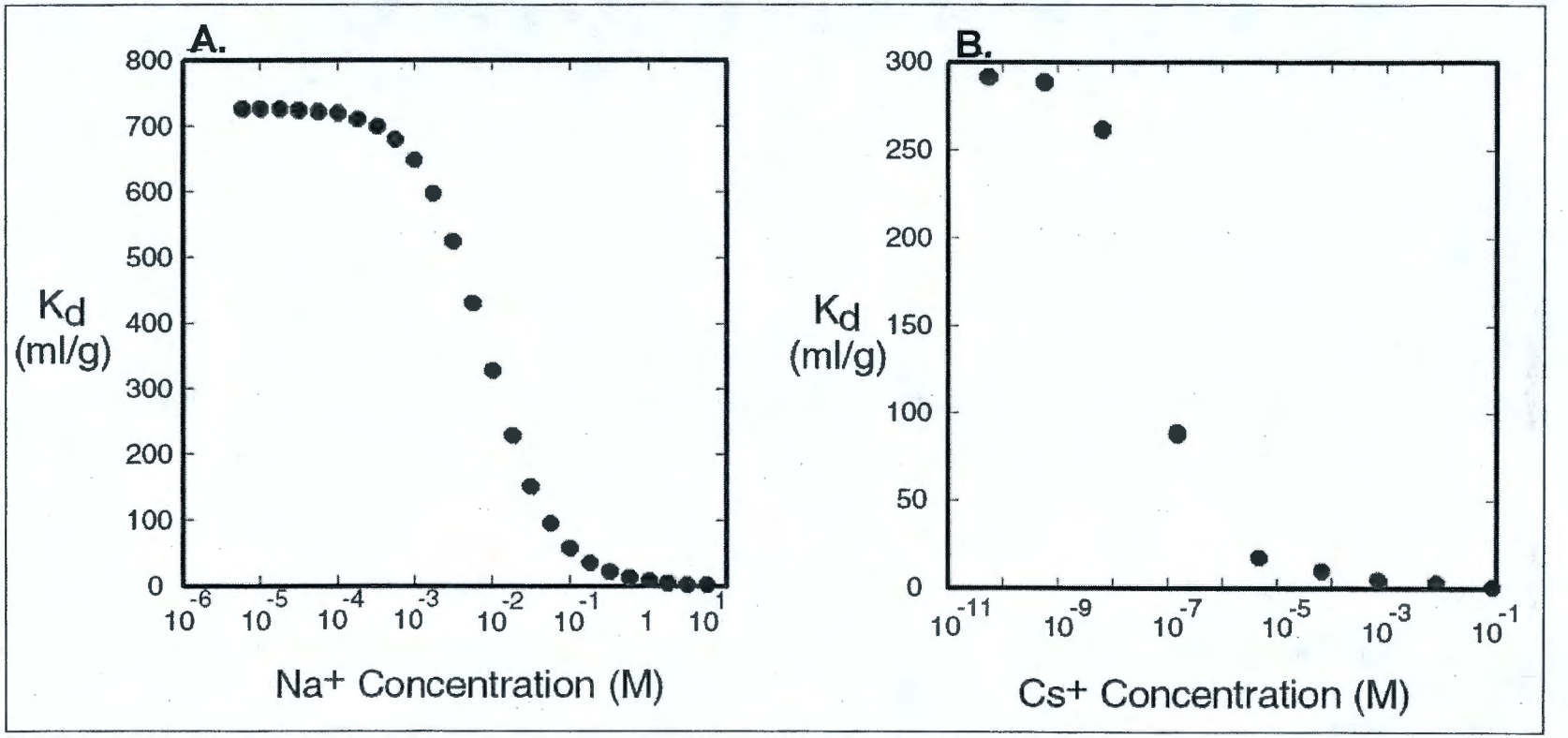

Figure D.3.3.3. Cesium Reactive Transport Through Hanford Sediments in $NaNO_3$ and Mixed $(K,Na)NO_3$ Solutions.

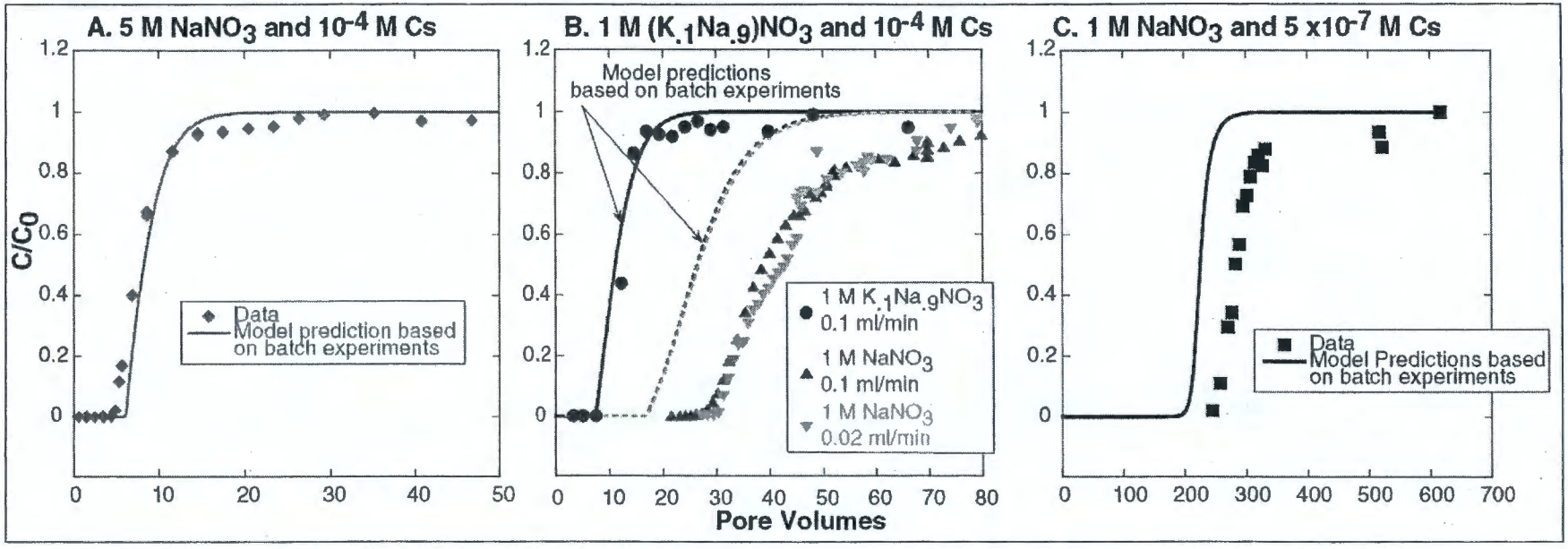

Note: Comparison of cesium breakthrough curves predicted by the multi-cation exchange model derived from batch experiments (lines) with experiments (symbols).

The variable agreement between the model predictions and experiments appears to be partly an artifact of fitting the batch data on a logarithmic scale. Our fits to the batch data on a log-log plot are visually very close (with the exception of 0.01 M Cs-Na exchange), with discrepancies on the order of 0.1 log unit or less. The global fit of the batch data slightly underpredicts exchange in the 1 M $NaNO_3$ batch experiments and slightly overpredicts exchange in the 5 M case. Although these discrepancies are small in log space, they translate into significant differences in the prediction of the total mass of exchange Cs and the resulting retardation in the column experiments. We evaluated this effect by weighting the batch exchange experiments at the $NaNO_3$ concentration corresponding to the conditions of the column experiment (Table D.3.3.4). Weighting the data in this fashion improves the match between the observed and calculated retardation, but it does completely eliminate the discrepancies. Additionally, this approach limits the global application of the ion exchange model over a wide range of solution compositions that are required to model Cs migration beneath the Hanford tanks.

Table D.3.3.4. Observed versus Calculated Retardation of Cesium for Case: Slowly Reversible Sites are Included in the Batch Fit Optimized for 1 M Salt Concentrations

Exp. No	Inlet salt solution	Observed retardation	Model retardation[a]	Model retardation[b]
1	1 M $NaNO_3$	42.8	34.3	
2	1 M $NaNO_3$	40.3	35.5	40.5
3	5 M $NaNO_3$	7.6	8.3	
5	1 M $NaNO_3$	282	230	262
6	0.1 M KNO_3 0.9 M $NaNO_3$	12.6	11.3	

[a]Batch fit optimized for salt concentration.
[b]Batch fit corrected for irreversible sites and optimized for salt concentration.

D.3.3.3.3 Multi-Cation Cesium Exchange Model—Column-Weighted Parameters. To further evaluate the ion exchange model, we modify our Cs-Na-K-Ca exchange model by fitting the selectivity coefficients and the cation exchange capacity with weighted results from our column experiments (Figure D.3.3.4 and Table D.3.3.2). Batch experiments are included in the fitting procedure because the column experiments do not cover the entire range of cation concentrations. The inclusion of the column-weighted data improves the match between predicted and observed Cs retardation in the 5 M $NaNO_3$, 1 M $NaNO_3$, and the mixed 0.1 M KNO_3 and 0.9 M $NaNO_3$ experiments. There are two significant differences between the model parameters fitted with the batch data and those fitted with the column data. One is the increase in the concentration of site 3 from 88.6 to 102 μeq/g. A second difference is the higher affinity for Cs over Na on site 3 where the log K increases from 1.64 to 2.10. Both of these predict a higher overall mass of Cs on exchange sites for a given aqueous concentration of Cs and thus higher Cs retardation. Changes in the selectivity coefficients for the Cs-K and Cs-Ca exchange reactions are directly linked to the higher CEC in the column-derived parameters. This reflects the non-uniqueness of the model, since the column experiments (102 μeq/g) provided no new data for the Cs-K-Ca systems (in the experiment containing K, the experiment agreed with the

model prediction based on the batch data). The higher CEC determined from a fit of the column experiments (102 μeq/g) is supported by the CEC estimated from the pretreatment phase of the column experiments (Figure D.3.3.5). The equivalent concentrations of eluted K, Ca, Mg, and Na in the pretreatment phase using 1 M $NaNO_3$ and 1 M KNO_3 in multiple column experiments equals 99 ± 13 μeq/g. However, caution must be used in interpreting results based on the CEC alone because of the non-uniqueness of the fitting parameters—it is the combination of fitted CEC and selectivity coefficients that determine the predicted cesium retardation. It is doubtful that soluble salts contilente to an erroneously large CeC, because cation concentrations measured in sediments in contact with distilled waters are quite small.

D.3.3.3.4 Cesium Exchange to Frayed-Edge Sites on Micas and to Basal Layers of Expansible Layer Silicates. We have tested the Cs exchange model in the Cs-Na binary system at two different initial Cs concentrations (5×10^{-7} and 10^{-4} M) and two different salt concentrations (1 and 5 M $NaNO_3$). These two Cs concentrations were selected to test the ability of the model to predict Cs mobility where retardation is dominated by exchange to the less abundant, high affinity, frayed-edge sites on micas (5×10^{-7} M) and by sorption to the abundant, lower affinity exchange sites on expansible layer silicates (10^{-4} M) (Figure D.3.3.4). We find good agreement between the revised model predictions and the experiment for Cs retardation (Figure D.3.3.4), indicating that this model may be applied over the range of Cs and salt concentrations present in WMA S-SX tank wastes leaking into the vadose zone sediments.

D.3.3.3.5 The Effect of Potassium on Cesium Exchange in High Salt Solutions. Potassium will enhance the mobility of Cs because it has a higher affinity for the exchange sites on micas and clays than does either Na or Ca. Our multi-cation exchange model predicts that in solutions with equal concentrations of K and Cs, K will displace about 10% of the Cs on the exchange sites (batch parameters, Table D.3.3.3). Since the tank wastes contain elevated concentrations of K as well as in Na (Section D.7.3), we conducted exchange experiments in the K-Cs-Na system to further test the ion exchange model. Another source of K in the contaminant plume is from the dissolution of mica and feldspar minerals in the highly alkaline and thermally hot waste stream. Validation and improvement of the ion exchange model with ternary K-Cs-Na experiments at neutral pH are needed before it can be realistically applied to high-base experiments.

Figure D.3.3.4 compares the column transport behavior of Cs in binary (Cs-Na) and ternary (K-Cs-Na) electrolyte systems. The initial Cs concentration (10^{-4} M) and total salt concentration (1 M) are the same in both experiments. In salt solutions containing 0.1 M KNO_3 and 0.9 M $NaNO_3$ Cs retardation is one-third of its retardation in 1 M $NaNO_3$. We see excellent agreement between the predicted breakthrough and the experimental breakthrough.

D.3.3.3.6 Cesium Exchange in High-Base Solutions. It is important to establish whether the multi-cation Cs exchange model can be extrapolated to the high-base concentrations reported to exist in the S and SX tank farms waste (Section D.7.3). While pH does not have a direct effect on Cs exchange, it can have an indirect effect through aqueous complexation or mineral dissolution. In the nitrate-dominated system considered here, the pH dependence of complexation is minimal (although there is some complexation as $CsOH_{aq}$ and $NaOH_{aq}$). Mineral dissolution and precipitation reactions can affect Cs mobility by altering the number and distribution of sites and by providing a source for dissolved K that competes for Cs exchange.

Figure D.3.3.4. Cesium Reactive Transport Through Hanford Sediments in $NaNO_3$ and Mixed $(K,Na)NO_3$ Solutions. Comparison of Cesium Breakthrough Curves Predicted by the Multi-Cation Exchange Model Derived from Fits Weighted to the Column Experiments (lines) with Experiments (symbols).

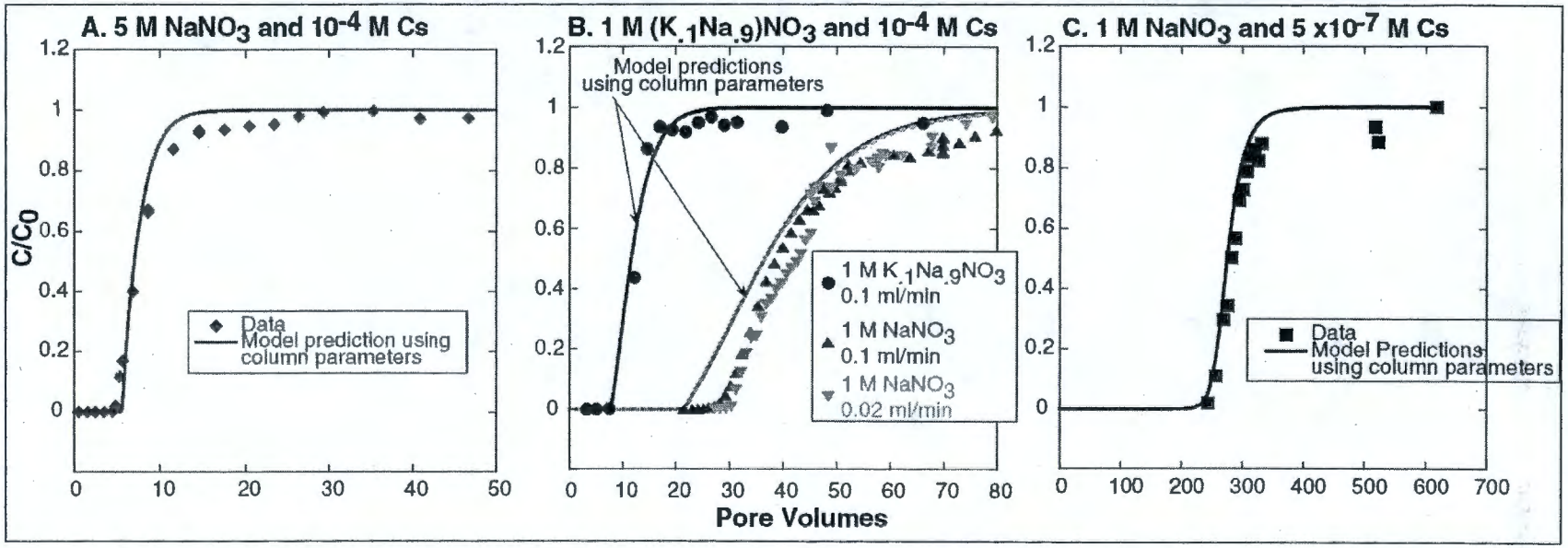

Figure D.3.3.5. The Caption Exchange Capacity Measured From the Equivalent Concentration of Ca, K, Mg, Exchanged for Na in 1 M $NaNO_3$ Flushes of the Sediment Column, and Na Exchange for K in 1 M KNO_3 Flushes of the Sediment Column.

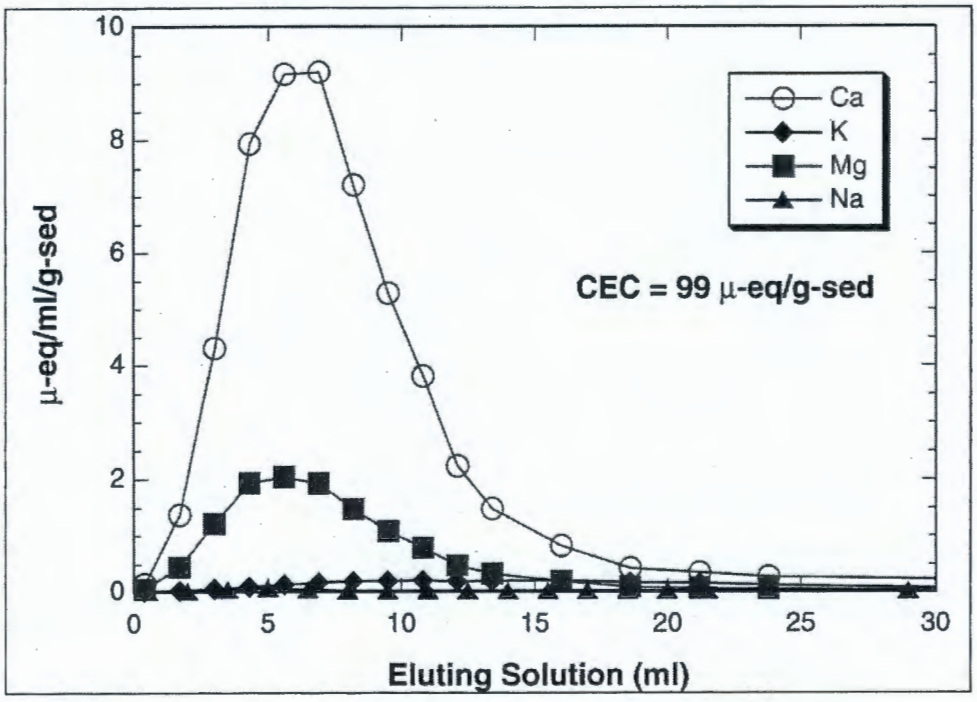

Note: The $NaNO_3$ and KNO_3 flushes were conducted in separate experiments with fresh sediments.

Figure D.3.3.6 compares Cs breakthrough curves and associated model predictions from the 1 M NaOH experiment (pH 13.7) and the 1 M $NaNO_3$ experiments (pH 8) both with Cs = 10^{-4} M. Cs retardation was underpredicted in the 1 M $NaNO_3$ experiments and overpredicted in the 1 M NaOH experiments by about the same amount (10 to 15%). This suggests that the model can be extended to the alkaline tank waste, because the reactive transport behavior of Cs was not significantly affected by the presence of base and the associated mineral alteration. The model used in Figure D.3.3.6 incorporated the measured OH^- and K^+ (1.5×10^{-4} M) at steady-state, but did not explicitly account for mineral dissolution or precipitation. About 4 wt% of the sediment dissolved based on the composition of the output solutions. During the first few hours of reaction there was rapid mineral dissolution and re-precipitation in the sediments. SEM and EDS analyses of the sediments at the end of the experiment revealed a precipitate that was rich in silica, Fe, Mg, and Ca. This precipitate is probably amorphous, because it was not detected by XRD (Personal Communication, D. Bish, LANL). The concentration of dissolved K in the high base experiments (1.5×10^{-4} M) had a small but detectable effect, lowering slightly the Cs retardation. Enhanced retardation in the 1 M NaOH experiments compared with the 1 M $NaNO_3$ experiments is consistent with the moduate increases in CEC reported in base-treated sediments in Section D.3.1.

Figure D.3.3.6. Comparison of Cesium Reactive Transport Through Hanford Sediments in 1 M $NaNO_3$ and 1 M NaOH Solutions.

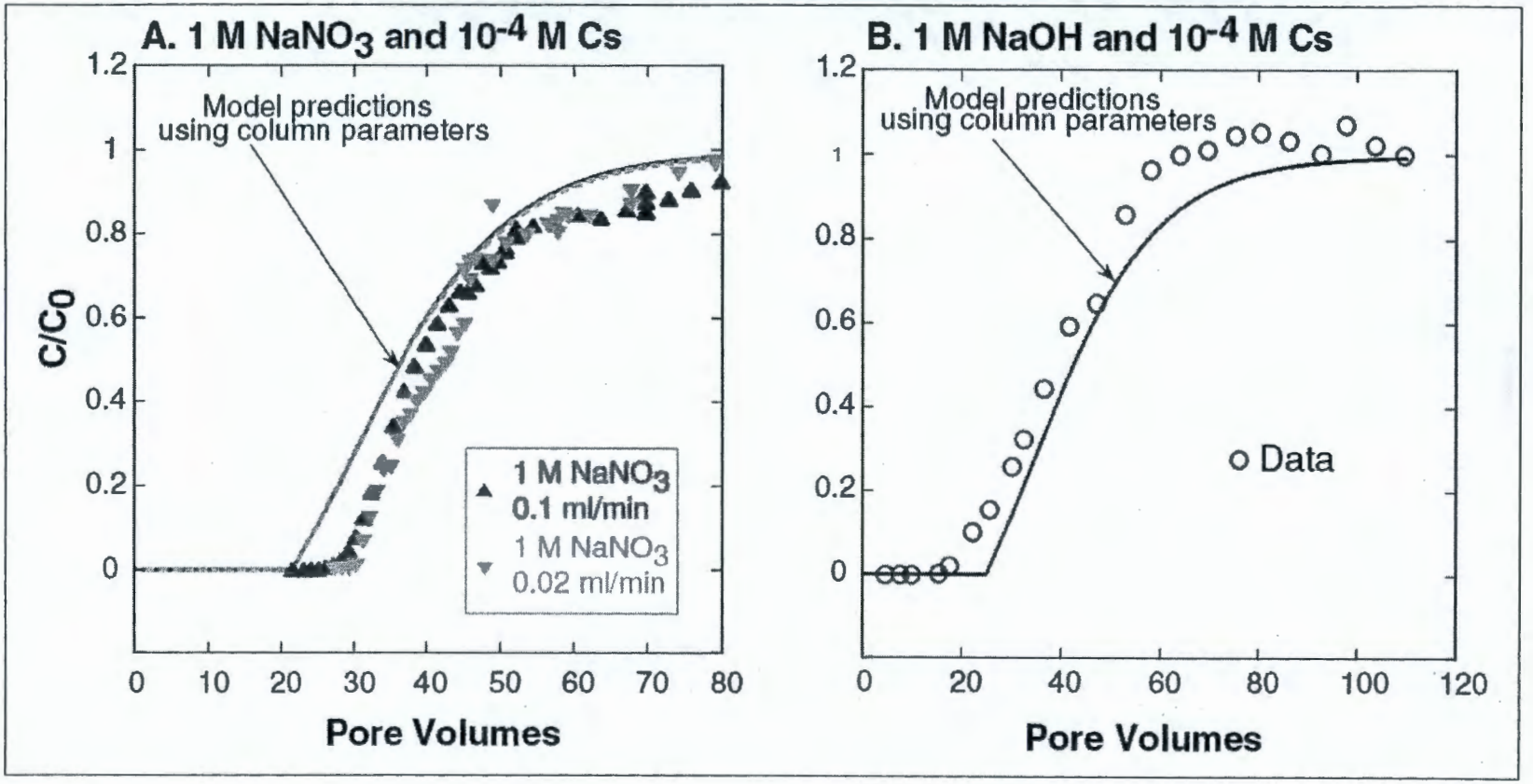

Note: Cesium breakthrough curves predicted by the multi-cation exchange model derived form fits weighted to the Column Experiments are shown by lines. The experimental data is shown by symbols.

D.3.3.3.7 Reversibility of Cesium Exchange. The Cs exchange model presented here assumed Cs exchange to the frayed-edge mica sites and to basal clay surfaces was rapid and reversible. It does not consider the impacts of poorly reversible Cs exchange. Laboratory studies show that Cs may diffuse within mica microfissure, interlamellar, and collapsed frayed-edge sites effectively fixing the Cs to the solids (Lomenick and Tamura 1965; Klobe and Gast 1970; Le Roux et al. 1970; Comans et al. 1991; Smith and Comans 1996). Preliminary measurements of Cs desorption from contaminated WAM S-SX sediments (41-09-39 and SX-108) indicate partial fixation of the sorbed Cs pool (McKinley et al. 2001). It is important to assess the reversibility of Cs exchange as a basis for predicting future mobility.

Figure D.3.3.7 shows Cs breakthrough and desorption for three experiments, 10^{-4} M Cs and 5 M $NaNO_3$, 5×10^{-7} M Cs and 1 M $NaNO_3$, and 10^{-4} M Cs and 1 M NaOH, as well as their respective model predictions based on the column parameters. In our reactive transport experiments, Cs exchange is fully reversible only in experiments where Cs and competing salt concentrations are high. In the 10^{-4} M Cs and 5 M $NaNO_3$ experiment, 98% of the sorbed Cs was desorbed when flushed with 5 M $NaNO_3$. Under these conditions, Cs sorption was dominated by exchange to basal sites on the expandable clays. At lower Cs and salt concentrations, however, Cs sorption was dominated by exchange at high affinity, frayed-edge mica sites. In the experiment using 5×10^{-7} M Cs and 1 M $NaNO_3$, about 70% of the sorbed Cs was desorbed by 1 M $NaNO_3$. As indicated by equilibrium modeling, most of the residual sorbed Cs remains there because of the high site affinity, not because of irreversible behavior. Because of the high binding affinity of the frayed-edge sites, many pore volumes are required to completely remove Cs. However, there was some evidence for irreversibility as indicated by the discrepancy between the equilibrium modeling results and the observed Cs concentrations during desorption. This is best shown in Figure D.3.3.7b. During the sorption phase (282 to 617 pore volumes), the lower Cs concentrations in the effluent compared to the model results may indicate that some Cs is incorporated in poorly reversible exchange complexes. Similarly, during the desorption phase, the observed Cs concentrations are higher than those predicted by the equilibrium modeling, indicating slow Cs desorption.

Figure D.3.3.7. Reversibility of Cs Exchange when Flushing the Sediments with 5 M $NaNO_3$ (A), 1 M $NaNO_3$ (B) and 1 M NaOH (C) Solutions at the End of the Sorption Experiments. Experimental Data are Shown with the Symbols. Model Predictions Using the Column Parameters are Shown with the Lines.

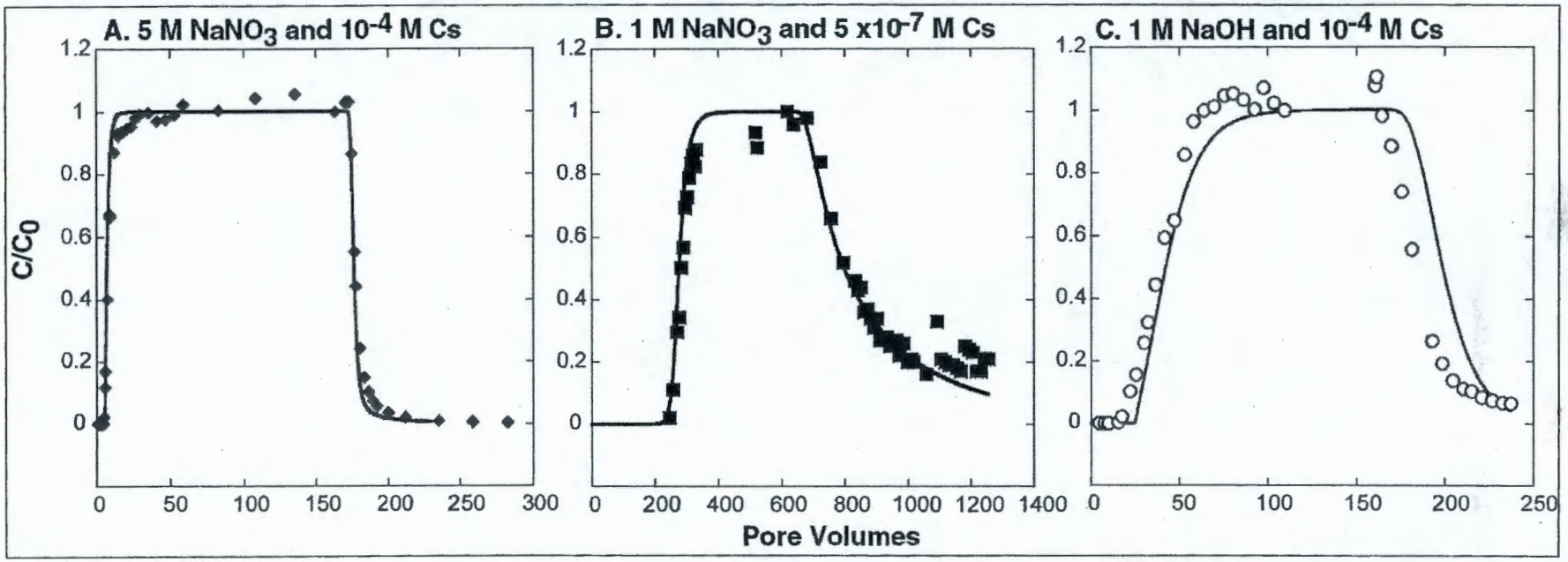

In the high base experiment using 1 M NaOH and 10^{-4} M Cs, most of the Cs sorption should occur on reversible, low affinity sites. However, only about 72% of the Cs was desorbed by 1 M NaOH (Figure D.3.3.7c). Unlike the 5×10^{-7} M and 1 M $NaNO_3$ experiment (Figure D.3.3.7b), which exhibited a constant release of Cs during the last half of the experiment, the release of Cs approached zero in the outflow solution of the 1 M NaOH experiment. The relatively large amount of Cs that did not desorb (28%) indicates Cs immobilization due to alteration of the sediments by base reaction. These results are consistent with exchange experiments conducted with contaminated sediments (41-09-39 and SX-108) which showed higher release of Cs when the sediments where treated with an NH_4-acetate extraction (Section D.3.6).

The discrepancy between the equilibrium modeling and observed results was used to assess the concentration of slowly reversible exchange sites. During the sorption stage between 282 and 617 pore volumes, the discrepancy between the model and the results indicated the sorption of 7.5×10^{-6} moles total Cs to slowly reversible sites. On the desorption limb, the discrepancy corresponded to 9.5×10^{-6} moles total Cs. In Experiment 2, carried out with 10^{-4} M Cs, the discrepancy during the sorption phase corresponded to 4×10^{-4} moles total Cs. These masses of Cs associated with the slowly reversible sites were minimum values, since their concentrations are not easily discovered from the breakthrough of Cs.

We have established that a discrepancy exists between the batch-based ion exchange model and the experimental column data. In this analysis we have applied "corrections" for sorption to the slowly reversible sites (Table D.3.3.4). Using the discrepancy between the equilibrium model and the observed results for the 5×10^{-7} M Cs and 1 M $NaNO_3$ experiment (Experiment 5), we calculated an average rate of Cs sorption to these sites of 4.9×10^{-8} mol/hr from 282 to 617 pore volumes. The application of this rate of Cs incorporation into the slowly reversible sites increased the predicted breakthrough from 230 to about 262 pore volumes. This retardation value is within 7% the experimentally observed retardation of 282 pore volumes (Table D.3.3.4). We applied the same analysis to Experiment 2 where the aqueous Cs concentration was higher, 10^{-4} M Cs. In this case, we calculated an average rate of Cs exchange at these sites equal to 1.3×10^{-5} mol/hour. When this "correction" was applied, the predicted retardation shifts to about 40.5, in agreement with the experimental value (Table D.3.3.4). Note that this interpretation of the batch-column discrepancy relies on a kinetic chemical process as opposed to diffusion-controlled transport into immobile zones within the sediment. A rate-limited process based on diffusion through porous media would have no effect in a batch system where stirring makes the sediment material fully accessible to the bulk solution.

Additional evidence for slowly reversible Cs exchange was observed in column experiments with 10^{-4} M Cs and 1 M $NaNO_3$ run at two different flow rates (Figure D.3.3.6a). In Experiment 1 (see Table D.3.3.1) run at 0.02 ml/min, the retardation of Cs was slightly greater (R= 43) than that observed in Experiment 2 run at 0.1 ml/min (R=40). The higher retardation may have resulted from the longer time available for Cs sorption to slowly reversible sites. Note also that Experiment 1 (which was run at a slower flow rate and over a longer period of time than Experiment 2) showed slightly better agreement with the equilibrium reactive transport model than did Experiment 2. Finally, Experiment 5, which was designed to increase the relative importance of the FES versus clay sites by using a lower Cs concentration, showed the strongest kinetic effects.

D.3.3.4 Conclusions and Implications

One of the most significant implications of this work is the confirmation that the ^{137}Cs distribution coefficient is not constant over the range of Na, K, Ca, and Cs concentrations found in the tank farm inventory and in the vadose zone pore water at the S and SX tank farms. Vadose zone processes, such as dilution from infiltrating rainwater (or water leaking from pipes) or concentration from boiling waste, will dramatically alter the ^{137}Cs K_d over time and space. Moreover, a ^{137}Cs K_d determined directly from the contaminated sediments is suspect unless proper adjustments are made, because those determinations typically involve dilutions as part of the analytical procedure. A 10× dilution, for example, could easily result in overestimating the K_d by a factor of 3 to 10. Similar cautions apply even when no dilutions for analytical purposes are carried out, because infiltration of rainwater in the vadose zone is likely to have diluted cation concentrations from what they were at the time of the leak. It is quite probable that a K_d determined from present day contaminated sediments might significantly overestimate the Cs retardation at the time of the tank leaks.

The multi-cation exchange model captures much of the chemical effects responsible for the dependence of ^{137}Cs K_d on competing cation and Cs concentrations and is a significant improvement over the use of a constant K_d to model ^{137}Cs form tank leaks to the vadose zone sediments. However, there is some mismatch between the predictions derived from a global fit of batch data covering a wide range of Cs and salt concentrations and our 1-D column experiments. Part of the mismatch appears to be related to the sorption of Cs at slowly reversible sites, which has not yet been included in the modeling except in an empirical sense (e.g., Table D.3.3.4). Additional experimental data is needed to better quantify these sites. In the absence of new experimental data, model parameters based on weighted column experiments can be used in field-scale analyses of transport to provide a more direct measure of retardation of Cs Hanford sediments (Sections D.3.7 and D.7.4).

The following example shows that the multi-cation exchange model describes ^{137}Cs retardation that is consistent with ^{137}Cs observations at the SX tank farm. Our column experiments indicate that high competing cation concentrations associated either with the tank liquors or resulting from reactions in the sediment underlying the tank cause a significant decrease in the retardation of Cs. The tank SX-115 leak apparently contained about 3.5 M $NaNO_3$ and 8×10^{-5} M Cs. Our model for Cs migration suggests a dimensionless Cs K_d of about 10 prior to any dilution of the tank liquors by vadose zone processes. This qualitatively agrees with the strong retardation of Cs observed below tank SX-115. In addition, some retardation of Na is expected upon dilution of the leaked waste, again in agreement with observations made in borehole WB 23-19 (Serne et al. 2001a, b). In contrast, leaking tank liquors at SX tank farm was at or above the boiling temperature and was extremely concentrated, with some estimates giving $NaNO_3$ concentrations at or close to equilibrium with respect to solid $NaNO_3$ (about 19.5 molal at 100 °C; Section D.7.3) and 7×10^{-4} M Cs. At these very high $NaNO_3$ concentrations, one does not expect to see any retardation of Na, in agreement with field observations that show Na peaks are coincident with nitrate peaks. One also expects significantly less retardation of Cs as well. Extrapolating the column-weighted fits of Cs exchange to 15 M yields a predicted Cs retardation of between 2 and 3. This value is close to the observed retardation below tank SX-108 of 2.5 to 3 (Serne et al. 2001a, b). While this prediction is uncertain until we have direct experimental confirmation of Cs retardation at these $NaNO_3$ concentrations and at higher temperature, the ion exchange model

presented here suggests that the high salt concentrations account for the bulk of the enhanced Cs mobility observed, particularly below tank SX-108.

An important aspect of the present study has been to provide additional scientific justification for the ion exchange model proposed by (Zachara et al. 2001) to describe Cs migration in Hanford sediments. We believe the combination of reactive transport modeling and column flow-through experiments provide very strong support for the applicability of the ion exchange model. As summarized above, our results suggest that the bulk of the enhanced migration of Cs observed below tanks like tank SX-108 is the result of the very high salt concentrations in these tanks. Tanks with lower salt concentrations than tank SX-108 show correspondingly higher Cs retardation. The multi-site ion exchange model also indicated that relatively dilute fluids of the kind associated with natural infiltration are unlikely to mobilize Cs in the subsurface. The ion exchange model, however, does suggest that considerable caution should be used in designing any sluicing methods, since re-injection of a concentrated sluicing solution is likely to result in further Cs migration.

D.3.3.5 References

Appelo, C. A. J., and D. Postma, 1996, *Geochemistry, Groundwater and Pollution*, Rotterdam, A. A. Balkema.

Klobe, W. D., and R. G. Gast, 1970, "Conditions Affecting Cesium Fixation and Sodium Entrapment in Hydrobiotite and Vermiculite," *Soil Science Society of America Proceedings*, Vol. 34:746-750.

Comans, R. N. J., M. Haller, and P. DePreter, 1991, "Sorption of Cesium on Illite: Non-Equilibrium Behavior and Reversibility," *Geochimica et Cosmochimica Acta*, Vol. 55:433-440.

Felmy, A. R., 1995, "GMIN, A Computerized Chemical Equilibrium Program Using a Constrained Minimization of the Gibbs Free Energy: Summary Report," *Chemical Equilibrium and Reaction Models*, Soil Science Society of America, Madison, Wisconsin.

Le Roux, J., C. I. Rich, and P. H. Ribbe, 1970, "Ion Selectivity by Weathered Micas as Determined by Microprobe Analysis," *Clays and Clay Minerals*, Vol. 18:333-338.

Lomenick, T. F., and T. Tamura, 1965, "Naturally Occurring Fixation of ^{137}Cs on Sediments of Lacustrine Origin," *Soil Science Society of America Proceedings*, Vol. 29:383-387.

McKinley, J. P., R. J. Serne, J. M. Zachara, C. J. Zeissler, and R. M. Lindstrom, 2001, "The Distribution and Retention of ^{137}Cs in Sediments Beneath Leaked Waste at the Hanford Site," *Environmental Science and Technology*, (Submitted).

Serne, R. J., H. T. Schaef, B. N. Bjornstad, B. A. Williams, D. C. Lanigan, D. G. Horton, R. E. Clayton, V. L. LeGore, M. J. O'Hara, C. F. Brown, K. E. Parker, I. V. Kutnyakov, J. N. Serne, A. V. Mitroshkov, G. V. Last, S. C. Smith, C. W. Lindenmeier, J. M. Zachara, and D. B. Burke, 2001a, *Characterization of Uncontaminated Sediments from the Hanford Reservation-RCRA Borehole Core and Composite Samples*, PNNL-2001-1, Pacific Northwest National Laboratory, Richland, Washington.

Serne, R. J., G. V. Last, G. W. Gee, H. T. Schaef, D. C. Lanigan, C. W. Lindenmeier, R. E. Clayton, V. L. LeGore, R. D. Orr, M. J. O'Hara, C. F. Brown, D. B. Burke, A. T. Owen, I. V. Kutnyakov, and T. C. Wilson, 2001b, *Geologic and Geochemical Data Collected from Vadose Zone Sediments from Borehole SX 41-09-39 in the S/SX Waste Management Area and Preliminary Interpretations*, PNNL-2001-2, Pacific Northwest National Laboratory, Richland, Washington.

Smith, J. T., and R. N. J. Comans, 1996, "Modeling the Diffusive Transport and Remobilization of ^{137}Cs in Sediments: The Effects of Sorption Kinetics and Reversibility," *Geochimica et Cosmochimica Acta*, Vol. 60:995-1004.

Steefel, C. I, 2001, *CRUNCH: Software for Modeling Multicomponent-Multidimensional Reactive Transport. 1 ed. User's Manual*, Lawrence Livermore National Laboratory (In press).

Zachara, J. M., S. C. Smith, C. Liu, J. P. McKinley, R. J. Serne, and P. L. Gassman, 2001, "Sorption of Cs^+ to Micaceous Subsurface Sediments from the Hanford Site, USA," *Geochimica et Cosmochimica Acta*, (Submitted).

D.3.4 CS^+ TRANSPORT IN UNSATURATED SEDIMENTS FROM THE S AND SX TANK FARMS

Amy P. Gamerdinger[1]

[1]Department of Chemistry, Washington State University, Richland, Washington 99352

D.3.4.1 Introduction

Regions of stagnant or immobile water develop in unsaturated sediments (Nielsen and Biggar 1961; Biggar and Nielsen 1962; Gaudet et al. 1977; Bond and Wierenga 1990). Immobile water may exist in thin liquid films around soil particles, in dead-end pores, or as relatively isolated regions associated with unsaturated flow (Nielsen et al. 1986). Mass transfer in and out of the immobile water domain is diffusion-limited; advective transport is restricted to the mobile water domain. A two-region transport model is used to describe this hydrodynamic condition.

Recent research on Hanford sediments illustrates an increase in the fraction of immobile water with decreasing water content (Gamerdinger and Kaplan 2000). Retardation due to sorption during unsaturated transport has not been widely investigated in systems with a significant fraction of immobile water. Uranium (U[VI]) transport in unsaturated sediments at higher water contents (greater than 50% moisture saturation) was generally predicted from sorption and transport that was determined in saturated systems (Gamerdinger et al. 2001a, b). This corresponded to conditions where transport was described with a single flow domain (all water present in the mobile domain). At lower water contents (less than 30% moisture saturation), retardation was less than predicted from sorption parameters that were determined in saturated systems (Gamerdinger et al. 2001b). This corresponded to conditions where a significant fraction of the water was present in the immobile water domain.

The above observations were made in systems where the solute was introduced to the sediment column during transport. There are two related mechanisms to explain changes in sorption during transport that are not predicted from measurements in saturated systems, and changes that are only apparent in systems with a significant fraction of immobile water. One is rate-limited mass transfer of the solute to sorption sites that are associated with the immobile water domain.

The significance of rate-limited mass transfer is determined by the average pore water velocity and the fraction of water in the immobile domain. The velocity of the solute in the mobile domain increases in proportion to the fraction water in the immobile water domain. For example, if the fraction of water in the mobile domain is 0.2, the velocity of solutes in the mobile domain increases by a factor of 5 relative to the average pore water velocity. Solutes moving through the mobile domain at the faster velocity have diffusion-limited access to sorption sites that are associated with the immobile water domain. Previous research with U(VI) indicated decreased sorption with increasing velocity; the changes with velocity at several moisture contents were consistent with the rate-limited mass transfer mechanism (Gamerdinger et al. 2001a).

The other possible mechanism to explain decreased sorption under conditions where a significant fraction of the water is present in the immobile water domain is a complete loss of access to

sorption sites in the immobile water domain. This contrasts diffusion-limited access, described above. If pore water in the immobile water domain is physically disconnected from the mobile domain, solutes that enter the system through the mobile domain do not have access to sorption sites in the immobile water domain. These solutes would appear to be excluded from a fraction of the pore volume. This mechanism has been suggested in research on U(VI) transport in unsaturated coarse–and fine-textured sandy sediments at moisture contents equivalent to 14 and 22% moisture saturation, respectively (Gamerdinger et al. 2001b). To date, this phenomenon has only been demonstrated in coarse-textured sandy sediments.

The objective of this research was to investigate Cs^+ transport in unsaturated sediments under geochemical conditions analogous to the water saturated column experiments discussed in Section D.3.3. Retardation under hydrodynamic conditions where a significant fraction of water was associated with an immobile water domain was of particular interest as these conditions are implied by the low moisture contents recorded in sediments from the SX-108 core. One goal was to determine whether Cs^+ transport at low unsaturated water contents (less than 30% moisture saturation) was predictable from batch and column measurements performed under saturated moisture conditions.

D.3.4.2 Experimental Procedures

D.3.4.2.1 Materials and Methods. The materials and geochemical conditions were selected to be consistent with previous (Zachara et al. 2001) and ongoing investigations of Cs^+ sorption in Hanford sediments (Sections D.3.1 and D.3.3). The less than 2 mm size fraction of the air-dried "Above B" composite sediment (D.2.2) was used without additional treatment. The aqueous solution for all experiments was 5 M $NaNO_3$. Solutions of 5.4×10^{-5} M Cs^+ were prepared by dissolving CsI in 5 M $NaNO_3$. Pentafluorobenzoic acid (PFBA) was used as a conservative, non-sorbing tracer in separate experiments to assess hydrodynamic conditions. Cs^+ concentrations were determined by ICP-MS; PFBA concentrations were determined by HPLC with UV detection at 254 nm.

D.3.4.2.2 Transport Experiments in Re-Packed, Unsaturated Columns. Retardation during transport in unsaturated sediments was determined using a centrifuge method; the experimental system and method are described in detail elsewhere (Gamerdinger and Kaplan 2000). A brief description of the approach follows and is similar to that used for saturated column (miscible displacement) experiments (Section D.3.3). Columns (length, L = 6.0 cm, radius, r = 2.25 cm, bulk volume, V_{bulk}, 95.43 cm^3) had mesh at the inflow and outflow; the outflow was lined with grade 230 filter paper (Whatman, Inc., Clifton, New Jersey). Columns were packed with the "Above B" composite sediment and were completely saturated with $NaNO_3$ solution. Sediment bulk density, ρ (g/cm), and volumetric water content, θ (cm^3/cm), were determined from the mass of the sediment and/or water. The percent moisture saturation was calculated from the ratio of θ (water-filled porosity), to the total porosity, ϕ, which was calculated from the bulk density and an assumed particle density of 2.65 g/cm^3.

With the centrifuge method (Model L8-UFA, Beckman Coulter, Inc., Fullerton, CA), water content is influenced by centrifugal force and the fluid flux, q (cm/hr), which was controlled with a volumetric infusion pump (AVI 210A, 3M, St. Paul, Minnesota). Columns were first saturated by passing four saturated pore volumes through the column; columns were then placed in the

centrifuge. A pore volume is defined as the volume of water within the porous media at a particular water content. Additional $NaNO_3$ was passed through the column during equilibration to attain steady-state conditions. Unsaturated transport experiments were initiated when the columns had reached a steady-state, average water content. Experiments at the different water content and velocity conditions were executed consecutively on the same column. Cs^+ and PFBA were applied as step inputs (separate experiments) where the pulse length, t_o, is defined as the volume of the step input, expressed as the number of column pore volumes. Practical considerations resulted in variation of t_o. Effluent was collected manually and analyzed for Cs^+ or PFBA. For each effluent sampling, rotation of the centrifuge and flow were stopped. Prior evaluation indicates no significant effect of stopping flow on the transport of non-retarded, conservative solute tracers (Gamerdinger and Kaplan 2000). The stop-flow interval provided additional time for rate-limited mass transfer of U(VI), however; the effect on retardation was dependent on the length of the stop-flow interval relative to the average pore water velocity (i.e., greater impact for faster velocity experiments).

D.3.4.3 Results

Results of transport experiments are expressed as breakthrough curves (Figures D.3.4.1 to D.3.4.3). The measured parameters that define the experimental conditions, and parameters determined from the breakthrough curves, are listed in Table D.3.4.1. They are defined as introduced in the text and are summarized as footnotes in Table D.3.4.1. The experiments are identified by the prefix of "CC" for Cs^+, and "CP," for PFBA, followed by the percent moisture saturation. For example, CC-26 represents a Cs^+ transport experiment at 26% moisture saturation. Percent moisture saturation is defined as the percent of the total porosity that is water-filled. The percent recovery of the analyte in the effluent was based on the area under the BTC compared with the measured step input. The retardation factor, R, is defined as the average velocity of water relative to that of the solute. R values are based on the center-of-mass and were determined from the mathematical first moment (Valocchi 1985).

D.3.4.3.1 Conservative Tracer Transport and Hydrodynamic Properties. Results of the tracer experiments are presented in Figure D.3.4.1 and Table D.3.4.1. Recovery was 98% at both water contents (CP-65, CP-28). Retardation factors were approximately one and indicate solute transport at the velocity of water. R values less than 1 suggest exclusion of the solute from a fraction of the water-filled pore volume. The exclusion phenomenon that was observed previously in unsaturated coarse–and fine-textured sandy sediments from Hanford (Gamerdinger et al. 2001b) was not observed for the "Above B" composite sediment at 28% moisture saturation (CP-28). Complete particle size characterization (% sand, silt, clay) was not available; however, the composite sediment appeared to contain a greater fraction of silt-sized particles than the coarse and fine sands. Because of the sediment texture, water content, and hydrodynamic condition (solute exclusion not observed), the "Above B" composite sediment was not suitable for evaluating the phenomenon of "disconnected" pore water. When this occurs, solutes are excluded from a fraction of the pore volume and, therefore, sorption sites associated with a portion of the immobile water domain. This exclusion phenomenon has been demonstrated in sand-textured sediments and results in accelerated transport due to decreased sorption: solutes in the mobile domain do not have access to sorption sites that are associated with disconnected pore water. Because there is a significant fraction of immobile water at less than or equal to 28% saturation, the "Above B" composite sediment is suitable for evaluating diffusion-limited access to sorption sites in the immobile water domain.

Table D.3.4.1. Measured and Calculated Parameters for PFBA and Cs^+ Transport Experiments on the "Above B" Composite Sediment.

Expt.	Analyte	Sat. (%)	F ($cm^3\ hr^{-1}$)	ρ_b ($g\ cm^{-3}$)	θ (st. dev.)	V_w (mL)	V ($cm\ hr^{-1}$)	t_o (V_w)	Recovery (%)	R	P	β	ω
CP-65	PFBA	65.3	74.4	1.609	0.256 (0.004)	24.47	18.24	2.91	98	1.05	18	-	-
CP-28	PFBA	27.6	33.0	1.609	0.109 (0.001)	10.36	19.11	3.17	98	1.06	9	0.182	1.24
CC-66	Cs^+	65.6	74.4	1.609	0.258 (0.001)	24.61	18.14	29.26	97	11.6	18	-	-
CC-26	Cs^+	25.8	33.0	1.609	0.101 (0.007)	9.68	20.44	45.97	92	13.2	9	0.183	1.24
CC-23	Cs^+	22.8	6.9	1.609	0.089 (0.003)	8.54	4.85	25.47	74	24.1	9	0.182	1.24

[a]F = flow rate, ρ_b = bulk density; θ = average volumetric water content (standard deviation); V_w = average pore volume; v = average pore water velocity; t_o = step input; R = retardation factor.

Figure D.3.4.1. Conservative Tracer (pentafluorobenzoic acid) Transport Through the "Above B" Composite Sediment at Two Moisture Contents.

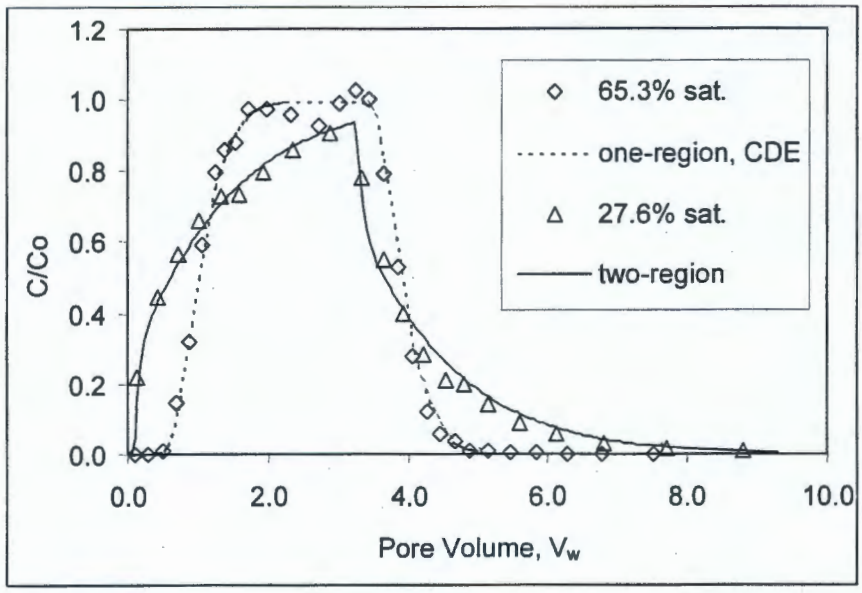

Note: Transport at 65% saturation is consistent with a one-region flow domain and is described with the convection-dispersion transport equation (CDE). At 27.6% saturation, the left-shift and tailing suggest mobile-immobile water, requiring a two-region transport model.

Hydrodynamic parameters were determined from the breakthrough curves (BTCs) of the tracers. At 65% moisture saturation (CP-65), the conventional single-flow domain form of the convection-dispersion equation, CDE, was adequate for characterizing the BTC. The dimensionless Peclet number, P, which includes hydrodynamic dispersion, D ($P = \nu L / D$, where ν is the average pore water velocity), was determined by a single-parameter curve fit.

At 28% moisture saturation (CP-28), the conventional CDE failed to capture the early breakthrough and tailing phenomena that is characteristic of mobile-immobile water (Figure D.3.4.1); a two-region model was applied to describe the BTC. The criteria for using a two-region model is when the Peclet number determined with the CDE is less than 2, and the fraction immobile water determined with the two-region model is greater than 10% (Gamerdinger and Kaplan 2000). The dimensionless parameters, β and ω, were determined by curve-fitting. β defines the fraction of mobile water, subscript m, ($\beta = \theta_m/\theta$, where θ is the volumetric water content); ω is the dimensionless coefficient for mass transfer between mobile and immobile water domains ($\omega = \alpha L/q$, where α is the mass transfer coefficient (1/hr), L is the column length, and q is the water flux). For these cases, the Peclet number, P, was calculated directly from the slope of the BTC where c/c_o was equal to 0.5 (Gamerdinger and Kaplan 2000).

Hydrodynamic parameters (P, β, ω) are presented in Table D.3.4.1. As anticipated, hydrodynamic dispersion and the fraction of immobile water increase with decreasing water content. Nearly 82% of the water in the sediment at 28% saturation is associated with the immobile domain (Table D.3.4.1, CP-28, $\beta = 0.182$). Although the average pore water velocity was controlled across experiments (Table D.3.4.1, range of 18.1 to 20.4 cm/hr), it is important to

recognize that advective transport is limited to the mobile domain, and the velocity of solute in the mobile domain ($v_m = v / \phi_m$) at 28% moisture saturation (CP-28) is 105 cm/hr, which is quite rapid.

D.3.4.3.2 Cs^+ Transport and Retardation. Cs^+ transport at 66 and 26% moisture saturation is illustrated in Figure D.3.4.2 (CC-66 and CC-26, Table D.3.4.1). The BTCs indicate that a small fraction of the Cs^+ continued to elute from the column when the experiments were terminated (recovery was 97 and 92% for CC-66 and CC-26, respectively). This suggests that a fraction of the sorption is less reversible, as shown by Zachara et al. (2001).

Cs^+ retardation during transport in unsaturated columns was determined and compared with predictions that were based on retardation in saturated columns (LLNL; Section D.3.3). The approach used here is limited to the use of readily available transport models and parameters that could be determined from the retardation factor (e.g., a bulk, equilibrium distribution coefficient, or K_d value). The retardation factor that was determined for saturated conditions (R=7) was used to determine a K_d value. The K_d value was then used to estimate expected retardation for transport experiments at lower water contents. This approach accounts for changes in retardation that are expected due to the change in the soil:water or mass:volume ratio. Isotherm nonlinearity is recognized and will be incorporated in subsequent modeling of Cs^+ transport.

Cs^+ transport at 66% moisture saturation is shown in Figure D.3.4.2A. The observed retardation (R = 11.6, Table D.3.4.1) agrees well with the independent prediction that was based on retardation determined in a saturated column (R = 10.5). The model prediction assumes a linear isotherm and does not account for nonlinear sorption behavior, which is known to be significant for Cs^+. Isotherm nonlinearity contributes to the asymmetry that is apparent in the observed breakthrough curve.

Cs^+ transport at 26% moisture saturation is shown in Figure D.3.4.2B. As discussed for the conservative tracer, the early breakthrough on the front and prolonged tailing on the back of the BTC are indicative of rate-limited mass transfer. The observed retardation (R = 13.2, Table D.3.4.1) is almost a factor of 2 lower than predicted from retardation in the saturated column (R = 25.2). Under-estimation of Cs^+ transport is illustrated by independent model predictions with R = 25.2 using both one-region (conventional CDE) and two-region transport models. Hydrodynamic parameters for the two-region model were determined from conservative tracer data. A semi-independent prediction with the two-region model and R equal to the observed value of 13.2 also failed to capture the observed transport behavior. This is likely because the model does not account for isotherm nonlinearity.

Even though the *average* pore-water velocity was consistent for the three moisture contents (100%, 66%, and 26% saturation), at 26% saturation the velocity of the solute in the mobile domain is accelerated by a factor of 5 (80% of the pore water is associated with the immobile water domain). This illustrates how a significant fraction of immobile water accelerates solute transport and decreases sorption because of diffusion-limited access to sorption sites associated with the immobile water domain. If all of the pore space is accessible by diffusion (as indicated by conservative tracer data), reducing the pore water velocity should result in increased sorption. This was evaluated with an additional experiment at a slower pore water velocity.

Figure D.3.4.2. Cs^+ Transport Through the "Above B" Composite Sediment at 66% (A) and 26% (B) Moisture Saturation.

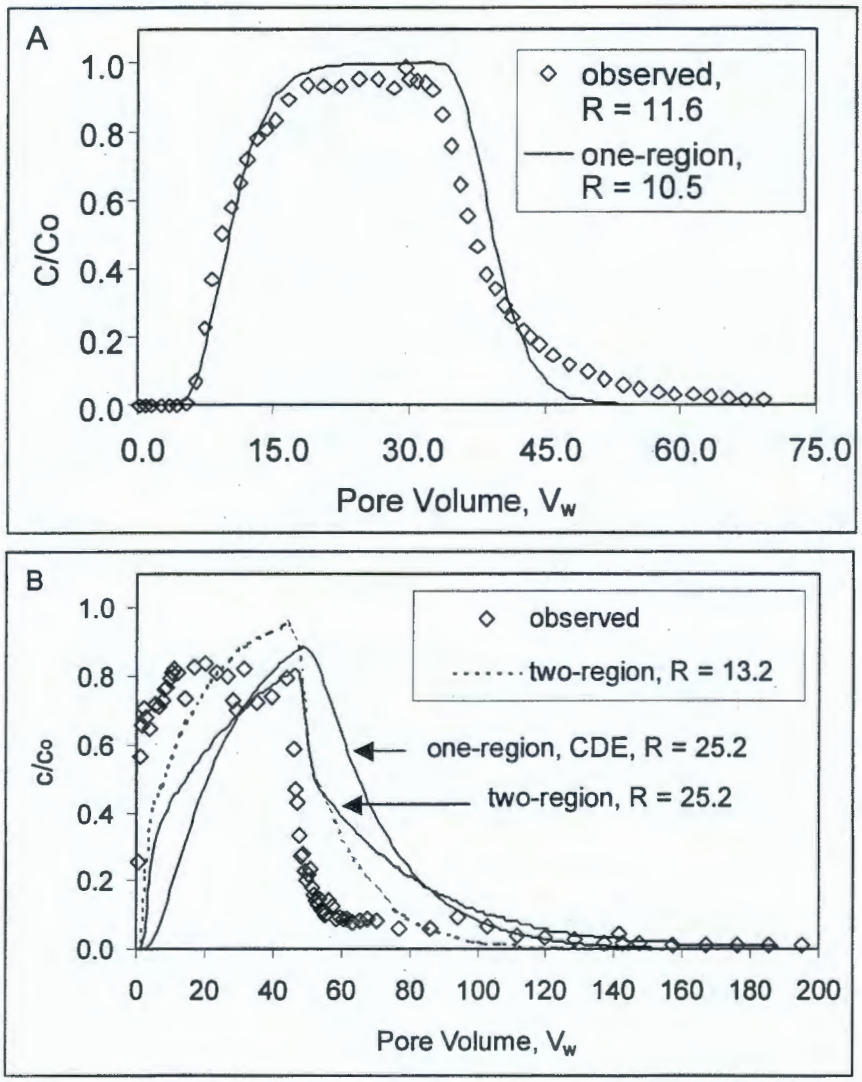

Note: A. Transport at 66% saturation is predicted from retardation in saturated columns and is described with the convection-dispersion transport equation (CDE). B. Retardation at 26% saturation is not predicted from saturated columns (R = 25.2); Transport is faster by a factor of 2. Even when accounting for the hydrodynamic effect of mobile-immobile water (R = 13.2, Two-Region), the breakthrough curve is not well described, likely because the model does not account for isotherm nonlinearity.

Cs^+ transport at 23% moisture saturation and a reduced pore water velocity of 4.85 cm/hr is shown in Figure D.3.4.3. The observed retardation (CC-23, $R = 24.1$, Table D.3.4.1) is somewhat less than predicted by Cs^+ transport in a saturated column (predicted $R = 30.3$); however, the experiment was terminated early due to mechanical problems and recovery was only 74%. This demonstrates increased retardation due to a reduction in v by a factor of approximately 4; the solute velocity in the mobile domain is 26.6 cm/hr, similar to that for the saturated case (Section D.3.3). This is consistent with the mechanism of rate-limited mass transfer that has been demonstrated in silt-textured sediments for unsaturated moisture conditions with mobile-immobile water (Gamerdinger et al. 2001a).

Figure D.3.4.3. Cs^+ Transport Through the "Above B" Composite Sediment at 23% Moisture Saturation and an Average Pore Water Velocity of 4.85 cm/hr.

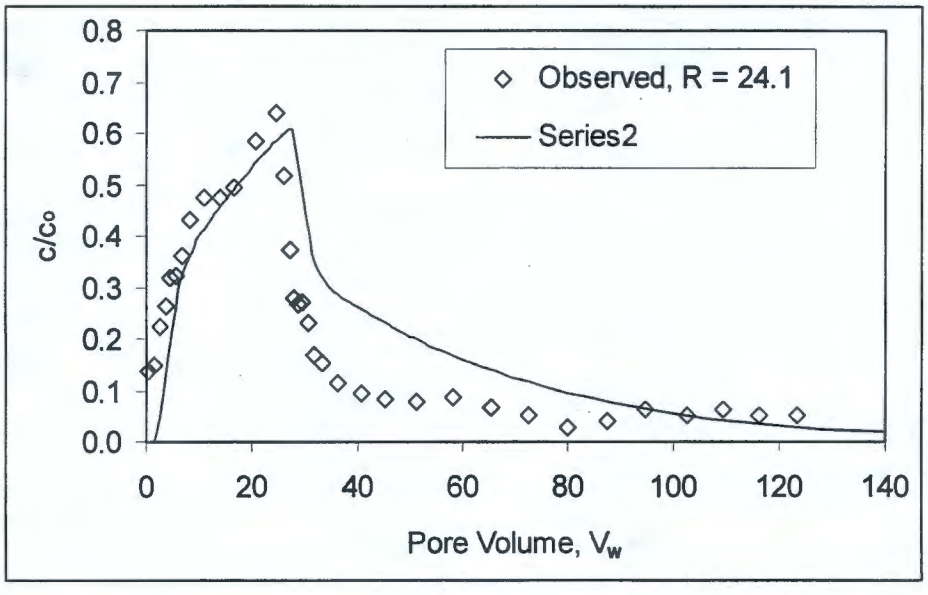

Note: Compared with Figure D.3.4.2B, decreasing the velocity by a factor of approximately 4 resulted in increased sorption of Cs^+. The observed retardation is less than predicted based on transport in saturated columns.

D.3.4.4 Conclusions and Implications

Cesium (Cs^+) transport was determined in unsaturated laboratory columns at 66% and approximately 24% moisture saturation. Re-packed sediment columns were equilibrated with a 5 M solution of $NaNO^3$; Cs^+ was applied as CsI at a concentration of 5.4×10^{-5} M (approximately 14 mg/L). The geochemical conditions were comparable to those used in other S&T Program investigations reported in Sections D.3.1 and D.3.3.

At 66% moisture saturation, Cs^+ retardation and transport were well predicted from Cs^+ retardation that was determined in saturated columns. At this higher water content (greater than 50% moisture saturation), the hydrodynamics are similar to a saturated system in that all of the water is associated with a single, mobile, flow domain. This is significant because it adds to the limited database indicating that transport at water contents greater than approximately 50 to 60% moisture saturation is predicted from transport behavior in saturated systems. This result

also provides further validation of the centrifuge method as an approach for studying transport through unsaturated sediments.

At approximately 24% moisture saturation, more than 80% of the pore water was associated with a stagnant, or immobile water domain. This hydrodynamic condition is characterized with a two-region (mobile-immobile) transport model and is consistent with other research indicating a significant fraction of immobile water at lower water contents (less than 30% moisture saturation). At 26% saturation and approximately the same velocity as for 100%, Section D.3.3, and 66% saturation, Cs^+ retardation and transport was poorly predicted from retardation that was determined in saturated columns; Cs^+ mobility was accelerated by a factor of 2. When velocity was reduced by a factor of 4, such that the velocity in the mobile domain approximated that for the saturated condition, retardation increased and was more consistent with predictions based on transport in saturated columns. For the hydrodynamic conditions obtained in the "Above B" composite sediment, there was no evidence of disconnected pore water, consistent with other results for sediments with silt-sized particles. It was not possible to evaluate the effect of disconnected pore water (solutes completely excluded from a fraction of the pore space) on Cs^+ transport, which can result in transport that is accelerated by a factor of 2, regardless of the pore water velocity.

This research demonstrates that solutes that are transported via the mobile water domain in unsaturated sediments have limited access to sorption sites that are associated with the immobile water domain. Sorption is reduced and transport is further accelerated, (e.g., to a greater extent than restricting transport to the mobile water domain). This has important implications for our general understanding of sorption during transport in unsaturated sediments and interactions between hydrodynamic and geochemical processes. The results are consistent with a rate-limited mass transfer mechanism that is specific to unsaturated sediments where a significant fraction of water is associated with the immobile water domain. This is of particular importance to contaminant transport through the vadose zone at Hanford, and may be one of several factors that contribute to accelerated contaminant transport.

D.3.4.5 References

Biggar, J. W., and D. R. Nielsen, 1962, "Miscible Displacement: II. Behavior of Tracers," *Soil Science Society of America Proceedings*, Vol. 26:125-128.

Bond, W. J., and P. J. Wierenga, 1990, "Immobile Water During Solute Transport in Unsaturated Sand Columns," *Water Resources Research*, Vol. 26:2475-2481.

Gamerdinger, A. P., and D. I. Kaplan, 2000, "Application of a Continuous-Flow Centrifugation Method for Solute Transport in Disturbed, Unsaturated Sediments and Illustration of Mobile-Immobile Water," *Water Resources Research*, Vol. 36:1747-1755.

Gamerdinger, A. P., and D. I. Kaplan, 2001, "Physical and Chemical Determinants of Colloid Transport and Deposition in Water-Unsaturated Sand and Yucca Mountain Tuff," *Environmental Science and Technology*, (In press).

Gamerdinger, A. P., D. I. Kaplan, D. M. Wellman, and R. J. Serne, 2001a, "Two-Region Flow and Rate-Limited Sorption of Uranium (VI) During Transport in Hanford Groundwater and An Unsaturated Silt Loam," *Water Resources Research*, (In press).

Gamerdinger, A. P., D. I. Kaplan, D. M. Wellman, and R. J. Serne, 2001b, "Two-Region Flow and Decreased Sorption of Uranium (VI) During Transport in Hanford Groundwater and Unsaturated Sands," *Water Resources Research*, (In press).

Gaudet, J. P., H. Jegat, G. Vachaud, and P. J. Wierenga, 1977, "Solute Transfer, With Exchange Between Mobile and Stagnant Water, Through Unsaturated Sand," *Soil Science Society of America Journal*, Vol. 41:665-671.

Nielsen, D. R., and J. W. Biggar, 1961, "Miscible Displacement In Soils: I. Experimental Information," *Soil Science Society of America Proceedings*, Vol. 25:1-5.

Nielsen, D. R., M. T. van Genuchten, and J. W. Biggar, 1986, "Water Flow and Solute Transport Processes in the Unsaturated Zone," *Water Resources Research*, Vol. 22:895-1085.

Zachara, J. M., S. C. Smith, C. Liu, J. P. McKinley, R. J. Serne, and P. L. Gassman, 2001, "Sorption of Cs^+ to Micaceous Subsurface Sediments from the Hanford Site, USA," *Geochimica et Cosmochimica Acta*, (Accepted).

D.3.5 MINERALOGIC RESIDENCE OF ^{137}CS IN CONTAMINATED SEDIMENTS

James P. McKinley[1], John M. Zachara[1], Jean A. Kimerling[1], and Bruce W. Arey[1]

[1]Pacific Northwest National Laboratory, Richland, Washington 99352

D.3.5.1 Introduction

The mineralogic residence of ^{137}Cs is a significant factor in determining its future mobility: micaceous minerals are much more energetic binders of Cs than other common silicates. The coarse-textured, micaceous sediments that make up the regional surface deposits underlying the SX tank farm (Tallman et al. 1979; Freeman-Pollard et al. 1994), have to large degree sorbed and concentrated the $^{137}Cs^{+}$ from leaked tank waste, limiting vertical migration to distances of approximately 6 – 20 m (20 – 65 ft). Because Cs^{+} is soluble, the retardation of Cs^{+} movement in vadose zone pore water and underlying groundwater is controlled by sorption, and Cs^{+} is preferentially sorbed by phyllosilicate minerals, which include expansible layer silicates such as smectite and vermiculite, and non-expansible micas, such as biotite and muscovite.

The sorption of Cs to phyllosilicates has been actively researched since the advent of anthropogenic ^{137}Cs in the environment (Sawhney 1970; Evans et al. 1983; Comans and Hockley 1992; Cornell 1993). The consensus on the retention of $^{137}Cs^{+}$ by sediments is that frayed edge sites (weathered sites at the edges of mica flakes) strongly bind Cs^{+}, preventing its rapid re-release. In the sub-tank sediments at Hanford, where micaceous minerals are common, it is not clear that sorption to micas has controlled ^{137}Cs mobility. Other reactions, such as Cs^{+} incorporation into authigenic zeolites or aluminosilicates formed by waste-sediment interaction could also be significant. We investigated the retention of ^{137}Cs by individual particles within contaminated sediments from SX-108 slant borehole and 41-09-39 without preconception about which mineral phases would prove to be radioactive. After screening, individual radioactive particles were isolated and examined to determine their mineralogy. The initial work was conducted using samples from borehole 41-09-39 (McKinley et al. 2001), and subsequent work was done with samples from SX-108 slant borehole.

D.3.5.2 Experimental Procedures

Sediments from borehole 41-09-39 were examined that had been size fractionated by wet sieving. SX-108 borehole samples were not sieved. Sediments from both boreholes were disseminated onto glass slides and fixed, using collodion in amyl acetate. Individual radioactive particles were identified using either a Fujifilm BAS-5000 (25 μm resolution) or Molecular Dynamics Storm (50 μm resolution) digital autoradiography system. The phosphor-plate media were exposed to disseminated sediments to construct a "map" of radioactive particles for each sample slide. Particles identified as "positive" or "negative" with respect to radioactivity were then removed to separate slides, and the exposure was repeated to confirm whether the identifications were correct. Finally, single radioactive particles were separated and mounted individually. Individual particles were identified mineralogically using optical microcopy, and in some cases examined by scanning electron microscopy. For 41-09-39, individual micas were removed from the 106-250 μm and 250-500 μm size fractions, identified by color as biotite (black), vermiculite (rust), or muscovite (clear), and used to test the hypothesis that all micas

were radioactive because they preferentially retained ^{137}Cs. The individual mica particles were also counted for gamma activity in a low-level counting facility at the National Institute for Standards and Technology at Gaithersburg, Maryland.

D.3.5.3 Results

Inspection of the digitized phosphor-plate images provided a means of rapid detection and identification of $^{137}Cs^{+}$-sorbing particles. Individual clasts were classified as "positive" (generating a radiological response) or "negative." In 41-09-39, sediment clasts that showed positive autoradiography results were morphologically and mineralogically distinct from negative clasts. As shown in Figure D.3.5.1a, from the 53 - 106 μm fraction, but consistent with results from all the size fractions, the negative clasts were predominantly particles of quartz and plagioclase feldspar, with some surface staining by fine iron oxide. The positive clasts consisted of mineral fragments bound together by clay-sized materials, presumably smectite. The positive clasts were also consistently larger than the maximum size nominally allowed by the sieving procedure: they were relatively large agglomerates of finer clasts cemented by smectite (Figure D.3.5.1b). Smectite apparently flocculated during or after the wet sieving process, forming agglomerates with other phases and yielding anomalously large grain sizes. Close examination of the agglomerates showed an abundance of mica. The grains in Figure D.3.5.1b were partially disaggregated during manipulation, revealing the presence of micas as either translucent large flakes or as small, dark constituent flakes at the surface of the clumped material. Individual non-micaceous silicate grains were also separated from the clumps. These grains were of size comparable to negative grains in Figure D.3.5.1a. Examination of disaggregated positive grains using optical and electron microscopy showed them to consist of quartz and plagioclase, as well as mica and smectite. Some agglomerated samples were crushed and their components screened autoradiographically (data not shown); smectite separated from these particles did not give positive results.

The examination of positive clasts from 41-09-39 suggested that the selection of individual clasts for single-clast autoradiography and gamma counting might be biased toward agglomerated small particles, since the strongest radiological results would tend to come from relatively large clumps including numerous positive components. We determined the relative significance of different components by logically evaluating the autoradiography results and by performing additional autoradiography measurements. The primary silicates (quartz and feldspar) could be ruled out as sources of radiation by analogy to negative clasts. The retention of $^{137}Cs^{+}$ by micas was tested directly by picking mica flakes from the 0.106 - 0.250 mm and 0.250 - 0.500 mm size fractions (Figure D.3.5.2). The micas were all confirmed to significantly retain $^{137}Cs^{+}$ by producing visible radiation-induced spots on autoradiography plates. Biotite and vermiculite showed strongly positive results, with muscovite retaining less $^{137}Cs^{+}$ than the other micas. During physical manipulation, "vermiculite" flakes often delaminated, and were observed to consist of a rusty cover or sheath of vermiculite over a relatively pristine core of biotite. The retention of $^{137}Cs^{+}$ that was ascribed to vermiculite was resulted from retention by biotite or a composite of biotite and vermiculite. The three micas, in any case, showed a higher affinity than all other phases for $^{137}Cs^{+}$.

Figure D.3.5.1. Comparison of Positive (Radioactive) Sediment Grains with Negative (Non-Radioactive) Grains From Borehole 41-09-39, 53 – 106 μm size Fraction.

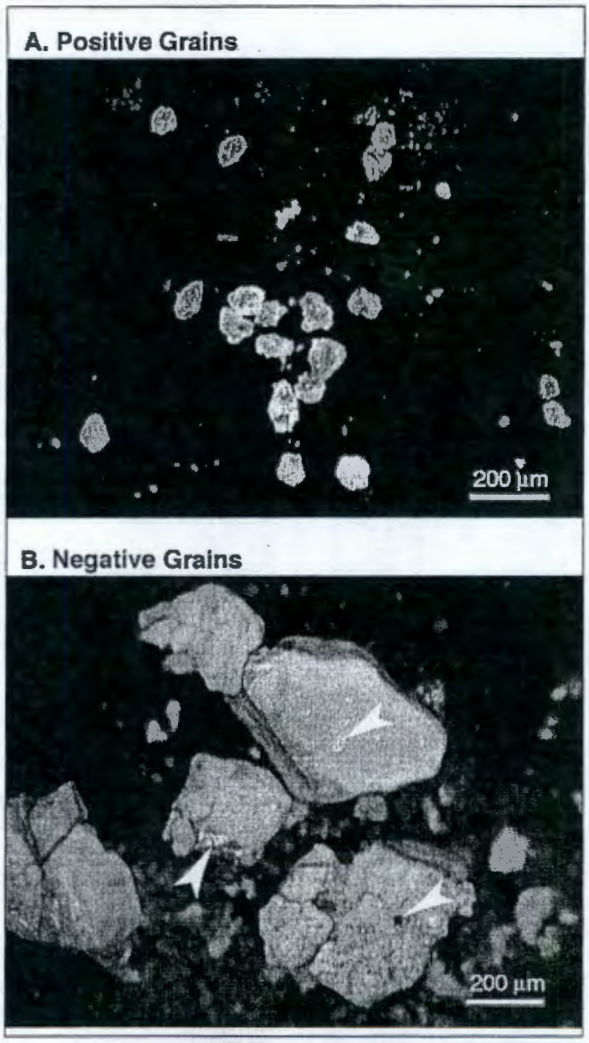

Note: Negative grains are monomineralic silicates; Positive grains are clay-cemented agglomerates containing mica flakes (arrows).

Figure D.3.5.2. Comparison of Autoradiography Results From Single Mica Flakes.

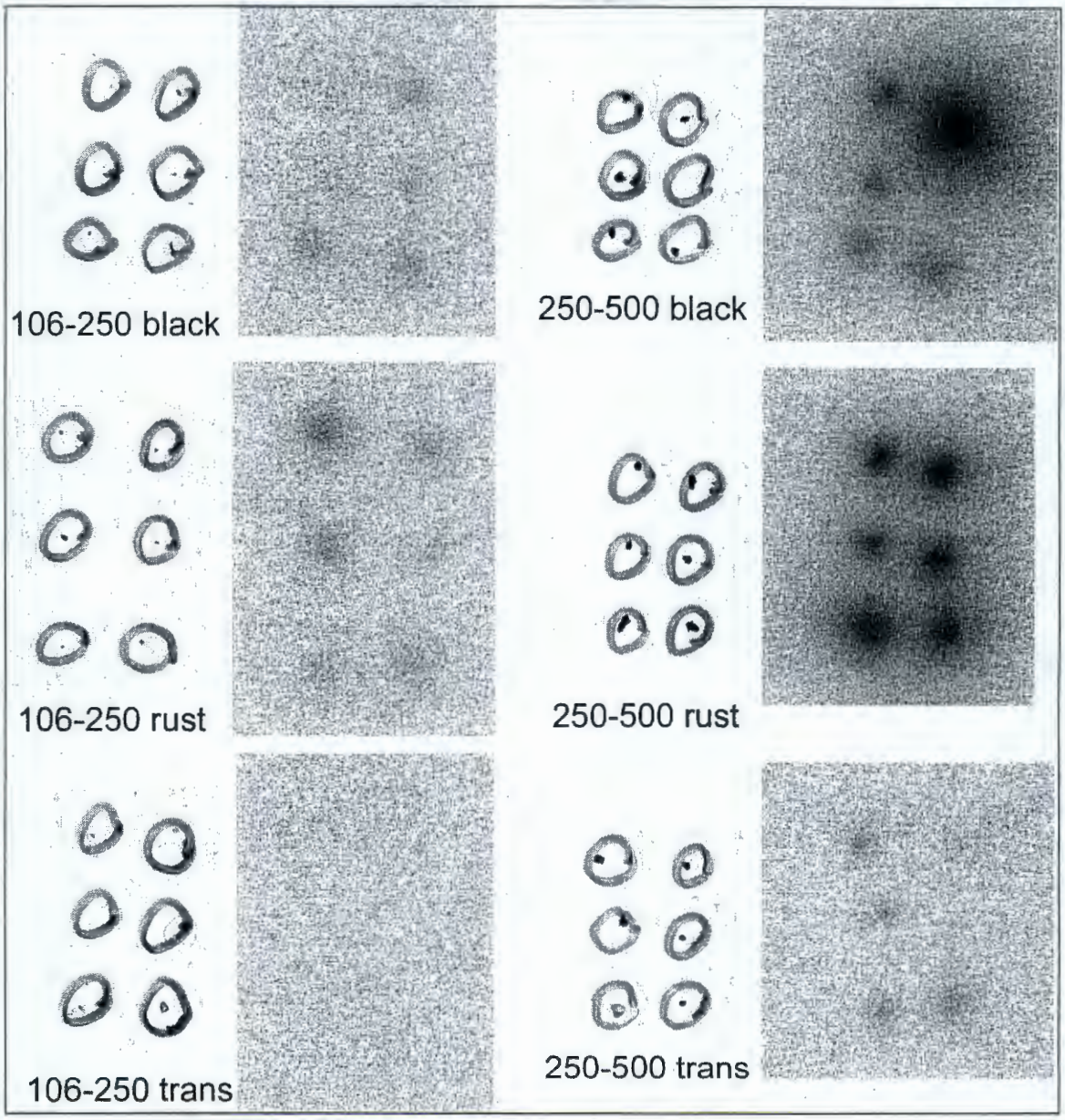

Note: Notations are: 106-250, etc. sieve-size sediment fractions from which micas were picked; Black: Biotite, Rust: Vermiculite, Trans: Muscovite. Each digital autoradiograph is paired with a Macroscopic Photomicrograph of the slide from which it was developed. Each slide contained six Mica flakes, circled. The density of the autoradiography spots is proportional to the activity of the imaged flakes.

Results for SX-108 slant borehole identified mica as the only significant retainer of ^{137}Cs (Figure D.3.5.3). All of the negative grains were non-micaceous silicates, as was the case for 41-09-39 samples. Since these sediments were not size-fractionated by wet sieving, no flocculation occurred. All of the positive grains were micas, with some micas including a small mass of adhering smectite.

The autoradiography method was used to identify radioactive particles, but could not discriminate between alpha, beta, and gamma radiation. The origin of detected radiation and its activity were confirmed by using low-level gamma counting. The integration of the single-grain exposure intensities (pixel densities) on autoradiography images provided a numerical value for radiation intensity (denoted photostimulated luminescence [PSL] units). These numerical results had good correspondence to gamma counting measurements of ^{137}Cs (Figure D.3.5.2; $r^2 = 0.83$). PSL intensities may have originated from beta or gamma radiation or both. The decay of ^{137}Cs to metastable ^{137}Ba includes emission of a 0.514 MeV β^- and a neutrino, followed by the isomeric transition of the ^{137}Ba by emission of a 662 KeV γ photon, detectable by gamma counting (Lederer et al. 1978). PSL measurements were more sensitive than gamma counting, and thus could estimate ^{137}Cs activities that were detectable by the phosphor system when these same activity levels were too small to be detected by gamma spectrometry (Figure D.3.5.4) (Zeissler et al. 2001).

Although all of the categorically positive clasts for SX-108 slant borehole were micaceous and all of the categorically negative clasts for both boreholes were silicates other than phyllosilicates, the clasts from the two boreholes were slightly different in their autoradiography results. The negative clasts from 41-09-39 were below detection (i.e., emitted less than approximately 0.05 Bq). Many of the negative clasts from SX-108 slant borehole, however, yielded a faint positive signal (Figure D.3.5.5). These clasts were examined by SEM to determine whether a secondary phase capable of retaining ^{137}Cs was present. Photomicrographs of quartz clasts from samples 03 (Figure D.3.5.6) and 07 (Figure D.3.5.7) show the presence on grain surfaces of numerous but very small (less than 10 μm) secondary crystals. These minerals have blocky habits and a composition (Na, Al, Si, O by energy dispersive spectroscopy, inset in Figures D.3.5.6 and D.3.5.7) that was consistent with zeolites identified in laboratory experiments of mineral-waste interaction performed with caustic tank-waste simulants (Section D.1.1). The retention of ^{137}Cs by the observed phases could not be confirmed; however, zeolites can sorb Cs^+ and the presence of ^{137}Cs on these clasts suggests that this phase may be responsible.

The absence of radioactivity on "negative" grains from 41-09-39 samples was puzzling. The samples examined from that borehole, however, had been size fractionated by sieving in the presence of water. It is possible that zeolites present on the surfaces of silicate clasts were either solublized or physically removed during the sieving procedure. Alternatively, OH^- concentrations in the wastes that migrated through the 41-09-39 sediments may have been too low to induce significant mineral dissolution and precipitation.

Figure D.3.5.3. Photomicrographs of Particles Screened Using Digital Autoradiography to Identify Minerals Retaining ^{137}Cs.

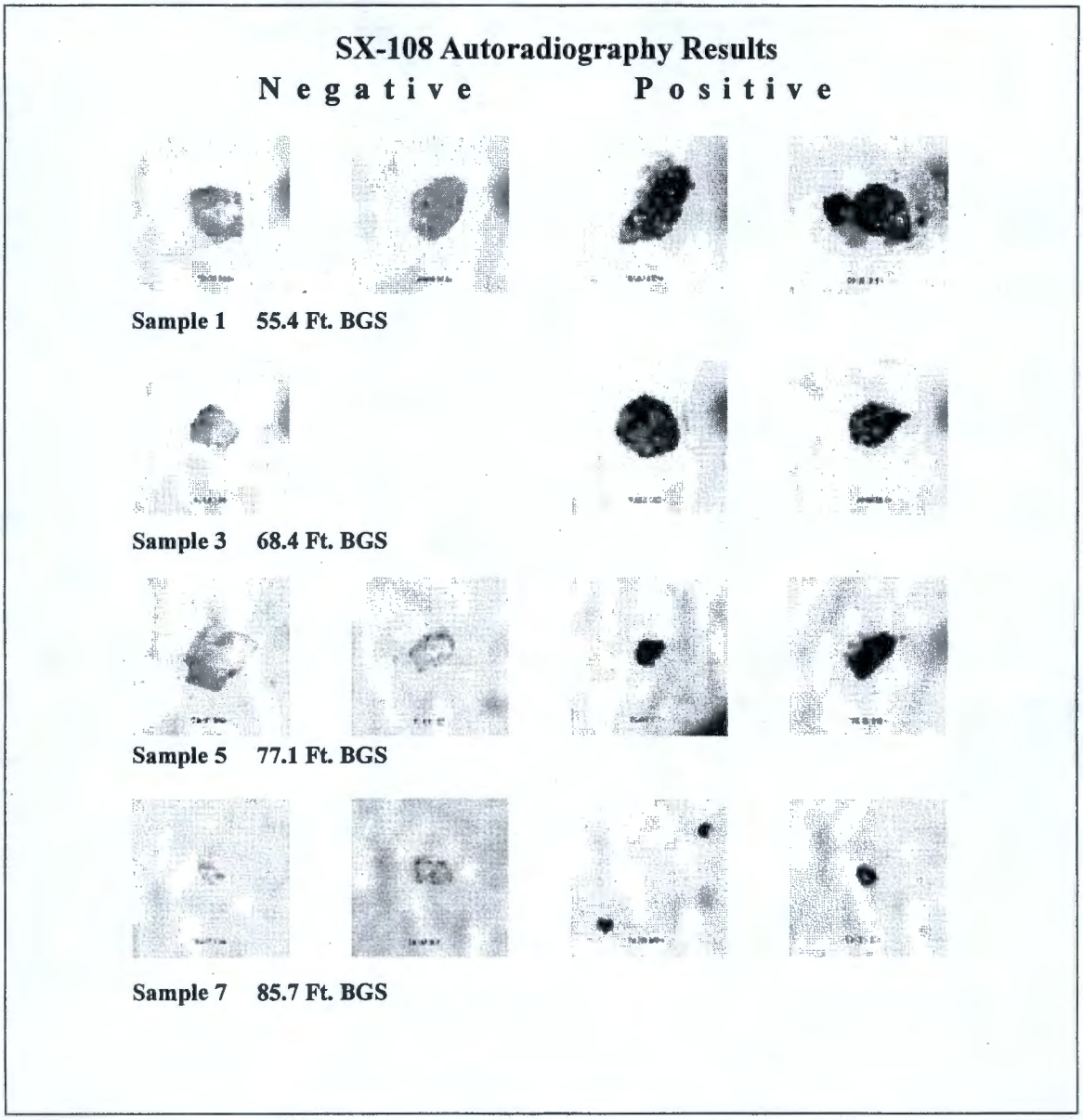

Note: Grains that were identified as non-radioactive are denoted negative, and radioactive grains are positive. All negative grains are non-micaceous silicates, and all positive grains are micas alone or micas with minor adhering smectite.

Figure D.3.5.4. Comparison of Photostimulated Luminescence Data to Low Level Gamma Counting Results.

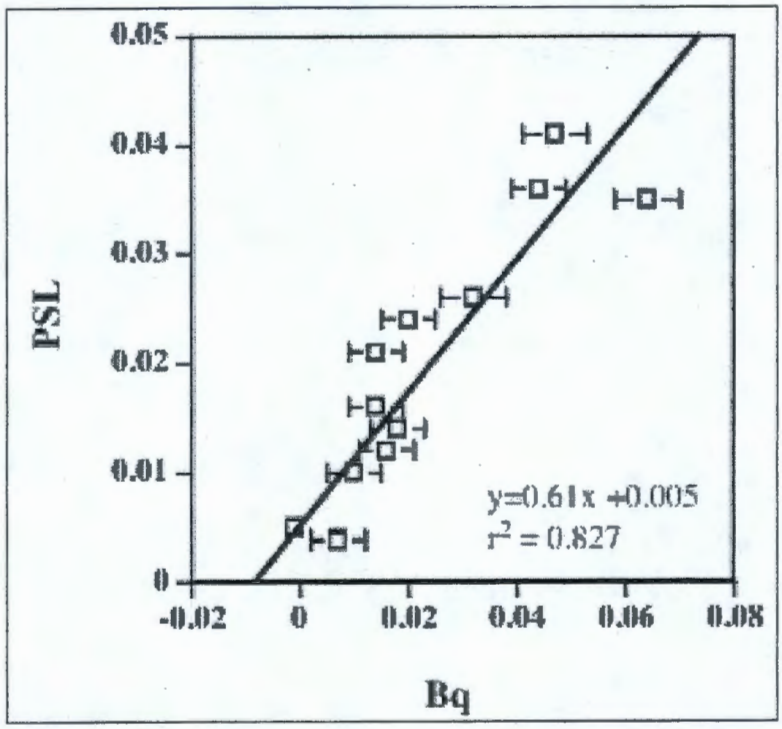

Note: The autoradiography method detected radioactive particles at a level below the detection limit low-level gamma counting, which was ca. 0.01 Bq. Gamma counting confirmed that radiation was emitted by the decay of ^{137}Cs.

Figure D.3.5.5. Autoradiograph of Clasts From SX-108 that were Previously Screened and Mapped as "Positive" or "Negative."

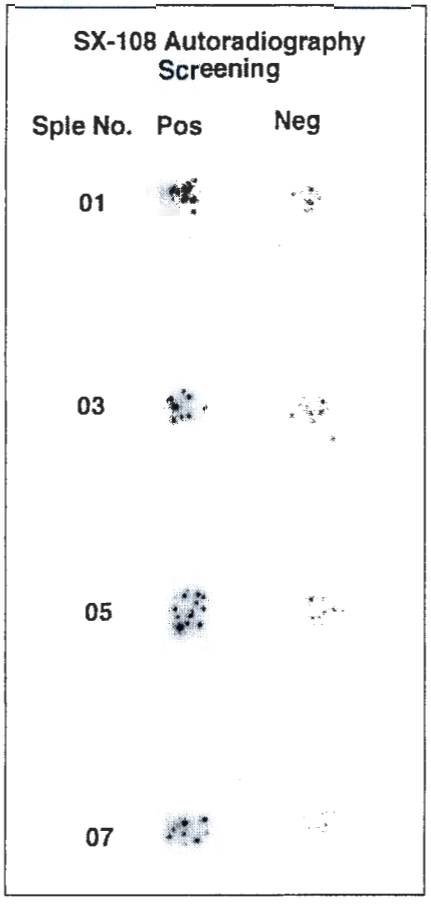

Note: The image brightness has been adjusted to show faint positive signals from negative grains.

Figure D.3.5.6. SEM Images of a Quartz Grain in SX-108 Sample 03, Showing the Presence on the Grain Surface of Secondary Minerals, Apparently Zeolite.

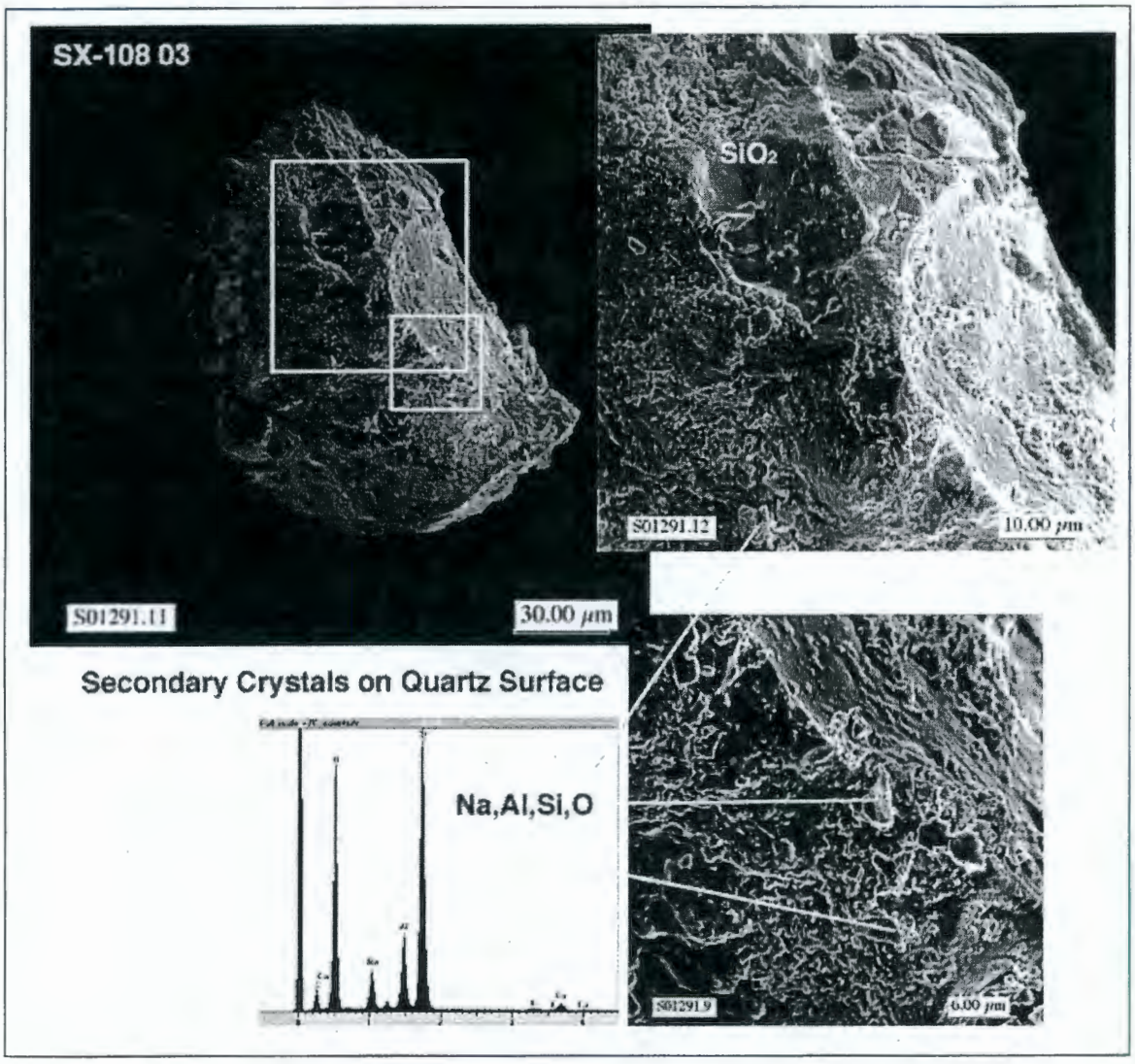

Figure D.3.5.7. Secondary Zeolite on the Surface of a Quartz Grain From SX-108 Sample 07.

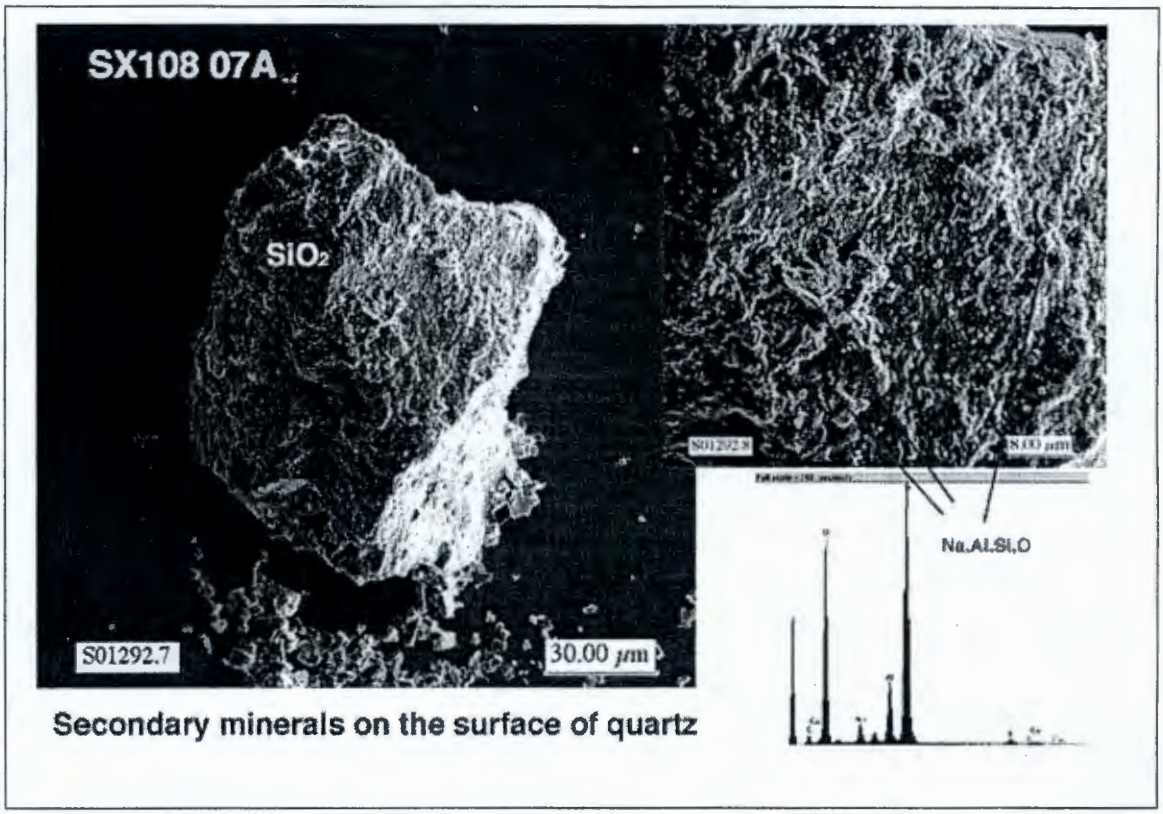

D.3.5.4 Conclusions and Implications

This study confirms the preferential retention of ^{137}Cs by micaceous minerals the SX tank farm sediments. ^{137}Cs was concentrated in micas during the interaction of tank wastes with sub-tank sediments, to the exclusion of more abundant smectites. The competitive retention of Cs by micas is consistent with the published observations of strong binding by micas in both the laboratory and contaminated settings. No other mineral phases were found to significantly sorb $^{137}Cs^{+}$ from tank waste. Small activity was associated with minute zeolite crystals on the surfaces of some silicates such as quartz. These zeolites may have precipitated during alkaline waste-sediment reaction and retained some $^{137}Cs^{+}$.

The future release of fluids to the SX tank farm vadose zone through waste retrieval or infiltration could pose threat of $^{137}Cs^{+}$ remobilization. Our studies of the mineralogic residence of sorbed $^{137}Cs^{+}$ support the following implications. First, the competitive desorption of $^{137}Cs^{+}$ may be limited by the strong preference of micas for Cs^{+} over other cations. Second, $^{137}Cs^{+}$ desorbed from micas and sparse zeolites may be rapidly resorbed by previously un-impacted sediments downgradient from the site of desorption; the presence of high-energy sites on these micas may effectively remove $^{137}Cs^{+}$ from dilute solutions.

D.3.5.5 Acknowledgement

These studies were supported, in part, by the DOE EMPD through a FY 97 funded project: "Function Mechanisms and Desorption Rates of Sorbed Cs in High Level Waste Contaminated Sediments: Implications to Future Behaviors and In-Ground Stability" (Zachara, McKinley, Ainsworth, and Serne).

D.3.5.6 References

Comans, R. N. J., and D. E. Hockley, 1992, "Kinetics of Cesium Sorption to Illite," *Geochimica et Cosmochimica Acta*, Vol. 56:1157-1164.

Cornell, R. M., 1993, "Adsorption of Cesium on Minerals: A Review," *Journal of Radioanalytical Nuclear Chemistry*, Vol. 171:483-500.

Evans, D. W., J. J. Alberts, and A. I. C. Roy, 1983, "Reversible Ion-Exchange Fixation of Cesium-137 Leading to Mobilization from Reservoir Sediments," *Geochimica et Cosmochimica Acta*, Vol. 47:1041-1049.

Freeman-Pollard, J. R., J. A. Caggiano, and S. J. Trent, 1994, *Engineering Evaluation of the GAO/RCED-89-157, Tank 241-T-106 Vadose Zone Investigation*, Report No. BHI-00061, Rev. 00, Bechtel Hanford Inc., Richland, Washington.

Lederer, C. M., V. S. Shirley, E. Browne, J. M. Dairiki, R. E. Doebler, A. A. Shihab-Elden, L. J. Jardine, J. K. Tuli, and A. B. Buyrn, 1978, *Table of Isotopes, Seventh Edition*, John Wiley & Sons, New York.

McKinley, J. P., C. J. Zeissler, J. M. Zachara, R. J. Serne, R. M. Lindstrom, H. T. Schaef, and R. D. Orr, 2001, "The Distribution and Retention of ^{137}Cs in Sediments Beneath Leaked Waste Tanks at the Hanford Site, Washington," *Environmental Science and Technology*, (In press).

Sawhney, B. L, 1970, "Potassium and Cesium Ion Selectivity in Relation to Clay Mineral Structure," *Clays and Clay Minerals*, Vol. 18:47-52.

Tallman A. M., K. R. Fecht, M. C. Marratt, and G. V. Last, 1979, *Geology of the Separations Areas, Hanford Site, South-Central Washington*, RHO-ST-23, Rockwell Hanford Operations, Richland, Washington.

Zeissler, C. J., R. M. Lindstrom, and J. P. McKinley, 2001, "Radioactive particle analysis by digital autoradiography," *Journal of Radioanalytical and Nuclear Chemistry*, Vol. 248, No. 2, 407-412.

D.3.6 DESORPTION AND LEACHING OF CS+ FROM WMA S-SX SEDIMENTS

Calvin C. Ainsworth[1], Chongxuan Liu[1], Steven C. Smith[1], Odeta S. Qafoku[1], John M. Zachara[1], and James E. Szecsody[1]

[1]Pacific Northwest National Laboratory, Richland, Washington 99352

D.3.6.1 Introduction

The Cs^+ sorption process in geologic materials consists of a forward adsorption reaction and backward desorption reaction. Both of these reactions can be characterized by a two stage kinetic process: a fast reaction related to accessible external sites associated with the basal planes of 2:1 clay minerals (e.g., smectite, vermiculites, etc.) and a slow, diffusion controlled transport to/from frayed edge sites (FES) of micas (Zachara et al. 2001; Cornell 1993; Comans and Hockley 1992; Comans et al. 1991; Evans et al. 1983). Contrary to earlier conclusions, Cs does not seem to exchange with dehydrated interlayer sites of micas (Cornell 1993; Comans et al. 1991). Investigations by Coleman and Le Roux (1965; as reported by Cornell 1993) and Brouwers et al. (1983) have shown that Cs replacement is controlled by ion exchange equilibrium, and this equilibrium is reversible, albeit slowly, with time.

The vadose zone sediments in the S and SX tank farms are a complex mineral composite, including unstable primary phases (e.g., feldspars, micas, etc.) that are slowly weathering and more stable secondary phases (e.g., Al and Fe oxides, poorly crystalline SiO_2, and smectites). The harsh nature of tank leaked fluids (high base, high Na concentrations etc.) from the tanks in SX farm has driven dissolution and precipitation reactions that occurred concomitantly with Cs adsorption. Because of the disparate rates of Cs adsorption and mineral dissolution-precipitation, Cs may have become occluded from the surrounding environment by precipitation of secondary minerals on the surfaces and edges of Cs bearing sorbents. This "armoring" against Cs desorption would limit the pool of sorbed Cs available fore future mobilization and transport.

Here we report on new studies of Cs desorption from ^{137}Cs-contaminated WMA S-SX sediments. These studies investigated Cs desorption in batch and small column reactors with different exchanging cations (Na^+, K^+ and Rb^+). The potential for particle armoring as a control on Cs desorption was evaluated using acid ammonium oxalate $[(NH_4)_2C_2O_4]$ as the extractant. Time-dependent desorption is described by coupling the multi-site exchange model (discussed in Section D.3.1) with a radial diffusion model approximated by a pseudo-1st-order rate. These results provide insights into the time dependence of Cs release from WMA S-SX sediments.

D.3.6.2 Experimental Procedures

The collection and analyses of sediments from the SX-108 borehole and 41-09-39 borehole are discussed elsewhere (Serne et al. 2001a, b). Materials used in these investigations were SX-108 sediments 3A, 7A, and 8A and 41-09-39 sediments 6AB, 7ABC, and 9ABC. Subsamples of the field moist material were air-dried to a constant weight and sieved to pass a 2 mm mesh. Gravels greater than 2 mm were removed from the air-dried material during the sieving process. The sieved material was thoroughly mixed to obtain a homogeneous sample. Total ^{137}Cs activity for these sediments is reported in Section D.3.1 (Table D.3.1.4). However, the Cs inventory of the

sediments also includes the Cs isotopes 133, 135. The total Cs determined by mass spectrometry (discussed in Section D.6.1) is 23.72, 13.66, 16.02, and 0.877 nmoles Cs/g sediment for 7A, 3A, 7ABC, and 9ABC, respectively.

D.3.6.2.1 Cesium Desorption Experiments. Batch-type desorption experiments were performed by suspending approximately 0.5 g sediment in 5 g solutions of 0.5 mol/L KNO_3, 0.5 mol/L $RbNO_3$, or 0.25 mol/L $(NH_4)_2C_2O_4$ in Oak Ridge centrifuge tubes. Tubes were sealed and agitated at 25 C. At prescribed time intervals (0.02, 0.10, 0.21, 1, 4, 8, 16, 32, and 47 days; [$(NH_4)_2C_2O_4$ extraction was followed for 64 days instead of 47 days]) tubes were centrifuged (5000 rcf for 10 min), about 0.5 mL supernate was removed to tared gamma counting tubes, weighed, and aqueous ^{137}Cs activity determined by gamma-ray spectroscopy. After counting, the solutions were returned to the centrifuge tubes and the samples mixed vigorously for several minutes, and then returned to slow agitation. Sediments 3A, 7A, 7ABC, and 9ABC were studied in duplicate. After 47 days, enough solid KNO_3 or $RbNO_3$ was added to each tube to increase the total K or Rb aqueous concentrations to 2 mol/L and the aqueous phase was monitored as before for an additional 8 days.

A second set of suspensions of each of the four sediments was prepared with the ammonium oxalate electrolyte for destructive sampling to allow determination of the aqueous concentrations of elements of interest, e.g., Fe, Al, Ba, Ca, Cr, K, Mg, Na, and Si. Each suspension was composed of 0.5 g of sediment and 5 mL of electrolyte. Duplicate suspensions were centrifuged at 5000 rcf for 30 minutes at selected time intervals (2.5 hours, 10 hours, 2 days, 8 days, 33 days, and 64 days). The supernatant was carefully transferred to a plastic syringe fitted with a 0.2 μm filter. The first 1 mL of filtrate was discarded and the remaining collected in a plastic tube. The $^{137}Cs_{aq}$ activity was determined as previously described. The filtrate was analyzed for concentrations of the elements previously mentioned using ICP-AES.

D.3.6.2.2 Cesium Leaching from Columns. Approximately 2g of air-dry sediments (7A, 8A, 6AB, 7ABC) were packed into 3.1 cm length by 0.78 cm diameter polypropylene columns. The columns were connected to a peristaltic pump on one side and a fraction collector on the other. They were continually leached with 0.5 mol/L $NaNO_3$ solution for about 25 to 30 pore volumes at a flow rate of 0.1 ml min^{-1} (residence time ≈ 6 min). Right before columns were connected to the leaching solution, 10 mL of pure CO_2 gas was injected through columns to displace the air from the sediment pore space. A uniform movement of the leaching solution through the packed, air-dried sediments was observed. Sediment leachates were collected every six minutes and the mass of collected solutions determined to better estimate flow rate. After all the leachates were collected, columns were flushed with 1.0 mol/L $NaNO_3$ or KNO_3 and the electrical conductivity monitored to estimate conservative tracer breakthrough. This procedure was followed by flushing the columns with deionized water, then weighing the columns, and determining the pore space as the difference between wet and air-dry sediments. The leachates were analyzed for ^{137}Cs via gamma-ray spectroscopy. Two additional columns, packed with sediments 7A and 7ABC, were leached as above but with 0.5 mol/L KNO_3 for 20 pore volumes followed by 0.25 mol/L $(NH_4)_2C_2O_4$ (adjusted to pH 3) for an additional 20 to 25 pore volumes; all other procedures were performed as described.

The effect of temperature on Cs leaching was studied using two columns (as described above) packed with SX-108 7A sediment. With the initial temperature set at about 15 °C, 0.5 mol/L

$NaNO_3$ solution was passed through a column at 0.1 ml min^{-1}. Once a steady-state Cs effluent concentration was approximated (~100 min), a stop-flow event was initiated. After 2.5 h, flow was restored and effluent monitored to determine effluent return to a quasi-steady-state condition. At this point, the temperature was increased to about 35 °C, effluent monitored to determine return to a quasi-steady-state condition, where a stop-flow event was again initiated. This cycle was repeated once again at 55 °C. The second column followed a similar procedure except after initial leaching (~100 min) at 15 °C the temperature was increased to 55 C. After a quasi-steady-state Cs concentration was obtained, a series of three stop-flow events were performed as before, but with the temperature being decreased (55 °C to 35 °C to 15 °C) after each event. Temperature changes were accomplished by submerging the column and the inflow line (about 2 m long) in a temperature-controlled bath; temperature equilibration was determined by monitoring the effluent temperature (~50 min).

D.3.6.3 Results

D.3.6.3.1 Cesium Desorption with 0.5 M KNO_3 or $RbNO_3$. The desorption of Cs resulting from exposure to 0.5 mol/L K- or $RbNO_3$ exhibited a rapid exchange between the surface Cs and K or Rb, followed by a continuous slow release of Cs from the surface (Figure D.3.6.1). Generally, $RbNO_3$ solutions caused greater exchange of Cs between the sediment and the solution during the initial 24 hours. This results from the higher selectivity of Rb over K and is related foremost to the hydration energies of the cations, K greater than Rb greater than Cs (Cornell 1993). The exception to this trend is observed for tank SX-108 sample 3A. This sediment is one of the most highly weathered sediments collected; scanning electron microscopy (Section D.1.1) shows deteriorated mica edges, surface pits, and copious secondary mineral phases. Mineral alteration may have changed the relative exchange affinities of Cs, K, and Rb.

Further Cs release, after the initial 47-day equilibration, was affected by increasing the [K]aq or [Rb]aq concentrations to 2 mol/L (Figure D.3.6.1). After electrolyte addition, the sediments exhibited the same type of desorption profile observed after the first electrolyte addition; that is, a rapid exchange followed by continuous slow release. However, sediments 3A and 7A displayed unusual behavior. The addition of 2.0 mol/L KNO_3 released more Cs from the 3A sediment than Rb, even though at 47 days the two cations had exchanged the same quantity of Cs. For 7A, the 2.0 mol/L K- and $RbNO_3$ desorbed the same amount of Cs after 8 days, but Rb was far more competitive for Cs than K was at the initial 0.5 mol/L concentration. Both of these findings were unexpected, and, at this point, the cause(s) remain unresolved.

Figure D.3.6.1. Desorption of $^{137}Cs^{+}$ From WMA S-SX Sediments as a Function of Exchangeable Cation (K or Rb), Time and Ionic Strength (less than 47 days, K^{-} or $RbNO_3$ = 0.5 mol/L; greater than 47 days, K^{-} or $RbNO_3$ = 2.0 mol/L).

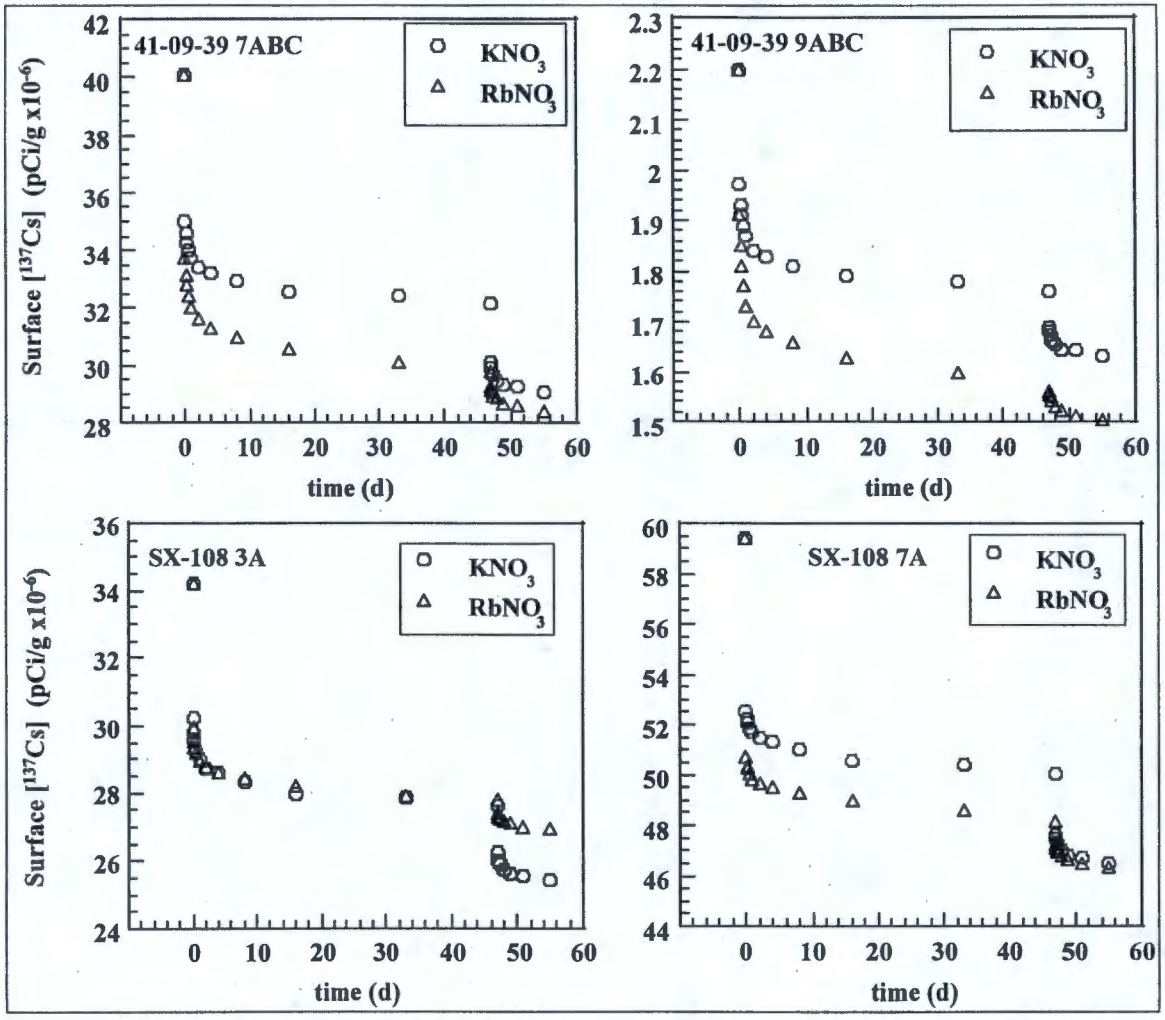

The percentage of Cs that was desorbed over the first two days (arbitrarily set as the initial exchange) varied with exchange cation (K or Rb) and sediment (Table D.3.6.1). With the exception of sediment 3A, the $RbNO_3$ solution extracted more Cs than KNO_3. The interesting point about these data was the apparent incongruity regarding Cs release from 9ABC. This sediment had the lowest mole fraction Cs (X_{Cs}) on the exchange complex of any of the sediments investigated; log X_{Cs} = -3.75, -3.82, -3.81 and -4.95 for 7A, 3A, 7ABC, and 9ABC, respectively. This X_{Cs} translates into almost a 0.5 log unit increase in Cs^+ binding affinity for 9ABC as measured by a conditional exchange constant, K_c (Section D.3.1). Increased binding affinity should translate to a smaller percentage of Cs desorbed from this sediment. In addition, the adsorption density (X_{Cs}) in the other three sediments were relatively similar, and therefore should release comparable concentrations of Cs. Yet, the tank SX-108 sediments lagged behind the other sediments in the percentage Cs released.

Table D.3.6.1. Percentage of ^{137}Cs Desorbed During the Initial Exchange with 0.5 mol/L K- or $RbNO_3$ and 2 mol/L K- or $RbNO_3$.

Sediment	0.5 mol L^{-1}		2 mol L^{-1}	
	K	Rb	K	Rb
	%			
SX-108				
7A	14.1	16.7	18.2	20.0
3A	17.0	16.6	21.5	20.1
41-09-39				
7ABC	17.7	22.4	24.1	25.5
9ABC	17.5	24.1	20.6	28.7

The interaction of $(NH_4)_2C_2O_4$ with the same four sediments extracted 44.6%, 60.8%, 55.9%, and 44.1% of the Cs after 64 days for 7ABC, 9ABC, 3A, and 7A, respectively (Figure D.3.6.2; Table D.3.6.2). All of the sediments exhibited signs of continued release of Cs to at least 64 days unlike the results within K- or $RbNO_3$. The use of $(NH_4)_2C_2O_4$ was based on two premises: (1) layer lattice silicates exhibit similar selectivities for the NH_4^+ and K^+ ions (Bruggenwart and Kamphorst 1979) and (2) $(NH_4)_2C_2O_4$ dissolves poorly crystalline oxides without significant damage to layer silicates if limited to about 2-hours (Loeppert and Inskeep 1996). From the percentage of total solids dissolved after 33 days (Table D.6.3.2), the extraction cannot be considered benign. However, the initial [Cs]aq activity that was determined at 2.4 hours (Table D.3.6.2) showed substantially greater Cs release than KNO_3 (approximately 7%) or $RbNO_3$ (approximately 4%). Because ion selectivity increases as $Cs^+ > Rb^+ > K^+ \approx NH_4^+$, the larger initial [Cs]aq concentrations observed in the $(NH_4)_2C_2O_4$ solutions suggested that secondary mineral precipitates were dissolved that allowed greater exchange of the sorbed ^{137}Cs. The action of the $(NH_4)_2C_2O_4$ in dissolving poorly crystalline oxides appears to expose Cs

containing surface and edge sites to exchange with the NH_4^+ cation. While Cs containing mineral particles coated with secondary mineral precipitates resulting from waste-sediment reactions and natural weathering inhibits Cs^+ exchange with the aqueous phase, the amount of Cs armored against exchange appears to be minimal.

Table D.3.6.2. Percentage of ^{137}Cs Released to Solution by $(NH_4)_2C_2O_4$, KNO_3 and $RbNO_3$ at Selected Times and the Percentage of Solids Dissolved After 33 Days Exposure to 0.25 mol/L $(NH_4)_2C_2O_4$.

Sediment	^{137}Cs Released					Solids Dissolved[1]
	$(NH_4)_2C_2O_4$			KNO_3	$RbNO_3$	$(NH_4)_2C_2O_4$
	2.4 hr	33 days	64 days	2.4 hr	2.4 hr	33 days
	%					
41-09-39						
7ABC	21.3	40.0	44.6	13.8	17.3	2.03
9ABC	19.6	52.5	60.8	12.3	16.2	1.73
SX-108						
3A	19.5	49.2	55.9	12.8	13.6	2.41
7A	19.3	37.4	44.1	12.1	15.2	2.77

[1]percentage of solids dissolved as Fe, Al, and Si oxides after 33 days.

D.3.6.3.2 Kinetic Modeling of Cs Desorption in K and Rb Electrolytes. The kinetic data for Cs desorption by 0.5 mol/L KNO_3 or $RbNO_3$ (Figure D.3.6.1) was simulated based on the assumption that Cs in the contaminated sediments consists of three populations: equilibrium-controlled exchangeable Cs, kinetic-controlled exchangeable Cs, and a Cs pool termed "non-exchangeable" (this pool includes Cs armored against exchange discussed above). Similar models have been used successfully to simulate ^{137}Cs transport in undisturbed soil columns contaminated during the Chernobyl accident (Toso and Velasco 2001). Assuming that the kinetic-controlled exchangeable Cs can be modeled using a first order rate law, then Cs desorption can be described as

$$[Cs]_{aq} = [Cs]_{aq}^{equi} + [Cs]_{aq}^{kinetic} \qquad (D.3.6.1)$$

$$\frac{d[Cs]_{aq}^{kinetic}}{dt} = k_1\left([Cs]_{aq}^{kinetic}(t=0) - [Cs]_{aq}^{kinetic}\right) \qquad (D.3.6.2)$$

where $[Cs]_{aq}^{equi}$ is the equilibrium-controlled exchangeable Cs, $[Cs]_{aq}^{kinetic}$ is the kinetic-controlled exchangeable Cs, $[Cs]_{aq}^{kinetic}(t=0)$ is the maximum kinetic-controlled exchangeable Cs, and k_1 is the first order rate constant. Equations D.3.6.1 and D.3.6.2 can be solved to obtain

Figure D.3.6.2. Ammonium Oxalate Extraction of ^{137}Cs From S-SX Sediments.

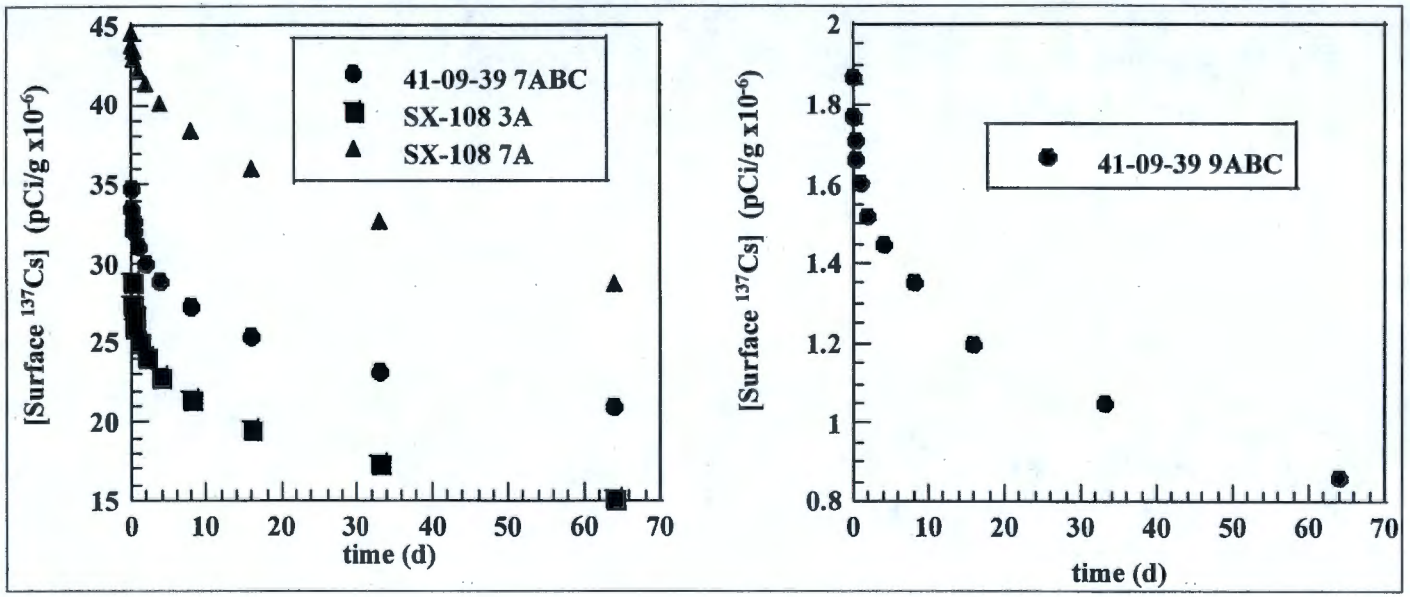

$$[Cs]_{aq} = [Cs]_{aq}^{exch} - [Cs]_{aq}^{kinetic}(t=0)\exp(-k_1 t) \qquad \text{(D.3.6.3)}$$

where $[Cs]_{aq}^{exch}$ is the total amount of exchangeable Cs (including equilibrium- and kinetic-controlled exchangeable Cs). Model (3) contains three parameters: the total amount of equilibrium- and kinetic- controlled Cs, and the rate parameter k_1. These 3 parameters were estimated by fitting to experimental data. Because the $[Cs]_{aq}^{exch}$, and $[Cs]_{aq}^{kinetic}$ were estimated from data with specific ionic strength and sample conditions, an ion exchange model (Section D.3.1) was used in back-calculating the total exchangeable Cs and total kinetic-controlled exchangeable Cs.

D.3.6.3.3 Cs Ion Exchange Model. The Cs ion exchange simulation was based on a 2-site model with its parameters determined previously or from the literature (exchange parameters between Cs, Na, and K were extracted from Zachara et al. [2001]; exchange parameters between Rb and Cs or Na or K were taken from Brouwers et al. [1983]). For each value of $[Cs]_{aq}^{exch}$ or $[Cs]_{aq}^{kinetic}$ estimated from the kinetic model, a corresponding total exchangeable or kinetic-controlled Cs concentration, $[Cs]_{aq}^{exch}$ or $[Cs]_{aq}^{kinetic}$, was calculated from the exchange model as described below.

Cs-Mi exchange on site I (Mi = Na, K, Rb)

$$N_{Mi}^{I}[Cs^+]K_c^I(Cs-Mi) = N_{Cs}^{I}[Mi^+] \qquad \text{(D.3.6.4)}$$

Cs-Mi exchange on site II

$$N_{Mi}^{II}[Cs^+]K_c^{II}(Cs-Mi) = N_{Cs}^{II}[Mi^+] \qquad \text{(D.3.6.5)}$$

Mass balance on exchange site I

$$N_{Cs}^{I} + \sum_{i=1}^{L} N_{Mi}^{I} = 1 \qquad \text{(D.3.6.6)}$$

Mass balance on exchange site II

$$N_{Cs}^{II} + \sum_{i=1}^{L} N_{Mi}^{II} = 1 \qquad \text{(D.3.6.7)}$$

Mass balance of Cs

$$\left(E^I N_{Cs}^{I} + E^{II} N_{Cs}^{II}\right) CECW_s + V[Cs^+] = T_{Cs} W_s \qquad \text{(D.3.6.8)}$$

Mass balance of Mi

$$\left(E^I N^I_{Mi} + E^{II} N^{II}_{Mi}\right) CEC W_s + V[Mi^+] = T_{Mi} W_s \qquad \text{(D.3.6.9)}$$

where N^I_{Cs} and N^I_{Mi} are the equivalent fractions of Cs and Mi on site I, respectively; N^{II}_{Cs} and N^{II}_{Mi} are the equivalent fractions of Cs and Mi on site II, respectively; E^I and E^{II} are the equivalent fractions of site I and site II with regard to the total soil CEC; W_s is the dry soil weight, V is aqueous volume, and T_{Mi} is the total initial concentrations of Mi in soil; K^I_c and K^{II}_c are conditional exchange constants on site I and site II, respectively; N^I_i and N^{II}_i are the equivalent fraction of ion Mi on site I and II, respectively; [Mi] is the aqueous concentration of Mi in solution; and (Cs^+) is the aqueous concentration of Cs, which equals $[Cs]^{exch}_{aq}$ W_s/V or $[Cs]^{kinetic}_{aq}$ W_s/V. The calculated TCs was the total Cs concentration corresponding to $[Cs]^{exch}_{aq}$ or $[Cs]^{kinetic}_{aq}$.

The above kinetic model well described experimental results out to about 16 days (386 hours, Figure D.3.6.3) with estimated parameters summarized in Table D.3.6.3. For all sediments, several general trends were pertinent to the above analysis.

Table D.3.6.3. Estimated Properties for the Three-Site (pool) Cs Desorption Model.

	K		Rb		K	Rb
	Exchangeable	Kinetic Fraction	Exchangeable	Kinetic Fraction	Overall mass	Overall mass
	^{137}Cs(pCi/g)				transfer rate (per hour)	
SX-108 07A	3.05×10^{7}	2.42×10^{6}	1.17×10^{7}	1.70×10^{6}	0.009	0.009
SX-108 03A	1.79×10^{7}	6.14×10^{6}	6.38×10^{6}	1.50×10^{6}	0.026	0.019
41-09-39 7ABC	2.22×10^{-7}	5.81×10^{6}	1.03×10^{7}	2.96×10^{6}	0.02	0.019
41-09-39 9ABC	1.26×10^{6}	4.39×10^{5}	5.91×10^{5}	2.56×10^{5}	0.029	0.026

First, the total K-exchangeable Cs was required to be between 19 to 23% of the total Cs on the exchange complex in order to achieve reasonable model simulations, while the total Rb-exchangeable Cs was required to be between 19 to 27% of the total Cs. This small difference in the computed exchangeability of Cs in the K^+ and Rb^+ electrolyte reflect the difference in selectivity of Rb, K, and Cs and that the Rb exchange coefficients were not determined for the geologic materials, but rather, extracted from the literature. In addition, the calculated percentages of K and Rb exchangeable Cs could be affected by: (1) potential CEC errors used in the model (Na-CEC was used and actual samples may contain higher CECs because K, Rb, and Cs can occupied more sites than Na); and (2) other cations present in solution that were not considered in the ion exchange calculation, but may affect Cs displacement, such as Ca^{2+}.

Figure D.3.6.3. Aqueous Exchange Data and Results of Three-Site Model Simulations for KNO_3 or $RbNO_3$ Exchange with ^{137}Cs Contaminated Sediments a) SX-108 3A, b) SX-108 7A, c) 41-09-39 7ABC, and d) 41-09-39 9ABC.

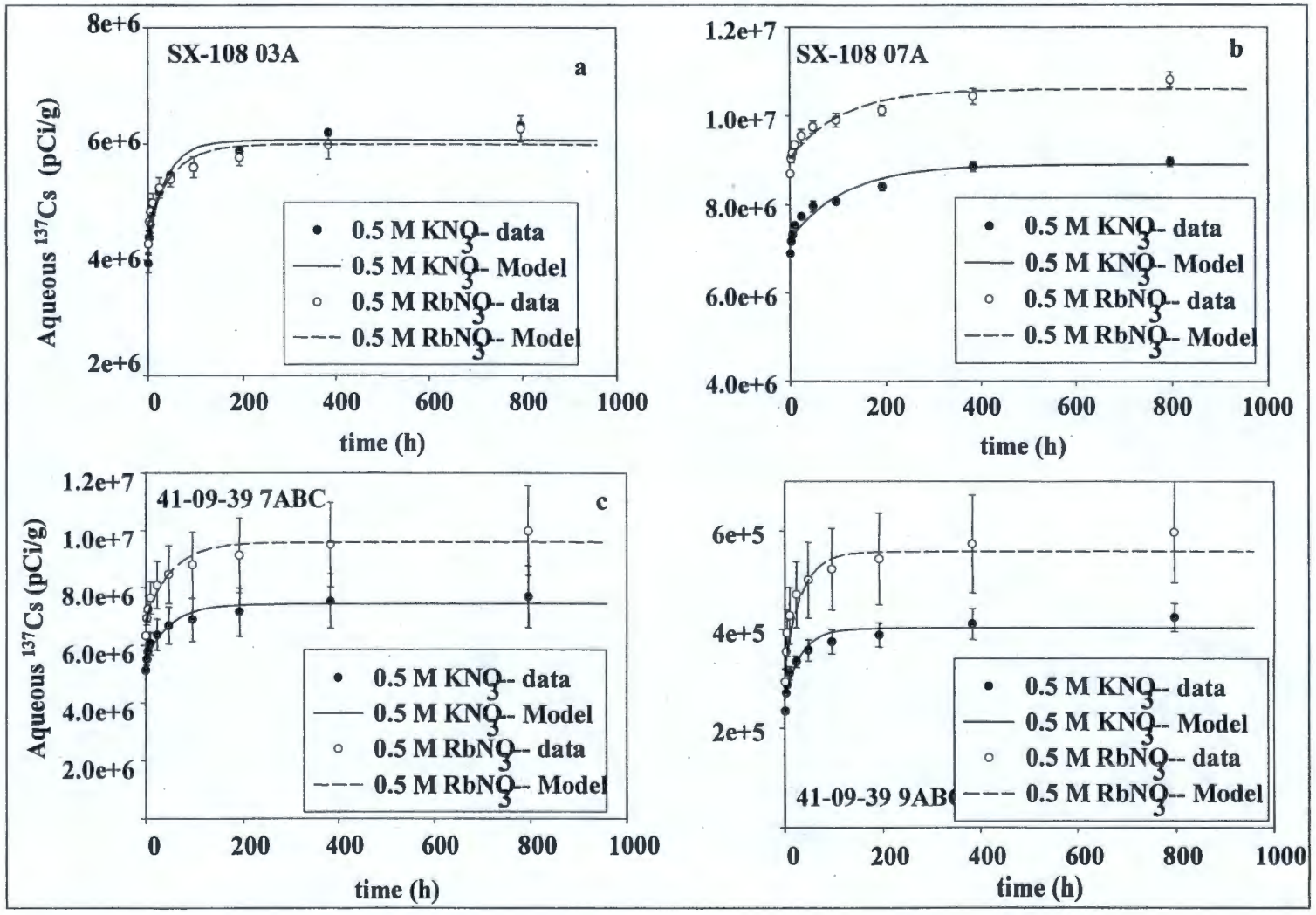

Second, the overall mass exchange coefficient (pseudo-1st order rate coefficient) for the kinetic-controlled exchangeable Cs indicated a slow Cs desorption step (rate constant ranges between 0.01-0.03 h^{-1}, or a $t_{1/2}$ = 23.1 and 69.3 hours). This slow Cs desorption is attributed to a film diffusion of Cs from a sorbed site to the bulk aqueous phase. Reported literature values of Cs adsorption and desorption rate coefficients range widely depending on the models and experimental procedures used. Generally, the kinetics of ion exchange can be divided into three individual processes (Sposito 1994): (1) film diffusion, which is ion diffusion from bulk solution to sorption sites; (2) kinetic complexation reactions at sorption sites; and (3) ion diffusion into intraparticle sorption sites. The desorption process is simply the reverse. Based on an experimental procedure developed by Ogwada and Sparks (1986), Liu et al. (1994) modeled rate coefficients for these individual processes for illite-containing and montmorillonite-containing soils. The determined rate coefficients were film diffusion 0.24-0.96/hr (half-life = 0.72^{-3} hours), intraparticle diffusion 1.68-3.84/hr (half-life = 0.18-0.42 hours), and kinetic sorption 10.8 hr (half-life = 0.06 hours). Based on the determined rate coefficient for film diffusion, Liu et al. (1994) calculated that the film diffusion coefficient was between 4.8-5.2 × 10^{-12} cm^2/s. The rate coefficient for the present study, based on our modeling results, was approximated by a film diffusion process, suggesting that film diffusion may be the rate-limiting process for Cs release from the Hanford sediments.

Coman and Hockley (1992) studied the long-term kinetic behavior of Cs and found that the kinetic sorption of Cs on illite could be divided into two steps. The fast sorption/desorption of Cs was suggested to be between bulk solution and surface sorption sites with a rate constant about 0.04-0.4/hr (half-life = 1.7-17 hours). This was followed by a slow step of Cs "fixation" with a rate constant of about 0.00015-0.0002/hr (half-life = 3465-4620 hour). The rate coefficient of the fast sorption/desorption step was close to our value (0.01-0.04/hr). However, Cs desorption in the current study appears to continue for greater than 30 days. In the current studies, the initial exchange and fast desorption step (modeled data), was followed by a long-term, slow desorption period similar to that observed by Coman and Hockley (1992) suggesting that the Cs "fixation" was reversible, but with a smaller rate than previously reported.

The later desorption data (8 to 47 days) for the all sediments was used to estimate a first-order rate constant (Table D.3.6.4) for the slow desorption process. The calculated rate constants define an extremely slow process, and one that is far reduced below that expected by film diffusion. The $t_{1/2}$ calculated from the pseudo-1st order rate constants illustrate the slowness of this reaction (Table D.3.6.4). Our results are less than an order of magnitude smaller than that observed for illite (Coman and Hockley 1992). The slowness of this observed desorption process is thought to result from the long inground exposure (greater than 30 years), the elevated temperature of the sediments during aging (50 to 80 °C), and the harsh chemical environment caused by the leaked fluids (hyperalkaline, hypersaline). It is significant that the $t_{1/2}$ for 9ABC was substantially less than that of the other sediments. Based on the concentrations of the other contaminants (e.g., Cr, Tc, Na), 9ABC appears to have been far less affected by the leaked tank wastes.

Table D.3.6.4. Pseudo-First Order Rate Constants and Half-Lives of the Slow Desorption Reaction Observed in WMA S-SX Sediments.

Sediment	Exchange Cation	Rate Constant per day	$t_{1/2}$ days
SX-108			
7A	K	4.14×10^{-4}	1674
	Rb	5.55×10^{-4}	1247
3A	K	5.63×10^{-4}	1232
	Rb	5.69×10^{-4}	1218
41-09-39			
7ABC	K	5.51×10^{-4}	1258
	Rb	9.75×10^{-4}	710
9ABC	K	6.94×10^{-4}	998
	Rb	1.39×10^{-4}	500

Our kinetic model was developed by utilizing aqueous ^{137}Cs data generated from the 0.5 mol/L K- or $RbNO_3$ exchange studies (Figure D.3.6.1). The data allowed the calculation of the total sediment Cs concentrations for the different sorbed populations considered by the model (Table D.3.6.3). The model and its fitted population estimates were used to simulate the desorption of ^{137}Cs from the same four sediments in the presence of increased electrolyte added after 47 days (2.0 mol/L K- or RbNO3 Figure D.3.6.4; K data only). The Cs→K exchange-desorption was well described by the model in all four sediments without any parameter adjustment. The model clearly embodies the primary features and phenomenology involved in the desorption process. From these results, we estimate that: (1) the exchangeable pool represents 20 to 30% of the total sediment Cs, (2) the kinetic fraction represents 20 to 35% of the total sediment Cs, and (3) the long-term fraction (by difference) represents 35 to 50% of the total sediment Cs. Of this latter fraction, it appears that only 6% to 10% can be directly attributable to secondary mineral precipitation related occlusion.

Figure D.3.6.4. Aqueous Exchange Data and Results of Three-Site Model Simulations for KNO_3 or $RbNO_3$ Exchange at 0.1 M (0 to 47 days) and 2.0 M (47 to 64 days) with ^{137}Cs Contaminated Sediments.

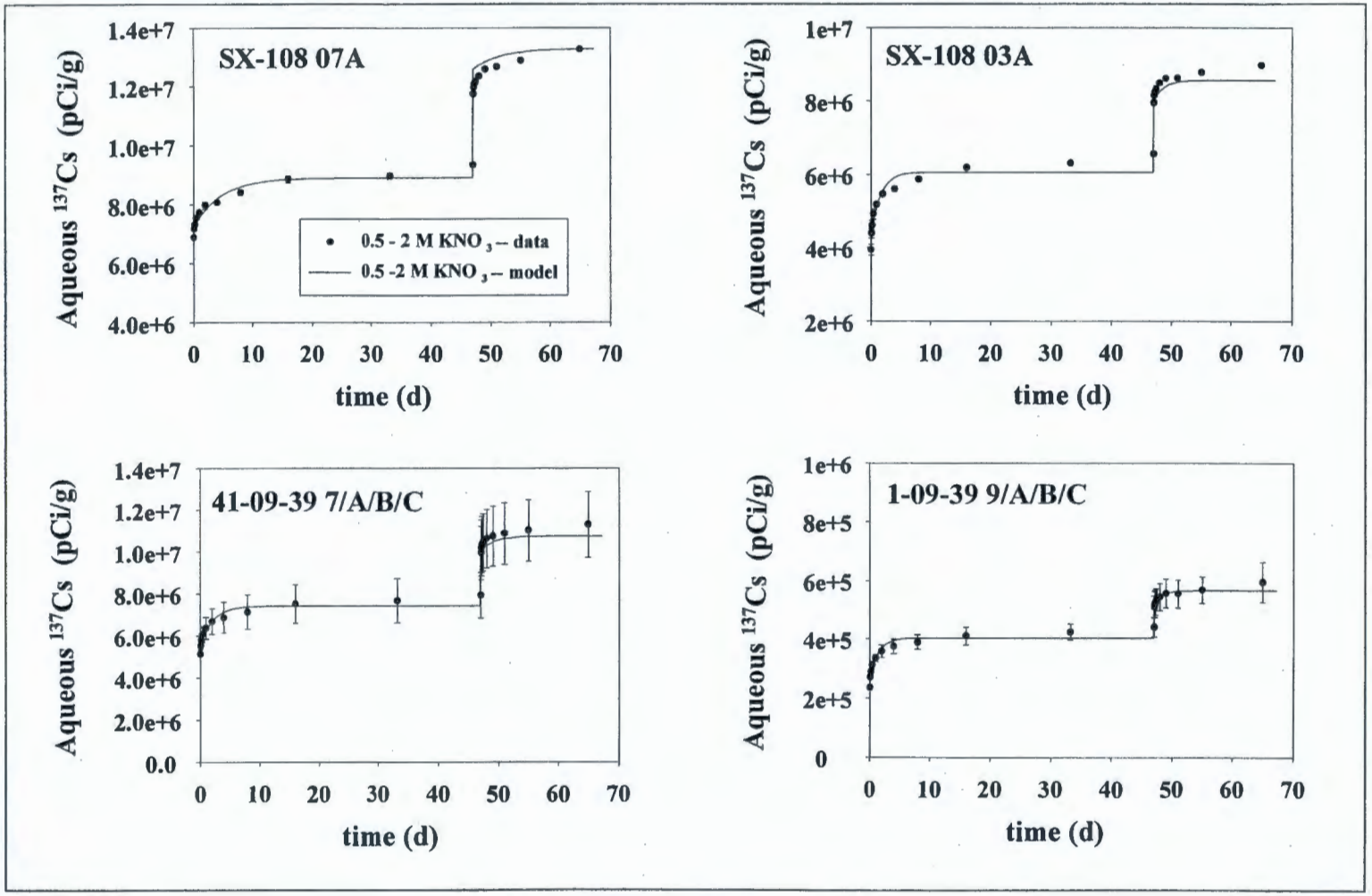

D.3.6.3.4 Cs Leaching from Columns. The leaching profile of ^{137}Cs by 0.5 mo/L $NaNO_3$ as a function of pore volume (pv) was characterized by an initial flush of ^{137}Cs followed by a long tail of decreasing ^{137}Cs activities (Figure D.3.6.5). The initial pulse of ^{137}Cs activity from these columns was the result of Na^+ exchange for Cs^+ on the easily accessible exchange sites. However, residual Na associated with the leaked fluids may have increased Cs^+ exchange over that expected from 0.5 mol/L $NaNO_3$. The residual Na concentration in these two sediments increased the initial Na_{aq} concentrations to at least 3.6 mol/L and 0.84 mol/L for 7A and 7ABC, respectively. While these quickly decreased (in 4-5 pv) to the influent Na concentration (0.5 mol/L), the initially high Na concentrations increased the initial flush of Cs over that expected for the influent solution. Sediment with 0.5 mol/L $NaNO_3$ or 5.0 mol/L $NaNO_3$ in batch mode showed that the higher electrolyte concentration solubilized ten-times more ^{137}Cs (see Section D.3.1, Figure D.3.1.4).

Despite the high initial flushing of ^{137}Cs, the total amount of Cs leached from the sediments was small compared to the total (Table D.3.6.5). For all columns, the initial four pore volumes accounted for about 1/3 of the Cs leached for the entire study and >1% of the total Cs. Four pore volumes represents that necessary to leach the residual Na from the columns. Based on modeling of the static-studies above (Figures D.3.6.3 and D.3.6.4), the Cs being leached from the columns was probably that associated with the easily exchangeable fraction, since the calculated diffusion-limited desorption rate constants for these sediments were small (0.01-0.03/hr, or a $t_{1/2}$ = 23.1- 69.3 hours). The residence time in these small columns was approximately 6 minutes; the entire study, up to the stopped flow event (at the 19th or 20th pore volume) took two hours. While stopping the flow for 19 hours did increase in Cs leaching, the increase in aqueous phase ^{137}Cs was small and transient. Depending on the mass transfer rates (film diffusion) for the individual sediments, the impact of 19 hours stopped-flow event is about what would be expected.

Table D.3.6.5. ^{137}Cs Activities (pCi/g) in 4 WMA S-SX Sediments, and Aqueous Concentrations (pCi/L and %) of ^{137}Cs Leached From Sediments by 0.5 mol/L $NaNO_3$.

Sediment	Total ^{137}Cs in sediment	^{137}Cs leached from sediments		^{137}Cs leached	
		Total	Initial[a]	Total	Initial[a]
	pCi/g			%	
SX-108					
7A	5.9×10^{7}	1.4×10^{6}	4.7×10^{5}	2.3	0.8
8A	5.6×10^{5}	4.7×10^{3}	1.4×10^{3}	0.8	0.3
41-09-39					
6AB	8.3×10^{4}	9.6×10^{2}	3.5×10^{2}	1.2	0.4
7ABC	4.0×10^{7}	6.0×10^{5}	1.6×10^{5}	1.5	0.4

[a]First 4 pore volumes

Figure D.3.6.5. ^{137}Cs **Leaching Profile From Sediments, a) 41-09-39 7ABC, and b) SX-108 7A with 0.5 mol/L** $NaNO_3$.

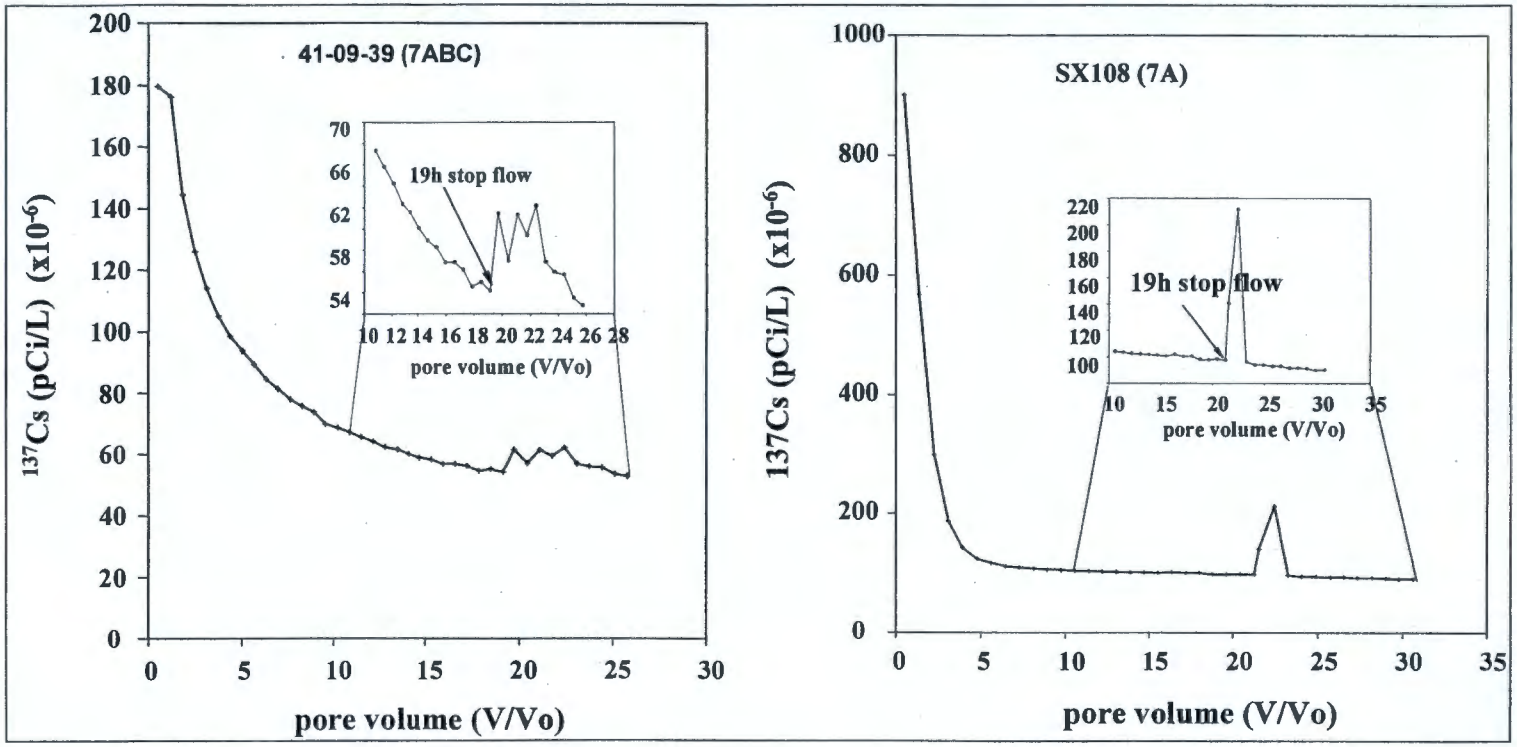

The leaching of ^{137}Cs from sediments 7A and 7ABC by 0.5 mol L^{-1} KNO_3 was similar to the $NaNO_3$ system (Figure D.3.6.6). As with the static exchange studies (Section D.3.1, Figure D.3.1.4), K^+ displaced more $^{137}Cs^+$ than Na^+. In comparison to Na^+, K^+ leached almost ten times more $^{137}Cs^+$ in the initial 4 pore volumes and throughout the flow study (Table D.3.6.6). Given that the overall mass transfer rates for Na^+, K^+, and Rb^+ (see modeling results for K^+ and Rb^+; Table D.3.6.3) were similar and that the leaching observed in the columns was the result of ion exchange with easily accessible exchange sites, the difference between the $NaNO_3$ and KNO_3 columns may be attributed exclusively to the differences in K^+ and Na^+ exchange selectivity.

Figure D.3.6.6. ^{137}Cs Leaching Profile From Sediment SX-108 7A by a) 0.5 mol/L KNO_3 (initial; 20 pv), and b) 0.25 mol/L $(NH_4)_2C_2O_4$ (greater than 20 pv).

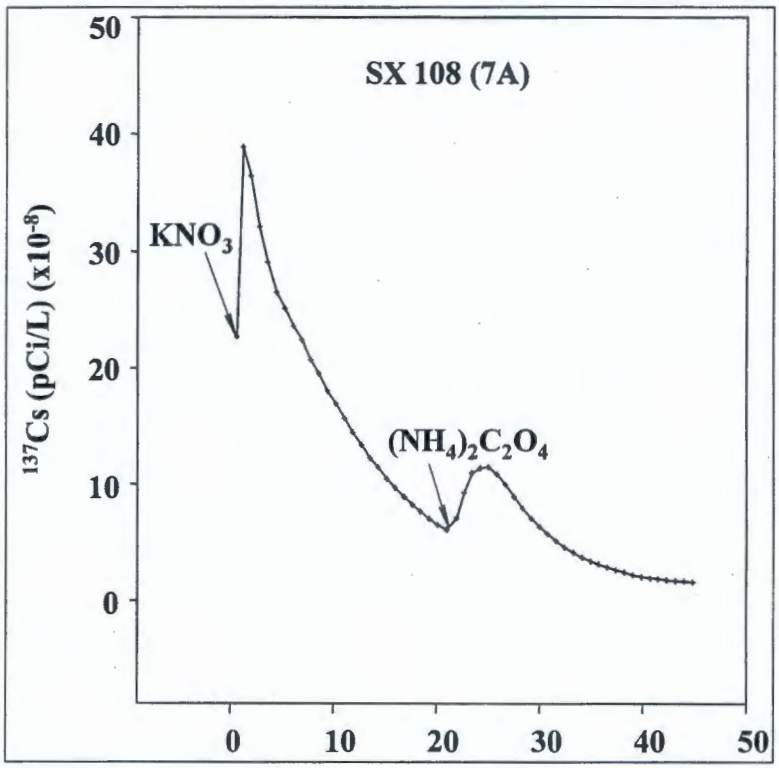

Table D.3.6.6. ^{137}Cs Activities (pCi/g) in 2 WMA S-SX Sediments, and Aqueous Concentrations (pCi/L and %) of ^{137}Cs Leached From Sediments by 0.5 mol/L KNO_3 Followed by 0.25 mol/L $(NH_4)_2C_2O_4$.

Sediment	^{137}Cs in sediment	^{137}Cs leached from column experiments				^{137}Cs leached[b]			
		Total	Initial[a]	^{137}Cs[c]	^{137}Cs[d]	Total	Initial[a]	^{137}Cs[c]	^{137}Cs[d]
	pCi/g					%			
SX108									
7A	5.9×10^7	5.9×10^7	4.2×10^6	1.1×10^7	3.7×10^6	25.1	7.1	18.8	6.3
41-09-39									
7ABC	4.0×10^7	8.3×10^6	1.2×10^6	4.2×10^6	4.1×10^6	20.8	2.9	10.5	10.3

[a]First 4 pore volumes
[b]Versus total ^{137}Cs in sediment
[c]Total leached from 0.5 mol/L KNO_3 solution
[d]Total leached from 0.25 mol/L $(NH_4)2C_2O_4$

The change of leaching solution from 0.5 mol/L KNO_3 to 0.25 mol/L $(NH_4)_2C_2O_4$ was designed to estimate the impact of secondary mineral overgrowth on Cs desorption (Figure D.3.6.6). As the $(NH_4)_2C_2O_4$ moved through the column, there was a smooth increase in Cs leaching followed by a return to almost the exact same leaching profile observed prior to its injection. While this may be fortuitous, more likely, it is a reflection of similar exchange selectivity coefficients between K^+ and NH_4^+. In these studies, unlike the long-term (100 day) $(NH_4)_2C_2O_4$ batch system, dissolution of minerals resulting from the low pH (pH 3) should not be of consequence (Loeppert and Inskeep 1996) since the column residence time was short. Hence, these data suggest that the increased leaching of Cs was due to the removal of poorly crystalline oxides that blocked a fraction of Cs-containing sorption sites. The increase in Cs exchange related to oxide removal was about 6.3 and 10.3% of the total exchangeable Cs for sediments 7A and 7ABC, respectively, which is about that estimated from the batch studies discussed above.

The effect of increasing temperature on Cs release from columns packed with sediment SX-108 7A, after the initial flush of Cs (about 8 pore volumes), is shown in Figure D.3.6.7. As temperature was increased from 14 °C to 34 °C to 55 °C, steady-state Cs effluent concentrations quickly stabilized at increasingly greater concentrations. Conversely, as temperature was decreased in 10 °C increments, steady-state Cs effluent concentrations quickly stabilized at decreasing levels. While difficult to see from the plots in D.3.6.7, the maximal Cs concentration resulting from a 2.5 h stop-flow followed the same behavior as Cs steady-state concentrations with temperature change. The observed changes in effluent Cs concentration where smooth, and indifferent to the order of temperature change, suggesting that the governing reactions were unaffected by the small surface Cs concentration changes observed over the life of these studies.

Figure D.3.6.7. Column Cs Leaching and Stop-Flow Profiles for Sediment SX-108 7A by 0.5 mol/L $NaNO_3$ at Three Temperatures.

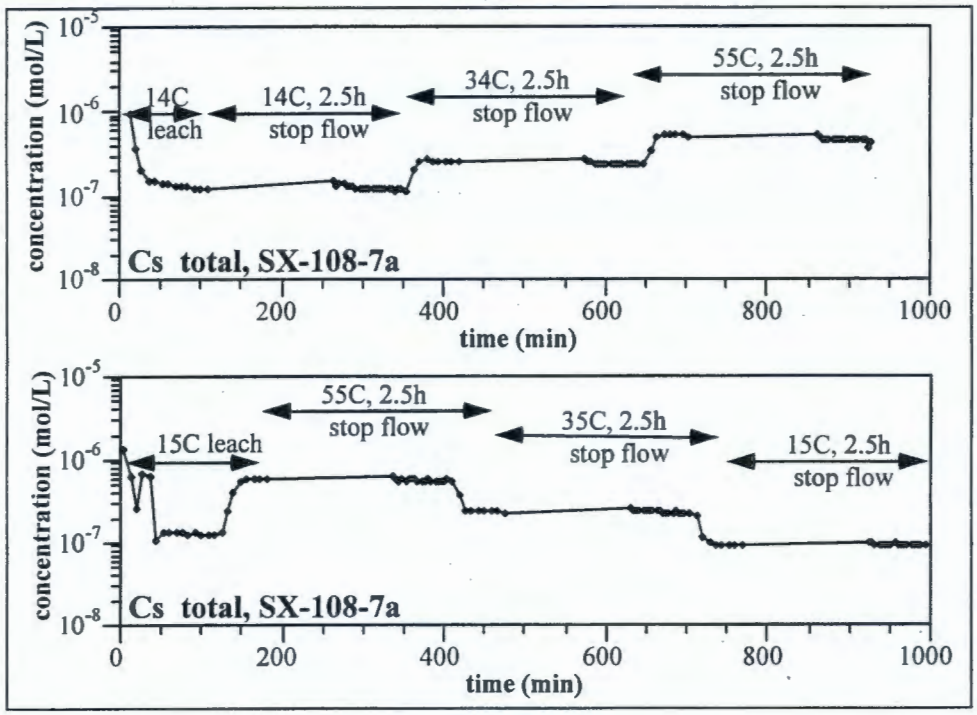

Two methods were used to calculate pseudo-first order rate coefficients from the column Cs data. One method assumed that a steady state concentration (and leaching rate) was obtained at each temperature during advective flow. A first-order model was fit using the leaching concentration and the column residence time. The second method used to calculate rate coefficients considered the concentration reached in solution during the stop flow event (2.5 hours). This static method uses the maximum concentration achieved during stop flow (as measured once flow was reinitiated). Rate constants and half-lives ($t_{1/2}$) for both methods are tabulated in Table D.3.6.7. The steady-state pseudo-first order rate coefficients are about an order of magnitude greater than those determined from stop-flow data. These differences are believed to arise due to advection continually removing mass from the column, causing greater diffusional gradients, and faster rates than typically observed for static (stop-flow) methods. Yet, it is the steady-state flow method that yields rate coefficients similar to those determined for the batch studies and modeling (Section D.3.6.3.3) for the kinetic-controlled exchangeable Cs (0.01 to 0.03 h^{-1}, or $t_{1/2}$ = 23.1 to 69.3 h).

Table D.3.6.7. Pseudo-First Order Rate Constants and half-life ($t_{1/2}$) as a Function of Temperature From Column Leaching of Cs For Sediment SX-108 7A.

Temperature (C)	Rate Constant : Steady-State (h^{-1})	Rate Constant : Stop-Flow (h^{-1})	Steady-State $t_{1/2}$ (h)	Stop-Flow $t_{1/2}$ (h)
Increasing T				
14	$1.50x10^{-2}$	$1.07x10^{-3}$	46.1	647
34	$3.16x10^{-2}$	$1.85x10^{-3}$	21.9	375
55	$6.55x10^{-2}$	$3.70x10^{-3}$	10.6	187
Decreasing T				
55	$6.83x10^{-2}$	$4.29x10^{-3}$	10.1	162
35	$2.77x10^{-2}$	$1.76x10^{-3}$	25.1	394
15	$1.07x10^{-2}$	$6.85x10^{-4}$	64.6	1011

Plotting the rate coefficients for steady-state and stop-flow data versus the reciprocal of temperature (in ^{0}K) yields two Arrhenius plot whose slopes represents a measure of the effective activation energy ($E_{act,eff}$) for Cs release (Figure D.3.6.8). The $E_{act,eff}$ for steady-state data were 15.5 kJ/mol and 19.5 kJ/mol for increasing and decreasing T, respectively; for stop-flow data $E_{act,eff}$= 12.5 kJ/mol and 19.4 kJ/mol for increasing and decreasing T, respectively. The Arrhenius plots for these data show that (1) the direction of temperature change (increasing or decreasing) did not impact the slope, and (2) even though the two methods of determining rate coefficients yielded coefficients about an order of magnitude different, the Arrhenius plot slopes are essentially identical. The average $E_{act,eff}$ = 16.7 kJ/mol, which is only slightly greater than that typically reported for diffusion-controlled reactions (10 – 12 kJ/mol).

Figure D.3.6.8. Arrhenius Plot (log k vs. 1/T) for Column Cs Leaching From Sediment SX-108 7A by 0.5 mol/L $NaNO_3$ at Three Temperatures Based on a) Stop-Flow Data (▼,▲) and b) Steady-State Flow Data (∇, Δ).

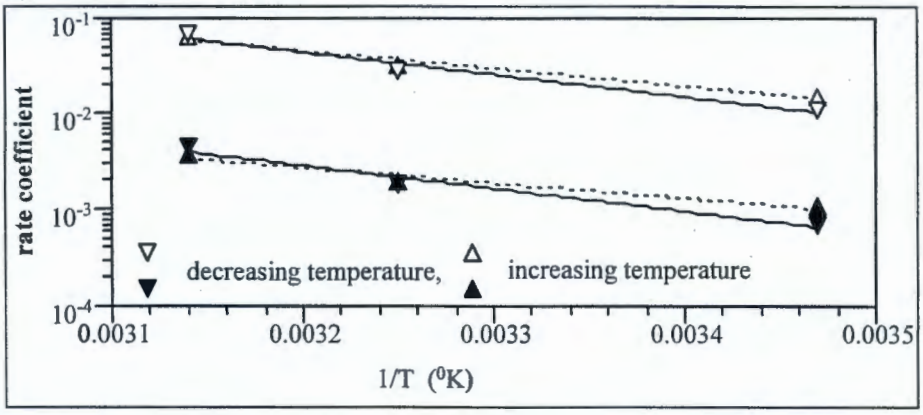

Taken as a whole, the flow studies corroborate the results and conclusions of the previously discussed batch studies. The initial release of Cs appears to be governed by surface exchange sites and is a rapid reaction. The slower kinetic-controlled Cs exchange is diffusion controlled and appears very uniform with an $E_{act,eff}$ that is approximately that associated with diffusion-controlled reactions. In addition, the amount of Cs that is apparently armored by secondary precipitates against desorption is small; perhaps as much as 10%. While the Cs in the sediments is desorbable, the process is extremely slow.

D.3.6.4 Conclusions and Implications

(1) Cs desorption may be simulated using a model containing three sorbed populations of Cs: (1) equilibrium-controlled exchangeable Cs, (2) kinetic-controlled (diffusion) exchangeable Cs, and (3) slowly exchangeable Cs. All three populations appeared to be exchangeable, although release from the latter pool was extremely slow ($t_{1/2} \approx 1000$ days).

(2) While the cations Rb^+, K^+, and Na^+ exhibited different exchange selectivity coefficients (Rb greater than K greater than Na) against Cs, the concentrations of the kinetically controlled Cs populations were largely unaffected by cation type.

(3) Based on modeling of batch desorption experiments, the easily exchangeable Cs pool was about 20 to 30% of the total Cs, the diffusion controlled Cs (or kinetic fraction) pool was approximately 20 to 35% of the total Cs, and the slowly exchangeable pool was 35 to 50% of the total Cs. Only about 10% of the slowly exchangeable Cs pool could be attributed to Cs occlusion by secondary mineral formation.

(4) While the Hanford sediments have a high sorption affinity for Cs, approximately 50% of the sorbed ^{137}Cs is exchangeable with the aqueous phase and could be remobilized using solutions of highly selective cations (K or Rb) or high ionic strength.

The studies reported here were designed, for the most part, to maximize Cs desorption from contaminated sediments. Clearly, a pure K^+ or Rb^+ solution will not develop in the pore waters underlying the S and SX tank farms. However, the small column studies using 0.5 mol/L $NaNO_3$ may, in fact, reasonably mimic leaching conditions that may develop from accidental spills during tank waste removal or from meteoric recharge. Residual Na from leaked waste solutions are seen in most sediments studied. This residual Na will be mobilized during sediments upon rewetting, and as with the column studies, increase the $[Na]_{aq}$ concentrations above those normally observed in pore waters.

Even with elevated Na concentrations, only a small percentage of the sorbed ^{137}Cs inventory was leachable. After the initial flush of easily exchangeable ^{137}Cs, the desorbed concentrations of ^{137}Cs would rapidly decrease to concentrations controlled by film diffusion. The more recalcitrant Cs pool, will not contribute to Cs transport because of its extremely slow desorption kinetics. Dissolution of secondary minerals and the subsequent increase in easily exchangeable Cs, as seen with $(NH_4)_2C_2O_4$, should not occur in these sediments since the existing sediment pH is slightly basic and the secondary minerals are stable under the observed conditions. Even though the entire Cs pool is believed to be exchangeable with time, and therefore available for

transport, the high Cs exchange selectivity coefficients exhibited by underlying uncontaminated sediments will retard Cs transport.

D.3.6.5 References

Brouwers, E., B. Baeyens, A. Maes and A. Cremers, 1983, "Cesium and Rubidium Ion Exchage in Illite Clay," *Journal of Physical Chemistry*, Vol. 87:1213-1219.

Bruggenwart, M. G. M., and A. Kamphorst, 1979, "Survey of Experimental Information on Cation Exchange in Soil Systems," In *Soil Chemistry B. Physico-Chemical Models, Elsevier*, Scientific Co., G. H. Bolt, ed., New York, pp. 141-192.

Comans, R. N. J., and D. E. Hockley, 1992, "Kinetics of Cesium Sorption on Illite," *Geochimica et Cosmochimica Acta*, Vol. 56:1157-1164.

Comans, R. N. J., M. Haller, and P. De Preter, 1991, "Sorption of cesium on illite: Non-equilibrium behavior and reversibility," *Geochimica et Cosmochimica Acta*, Vol. 55:433-440.

Cornell, R. M., 1993, "Adsorption of Cesium on Minerals: A Review," *Journal of Radioanalytical Nuclear Chemistry Articles*, Vol. 171:483-500.

Evans, D. W., J. J. Alberts, and R. A. Clark, 1983, "Reversible Ion-Exchange Fixation of Cesium-137 Leading to Mobilization from Reservoir Sediments," *Geochimica et Cosmochimica Acta*, Vol. 47:1041-1049.

Liu, D. C., C. N. Hsu, and C. L. Chung, 1994, "Ion-Exchange and Sorption Kinetics of Cesium and Strontium in Soils," *Applied Radiation Isotope*, Vol. 46:839-846.

Loeppert, R. L., and W. P. Inskeep, 1996, "Iron," In D. L. Sparks et al., ed., *Methods of Soil Analysis; Part 3—Chemical Methods,* SSSA Book Series: 5, Soil Science Society of America, Inc., Madison, Wisconsin, pp. 639-664.

Ogwada, R. A., and D. L. Sparks, 1986, "Kinetics of Ion Exchange on Clay Minerals and Soil: II. Elucidation of Rate-Limiting Steps," *Soil Science Society of America Journal*, Vol. 50:1162-1166.

Serne, R. J., H. T. Schaef, B. N. Bjornstad, B. A. Williams, D. C. Lanigan, D. G. Horton, R. E. Clayton, V. L. LeGore, M. J. O'Hara, C. F. Brown, K. E. Parker, I. V. Kutnyakov, J. N. Serne, A. V. Mitroshkov, G. V. Last, S. C. Smith, C. W. Lindenmeier, J. M. Zachara, and D. B. Burke, 2001a, *Characterization of Uncontaminated Sediments from the Hanford Reservation-RCRA Borehole Core and Composite Samples*, PNNL-2001-1, Pacific Northwest National Laboratory, Richland, Washington.

Serne, R. J., G. V. Last, G. W. Gee, H. T. Schaef, D. C. Lanigan, C. W. Lindenmeier, R. E. Clayton, V. L. LeGore, R. D. Orr, M. J. O'Hara, C. F. Brown, D. B. Burke, A. T. Owen, I. V. Kutnyakov, and T. C. Wilson, 2001b, *Geologic and Geochemical Data Collected from Vadose Zone Sediments from Borehole SX 41-09-39 in the S/SX Waste Management Area and Preliminary Interpretations*, PNNL-2001-2, Pacific Northwest National Laboratory, Richland, Washington.

Sposito, G., 1994, "Chemical Equilibria and Kinetics in Soils," Oxford University Press, New York and Oxford.

Toso, J. P., and R. H. Velasco, 2001, "Describing the Observed Vertical Transport of Radiocesium in Specific Soils with Three Time-Dependent Models," *Journal of Environmental Radioactivity*, Vol. 53:133-144.

Zachara, J. M., S. C. Smith, J. P. McKinley, R. J. Serne, and P. L. Gassman, 2001, "Sorption of Cs+ to Micaceous Subsurface Sediments From the Hanford Site," *Geochimica et Cosmochimica Acta*, (Accepted).

D.3.7 EFFECT OF HIGH SODIUM CONCENTRATIONS ON THE MOBILITY OF CESIUM: ONE-DIMENSIONAL REACTIVE TRANSPORT SIMULATIONS

Peter C. Lichtner[1]

[1]Los Alamos National Laboratory, Los Alamos, New Mexico 87545

D.3.7.1 Introduction

Leaked ^{137}Cs has been observed in boreholes at WMA S-SX at depths greater than anticipated based on previous estimates using constant K_d transport models. The depth of penetration of cesium appears to be different depending on the tank waste composition. Tank SX-115 shows little migration of cesium, whereas for tank SX-108 cesium appears to have migrated several tens of meters beneath the tank. It is important to understand what controls the mobility of Cs in the Hanford vadose zone in order to understand the potential hazard Cs could pose to the environment and also to facilitate remediation efforts to clean up the site.

There are several plausible explanations for the observed differences in Cs mobility. One possibility is that competitive sorption effects could enhance the mobility of Cs in the presence of high sodium concentrations. This possibility is considered in more detail in this report. Competition for a limited number of sorption sites between radionuclides and cations in the background electrolyte solution leaked from the tanks could greatly reduce the retardation of cesium. This is consistent with observations in that the fluid leaked from tank SX-115 is much more dilute compared to tank SX-108. Other possibilities include reaction of the tank fluids with the sediments beneath the tanks, thereby altering their sorptive properties, colloid-facilitated transport, and complexing reactions.

In this contribution, the two phase, reactive flow and transport model FLOTRAN (Lichtner 2001) is used to describe the interaction of the leaked tank fluid with host sediments and ambient groundwater in the vadose zone. The effect of high ionic strength fluid leaked from tanks on the mobility of radionuclides is investigated. In this preliminary effort focus is on the radionuclide cesium. A simplified, one-dimensional (1D) model is considered. The model incorporates flow of liquid water, water vapor, air, and heat, in addition to multicomponent reactive chemistry. Both Pitzer and Debye-Hückel activity coefficient algorithms are included in the model calculations. Finally, an estimate of the colloid concentration necessary to affect significantly the mobility of cesium is presented.

D.3.7.2 The K_D Approximation

In an ion exchange process, chromatographic separation takes place between the exchanging cations with distance and time. The extent of separation depends on the affinity of each cation to the exchange surface, the exchange capacity of the medium, and length of time involved. In certain cases it is possible to predict the mobility of each cation based on its distribution coefficient, defined as the ratio of sorbed to aqueous concentration. Cations with larger distribution coefficients move more slowly compared to ones with smaller coefficients. However, in order to use the distribution coefficient approach to estimate mobility, it is necessary that the bulk solution composition remain relatively constant with distance and time.

This requirement is most certainly not met at Hanford for situations in which high ionic strength fluids have leaked from the tanks.

To investigate the dependence of the distribution coefficient on solution composition, exchange of Na and Cs is considered using the three-site sorption model developed by Zachara et al. (2001) for the Hanford sediments. The exchange parameters used in the model are listed in Table D.3.7.1. The distribution coefficient in dimensionless units for the i^{th} cation, valid for monovalent exchange and ignoring complexing, is given by the expression

$$K_i = \frac{(1-\phi)\rho_r}{\phi} \sum_{\alpha} \left| \frac{Q_\alpha k_i^\alpha}{\sum_l k_l^\alpha c_l} \right| \qquad \text{(D.3.7.1)}$$

where Q_α refers to the cation exchange capacity of site α, k_i^α is the selectivity coefficient of the ith cation with concentration c_i, sediment particle density is denoted by ρ_r, and porosity by ϕ. The sum is taken over the distinct sorption sites.

Table D.3.7.1. Ion Exchange Parameters for Cs, Na, K, and Ca on Hanford Sediments. Parameters Kindly Provided by Carl Steefel (private communication).

Cation	Log Species Selectivity Coef.		
	Site 1	Site 2	Site 3
Na+	-6.87373	-3.57769	-1.66068
K+	-4.74122	-1.00000	-0.99987
Ca++	-7.52000	-4.58638	-1.50441
Cs+	0.0	0.0	0.0
CEC [mol/kg solid]	2.720e-5	1.3371e-4	7.7844e-2

Plotted in Figure D.3.7.1 along the vertical axis is the logarithm of the retardation factor for Cs, $R=1+K_{Cs}$, against the concentration of Cs and Na along the x- and y-axes, respectively, with the parameter values given in Table D.3.7.1. A porosity of 40% and density of 1.54 g/cm^3 is used in obtaining the retardation. As can be seen from the figure, Cs retardation ranges over four orders of magnitude. Cs becomes more strongly retarded as its own concentration decreases and as the concentration of Na decreases. However, as the concentration of Na increases, Cs mobility as measured by the distribution coefficient rapidly decreases.

Figure D.3.7.1. Retardation Factor for Cs Exchanging with Na on Hanford Sediments.

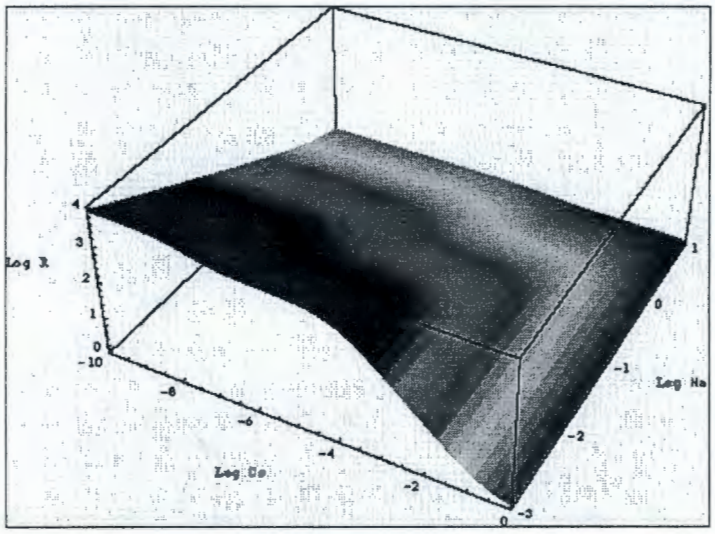

In the environment of the Hanford tank farms, the concentrations of both Cs and Na were highly variable over time and depth within the vadose zone. Leaks from the tanks took place over relatively short periods of time releasing short duration pulses from weeks to months or years of variable composition tank effluents into the vadose zone. Under such conditions, the mobility of Cs would also have been highly variable. During a pulse release with high Na concentration, Cs mobility could be greatly enhanced. However, because of the slight difference in the Na and Cs distribution coefficients, Cs would still be slightly more retarded compared to Na. As time increased and the leak halted, the chromatographic separation between the Na and Cs plumes would increase. Eventually, given sufficient time and travel distance, the two plumes would become completely separated with cesium left behind in a dilute solution with a greatly reduced mobility. The picture that emerges from this qualitative consideration of the distribution coefficient, is that during the initial release of fluid from the tank, Cs would migrate rapidly as long as it was in the presence of high Na concentrations. But as chromatographic separation set in after the leak had ceased, cesium would become highly retarded. How far Cs could actually migrate through the vadose zone would appear to depend on a number of factors including the leak composition, rate, and duration, surface infiltration rate, and sediment sorptive properties.

D.3.7.3 Model Description

The SX tank farm consists of 15 single-shell tanks with different heat loads (see Sections D.7.1 and D.7.2), some of which have leaked radioactive fluid into the vadose zone. Because of the finite number of tanks and their variable heat loads and the varying positions of suspected leaks from the tanks, it is not possible in a rigorous sense to reduce the size of the problem by symmetry considerations. Nevertheless, to gain insight into the processes taking place within the vadose zone, simplifications are necessary to reduce the system to a manageable size for which relatively rapid simulations can be performed which captures the basic physics and chemistry involved. Use of a 1D model is clearly a gross simplification compared to two- or three-dimensional (2D or 3D) models and therefore should not be considered quantitatively accurate. However, because of the vastly reduced computational effort required for a 1D model

compared to 2D or 3D models, the 1D model allows sensitivity analyses to be more easily performed with incorporation of multiphase-multicomponent chemistry. In what follows 1D simulations are carried out along a vertical column from the ground surface to the water table. Fluid is injected at a depth corresponding to the base of the tank. Combined with surface infiltration, the interaction of fluid with sediments is simulated to describe the migration of Cs as it is released from the tank. To obtain appropriate leak rates, the model is calibrated against observations from well 299-W23-19, which is located next to tank SX-115.

Calculations are performed using the computer code FLOTRAN (Lichtner 2001), a two-phase, multicomponent, reactive flow and transport numerical model. Processes included in the code include two-phase, nonisothermal, flow of mass and heat in variably saturated porous media, and (enhanced) binary diffusion of water vapor and air. The flow equations are coupled to equations describing multicomponent reactive transport through field variables pressure, temperature, liquid and gas velocities, saturation state, and liquid and gas densities. The reactive transport equations account for such processes as aqueous speciation, reactions with minerals, ion exchange and surface complexation, and colloid-facilitated transport. The transport equations, in turn, can be coupled to the flow equations through changes in material properties such as porosity, permeability, tortuosity, and fluid density although this possibility is not considered in the simulations carried out below.

The stratigraphic sequence used in the calculations is listed in Table D.3.7.2. Not included in the present simulations is the possible presence of a thin compacted layer beneath the tanks. The compacted layer has been estimated to be approximately 0.5-1 m thick. However, the physical properties of the compact layer (porosity, permeability, capillary parameters, density) are presently unknown.

Table D.3.7.2. Stratigraphic Sequence Used in the Calculations.

Formation	Abbreviations	Thickness [m]
Backfill	BF	16.2
Hanford Fine Sand	HF	23.0
Plio-Pleistocene	PP	6.0
Upper Ringold Gravel	URG	3.0
Middle Ringold	MRG	20.0

Material properties for soil, hydraulic, and thermal parameters used in the calculations are listed in Table D.3.7.3. Parameters α and λ refer to the phenomenological van Genuchten equation relating capillary pressure and saturation. Effective binary gas diffusion is considered with gaseous diffusion constant $D_g^0 = 2.13 \times 10\text{-}5\ m^2\ s^{-1}$. Vapor pressure lowering resulting from capillary suction was included in the simulations as described by Kelvin's equation. An even more important effect, but not yet incorporated in the simulations, could be the effect of salts on vapor pressure.

Table D.3.7.3. Parameters for Material and Thermal Properties for Intrinsic Rock Density rr, Heat Capacity c, Thermal Conductivity κ, Porosity ϕ, Residual Saturation s_r, van Genuchten Parameters α and π, and Saturated Permeability k_{sat}.

Formation	ρ_r	c	κ dry	κ wet	ϕ	s_r	α	λ	k_{sat}
	g/cm^3	J/kg/K	W/m/K	W/m/K	-	-	1/m	-	m^2
BF	2.85	800	0.2	2.	0.258	0.077	1.008e-3	0.659	1.24e-12
HF	2.85	800	0.2	2.	0.358	0.084	9.408e-5	0.469	3.37e-13
PP	2.85	800	0.2	2.	0.422	0.259	6.851e-5	0.456	3.73e-14
URG	2.85	800	0.2	2.	0.262	0.213	2.966e-5	0.386	1.44e-13
MRG	2.85	800	0.2	2.	0.164	0.061	6.340e-5	0.392	2.00e-13

D.3.7.4 Calibration to Well 299-W23-19

In this Section, 1D reactive transport simulations are carried out for tank SX-115. The simulations are based on a simplified chemical system compared to the actual tank composition. Included, in addition to several aqueous complexing reactions, are ion exchange reactions involving cations Cs^+, Na^+, K^+, and Ca^{2+}, and precipitation and dissolution of calcite. Results using the Pitzer model are compared with the Debye-Hückel activity coefficient algorithm.

D.3.7.4.1 Model Calibration. Because the geometry of the system is inherently 3D, it is not possible to use the actual leak volumes and rates in 1D simulations. To obtain these parameters for the 1D model, it is necessary to calibrate the model against field observations. Extensive data for concentration of solute species with depth is available from well 299-W23-19, located in the vicinity of tank SX-115 (Serne et al. 2001). The timing of the leak for tank SX-115 is thought to have occurred in 1965, and leak volume and duration are estimated to be 60,000 gallons over a two-week period. The position of the leak is thought to be close to the edge of the tank near the well.

As suggested here, the model parameters for leak rate and duration, average infiltration rate, and solution composition of the leaking fluid are rather tightly constrained by field observations. From the observed profile for NO_3^-, a conservative species that does not take part in exchange, several parameters can be determined. The width of the NO_3^- profile is used to fix the leak duration, and the depth of the peak concentration determines both the infiltration and leak rate. A time span of 35 y is assumed. For the leak rate a value of 8.4×10^{-4} kg/s is obtained, and for the leak duration a value of 1.213×10^6 s, or just over two weeks, in agreement with the estimated value. With these values a total leak volume of 247.6 gallons is released in the 1D model, much smaller than the 60,000 gallons estimated to have leaked. This reduced value is a consequence of neglecting lateral spreading in the 1D model. An infiltration rate of 0.08 m/yr gave the best fit to the nitrate profile. With these values the travel time to the water table for a conservative tracer released from the surface without the tank present is found to be 100 years, and 68 years when released from a depth coinciding with the base of the tank in the presence of the leak.

In addition, the solution composition of the leak can be constrained by the Serne et al. (2001) field data. The concentration of NO_3^- in the leak is adjusted to match the observed peak concentration. Likewise the pH of the leak composition is adjusted to match the observed pH peak at depth. The sodium concentration is determined by charge balance. The initial and source fluid compositions are given in Tables D.3.7.4 and D.3.7.5, respectively. The mineral calcite is allowed to form as a secondary phase, but is assumed not to be present initially.

Initial flow conditions and moisture profile are determined by first running the model without the tank in place at a constant rate of infiltration. An infiltration rate of 8 cm/yr is imposed at the ground surface with a constant temperature of 12.8 °C. At the water table the temperature is fixed at 17 °C. A steady-state profile for moisture content, temperature, and counter flow of vapor and liquid is obtained which is then used with the tank in place. The initial saturation profile is shown in Figure D.3.7.2 along with profiles at 1 and 10 years following release of fluid from the tank using the material properties and van Genuchten parameters listed in Table D.3.7.3. After approximately 10 years the moisture profile has returned to its steady state value. For the 1D model, 136 nodes in the vertical direction are used with equal spacing of 0.5 m. Two zones of elevated moisture content, located at a depth of approximately 43-48 m, coincide with the Plio-Pleistocene and Upper Ringold Gravel stratigraphic units. The water table is located at a depth of approximately 62.4 m. In these preliminary simulations the tank temperature was fixed at 25 °C.

Table D.3.7.4. Initial Fluid Concentration.

solution density = 1.0008 [g/cm^3]
mole fraction H2O = 9.9960E-01
activity of water = 9.9962E-01 osmotic coefficient = 9.3347E-01
pH = 7.5000

species	molality	tot	act. coef.	act. ratio/H+	constraint
Ca++	2.9973E-03	3.0000E-03	5.8420E-01	1.2354E+01	1 total
Mg++	2.0000E-03	2.0000E-03	5.8236E-01	1.2178E+01	1 total
K+	2.6700E-03	2.6700E-03	8.6355E-01	4.8651E+00	1 total
Na+	9.9999E-04	1.0000E-03	8.6524E-01	4.4385E+00	1 total
H+	3.6430E-08	2.9655E-05	8.6804E-01	0.0000E+00	8 pH
NO3-	9.9993E-05	1.0000E-04	8.7227E-01	-1.1439E+01	1 total
Cl-	1.3007E-02	1.3007E-02	8.8160E-01	-9.3244E+00	-1 chrg
HCO3-	5.5506E-04	5.9304E-04	8.8376E-01	-1.0694E+01	4 CO2(g)
Cs+	1.0000E-16	1.0000E-16	8.5776E-01	-8.5615E+00	1 total
H2O	5.5508E+01	5.5508E+01	1.0000E+00	1.7444E+00	7 conc

complex	molality	act. coef.	act/H+	log K
CO2(aq)	3.39881E-05	1.0022	-4.4687	6.3414
CaCO3(aq)	2.66200E-06	1.0000	-5.5748	-7.0088
CO3--	1.32961E-06	0.55218	-20.753	-10.325
OH-	3.77977E-07	0.85363	-13.861	-13.991
NaNO3(aq)	6.81895E-09	1.0000	-8.1663	-1.0440

mineral saturation indices

mineral	SI	log K
Calcite	-4.20274E-01	-1.85424E+00
Halite	-6.59370E+00	-1.59027E+00
NaNO3(s)	-8.21280E+00	-1.09056E+00

gas	log partial pressure	pressure [bars]	log K
CO2(g)	-3.000	1.0000E-03	7.8092

Table D.3.7.5. Calibrated Source Term Representing the Tank Leak Composition.

```
solution density     =  1.0638      [g/cm^3]
mole fraction H2O    =   9.7402E-01
activity of water    =   9.7519E-01 osmotic coefficient =   9.4187E-01
pH = 10.0000
-----------------------------------------------------------------------
species      molality      tot     act.  coef.  act.  ratio/H+ constraint
-----------------------------------------------------------------------
Ca++        3.5099E-04 3.5800E-04 1.1157E-01 1.6242E+01  1 total
Mg++        1.0000E-04 1.0000E-04 4.1546E-02 1.5696E+01  1 total
K+          1.0000E-03 1.0000E-03 5.1290E-01 6.8482E+00  1 total
Na+         7.2778E-01 7.5000E-01 6.8217E-01 9.7102E+00  1 total
H+          1.4183E-10-1.1018E-03 7.0508E-01 0.0000E+00  8 pH
NO3-        7.2639E-01 7.4860E-01 6.8177E-01-9.9871E+00 -1 chrg
Cl-         1.0000E-03 1.0000E-03 6.3532E-01-1.2848E+01  1 total
HCO3-       3.5585E-04 1.3105E-03 5.1299E-01-1.3297E+01  3 Calcite
Cs+         1.0000E-04 1.0000E-04 4.0752E-01 5.8482E+00  1 total
H2O         5.5508E+01 5.5508E+01 1.0000E+00 1.7444E+00  7 conc

complex               molality   act.  coef.  act/H+       log K
-----------------------------------------------------------------------
NaNO3(aq)            2.22157E-02   1.0000     -1.6533     -1.0440
CO3--                9.47629E-04  9.11747E-02 -22.720     -10.325
OH-                  1.47247E-04  0.67599     -13.680     -13.991
CaCO3(aq)            7.00620E-06   1.0000     -5.1545     -7.0088
CO2(aq)              3.55139E-08   1.1570     -7.4496      6.3414
-----------------------------------------------------------------------

              mineral saturation indices
mineral                    SI           log K
-----------------------------------------------------------------------
Calcite                0.00000E+00   -1.85424E+00
NaNO3(s)              -1.69986E+00   -1.09056E+00
Halite                -5.09138E+00   -1.59027E+00

 gas   log partial pressure  pressure [bars]   log K
-----------------------------------------------------------------------
CO2(g)        -5.919           1.2063E-06      7.8092
```

Figure D.3.7.2. Steady-State Saturation Profile, and Saturation Profiles at 1 and 10 Years Following the Release of Fluid From the Tank. A Constant Infiltration Rate of 8 mm/y is Imposed at the Surface.

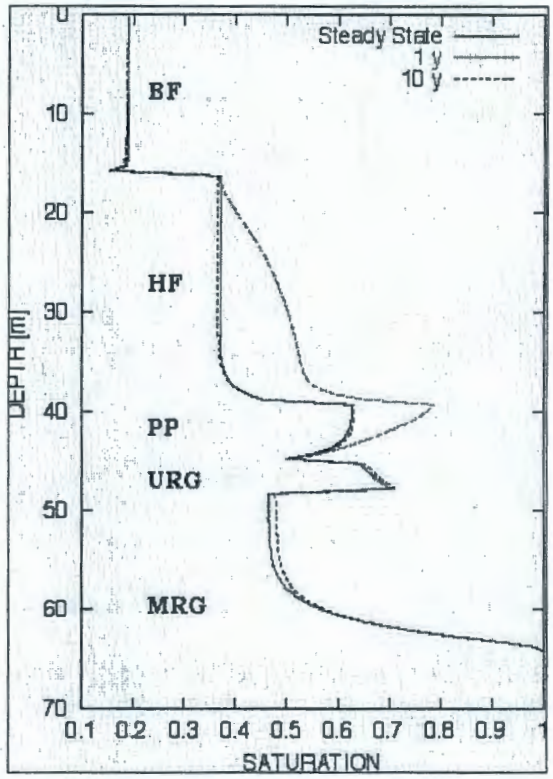

D.3.7.4.2 Results. The results of the fit to the Serne (2001) data from well 299-W23-19 are shown in Figure D.3.7.3. Concentration profiles for species NO_3^-, Na^+, Ca^{2+}, and pH are shown along with field observations from well 299-W23-19 (Serne 2001). While generally speaking the numerical simulation appears to capture the main features of the field data there are some differences. The simulation does not succeed in describing the broad peak in the Na^+ concentration profile, nor does it capture the smaller peak at greater depth. The upper portion of the NO_3^- is not well described either. There is a small displacement between the Na^+ and NO_3^- peaks indicating that Na^+ is slightly retarded. Note that the peak concentrations are less than the source term values by almost a factor of two for nitrate resulting from dilution effects, and roughly a factor of 7.5 for Na^+ resulting from sorption of Na^+ on mineral surfaces as well as dilution. The pH profile was rather remarkably reproduced. The sharp rise in pH (at 21 m) was caused by dissolution of calcite at the leading edge of the zone where secondary calcite formed. The pH gradually decreases as calcite precipitates and begins to increase again as the reaction slows. Calcite disappears and stops reacting at a depth of approximately 47.5 m. The results for the Pitzer and Debye-Hückel activity coefficient algorithms are seen to be quite close to one another.

Figure D.3.7.3. Solute and pH Profiles for an Elapsed Time of 35 Years. Symbols Indicate Experimental Data From Serne (2001). The Symbols P and DH Indicate Pitzer and Debye-Hückel Activity Coefficients, Respectively.

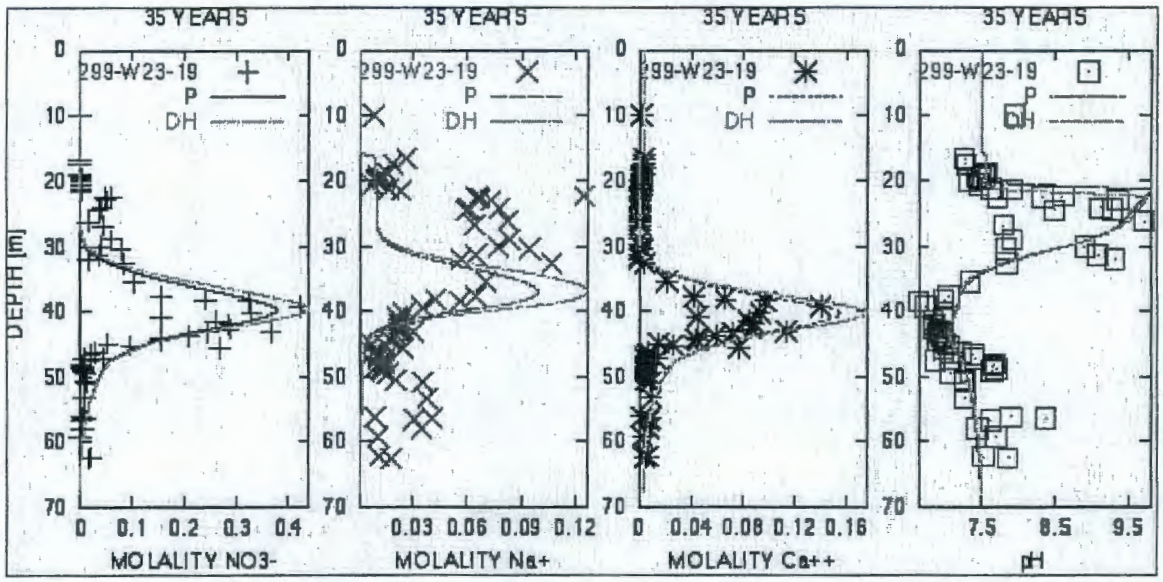

D.3.7.5 Effect of Background Electrolyte Concentration on Cesium Mobility

To investigate the effect of high sodium concentrations on the mobility of cesium, varying source term concentrations of sodium nitrate were used. The injection interval was set at 1 year keeping the total mass of fluid injected the same as in the calibration problem. All other variables were kept fixed to the values used in the calibration problem. Radioactive decay of ^{137}Cs was not taken into account in the calculations. With a half-life of 30.2 years, roughly 300 years are required for ^{137}Cs to decay to negligible levels.

Results of the simulations are presented in Figures D.3.7.4 through D.3.7.8, showing aqueous and sorbed cesium concentrations and aqueous Na concentrations plotted as a function of depth for 35, 50, and 75 years. Sodium concentrations ranged from 0.75 M, corresponding to the calibration problem, to 20 M, which could easily have leaked from tank SX-108 (see Section D.7.3). As is apparent from the figures, with increasing Na^+ concentration, Cs^+ mobility increases. For lower concentrations of Na^+, however, Cs^+ becomes more retarded compared to Na^+, resulting in rapid chromatographic separation of the two ions. As a consequence, Cs^+ is left behind in a dilute solution in which it is highly retarded. This is apparent in Figures D.3.7.4, D.3.7.5, and D.3.7.6. However, for more concentrated solutions, it is possible for cesium to penetrate more deeply into the vadose zone as can be seen in Figures D.3.7.7 and D.3.7.8. However, even in these cases Cs^+ began to lag behind Na^+ and becomes more strongly sorbed with depth.

Figure D.3.7.4. Calculated Na and Cs Profiles with Depth for Elapsed Times of 35, 50, and 75 Years for Tank SX-115.

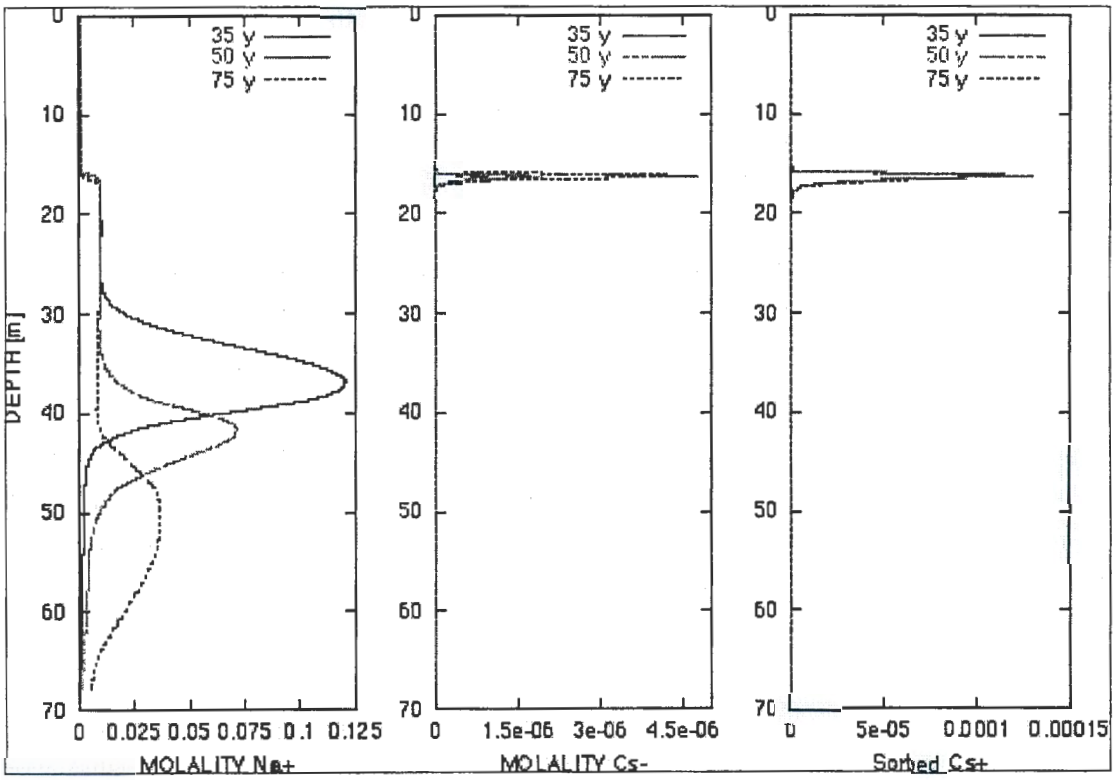

Figure D.3.7.5. Calculated Na and Cs Profiles with Depth for 5 Molal Sodium Nitrate Source Concentration.

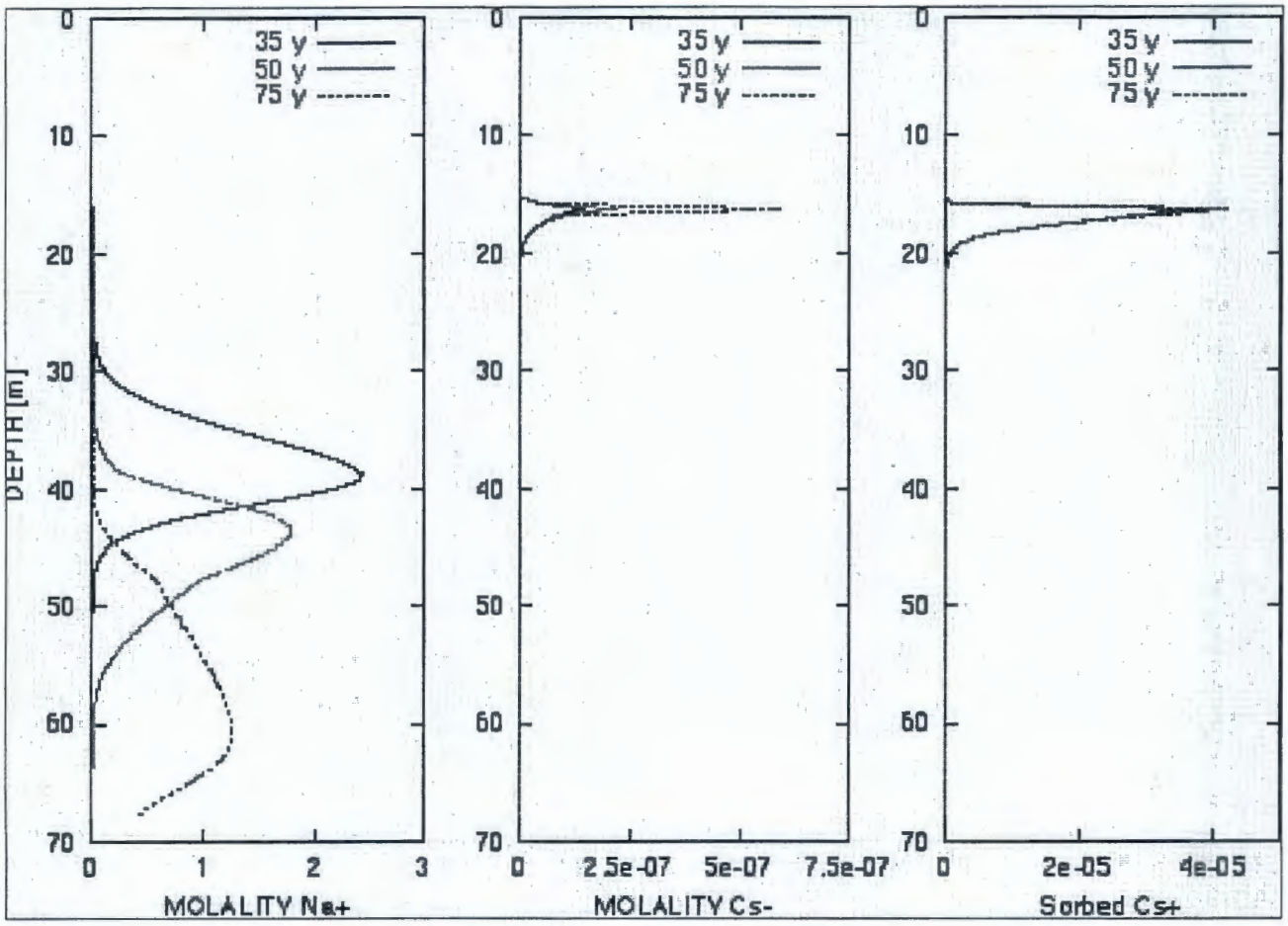

Figure D.3.7.6. Calculated Na and Cs Profiles with Depth for 10 Molal Sodium Nitrate Source Concentration.

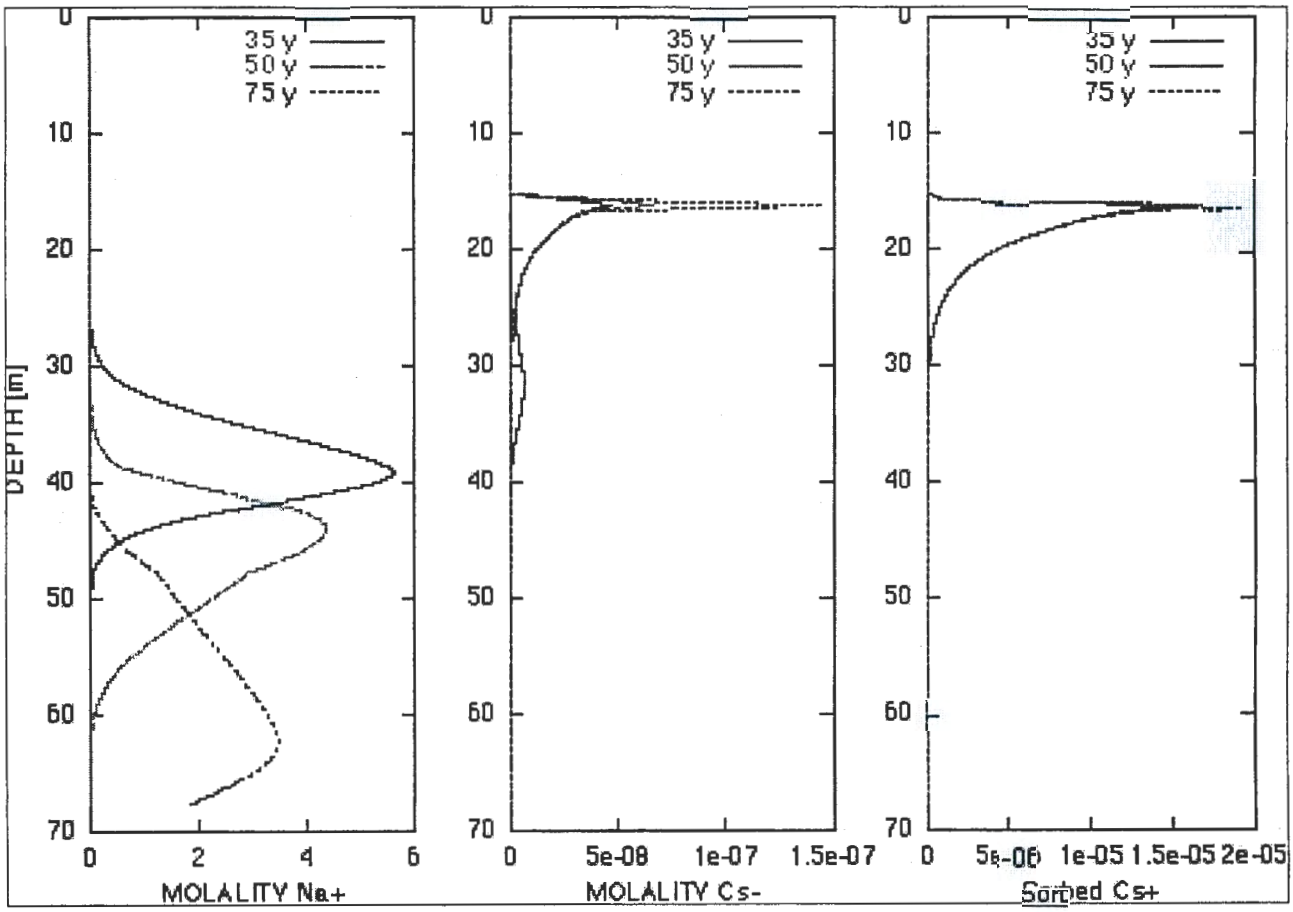

Figure D.3.7.7. Calculated Na and Cs Profiles with Depth for 15 Molal Sodium Nitrate Source Concentration.

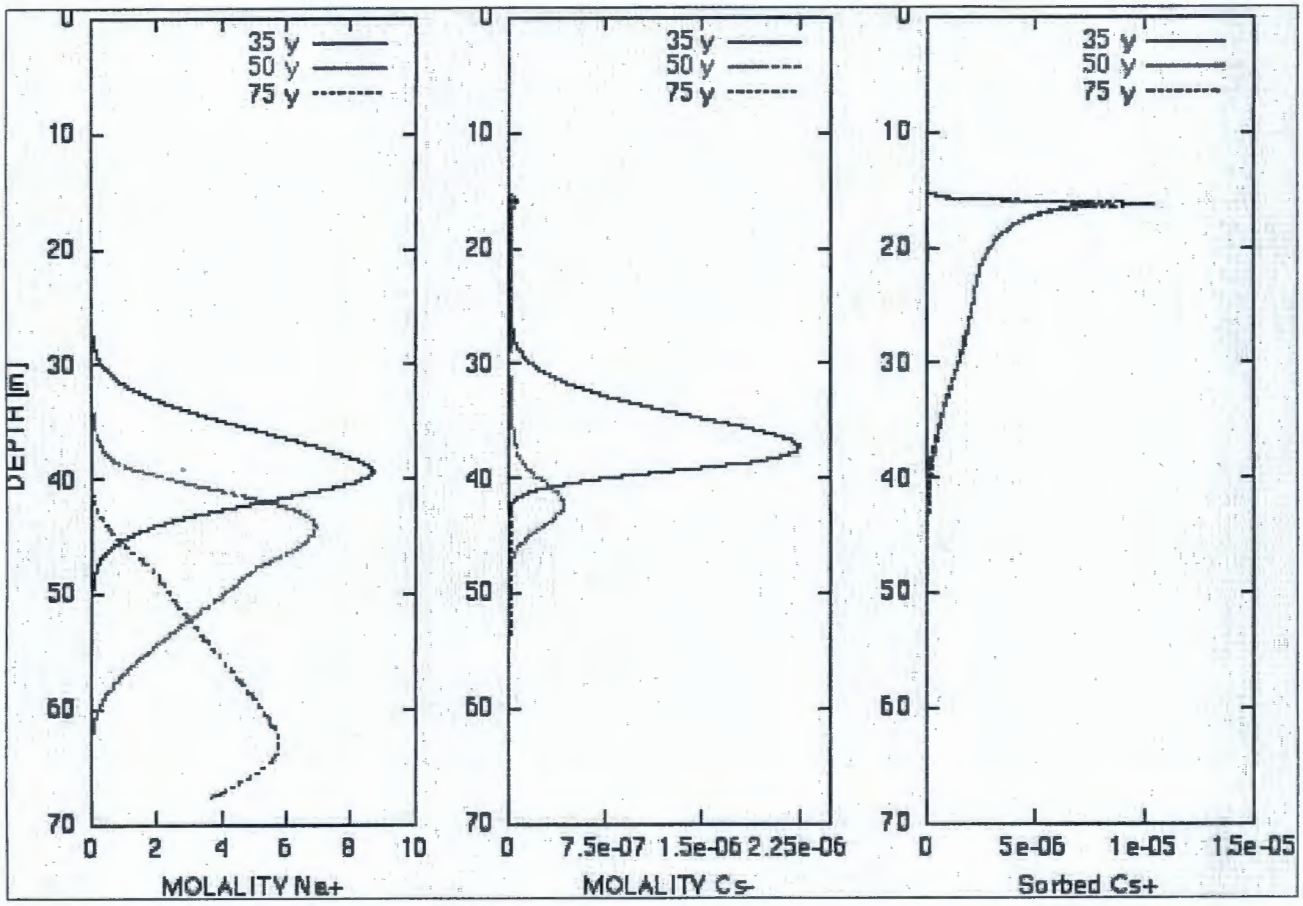

Figure D.3.7.8. Calculated Na and Cs Profiles with Depth for 20 Molal Sodium Nitrate Source Concentration.

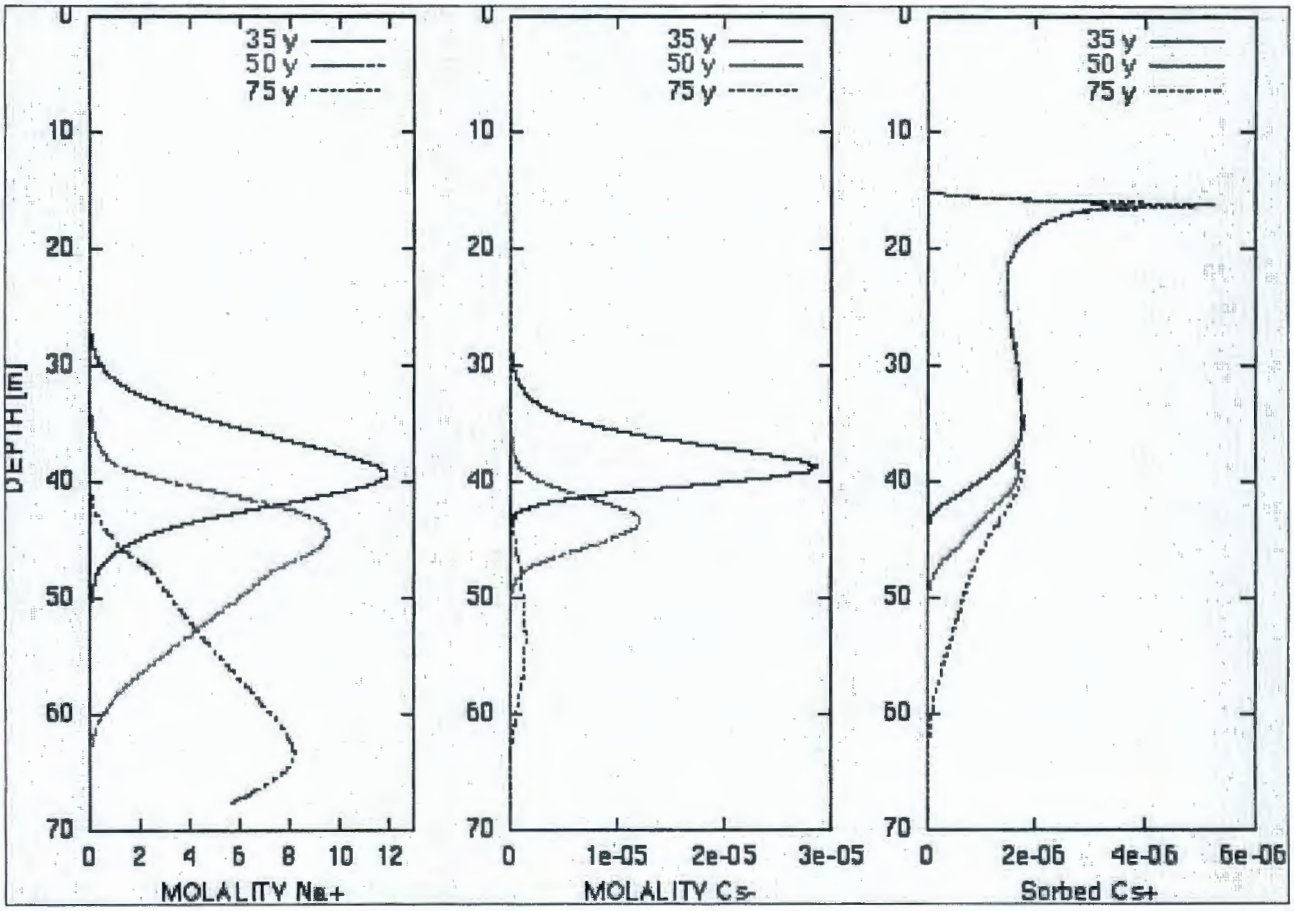

The relation between the aqueous and sorbed Cs^+ concentration profiles is noteworthy. As the Na^+ source concentration increases, the sorbed Cs^+ concentration penetrates more deeply into the vadose zone. Near the base of the tank close to the source of the leak, Cs^+ becomes highly retarded once the Na^+ pulse has advanced beyond the injection point. For this reason, Cs^+ is not completely displaced from its point of release. The aqueous Cs^+ concentration rapidly becomes attenuated with depth as more cesium becomes sorbed on the sediments after the Na^+ plume has passed. The sorbed Cs^+ profile formed a quasi-stationary state as time increased and remained in the vadose zone in the presence of dilute ambient groundwater.

Breakthrough curves for 20 M and 25 M sodium nitrate source concentrations are shown in Figure D.3.7.9. A pulse concentration of Cs^+ is released at the water table for these high Na^+ concentrated solutions, which rapidly becomes attenuated with decreasing Na^+ concentration. It should be noted that these results are qualitatively different than would be obtained with a constant K_d description of ion exchange. It was found that Cs^+ mobility is nearly independent of the leak duration over a two week to one year period, provided the source injection rate is scaled so that the same total mass of fluid is injected.

Figure D.3.7.9. Cs Breakthrough Curves at the Water Table Corresponding to a Depth of 62.5 m for 20 Molal and 25 Molal Sodium Nitrate Source Concentrations.

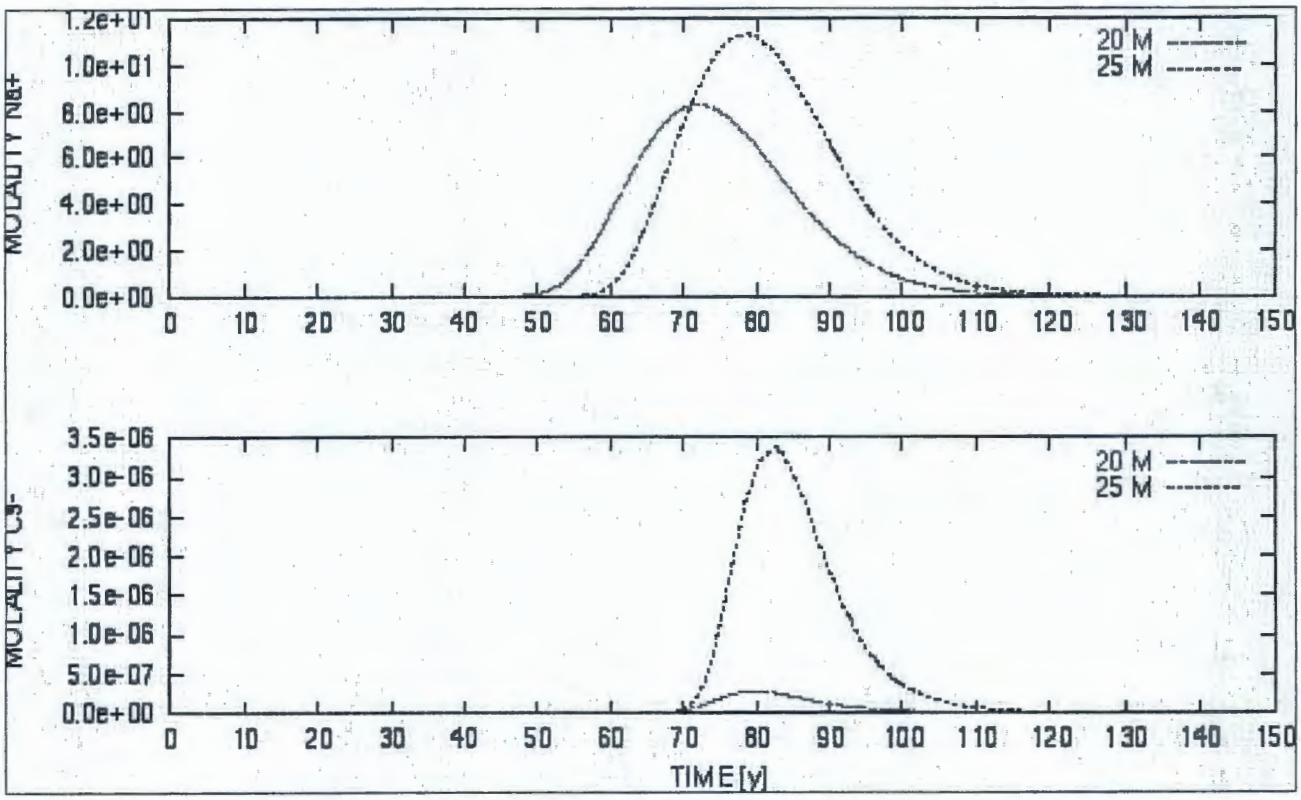

D.3.7.6 Colloid-Facilitated Transport of Cesium

Another mechanism that could possibly explain the migration of cesium in the vicinity of the tank SX-108 is colloid-facilitated transport. For the case when exchange reactions are fast described by local equilibrium, the effective retardation factor taking into account exchange on colloid and mineral surfaces is given by

$$R_i^{eff} = 1 + \frac{K_i^{min}}{1 + K_i^{coll}} \qquad \text{(D.3.7.2)}$$

where K_i^{min} and K_i^{coll} refer to the distribution coefficients associated with minerals and colloids, respectively. To obtain this expression it is assumed that colloids and groundwater move at the same average Darcy velocity. From this expression it is apparent that for colloids to appreciably affect radionuclide mobility, the colloid distribution coefficient should be the same order of magnitude as the mineral distribution coefficient or greater. This observation enables an estimate of the colloid concentration necessary to affect cesium mobility.

The distribution coefficient for colloids has a similar form as the distribution coefficient for exchange on mineral surfaces except that in this case it is proportional to the colloid concentration. Thus

$$K_i^{coll} = W_{coll} C_{coll} \sum_{\alpha} \left[\frac{Q_{\alpha}^{coll} k_i^{\alpha}}{\sum_l k_l^{\alpha} c_l} \right] \qquad \text{(D.3.7.3)}$$

where the colloid concentration is denoted by C_{coll}, W_{coll} refers to the colloid formula weight, and Q_{α}^{coll} the colloid exchange capacity associated with site α. Assuming that exchange on colloids obeys a similar sorption isotherm as on minerals, equating colloid and mineral distribution coefficients yields the following expression for the colloid concentration where a single exchange site is assumed

$$C_{coll} = \frac{\rho_r (1-\phi) Q_{min}}{W_{coll} Q_{coll}} \qquad \text{(D.3.7.4)}$$

The magnitude of colloid concentration necessary for equal mineral and colloid distribution coefficients, may be obtained by calculating the fraction of the pore volume occupied by colloids. It follows that

$$\phi_{coll} = \frac{W_{coll} C_{coll}}{\rho_{coll}} = \frac{(1-\phi)}{\phi} \frac{\rho_r Q_{min}}{\rho_{coll} Q_{coll}} \cong \frac{1-\phi}{\phi} \qquad \text{(D.3.7.5)}$$

where ρ_{coll} is the intrinsic colloid density. The latter result is obtained by assuming that the exchange capacities and intrinsic densities for colloids and sediment are similar: $Q_{coll} \approx Q_{min}$, and $\rho_{coll} \approx \rho_{min}$.

According to this result, the entire pore space would be filled with colloids for a porosity of 50% (ρ_{coll}). At lower porosities the condition of equal distribution coefficients is impossible to achieve. This result indicates that a rather large colloid concentration is required if colloids are to compete with minerals for sorption, and thus to affect in a significant way the mobility of cesium. Thus it would appear that a significant influence of colloids on the mobility of cesium can be ruled out, unless cesium is much more strongly sorbed to colloids compared to mineral surfaces in the sediment. It should also be noted, however, that this analysis assumes sorption is reversible. Should sorption on colloids be irreversible, then smaller colloid concentrations could have a significant influence since colloids would not have to compete with minerals in this case.

D.3.7.7 Conclusion and Implications

By utilizing field data from the 299-W23-19 well in the neighborhood of tank SX-115, it was possible to calibrate flow parameters and source term to a 1D reactive flow and transport model. The model was then used to analyze the mobility of Cs^+ with varying salinity of the background electrolyte solution used in the source term. It was found that only for very high Na^+ concentration was it possible for Cs^+ to advance to the water table. However, the aqueous Cs^+ concentration rapidly became attenuated with depth, as more Cs^+ exchanged with the sediments following passage of the Na^+ plume. The sorbed Cs^+ profile formed a quasi-stationary state, remaining in the vadose zone in the presence of dilute ambient groundwater. Finally, it was concluded that colloids under conditions of reversible exchange reactions, are not likely to

provide a feasible mechanism to enhance Cs^+ migration because of the extremely large colloid concentrations that would be required. This conclusion, however, was predicated on the assumption of reversible sorption.

It should be emphasized that the results of numerical simulations presented in this contribution are preliminary in nature. Several possibly important aspects were not included in the simulations reported here. The most obvious is the 1D simplification used in the simulations. This was partly corrected for by calibrating the model against field data. However, dilution effects caused by lateral spreading cannot be accounted for in these simulations. In addition, calculations were based on isothermal conditions and did not take into account heat released from the tanks. This could be important in accounting for moisture redistribution and effects on chemical interaction. Finally, alteration of surfaces of sorbing minerals by the caustic fluid leaked from the tank was not included in the model.

D.3.7.8 References

Lichtner, P. C., 2001, *FLOTRAN User Manual*, LA-UR-01-2349, Los Alamos National Laboratory, Los Alamos, New Mexico.

Serne, R. J., 2001, *S-SX Sediment Characterization Results and Issues*, Pacific Northwest National Laboratory, Richland, Washington.

Zachara, J. M., S. C. Smith, J. P. McKinley, R. J. Serne, and P. L. Gassman, 2001, "Sorption of Cs^+ to Micaceous Subsurface Sediments from the Hanford Site," *Geochimica et Cosmochimica Acta*, (Accepted).

D.3.8 CONCLUSIONS OF S&T INVESTIGATIONS OF CS ADSORPTION AND TRANSPORT IN S-SX SEDIMENTS

$^{137}Cs^{+}$ is the radioactive contaminant that has been released to the vadose zone in the highest concentrations in the S and SX tank farms. In-ground inventory estimates developed in other sections of this FIR suggest that 89 kCi or more of $^{137}Cs^{+}$ may be sorbed to sediments beneath the S and SX tank farms. Because of its' hard gamma emission and large in-ground concentration, considerable concern exists regarding the future migration of ^{137}Cs. $^{137}Cs^{+}$ is also a reference contaminant in the tank farms because it is one of the few radionuclides whose depth distribution can be monitored in-situ by spectral gamma analyses. Often, estimates of the concentration, inventory, and depth penetration of other "gamma invisible" radionuclides (e.g., ^{99}Tc) are derived from the $^{137}Cs^{+}$ concentration profile. For these reasons it is important to understand the geochemistry of $^{137}Cs^{+}$, and to develop models that describe its i.) distribution between soil and water that determines retardation and transport and ii.) desorption rates from sediment and potential for future migration.

Through study of uncontaminated sediment from the S and SX tank farms ("Above B" composite), we have learned that $^{137}Cs^{+}$ adsorbs to Hanford sediment by a highly selective ion exchange process to micas and smectites. The concentration of the adsorption sites is small (10^{-5} mol/g). The highest affinity sites reside on the micas and these are present at 10^{-9} mol/g. While small in concentration, these sites provide a high sorption potential for $^{137}Cs^{+}$. The overall extent of adsorption is strongly controlled by Na^{+} and Cs^{+} concentration as these participate in mass action reactions on the same set of adsorption sites. Na^{+} exhibits a strong competitive effect on $^{137}Cs^{+}$ adsorption; Na^{+} concentrations in excess of 10 mol/L virtually eliminate adsorptive retardation by Hanford sediments. These effects can be described by multi-site, multi-component ion exchange theory and a Cs^{+} adsorption model of this type was developed for Hanford sediments that well describes Cs^{+} adsorption over the range of Cs^{+} and electrolyte concentration found in tank waste. This equilibrium model well described $^{137}Cs^{+}$ transport through columns of Hanford sediment at 100% and 64% water saturation under various ionic regimes. In contrast, $^{137}Cs^{+}$ transport at 24% water saturation was more rapid then expected (model predicted), because immobile water prevented access of $^{137}Cs^{+}$ to high affinity sorption sites. High base interaction with the sediments designed to simulate REDOX waste reactions had minimal effects on $^{137}Cs^{+}$ ion exchange adsorption.

Contaminated sediments were studied from boreholes 41-09-39 and SX-108 slant ranging in $^{137}Cs^{+}$ content from 10^{5} to 10^{8} pCi/g. The isotopic composition of exchangeable Cs^{+} (^{137}Cs, ^{135}Cs, ^{133}Cs) was measured in these sediments, and ^{137}Cs represented 20.8 % of the total Cs pool. ^{137}Cs-containing mineral phases were isolated and identified from a number of core sections with varying distances from the leaked tanks. The ^{137}Cs-containing phases were invariably micas of various types with biotite and weathered biotite giving the highest counts. The high Na^{+} in the REDOX wastes had suppressed all ^{137}Cs adsorption except that to the highest affinity sites in the sediment. Desorption studies were performed with four contaminated sediments with different degrees of apparent mineral transformation by waste reaction. The degree of mineral transformation had little discernable impact on the extent or rate of ^{137}Cs desorption. Approximately 30-50 % of the adsorbed ^{137}Cs was immediately desorbable (electrolyte dependent) and conformed to predictions from the multi-site Cs^{+} exchange model. The remaining sorbed ^{137}Cs pool (50-70%) was not irreversibly sorbed, but was slowly exchangeable

and exhibited a kinetic half-life of 500-1674 days. Electron and X-ray microprobe analyses of Cs^+- contaminated sediments, and chemical extraction of the same suggested that the poorly exchangeable fraction resided in intra-particle channels (micas) and on sorbent regions coated with secondary mineral precipitates resulting from waste sediment reaction. The desorption behavior was described with a first-order kinetic model that was linked to the equilibrium, multi-site Cs^+ adsorption model.

The multi-site Cs^+ adsorption model was used to predict in-situ ^{137}Cs K_d values for the SX-108 core samples that compared favorably with those measured by water and acid extraction by Serne et al. (2001d). The model was also used in 1D transport simulations to describe ^{137}Cs migration beneath a leaked SX tank where the Na^+ concentration in the REDOX waste was varied as a sensitivity exercise (the Na^+ concentrations of leaked tanks SX-108, SX-109, and SX-115 are not well known). The simulations resulting from a REDOX waste Na^+ concentration of 15-20 mol/L best approximated the in-ground ^{137}Cs distribution. This latter modeling exercise did not include multi-dimensional hydrologic phenomena resulting from fine- and coarse-scale sediment layering that may have influenced or controlled waste migration patterns.

Research in this section has shown that expedited $^{137}Cs^+$ migration has occurred beneath the S and SX tank farms for at least three chemical reasons: (1) ^{137}Cs migration is very sensitive to Na^+ concentration and the impact of high Na^+ was not taken into account in previous modeling exercises; (2) Na^+ concentrations in leaked REDOX wastes were underestimated in the past; new estimates based on mass balance calculations (D.7.3) and characterization measurements (Serne et al. 2001d) suggest that Na^+ concentrations in SX-108 supernatant may have approached 20 mol/L; and (3) the total concentration of Cs in the supernatant was underestimated because the mass contributions of ^{133}Cs and ^{135}Cs were not accounted for. Physical explanations, such as adsorption site bypass under low water content, and preferential flow paths may also have been at play.

In terms of future behavior, desorption measurements indicate that almost all of the adsorbed ^{137}Cs is exchangeable with the aqueous phase over long contact times, (e.g., > 500 days). Thus, it is available for mobilization and transport if sufficient ionic conditions develop. However, high levels (>5-10 mol/L) of soluble Na^+ would be required to mobilize the adsorbed ^{137}Cs. Because the existing Na^+ plume from REDOX waste lies deeper than ^{137}Cs because of chromatographic separation (Serne et al. 2001d; see also Figures D.3.7.7 and D.3.7.8), conditions are unlikely to develop that will mobilize adsorbed ^{137}Cs unless high salt solutions are released to the vadose zone during tank sluicing. The volume of, and Na^+ concentrations in, sluicing losses should be minimized. The equilibrium multi-site Cs^+ adsorption model and the kinetic desorption model may be used in sensitivity calculations to explore the potential mobilizing effect of sluicing losses of different volumes and compositions.

D.4.0 GEOCHEMISTRY AND REACTIVE TRANSPORT BEHAVIOR OF CHROMIUM

Hexavalent Cr [Cr(VI)] in the form of potassium dichromate was used as an oxidant in the REDOX process to manipulate the valence states of Pu and U. Approximately 50% of the Cr(VI) was reduced in processing; the residual Cr(VI) was discharged to the S and SX tank farms in tank waste. Cr(VI) was soluble in the tank waste and remained in the supernate. The estimated Cr concentration at the time of the leak(s) range from 5.09×10^{-2} mol/L to 4.13×10^{-1} mol/L. While estimates of leak volume (and hence, the mass of Cr) varies depending on the assumptions and inventory estimates, the estimated total mass of Cr lost to the vadose zone from tanks S-104, SX-107, SX-108, SX-109, SX-113, and SX-115 is 2,685 kg (Jones et al. 2000).

Chromate is, under normal Hanford soil and soil pore water conditions, a mobile anion. For this reason, five or more distinct Cr(VI) plumes exist in the 100 areas that discharge to the Columbia River. This Cr(VI) resulted from the disposal of CrO_4^{2-}, used as a corrosion inhibitor, to the soil surface. Given the high estimated electrolyte concentration and pH of the tank fluids (Section D.7.3), chromate could be even more mobile in the WMA S-SX vadose zone than observed in the 100 Areas. There is only a limited understanding of the behavior of $Cr(VI)O_4^{2-}$ in sediments under conditions as harsh as those imposed by leaking tank fluids. The in-ground inventory of Cr(VI) in the WMA S-SX vadose zone is of concern because of its high mobility and known toxicity. Issues regarding $Cr(VI)O_4^{2-}$ mobility and possible geochemical reactions occurring at the time of the leaks are being investigated under several U.S. DOE EMSP projects. Current concerns, however, center on the potential for in-ground inventories to be remobilized by infiltrating meteoric water or possible spills because of tank waste sluicing.

A series of research activities directed at developing a more complete understanding of Cr geochemistry and reactive transport in sediments influenced by the hyperalkaline, hypersaline tank fluids has been performed and is reported here. Current information on Cr behavior under the extreme conditions suspected during SX tank leaks is inadequate to determine: (1) the rates and extent of Cr reactions at the time of the leaks, (2) the current geochemical status of leaked Cr in the vadose zone, and (3) the susceptibility of WMA S-SX vadose zone Cr to future migration. This new research is ongoing and has involved Hanford S&T Program and EMSP investigators and the use of uncontaminated (B8812) and contaminated (SX-108 slant, 41-09-39) vadose zone sediments. The results and implications of this research are described in the following sections: speciation of chromium in Hanford tank farm SX-108 slant and 41-09-39 core samples determined by X-ray absorption spectroscopy; desorption and leaching of Cr from WMA S-SX sediments; fate and transport of C(VI) in Hanford sediments treated with Al-rich, alkaline and saline solutions; and Cr(VI) reduction in homogenous and heterogeneous Fe(II) systems under alkaline conditions at 50 °C.

D.4.1 SPECIATION OF CHROMIUM IN HANFORD TANK FARM SX-108 SLANT AND 41-09-39 CORE SAMPLES DETERMINED BY X-RAY ABSORPTION SPECTROSCOPY

Jeffrey G. Catalano[1], Jeffrey A. Warner[1], Chia-chen Chen[2], Isao Yamakawa[2], Matthew Newville[3], Steven R. Sutton[3], Calvin C. Ainsworth[4], John M. Zachara[4], Samuel J. Traina[2], and Gordon E. Brown, Jr.[1,5]

[1]Department of Geological & Environmental Sciences, Stanford University, Stanford, California 94305-2115

[2]The Ohio State University, Columbus, Ohio 43210-1085

[3]Advanced Photon Source, Argonne National Laboratory, Argonne, Illinois 60439

[4]Pacific Northwest National Laboratory, Richland, Washington 99352

[5] Stanford Synchrotron Radiation Laboratory, Stanford, California 94309-0210

D.4.1.1 Introduction

Chromium was present in relatively high concentrations in the REDOX tank wastes at WMA S-SX and has been found at concentrations as high as 37,000 ppm in contaminated sediments in the vadose zone beneath SX-108 and SX-109 (Serne et al. 2001a, b). At the high pH values of the tank supernate, aqueous chromium is expected to be dominantly in the chromate (CrO_4^{2-}) form (Baes and Mesmer 1986). This form of chromium is highly mobile in aquatic systems (Richard and Bourg 1991) and acutely toxic (Paschin et al. 1983), teratogenic (Abbasi and Soni 1984), and carcinogenic (Ono 1988). In order to assess the environmental impact of chromium in tank leachates that have been released to the vadose zone, a quantitative knowledge of chromium speciation is essential. More specifically, it must be determined to what extent Cr(VI) species have been reduced, via electron transfer reactions, to Cr(III) species in the sediments in the vadose zone. In contrast to Cr(VI), Cr(III) species should be relatively immobile in Hanford subsurface sediments and of low toxicity to biological organisms.

Although the reduction of Cr(VI) to Cr(III) can occur via both abiotic and biotic pathways (Fendorf et al. 2000), it is likely that abiotic pathways are dominant in the Hanford vadose zone due to the low levels of microorganisms and electron donors present (see Section D.5.1). A possible abiotic pathway is the reaction of Cr(VI) species with the surfaces of Fe(II)-bearing minerals such as magnetite (Fe_3O_4) (Peterson et al. 1996; 1997a) and phyllosilicates such as chlorite and montmorillonite (Brigatti et al. 2000a, b), and biotite and phlogopite (Ilton and Veblen 1994; Ilton et al. 1997). This reaction involves the transfer of an electron from three Fe(II) to one Cr(VI), resulting in Cr(III). Another potential abiotic pathway involves the reaction of aqueous Cr(VI) species with aqueous Fe(II) ions released by the dissolution of Fe(II)-containing minerals (Eary and Rai 1989; Fendorf and Li 1996). Ferrous iron-bearing minerals such as magnetite, ilmenite, biotite, and chlorite are known to occur in WMA S-SX sediments (Section D.1.1), but the extent of Cr(VI) reduction in contaminated areas of the vadose zone is not known. It is possible that such reduction is hindered by the presence of carbonate surface coatings on these Fe(II)-bearing minerals (Doyle et al. 2000) or that the surfaces of

Fe(II)-bearing minerals become quickly passivated early in the Cr(VI) reduction process by the formation of a thin layer of amorphous Cr(III)-oxyhydroxide (Peterson et al. 1997b; Kendelewicz et al. 2000; Brown et al. 2000). The presence of significant percentages of Cr(VI) relative to total Cr in the vadose zone sediments, as discussed below, suggests that the inorganic and organic reductants present are not capable of reducing the quantities of Cr(VI) that have been introduced or that the reduction process is in some way inhibited.

In order to determine the relative concentration of Cr(VI) vs. Cr(III) in representative samples from contaminated zones beneath the Hanford tank farm, we carried out a detailed synchrotron-based X-ray absorption fine structure (XAFS) spectroscopy study of eight subsurface samples from the Hanford SX tank farm – six from the SX-108 slant borehole (samples SX-108-6A, -7A, -8A, -9A, -13A, and -14A) and two from borehole 41-09-39 (samples 41-09-39-6AB and 41-09-39-7ABC). The concentrations of chromium in these samples (in mg Cr/g sediment), as determined by x-ray fluorescence analysis are 1186 (41-09-39-6AB, 2090 (41-09-39-7ABC), 955 (SX-108-6A), 1297 (SX-108-7A), 2098 (SX-108-8A), 1394 (SX-108-9A), 931 (SX-108-13A), and 565 (SX-108-14A).

At these concentration levels, the technique of choice for determining the relative proportions of Cr(VI) vs. Cr(III) in mineralogically complex samples of this type is XAFS spectroscopy, which is element-selective, nondestructive, requires no significant sample preparation, and can be measured under ambient conditions (Brown et al. 1988). The basic XAFS experiment involves exposure of a powdered sample or thin section to a very intense monochromatic beam of x-rays from a synchrotron source. The energy of the x-ray beam is varied in steps using a crystal monochromator over a selected energy range that typically begins 20 to 30 eV below the absorption edge of the element of interest and increases to several hundred eV above the absorption edge. The energy steps used vary from several tenths of an eV to several eV. When the energy of the incident x-ray beam matches the energy with which core-level electrons (e.g., 1s) are held, core electrons are excited to valence or continuum levels, in which case they are scattered by atoms surrounding the excited atom. This excitation process results in the absorption of x-rays, and there is a corresponding steep rise in x-ray absorbance at this energy in the absorbance vs. incident x-ray energy spectrum. The fine structure in the spectrum above the absorption edge is due to the constructive and destructive interference of photoelectron waves as photoelectrons are scattered among the neighboring atoms around the absorbing atom. When the neighboring atoms around an absorbing atom such as Cr differ in number or in distances from the central absorber in two different samples, the resulting x-ray absorption fine structure spectra will exhibit significant differences that can be analyzed to quantify these structural differences.

The absorption edge position shifts to higher energy with increasing oxidation state of an element. In the case of chromium, for example, the inflection point of the absorption edge of Cr(III) occurs at ≈ 5998 eV and that of Cr(VI) occurs at ≈ 6005 eV. However, a more sensitive indicator of Cr(VI) vs. Cr(III) is a "pre-edge" feature that occurs at ≈ 5993 eV and varies in intensity depending on the Cr(VI):Cr(III) ratio. The dipole matrix elements that govern the probability of the 1s → 3d electronic transitions responsible for the pre-edge feature indicate that the probability of this transition should be greatest when Cr(VI) is coordinated by four oxygens in approximate T_d point symmetry, resulting in the highest integrated intensity and height of the pre-edge feature. In contrast, Cr(III) is coordinated by six oxygens in approximate O_h point symmetry, and the probability of 1s → 3d electronic transitions is low for this coordination

geometry, resulting in a much smaller integrated intensity and height of the pre-edge feature. One can calibrate the variation in pre-edge intensity or height as a function of the Cr(VI):Cr(III) ratio in a series of samples prepared by mechanically mixing known proportions of Cr(VI)-containing and Cr(III)-containing minerals. Such a calibration is shown in Figure D.4.1.1.

Figure D.4.1.1. Cr Pre-edge Height Calibration for Beamline 11-2 at the Stanford Synchrotron Radiation Laboratory: (left) Variation of Pre-Edge Peak Height of Cr K-Edge XANES Spectra as a Function of Cr(VI)/Total Cr. (right) Plot of Cr(VI)/Total Cr versus Cr Pre-Edge Peak Height (from Peterson 1996).

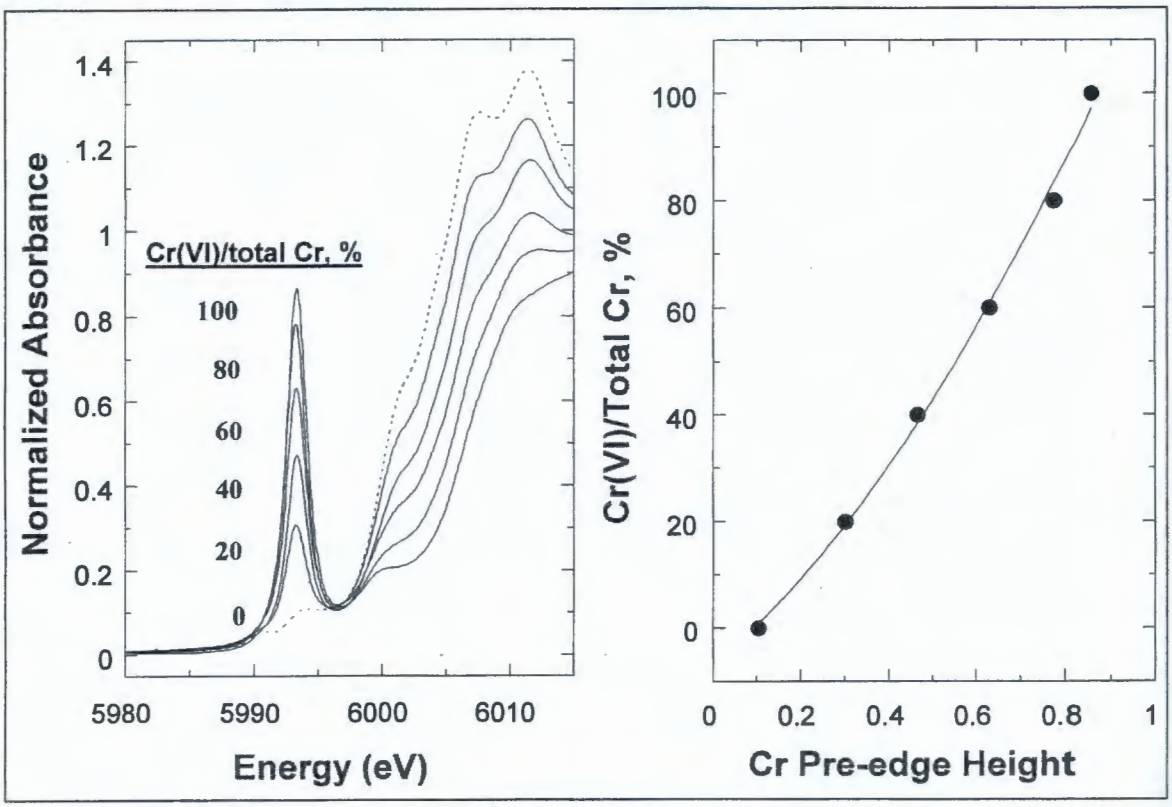

By measuring the XANES (x-ray absorption near-edge structure) spectra of the four Hanford S and SX tank farms borehole samples on the new Molecular Environmental Science beam line (11-2) at the Stanford Synchrotron Radiation Laboratory (Bargar et al. 2001), or on the general XAFS beamline (4-3), and using a calibration curve of the type described above, we determined quantitatively the Cr(VI):Cr(III) ratios of these samples. The results of this study are reported below.

In a separate series of experiments, we examined the spatial distribution of Cr(VI) and Cr(III) species in thin sections of four of the Hanford tank farm borehole samples prepared at PNNL using a highly focused beam of x-rays. This method is known as x-ray micro-fluorescence elemental mapping and was accomplished on the undulator beam line at GSECARS Sector 13 (Advanced Photon Source, Argonne National Laboratory, Argonne, Illinois). Using a 10 μm × 10 μm x-ray beam tuned to an energy just above the Fe K-absorption edge (7,112 eV), we mapped K, Ca, Ti, Cr, Fe, and Mn in 300 μm × 300 μm areas on the four thin sections. In separate experiments, we also measured Cr K-edge micro-XANES spectra of a number of points on these thin sections to determine Cr speciation. Bulk Cr K-edge XANES spectra of the thin sections were collected at the Stanford Synchrotron Radiation Laboratory to evaluate the effects of sample preparation on the Cr speciation in the thin sections. The results of these experiments are reported below.

D.4.1.2 Chromium XANES Spectroscopic Analyses of Untreated Samples

D.4.1.2.1 Experimental Procedure. Contaminated sediment samples from the Hanford S and SX tank farms boreholes described above were packed in doubly contained sample holders and shipped from PNNL to the Stanford Linear Accelerator Center for XAFS analysis. The radiation levels of 0.25 g portions of the four powdered samples were as follows: 41-09-39-7ABC (1.7×10^7 pCi/g ^{137}Cs + 1160 pCi/g ^{99}Tc); 41-09-39-6AB (1.1×10^4 pCi/g ^{137}Cs + 3586 pCi/g ^{99}Tc); SX-108-6A (5.3×10^7 pCi/g ^{137}Cs + 77.8 pCi/g ^{99}Tc); SX-108-7A (2.1×10^7 pCi/g ^{137}Cs + 1160 pCi ^{99}Tc); SX-108-08A (5.5×10^5 pCi/g ^{137}Cs + 2116 pCi ^{99}Tc); SX-108-9A (171 pCi/g ^{137}Cs + 4240 pCi/g ^{99}Tc); SX-108-13A (440 pCi/g ^{137}Cs + 7500 pCi/g ^{99}Tc); SX-108-14A (837 pCi/g ^{137}Cs + 7510 pCi/g ^{99}Tc). The volume of each sample examined was approximately 15 mm × 2 mm × 1 mm (the volume illuminated by the x-ray beam at SSRL) and the bulk density of each sample was approximately 1.6 g/cm^3. These samples were held in Teflon sample holders with 10 mil Mylar windows and were sequentially placed in a sample positioner for XAFS experiments. An Ar-filled Stern-Heald-type x-ray fluorescence detector (Lytle et al. 1984) or a 13-element Ge detector was used to monitor Cr Kα fluorescence as a function of incident x-ray energy. A 3 μx-thickness V filter was placed between the sample and the detector to minimize scattering and thus reduce background radiation. The sample container was purged with He prior to data collection, and He was flowed through the sample container during data collection to minimize air scatter.

Cr K-XANES spectra were measured on the Molecular Environmental Science Beam Line (BL 11-2) (Bargar et al. 2001) or a general XAFS beamline (BL 4-3) over the energy range 5900 eV to 6350 eV using a Si (220) double-crystal monochromator (cryogenically cooled on BL 11-2), with the SPEAR ring operating at 80 to 100 mA electron current and 3 GeV energy. The vertical slit before the monochromator was adjusted to 1 mm height to maximize energy

resolution. A step size of 0.15 eV was used in the energy region 5980 to 6010 eV, and a step size of 1 eV was used over the energy region 6010 to 6350 eV. An integration time of 4 seconds was used at each step. Because the samples were too thick (2 mm), it was not possible to simultaneously collect x-ray fluorescence data from the sample and transmission data from a Cr metal foil used for energy calibration. However, foil edges were collected within 40 minutes of XANES measurements for each sample, and the drift of the monochromator was found to be negligible during this time frame. The first inflection point of the Cr metal foil edge was set to 5989 eV. The deviation from this value was recorded (it was typically around 0.3 to 0.5 eV too small), and the sample spectra were calibrated in energy using this inflection point energy value. Two scans of each sample were recorded and averaged as described below. Reduction of REDOX-sensitive elements like Cr can occur in the intense x-ray beam of a synchrotron and must be monitored in these types of experiments. No evidence of beam-induced Cr(VI) to Cr(III) reduction was observed over the relatively short time exposures (15 to 20 minutes) necessary to collect the Cr K-XANES spectra on the eight Hanford S and SX tank farms borehole samples.

D.4.1.2.2 Data Analysis and Results. The methods of Peterson et al. (1997a) were used to analyze the Cr(VI) content of the Hanford borehole samples. The sample data (typically two scans) were averaged using the computer code MAVE, which is a subroutine in the XAFS data analysis package EXAFSPAK (George and Pickering 1993). No dead time corrections were made. The peak of the pre-edge feature was selected as the calibration point in the EXAFSPAK subroutine MCALIB, as this feature's position should not have changed during the experiment. The position observed was then shifted by the amount of offset measured in the Cr foil (for example, if the feature occurred at 5992.86 eV, and the Cr foil edge was 0.38 eV too low, the data were shifted by + 0.38 eV, resulting in a pre-edge position of 5993.24 eV). The average pre-edge peak position for all eight samples was found to be 5993.3 ± 0.1 eV (see Table D.4.1.1).

Table D.4.1.1. Results of Cr(VI) Determination From XAFS "Pre-Edge" Heights.

Sample	SSRL Beamline	Pre-edge Position (eV)	Normalized Pre-edge Height	% Cr(VI)
41-09-39-6AB	11-2	5993.2 ± 0.1	0.624	51
41-09-39-7ABC	11-2	5993.2 ± 0.1	0.684	58
SX-108-6A	4-3	5993.3 ± 0.1	0.520	54
SX-108-7A	11-2	5993.2 ± 0.1	0.367	25
SX-108-8A	11-2	5993.3 ± 0.1	0.639	53
SX-108-9A	4-3	5993.3 ± 0.1	0.653	71
SX-108-13A	4-3	5993.3 ± 0.1	0.635	69
SX-108-14A	4-3	5993.3 ± 0.1	0.583	62

The averaged data were then analyzed using the EXAFSPAK subroutine PROCESS by background subtraction using a polynomial pre-edge fit of the data up to 5960 eV. A spline was